

MODERN ACOUSTICAL
TECHNIQUES FOR THE
MEASUREMENT OF
MECHANICAL PROPERTIES

Edited by
MOISES LEVY
HENRY E. BASS
RICHARD STERN

VOLUME 39
EXPERIMENTAL METHODS IN THE PHYSICAL SCIENCES

Treatise Editors
ROBERT CELOTTA
THOMAS LUCATORTO



ACADEMIC PRESS

Experimental Methods in the Physical Sciences

VOLUME 39

MODERN ACOUSTICAL TECHNIQUES FOR THE
MEASUREMENT OF MECHANICAL PROPERTIES

EXPERIMENTAL METHODS IN THE PHYSICAL SCIENCES

Robert Celotta and Thomas Lucatorto, *Editors in Chief*

Founding Editors

L. MARTON

C. MARTON

Volume 39

Modern Acoustical Techniques for the Measurement of Mechanical Properties

Edited by

Moises Levy

University of Wisconsin-Milwaukee

Henry E. Bass

University of Mississippi

Richard Stern

Pennsylvania State University



ACADEMIC PRESS

A Harcourt Science and Technology Company

San Diego San Francisco New York Boston London Sydney Tokyo

This book is printed on acid-free paper. ☺

Compilation copyright © 2001 by ACADEMIC PRESS

All rights reserved.

No part of this publication may be reproduced or transmitted in any form or by any means, electronic or mechanical, including photocopy, recording, or any information storage and retrieval system, without permission in writing from the publisher.

The appearance of the code at the bottom of the first page of a chapter in this book indicates the Publisher's consent that copies of the chapter may be made for personal or internal use of specific clients. This consent is given on the condition, however, that the copier pay the stated per copy fee through the Copyright Clearance Center, Inc. (222 Rosewood Drive, Danvers, Massachusetts 01923), for copying beyond that permitted by Sections 107 or 108 of the U.S. Copyright Law. This consent does not extend to other kinds of copying, such as copying for general distribution, for advertising or promotional purposes, for creating new collective works, or for resale. Copy fees for pre-2001 chapters are as shown on the title pages. If no fee code appears on the title page, the copy fee is the same as for current chapters. 1079-4042/01 \$35.00.

Explicit permission from Academic Press is not required to reproduce a maximum of two figures or tables from an Academic Press chapter in another scientific or research publication provided that the material has not been credited to another source and that full credit to the Academic Press chapter is given.

The articles in this book are selected from the Academic Press multi-volume work titled *Handbook of Elastic Properties of Solids, Liquids, and Gases*, edited by M. Levy, H. Bass, and R. Stern and are uniquely arranged to focus on modern acoustical techniques for the measurement of mechanical properties.

Academic Press

A division of Harcourt, Inc.

525 B Street, Suite 1900, San Diego, California 92101-4495, USA

<http://www.academicpress.com>

Academic Press

Harcourt Place, 32 Jamestown Road, London NW1 7BY, UK

<http://www.academicpress.com>

International Standard Book Number: 0-12-475986-6

International Standard Serial Number: 1079-4042/01

PRINTED IN THE UNITED STATES OF AMERICA

01 02 03 04 05 EB 9 8 7 6 5 4 3 2 1

CONTENTS

CONTRIBUTORS	xi
VOLUMES IN SERIES	xiii
PREFACE	xvii
CONVERSION FACTORS	xxi
1. Introduction to Fundamentals of Elastic Constants	
by MOISES LEVY	
1.1 Introduction	1
1.2 Generalized Hooke's Law	2
1.3 Crystal Structures	6
1.4 Reduced Elastic Constant Matrices	10
1.5 Equations of Motion and Plane Waves in an Infinite Solid	14
1.6 Absorption	27
1.7 Group Velocity	31
1.8 Phenomenological Relations between Phase Velocity and Attenuation	33
1.9 Units	35
References	35
2. Point-Source/Point-Receiver Methods	
by A. G. EVERY, K. Y. KIM, and W. SACHSE	
2.1 Introduction	37
2.2 Dynamic Green's Functions: Formal Solutions	38
2.3 Response to a Periodic Force: Numerical Implementation and Comparison with Experiment	41

2.4	Time Domain Response: Numerical Implementation and Comparison with Experiment	47
2.5	Surface Response	58
2.6	Plate Modes	60
2.7	Conclusions	61
	References	62
3.	Laser-Based Surface Acoustic Waves in Materials Science by ALEXEY LOMONOSOV, ANDREAS P. MAYER, and PETER HESS	
3.1	Introduction	65
3.2	Experimental	71
3.3	SAWs in Anisotropic Solids	90
3.4	SAWs in Dispersive Media	100
3.5	Nonlinear SAWs	119
	References	130
4.	Quantitative Acoustic Microscopy by PAVEL V. ZININ	
4.1	Introduction	136
4.2	Basic Principles of Quantitative Acoustic Microscopy . .	137
4.3	Elastic Properties of Anisotropic Layered Media by Acoustic Microscopy	155
4.4	Acoustic Microscopy of Isotropic Layered Media	160
4.5	Acoustic Microscopy of Anisotropic Solids	168
4.6	Nonplanar Surfaces	176
4.7	Comparison with Other Techniques	179
	References	180
5.	Resonant Ultrasound Spectroscopy (RUS) by A. MIGLIORI, T. W. DARLING, J. P. BAIARDO, and F. FREIBERT	
5.1	Introduction	189

5.2	Motivation for the Use of Resonances to Study Elastic Moduli	189
5.3	Measurements	193
5.4	Computation of Resonances and Data Analysis	204
5.5	Examples of Applications of RUS	212
	References	219
6.	Elastic Properties and Thermodynamics by VEERLE KEPPENS and A. MIGLIORI	
6.1	Introduction	221
6.2	Vibrational Modes, Phonons, and Elastic Moduli	221
6.3	Phase Stability of Pu at Higher Temperatures	225
6.4	Elastic Moduli and Local Modes	228
6.5	Local Modes in Filled Skutterudites	230
6.6	Summary	234
	References	235
7.	Speed of Sound as a Thermodynamic Property of Fluids by DANIEL G. FRIEND	
7.1	Introduction	237
7.2	Wave Equation in a Fluid	238
7.3	Equations of State for Fluids	245
7.4	Speed of Sound in Fluids	254
7.5	Conclusions	264
7.6	Tables of the Speed of Sound in Important Fluids	266
	Additional Reading	305
	References	305
8.	Noninvasive Determination of Sound Speed in Liquids by DIPEN N. SINHA and GREGORY KADUCHAK	
8.1	Introduction	307
8.2	Theory	309

8.3	Experimental	320
8.4	Results and Discussion	323
8.5	Conclusions	325
	Appendix	328
	References	331
9.	Introduction to the Elastic Constants of Gases by HENRY E. BASS	
9.1	Introduction	335
9.2	Ideal Gas	336
9.3	Real Gas Corrections	338
9.4	Contribution of Transport Processes on Speed of Sound .	339
9.5	Changes in Elastic Properties Due to Relaxation Processes	342
9.6	Measurements at Moderate Pressures	348
9.7	Typical Results	351
9.8	Diffusion	363
9.9	Gases at Low Pressure	364
9.10	Systems Not in Equilibrium	372
9.11	Summary	373
	References	373
10.	Acoustic Measurements in Gases by M. R. MOLDOVER, K. A. GILLIS, J. J. HURLY, J. B. MEHL, and J. WILHELM	
10.1	Introduction and Scope	377
10.2	Acoustic Measurements and Thermodynamic Properties of Dilute Gases	379
10.3	Measuring the Speed of Sound	384
10.4	Resonance Measurements of Transport Properties	391
10.5	Acoustic Thermometry	399

10.6 Acoustic Determination of the Universal Gas Constant R	404
10.7 Concluding Remarks	406
10.8 Preface to Tables	407
References	426
INDEX	429

This Page Intentionally Left Blank

CONTRIBUTORS

Numbers in parentheses indicate the pages on which the authors' contributions begin.

- J. P. BAIARDO (189), *Los Alamos National Laboratory, Los Alamos, New Mexico*
HENRY E. BASS (335), *National Center for Physical Acoustics, The University of Mississippi, University, Mississippi*
T. W. DARLING (189), *Los Alamos National Laboratory, Los Alamos, New Mexico*
A. G. EVERY (37), *Department of Physics, University of the Witwatersrand, Johannesburg, South Africa*
F. FREIBERT (189), *Los Alamos National Laboratory, Los Alamos, New Mexico*
DANIEL G. FRIEND (237), *Physical and Chemical Properties Division, Chemical Science and Technology Laboratory, National Institute of Standards and Technology, Boulder, Colorado*
K. A. GILLIS (377), *Process Measurements Division, National Institute of Standards and Technology, Gaithersburg, Maryland*
PETER HESS (65), *Institute of Physical Chemistry, University of Heidelberg, Heidelberg, Germany*
J. J. HURLY (377), *Process Measurements Division, National Institute of Standards and Technology, Gaithersburg, Maryland*
GREGORY KADUCHAK (307), *Electronic Materials and Devices Group, Los Alamos National Laboratory, Los Alamos, New Mexico*
VEERLE KEPPENS (221), *University of Mississippi, NCPA, University, Mississippi*
K. Y. KIM (37), *Department of Theoretical and Applied Mechanics, Cornell University, Ithaca, New York*
MOISES LEVY (1), *Physics Department, University of Wisconsin-Milwaukee, Milwaukee, Wisconsin*
ALEXEY LOMONOSOV (65), *General Physics Institute, Moscow, Russia*
ANDREAS P. MAYER (65), *Institute of Theoretical Physics, University of Regensburg, Regensburg, Germany*
J. B. MEHL (377), *Process Measurements Division, National Institute of Standards and Technology, Gaithersburg, Maryland*
A. MIGLIORI (189, 221), *Los Alamos National Laboratory, Los Alamos, New Mexico*

- M. R. MOLDOVER (377), *Process Measurements Division, National Institute of Standards and Technology, Gaithersburg, Maryland*
- W. SACHSE (37), *Department of Theoretical and Applied Mechanics, Cornell University, Ithaca, New York*
- DIPEN N. SINHA (307), *Electronic Materials and Devices Group, Los Alamos National Laboratory, Los Alamos, New Mexico*
- J. WILHELM (377), *Process Measurements Division, National Institute of Standards and Technology, Gaithersburg, Maryland*
- PAVEL V. ZININ (135), *School of Ocean and Earth Science and Technology, University of Hawaii, Honolulu, Hawaii*

VOLUMES IN SERIES

EXPERIMENTAL METHODS IN THE PHYSICAL SCIENCES

(formerly Methods of Experimental Physics)

Editors-in-Chief

Robert Celotta and Thomas Lucatorto

Volume 1. Classical Methods

Edited by Immanuel Estermann

Volume 2. Electronic Methods, Second Edition (in two parts)

Edited by E. Bleuler and R.O. Haxby

Volume 3. Molecular Physics, Second Edition (in two parts)

Edited by Dudley Williams

Volume 4. Atomic and Electron Physics — Part A: Atomic Sources and
Detectors; Part B: Free Atoms

Edited by Vernon W. Hughes and Howard L. Schultz

Volume 5. Nuclear Physics (in two parts)

Edited by Luke C.L. Yuan and Chien-Shiung Wu

Volume 6. Solid State Physics — Part A: Preparation, Structure,
Mechanical and Thermal Properties; Part B: Electrical, Magnetic and
Optical Properties

Edited by K. Lark-Horovitz and Vivian A. Johnson

Volume 7. Atomic and Electron Physics — Atomic Interactions (in two
parts)

Edited by Benjamin Bederson and Wade L. Fite

Volume 8. Problems and Solutions for Students

Edited by L. Marton and W.F. Hornyak

Volume 9. Plasma Physics (in two parts)

Edited by Hans R. Griem and Ralph H. Lovberg

Volume 10. Physical Principles of Far-Infrared Radiation

Edited by L.C. Robinson

Volume 11. Solid State Physics

Edited by R.V. Coleman

Volume 12. Astrophysics — Part A: Optical and Infrared Astronomy

Edited by N. Carleton

Part B: Radio Telescopes; Part C: Radio Observations

Edited by M.L. Meeks

Volume 13. Spectroscopy (in two parts)

Edited by Dudley Williams

Volume 14. Vacuum Physics and Technology

Edited by G.L. Weissler and R.W. Carlson

Volume 15. Quantum Electronics (in two parts)

Edited by C.L. Tang

Volume 16. Polymers — Part A: Molecular Structure and Dynamics; Part

B: Crystal Structure and Morphology; Part C: Physical Properties

Edited by R.A. Fava

Volume 17. Accelerators in Atomic Physics

Edited by P. Richard

Volume 18. Fluid Dynamics (in two parts)

Edited by R.J. Emrich

Volume 19. Ultrasonics

Edited by Peter D. Edmonds

Volume 20. Biophysics

Edited by Gerald Ehrenstein and Harold Lecar

Volume 21. Solid State: Nuclear Methods

Edited by J.N. Mundy, S.J. Rothman, M.J. Fluss, and L.C. Smedskjaer

Volume 22. Solid State Physics: Surfaces

Edited by Robert L. Park and Max G. Lagally

Volume 23. Neutron Scattering (in three parts)

Edited by K. Skold and D.L. Price

Volume 24. Geophysics — Part A: Laboratory Measurements; Part B:
Field Measurements

Edited by C.G. Sammis and T.L. Henyey

Volume 25. Geometrical and Instrumental Optics

Edited by Daniel Malacara

Volume 26. Physical Optics and Light Measurements

Edited by Daniel Malacara

Volume 27. Scanning Tunneling Microscopy

Edited by Joseph Stroscio and William Kaiser

Volume 28. Statistical Methods for Physical Science

Edited by John L. Stanford and Stephen B. Vardaman

Volume 29. Atomic, Molecular, and Optical Physics — Part A: Charged
Particles; Part B: Atoms and Molecules; Part C: Electromagnetic
Radiation

Edited by F.B. Dunning and Randall G. Hulet

Volume 30. Laser Ablation and Desorption

Edited by John C. Miller and Richard F. Haglund, Jr.

Volume 31. Vacuum Ultraviolet Spectroscopy I

Edited by J.A.R. Samson and D.L. Ederer

Volume 32. Vacuum Ultraviolet Spectroscopy II

Edited by J.A.R. Samson and D.L. Ederer

Volume 33. Cumulative Author Index and Tables of Contents, Volumes
1–32

Volume 34. Cumulative Subject Index

Volume 35. Methods in the Physics of Porous Media

Edited by Po-zen Wong

Volume 36. Magnetic Imaging and Its Applications to Materials

Edited by Marc De Graef and Yimei Zhu

Volume 37. Characterization of Amorphous and Crystalline Rough
Surface: Principles and Applications

By YiPing Zhao, Gwo-Ching Wang, and Toh-Ming Lu

Volume 38. Advances in Surface Science

Volume 39. Modern Acoustical Techniques for the Measurement of
Mechanical Properties

Edited by Moises Levy, Henry E. Bass, and Richard Stern

PREFACE

Ever since it was established that the velocity of sound is proportional to the square root of the ratio of the effective elastic constant to the effective density, acoustic techniques have been used to determine the elastic properties of materials, be they solids, liquids, or gases or even a mixture of these. In this volume, which has been extracted from the *Handbook of Elastic Properties of Solids, Liquids, and Gases*, edited by M. Levy, H. E. Bass, and R. Stern and published by Academic Press, we present some of the modern acoustic techniques used by contemporary researchers to extract the elastic properties of solids and fluids. Those of you who may develop an interest in the elastic properties of biological materials, of stellar objects, of quasicrystals, of fullerenes, and of low-dimensional materials would have to look at the four-volume handbook, which contains chapters on these topics plus others on building materials, alloys, organic materials, and earth and marine science.

The rationale for compiling this volume was based on the fact that the readership of the series *Experimental Methods in the Physical Sciences* may not be acquainted with the acoustic techniques covered in this volume and would not normally be exposed to the handbook. Therefore the editors thought it desirable to produce this volume, which includes most of the introductory chapters in the handbook plus some chapters describing unique acoustic techniques developed recently to study surfaces, single crystals, and materials with somewhat unusual physical properties. Although this volume is supposed to concentrate on experimental techniques, it is well known, at least to theorists, that extracting information about the fundamental properties of the materials being investigated requires a healthy amount of theoretical insight. This is evident throughout this volume, where thermodynamics also plays a prominent role in at least two of the chapters.

If this volume had subheadings, then the last four chapters would be included under the general heading of fluids. In my opinion, these four chapters form an excellent self-contained description of the elastic properties of fluids, starting with the thermodynamic treatment of sound speed in fluids, continuing with the noninvasive determination of sound speed in liquids and then with a comprehensive introduction to the propagation and absorption of sound in gases, and finishing with a description of exquisitely elegant and precise acoustic measurements in gases in the final chapter.

This volume starts with an introduction to the concepts used to develop a description of the elastic properties of a material and their relation to the velocity of sound in isotropic and anisotropic materials. The elastic constants

in real materials may be complex, with the real components primarily related to the velocity of sound and the imaginary components related to the absorption of sound. Whenever possible, empirical rules of thumb are presented and then related to standard elastic constant models.

The next four chapters discuss unique dynamic acoustic techniques that have been perfected recently with the advent of the modern personal computer. In Chapter 2, point sources, produced by the fracture of capillaries or pencil lead or by pulsed laser, electron, or x-ray beams, are used to generate both longitudinal and shear waves propagating omnidirectionally. An array of sensors is then used to detect the shape and velocity of the generated waveforms. After formidable computer manipulation, this information can be related to the material's elastic anisotropy and microstructure.

Chapter 3 discusses the generation and detection of surface acoustic waves (SAWs) using various laser configurations. This is done to study the characteristics of surface acoustic waves, which currently have numerous practical applications in signal processing devices. SAWs are also used to determine the elastic constants of very thin films and coatings. The inherent dispersion of SAWs, which may be exacerbated by propagating through layered media or over rough surfaces, is discussed, as well as nonlinear effects in SAWs.

The elastic characterization of solid media by three types of acoustic microscopy is covered in Chapter 4. In the first method, conventional acoustic microscopy, the velocity of SAW is extracted from the interference pattern made by the reflected normal incident beam with the secondary beam emanating from the SAW excited by the same incident beam. The second technique is time-resolved microscopy, which uses one acoustic lens to transmit and receive acoustic pulses to measure the velocities of bulk waves, which may even travel through solid layers. In the third type, two-lens acoustic microscopy, one lens transmits the sound pulse and the other lens is used as a receiver. These lenses are used in different configurations to measure the reflection coefficients of anisotropic solids, to produce fascinating pictures of bulk waves in anisotropic solids, and to depict the complex angle and frequency dependence of SAWs generated on a crystal surface.

Resonant ultrasound spectroscopy (RUS) is presented in Chapter 5. This technique is a modern evolution of classical resonant techniques. The elastic tensors of single crystal samples as small as 1 mm on a side may be determined with a single set of measurements. RUS may even be used effectively with samples with triclinic symmetry, which have the minimum elastic symmetry and therefore the largest number of independent elastic constants. Conventional techniques would require at least 18 independent measurements to extract the 18 or 21 elastic constants in the elastic tensor. Although the shapes of the samples could be spherical or cylindrical, measurements are typically made on rectangular parallelepipeds. The diagonal corners of such a sample

are held between a transmitting transducer and a receiving one. The transmitting transducer is then excited by a swept frequency oscillator that covers the lowest 40 or 50 resonant modes of the sample, which are detected by the receiving transducer. The elastic moduli are then determined from this RUS spectrum. The key to this technique is the ability of modern personal computers to perform calculations nearly as rapidly as the original supercomputers. Equally important is the fact that modern integrated electronics allows the rapid acquisition of RUS data. Not only is the RUS technique used to determine elastic constants, but also once the RUS spectrum of a good specimen is obtained, it can be used as a quality control template for subsequent specimens, such as for steel ball bearings or other specimens with more esoteric shapes.

As described in Chapter 6, the RUS technique has been used to determine the elastic properties of two unusual systems, filled skutterudites, which possess low-frequency anharmonic local modes without undergoing any phase transitions, and plutonium, a metal that has at least five unusual zero-pressure phases between low temperatures and its melting point. This work is a tour de force, demonstrating how measurements of the values and the temperature dependence of the elastic constants may contribute to the understanding of the electronic structure and thermodynamics of some solids.

As mentioned earlier, the next four chapters could be placed under the general heading of fluids. The first of these, Chapter 7, considers sound speed as a thermodynamic property of fluids. The speed of sound is derived over a wide range of temperatures and pressures from the Helmholtz free energy for argon, nitrogen, water, and air in both the saturated liquid and the vapor state. In fact, precise experimental measurements of the speed of sound in a fluid may also contribute to a better determination of the shape of its Helmholtz free energy surface.

In Chapter 8, a clever nonintrusive technique for characterizing liquids in sealed containers is described. This technique uses swept frequency acoustic interferometry to rapidly and accurately determine the sound speed and attenuation of a liquid inside a container over a wide frequency range, and from the value of the attenuation extrapolated to zero frequency, the density of the liquid may be evaluated. Thus, this technique not only yields three important liquid properties but also yields enough information to uniquely identify a liquid by plotting these properties in the three-dimensional space of sound speed, attenuation, and density.

The propagation of sound in gases is discussed in Chapter 9, both in the continuum or hydrodynamic limit, where the mean free path between collisions is smaller than the sound wavelength, and in the noncontinuum or nonhydrodynamic limit, where the mean free path is comparable to or larger than the wavelength. In addition, the absorption of sound due to molecular relaxation

processes is thoroughly described, and the effects of relaxation processes on sound propagation through diatomic and triatomic gases and their mixtures, even with monatomic gases, are explored.

Some deceptively simple and brilliantly ingenious acoustic devices and techniques for extracting the thermodynamic properties and transport properties of gases are presented in Chapter 10, the last chapter of this volume. A cylindrical resonator is routinely used to measure sound speed to better than 0.01%. A dumbbell-shaped resonator is used to measure gas viscosity to better than 1%. Adding a honeycombed-shaped array of hexagonal ducts between the double resonators and exciting its odd and even harmonics make it possible to determine both the viscosity and the thermal conductivity of a gas in the same geometric configuration. The ratio of these two values yields an important hydrodynamic value for the gas, the Prandtl number. Finally, a resonant sphere, which lends itself to exact theoretical analysis of the experimental corrections required to accurately evaluate its radially symmetric modes, has produced the most accurate measurement of the speed of sound ever made. It was determined to better than one part per million, and consequently, these measurements have yielded the internationally accepted value of the universal gas constant, which is therefore known to better than two parts per million.

The 10 chapters in this volume were selected from the 75 chapters in the *Handbook of Solids, Liquids, and Gases*. However, it is still hoped that even this modest number has piqued your interest in the fascinating area of modern acoustics and conveyed the excitement engendered by our ability to use modern acoustic techniques to probe deeply into the physical and thermodynamic nature of matter.

MOISES LEVY

CONVERSION FACTORS BETWEEN SI AND CGS

Quantity	Multiply SI	by	to obtain CGS
Length	meter (m)	10^2	centimeter (cm)
Mass	kilogram (kg)	10^3	gram (g)
Time	second (s)	1	second (s)
Force	newton (N)	10^5	dyne
Energy	joule (J)	10^7	erg
Power	watt (W)	10^7	erg/s
Volume density	kg/m^3	10^{-3}	g/cm^3
Pressure	pascal (Pa)	10	dyne/cm^2
Speed	m/s	10^2	cm/s
Energy density	J/m^3	10	erg/cm^3
Elastic modulus	Pa	10	dyne/cm^2
Coefficient of viscosity	Pa·s	10	dyne·s/cm^2
Volume velocity	m^3/s	10^6	cm^3/s
Acoustic intensity	W/m^2	10^3	$\text{erg}/(\text{s·cm}^2)$
Mechanical impedance	N·s/m	10^3	dyne·s/cm
Specific acoustic impedance	Pa·s/m	10^{-1}	dyne·s/cm^3
Acoustic impedance	Pa·s/m^3	10^{-5}	dyne·s/cm^5
Mechanical stiffness	N/m	10^3	dyne/cm

Some Useful Conversions:

1 in. = 2.5400 cm
 1 ft = 0.3048 m
 1 yd = 0.9144 m
 1 fathom = 1.829 m
 1 mi (statute) = 1.609 km
 1 mi (nautical international) = 1.6093 km
 1 nm = 6076 ft = 1.852 km
 1 mph = 1.6093 km/h = 0.4470 m/s
 1 knot = 1 nm/h = 1.1508 mph = 1.852 km/h = 0.5144 m/s
 1 atm = 14.70 psi = 29.92 in. Hg (32 °C) = 33.90 ft H₂O = 1.033×10^4 kgf/m² = 1.0133 bar
 1 bar = 1×10^6 dyne/cm² = 14.50 psi = 1×10^5 Pa
 1 neper/m = 8.7 dB/m

Metric (SI) Multipliers

Prefix	Abbreviation	Value
Tera	T	10^{12}
Giga	G	10^9
Mega	M	10^6
Kilo	k	10^3
Hecto	h	10^2
Deka	da	10^1
Deci	d	10^{-1}
Centi	c	10^{-2}
Milli	m	10^{-3}
Micro	μ	10^{-6}
Nano	n	10^{-9}
Pico	p	10^{-12}
Femto	f	10^{-15}

This Page Intentionally Left Blank

1. INTRODUCTION TO FUNDAMENTALS OF ELASTIC CONSTANTS

Moises Levy

Physics Department
University of Wisconsin-Milwaukee
Milwaukee, Wisconsin

1.1 Introduction

The velocity of sound in an infinite medium is proportional to the square root of the ratio of an effective elastic constant to an effective density. This is true for solids, liquids, and gases. Even single crystals, glasses, and porous and heterogeneous materials follow this relation. In fact, in most cases, the most precise values of the elastic constants are obtained from a measurement of the sound velocity. Once the elastic constants are obtained, other relevant parameters such as the Young's modulus, the Poisson ratio, and the bulk modulus may be determined.

A discussion of Hooke's law is given in Section 1.2 of this chapter. Formulated by Robert Hooke in 1676, this law is the basic statement of linear elasticity. One hundred years later Thomas Young realized that the proportionality could be extended to an anisotropic medium so that the stress (σ) and strain (ϵ) are related by $\sigma = c_{ij}\epsilon_j$, where the proportionality constants (c_{ij}) are the elastic constants. Although most materials are intrinsically nonlinear, the law is a good approximation to the behavior of most types of materials within the range of recoverable, small strains. This section presents elastic constants in matrix form.

Section 1.3 gives a brief review of crystal structures and their symmetries. This review is necessary to the discussion in Section 1.4 of reduced elastic constant matrices for seven different crystal systems: triclinic, monoclinic, orthorhombic, trigonal, tetragonal, hexagonal, and cubic. The structure of all crystals can be described in terms of a lattice with a group of atoms attached to each lattice point. In 1845, Auguste Bravais recognized that the seven crystal systems in three dimensions could be further subdivided into 14 space lattices that are now called Bravais lattices.

Section 1.5 begins with a discussion of the wave equation for an anisotropic medium. The most general solution to these equations was obtained by Elwin Bruno Christoffel in 1877 [1]. This section goes on to describe elastic waves propagating through cubic and hexagonal crystals. Young's modulus, the Poisson ratio, and the bulk modulus are defined. Finally, the wave equations for

longitudinal and transverse waves in isotropic media are investigated in order to elucidate their nature as compressional irrotational waves and distortional rotational waves, respectively.

When sound waves propagate through a medium, absorption of energy by the body may occur. In Section 1.6, absorption in plane shear and longitudinal waves is derived by adding viscous losses to the wave equation. A simple method for obtaining the attenuation coefficient from rate of energy loss considerations is presented and the relation between attenuation and the quality factor is introduced.

Section 1.7 discusses group velocity and its relation to wave packets from a pulsed signal propagating through a medium. Section 1.8 discusses the phenomenological relations between phase velocity and attenuation and Section 1.9 gives a brief description of units.

1.2 Generalized Hooke's Law

1.2.1 Elastic Constants

Stress and strain in a solid body can be resolved into six components: three compressional or dilatational and three shear.

The stress components are identified as σ_{ij} and may be defined with the help of Figure 1.1. As may be seen in this figure, the first subscript identifies the direction of the stress and the second identifies the direction perpendicular to the plane upon which the stress is acting. Thus, σ_{zy} is a stress in the z -direction acting on the plane perpendicular to the y -axis. In the figure, it is apparent that there are nine stresses; however, since it is assumed that the block is not rotating, $\sigma_{ij} = \sigma_{ji}$, the stress components are reduced to six: three compressional, σ_{xx} , σ_{yy} and σ_{zz} , and three shear, σ_{yz} , σ_{xz} and σ_{xy} .

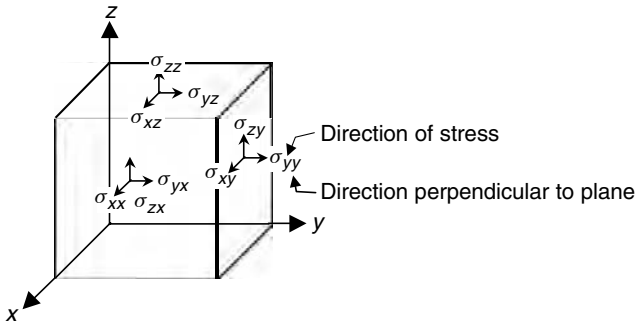


FIG. 1.1. Direction of stress components.

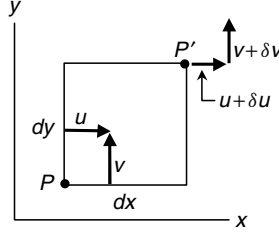


FIG. 1.2. Identification of strain.

The strain components are identified as ϵ_{jj} and may be derived and defined with the help of the diagram in Figure 1.2. Consider two points, P and P' , that for simplicity are located on the $y-x$ plane. Assume that point, $P(x, y, z)$, has a displacement of u, v, w in the x, y, z directions, respectively; and similarly, assume that $P' = P + \delta P = P'(x + dx, y + dy, z + dz)$ has displacements $u + \delta u, v + \delta v, w + \delta w$. If $\delta_i = 0$, then the rectangle identified by P and P' has just been moved. In order for the displacements to produce a deformation, some of the δ s must be unequal to zero. By Taylor's expansion, we find that

$$\begin{aligned} [u + \delta u] - u &= \frac{\partial u}{\partial x} dx + \frac{\partial u}{\partial y} dy + \frac{\partial u}{\partial z} dz = \nabla u \cdot \delta \vec{r} \\ \delta v &= \frac{\partial v}{\partial x} dx + \frac{\partial v}{\partial y} dy + \frac{\partial v}{\partial z} dz = \nabla v \cdot \delta \vec{r} \end{aligned}$$

and

$$\delta w = \frac{\partial w}{\partial x} dx + \frac{\partial w}{\partial y} dy + \frac{\partial w}{\partial z} dz = \nabla w \cdot \delta \vec{r}$$

In the above, we have used

$$\begin{aligned} \vec{r} &= x\hat{i} + y\hat{j} + z\hat{k} \\ \delta \vec{r} &= dx\hat{i} + dy\hat{j} + dz\hat{k} \end{aligned}$$

and the divergence

$$\nabla = \frac{\partial}{\partial x}\hat{i} + \frac{\partial}{\partial y}\hat{j} + \frac{\partial}{\partial z}\hat{k}$$

The three compressional or dilatational strains are defined as

$$\epsilon_{xx} = \frac{\partial u}{\partial x}; \quad \epsilon_{yy} = \frac{\partial v}{\partial y}; \quad \epsilon_{zz} = \frac{\partial w}{\partial z}$$

and, the three shear strains

$$\epsilon_{yz} = \frac{\partial w}{\partial y} + \frac{\partial v}{\partial z}; \quad \epsilon_{zx} = \frac{\partial u}{\partial z} + \frac{\partial w}{\partial x}; \quad \epsilon_{xy} = \frac{\partial v}{\partial x} + \frac{\partial u}{\partial y}$$

When using tensor notation, definitions of ϵ_{yz} , ϵ_{zx} and ϵ_{xy} differ by a factor of 1/2 from the preceding since deformation-produced rotations about the three axes are given by

$$\bar{\omega}_x = \frac{1}{2} \left(\frac{\partial w}{\partial y} - \frac{\partial v}{\partial z} \right)$$

$$\bar{\omega}_y = \frac{1}{2} \left(\frac{\partial u}{\partial z} - \frac{\partial w}{\partial x} \right)$$

and

$$\bar{\omega}_z = \frac{1}{2} \left(\frac{\partial v}{\partial x} - \frac{\partial u}{\partial y} \right)$$

According to Hooke's law, the stress is proportional to the strain for small displacements. In the generalized form, this proportionality principle is extended to the six stresses and strains. Thus, the generalized Hooke's law may be written as

$$\sigma_{xx} = C_{11}\epsilon_{xx} + C_{12}\epsilon_{yy} + C_{13}\epsilon_{zz} + C_{14}\epsilon_{yz} + C_{15}\epsilon_{zx} + C_{16}\epsilon_{xy},$$

$$\sigma_{yy} = C_{21}\epsilon_{xx} + C_{22}\epsilon_{yy} + C_{23}\epsilon_{zz} + C_{24}\epsilon_{yz} + C_{25}\epsilon_{zx} + C_{26}\epsilon_{xy},$$

$$\sigma_{zz} = C_{31}\epsilon_{xx} + C_{32}\epsilon_{yy} + C_{33}\epsilon_{zz} + C_{34}\epsilon_{yz} + C_{35}\epsilon_{zx} + C_{36}\epsilon_{xy},$$

$$\sigma_{yz} = C_{41}\epsilon_{xx} + C_{42}\epsilon_{yy} + C_{43}\epsilon_{zz} + C_{44}\epsilon_{yz} + C_{45}\epsilon_{zx} + C_{46}\epsilon_{xy},$$

$$\sigma_{zx} = C_{51}\epsilon_{xx} + C_{52}\epsilon_{yy} + C_{53}\epsilon_{zz} + C_{54}\epsilon_{yz} + C_{55}\epsilon_{zx} + C_{56}\epsilon_{xy},$$

$$\sigma_{xy} = C_{61}\epsilon_{xx} + C_{62}\epsilon_{yy} + C_{63}\epsilon_{zz} + C_{64}\epsilon_{yz} + C_{65}\epsilon_{zx} + C_{66}\epsilon_{xy}.$$

The constants of proportionality, c_{ij} , are known as the elastic constants. Because for small displacement the elastic energy density U is a quadratic function of the strains, and the elastic constants are given by the second partial derivatives of U (therefore known as second-order constants), then it can be shown that

$$c_{ij} = c_{ji}$$

Thus, the 36 elastic constants given in matrix form can be reduced to 6 diagonal elements and 15 off-diagonal elements. For different crystal structures, the number can be reduced further. Therefore, we shall review crystal structures in the next section. In matrix form, these elastic constants may be written

as follows:

$$\begin{pmatrix} C_{11} & C_{12} & C_{13} & C_{14} & C_{15} & C_{16} \\ C_{21} & C_{22} & C_{23} & C_{24} & C_{25} & C_{26} \\ C_{31} & C_{32} & C_{33} & C_{34} & C_{35} & C_{36} \\ C_{41} & C_{42} & C_{43} & C_{44} & C_{45} & C_{46} \\ C_{51} & C_{52} & C_{53} & C_{54} & C_{55} & C_{56} \\ C_{61} & C_{62} & C_{63} & C_{64} & C_{65} & C_{66} \end{pmatrix}$$

1.2.1.1 Reduced Tensor Notation. The generalized form of Hooke's law may be written in reduced tensor notation and using the so-called Voigt notation,

$$\sigma_i = C_{ij} \epsilon_j \quad (1.1)$$

where $i, j = 1$ to 6 . In addition, the subscripts, i and j that run from 1 through 6 , correspond to xx, yy, zz, yz, zx , and xy , respectively, in our previous notation. The actual stress strain tensor is a fourth-rank tensor, so it should be written as

$$\sigma_{ij} = C_{ijkl} \epsilon_{kl}$$

However, since elastic constants are determined by the ratio of the stresses to strains, it is possible to interchange the first two and last two indices because both stresses and strains are symmetrical tensors. Therefore, it is possible to write the elastic constant terms with only two indices, C_{ij} , where the indices can take on values from 1 to 6 ; this then results in Eq. 1.1.

1.2.2 Elastic Compliance

For some applications, it is sometimes preferable to express strains in terms of the stresses. This can be done by solving Eq. 1.1 simultaneously for the strains and the resulting equation is

$$\epsilon_i = S_{ij} \sigma_j \quad (1.2)$$

where the S_{ij} are known as the elastic compliance constants. Written in full, Eq. 1.2 becomes the following:

$$\begin{aligned} \epsilon_1 &= S_{11}\sigma_1 + S_{12}\sigma_2 + S_{13}\sigma_3 + S_{14}\sigma_4 + S_{15}\sigma_5 + S_{16}\sigma_6 \\ \epsilon_2 &= S_{21}\sigma_1 + S_{22}\sigma_2 + S_{23}\sigma_3 + S_{24}\sigma_4 + S_{25}\sigma_5 + S_{26}\sigma_6 \\ \epsilon_3 &= S_{31}\sigma_1 + S_{32}\sigma_2 + S_{33}\sigma_3 + S_{34}\sigma_4 + S_{35}\sigma_5 + S_{36}\sigma_6 \\ \epsilon_4 &= S_{41}\sigma_1 + S_{42}\sigma_2 + S_{43}\sigma_3 + S_{44}\sigma_4 + S_{45}\sigma_5 + S_{46}\sigma_6 \\ \epsilon_5 &= S_{51}\sigma_1 + S_{52}\sigma_2 + S_{53}\sigma_3 + S_{54}\sigma_4 + S_{55}\sigma_5 + S_{56}\sigma_6 \\ \epsilon_6 &= S_{61}\sigma_1 + S_{62}\sigma_2 + S_{63}\sigma_3 + S_{64}\sigma_4 + S_{65}\sigma_5 + S_{66}\sigma_6 \end{aligned} \quad (1.3)$$

There are computer and software programs that easily invert the sets of matrices in Eqs. 1.1 and 1.3. However, for completeness, it should be noted that the elastic compliance constants are given by

$$S_{ij} = \frac{(-1)^{i+j} \Delta_{ij}^c}{\Delta^c},$$

where Δ^c is the determinant of the C_{ij} terms,

$$\Delta^c = \begin{vmatrix} C_{11} & C_{12} & C_{13} & C_{14} & C_{15} & C_{16} \\ C_{21} & C_{22} & C_{23} & C_{24} & C_{25} & C_{26} \\ C_{31} & C_{32} & C_{33} & C_{34} & C_{35} & C_{36} \\ C_{41} & C_{42} & C_{43} & C_{44} & C_{45} & C_{46} \\ C_{51} & C_{52} & C_{53} & C_{54} & C_{55} & C_{56} \\ C_{61} & C_{62} & C_{63} & C_{64} & C_{65} & C_{66} \end{vmatrix}$$

and Δ_{ij}^c is the minor obtained by suppressing the i^{th} row and the j^{th} column. It follows that $S_{ij} = S_{ji}$ since $c_{ij} = c_{ji}$.

1.3 Crystal Structures

In three dimensions, there are 32 symmetric point groups that can be subdivided into fourteen Bravais or space lattices. These lattices are further grouped into seven crystal systems: triclinic, monoclinic, orthorhombic, tetragonal, cubic, trigonal, and hexagonal. The three dimensional Bravais lattices are listed in Table 1.1. This table includes the number of lattices in each system, the lattice symbols, the restrictions on the conventional unit cell axes and angles, the lengths and angles which must be specified in order to describe a particular crystal structure, and, in the last column, the highest symmetry point group of the lattice. Figure 1.3 describes the relation between the axes

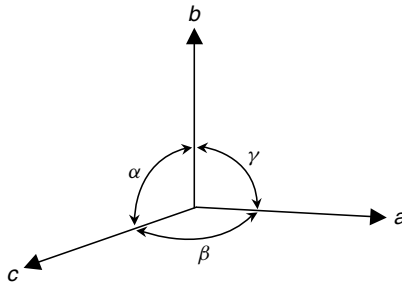


FIG. 1.3. Relation between axes and angles in conventional unit cell.

TABLE 1.1. Symmetry Point Groups Associated with the Seven Crystal Systems: 32 Point Groups in 3 Dimensions

System	International Symbol		Schoenflies symbol
	Short	Full	
Triclinic	$\bar{1}$	$\bar{1}$	C_1
			$C_i(S_2)$
Monoclinic	2	2	C_2
	m	m	$C_s(C_{1h})$
Orthorhombic	$\frac{2}{m}$	$\frac{2}{m}$	C_{2h}
	222	222	$D_2(V)$
	mm2	mm2	C_{2v}
	mmm	$\frac{2}{m} \frac{2}{m} \frac{2}{m}$	$D_{2h}(V_h)$
Tetragonal	4	4	C_4
	$\bar{4}$	$\bar{4}$	S_4
	$\frac{4}{m}$	$\frac{4}{m}$	C_4
	422	422	D_4
	4mm	4mm	C_{4v}
	$\bar{4}2m$	$\bar{4}2m$	$D_{2d}(V_d)$
	$\frac{4}{mmm}$	$\frac{4}{m} \frac{2}{m} \frac{2}{m}$	D_{4h}
Trigonal	$\frac{3}{\bar{3}}$	$\frac{3}{\bar{3}}$	C_3
	32	32	$C_{3i}(S_6)$
	3m	3m	D_3
			C_{3v}
	$\bar{3}m$	$\frac{2}{3} \frac{2}{m}$	D_{3d}
Hexagonal	6	6	C_6
	$\bar{6}$	$\bar{6}$	C_{3h}
	$\frac{6}{m}$	$\frac{6}{m}$	C_{6h}
	622	622	D_6
	6mm	6mm	C_{6v}
	$\bar{6}m2$	$\bar{6}m2$	D_{3h}
	$\frac{6}{mmm}$	$\frac{6}{m} \frac{2}{m} \frac{2}{m}$	D_{6h}
Cubic	23	23	T
	m3	$\frac{2}{m} \bar{3}$	T_h
	432	432	O
	$\bar{4}3m$	$\bar{4}3m$	T_d
	m3m	$\frac{4}{m} \frac{2}{\bar{3}} \frac{2}{m}$	O_h

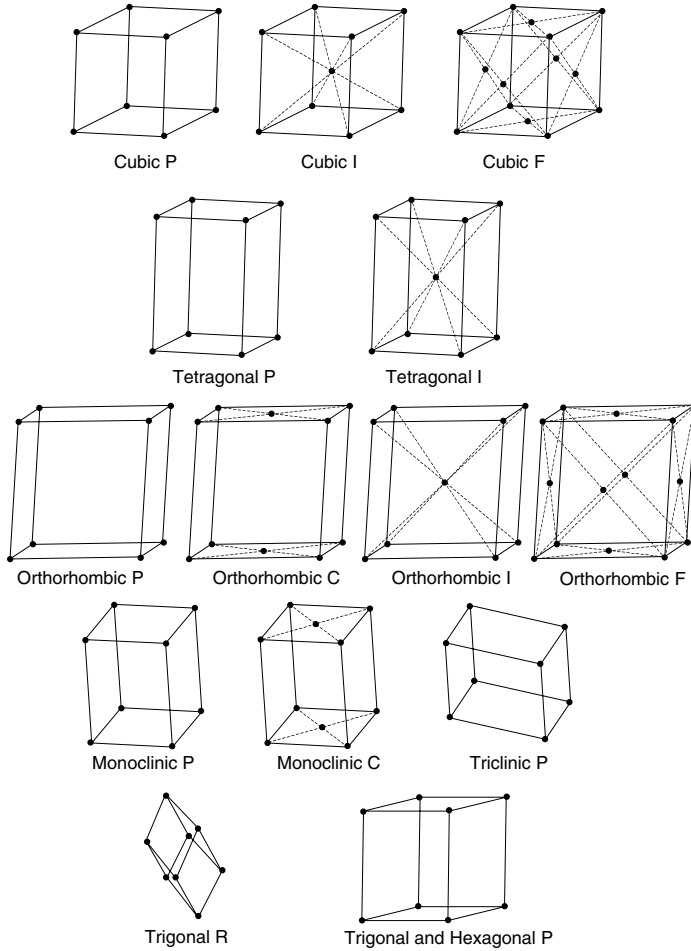


FIG. 1.4. The fourteen Bravais lattices.

and the angles of the conventional unit cells, and Figure 1.4 illustrates the fourteen Bravais lattices.

Table 1.2 identifies the different symmetry point groups associated with each crystal system that leave the system invariant. For completeness, the

TABLE 1.2. Conventional Unit Cells for the Fourteen Bravais Lattices

System	Number of lattices in system	Lattice symbols	Nature of unit-cell axes and angles	Lengths and angles to be specified	Symmetry of lattice
Triclinic	1	P	$a \neq b \neq c$ $\alpha \neq \beta \neq \gamma$	a, b, c α, β, γ	$\bar{1}$
Monoclinic	2	P	$a \neq b \neq c$	a, b, c	$\frac{2}{m}$
		C	$\alpha = \gamma = 90^\circ \neq \beta$	β	
		P			
Orthorhombic	4	C	$a \neq b \neq c$	a, b, c	mmm
		I	$\alpha = \beta = \gamma = 90^\circ$		
		F			
Tetragonal	2	P	$a = b \neq c$	a, c	$\frac{4}{mmm}$
		I	$\alpha = \beta = \gamma = 90^\circ$		
		P			
Cubic	3	I	$a = b = c$	a	$m\bar{3}m$
		F	$\alpha = \beta = \gamma = 90^\circ$		
			$a = b = c$		
Trigonal	1	R	$\alpha = \beta = \gamma$	a	$\bar{3}m$
			$< 120^\circ, \neq 90^\circ$	α	
			$a = b \neq c$		
Hexagonal	1	P	$\alpha = \beta = 90^\circ$	a, c	$\frac{6}{mmm}$
			$\gamma = 120^\circ$		

short and full international symbols and the Schoenflies symbol nomenclature are included. There are five types of symbols used; they identify the following symmetry operations about a lattice point that returns the lattice unto itself [2, 3].

The symbols, 1, 2 (diad), 3 (triad), 4 (tetrad), and 6 (hexad), denote rotation axes. They represent one-, two-, three-, four-, and sixfold rotation axes corresponding to rotations by 360° , 180° , 120° , 90° and 60° about a lattice point. The reflection plane is denoted by m . It is in a plane through a lattice point. The inversion center is denoted by $\bar{1}$. If the operation $\vec{r} \rightarrow -\vec{r}$ brings the crystal structure onto itself, then the crystal possesses inversion symmetry. Here \vec{r} is the position of an arbitrary point in the crystal relative to the lattice point. The rotation-inversion axes are denoted by the symbols, $\bar{1}, \bar{2}, \bar{3}, \bar{4}, \bar{6}$. Thus, self-coincidence is attained by a rotation followed by an inversion. The symbol $\bar{2}$ does not appear in the table since it is equal to m . The rotation axis with mirror plane normal to it is denoted by $\frac{2}{m}, \frac{4}{m},$ and $\frac{6}{m}$.

The international point group notation is summarized as follows with X standing for the rotation axis.

Rotation Axis	X
Rotation-Inversion Axis	\overline{X}
Rotation Axis with Mirror Plane Normal to It	$\frac{X}{m}$
Rotation Axis with Diad Axis(es) Normal to It	$X2$
Rotation Axis with Mirror Plane(s) Parallel to It	$\frac{Xm}{2}$
Rotation-Inversion Axis with Diad Axis(es) Normal to It	$\frac{\overline{X}}{2}$
Rotation-Inversion Axis with Mirror Plane(s) Parallel to It	$\overline{X}2$
Rotation Axis with Mirror Plane Normal to it and Mirror Plane(s) Parallel to It	$\frac{X}{m}m$

Again, for completeness, it should be pointed out that if the lattices are infinite they can be further subdivided into 230 space groups that leave the lattice invariant through a combination of point-group operations, full and partial primitive translations, rotations, and reflections. For example, even for a finite unit cell, each of the point group operations listed in Table 1.2 can be applied to the corresponding lattices listed in Table 1.1, yielding 66 space groups for the 3 dimensional unit cells. By considering the orientation of the Bravais lattice when the point group operation is applied, 7 additional space groups are obtained that yield a total of 73 space groups. The other 157 space groups for the infinite lattice are obtained by judiciously applying the operations listed above. Now we are in a position to write down the elastic constant matrices for the different crystal structures.

1.4 Reduced Elastic Constant Matrices

It was necessary to define crystal structures and their symmetries in the previous section before we could write down the reduced elements in the elastic constant matrices for the different crystal structures. As will be seen, five of the seven crystal systems only require one reduced elastic constant matrix each. Two, the trigonal and the tetragonal, require two matrices each. For completeness, the matrix for isotropic materials is also included. This requires only two elastic constants, either C_{11} and C_{12} or λ and μ , the Lamé constants, where $\mu = \frac{1}{2}(C_{11} - C_{12})$ and $\lambda = C_{12}$.

1.4.1 Triclinic

$$\begin{vmatrix} C_{11} & C_{12} & C_{13} & C_{14} & C_{15} & C_{16} \\ C_{12} & C_{22} & C_{23} & C_{24} & C_{25} & C_{26} \\ C_{13} & C_{23} & C_{33} & C_{34} & C_{35} & C_{36} \\ C_{14} & C_{24} & C_{34} & C_{44} & C_{45} & C_{46} \\ C_{15} & C_{25} & C_{35} & C_{45} & C_{55} & C_{56} \\ C_{16} & C_{26} & C_{36} & C_{46} & C_{56} & C_{66} \end{vmatrix}$$

The triclinic matrix has 21 elastic constants. This is the conventional wisdom. However, Landau and Lifshitz state that this number should be reduced by three to 18 because the choice of the Cartesian orthogonal axes, x , y , and z , is arbitrary and these could be interchanged, thus reducing the number by three [6].

1.4.2 Monoclinic

$$\begin{vmatrix} C_{11} & C_{12} & C_{13} & 0 & C_{15} & 0 \\ C_{12} & C_{22} & C_{23} & 0 & C_{25} & 0 \\ C_{13} & C_{23} & C_{33} & 0 & C_{35} & 0 \\ 0 & 0 & 0 & C_{44} & 0 & C_{46} \\ C_{15} & C_{25} & C_{35} & 0 & C_{55} & 0 \\ 0 & 0 & 0 & C_{46} & 0 & C_{66} \end{vmatrix}$$

The monoclinic system has 13 elastic constants. By a suitable choice of the coordinate axes, these could be reduced to 12.

1.4.3 Orthorhombic

$$\begin{vmatrix} C_{11} & C_{12} & C_{13} & 0 & 0 & 0 \\ C_{12} & C_{22} & C_{23} & 0 & 0 & 0 \\ C_{13} & C_{23} & C_{33} & 0 & 0 & 0 \\ 0 & 0 & 0 & C_{44} & 0 & 0 \\ 0 & 0 & 0 & 0 & C_{55} & 0 \\ 0 & 0 & 0 & 0 & 0 & C_{66} \end{vmatrix}$$

Orthorhombic has nine elastic constants.

1.4.4 Trigonal

The trigonal system requires two reduced elastic constant matrices. The one for the symmetry point groups, 3 and $\bar{3}$, is

$$\begin{vmatrix} C_{11} & C_{12} & C_{13} & C_{14} & -C_{25} & 0 \\ C_{12} & C_{11} & C_{13} & -C_{14} & C_{25} & 0 \\ C_{13} & C_{13} & C_{33} & 0 & 0 & 0 \\ C_{14} & -C_{14} & 0 & C_{44} & 0 & C_{25} \\ -C_{25} & C_{25} & 0 & 0 & C_{44} & C_{14} \\ 0 & 0 & 0 & C_{25} & C_{14} & \frac{1}{2}(C_{11} - C_{12}) \end{vmatrix}$$

The reduced elastic constant matrix for these two trigonal point groups has seven constants. By a suitable choice of coordinates, these could be reduced to six. The other matrix for the trigonal symmetry point groups, $3m$, 32 and $\bar{3}2/m$, is

$$\begin{vmatrix} C_{11} & C_{12} & C_{13} & C_{14} & 0 & 0 \\ C_{12} & C_{11} & C_{13} & -C_{14} & 0 & 0 \\ C_{13} & C_{13} & C_{33} & 0 & 0 & 0 \\ C_{14} & -C_{14} & 0 & C_{44} & 0 & 0 \\ 0 & 0 & 0 & 0 & C_{44} & C_{14} \\ 0 & 0 & 0 & 0 & C_{14} & \frac{1}{2}(C_{11} - C_{12}) \end{vmatrix}$$

Thus, the conventional reduced elastic constant matrix for these three trigonal point groups has six constants. Therefore, by a suitable choice of coordinate axes, all the point groups in the trigonal system have the same number of elastic constants, six.

1.4.5 Tetragonal

The tetragonal system also requires two reduced elastic constant matrices. The one for the symmetry point groups, 4 , $\bar{4}$, $\frac{4}{m}$, is

$$\begin{vmatrix} C_{11} & C_{12} & C_{13} & 0 & 0 & C_{16} \\ C_{12} & C_{11} & C_{13} & 0 & 0 & -C_{16} \\ C_{13} & C_{13} & C_{33} & 0 & 0 & 0 \\ 0 & 0 & 0 & C_{44} & 0 & 0 \\ 0 & 0 & 0 & 0 & C_{44} & 0 \\ C_{16} & -C_{16} & 0 & 0 & 0 & C_{66} \end{vmatrix}$$

The conventional reduced elastic constant matrix for these three trigonal point groups has seven constants. By a suitable choice of coordinates, these could be reduced to six. The other matrix for the tetragonal point groups, $\bar{4}2m$, 422 , $\frac{4}{m}2\frac{2}{m}$ is

$$\begin{vmatrix} C_{11} & C_{12} & C_{13} & 0 & 0 & 0 \\ C_{12} & C_{11} & C_{13} & 0 & 0 & 0 \\ C_{13} & C_{13} & C_{33} & 0 & 0 & 0 \\ 0 & 0 & 0 & C_{44} & 0 & 0 \\ 0 & 0 & 0 & 0 & C_{44} & 0 \\ 0 & 0 & 0 & 0 & 0 & C_{66} \end{vmatrix}$$

There are six constants in this matrix. Again, by a suitable choice of the coordinate axis, all the point groups in the tetragonal system have the same number of elastic constants, six.

1.4.6 Hexagonal

$$\begin{vmatrix} C_{11} & C_{12} & C_{13} & 0 & 0 & 0 \\ C_{12} & C_{11} & C_{13} & 0 & 0 & 0 \\ C_{13} & C_{13} & C_{33} & 0 & 0 & 0 \\ 0 & 0 & 0 & C_{44} & 0 & 0 \\ 0 & 0 & 0 & 0 & C_{44} & 0 \\ 0 & 0 & 0 & 0 & 0 & \frac{1}{2}(C_{11} - C_{12}) \end{vmatrix}$$

The hexagonal system has five constants.

1.4.7 Cubic

$$\begin{vmatrix} C_{11} & C_{12} & C_{12} & 0 & 0 & 0 \\ C_{12} & C_{11} & C_{12} & 0 & 0 & 0 \\ C_{12} & C_{12} & C_{11} & 0 & 0 & 0 \\ 0 & 0 & 0 & C_{44} & 0 & 0 \\ 0 & 0 & 0 & 0 & C_{44} & 0 \\ 0 & 0 & 0 & 0 & 0 & C_{44} \end{vmatrix}$$

The cubic system has three constants.

1.4.8 Isotropic

$$\begin{vmatrix} C_{11} & C_{12} & C_{12} & 0 & 0 & 0 \\ C_{12} & C_{11} & C_{12} & 0 & 0 & 0 \\ C_{12} & C_{12} & C_{11} & 0 & 0 & 0 \\ 0 & 0 & 0 & \frac{C_{11} - C_{12}}{2} & 0 & 0 \\ 0 & 0 & 0 & 0 & \frac{C_{11} - C_{12}}{2} & 0 \\ 0 & 0 & 0 & 0 & 0 & \frac{C_{11} - C_{12}}{2} \end{vmatrix}$$

The isotropic system has two constants. And, using the following definitions for the Lamé constants, $\mu \equiv C_{44}$, $\lambda \equiv C_{12}$, $2C_{44} = C_{11} - C_{12}$, and $C_{11} = 2C_{44} + C_{12} = \lambda + 2\mu$, the isotropic matrix becomes

$$\begin{vmatrix} (\lambda + 2\mu) & \lambda & \lambda & 0 & 0 & 0 \\ \lambda & (\lambda + 2\mu) & \lambda & 0 & 0 & 0 \\ \lambda & \lambda & (\lambda + 2\mu) & 0 & 0 & 0 \\ 0 & 0 & 0 & \mu & 0 & 0 \\ 0 & 0 & 0 & 0 & \mu & 0 \\ 0 & 0 & 0 & 0 & 0 & \mu \end{vmatrix}$$

Again, there are two constants, λ and μ .

1.5 Equations of Motion and Plane Waves in an Infinite Solid

Consider the forces on a cube in the x -direction, as shown in Figure 1.5, where the displacement in the x -direction is u . The equation of motion is derived from Newton's second law. The mass of the cube, $\rho dx dy dz$, where ρ is the density times its acceleration, $\frac{\partial^2 u}{\partial t^2}$, is given by the net force on the cube in the x -direction,

$$\rho \frac{\partial^2 u}{\partial t^2} dx dy dz = \left(\frac{\partial \sigma_{xx}}{\partial x} dx \right) dy dz + \left(\frac{\partial \sigma_{xy}}{\partial y} dy \right) dx dz + \left(\frac{\partial \sigma_{xz}}{\partial z} dz \right) dx dy$$

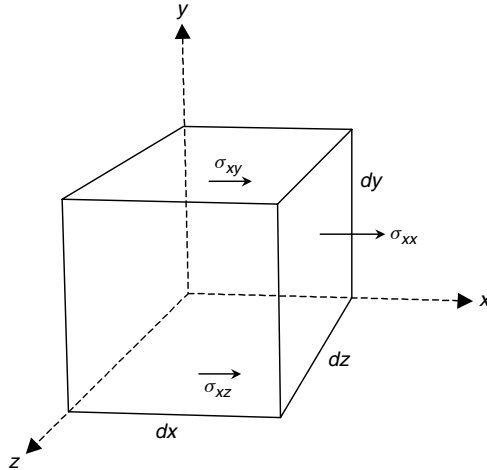


FIG. 1.5. Cube used for deriving wave equation.

On the right hand side of the equation, the terms in parentheses correspond to the net stress on a set of parallel surfaces whose area is given by the product of the next two differentials. After dividing by the volume of the cube, $dx dy dz$, we obtain

$$\rho \frac{\partial^2 u}{\partial t^2} = \frac{\partial \sigma_{xx}}{\partial x} + \frac{\partial \sigma_{xy}}{\partial y} + \frac{\partial \sigma_{xz}}{\partial z}$$

Similarly for the other two directions,

$$\rho \frac{\partial^2 v}{\partial t^2} = \frac{\partial \sigma_{yy}}{\partial y} + \frac{\partial \sigma_{yz}}{\partial z} + \frac{\partial \sigma_{yx}}{\partial x}$$

and

$$\rho \frac{\partial^2 w}{\partial t^2} = \frac{\partial \sigma_{zz}}{\partial z} + \frac{\partial \sigma_{zx}}{\partial x} + \frac{\partial \sigma_{zy}}{\partial y}$$

The generalized Hooke's law gives a relation between the stresses, ω , and the strains, ϵ , that in turn can be expressed in terms of the displacements, u , v , and w . The most general solution to this set of equations of motion was obtained by Christoffel [1, 5]. By calling l , m , and n the direction cosines with respect to the x -, y -, and z -axes of the normal to the plane wave, then a distance along the normal has the value

$$s = lx + my + nz$$

and

$$l^2 + m^2 + n^2 = 1$$

Furthermore, if the particle velocity, ξ , of a point on the surface of the plane wave has the direction cosines, α , β , γ , with respect to the x -, y -, and z -axes, then,

$$\xi = \alpha u + \beta v + \gamma w$$

and

$$\alpha^2 + \beta^2 + \gamma^2 = 1$$

The equations of motion may then be written, as shown by Christoffel, in terms of u , v , w and s , instead of the strains, by introducing a series of moduli, λ_{11} to λ_{33} , that are functions of the elastic stiffness, c_{ij} , and the direction cosines l , m , and n . Thus, the equations of motion take the form [5]

$$\begin{aligned} \rho \frac{\partial^2 u}{\partial t^2} &= \lambda_{11} \frac{\partial^2 u}{\partial s^2} + \lambda_{12} \frac{\partial^2 v}{\partial s^2} + \lambda_{13} \frac{\partial^2 w}{\partial s^2} \\ \rho \frac{\partial^2 v}{\partial t^2} &= \lambda_{12} \frac{\partial^2 u}{\partial s^2} + \lambda_{22} \frac{\partial^2 v}{\partial s^2} + \lambda_{23} \frac{\partial^2 w}{\partial s^2} \end{aligned}$$

and

$$\rho \frac{\partial^2 w}{\partial t^2} = \lambda_{13} \frac{\partial^2 u}{\partial s^2} + \lambda_{23} \frac{\partial^2 v}{\partial s^2} + \lambda_{33} \frac{\partial^2 w}{\partial s^2}$$

where

$$\begin{aligned}\lambda_{11} &= l^2 C_{11} + m^2 C_{66} + n^2 C_{55} + 2mnC_{56} + 2nlC_{15} + 2lmC_{16} \\ \lambda_{22} &= l^2 C_{66} + m^2 C_{22} + n^2 C_{44} + 2mnC_{24} + 2mlC_{46} + 2lmC_{26} \\ \lambda_{33} &= l^2 C_{55} + m^2 C_{44} + n^2 C_{33} + 2mnC_{34} + 2nlC_{35} + 2lmC_{45} \\ \lambda_{12} &= \lambda_{21} = l^2 C_{16} + m^2 C_{26} + n^2 C_{45} + mn(C_{44} + C_{25}) + nl(C_{14} \\ &\quad + C_{56}) + lm(C_{12} + C_{66}) \\ \lambda_{13} &= \lambda_{31} = l^2 C_{15} + m^2 C_{46} + n^2 C_{35} + mn(C_{45} + C_{35}) + nl(C_{13} + C_{55}) \\ &\quad + lm(C_{14} + C_{56})\end{aligned}$$

and

$$\begin{aligned}\lambda_{23} &= \lambda_{32} = l^2 C_{56} + m^2 C_{24} + n^2 C_{34} + mn(C_{44} \\ &\quad + C_{23}) + nl(C_{36} + C_{45}) + lm(C_{25} + C_{46})\end{aligned}$$

There are three velocities, some of which may be degenerate, that propagate along any direction. The three velocities satisfy the following matrix equation

$$\begin{vmatrix} \lambda_{11} - \rho v^2 & \lambda_{12} & \lambda_{13} \\ \lambda_{12} & \lambda_{22} - \rho v^2 & \lambda_{23} \\ \lambda_{13} & \lambda_{23} & \lambda_{33} - \rho v^2 \end{vmatrix} = 0 \quad (1.5)$$

The particle motions associated with the three different waves are perpendicular to each other, but only in special cases are they also perpendicular or parallel to the direction of propagation [6]. The direction cosines, α , β , and γ , for the particle velocity, ξ , may be obtained from the following set of equations:

$$\begin{aligned}\alpha \lambda_{11} + \beta \lambda_{12} + \gamma \lambda_{13} &= \alpha \rho v_i^2 \\ \alpha \lambda_{12} + \beta \lambda_{22} + \gamma \lambda_{23} &= \beta \rho v_i^2 \\ \alpha \lambda_{13} + \beta \lambda_{23} + \gamma \lambda_{33} &= \gamma \rho v_i^2\end{aligned}$$

where $i = 1, 2, 3$ and v_i are solutions of the velocity equation.

1.5.1 Elastic Waves in Cubic Crystals

For a cubic crystal there are three elastic constants, $C_{11} = C_{22} = C_{33}$, $C_{44} = C_{55} = C_{66}$, and $C_{12} = C_{13}$. Therefore, the expressions for the λ_{ij} elastic

parameters become

$$\lambda_{11} = l^2 C_{11} + (m^2 + n^2) C_{44}$$

$$\lambda_{22} = m^2 C_{11} + (l^2 + n^2) C_{44}$$

$$\lambda_{33} = n^2 C_{11} + (l^2 + m^2) C_{44}$$

$$\lambda_{12} = lm(C_{12} + C_{44})$$

$$\lambda_{13} = nl(C_{12} + C_{44})$$

and

$$\lambda_{23} = mn(C_{12} + C_{44})$$

Inserting the values into Eq. 1.5 yields the following equation for the three velocities along any orientation:

$$0 = \begin{vmatrix} l^2 C_{11} + (m^2 + n^2) C_{44} - \rho v^2 & lm(C_{12} + C_{44}) & nl(C_{12} + C_{44}) \\ lm(C_{12} + C_{44}) & (l^2 + n^2) C_{44} + m^2 C_{11} - \rho v^2 & mn(C_{12} + C_{44}) \\ nl(C_{12} + C_{44}) & mn(C_{12} + C_{44}) & (l^2 + m^2) C_{44} + n^2 C_{11} - \rho v^2 \end{vmatrix}$$

A pure longitudinal wave is defined as one in which the particle velocity is parallel to the propagation direction. A pure shear wave has the particle velocity perpendicular to the propagation direction. A cubic crystal has three orientations along which a pure longitudinal and two pure shear waves can be transmitted. These are [100], $l = 1, m = n = 0$; [110], $l = m = \frac{1}{\sqrt{2}}, n = 0$; and [111], $l = m = n = \frac{1}{\sqrt{3}}$. Along the [100] direction, the velocity and respective particle velocities are

$$v_1 = v_{\text{long}} = \sqrt{\frac{C_{11}}{\rho}} \quad \alpha = 1 \text{ or } \xi \text{ along [100]}$$

$$v_2 = v_{\text{shear}} = \sqrt{\frac{C_{44}}{\rho}} \quad \beta = 1 \text{ or } \xi \text{ along [010]}$$

and

$$v_3 = v_{\text{shear}} = \sqrt{\frac{C_{44}}{\rho}} \quad \gamma = 1 \text{ or } \xi \text{ along [001]}$$

Along the [110] direction, the velocity and respective particles velocities are

$$v_1 = v_{\text{long}} = \sqrt{\frac{C_{11} + C_{12} + 2C_{44}}{2\rho}} \quad \alpha = \beta = \frac{1}{\sqrt{2}}; \xi \text{ along [110]}$$

$$v_2 = v_{\text{shear}} = \sqrt{\frac{C_{44}}{\rho}} \quad \gamma = 1; \xi \text{ along [001]}$$

and

$$v_3 = v_{\text{shear}} = \sqrt{\frac{C_{11} - C_{12}}{2\rho}} \quad \alpha = \frac{1}{\sqrt{2}}, \quad \beta = \frac{1}{\sqrt{2}}; \quad \xi \text{ along } [1\bar{1}0]$$

This is a significant orientation for cubic crystals with regard to the measurement of the elastic constants, since all three elastic constants may be measured by propagating one longitudinal and two shear waves along the $[110]$ direction. Along the $[111]$ direction, the velocity and respective particle velocities are

$$v_1 = v_{\text{long}} = \sqrt{\frac{C_{11} + 2C_{12} + 4C_{44}}{3\rho}} \quad \alpha = \beta = \gamma = \frac{1}{\sqrt{3}}; \quad \xi \text{ along } [111]$$

and

$$v_2 = v_3 = v_{\text{shear}} = \sqrt{\frac{C_{11} - C_{12} + C_{44}}{3\rho}} \quad \alpha + \beta + \gamma = 0;$$

ξ can be any direction in the (111) plane

It has been determined by Parker and Mayer that the sum of the squares of the three velocities in a cubic crystal along any direction of propagation ($v_1^2 + v_2^2 + v_3^2$) is a constant [4]. Therefore, the end point of the propagation vector may lie anywhere in a sphere around the origin, and the sum of the squares of the velocities will be invariant. Thus, once the sum is obtained, only two velocities have to be measured along any directions and the third may be computed.

1.5.2 Elastic Waves in Hexagonal Crystals

For hexagonal crystals or materials exhibiting transverse isotropy, such as sinter-forged or melt-textured high T_c superconductors, a pure longitudinal and two pure transverse waves can be transmitted along the unique axis and any axis perpendicular to it. There are five independent elastic constants for this system:

$$C_{11} = C_{22}, C_{12}, C_{13} = C_{23}, C_{33}, C_{44} = C_{55}, \text{ and } C_{66} = \left(\frac{C_{11} - C_{12}}{2} \right)$$

Along the $[001]$ direction, known as the unique axis,

$$v_1 = v_{\text{long}} = \sqrt{\frac{C_{33}}{\rho}} \quad \xi \text{ along } [001]$$

and

$$v_2 = v_3 = v_{\text{shear}} = \sqrt{\frac{C_{44}}{\rho}} \quad \xi \text{ along any direction in the } (001) \text{ plane.}$$

Along the [100] direction or any other direction perpendicular to the [001] axis,

$$v_1 = v_{\text{long}} = \sqrt{\frac{C_{13}}{\rho}} \quad \xi \text{ along [100]}$$

$$v_2 = v_{\text{shear}} = \sqrt{\frac{C_{44}}{\rho}} \quad \xi \text{ along [001]}$$

and

$$v_3 = v_{\text{shear}} = \sqrt{\frac{C_{11} - C_{12}}{2\rho}} \quad \xi \text{ along [010]}$$

For any wave propagating along the [100] plane, the longitudinal wave will have the particle velocity parallel to its propagation direction; the particle velocity for one shear wave will be parallel to the unique axis. For the other, the particle velocity will be perpendicular to the propagation direction and in the [100] plane.

As discussed earlier, sound velocity measurements are used to determine the elastic constants in single crystals. We saw that measurements along the [110] direction in a cubic crystal can determine all three elastic constants of a cubic crystal. For a hexagonal crystal, there is no unique direction that can determine all five elastic constants, as would be expected since each direction can yield at most three independent equations involving the elastic constants. One might hope that a crystal could be cut as a rectangle parallelogram that could yield at least five independent equations. However, this is not possible. One example is given by the two directions chosen above. A crystal may certainly be cut with [001], [100], and [010] parallel surfaces. However, propagation of sound waves along these directions would only yield four independent equations, as mentioned above. Fortunately, these four equations contain only four of the five elastic constants so that it is possible to solve for them uniquely. In order to determine the fifth one, a wave is transmitted along an axis that is 45° between the [100] and the [001] directions. Thus $l = n = \frac{1}{\sqrt{2}}$ and $m = 0$. The three velocities along this direction would be

$$v_1 = \sqrt{\frac{C_{11} - C_{12} + 2C_{44}}{4\rho}}$$

and

$$v_{2,3} = \sqrt{\frac{\frac{C_{11} + C_{33} + 2C_{44}}{2} \pm \sqrt{\left(\frac{C_{11} - C_{33}}{2}\right)^2 + (C_{33} + C_{44})^2}}{2\rho}}$$

For these three velocities, the particle velocities have the direction cosines

$$v_1 : \beta = 1, \text{ shear,}$$

$$v_2 : \alpha = \gamma \left[\frac{C_{11} - C_{33}}{2(C_{13} + C_{44})} + \sqrt{1 + \left(\frac{C_{11} - C_{33}}{2(C_{13} + C_{44})}\right)^2} \right]$$

and

$$v_3 : \alpha = -\gamma \left[\frac{C_{33} - C_{11}}{2} + \sqrt{1 + \left(\frac{C_{11} - C_{33}}{2(C_{13} + C_{44})}\right)^2} \right]$$

Together with the relation for direction cosines, $\alpha^2 + \beta^2 + \gamma^2 = 1$, the preceding equations uniquely determine the values for u , v , and w for each of the waves. It is easy to see that v is a shear wave, since the particle motion is along the y -axis and perpendicular to the propagation direction. Remembering that the particle motions for the three waves have to be mutually orthogonal, we can conclude that $\beta = 0$ for both v_2 and v_3 . Thus, their particle motion is contained in the x, z plane. If c_{11} is nearly equal to C_{33} , then, the above equations for particle motion reduce to

$$v_2 : \alpha \cong \gamma \text{ pseudo-longitudinal}$$

and

$$v_3 : \alpha \cong -\gamma \text{ pseudo-shear.}$$

However, if this is not the case then a longitudinal or shear transducer will couple to both types of waves and acoustic birefringence occurs. But, experimentally, it is possible to discriminate between the two types of waves being generated, since a longitudinal transducer will couple more strongly to v_2 and a shear transducer will couple more strongly to v_3 . A similar technique may be extended to crystals of lower symmetry for measurements of their elastic constants. For the hexagonal, tetragonal (six and seven elastic constants), and trigonal systems, the sum of the squares of the velocity is constant only for a given definite cosine about the c -axis. Therefore, the wave propagation vector has to describe cones around the unique axis for this sum to be constant [4].

1.5.3 Elastic Waves in Isotropic Media

1.5.3.1 Elastic Isotropy. We start with the wave equation for a cubic crystal, which we can write down by inspection of the matrix equations for the wave velocities,

$$\rho \frac{\partial^2 u}{\partial t^2} = C_{11} \frac{\partial^2 u}{\partial x^2} + C_{44} \left(\frac{\partial^2 u}{\partial y^2} + \frac{\partial^2 u}{\partial z^2} \right) + (C_{12} + C_{44}) \left(\frac{\partial^2 v}{\partial x \partial y} + \frac{\partial^2 w}{\partial x \partial z} \right)$$

$$\rho \frac{\partial^2 v}{\partial t^2} = C_{11} \frac{\partial^2 v}{\partial y^2} + C_{44} \left(\frac{\partial^2 v}{\partial x^2} + \frac{\partial^2 v}{\partial z^2} \right) + (C_{12} + C_{44}) \left(\frac{\partial^2 u}{\partial x \partial y} + \frac{\partial^2 w}{\partial y \partial z} \right)$$

and

$$\rho \frac{\partial^2 w}{\partial t^2} = C_{11} \frac{\partial^2 w}{\partial z^2} + C_{44} \left(\frac{\partial^2 w}{\partial x^2} + \frac{\partial^2 w}{\partial y^2} \right) + (C_{12} + C_{44}) \left(\frac{\partial^2 u}{\partial x \partial z} + \frac{\partial^2 v}{\partial y \partial z} \right)$$

By adding and subtracting the proper terms, the first of these equations can be rewritten as follows,

$$\begin{aligned} \rho \frac{\partial^2 u}{\partial t^2} &= C_{11} \frac{\partial^2 u}{\partial x^2} + C_{44} \left(\frac{\partial^2 u}{\partial y^2} + \frac{\partial^2 u}{\partial z^2} + \frac{\partial^2 u}{\partial x^2} \right) - C_{44} \frac{\partial^2 u}{\partial x^2} \\ &\quad + (C_{12} + C_{44}) \frac{\partial}{\partial x} \left(\frac{\partial v}{\partial y} + \frac{\partial w}{\partial z} + \frac{\partial u}{\partial x} \right) - (C_{12} + C_{44}) \frac{\partial^2 u}{\partial x^2} \end{aligned}$$

or

$$\rho \frac{\partial^2 u}{\partial t^2} = (C_{11} - C_{12} - 2C_{44}) \frac{\partial^2 u}{\partial x^2} + C_{44} \nabla^2 u + (C_{12} + C_{44}) \frac{\partial}{\partial x} \nabla \cdot \vec{S} \quad (1.6)$$

where $\vec{s} = u\vec{i} + v\vec{j} + w\vec{k}$. Elastic isotropy is obtained if $C_{11} - C_{12} = 2C_{44}$ because then the first term in Eq. 1.6 drops out and we can now write the whole sum for the three components as

$$\begin{aligned} \rho \frac{\partial^2 \vec{s}}{\partial t^2} &= C_{44} \nabla^2 \vec{s} + (C_{12} + C_{44}) \left(\vec{i} \frac{\partial}{\partial x} + \vec{j} \frac{\partial}{\partial y} + \vec{k} \frac{\partial}{\partial z} \right) \nabla \cdot \vec{s} \\ &= C_{44} \nabla^2 \vec{s} + (C_{12} + C_{44}) \nabla \nabla \cdot \vec{s} \end{aligned}$$

Using the vector identity,

$$\nabla^2 \vec{s} = \nabla \nabla \cdot \vec{s} - \nabla \times \nabla \times \vec{s} \quad (1.7)$$

we finally obtain the Christoffel–Pochhammer wave equation for compressible isotropic media:

$$\rho \frac{\partial^2 \vec{s}}{\partial t^2} = (C_{12} + 2C_{44}) \nabla \nabla \cdot \vec{s} - C_{44} \nabla \times \nabla \times \vec{s} \quad (1.8)$$

This equation is invariant under rotation.

The condition imposed on the cubic wave equation for elastic isotropy was $C_{11} - C_{12} = 2C_{44}$. In fact, the elastic anisotropy factor, A , is defined as the ratio of the two sides of Eq. 1.8:

$$A = \frac{2C_{44}}{C_{11} - C_{12}}$$

Furthermore, according to Cauchy, in a crystal of cubic symmetry if all the interatomic forces act along lines joining the centers of the atoms, as may be found in some ionic crystals, then $C_{12} = C_{44}$. If the cubic crystal were elastically isotropic then $C_{11} = 3C_{44}$ and then the velocity of the transverse wave would be equal to $\frac{v_s}{v_l} = \left(\frac{1}{3}\right)^{1/2} = 0.577$ times the velocity of the longitudinal wave. The usual value is $1/2$.

Using the isotropy condition, $C_{11} - C_{12} = 2C_{44}$, the Lamé constants are defined as $\mu \equiv C_{44}$ and $\lambda \equiv C_{12}$, and therefore, $C_{11} = 2C_{44} + C_{12} = 2\mu + \lambda$. If we note that the change in volume, V , of a rectangular parallelepiped undergoing strains, ϵ_{xx} , ϵ_{yy} and ϵ_{zz} , is given by

$$\Delta = \frac{dV}{V} = \epsilon_{xx} + \epsilon_{yy} + \epsilon_{zz} = \Delta \cdot \vec{S} \quad (1.9)$$

Then, the generalized Hooke's law for an isotropic crystal may be rewritten as

$$\begin{aligned} \sigma_{xx} &= \lambda \Delta + 2\mu \epsilon_{xx}, \\ \sigma_{yy} &= \lambda \Delta + 2\mu \epsilon_{yy}, \\ \sigma_{zz} &= \lambda \Delta + 2\mu \epsilon_{zz}, \\ \sigma_{yz} &= \mu \epsilon_{yz}, \\ \sigma_{zx} &= \mu \epsilon_{zx}, \end{aligned} \quad (1.10)$$

and

$$\sigma_{xy} = \mu \epsilon_{xy}$$

1.5.3.2 Young's Modulus, Poisson Ratio, and Bulk Modulus. Young's modulus is defined with the help of Figure 1.6, where the cylinder is stressed along the x -direction, while the surfaces are stress free in the y - and z -directions. Young's modulus is given by

$$y = \frac{\sigma_{xx}}{\epsilon_{xx}}.$$

Placing these conditions in Eqs. 1.9 and 1.10, we find

$$y = \mu \frac{(3\lambda + 2\mu)}{\lambda + \mu}$$

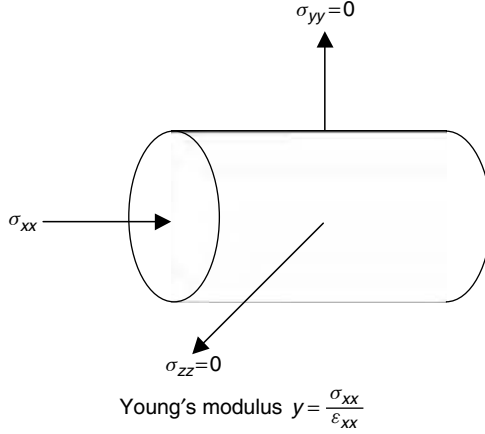


FIG. 1.6. Cylinder for deriving Young's modulus.

The Poisson ratio is defined as

$$\nu = \frac{-\epsilon_{yy}}{\epsilon_{xx}} = \frac{\lambda}{2(\lambda + \mu)}$$

For discussion, this may be rewritten as

$$\nu = \frac{1}{2\left(1 + \frac{\mu}{\lambda}\right)}$$

Thus, the Poisson ratio depends on the ratio of the two Lamé constants. A substance with a shear constant equal to zero has $\nu = 1/2$. This value of ν conserves the total volume, as may be seen in Figure 1.6. Liquids have $\nu = 1/2$, and even soft rubber has $\nu = 1/2$. If μ approaches infinity, then ν approaches zero. If the Cauchy conjecture for central forces is used, then $\mu = \lambda$ and $\nu = 0.25$. As may be seen in the next section, the ratio of the two velocities is given by

$$\frac{v_s}{v_l} = \frac{\mu}{\lambda + 2\mu} = \frac{\frac{1}{2} - \nu}{1 - \nu}$$

In most isotropic homogeneous solid substances the usual value for the Poisson ratio is $\frac{1}{3}$. This yields a value of $1/2$ for the ratio of the velocity of a transverse wave to a longitudinal wave in an isotropic medium. As a rule, transverse waves are slower than longitudinal waves and usually travel at half the speed.

The bulk modulus, K , is defined as the ratio of a uniform pressure or stress divided by the change in volume. As seen in Figure 1.7, this may be

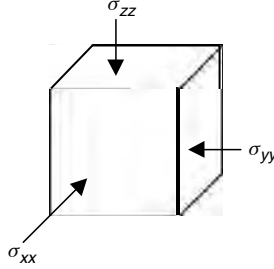


FIG. 1.7. Cube for deriving bulk modulus.

written as

$$K = \frac{p}{\Delta} = \frac{\sigma_{xx}}{\Delta} = \frac{\sigma_{yy}}{\Delta} = \frac{\sigma_{zz}}{\Delta}$$

Using Eqs. 1.9 and 1.10, we see that

$$\sigma_{xx} + \sigma_{yy} + \sigma_{zz} = 3\Delta\Delta + 2\mu\Delta + 3\sigma_{xx}$$

and, therefore

$$K = \lambda + \frac{2}{3}\mu$$

1.5.3.3 Wave Equations. Using the vector identity in Eq. 1.7, and the relation for the dilatation in Eq. 1.9, $\Delta = \Delta \cdot \vec{s}$, the Christoffel–Pochhammer wave equation, Eq. 1.8, may be rewritten in terms of the Lamé constants as

$$\rho_0 \frac{\partial^2 \mu}{\partial t^2} = (\lambda + \mu) \nabla \Delta + \mu \Delta^2 \vec{s} \quad (1.11)$$

For displacement in the x -direction, this may be rewritten as

$$\rho_0 \frac{\partial^2 u}{\partial t^2} = (\lambda + \mu) \frac{\partial}{\partial x} \left(\frac{\partial u}{\partial x} + \frac{\partial v}{\partial y} + \frac{\partial w}{\partial z} \right) + \mu \left(\frac{\partial^2 u}{\partial x^2} + \frac{\partial^2 v}{\partial y^2} + \frac{\partial^2 w}{\partial z^2} \right)$$

For a longitudinal wave,

$$u = u_0 e^{i(\omega t - k_x x)}$$

and

$$\rho_0 \omega^2 = (\lambda + 2\mu) k_x^2$$

or

$$v_l = \frac{\omega^2}{k_x^2} = \frac{\lambda + 2\mu}{\rho_0}$$

and in terms of the bulk modulus, K , this may be rewritten as

$$v_l^2 = \frac{K + \frac{4}{3}\mu}{\rho_0}$$

For transverse waves polarized in the x -direction and propagation in the y -direction,

$$u = u_0 e^{i(\omega t - k_y y)}$$

and

$$v_l^2 = \frac{\omega^2}{k_y^2} = \frac{\mu}{\rho_0}$$

Because the medium is isotropic and homogeneous, there are only two types of bulk waves that may propagate through it: a longitudinal wave with velocity $v_l = \sqrt{\frac{\lambda+2\mu}{\rho_0}}$ and a transverse wave with velocity $v_s = \sqrt{\frac{\mu}{\rho_0}}$. Although the x -direction was chosen for the above derivation, had any other direction been chosen the results would have been exactly the same because of the isotropy condition.

Manipulations of the Christoffel–Pochhammer equation provide some insight into the nature of longitudinal waves and transverse or shear waves in an isotropic medium which could be extended to pure longitudinal and transverse waves in single crystals.

1.5.3.3.1 Longitudinal Waves. Longitudinal waves are irrotational dilatational waves. The fact that longitudinal waves are dilatational may be seen by taking the divergence of the Christoffel–Pochhammer wave equation, Eq. 1.11:

$$\begin{aligned} \rho_0 \frac{\partial^2 \nabla \cdot \vec{s}}{\partial t^2} &= (\lambda + \mu) \nabla \cdot \nabla \Delta + \mu \nabla \cdot (\nabla \cdot \nabla) \vec{s} \\ &= (\lambda + \mu) \nabla \cdot \nabla \Delta + \mu \nabla \cdot \nabla \nabla \cdot \vec{s} \\ \rho_0 \frac{\partial^2 \Delta}{\partial t^2} &= (\lambda + 2\mu) \nabla^2 \Delta \end{aligned}$$

Therefore, the velocity of the dilatational wave is $\sqrt{\frac{\lambda+2\mu}{\rho}}$. Because this is the velocity of a longitudinal wave and there are only two possible waves that can propagate through the bulk of an isotropic medium, it follows that the dilatational wave is a longitudinal wave.

The irrotational nature of longitudinal waves may be shown by considering a wave whose displacements exhibit no rotation. Namely, $\nabla \times \vec{s} = \vec{\omega} = 0$, but $\nabla \neq 0$. Then, \vec{s} may be expressed as the gradient of a potential $\vec{s} = \Delta \phi$. Now

Eq. 1.11 becomes

$$\begin{aligned}\rho_0 \frac{\partial^2 \nabla \phi}{\partial t^2} &= (\lambda + \mu) \nabla (\nabla \cdot \nabla \phi) + \mu (\nabla \cdot \nabla \nabla \phi) \\ \nabla \rho \frac{\partial^2 \phi}{\partial t^2} &= (\lambda + 2\mu) \nabla (\nabla \cdot \nabla \phi)\end{aligned}$$

Therefore,

$$\rho \frac{\partial^2 \phi}{\partial t^2} = (\lambda + 2\mu) \nabla^2 \phi$$

This yields a velocity of $\sqrt{\frac{\lambda+2\mu}{\rho}}$, which is that of a longitudinal wave; therefore, a longitudinal wave is an irrotational dilatational wave.

1.5.3.3.2 Transverse Waves. Transverse waves are equivoluminal (nondilatational), distortional (rotational) waves. It can be shown that transverse waves are distortional or rotational waves by taking the curl of Eq. 1.11:

$$\rho \frac{\partial^2 \nabla \times \vec{s}}{\partial t^2} = (\lambda + 2\mu) \nabla \times \nabla \Delta - \mu \nabla \times \nabla \times \nabla \times \vec{s}$$

The first term on the right-hand side vanishes since $\nabla \times \nabla = 0$. And, remembering that $\nabla \times \vec{s} = \vec{\omega}$,

$$\rho \frac{\partial^2 \vec{\omega}}{\partial t^2} = -\mu \nabla \times \nabla \times \vec{\omega}$$

which, after noting that $\nabla \nabla \cdot \vec{\omega} = \nabla \cdot \nabla \times \vec{s} = 0$ and using Eq. 1.7, reduces to

$$\rho \frac{\partial^2 \vec{\omega}}{\partial t^2} = \mu \nabla^2 \vec{\omega}$$

This yields the velocity of a transverse wave and, therefore, transverse waves are rotational or distortional.

It is simple to show that transverse waves are equivoluminal. If Δ is set equal to zero in Eq. 1.11, then this equation becomes

$$\rho \frac{\partial^2 \vec{s}}{\partial t^2} = -\mu \nabla^2 \vec{s}$$

Again, the wave velocity of a transverse wave is obtained and it may be concluded that a transverse wave is equivoluminal or nondilatational, and distortional or rotational in an isotropic homogeneous medium.

Although the above characteristics were derived for isotropic media, they may also be attributed to pure longitudinal and transverse waves in single

crystals: pure longitudinal waves are dilatational and irrotational, and pure transverse waves are equivoluminal and distortional.

1.6 Absorption

Although Eq. 1.1 describes the relation between stress and strain in an elastic solid, it does not take into account the possible absorption of energy by the medium during sound wave propagation through the medium. A convenient model to account for this absorption is to assume that the energy loss is being produced by a process that is dependent on the time derivative of the strains, such as a viscous process. In this case, Eq. 1.1 can be recast as

$$\sigma_i = c_{ij} \epsilon_j + c'_{ij} \dot{\epsilon}_j \quad (1.12)$$

where $\dot{\epsilon}_j$ is the time derivative of the strain and c'_{ij} are the associated loss constants. The c'_{ij} have the same symmetry characteristics as the c_{ij} .

Let us now apply Eq. 1.12 to an isotropic material with viscous losses in order to find relations between absorption coefficients and these elastic loss constants. For an isotropic medium, Eq. 1.12 reduces to

$$\begin{aligned} \sigma_1 &= \lambda \Delta + 2\mu \epsilon_1 + \mu_1 \dot{\Delta} + 2\mu_0 \dot{\epsilon}_1 \\ \sigma_2 &= \lambda \Delta + 2\mu \epsilon_2 + \mu_1 \dot{\Delta} + 2\mu_0 \dot{\epsilon}_2 \\ \sigma_3 &= \lambda \Delta + 2\mu \epsilon_3 + \mu_1 \dot{\Delta} + 2\mu_0 \dot{\epsilon}_3 \\ \sigma_4 &= \mu \epsilon_4 + \mu_0 \dot{\epsilon}_4 \\ \sigma_5 &= \mu \epsilon_5 + \mu_0 \dot{\epsilon}_5 \text{ and} \\ \sigma_6 &= \mu \epsilon_6 + \mu_0 \dot{\epsilon}_6 \end{aligned} \quad (1.13)$$

where μ_0 is the shear viscosity and μ_1 is the dilatational coefficient of viscosity. In the above, we have made use of Eq. 1.10 in the reduced notation described in Eq. 1.1 and $\dot{\Delta} = \frac{\partial}{\partial t}(\epsilon_{xx} + \epsilon_{yy} + \epsilon_{zz}) = \frac{\partial}{\partial t}(\epsilon_1 + \epsilon_2 + \epsilon_3)$ and $\dot{\epsilon}_i = \frac{\partial}{\partial t} \epsilon_i$

1.6.1 Plane Shear Waves

For a plane sinusoidal shear wave propagating in the z -direction with the particle motion in the y -direction, the equation of motion can be written as

$$\rho \frac{\partial^2 v}{\partial t^2} = \frac{\partial \sigma_4}{\partial z}$$

and for $v = v_0 e^{i(\omega t - kz)}$, where $k = k_1 + ik_2$,

$$-\rho\omega_2 v = -k^2(\mu v + i\omega\mu_0 v)$$

Therefore,

$$\begin{aligned} k^2 &= \frac{\rho\omega^2}{\mu + i\omega\mu_0} \\ k &= \frac{\frac{\omega}{\sqrt{\mu/\rho}}}{\sqrt{1 + \frac{i\omega\mu_0}{\mu}}} = k_1 + ik_2 \end{aligned} \quad (1.14)$$

and

$$v = v_0 e^{i(\omega t - k_1 z)} + k_2 z$$

If $\frac{\omega\mu_0}{\mu} \ll 1$, then Eq. 1.14 becomes

$$k_1 \cong \frac{\omega}{\sqrt{\mu/\rho}} = \frac{\omega}{v_s}$$

and

$$k_2 \cong -\frac{\omega^2\mu_0}{2\rho v_s^3}$$

and because the attenuation coefficient, α , is proportional to the energy absorption, then $\alpha = -2k_2$ and

$$\alpha = \frac{\omega^2\mu_0}{\rho v_s^3}$$

If α is measured, then

$$\mu_0 = \frac{\alpha\rho v_s^3}{\omega^2}$$

For larger values the binomial expansion is not valid, so one has to solve Eq. 1.14 obtaining

$$k = k_1 + k_2 = \frac{\omega}{\sqrt{\frac{\mu}{\rho}}} \frac{1}{\left[1 + \left(\frac{\omega\mu_0}{\mu}\right)^2\right]^{1/4}} \left(\cos \frac{\theta}{2} - i \sin \frac{\theta}{2}\right)$$

where $\tan \theta = \frac{\omega\mu_0}{\mu}$.

1.6.2 Plane Longitudinal Waves

For a plane longitudinal wave propagating in the x -direction,

$$\begin{aligned} u &= u_0 e^{i(\omega t - kx)}, \\ \rho \frac{\partial^2 u}{\partial t^2} &= \frac{\partial \sigma_1}{\partial x} = \lambda \frac{\partial^2 u}{\partial x^2} + 2\mu \frac{\partial^2 u}{\partial x^2} + \frac{\partial}{\partial t} \left[\mu_1 \frac{\partial^2 u}{\partial x^2} + 2\mu_0 \frac{\partial^2 u}{\partial x^2} \right] \\ -\rho \omega^2 &= -(\lambda + 2\mu)k^2 - i\omega k^2(\mu_1 + 2\mu_0) \end{aligned}$$

and

$$\rho \omega^2 = (\lambda + 2\mu)k^2 \left[1 - i\omega \left(\frac{\mu_1 + 2\mu_0}{\lambda + 2\mu} \right) \right]$$

Remembering that

$$v_l^2 = \frac{\lambda + 2\mu}{\rho}$$

then

$$\begin{aligned} k^2 &= \frac{1}{v_l^2} \frac{\omega^2}{\left[1 - i\omega \left(\frac{\mu_1 + 2\mu_0}{\lambda + 2\mu} \right) \right]} \\ k &= \frac{1}{v_l} \frac{\omega}{\left[1 - i\omega \left(\frac{\mu_1 + 2\mu_0}{\lambda + 2\mu} \right) \right]^{1/2}} \end{aligned}$$

and

$$\begin{aligned} k_1 + ik_2 &= \frac{\omega}{v_l} + \frac{1}{2} \frac{\omega^2}{v_l} i \left(\frac{\mu_1 + 2\mu_0}{\lambda + 2\mu} \right) \\ &\cong \frac{\omega}{v_l} + \frac{1}{2} \frac{\omega^2}{\rho v_l^3} i (\mu_1 + 2\mu_0) \\ k_1 &= \frac{\omega}{v_l} \end{aligned}$$

and

$$k_2 = \frac{1}{2} \frac{\omega^2}{\rho v_l^3} i (\mu_1 + 2\mu_0) \quad 1.15)$$

Remembering that the bulk modulus $K = \lambda + \frac{2}{3}\mu$, we may define a bulk viscosity, μ_2 , as

$$\mu_2 = \mu_1 + \frac{2}{3}\mu_0$$

and now Eq. 1.15 may be rewritten in terms of μ_2 as

$$k_2 = \frac{1}{2} \frac{\omega^2}{\rho v_l^3} \left(\mu_2 + \frac{4}{3} \mu_0 \right)$$

For certain cases, such as ideal gases and free electrons, $\mu_2 = 0$ and then

$$k_2 = \frac{2}{3} \frac{\omega^2}{\rho v_l^3} \mu_0$$

for longitudinal waves as compared to

$$k_2 = \frac{1}{2} \frac{\omega^2}{\rho v_s^3} \mu_0$$

for shear waves. Thus, the ratio of the attenuation for shear waves to that for longitudinal waves is given by

$$\frac{\alpha_s}{\alpha_l} = \frac{3}{4} \left(\frac{v_l}{v_s} \right)^3$$

and if our rule of thumb holds that $v_l \cong 2v_s$, then

$$\frac{\alpha_s}{\alpha_l} \cong 6$$

1.6.3 Attenuation, Energy, and Quality Factor

The energy attenuation coefficient, α , was obtained directly from the wave equation by adding a loss term that had an odd number of partial derivatives which immediately introduced an imaginary component to the resulting equation for a harmonic wave. This yields a complex wave vector that results in the decay of the wave's amplitude. This decay factor is given by k_2 which, in turn, means that the intensity of the wave is attenuated by $\alpha = 2k_2$ in a unit distance, since the intensity is proportional to the square of the amplitude.

There is another straightforward approach for evaluating the absorption coefficient, α , if we start with the relation for the energy in a decaying wave,

$$E = E_0 e^{-\alpha' t}$$

where E_0 is the initial energy, E is the instantaneous energy, t is the time, and α' is the attenuation per unit time. Then the rate of energy loss, Q , is given by

$$Q = \frac{\partial E}{\partial t} = -\alpha' E_0 e^{-\alpha' t} = -\alpha' E$$

and

$$\alpha' = -\frac{Q}{E}$$

and to convert the attenuation-per-unit time, α' , to the attenuation-per-unit distance, we divide α' by v , the velocity of sound. Thus,

$$\alpha = \frac{\alpha'}{v} = -\frac{Q}{vE}$$

Therefore, in some instances it may be more convenient to derive a relation for the attenuation coefficient by evaluating the rate of energy loss and dividing it by the energy in the wave and the velocity of sound. For examples of this approach see Pippard and Levy [7, 8].

The attenuation coefficient may be measured directly by observing the decay of the oscillations of a vibrating object, or the decay of a pulse or traveling wave through a medium. However, it is also possible to obtain the attenuation coefficient from the shape of a resonance curve plotted as a function of the imposed sound frequency. The quality factor of such a curve is defined as

$$Q = \frac{\omega_0}{\omega_2 - \omega_1}$$

where ω_0 is the resonant frequency, and ω_2 and ω_1 are the two frequencies, respectively, above and below the resonance at which the average power has dropped to one-half its resonance value.

In terms of α' and α , Q is given by

$$Q = \frac{\omega_0}{\alpha'} = \frac{\omega_0}{\alpha v}$$

And, therefore,

$$\alpha = \frac{\omega_0}{Qv}$$

Since $\alpha' = \frac{1}{\tau}$, where τ is the decay time of a wave, then $2Q = \frac{\omega_0 \tau}{\pi}$ or $2Q$ is equal to the number of cycles it takes for the amplitude wave to decay to $\frac{1}{e}$ of its original value.

1.7 Group Velocity

Until now we have been discussing the velocity of an infinite sinusoidal wave that is given by the phase velocity

$$v = \frac{\omega}{k}$$

In some measurements, it is convenient to use a pulsed signal instead of a continuous one. The velocity of the wave packets, or pulses, is given by the group velocity that in one dimension can be written as

$$v_g = \left(\frac{d\omega}{dk} \right)_{k_0} \quad (1.16)$$

The derivative is evaluated at the central wave vector of the wave packet. It is assumed that the frequency spectrum contained in the wave packet is narrow. Otherwise, the wave packet frequency spectrum will broaden with time. Remembering that $k = \frac{2\pi}{\lambda}$ and $\omega = kv$, we may derive several equivalent expressions for the group velocity that may be more convenient than Eq. 1.16:

$$v_g = \frac{d}{dk}(vk) = v + k \frac{dv}{dk} = v - \lambda \frac{dv}{d\lambda} = \frac{dv}{d\left(\frac{1}{\lambda}\right)} = \frac{1}{\frac{dk}{d\omega}}$$

Equation 1.16 implies that if there is dispersion in the medium or if a plot of ω versus k is not linear, then the group velocity is not equal to the phase velocity. In this case, the group velocity is given by the slope of the curve of ω versus k . This dispersion, or change in velocity as a function of frequency or wavelength, may be due to intrinsic physical properties of the material or to configuration or geometric factors related to the dimensions of the sample as compared to the sound wavelength. An obvious example of configuration dispersion is observed in the propagation of sound through an isotropic cylindrical rod.

For long wavelengths the sound velocity of longitudinal waves corresponds to that of Young's modulus waves,

$$v_y = \sqrt{\frac{\gamma}{\rho}} = \sqrt{\frac{\mu(3\lambda + 2\mu)}{\rho(\lambda + \mu)}}$$

For short wavelengths, the sound velocity corresponds to that of longitudinal waves propagating through an infinite medium,

$$v_l = \sqrt{\frac{\lambda + 2\mu}{\rho}}$$

Thus, as the frequency is changed, the wavelength changes, and there will be a smooth transition from one velocity to the other resulting in a configuration-dispersion curve.

The group velocity in three dimensions is given by

$$\vec{V}_{\text{group}} = \Delta_k \omega(\vec{k})$$

It is important to emphasize that, in general, for an elastic wave propagating in an anisotropic solid, the phase and group velocities of the wave are not equal even if there is no dispersion.

1.8 Phenomenological Relations between Phase Velocity and Attenuation

For a plane wave propagating in the x -direction, the particle motion may be given by

$$u = u_0 e^{i(\omega t - kx)} \quad (1.17)$$

If this is to be a solution of the wave equation, then we must have

$$k^2 V^2 = \omega^2 \quad (1.18)$$

It is possible to obtain relations between the phase velocity of the attenuated harmonic wave and the attenuation coefficient by assuming that V is complex.

$$V = V_r + i V_i \quad (1.19)$$

where V_r is the real part and V_i is the imaginary part of the velocity. Let us first assume that in Eq. 1.19, ω is real and therefore k is complex,

$$k = k_r - i\alpha \quad (1.20)$$

and then the particle motion in Eq. 1.17 is

$$u = u_0 e^{-\alpha x} e^{i(\omega t - k_r x)}$$

This is a spatially attenuated wave. The phase velocity, V_p , of the wave is now given by

$$V_p = \frac{\omega}{k_r} \quad (1.21)$$

Substituting Eqs. 1.19 and 1.20 into Eq. 1.18, we find

$$(k_r^2 - \alpha^2 - 2ik_r\alpha)(V_r^2 - V_i^2 + 2iV_rV_i) = \omega^2$$

Solving this, we find

$$\alpha = \frac{\omega V_i}{V_r^2 + V_i^2} = \frac{\omega V_i}{|V|^2} \quad (1.22)$$

and

$$k_r = \frac{\omega V_r}{V_r^2 + V_i^2} = \frac{\omega V_r}{|V|^2} \quad (1.23)$$

Therefore, the phase velocity from Eq. 1.21 becomes

$$V_p = \frac{|V|^2}{V_r} \quad (1.24)$$

If $\frac{|V|^2}{V_r}$ is independent of frequency, the medium through which the sound passes is said to be nondispersive. However, most absorption mechanisms do depend on frequency, and consequently, V_p varies with frequency. Therefore, the medium is said to be dispersive. We can write Eq. 1.10a in a more convenient form,

$$V_p = V_r \left(1 + \frac{V_i^2}{V_r^2} \right) \quad (1.25)$$

in order to determine the relation between V_p and α when $V_i \ll V_r$. In this case, Eqs. 1.22 and 1.23 become

$$\alpha \cong \frac{\omega V_i}{V_r^2}$$

and

$$k_r \cong \frac{\omega}{V_r}$$

Making the appropriate substitutions, Eq. 1.25 becomes

$$V_p = V_r \left[1 + \frac{\alpha^2}{k_r^2} \right] \quad (1.26)$$

Thus, in the absence of absorption, $V_p = V_r$, and as absorption is increased then the phase velocity is increased first according to Eq. 1.26 and then according to Eq. 1.29.

The preceding analysis applies to a traveling wave. For a standing wave we should assume that k is real and ω complex.

$$\omega = \omega_r + i\omega_i$$

and then

$$u = u_0 e^{-\omega_i t} e^{i(\omega_r t - kx)}$$

yielding a temporally damped harmonic wave. Going through the same procedure, we find

$$\omega_i = k V_i$$

and

$$\omega_r = k V_r$$

and for standing waves the phase velocity becomes

$$V_p = \frac{\omega_r}{k} = V_r$$

Again, it should be emphasized that this independence of the phase velocity from attenuation applies only to standing waves.

1.9 Units

The contributors to this book have been encouraged to use SI units wherever practicable. However, there is a wide diversity in the specialties that are covered, and each has adopted a set of units that is most useful or common in its field. Therefore, the authors present the data in the units that have been adopted by their particular field. In all cases, they provide the appropriate conversion factors for converting their data into SI units. SI stands for *Système International* (International System), formerly called the meter-kilogram-second (MKS) system. In any case, useful conversions are included in the front matter of this volume (p. xxi).

This work was supported by the Office of Naval Research.

References

1. Christoffel, E.W. (1877). *Annali di matematica pura ed. Applicata Ser II* **8**: 193.
2. Burns, G., and Glazer, A.M. (1990). *Space Groups for Solid State Scientists*, second edition, p. 343, New York: Academic Press.
3. Kittel, C. (1956). *Introduction to Solid State Physics*, second edition, p. 617, New York: John Wiley and Sons, Inc.
4. Parker, P.M., and Mayer, W.G. (1962). Method for the determination of elastic constants for some crystallographic groups. *Acta Crystallogr.* **15**: 334–336.
5. Mason, W.P. (1950). *Physical Acoustics and the Propagation of Solid*, p. 402, Princeton: D. Van Northround Company, Inc.
6. Landau, L.D., and Lifshitz, E.M. (1970). *Theory of Elasticity*, second edition, London: Pergamon Press.
7. Pippard, A.B. (1955). Ultrasonic attenuation in metals. *Philos. Mag.* **46**: 1104–1114.
8. Levy, M. (1963). Ultrasonic attenuation in superconductors for $ql < 1$. *Phys. Rev.* **131-2**: 1497–1500.

This Page Intentionally Left Blank

2. POINT-SOURCE/POINT-RECEIVER METHODS

A. G. Every

Department of Physics
University of the Witwatersrand
Johannesburg, South Africa

K. Y. Kim and W. Sachse

Department of Theoretical and Applied Mechanics
Cornell University
Ithaca, New York

2.1 Introduction

This chapter deals with a suite of techniques that elicit information on the elastic properties of solids using pointlike excitation and detection of ultrasound. These point-source/point-receiver (PS/PR) techniques have shown great promise in several materials' inspection and characterization applications. One of their advantages is that a point source generates both longitudinal and shear waves in a specimen, and therefore information about both types of waves can, in principle, be extracted from a single waveform. Furthermore, PS/PR signals are simultaneously propagated in a wide range of directions in a specimen, and so one can use an array of sensors or scan either the source or the receiver over the specimen surface to determine the directional dependence of the speeds of propagation and amplitudes of various wave modes in a material. When a repetitive source is used, a number of signals measured at adjacent source–receiver configurations can be stacked together to obtain a so-called *scan image*, which portrays the detailed spatial and temporal characteristics of the elastic wavefield in a material, and this can be directly related to the material's anisotropy and macrostructure [1]. Although PS/PR techniques offer the advantage of simplicity in sample preparation and data collection, there is a trade-off, and that is added complexity in extracting information about the sample from the wavefield data.

The term PS/PR usually attaches to a technique that delivers acoustic energy to a region comparable in size to, or smaller than, the characteristic wavelength radiated, and to detection of the wavefield within a similarly small area. Incoherent excitation over a larger region, as occurs in phonon imaging [2, 3], can be categorized as PS/PR, provided that the coherence length is sufficiently

small and the observation distance is much greater than the source size. An essential characteristic of point excitation is that, instead of waves of a single wave normal being excited, as is the case with conventional pulse-echo techniques, the waveform is a superposition of waves with a broad spread of wave normals. Radiation of acoustic energy consequently takes place in a wide range of directions, and detection has similar wide-angle sensitivity. These techniques, in essence, measure a time or frequency domain dynamic Green's function (response function) of the solid. As such, PS/PR techniques explore phenomena that are not normally encountered in plane wave techniques. For an impulsive or suddenly applied force, the response displays a number of wave arrival singularities, which propagate outwards from the source at group velocity in each direction. Periodic excitation reveals internal diffraction effects. In the far field, the wave arrival rays and associated acoustic energy focusing dominate the observations. Transient techniques can be considered simulated acoustic emission [4]; they produce similar waveforms to actual acoustic emission or seismic events, but in a more controlled way.

There are a number of techniques available for performing PS/PR measurements. The fracture of a very small capillary [5, 6] or pencil lead [7] on the surface of a sample simulates a point force acting normal to the surface and having a step function time dependence. A focused pulsed laser beam of sufficient energy to cause ablation of a specimen's surface simulates a point impulse normal to that surface, and a horizontal double force is realized when the pulsed laser beam operates in the thermoelastic regime [8–10]. Much the same effect can be achieved with electron beams [11] and x-rays [12]. Pointlike detection can be achieved, for example, with piezoelectric “pinducers,” with small capacitive detectors [6], or by laser interferometry [13–15]. Focusing an acoustic beam through a transmission fluid onto a surface allows pulsed or periodic forces to be generated and surface displacements to be detected [16–20]. Optical techniques for excitation and detection have the advantage of being noncontact. Discussion of the comparative operational characteristics of a number of sources and receivers that can be used in PS/PR measurements can be found in [21].

To date, ultrasonic PS/PR measurements of elastic constants have been carried out on a number of crystals (see, e.g., [22–31]) and also on a variety of polymer and ceramic–ceramic matrix composite specimens (see, e.g., [32–35]). In the case of composites, signals possessing excellent signal-to-noise ratio are detected even when the materials exhibit high damping characteristics that make conventional ultrasonic measurements difficult or even impossible.

2.2 Dynamic Green's Functions: Formal Solutions

The phenomena we describe in this chapter, as mentioned earlier, can be interpreted directly or indirectly in terms of dynamic Green's functions. Some

of these phenomena are reasonably well accounted for by the Green's functions for an infinite anisotropic elastic continuum [36–38], whereas for others the surfaces play a vital role. Where necessary we will be treating the effects of surfaces either in an ad hoc matter, or invoke the dynamic Green's function for a half-space [39–42] in the interpretation. Our concluding discussion is on transient waves in thin anisotropic plates.

2.2.1 Infinite Continuum Green's Functions

The space-time response or Green's function $G_{ij}(\mathbf{x}, t)$ for an infinite anisotropic elastic continuum is governed by the equation

$$\left(\rho \delta_{mi} \frac{\partial^2}{\partial t^2} - c_{mki\ell} \frac{\partial^2}{\partial x_k \partial x_\ell} \right) G_{ij}(\mathbf{x}, t) = \delta_{mj} \delta(\mathbf{x}) F(t) \quad (2.1)$$

Physically $G_{ij}(\mathbf{x}, t)$ represents the i 'th Cartesian component of the displacement at point \mathbf{x} and time t in response to a concentrated force in the j 'th direction having time dependence $F(t)$, applied at the origin. The array of responses $G_{ij}(\mathbf{x}, t)$, $i, j = 1, 2, 3$, form a tensor of second rank. The formal solution to Eq. 2.1 in terms of integral transforms has been treated by a number of authors [36–38, 43–47], and the methods have been reviewed by Payton [48]. In brief, by carrying out a quadruple space-time Fourier transform on Eq. 2.1, solving the resultant algebraic equations, and then carrying out the inverse transform, one obtains

$$G_{ij}(\mathbf{x}, t) = \int G_{ij}(\mathbf{x}, \omega) f(\omega) e^{-i\omega t} d\omega \quad (2.2)$$

where

$$G_{ij}(\mathbf{x}, \omega) = \frac{1}{(2\pi)^3} \int d^3\mathbf{k} (L^{-1}(\mathbf{k}, \omega))_{ij} e^{i\mathbf{k} \cdot \mathbf{x}} \quad (2.3)$$

$$L_{mi}(\mathbf{k}, \omega) = c_{mki\ell} k_k k_\ell - \rho \omega^2 \delta_{mi} \quad (2.4)$$

and

$$f(\omega) = \frac{1}{2\pi} \int F(t) e^{i\omega t} dt \quad (2.5)$$

is the Fourier transform of the forcing function. Using the spectral resolution theorem [49], we can write

$$(L^{-1})_{ij} = \sum_{n=1}^3 \frac{\Lambda_{ij}^{(n)}}{\rho v^{(n)2} k^2 - \rho \omega^2} = \sum_{n=1}^3 \frac{s^{(n)2} \Lambda_{ij}^{(n)}}{\rho (k^2 - \omega^2 s^{(n)2})} \quad (2.6)$$

where the sum is taken over the three eigensolutions of the Christoffel tensor $\Gamma_{mi} = c_{mki\ell} n_k n_\ell$, and $v^{(n)}$ is the phase velocity, $s^{(n)} = 1/v^{(n)}$ the slowness, $\Lambda_{ij}^{(n)} = U_i^{(n)} U_j^{(n)}$, and $\mathbf{U}^{(n)}$ is the polarization vector for each mode. The integral over the magnitude of \mathbf{k} can be done analytically [36, 37], leading to the equation

$$G_{ij}(\mathbf{x}, \omega) = \frac{1}{8\pi^2 \rho} \sum_n \left\{ i\omega \int_{\cap} d\Omega s^{(n)3} \Lambda_{ij}^{(n)} e^{i\omega \mathbf{s}^{(n)} \cdot \mathbf{x}} + \frac{1}{x} \int_0^{2\pi} d\phi s^{(n)2} \Lambda_{ij}^{(n)} \right\} \quad (2.7)$$

for the frequency domain Green's function $G_{ij}(\mathbf{x}, \omega)$. The first of the two integrals is with respect to the direction of the slowness $\mathbf{s} = \mathbf{k}/\omega$, and is carried out over the unit hemisphere centered on the observation direction, with $d\Omega$ denoting the element of solid angle in which \mathbf{s} falls. The second integral is a line integral taken around the periphery of this hemisphere.

We evaluate $G_{ij}(\mathbf{x}, t)$ for a point force with step function time dependence

$$F(t) = \Theta(t) = \begin{cases} 0, & t < 0 \\ 1, & t > 0 \end{cases} \quad (2.8)$$

The Fourier transform of $\Theta(t)$ is $f(\omega) = -1/2\pi i\omega + \delta(\omega)/2$, and from Eq. 2.2 it follows that

$$G_{ij}(\mathbf{x}, t) = \frac{1}{8\pi^2 \rho} \sum_n \left\{ -\int_{\cap} d\Omega s^{(n)3} \Lambda_{ij}^{(n)} \delta(t - \mathbf{s} \cdot \mathbf{x}) + \frac{\Theta(t)}{x} \int_0^{2\pi} d\phi s^{(n)2} \Lambda_{ij}^{(n)} \right\}. \quad (2.9)$$

The response to an impulsive force $F(t) = \delta(t)$ is the time derivative of $G_{ij}(\mathbf{x}, t)$, and the response to other force distributions and time dependences can be obtained by integration.

2.2.2 Half-space Green's Functions

We take the Fourier domain surface Green's function for an anisotropic solid as our starting point for calculating the transient response of a half-space, following the method of Every *et al.* [39]. Generalizing to an arbitrary component of surface force, and to the response at an interior point of an anisotropic elastic half-space (*hs*) at a distance x_3 from the surface, we have

$$G_{ij}^{hs}(\mathbf{k}_{\parallel}, x_3, \omega) = \frac{i}{\omega} \sum_{n=1}^3 E_{ij}^{(n)} \exp\{ik_3^{(n)} x_3\} \quad (2.10)$$

$$E_{ij}^{(n)}(\mathbf{s}_{\parallel}) = \frac{\text{adj}(\mathbf{B})_j^{(n)} U_i^{(n)}}{\det |\mathbf{B}|} \quad (2.11)$$

and $\mathbf{s}_{\parallel} = \mathbf{k}_{\parallel}/\omega$. By Fourier transforming with respect to \mathbf{k}_{\parallel} and ω , and replacing the integration variable \mathbf{k}_{\parallel} by \mathbf{s}_{\parallel} , we arrive at the following integral expression:

$$G_{ij}^{hs}(\mathbf{x}, t) = -\frac{1}{4\pi^3} \int_{-\infty}^{\infty} d^2 s_{\parallel} \int_0^{\infty} d\omega \sum_{n=1}^3 E_{ij}^{(n)} \exp\{i\omega(\mathbf{s}_{\parallel} \cdot \mathbf{x}_{\parallel} + s_3^{(n)} x_3 - t)\} + I \quad (2.12)$$

for the response of the medium to a concentrated point force acting on the surface and having step function time dependence $\Theta(t)$. I is an integration constant. Without loss of generality, we can choose the observation point to be in the (x_1, x_3) plane, setting $x_2 = 0$. The integration over ω can be done analytically to yield

$$G_{ij}^{hs}(\mathbf{x}, t) = -\frac{1}{4\pi^3 |\mathbf{x}|} \text{Re} \int_{-\infty}^{\infty} d^2 s_{\parallel} \sum_{n=1}^3 \frac{i E_{ij}^{(n)}(\mathbf{s}_{\parallel})}{s_1 \sin \theta + s_3^{(n)} \cos \theta - t/|\mathbf{x}| + i0_+} + I \quad (2.13)$$

For the surface response ($x_3 = 0$) we can use causality to simplify further, finally obtaining

$$G_{ij}^{hs}(x_1, t > 0) = -\frac{1}{2\pi^2 |x_1|} \text{Re}\{\Phi_{ij}(t/x_1) - \Phi_{ij}(0)\} \quad (2.14)$$

where

$$\Phi_{ij}(s_1) = \int_{-\infty}^{\infty} ds_2 \sum_{n=1}^3 E_{ij}^{(n)}(s_1, s_2) \quad (2.15)$$

Calculated responses are presented later.

2.3 Response to a Periodic Force: Numerical Implementation and Comparison with Experiment

For an isotropic solid the angular integrals in Eq. 2.7 for the infinite continuum response function $G_{ij}(\mathbf{x}, \omega)$ can be performed analytically [4], but for anisotropic solids, except in certain special cases [48], these integrals require numerical methods for their evaluation. The first term in Eq. 2.7, because it involves 2D integration, is the most computationally demanding. The main reason for this is the rapid variation of the phase factor, which necessitates a fine grid size for the integration. Of interest to us here is the far field $\omega s x > 200\pi$ and the intermediate field $200\pi > \omega s x > 2\pi$.

2.3.1 The Far Field

For the far field we invoke the stationary phase approximation and limit the integration to small regions around directions in which the phase $\omega \mathbf{s} \cdot \mathbf{x}$ is

stationary. The contribution from all other directions is negligible because of the rapid phase variation of the integrand and resulting cancellation. At the stationary phase points, the outward normal to the slowness surface, which is the direction of the group velocity \mathbf{V} is parallel to the observation direction \mathbf{x} . Thus, to obtain the response at a point requires identifying the group velocities in that direction.

There are various methods for calculating the group velocity $\mathbf{V} = \nabla_{\mathbf{k}}\omega(\mathbf{k})$ for a wave, all of which involve expressing it parametrically in terms of quantities that are derivable from Christoffel's equation. The more frequently encountered are the following [50–52]. Differentiating Christoffel's equation yields

$$V_i = \frac{1}{\rho v} c_{ijkl} n_k U_j U_l \quad (2.16)$$

\mathbf{V} can also be obtained from the phase velocity equation by implicit differentiation. Arranging this equation to be homogeneous in the components of \mathbf{n} , one has

$$\mathbf{V} = \frac{\partial v}{\partial \mathbf{n}} \quad (2.17)$$

The fact that the group velocity is normal to the constant frequency and slowness surfaces leads to two other expressions for \mathbf{V} :

$$\mathbf{V} = -\frac{\nabla_{\mathbf{k}} D(\mathbf{k}, \omega)}{\partial D / \partial \omega} = \frac{\nabla_{\mathbf{s}} S(\mathbf{s})}{\mathbf{s} \cdot \nabla_{\mathbf{s}} S(\mathbf{s})} \quad (2.18)$$

where the dispersion relation $D(\mathbf{k}, \omega) = 0$ and the slowness equation $S(\mathbf{s}) = 0$.

In these small regions around the stationary phase points, the factor $s^3 \Lambda$ can be taken to be constant, and for a generic point the equation for the slowness surface can be approximated by $s_3 = L_1 s_1^2 + L_2 s_2^2$ in a locally oriented coordinate system with s_3 normal to the surface and s_1 and s_2 along the directions of the principal curvatures of the surface. L_1 and L_2 are the values of these principal curvatures, and their product, $K = L_1 L_2$, is the Gaussian curvature of the surface. The integral can now be performed analytically, yielding a contribution to $G_{ij}(\mathbf{x}, \omega)$ of the form [37, 44]

$$G \approx \frac{s \Lambda e^{i\omega \mathbf{s} \cdot \mathbf{x}}}{\rho x \sqrt{|L_1 L_2|}} \quad (2.19)$$

for each stationary phase point. The intensity or energy flux I associated with each contribution is proportional to $|G|^2$, and thus

$$I \approx \frac{1}{x|K|} \quad (2.20)$$

We will see that this result has a simple geometrical interpretation on the basis of ray acoustics, and that the variation of K in an anisotropic solid can have striking consequences.

2.3.2 Phonon Imaging

The acoustic anisotropy of crystals is revealed in a most graphic way in phonon imaging [2]. In this technique a focused laser or electron beam is used to heat a small spot on the surface of a single crystal specimen maintained at an ambient temperature of $\approx 2\text{K}$. The thermal phonons emanating from this heated region (they can be thought of as small wave packets with frequencies in the region of 100 GHz) travel ballistically through the crystal to the opposite face, where they are detected with a superconducting bolometer or tunnel junction detector. A phonon image depicts the directional dependence of the transmitted phonon intensity and is constructed by raster-scanning the source over the front surface and recording the detected signal as a gray-scale image. Figure 2.1(a) shows a measured phonon image for the crystal sapphire (Al_2O_3) [53], time-gated to display only the ST and FT phonon flux. The phonon intensity is highly nonuniform, mainly ascribable to the effect of phonon focusing discussed in the following text. The bright lines are caustics, where the flux is mathematically singular.

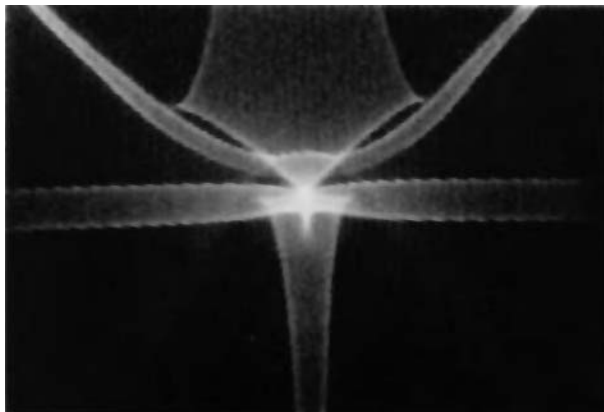
Phonon focusing has its origin in the nonspherical shape of the acoustic slowness surface. The rays pointing out of this surface can be taken to represent the group velocity vectors of the phonons making up the heat flux. It is evident that, where the curvature of the slowness surface is least, the group velocity vectors are strongly concentrated in direction, and consequently the energy flux in that direction is the greatest. This effect is known as phonon focusing, and it is the most important source of nonuniformity of the intensity in phonon images. A useful measure of focusing is given by the Maris phonon enhancement factor [3, 54]

$$A = \left| \frac{\delta\Omega_s}{\delta\Omega_v} \right| \quad (2.21)$$

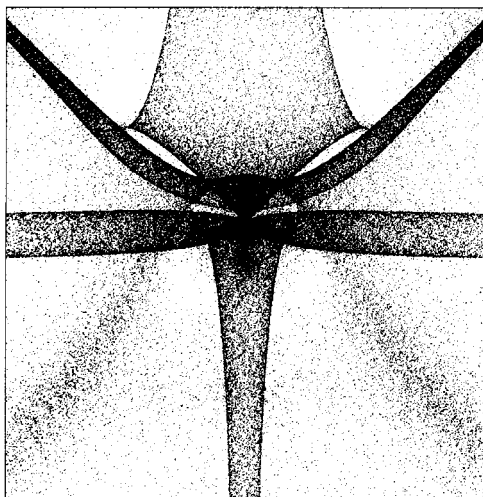
where $\delta\Omega_s$ is the solid angle subtended by an infinitesimal cone of slowness vectors and $\delta\Omega_v$ is the solid angle subtended by their associated group velocity vectors. From differential geometry it is readily established that [55, 56]

$$A = (s^3 V |K|)^{-1} \quad (2.22)$$

This geometrical argument thus leads to the same conclusion as the stationary phase approximation for the far field, namely, that the energy flux in any direction for a particular mode is inversely proportional to the magnitude of the Gaussian curvature, $|K|$, of the slowness surface.



(a)



(b)

FIG. 2.1. (a) Measured phonon image for the crystal sapphire (Al_2O_3), time-gated to display only the ST and FT phonon flux. Bright regions indicate directions of high phonon intensity. (b) Monte Carlo calculated focusing pattern for sapphire (darkness in this case is a measure of the phonon intensity).

Monte Carlo methods provide the simplest means of generating theoretical phonon intensity patterns of crystals [2]. A common point of departure in these computer simulations is to assume that the phonons emanating from the heat source have a uniform distribution of wave normals. The group velocities for a large number of uniformly distributed normals are computed, and the points

where these meet the viewing surface are sorted into a two-dimensional array of bins, and the result presented as a gray-scale image. Figure 2.1(b) shows the calculated focusing pattern for sapphire for the experimental geometry of Figure 2.1(a). The values of the elastic constants in this calculation have been adjusted to obtain the best fit to experiment. Actually, it is only the elastic constant ratios that can be determined in this way, since changing all the elastic constants by the same factor does not alter a phonon focusing pattern. The values of the elastic constants obtained are close to the low-temperature extrapolated values used in [53]. Interestingly, the fit is most sensitive to the value of C_{14} , an elastic constant that is not normally easy to measure accurately (the fitted value is -23.2 ± 0.3 GPa). Metzger and Huebener [57] have made similar adjustments to the values of the elastic constants in fitting calculated to measured phonon image of germanium. Their fitted values differ appreciably from literature values, and they conclude that this is the result of dispersion.

The most striking feature of the phonon images in Figure 2.1 is the complex pattern of caustics they contain. These intense bands are associated with lines of zero Gaussian curvature on the slowness surface [55]. The vanishing of K on these lines results in the energy flux being mathematically infinite. Caustics are essentially a far-field effect. The patterns they form for different crystal symmetries and degrees of anisotropy have been extensively studied by a number of authors. For a review, see [2].

2.3.3 Intermediate Field

Emerging from the far field, as the frequency is lowered or the observation point is brought closer to the source, each line caustic of a phonon focusing pattern unfolds into an Airy diffraction pattern [58, 59]. As the frequency is lowered further, the fringes broaden and merge, becoming fewer in number. To predict the diffraction pattern requires going beyond the stationary phase approximation and carrying out the numerical integration in Eq. 2.7. In the intermediate field the main contributions to the integral still come from the vicinity of stationary phase points, and one can, without much loss of accuracy, still restrict the integration to small but finite regions around each such point.

2.3.4 Scanning Transmission Acoustic Microscopy

Scanning transmission acoustic microscopy has been used by Hauser *et al.* [18] to study the frequency domain dynamic response of a number of anisotropic solids, including metal, insulating and semiconducting crystals, and fiber composites. Their experimental setup is shown in Figure 2.2(a). A pair of water immersion acoustic lenses, which are focused to small spots on opposite surfaces of the sample, are used to generate and detect ultrasonic tone bursts with central frequencies in the range of 5 to 25 MHz. One of the transducers

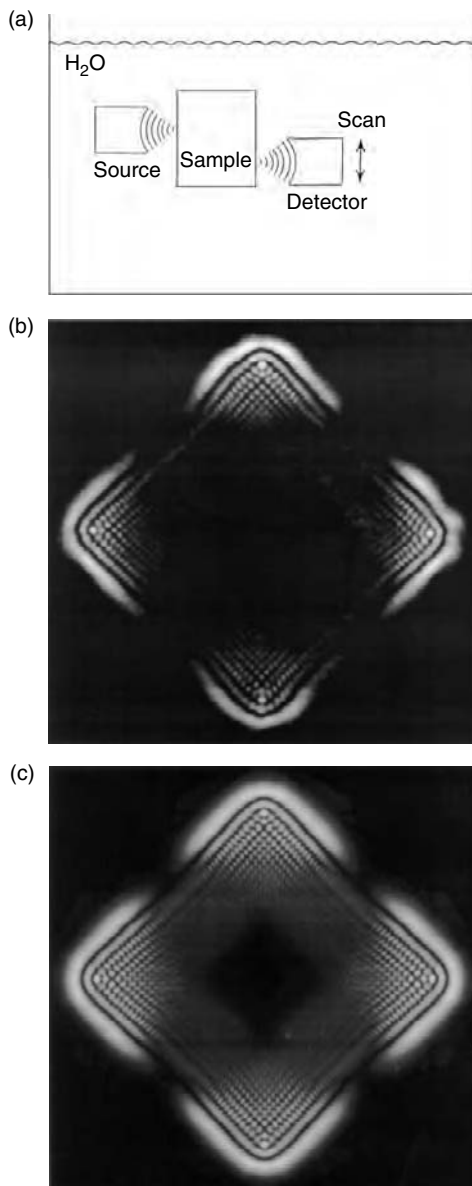


FIG. 2.2. (a) Experimental scanning transmission acoustic microscopy technique of Hauser *et al.* [18]. (b) Internal diffraction image of GaAs centered on the [100] direction, measured by Wuerz *et al.* [27, 28], (c) Their calculated image, based on optimized values of the elastic constants.

TABLE 2.1. Elastic Constants of GaAs

	$C_{11}(GPa)$	$C_{12}(GPa)$	$C_{44}(GPa)$
Wuerz <i>et al.</i> [27]	118.52	54.99	57.77
Tabulated values [60]	118	53.5	59.4

is kept fixed while the other is raster-scanned to yield a two-dimensional image of the ultrasonic flux pattern transmitted through the sample. The measured diffraction images are in good agreement with calculated Green's functions $G_{33}(\mathbf{x}, \omega)$ corresponding to the experimental parameters. The actual analysis carried out by Hauser *et al.* [18] is a little different from this, in that they also take account of the finite angular width of the incoming and outgoing beams in the water and of the angular dependence of the transmission across the fluid–solid interface. Wesner *et al.* [19] have used essentially the same technique to study a number of crystals, except that they retain phase information and operate at higher frequencies. Kim *et al.* [36] have studied the diffraction of SH waves in Si using piezoelectric shear transducers.

2.3.4.1 Recovery of Elastic Constants from Diffraction Images. Wuerz *et al.* [27, 28] have determined the elastic constants of GaAs by fitting a calculated diffraction image to measurement for that crystal. Figure 2.2(b) shows their measured image. They have used a simplex inversion algorithm to obtain the elastic constants, starting from remote values. Figure 2.2(c) is the best fit to their early time image, and the Table 2.1 shows the elastic constant values they obtain from this fit, which are in close agreement with tabulated values. In contrast to phonon imaging, all the elastic constants are obtained from a diffraction image, not simply the ratios. This is because the magnitudes of the elastic constants determine the fringe spacing. Interestingly, in their fit Wuerz *et al.* [27] use only information pertaining to the ST branch extending out to about 13° from the [100] direction, and yet are able to accurately recover all three of the elastic constants of GaAs. It is unlikely that one would be able to achieve the same accuracy with ST phase velocity measurements in the same angular range. The algorithm of Wuerz *et al.* [27] appears to be quite robust, although CPU intensive.

2.4 Time Domain Response: Numerical Implementation and Comparison with Experiment

2.4.1 Infinite Continuum Response

To evaluate $G_{ij}(\mathbf{x}, t)$ at a particular time, the first term in Eq. 2.9 can be reduced to a one-dimensional integral summed over directions for which

$t - \mathbf{s} \cdot \mathbf{x} = 0$. However, it is usual that the entire time dependence of $G_{ij}(\mathbf{x}, t)$ is required, in which case it is simpler, and not necessarily more demanding on computer time, to perform the two-dimensional integration as a sorting and counting process. The time interval between $t = 0$ and the arrival of the last wave, i.e., the largest value of $\mathbf{s} \cdot \mathbf{x}$, is divided into a number of slots. A uniform distribution of \mathbf{n} 's is generated, and for each of these the value of $\mathbf{s} \cdot \mathbf{x}$ determines the slot in which the corresponding value of $s^3 \Lambda_{ij}$ is accumulated. For times exceeding the maximum of $\mathbf{s} \cdot \mathbf{x}$, $G_{ij}(\mathbf{x}, t)$ has the constant value given by the second term in Eq. 2.9. By way of example, Figure 2.3(a) shows calculated infinite continuum responses $G_{33}(\mathbf{x}, t)$ for hexagonal zinc (x_3 axis taken along the principal crystallographic axis) [39] for three observation points, namely, $x_1 = 0$ mm, 5 mm, and 10 mm, with $x_2 = 0$ and $x_3 = 25.8$ mm.

Some of the striking features of these and other space-time Green's functions are the singularities they contain. These are called wave arrivals and are associated with points on the slowness surface where $\mathbf{s} \cdot \mathbf{x}$ is stationary. These wave arrival singularities propagate outwards from the source at the group velocities in each direction, and thus lie on the wave surface, i.e., the locus of ray vectors scaled by a factor t . Figure 2.4 shows the zonal section of the L and qT sheets of the wave surface of zinc [37] (the pure T sheet is not shown since these T waves are SH polarized and are not coupled to in G_{33}). The qT sheet is folded, giving rise to multiple wave arrivals near the [001] direction.

The analytical form of a wave arrival singularity is ascertained by approximating the equation of the slowness surface with a polynomial function in the region around the stationary phase point, and then integrating analytically [37, 48]. What emerges is that, for convex and concave regions of the slowness surface (L_1, L_2 both negative or both positive), $G_{ij}(\mathbf{x}, t)$ displays a discontinuity of magnitude proportional to $\Lambda/x\sqrt{|K|}$, together with a change in slope. The arrivals L and S are of this form, with the response being zero before the longitudinal arrival L and constant after the last shear arrival S. For saddle-shaped regions of the slowness surface (L_1, L_2 opposite in sign), $G_{ij}(\mathbf{x}, t)$ displays a logarithmic divergence, an example of which is the arrival I. Along the zonal axis of transversely isotropic solids such as zinc, for which the slowness surface is concave in the region of the zonal axis, there is a conical point in the ray surface, and this gives rise to the negative square root singularity of the arrival X, which is associated with the phenomenon of external conical refraction [61]. These wave arrivals correspond to intersections of the viewing direction with sheets of the wave surface of zinc as shown in Figure 2.4.

2.4.2 Half-Space Response

The sorts of experiments that measure the response functions of solids, more often than not, involve forces being applied and measurements being carried out at surfaces. One might expect, therefore, that half-space Green's

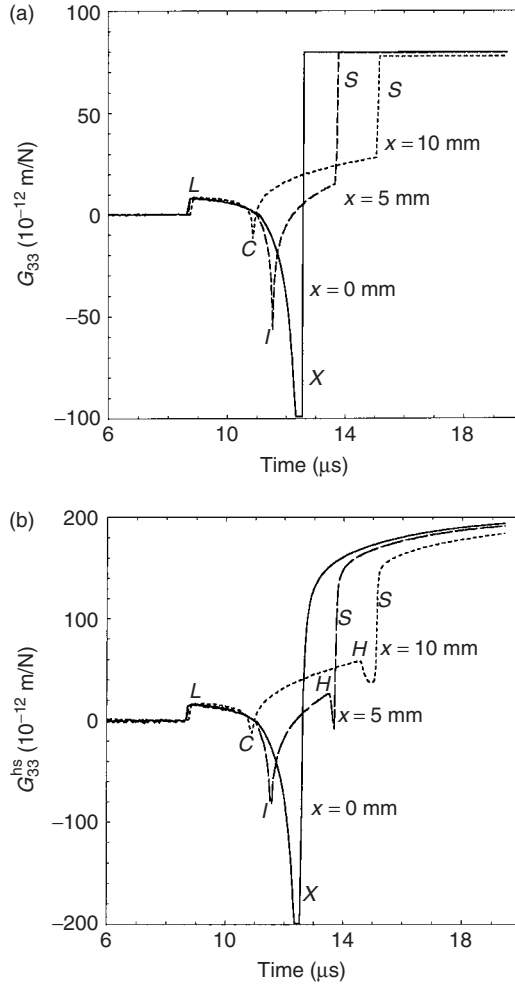


FIG. 2.3. (a) Calculated infinite continuum response function $G_{33}(\mathbf{x}, t)$ for hexagonal zinc, for three observation points $x_1 = 0 \text{ mm}$, 5 mm , and 10 mm , with $x_2 = 0$ and $x_3 = 25.8 \text{ mm}$. (b) Corresponding half-space Green's functions $G_{33}^{hs}(\mathbf{x}, t)$. The elastic constants are from [60].

functions or the Green's functions for a layer would more accurately model the results of these experiments. Calculation of the half-space Green's function for an interior point requires evaluation of the two-dimensional integral in Eq. 2.13. In the case of a generally anisotropic solid, this can be done entirely numerically [39] or, using the Cagniard-de Hoop method, to evaluate

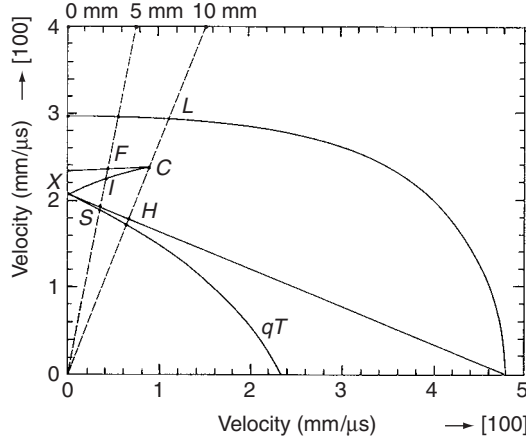


FIG. 2.4. Zonal section of the L and qT sheets of the wave surface of zinc.

one of the integrals analytically [40, 41]. The results obtained by the two approaches are identical. Figure 2.3(b) shows the calculated zinc half-space response functions $G_{ss}^{hs}(\mathbf{x}, t)$ for the same configurations as in Figure 2.3(a). Overall, the displacements are greater in magnitude by about a factor of 2 as compared with those for the infinite continuum, as one might expect. The bulk wave arrivals have the same analytic form and occur at the same times as for the half-space calculation, and for early times and near epicentral directions, the two response functions are almost indistinguishable. After the last T wave arrival, while the infinite continuum response $G_{33}(\mathbf{x}, t)$ is constant, the half-space response $G_{33}^{hs}(\mathbf{x}, t)$ approaches asymptotically a constant value. This last-mentioned feature is a diffraction effect originating at the surface.

For observation points well away from epicenter, where the surfaces of the sample play an increasingly important role, the two responses are no longer so similar. For the half-space an additional wavefront appears, called the head wave [62]. This is the sharp downward kink marked H in Figure 2.3(b) and the wave surface similarly labeled in Figure 2.4. A head wave can be thought of as being made up of a family of slower (transverse) waves trailing the faster (longitudinal) wave as it skims along the surface, much like in the formation of a supersonic cone. Zinc is somewhat unusual in that the head wave merges with the qT sheet of the wave surface at a point very close to the conical point [62]. These calculated responses are in very good agreement with waveforms measured in zinc by Kim *et al.* [63, 64], particularly with regard to the bulk and head wave arrivals.

Along the surface of the solid there is also the Rayleigh wavefront, which lags behind the slowest T wavefront, and which along the surface propagates

the dominant singularity. This is discussed in Section 2.5. For a thick plate, there are also numerous multipass wave arrivals, encompassing the various possible mode conversion sequences. The generalized ray approximation [47, 65] is a starting point for calculations of the complete waveform for a thick plate of arbitrary anisotropy, but to date there has not been much in the way of numerical implementation of this method for modeling experiment. The main difficulty is keeping track of the large number of poles that occur. In the case of viscoelastic solids, these poles lie off the real axis, and numerical integration becomes a viable option for computing the response of an anisotropic plate [35, 66]. The complex issue of poles is sidestepped in finite difference calculations (see, e.g., [67]).

2.4.3 Inversion of Capillary Fracture Waveform Data

A method of simulating a concentrated normal force on the surface of a sample with a step function time dependence is to place a thin glass capillary on the surface and press the sharp edge of a razor blade down on it until it breaks [5, 6]. At this instant the approximate point load on the surface drops abruptly to zero. The waveform that is generated is of large amplitude and can be accurately monitored with a small-aperture capacitive transducer placed elsewhere on the surface of the sample. This method has been applied to a variety of solids.

A complete waveform contains a great deal of information that can be used to recover elastic constants. Every and Kim [23] have determined elastic constants of silicon from individual capillary fracture-generated waveforms obtained on a (001)-oriented Si single crystal, confining their attention to near epicentral measurements and data extending only as far as the last T wave arrival, and interpreting this information on the basis of the infinite continuum Green's function, which is adequate in this region, where the HW does not exist.

Figure 2.5 shows a measured epicentral waveform for silicon and the outcome of a simple optimization process based on a succession of grid searches in which the elastic constants C_{12} and C_{44} have been determined by fitting the calculated infinite continuum Green's function to the measured waveform. The fit is close, and the values of C_{12} and C_{44} obtained are in good agreement with accepted values, 63GPa and 79.1GPa, respectively [60]. The position of the dip followed by the steep rise is most sensitive to the value of C_{44} , and the depth of the dip is mainly controlled by C_{12} . Interestingly, from phase velocity measurements in the (001) direction of a cubic crystal, it is not possible to obtain the value of C_{12} .

2.4.4 Observation of Wave Arrivals

In some experiments, it is only the singularities in a waveform, where most of the acoustic energy is concentrated, that can be clearly distinguished, the

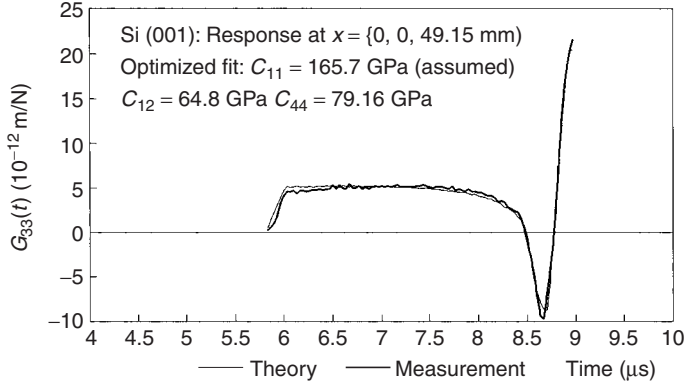


FIG. 2.5. Measured and calculated epicentral waveforms for Si(001).

remaining features being obscured by transducer ringing and other experimental artifacts. This is particularly true of laser ultrasound measurements [8–10]. A number of groups have consequently devoted their efforts to measuring wave arrivals, reconstructing part of the wave surface, and then working backwards to determine the elastic constants.

2.4.4.1 Laser Ultrasound Measurements. In recent years laser ultrasound measurements have been carried out on a number of anisotropic solids, including silicon and zinc single crystals and a variety of fiber composites [1, 68] (for a review, see Castagnede and Berthelot [69]). In the standard approach, as depicted in Figure 2.6(a), a focused Q-switched laser delivers a heat pulse to a small region on the surface of a specimen, causing a transient acoustic wave to be launched into the specimen. The wavefield is measured on the opposite face using interferometry or a small-aperture piezoelectric or capacitive transducer, which senses the normal displacement of the surface. Note that it is the thermally generated sound wave that is detected, not the thermal phonons making up the heat pulse as in phonon imaging. At low power densities the thermoacoustic generation mechanism predominates. The sudden rise in temperature of the surface brings about a localized radial stress field within the surface, and this results in acoustic radiation. At higher power densities, material is ablated from the surface, and this gives rise to an impulsive reaction force normal to the surface. The generation and detection processes are both axisymmetric in form, and only waves with a significant sagittal component to their polarizations feature in the observations.

Figure 2.6(b) shows typical waveforms obtained by Every *et al.* [1] on a 10-mm-thick (001)-oriented silicon single crystal with detection at epicenter and at 8 mm from epicenter. Although the wave arrivals are recognizable from the signal onsets, little information can be inferred directly from these

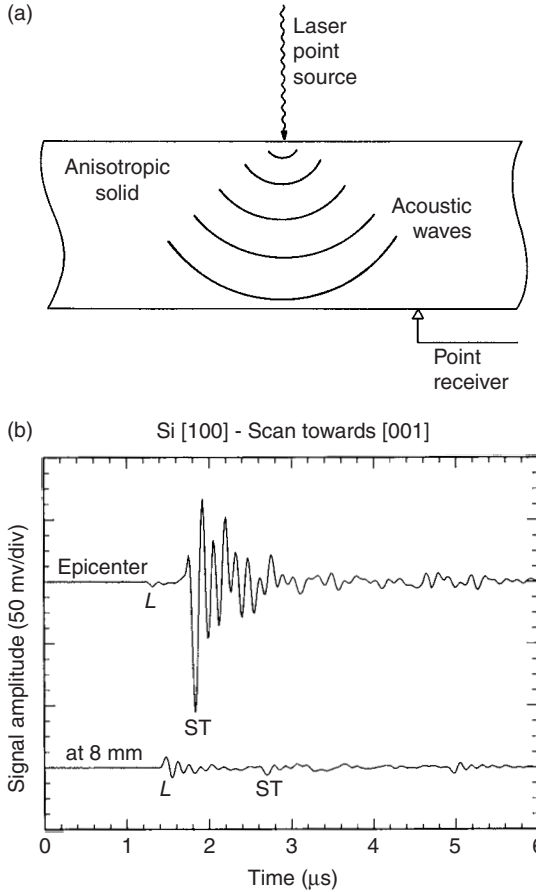


FIG. 2.6. (a) Schematic of a laser ultrasound experiment. (b) Laser ultrasound waveforms measured in a (001)-oriented Si crystal with a small-aperture piezoelectric transducer.

signals concerning the continuous portions of the waveforms in between the singularities.

Figure 2.7(a) shows a scan image obtained by stacking together a large number of waveforms for a closely spaced set of excitation points, and representing the resulting (x, t) response as a gray-scale image [1]. Figure 2.7(b) shows the theoretical wave arrivals obtained by a Monte Carlo procedure that assumes a uniform distribution of wave normals \mathbf{n} , and then plots as points the arrival times of those rays that come within the detector aperture for each value of x . The calculated scan image features the first L and ST

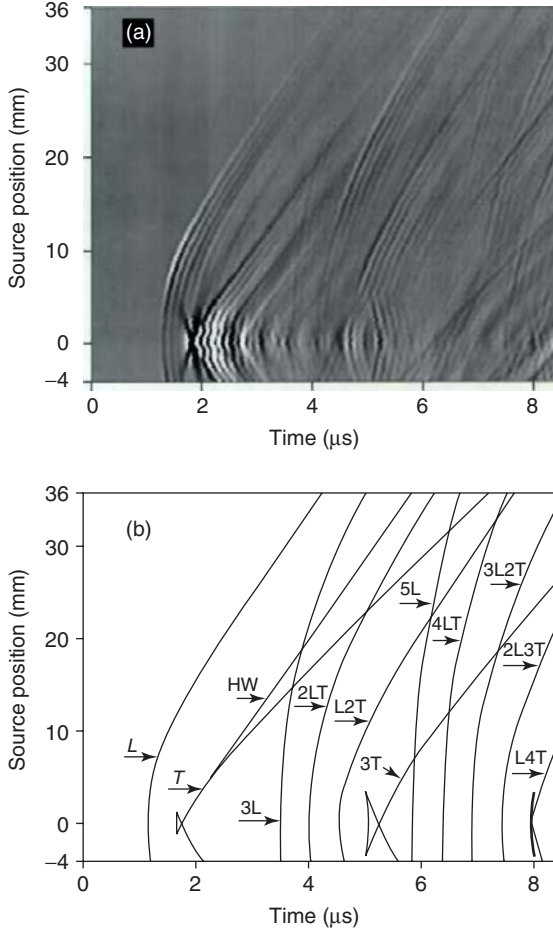


FIG. 2.7. (a) Scan image for a (001)-oriented 10-mm-thick Si crystal, generated from a closely spaced set of excitation points in the [100] direction. (b) Calculated scan image.

wave arrivals, the head wave (HW), and the arrivals of various mode conversion sequences for passage of the wavefield three and five times through the sample. The multipass and head waves are calculated using standard procedures for dealing with reflection in anisotropic solids [52]. These various wave arrivals are all in good agreement with the signal onsets in the measured scan image. There is no discernable presence of FT single- or multipass waves, or any mode conversion sequence or head wave involving FT waves. This is because the FT waves are almost perfectly shear-horizontally (SH) polarized,

and are therefore uncoupled from the axisymmetric mode of excitation and detection. The single- and multipass wave arrivals and head wave are all in good agreement with experiment. Castagnede *et al.* [70] have carried out a similar study on fiber composites using the Cagniard-de Hoop method to do the simulations.

In viscoelastic solids there is rounding of the wave arrivals due to dispersion. Guilbaud and Audoin [35] have used wavelet analysis to process waveforms measured on polymer matrix composites, thereby obtaining more accurate (frequency-dependent) wave arrival times. Another device for obtaining more accurate wave arrivals, used by Audoin *et al.* [71], is to locate peaks in the radiation power, calculated from the measured signal and its Hilbert transform.

2.4.5 Inversion to Obtain Elastic Constants from Group Velocity Data

The inverse problem of obtaining elastic constants from group velocity data is, in general, more complicated than for phase velocity data. The main reason is that, in cubic or lower-symmetry materials, the group velocity for a particular nonsymmetry direction cannot be obtained by analytic means; it needs to be computed numerically. One method of doing so is to choose a starting value of the wave normal \mathbf{n} , calculate the phase velocity $v(\mathbf{n})$ by diagonalizing the Christoffel tensor, obtain the group velocity \mathbf{V} by one of the methods described in Section 2.3.1, and then adjust \mathbf{n} until \mathbf{V} points in the required direction. Building on this procedure, Every and Sachse [24] have implemented the following double iterative strategy for recovering elastic constants $C_{\alpha\beta}$ from a set of measured group velocities. With a starting set of $C_{\alpha\beta}$'s, \mathbf{V} 's having the directions but not in general the magnitudes of the measured \mathbf{V} 's are obtained. A succession of steadily improving values of the $C_{\alpha\beta}$'s are then generated, which at each step reduce the mean square difference between the measured and calculated \mathbf{V} 's.

Table 2.2 shows the elastic constants of Si that Every and Sachse [24] have obtained from laser ultrasound measurements. They are in good agreement with tabulated values. This algorithm has been used on a number of materials, including composites with different ply-layup configurations [72, 32]. Figure 2.8 shows group velocity data measured in a cross-ply graphite-epoxy

TABLE 2.2. Elastic Constants of Si

	$C_{11}(GPa)$	$C_{12}(GPa)$	$C_{44}(GPa)$
Every and Sachse [24]	165.1	65.0	80.2
Tabulated values [60]	165	63	79.1

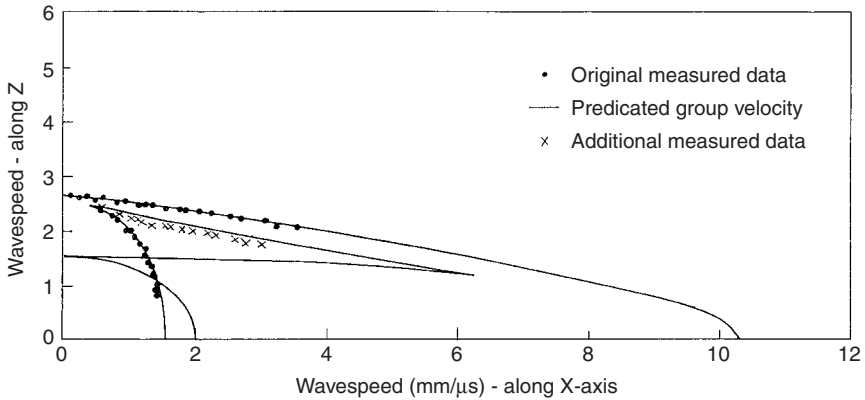


FIG. 2.8. Group velocity data measured in a cross-ply graphite–epoxy specimen by Niu [72].

specimen by Lin Niu [72], using capillary fracture generation and capacitive detection, together with her fitted group velocity curve. Her recovered values of the elastic constants are $C_{11} = C_{22} = 185$, $C_{33} = 12.0$, $C_{44} = C_{55} = 4.14$, and $C_{13} = C_{23} = 3.96$ GPa. A number of other authors have subsequently implemented similar schemes. Minachi *et al.* [73] have determined elastic constants of a number of unidirectional graphite–epoxy composite plates from the group velocities of longitudinal pulses that are generated at one surface of the sample, reflected from the opposite surface, and then detected elsewhere at the first surface using piezoelectric transducers. Their material is transversely isotropic, which simplifies the calculations a bit since the plane in which the wave normal lies is known.

In directions where the wave surface is folded, the algorithm described previously for determining the wave normals can become unstable because of the multiplicity of wave arrivals in these directions. An alternative approach, based on the Cagniard-de Hoop method, has been developed by Deschamps and Bescond [74], and is claimed to be more robust. It has been implemented on laser-generated data to obtain the elastic constants of silicon [71]. A pitfall that has to be carefully negotiated when using data from near cuspidal edges of the wave surface is that a sharp feature persists in the waveform well beyond the cuspidal edge [20, 37, 71], and it is difficult to distinguish this from an actual wave arrival.

In laser ultrasound, the first L arrival tends to be the clearest and most accurately measurable, with later arrivals being partially obscured by their proximity and by noise. Although it is tempting, therefore, to try to base an elastic constant determination on L data alone, Every and Sachse [75] and

Castagnede *et al.* [76] have shown that longitudinal velocities depend most sensitively on the partial set of elastic constants C_{11} , C_{22} , C_{33} , $(C_{12} + 2C_{66})$, $(C_{23} + 2C_{44})$, and $(C_{13} + 2C_{55})$, and it is only these constants that can be accurately recovered from longitudinal velocity data.

2.4.5.1 Symmetry Plane Measurements. For minimization of experimental error, it is recommended and indeed is quite a common practice in crystallography to determine the elastic constants from wave speeds measured in symmetry planes that contain symmetry axes. For media of orthorhombic or higher symmetry, the diagonal elements $C_{\alpha\alpha}$, $\alpha = 1, 2, \dots, 6$ are determined from measured speeds of longitudinal and transverse waves propagating in symmetry directions, since variations of these wave speeds with deviation of their wave normals from the symmetry direction are zero to first order. Along the principal axes, group and phase velocities coincide and the elastic constant $C_{\alpha\alpha}$ is given simply by ρv^2 for the relevant velocity. Determination of the mixed-index elastic constants $C_{\alpha\beta}$, $\alpha \neq \beta$, is carried out using measurements of the group velocities of quasi-longitudinal and quasi-transverse modes propagating along oblique directions in symmetry planes, for which directions of corresponding wave normals are found from an analytic equation expressed in terms of elastic constants that include both pure- and mixed-index elastic constants. The mixed-index elastic constants are then calculated from a closed-form analytic formula that relates them to the magnitude of the group velocity, its direction and corresponding wave normal. It is also noted that pure-index shear moduli, such as C_{44} , C_{55} , and C_{66} , can also be determined from measurements of group velocities of a shear-horizontally (SH) polarized pure transverse mode propagating along oblique directions in symmetry planes. Kim *et al.* [29–31] developed this procedure and determined the elastic constants of cubic silicon, hexagonal zinc, and an orthorhombic PEEK (poly ether ether ketone) composite from group velocities measured in symmetry planes of these materials.

For data pertaining to certain high-symmetry directions such as fourfold axes in cubic and tetragonal media, the sixfold axis in hexagonal media, and twofold axes in orthorhombic media, around which a transverse slowness sheet is concave-shaped, it is possible to derive closed-form expressions relating the group velocities to the $C_{\alpha\beta}$'s, not only for the modes whose \mathbf{n} 's lie in the symmetry direction, but also for the so-called oblique modes whose \mathbf{n} 's lie away from the axis in symmetry planes. These expressions allow the $C_{\alpha\beta}$'s to be obtained by analytic means [77, 78]. Litian Wang [79] has carried out a general analysis of this problem using Stroh's formalism. The inversion is simplest for wave arrivals whose normals lie in the symmetry directions, because in that case phase and group velocities coincide. Kim *et al.* [80] have obtained elastic constants of Si from multipass arrivals by this means. Aussel

and Monchalin [22], who were pioneers in the use of laser-generated ultrasound for elastic constant determination, also focused on measurements in symmetry directions.

2.5 Surface Response

When detection is carried out on the same surface as excitation, the response is dominated by Rayleigh surface acoustic waves (SAW) or pseudo-SAW (pSAW). The feature labeled RW represents the slowness curve of the SAW in the (001) surface of copper. It is the slowest propagating wave arrival and hence appears latest in the surface displacement signal. The family of SAW rays emanating from the point of excitation is normal to this curve. There are two regions in that diagram where the slowness curve is concave, whereas elsewhere it is convex. As a result, the SAW group velocity curve is folded in a complicated way near the $\langle 100 \rangle$ directions as shown in the inset in Figure 2.9(a), and the surface response to point excitation exhibits multiple SAW arrivals, as seen for the calculated response for the [100] direction, represented by the solid curve in Figure 2.9(a) [81]. The cuspidal points where the folding occurs correspond to points of inflection (zero curvature) in the RW slowness curves. In much the same way as for bulk phonon focusing, this is accompanied by intense focusing of SAW energy flux. SAW focusing has been extensively studied, both theoretically and experimentally, by Maznev and coworkers [82], and could provide a means for determining elastic constant ratios.

In and near the [110] direction, we see that the response is dominated by a pSAW, which lies within the band of bulk wave excitations. The calculated point force response for the [110] direction is shown by the chain dotted curve in Figure 2.9(a). Essentially identical results are obtained using the Cagniard-de Hoop technique [41]. The deep dip in this curve is the pSAW arrival, and the displacement continues to increase after this until the end of the bulk wave continuum.

In addition to the SAW arrivals, there are bulk L, FT, and ST wave arrivals that appear at earlier times in the surface response (points a, b, and c in Figure 2.9(a)). These are much less pronounced than the SAW arrivals.

Figure 2.9(b) shows the corresponding measured responses of the (001) surface of a Cu single crystal obtained by capillary fracture excitation and capacitive detection [81]. Apart from experimental rounding in the measured signals, the measured and calculated responses are in good agreement. Fitting calculated to measured surface responses is thus a way of obtaining the elastic constants of solids, whether the full waveform data are used or only the wave arrivals.

Chai and Wu [25], relying only on SAW arrivals, have measured the directional dependence of the group velocities of point focus laser-generated SAW

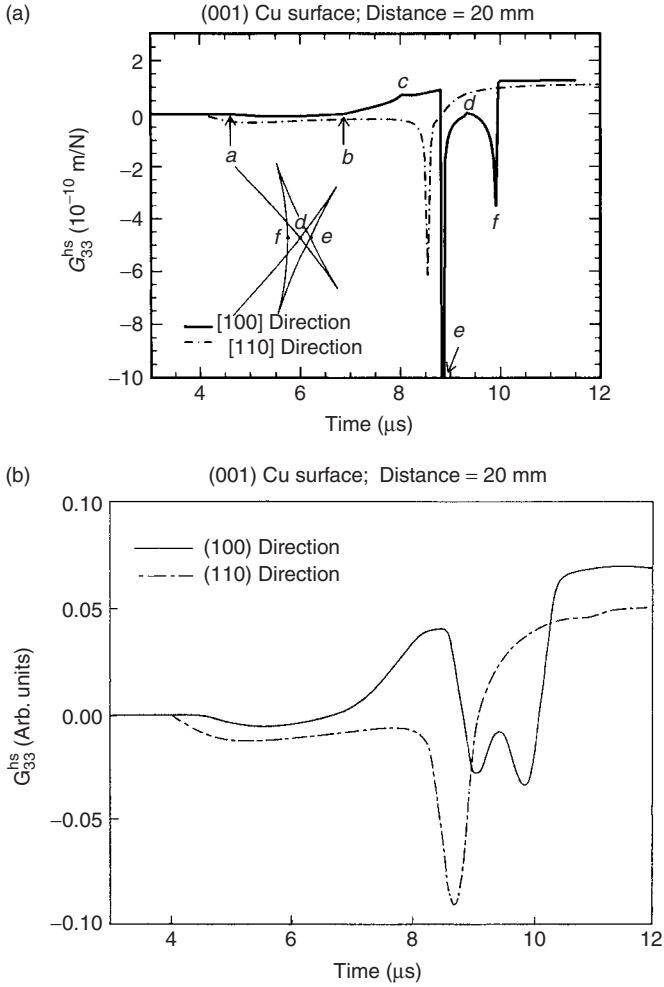


FIG. 2.9. (a) Calculated and (b) measured surface response of a (001)-oriented copper crystal in the [100] and [110] directions.

in the (111) surface of silicon and in a unidirectional fiber composite, and have used a simplex optimization method to recover the elastic constants of this solid. Their algorithm is similar to the one described earlier in this chapter for bulk waves. With starting values of $C_{\alpha\beta}$, they calculate a set of group velocities that point in the observation directions and thereby obtain the mean square difference χ^2 between calculated and measured velocities. The $C_{\alpha\beta}$ are then varied to progressively improve the fit and minimize χ^2 .

It is usually the case, except for highly anisotropic materials, that the SAW velocity is more sensitive to the shear moduli than longitudinal moduli such as C_{11} . It is therefore advantageous for the purpose of elastic constant determination if bulk longitudinal wave arrivals can also be measured in one or more directions. This approach has been effectively applied by Wu *et al.* [83] to determine the elastic constants of concrete using transient waves excited by ball impact and the use of a conical transducer.

2.6 Plate Modes

We consider here the response of a thin anisotropic plate to pointlike excitation by laser or other means. The characteristic wavelengths radiated are supposedly much greater than the thickness h of the plate, i.e., $kh \ll 1$, and so we are concerned only with the three lowest plate modes:

- (1) The flexural or antisymmetric mode A_0 . This mode is dispersive, with the absolute value of slowness being proportional to $\omega^{-1/2}$. Taking the z -direction normal to the plate, and the x - and y -directions in the plate, the directional dependence of the slowness \mathbf{s} of this mode is given by [84, 85]

$$\gamma_{11}s_x^4 + 4\gamma_{16}s_x^3s_y + 2(\gamma_{12} + 2\gamma_{66})s_x^2s_y^2 + 4\gamma_{26}s_xs_y^3 + \gamma_{22}s_y^4 = \frac{12\rho}{\omega^2h^2} \quad (2.23)$$

- (2) Two coupled horizontally polarized modes satisfying [84–86]

$$\begin{pmatrix} \Gamma_{11} - 1 & \Gamma_{12} \\ \Gamma_{21} & \Gamma_{22} - 1 \end{pmatrix} \begin{pmatrix} u_x \\ u_y \end{pmatrix} = 0 \quad (2.24)$$

$$\Gamma_{11} = (\gamma_{11}s_x^2 + 2\gamma_{16}s_xs_y + \gamma_{66}s_y^2)/\rho$$

$$\Gamma_{12} = \Gamma_{21} = (\gamma_{16}s_x^2 + (\gamma_{12} + \gamma_{66})s_xs_y + \gamma_{26}s_y^2)/\rho$$

$$\Gamma_{22} = (\gamma_{66}s_x^2 + 2\gamma_{26}s_xs_y + \gamma_{22}s_y^2)/\rho$$

The coefficients γ_{ij} are the stiffnesses appropriate to plane stress, and are functions of the elastic constants C_{ij} . For the practically important case of (x, y) being a symmetry plane of an orthotropic medium, $\gamma_{ij} = (C_{ij} - C_{i3}C_{j3}/C_{33})$ for $i, j = 1, 2$; $\gamma_{66} = C_{66}$, and $\gamma_{16} = \gamma_{26} = 0$. In the isotropic limit the last two modes are uncoupled and become the lowest symmetric Lamb mode S_0 and the lowest shear horizontal mode SH_0 .

Plate modes exhibit focusing, much as for SAW, with the focusing intensity being inversely proportional to the curvature of the slowness curve. In the case of the flexural mode and the slower of the two coupled modes, the slowness

curve can have concave regions, and consequently there can be focusing caustics. The characteristic patterns of these caustics for cubic symmetry materials have been worked out by Maznev and Every [85].

Measurements of the laser-generated dispersive flexural mode response of a silicon wafer have been carried out by Nakano and Nagai [87]. Chen and Man [88] have carried out measurements on the slower SH_0 -like mode in an anisotropic cold-rolled aluminium sheet.

Veidt and Sachse [33] have carried out an extensive study of the coupled plate modes in a Si wafer and in unidirectional graphite–epoxy laminates, using a pulsed laser beam as a dipole source and a small-aperture piezoceramic transducer as a monopolar source, as well as a piezoceramic sensor that responds to lateral and shear motion of the specimen surface. By these means they were able to generate scan images for the plate modes. They have modeled the wave arrivals with calculated plate mode group velocities. For the fiber composites, accurate fits were obtained both outside and within the cuspidal regions of the wave surface. Consistent values were obtained for the stiffness coefficients γ_{11} , γ_{22} , γ_{12} , and C_{66} .

2.7 Conclusions

The PS/PR approach to measuring the elastic properties of solids is now well established, and has proved of value in a number of applications. The advantages of PS/PR techniques are manifold and varied. Wave propagation over a wide range of directions can be studied and many elastic constants recovered in an experiment on a single specimen, obviating the need for accurate cutting and faceting of samples. Laser excitation and interferometric detection permit noncontact measurement of elastic constants. Elastic properties can be inferred from measurements carried out on one side of a specimen, which has obvious applications in the nondestructive inspection of structures for materials' degradation. PS/PR techniques exist for studying large specimens as well as small specimens, thin plates, and so on.

PS/PR techniques span the time domain (transient excitation) as well as the frequency domain (tone burst excitation), and in essence measure the time or frequency domain Green's function of a solid. The theoretical modeling that is required for extracting information about a specimen from measured data is generally much more complicated than for plane wave techniques, but easily within the capability of any modern personal computer. Measurements carried out in the far field, which encompasses phonon imaging, the measurement of wave arrivals by laser techniques, etc., can be interpreted on the basis of the ray approximation, which is a significant simplification. In the special case of data pertaining to symmetry directions, for which the phase and group

velocities coincide, the elastic constant recovery is the same as for plane wave techniques.

There remain many challenging problems both from an experimental point of view and in modeling and interpretation, but PS/PR techniques are sufficiently well established that one can anticipate their continued use in a wide variety of applications.

References

1. Every, A.G., and Sachse, W. (1991). *Phys. Rev.* **B44**: 6689; Every, A.G., Sachse, W., Kim, K.Y., and Thompson, M.O. (1990). *Phys. Rev. Lett.* **65**: 1446.
2. Wolfe, J.P. (1998). *Imaging of Phonons*, Cambridge: Cambridge University Press.
3. Maris, H.J. (1971). *J. Acoust. Soc. Am.* **50**: 812; Maris, H.J. (1986). In *Nonequilibrium Phonons in Nonmetallic Crystals*, Eisenmenger, W., and Kaplyanskii, A.A., eds., Amsterdam: North Holland.
4. Aki, K., and Richards, P. (1980). *Quantitative Seismology*, San Francisco: Freeman.
5. Breckenridge, F.R., Tschiegg, C.E., and Greenspan, M. (1975). *J. Acoust. Soc. Am.* **57**: 626.
6. Kim, K.Y., Niu, L., Castagnede, B., and Sachse, W. (1989). *Rev. Sci. Instrum.* **60**: 2785.
7. Hsu, N.N. (May, 1976). U.S. Patent 4,018,084.
8. Bunkin, F.V., Kolomenskii, A.A., and Mikhalevich, V.G. (1991). *Lasers in Acoustics* Chur: Harwood.
9. Hutchings, D.A. (1988). In *Physical Acoustics*, p. 21, vol. 18, Mason, W.P., and Thurston, R.N., eds., New York: Academic.
10. Scruby, C.B., Dewhurst, R.J., Hutchings, D.A., and Palmer, S.B. (1982). In *Research Techniques in Nondestructive Testing*, p. 281, vol. V, Sharpe, R.S., ed., New York: Academic.
11. Cargill, G.S. (1981). *Physics Today* **34**(10): 27.
12. Kim, K.Y., and Sachse, W. (1983). *Appl. Phys. Lett.* **43**, 1099.
13. Monchalin, J.P., Heron, R., and Muzak, N. (1985). *Rev. Sci. Instrum.* **56**: 543.
14. Dewhurst, R.J., Edwards, C., McKie, A.D.W., and Palmer, S.B. (1988). *J. Appl. Phys.* **63**: 1225.
15. Calder, C.A., Draney, E.C., and Wilcox, W.W. (1981). *J. Nucl. Mater.* **27**: 126.
16. Briggs, A. (1992). *Acoustic Microscopy*, Oxford: Clarendon.
17. Every, A.G., and Briggs, G.A.D. (1998). *Phys. Rev.* **B58**: 1601.
18. Hauser, M.R., Weaver, R.L., and Wolfe, J.P. (1992). *Phys. Rev. Lett.* **68**: 2604; Weaver, R.L., Hauser, M.R., and Wolfe, J.P. *Z. Phys.* **B90**: 27.
19. Wesner, J., Wurz, K.U., Hillmann, K., and Grill, W. (1993). In *Phonon Scattering in Condensed Matter*, vol. VII, Meissner, M., and Pohl, R.O. eds., Berlin: Springer-Verlag.
20. Kim, K.Y., Bretz, K.C., Every, A.G., and Sachse, W. (1996). *J. Appl. Phys.* **79**: 1857.
21. Sachse, W. (1987). *Ultrasonics International '87 Conference Proceedings*, p. 419, Guildford: Butterworth.
22. Aussel, J.D., and Monchalin, J.P. (1989). *Ultrasonics* **27**: 165.
23. Every, A.G., and Kim, K.Y. (1996). *Ultrasonics* **34**: 471.
24. Every, A.G., and Sachse, W. (1990). *Phys. Rev.* **B42**: 8196.

25. Chai, J.F., and Wu, T.T. (1994). *J. Acoust. Soc. Am.* **95**: 3232.
26. Audoin, B., Bescond, C., and Deschamps, M. (1996). *J. Appl. Phys.* **80**: 3760.
27. Wuerz, K.U., Wesner, J., Hillmann, K., and Grill, W. (1995). *Z. Phys.* **B97**: 487.
28. Grill, W., Hillmann, K., Wuerz, K.U., and Wesner, J. (1996). In *Advances in Acoustic Microscopy*, p. 167. vol. 2, Briggs, A., and Arnold, W., eds., New York: Plenum.
29. Kim, K.Y., Sribar, R., and Sachse, W. (1995). *J. Appl. Phys.* **77**: 5589.
30. Kim, K.Y. (1994). *Phys. Rev.* **B49**: 3713.
31. Kim, K.Y., Ohtani, T., Baker, A.R., and Sachse, W. (1995). *Res. Nondestr. Eval.* **7**: 13.
32. Sachse, W., Every, A.G., and Grabec, I. (1991). In *Enhancing Analysis Techniques for Composite Materials*, p. 77, NDE-Vol. 10, Schwer, L., Reddy, J.N., and Mal, A., eds., New York: ASME-AMD.
33. Veidt, M. and Sachse, W. (1994). *J. Acoust. Soc. Am.* **96**: 2318.
34. Sachse, W., Shiwa, M., Kishi, T., and Thompson, M.O. (1994). In *Nondestructive Characterization of Materials VI*, p. 291, Green, R.E., and Ruud, C.O., eds., New York: Plenum.
35. Guilbaud, S., and Audoin, B. (1999). *J. Acoust. Soc. Am.* **105**: 2226.
36. Kim, K.Y., Every, A.G., and Sachse, W. (1994). *J. Acoust. Soc. Am.* **95**: 1942.
37. Every, A.G., and Kim, K.Y. (1994). *J. Acoust. Soc. Am.* **95**: 2505.
38. Wang, C.-Y., and Achenbach, J.D. (1993). *Wave Motion* **18**: 273; (1995). *Proc. Roy. Soc. Lond.* **A449**: 441.
39. Every, A.G., Kim, K.Y., and Maznev, A.A. (1997). *J. Acoust. Soc. Am.* **102**: 1346; Maznev, A.A., and Every, A.G. (1997) *Int. J. Eng. Sci.* **35**: 321.
40. Mourad, A., and Deschamps, M. (1995). *J. Acoust. Soc. Am.* **97**: 3194.
41. Bescond, C., and Deschamps, M. (1998). *J. Acoust. Soc. Am.* **103**: 114.
42. Wang, C.-Y., and Achenbach, J.D. (1996). *Wave Motion* **24**: 227.
43. Buchwald, V.T. (1959). *Proc. R. Soc. Lond.* **A253**: 563.
44. Burrige, R. (1967). *Q. J. Mech. Appl. Math.* **20**: 42.
45. Duff, G.F.D. (1960). *Phil. Trans. Roy. Soc.* **252**: 249.
46. Tewary, V.K., and Fortunko, C.M. (1992). *J. Acoust. Soc. Am.* **91**: 1888.
47. Van der Hijden, J.H.M.T. (1987). *Propagation of Transient Elastic Waves in Stratified Anisotropic Media*, Amsterdam: North Holland.
48. Payton, R.G. (1983). *Elastic Wave Propagation in Transversely Isotropic Media*, The Hague: Martinus Nijhoff.
49. Yeats, F.R. (1984). *Phys. Rev.* **B29**: 1674.
50. Auld, B.A. (1990). *Acoustic Fields and Waves in Solids*, Malabar: Krieger.
51. Fedorov, F.I. (1968). *Theory of Elastic Waves in Crystals*, New York: Plenum.
52. Musgrave, M.J.P. (1970). *Crystal Acoustics*, San Francisco: Holden-Day.
53. Every, A.G., Koos, G.L., and Wolfe, J.P. (1984). *Phys. Rev.* **B29**: 2190.
54. Maris, H.J. (1971). *J. Acoust. Soc. Am.* **50**: 812.
55. Northrop, G.A., and Wolfe, J.P. (1980). *Phys. Rev.* **B22**: 6196.
56. Every, A.G. (1981). *Phys. Rev.* **B24**: 3456.
57. Metzger, W., and Huebener, R.P. (1988). *Z. Phys.* **B73**: 33.
58. Maris, H.J. (1983). *Phys. Rev.* **B28**: 7033.
59. Berry, M.V. (1976). *Adv. Phys.* **25**: 1.
60. Every, A.G., and McCurdy, A.K. (1992). *Landolt Bornstein, Numerical Data and Functional Relationships in Science and Technology*, vol. 29a, Berlin: Springer.
61. Kim, K.Y., Sachse, W., and Every, A.G. (1993). *Phys. Rev. Lett.* **70**: 3443; (1994). *Int. J. Mod. Phys.* **B8**: 2327.
62. Musgrave, M.J.P., and Payton, R.G. (1981). *Q. J. Mech. Appl. Math.* **34**: 235.

63. Kim, K.Y., and Sachse, W. (1994). *J. Appl. Phys.* **75**: 1435.
64. Kim, K.Y. (1994). *Wave Motion* **20**: 83.
65. Pao, Y.H., and Gajewski, R.R. (1977). In *Physical Acoustics*, p. 183, vol. 13, Mason, W.P., and Thurston, R.N., eds., New York: Academic; Pao, Y.-H., Gajewski, R.R., and Ceranoglu, A.N. (1978) *J. Acoust. Soc. Am.* **65**: 96.
66. Weaver, R.L., Sachse, W., and Kim, K.Y. (1996). *J. Appl. Mech.* **63**: 338; Weaver, R.L., Sachse, W., and Niu, L. (1989). *J. Acoust. Soc. Am.* **85**: 2255.
67. Chang, C., and Sun, C.T. (1988). *Composites Science and Technology* **33**: 213.
68. Sachse, W., Every, A.G., and Thompson, M.O. (1990). *Am. Soc. Mech. Eng. AMD-Vol.* **116**: 51.
69. Castagnede, B., and Berthelot, Y. (1992). *J. d'Acoustique* **5**: 417.
70. Castagnede, B., Deschamps, M., Mottay, E., and Mourad, A. (1994). *Acta Acustica* **2**: 83.
71. Audoin, B., Bescond, C., and Deschamps, M. (1996). *J. Appl. Phys.* **80**: 3760.
72. Niu, L. (1992). PhD Dissertation, Cornell University, Ithaca, New York.
73. Minachi, A., Hsu, D.K., and Thompson, R.B. (1994). *J. Acoust. Soc. Am.* **96**: 353.
74. Deschamps, M., and Bescond, C. (1995). *Ultrasonics* **33**: 205.
75. Every, A.G., and Sachse, W. (1992). *Ultrasonics* **30**: 43.
76. Castagnede, B., Every, A.G., and Sachse, W. (1992). *C.R. Acad. Sci. Paris*, t. **314**, Serie II: 865.
77. Kim, K.Y., and Sachse, W. (1993). *Phys. Rev.* **47**: 10993.
78. Kim, K.Y., Every, A.G., and Sachse, W. (1996). *Int. J. Mod. Phys.* **B10**: 235.
79. Wang, L. (1995). *J. Phys. Condens. Mat.* **7**: 3863.
80. Kim, K.Y., Sachse, W., and Every, A.G. (1993). *J. Acoust. Soc. Am.* **93**: 1393.
81. Every, A.G., Kim, K.Y., and Maznev, A.A. (1998). *Ultrasonics* **36**: 349.
82. Kolomenskii, A.A., and Maznev, A.A. (1993). *Phys. Rev.* **B48**: 14502; (1991). *JETP Lett.* **53**: 423; Maznev, A.A., and Every, A.G., *Solid State Commun.* **97**: 679.
83. Wu, T.T., Fang, J.S., Liu, G.Y., and Kuo, M.K. (1995). *J. Acoust. Soc. Am.* **98**: 2142; Wu, T.T., and Fang, J.S. (1997). *J. Acoust. Soc. Am.* **101**: 330.
84. Lekhnitskii, S.G., Tsai, S.W., and Cheron, T. (1968). *Anisotropic Plates*, New York: Gordon and Breach.
85. Maznev, A.A., and Every, A.G. (1995). *Acta Acustica* **3**: 387.
86. Wu, T.T., and Chiu, S.T. (1992). *Ultrasonics* **30**: 60.
87. Nakano, H., and Nagai, S. (1991). *Ultrasonics* **29**: 230.
88. Chen, H.Y., and Man, C.S. (1994). In *Rev. Prog. in QNDE*, p. 149, vol. 13A, Thompson, D.O., and Chimenti, D.E., eds., New York: Plenum.

3. LASER-BASED SURFACE ACOUSTIC WAVES IN MATERIALS SCIENCE

Alexey Lomonosov

General Physics Institute
Moscow, Russia

Andreas P. Mayer

Institute of Theoretical Physics
University of Regensburg
Regensburg, Germany

Peter Hess

Institute of Physical Chemistry
University of Heidelberg
Heidelberg, Germany

3.1 Introduction

3.1.1 Properties of Surface Acoustic Waves

3.1.1.1 Basics of SAWs. Surface acoustic waves (SAWs) are a class of waves that propagate along the interface of two elastic media, at least one of which is a solid. The long-wavelength elastic waves considered here can be treated within the framework of classical continuum elasticity theory. SAWs are solutions of the set of wave equations for the displacement components that usually satisfy the boundary conditions for a mechanically stress-free surface. The solutions can generally be presented as a linear combination of partial waves with wavevectors \mathbf{k}_{\parallel} parallel to the surface that propagate in the direction under consideration with the same phase velocity and decay exponentially in depth. In the following, planar surfaces are always parallel to the $x_1 - x_2$ plane. In this case the medium fills the half-space $x_3 > 0$. To a surface acoustic wave we attribute a wavevector $\mathbf{k}_{\parallel} = (k_1, k_2, 0)$ in the $x_1 - x_2$ plane and a frequency $\omega(\mathbf{k}_{\parallel})$. For Rayleigh waves and generalized Rayleigh waves, $\omega(\mathbf{k}_{\parallel}) = (v_R \mathbf{k}_{\parallel})k_{\parallel}$. The displacement field associated with a plane surface acoustic wave may be written in the form

$$u_j = \exp[i(\mathbf{k}_{\parallel} \cdot \mathbf{x} - \omega t)] w_j(x_3 | \mathbf{k}_{\parallel}) \quad (3.1)$$

In the case of (generalized) Rayleigh waves, the functions w_j are sums of exponentials,

$$w_j(x_3 | \mathbf{k}_{\parallel}) = \sum_r b_j(r) \exp[-\alpha(r)x_3] \quad (3.2)$$

with $\alpha(r)$ having positive real part. Hence, the displacement field is a superposition of up to three (in piezoelectric media up to four) inhomogeneous partial waves $\mathbf{b}(r) \exp[i(k_1 x_1 + k_2 x_2 + i\alpha(r)x_3 - \omega t)]$. For Rayleigh waves propagating along the planar surface of a homogeneous elastic medium, $\alpha(r) = k_{\parallel} \hat{\alpha}(r)$ and $\hat{\alpha}(r)$ is independent of k_{\parallel} . Unless stated otherwise, the functions $\mathbf{w}(x_3)$ are normalized such that the vectors $\mathbf{b}(r)$ are independent of k_{\parallel} . To simplify the notation, we shall use the symbol \mathbf{q} for the two-dimensional wavevector of the surface acoustic wave, rather than \mathbf{k}_{\parallel} .

Typically more than 90% of the energy of surface waves remains concentrated at a distance of the order of one wavelength below the surface. It should be noted that in all but the simplest cases an explicit calculation of SAW solutions is not possible and numerical computations are necessary (for reviews, see, for example, [1–8]).

3.1.1.2 Depth Penetration of SAWs. Among the most important surface waves are Rayleigh waves, which propagate on the stress-free planar surface of a semi-infinite isotropic half-space. The amplitude of the particle displacement decays exponentially and becomes negligible for depths more than a few wavelengths from the surface. The particle displacement is elliptically polarized. Normally the particle motion is decomposed into two orthogonal components in the sagittal plane, one in the direction of SAW propagation and one normal to the free surface. The major axes of the ellipses are normal to the surface. The typical depth dependence of the in-plane and normal displacement components in an isotropic material can be seen in Figure 3.1. This figure shows the varying aspect ratio of the ellipse with depth.

In anisotropic solids, the phase velocity and the form of displacements depend on the crystal plane used as the free surface and on the direction of the SAW wavevector in this plane (generalized Rayleigh waves). In an anisotropic crystal, the wavevector may no longer be parallel to the flow of wave energy or the group velocity. Directions with collinear phase and group velocity vectors are called pure mode directions. A feature often found in anisotropic crystals is an imaginary part in the decay constant $\alpha(r)$, which may be complex instead of purely real, resulting in the appearance of oscillations in the dependence of displacement components with depth (see Fig. 3.2). Nevertheless, the wave energy usually remains concentrated in the surface region. For certain propagation angles, however, Rayleigh-type waves exist with a velocity higher than that of the lowest transverse bulk mode. Apart from special cases, these waves have a small leakage of energy from the surface to the bulk and are called pseudo-surface waves (or leaky surface waves).

3.1.1.3 Thickness Dependence of SAW Propagation. If the depth of penetration of SAWs becomes comparable with the thickness of the substrate, boundary conditions at the second surface must be included in the theoretical treatment. The propagation velocity now depends on the thickness dimension

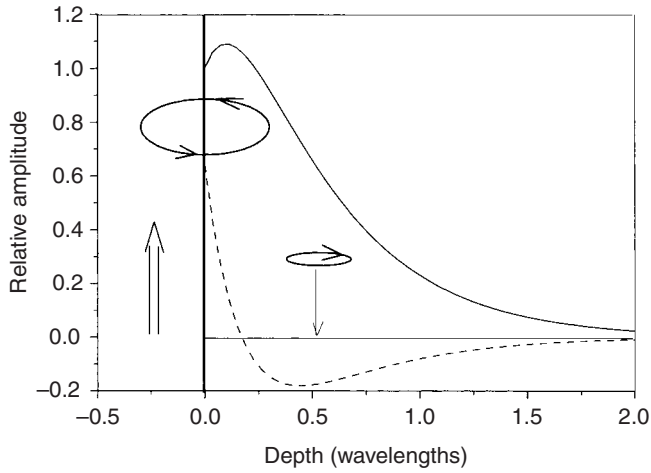


FIG. 3.1. Normal and in-plane displacement amplitudes in the sagittal plane as a function of depth for a SAW propagating in an isotropic substrate; particle trajectories for different depths are indicated. Normal component, solid line; in-plane component, dashed line.

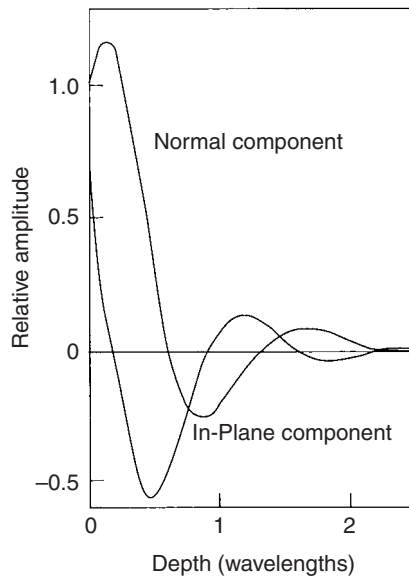


FIG. 3.2. Normal and in-plane displacement components in the sagittal plane as a function of depth for a SAW propagating in an anisotropic substrate.

of the plate; i.e., dispersion is observed and different modes of waves with symmetric and antisymmetric displacement distributions across the whole plate are possible. The symmetric modes with sagittal displacements have a symmetric in-plane component and an antisymmetric out-of-plane component with respect to the center line of the plate thickness, and therefore they are dilational in nature. The antisymmetric modes have antisymmetric in-plane and symmetric out-of-plane components, leading to a flexural plate motion. An infinite number of these plate or Lamb modes exist for such thin plates. With an increase in the thickness to about 2 to 3 wavelengths, the phase velocities of the lowest symmetric and antisymmetric modes asymptotically approach the velocity of the Rayleigh wave in a half-space of the material. In the following it is always assumed that the thickness of the substrate is much larger than the SAW wavelength. A series of papers has been published investigating Lamb modes in free-standing films or plates with laser methods [9–11]. This topic, however, will not be treated in more detail here.

3.1.2 Types of SAWs at Different Interfaces

3.1.2.1 Rayleigh-Type Waves. Besides Rayleigh waves in isotropic solids and generalized Rayleigh waves in anisotropic solids, SAWs in semi-infinite isotropic or anisotropic solids covered with a layer of material with different properties will be considered. Such layers may be added deliberately to modify the materials properties or may grow spontaneously on a reactive surface as, for example, the native oxide layer on a silicon wafer. Usually it is assumed that the film consists of a homogeneous solid of uniform thickness in intimate contact with the substrate.

Several kinds of surface waves may propagate in such a layered system. Here modes exist with particle displacements parallel to the propagation direction and normal to the free surface. They have characteristic properties in common with ordinary surface waves and plate modes. For long wavelengths, as compared to the film thickness, the particle motion extends far into the underlying substrate and the phase velocity approaches that of the bare substrate. In contrast, on going to high frequencies the particle motion will be more and more confined to the film region and the phase velocity comes nearer to that of the pure layer material. In principle, the wave can converge to a Stonely wave rather than to a surface wave of the layer material.

Since such a layer introduces a characteristic length scale, the layered medium becomes dispersive, where the phase velocity varies with the ratio between SAW wavelength and film thickness. Since the penetration depth varies with the SAW wavelength, different depths are probed simultaneously with a short SAW pulse containing a spectral distribution of wavelengths. Thus, in a layered system with a film thickness in the subwavelength region, dispersion of the phase velocity can be observed in a single broad-band pulse experiment.

A second characteristic feature of film systems, besides dispersion, is the existence of higher-order surface modes for sufficiently large values of the product of wavenumber q and film thickness d . This will now be discussed in more detail for a film loading the substrate, which causes normal dispersion. At a certain cutoff value qd , phase matching between higher-order modes and the bulk shear wave propagating parallel to the surface takes place. The coupled wave penetrates deep into the substrate with equal phase and group velocity. With increasing qd values the phase velocity of the higher modes decreases, as exhibited in Figure 3.3, and finally approaches the value of the bulk shear wave of the layer material. As an example, results are presented later on for polymer films on silicon. In the presence of a stiffening layer with anomalous dispersion, the phase velocity increases from the Rayleigh velocity of the substrate at $qd = 0$ to the shear velocity of the substrate with increasing qd . The example discussed later exhibiting this kind of behavior is a diamond-coated silicon substrate. For large qd values, the higher modes resemble plate modes of the layer under the influence of the substrate.

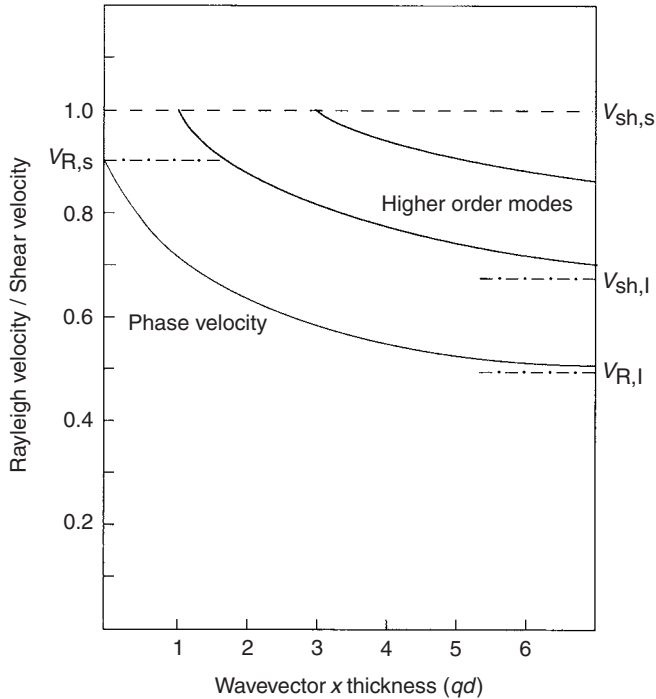


FIG. 3.3. Scheme of normal dispersion curves for higher order modes of an isotropic layer on an isotropic substrate.

3.1.2.2 Love Waves. In layered media, another type of guided wave exists, with a polarization different from that of Rayleigh waves, namely, the Love modes. In these waves the particle motion occurs at right angles to the propagation direction and parallel to the surface plane (perpendicular to the sagittal plane). Therefore, Love waves resemble horizontally polarized shear waves in the bulk, but are confined to the vicinity of the layer. A detailed theoretical treatment of laser-induced piezoexcitation of Love modes in heterogeneous systems is given in [12], confirming the possible application of laser-based Love waves to the remote diagnostics of films.

3.1.2.3 Other Interface Waves. There are also elastic waves that propagate along the plane interface between two condensed elastic media. The waves belonging to this group are guided and leaky waves at the interface between two solids (Stonely waves) and leaky Rayleigh and guided Scholte waves at the liquid–solid interface. Until recently only a very limited number of papers had been published on the optical detection of such waves [13, 14]. The laser-induced thermoelastic excitation of interface waves was considered for the first time in [15]. A general solution is derived for the acoustic field generated by potential sources distributed near the plane interface, in particular by thermoelastic stresses induced by the absorption of laser radiation. An analytical description of both the frequency spectrum and the time-domain profiles of the interface mechanical motion for pulsed excitation is presented. A formalism derived for laser-induced sound excitation in multilayered structures is applied specifically to the liquid–solid interface. It appears that the thermal expansion of the solid and liquid contributes in phase to the excitation of the Scholte wave. The theory further predicts that the laser-induced lateral wave in the liquid is suppressed at the frequency for which the Scholte wave penetration depth into the liquid is equal to the light penetration depth in the liquid.

This theory has been tested by pulsed laser excitation of Scholte waves on mercury–Plexiglas or mercury–fused silica interfaces and their subsequent detection by the laser probe beam deflection method. The shape of the Scholte pulse in the time domain and measured velocity as well as the attenuation of leaky Rayleigh waves were in good agreement with the theoretical predictions [16, 17].

3.1.3 Characteristic Features (Laser Ultrasound)

3.1.3.1 SAW Velocities. Velocities of elastic surface waves are in the range of $1\text{--}10 \times 10^3$ m/s, which is typical for transversal bulk waves in solids. As a consequence, SAWs propagate about 10^5 times slower than electromagnetic waves and hence possess an accordingly smaller wavelength at a comparable frequency. This fact is the basis of numerous practical applications of SAWs in signal processing devices, since SAW delay lines, filters, or

resonators are about 10^5 times smaller in size than corresponding electromagnetic devices working at the same frequency. For such technical applications, at present continuous SAWs are employed, which are generated and detected by suitable interdigital transducers (IDTs).

The phase velocity of a Rayleigh wave usually is about 5–13% below that of the slowest bulk wave, the transversal wave, and therefore cannot phase-match with any bulk wave. The fact that particles at the free surface are less constrained than in the interior of the material may be considered as a hint why normally the velocity of elastic surface waves is smaller than those of longitudinal and transversal bulk waves. A linear Rayleigh wave is dispersion-free, which means that an arbitrary surface pulse preserves its shape during propagation along the surface, because the phase velocity does not depend on frequency. The behavior of nonlinear SAW pulses, on the other hand, is much more complicated; they may form shocks during propagation in a nonlinear medium and even fracture the material.

3.1.3.2 SAW Frequencies. Typical frequencies of broad-band SAW pulses lie within the 5–500-MHz range, usually covering a spectral bandwidth of more than one decade simultaneously. Thus the corresponding wavelengths realized in a laser excitation process are, for example, about 1000–10 μm in silicon. The physical limitation is usually set by the minimal width of the laser focus employed in the thermoelastic excitation process. With narrow-band SAW trains, launched by interference of two laser pulses at the surface as counterpropagating waves, frequencies up to 5 GHz may be obtained, resulting in an acoustic wavelength of approximately 1 μm in silicon. The spectral bandwidth is determined in this case by the number of interference fringes in the surface grating and may be below 1% for a grating with 100 or more periods.

Since the penetration depth into the solid is on the order of the wavelength of the elastic surface waves, the extension of the acoustic field below the surface is typically in the micrometer to millimeter range. Therefore, the elastic waves considered here are in the continuum or long-wavelength limit of the microscopic surface vibrations, which require a lattice-dynamical treatment for their description at the molecular level. The subject of surface elastic waves nevertheless continues to play an important role because it provides the foundation of a variety of already existing devices and the basis for the future development of new technological applications.

3.2 Experimental

3.2.1 Pulsed Laser Excitation of Broad-band SAWs

Laser sources are widely used in investigations by means of SAWs of elastic properties of solids, various films, and coatings on surfaces. These

sources are noncontact; they allow a SAW transmitter of desired shape to be created and thus an acoustic beam with predetermined properties to be formed.

All laser-based methods of SAW generation in solids can be divided into two groups. The first group is connected with heating of the solid by the absorbed laser radiation and all consequences of this heating, such as thermal expansion, evaporation, and ablation. The second group combines the processes of interaction of the electromagnetic field with the lattice or electronic structure of the solid, including electrostriction, deformation due to carrier density modulation by laser radiation [18], and nonradiative recombination in semiconductors [19]. In this section we only consider thermal laser sources of SAWs, since they are more universal and in general more effective.

Among thermal methods it is convenient to distinguish between two limiting cases according to the relation between the absorbed energy density and specific heat of fusion and evaporation of the solid. The low-energy limit is the linear thermoelastic regime of SAW generation. All thermal and elastic parameters are assumed to be constant. Local pulsed heating causes transient thermal expansion and elastic stresses, which subsequently lead to emission of bulk and surface waves.

In the high-energy case, strong evaporation or ablation occurs in the irradiated area. The intense flow of vapor or ablated material generates a recoil momentum and a pressure pulse directed into the sample. The effects of the laser pulse are different in the two following cases: in the thermoelastic regime it produces an elevation of the surface, whereas under ablation conditions the surface is indented. Nevertheless, the longitudinal stress is always directed out of the irradiated area. It turns out that the pulse shapes are distinguishable for the two regimes. This allows for the determination of the prevalent mechanism in every specific case.

In the transition region from the thermoelastic to the ablation regime, the generation conditions are affected by many factors. The thermoelastic mechanism is suppressed by melting, and the recoil momentum is applied to a liquid phase. A phase transition also decreases the efficiency of SAW generation and significantly distorts the SAW pulse. These effects are considered in detail in [20].

3.2.1.1 Thermoelastic Regime. We consider an isotropic solid that occupies the half-space $x_3 > 0$. The laser beam is normal to the surface and is centered at $x_1 = x_2 = 0$. Laser radiation decays exponentially with depth into the solid so that the heat deposition can be written as $Q = \alpha I_0(1 - R) \exp(-\alpha x_3) H(x_1, x_2) I(t)$, where H and I represent the spatial light intensity distribution across the laser beam and its temporal profile, respectively, I_0 denotes the peak intensity, and R is the surface reflectance coefficient. In the adiabatic approximation the equation of motion for the displacement field

\mathbf{u} has the form

$$\rho \frac{\partial^2 u_i}{\partial t^2} = \frac{\partial \sigma_{ik}}{\partial x_k} \quad (3.3)$$

with the stress tensor

$$\sigma_{ij} = C_{ijkl} u_{kl} - \beta T C_{ijkl} \delta_{kl} \quad (3.4)$$

Here β is the bulk coefficient of thermal expansion, C_{ijkl} is the tensor of elastic moduli, and $u_{ij} = \partial u_i / \partial x_j$ denotes the strain. The first term is the conventional Hooke's law, and the second one is associated with the thermal expansion of a solid. The temperature deviation field T has to satisfy the equation of thermal conductivity:

$$\frac{\partial T}{\partial t} = D \Delta T + \frac{1}{\rho c_p} \alpha I_0 (1 - R) e^{-\alpha x_3} I(t) H(\mathbf{x}_{\parallel}) \quad (3.5)$$

where D denotes the thermal conductivity, ρ is mass density, c_p is the specific heat, and $\mathbf{x}_{\parallel} = (x_1, x_2)$.

If we restrict our discussion to the case of the solid–vacuum interface, the boundary conditions for the stress field reduce to $\sigma_{i3} = 0$ on $x_3 = 0$, $i = 1, 2, 3$; and for the temperature distribution $\partial T / \partial x_3 = 0$ at the surface $x_3 = 0$. Physically this means that the surface is not “loaded”; i.e., it is traction-free, and there is no heat flow through the surface.

The solution to this problem is given in [21]. These authors introduced scalar and vector potentials for the vibrational velocity and derived wave equations for them. The system of these two equations together with the thermal conductivity equation was solved using the Fourier transform with respect to x_1 , x_2 , and t , and the Laplace transform with respect to x_3 . In the approximation of strong light absorption $\alpha \gg \omega / v_R$, their solution for the vibrational velocity at the surface is given by

$$\begin{aligned} \dot{u}_3(t, |\mathbf{x}_{\parallel}|, \delta) &= \frac{\beta(1 - 4/3(v_T/v_L)^2)}{\rho c_p} I_0(1 - R) F \\ &\times \int_{-\infty}^{\infty} d\omega \int_0^{2\pi} d\xi \frac{i\omega^2}{v_R^2} \tilde{I}(\omega) \tilde{H}\left(\frac{\omega}{v_R}, \xi\right) \\ &\times \exp\left(-i\omega\left(t - \frac{|\mathbf{x}_{\parallel}|}{v_R} \cos(\delta - \xi)\right)\right) \end{aligned} \quad (3.6)$$

in the cylindric coordinate system $(|\mathbf{x}_{\parallel}|, \delta)$, where v_T , v_L , and v_R are the velocities of the shear, longitudinal, and Rayleigh waves, respectively, I_0 is the light intensity in the center of the beam, a tilde denotes Fourier transformation,

and

$$F = \left(\frac{v_R}{2v_T} \right)^2 \left(\left(2 - \left(\frac{v_R}{v_T} \right)^2 \right) \left(2 + \left(1 - \frac{v_R^2}{v_T^2} \right)^{-1} + \left(1 - \frac{v_R^2}{v_L^2} \right)^{-1} \right) - 8 \right)^{-1} \quad (3.7)$$

Let us consider the solution (Eq. 3.6) for a one-dimensional source of the following form:

$$H = \exp(-x_1^2/a^2), \quad I = \exp(-t^2/\tau^2) \quad (3.8)$$

where the duration of the laser pulse is 2τ and a is the half-width of the line source. In this case the integral in Eq. 3.6 can be evaluated analytically. The solution consists of two symmetric SAW pulses propagating in opposite directions along x_1 . The profile of each is given by

$$\begin{aligned} \dot{u}_3 = & -\frac{\sqrt{\pi}}{2} F I_0 a \tau \frac{\beta(1 - \frac{4}{3} v_T^2/v_L^2)}{\pi \rho c_p v_R} (\tau^2 + a^2/v_R^2)^{-3/2} \\ & \times \left(t - \frac{x_1}{v_R} \right) \exp \left(-\frac{(x_1 - v_R t)^2}{4(v_R^2 \tau^2 + a^2)} \right) \end{aligned} \quad (3.9)$$

The displacement calculated as the time integral of Eq. 3.9 is depicted in Figure 3.4. It has a Gaussian shape and is positive, and thus corresponds to an indentation of the surface. Note that if the laser pulse is short so that $\tau v_R \ll a$, the spatial profile of the vibrational velocity $\dot{u}_3 \propto H'$, and correspondingly the

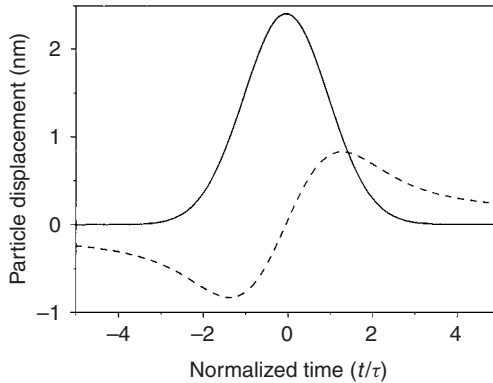


FIG. 3.4. Thermoelastic pulse profile in a straight-crested wave: normal displacement component, solid line; in-plane component, dashed line.

displacement is proportional to $H(x_1 - v_R t)$. Using the fact that \dot{u}_3 is an even function of $t' = t - x_1/v_R$, the maximal displacement can be expressed as

$$u_{3,\max} = \int_{-\infty}^0 \dot{u}_3(t') dt' = \frac{\sqrt{\pi}}{4} \frac{\beta (1 - \frac{4}{3} v_T^2/v_L^2) F}{\rho c_p} I_0 \frac{a\tau}{(a^2 + v_R^2 \tau^2)^{1/2}} \quad (3.10)$$

As can be seen from Eqs. 3.9 and 3.10, the efficiency does not depend on the light absorption coefficient α (if $\alpha \gg \omega/v_R$) and is determined on the one hand by the spatial and temporal parameters of the laser beam, and on the other by the elastic and thermal parameters of the medium.

Within this model, the laser radiation at the surface is described by the two parameters a and τ . In practice τ is determined by the type of laser used, whereas the width of the line source a can be adjusted to achieve the desired properties of the generated SAW pulse. Figure 3.5 shows the dependence of displacement amplitude on the parameter a for the two following cases. If one fixes the total energy of the laser pulse E_0 , the amplitude is a monotonically decreasing function of a and SAW generation becomes inefficient for $a > v_R \tau$. Taking as a typical example the Q -switched Nd:YAG laser and an aluminum sample, we assume $\tau \approx 5$ ns and $v_R \approx 2.9 \times 10^5$ cm/s, and the condition for efficient generation is given by $a < 15$ μ m (strip width less than 30 μ m). Focusing the laser beam into a thinner strip increases the peak intensity at the line center as $1/a$, and may cause destruction of the surface due to melting or ablation. To avoid surface damage, the pulse energy must be reduced proportionally to a to keep the flux constant. At the maximal admissible flux, the SAW amplitude dependence on a has the form presented in Figure 3.5 with a dashed line. In this case the amplitude increases linearly with a for small values of $a/(v_R \tau)$ since the absorbed energy is proportional to a , but for

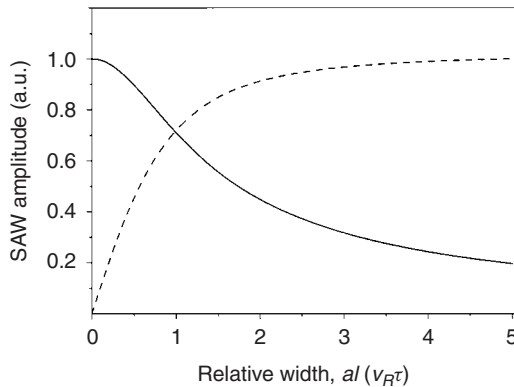


FIG. 3.5. Dependence of the thermoelastic pulse amplitude on the source width.

TABLE 3.1. Parameters of SAW Excitation by Means of Thermoexpansion (G_t) and Pressure Shock (G_a)

	Aluminum	Silicon	Quartz	Copper	Germanium
$G_t, \text{m}^3/\text{J}$	1×10^{-12}	1×10^{-13}	3.59×10^{-13}	4.86×10^{-13}	2.66×10^{-13}
$G_a, \text{m} \cdot \text{Pa}^{-1} \cdot \text{s}^{-1}$	1.16×10^{-8}	7.36×10^{-9}	1.47×10^{-8}	4.46×10^{-9}	5.86×10^{-9}

$a \gg \tau v_R$ the amplitude is determined solely by I_0 and its dependence on a is saturated. As follows from both amplitude dependences, the strip width can be reduced to the minimal possible quantity (corresponding to the solid curve in Figure 3.5) if the admitted light intensity is sufficiently lower than the surface destruction threshold. If the intensity must be limited, the optimal width has to be chosen as $a \approx v_R \tau$. The parameter $G_t = \beta F(1 - \frac{4}{3}v_T^2/v_L^2)(\rho c_p)^{-1}$ characterizes the influence of material properties on the SAW generation efficiency and has the physical meaning of a Grueneisen parameter. Table 3.1 gives the values of G_t for some materials.

Let us estimate the amplitude of a surface wave that can be achieved in the thermoelastic regime. We consider a laser pulse of 10-ns duration operating at a wavelength of 1.06 μm focused by a cylindrical lens into a strip on the sample surface. As sample material we take aluminum, which possesses relatively high values of G_t and light absorption α . As mentioned previously, the absorbed energy density is limited by the melting and ablation processes. According to [22], the peak intensity of the excitation laser pulse must not exceed 20 MW/cm^2 to hold the condition for thermoelastic excitation in aluminum. The reflectance coefficient for polished aluminum amounts to about 90%, and thus, for the parameters given and an optimal line source width, insertion of $a = v_R \tau$ in Eq. 3.10 provides a value for the maximal displacement of 2.5 nm.

According to the thermoelastic approach, the amplitude of the SAW pulse grows linearly with I_0 as predicted by Eq. 3.10. Experimental results confirm this dependence [23] until the light intensity reaches a certain value, where the amplitude remains almost constant for a wide range of intensities. This effect is explained in [20] as an effect of melting at the surface. A further increase of the light intensity leads to another mechanism of SAW generation—the ablative mechanism. Above a certain intensity the sample material starts to evaporate in an explosivelike manner, causing the recoil momentum and pressure pulse to occur normally to the surface.

3.2.1.2 Ablation Sources. The problem of calculating the magnitude of the recoil pressure caused by ablation is very cumbersome. Under real experimental conditions the material is ejected from the surface in different states, as a vapor, liquid, solid, or even a plasma. The thermal constants are undetermined, making it impossible to use the thermodynamic approach. In

the case of strong ablation, the plasma plume shields the surface from the incident light and continues to heat the surface after the end of the laser pulse.

A rough estimate for the case of weak ablation was given in [24]. Only the influence of the flow of vapor was considered, using the equilibrium thermal constants. According to this estimate, the pressure at the surface is given by

$$P_3 = \frac{(I_o I (1 - R) H)^2}{\rho (L + c_p (T_v - T_i))^2} \quad (3.11)$$

where L is the latent heat of evaporation, and T_v and T_i are the temperature of evaporation and the initial temperature, respectively.

We consider further the generation of the surface wave by a short pressure pulse applied normally to the surface with the magnitude defined by Eq. 3.11. The temporal profile of the recoil force is not directly connected to that of the laser pulse; therefore, we assume $P_3(\mathbf{x}_{\parallel}, t) = \Pi(\mathbf{x}_{\parallel})\delta(t)$, and the response to an arbitrary time dependence $P(t)$ can be evaluated by taking the convolution in time. We also neglect the influence of heating and take into account only the contribution of the impulsive force.

The equation of motion remains similar to Eq. 3.3, but the expression for the stress tensor does not contain the thermoelastic term: $\sigma_{ij} = C_{ijkl}u_{kl}$.

The effect of the recoil pressure appears as a boundary condition at the surface, which is no longer traction-free: $\sigma_{3,3} = \Pi(\mathbf{x}_{\parallel})\delta(t)$ for $x_3 = 0$. This boundary problem can be solved using a method similar to that in the thermoelastic case. Another approach was developed in [25], where the two-dimensional wave equation was derived for the in-plane components of a Rayleigh wave. The boundary problem thus reduces to an inhomogeneous wave equation with a term describing the source. The solution is given by

$$\mathbf{u}_{\parallel}(\mathbf{x}_{\parallel}, t) = \frac{v_R \Gamma}{8\pi^2 \rho v_T^2} \int i \frac{\mathbf{q}}{q} \tilde{\Pi}(\mathbf{q}) \sin(q v_R t) \exp(i \mathbf{q} \mathbf{x}_{\parallel}) d^2 \mathbf{q} \quad (3.12)$$

$$u_3(\mathbf{x}_{\parallel}, t) = \frac{v_R \Gamma}{8\pi^2 \rho v_T^2} \left(\frac{1 - v_R^2/v_L^2}{1 - v_R^2/v_T^2} \right)^{1/4} \int \tilde{\Pi}(\mathbf{q}) \sin(q v_R t) \\ \times \exp(i \mathbf{q} \mathbf{x}_{\parallel}) d^2 \mathbf{q} \quad (3.13)$$

Here Γ characterizes the elastic properties of the solid:

$$\Gamma = ((v_T^2 - v_R^2/2)((v_T^2 - v_R^2)^{-1} + (v_L^2 - v_R^2)^{-1}) - 2)^{-1} \quad (3.14)$$

In the case of a one-dimensional source $P = P(x_1)$, the expression for the in-plane displacement component can be derived in an explicit form:

$$u_1 = \frac{v_R \Gamma}{4\rho v_T^2} (\Pi(x_1 + v_R t) - \Pi(x_1 - v_R t)) \quad (3.15)$$

It consists of two symmetric pulses propagating in opposite directions along x_1 . The spatial profile of each pulse repeats the spatial distribution of the force applied to the surface. This distinguishes an ablation source from a thermoelastic one, for which the out-of-plane displacement component repeats the profile of the source. Another difference is that the ablation source itself has a spatial distribution that differs from the laser beam profile due to the substantially nonlinear character of the ablation process. According to Eq. 3.11, the pressure has a quadratic dependence on light intensity; hence the ablation source is $\sqrt{2}$ times narrower than the laser beam and, correspondingly, the SAW pulse is shorter than in the case of a linear source. Such a pulse shortening, when the mechanism of generation changes from thermoelastic to ablative, has been observed experimentally [20]. The parameter $G_a = v_R \Gamma (4\rho v_T^2)^{-1}$ characterizes the efficiency of SAW generation by means of an ablation source. It does not depend on any thermal properties of the substance and is determined solely by the elastic constants and density. Values of G_a are presented in Table 3.1 for the same materials as considered in the thermoelastic case.

Now we estimate the displacement amplitude in a SAW pulse generated by means of a one-dimensional ablation source in an aluminum plate. We consider a laser pulse of energy 30 mJ and $\tau = 5$ ns focused into a strip of 1-cm length and having a Gaussian profile with a width parameter $a = 15$ μm . In this case the absorbed power density attains 1.3×10^8 W/cm² in the middle of the strip, and the corresponding recoil peak pressure is estimated using Eq. 3.11 as 1.2×10^8 Pa. The displacement can be obtained by means of the time convolution of Eq. 3.12 with the temporal shape of the pressure pulse:

$$u_1(t - x_1/v_R) = \frac{v_R \Gamma}{4\rho v_T^2} \int P(x_1 - v_R(t - t'), t') dt' \quad (3.16)$$

where $P(x, t) = P_0 \exp(-2x^2/a^2) \cdot \exp(-2t^2/\tau^2)$. The out-of-plane component u_3 can be obtained using the general relation for one-dimensional Rayleigh waves in an isotropic solid:

$$u_3(t) = \frac{1}{\pi} \left(\frac{1 - v_R^2/v_T^2}{1 - v_R^2/v_L^2} \right)^{1/4} \int u_1(t - t')/t' dt' \quad (3.17)$$

In Figure 3.6 we present the calculated displacement components u_1 and u_3 . Their amplitude is comparable to that of the pulse shown in Figure 3.4, which is considered the maximal possible value within the thermoelastic approximation. Thus the intensity of 10^8 W/cm² is confirmed to cause a transition from the thermoelastic to the ablation regime of SAW generation for aluminum. With a further increase of the intensity, the ablative contribution becomes

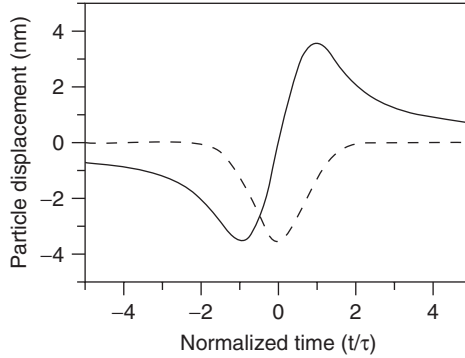


FIG. 3.6. Ablation pulse profile in a straight-crested wave: normal displacement component, solid line; in-plane component, dashed line.

dominant, since it grows proportionally to the square of intensity (Eq. 3.11), while the thermoelastic contribution is a linear function of light intensity. In contrast to a thermoelastic pulse (see Fig. 3.4), which represents a surface indentation, the ablation pulse profile is bipolar with a leading elevation part.

Solutions such as those given in Eqs. 3.9 and 3.15 can be used to simulate the surface waves in the near-field zone, defined by $x \ll k_0 l^2$, where l is the length of the source strip and k_0 is a low-limit value for the wavenumber. It is defined either by the frequency band of the generated pulse ($k_0 \approx a^{-1}$), or by the band of the detection setup ($k_0 \approx f_{\min}/v_R$). Diffraction effects are negligible in this area. Outside the near-field area, the shape of a SAW pulse suffers from the distortions caused by diffraction. Diffraction mainly affects the long-wavelength range of the pulse spectrum so that it loses the lower frequency part and the initially monopolar pulse gradually transforms into a bipolar profile. In order to simulate the influence of diffraction, it is necessary to take into account the finite size of the laser strip at the surface along x_2 .

As an illustration of the influence of diffraction, we consider the evolution of the SAW pulse generated by an axially symmetric thermoelastic Gaussian source. To obtain the displacement, Eq. 3.6 is integrated over t , and, using the identity $\int_0^\pi \exp(ikr \cdot \cos(\xi)) d\xi = \pi J_0(kr)$, we obtain

$$u_3(\mathbf{x}_{\parallel}, t) \sim \int \frac{|\omega|}{v_R} \exp[-\omega^2(\tau^2 + a^2/v_R^2)/4] J_0\left(\frac{\omega}{v_R} r_{\parallel}\right) e^{-i\omega t} d\omega \quad (3.18)$$

Outside the laser spot $r > a$, $kr > 1$ the Bessel function can be approximated as $J_0(kr) \approx (2/\pi)^{-1/2} (kr)^{-1/2} \cos(kr - \pi/4)$, and thus the surface displacement represents a running pulse of an almost steady shape with an amplitude decaying as $(a/r_{\parallel})^{-1/2}$. Numerical integration of Eq. 3.18 gives the pulse

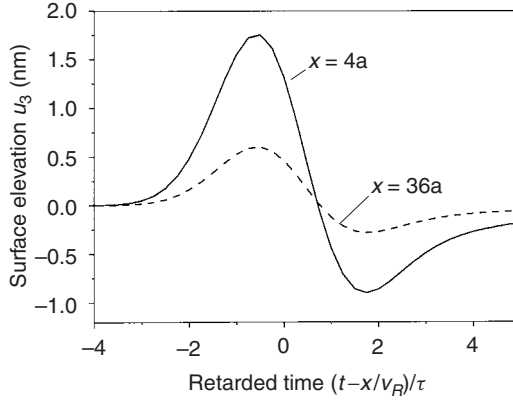


FIG. 3.7. Thermoelastic pulse profile in the far field.

profile in the far field, which is shown in Figure 3.7. The SAW pulse generated by a linear laser source of finite length l changes its shape from monopolar of the type presented in Figure 3.4 in the near field, $r \ll \pi l^2/a$, to bipolar, as shown in Figure 3.7, in the far field, $r_{\parallel} \gg \pi l^2/a$.

3.2.2 Transient Laser Gratings

Mode-locked laser pulses can be used for the generation of narrow-band SAWs. Since the SAW generation efficiency increases as laser intensity grows, picosecond (ps) laser pulses are normally used to excite transient laser gratings. In order to obtain periodic surface waves, the laser source at the surface must possess a periodic spatial intensity distribution. Such a source is produced by propagating the excitation beam through a diffraction grid [27] or by causing two or more coherent laser beams tilted with respect to each other to overlap in space and time at the surface [28, 29]. In the latter case the radiation of a pulsed laser is split by a 50% beam splitter, and then it is recombined at the sample surface, creating a one-dimensional interference pattern with light and dark regions. The laser intensity distribution at the surface is given by

$$I(\mathbf{x}_{\parallel}, t) = I_0(1 + \cos(2k \sin(\theta/2) \cdot x_1)) \exp(-t^2/\tau^2) \exp(-x_{\parallel}^2/a^2) \quad (3.19)$$

where I_0 is the intensity in the center, k is an optical wavenumber, and a and τ denote the beam radius and pulse duration, respectively.

As was discussed in the previous section, in the approximation of a short laser pulse, $\tau v_R k \sin(\theta/2) \ll 1$, the displacement field in a SAW is proportional to the spatial intensity distribution: $u_3 \propto I(x - v_R t)$, and thus the surface elevation at a fixed point consists of oscillations of frequency $f = v_R k \sin(\theta/2)/\pi$, modulated

by a Gaussian envelope of the form $\exp(-v_R^2 t^2/a^2)$. In the frequency domain this signal consists of a single spectral peak of full width $\Delta f = v_R/(2\pi a)$.

Narrow-band SAWs are widely applied in investigations of elastic, mechanical, and thermoelastic properties of thin films deposited on surfaces, as described in more detail in the section on SAW dispersion. In such experiments the dependence of the SAW velocity on the frequency is measured, and for this purpose the applied SAW must contain two spectral components or more, or the dispersion must be measured point by point, e.g., by changing the grating period, which depends on the angle between the two laser beams.

In [30] the transient grating source was produced by mixing three coherent excitation beams, which were obtained by diffraction of the excitation beam at a transmitting diffraction grid. The desired diffraction orders were then selected by a spatial mask and recombined at the surface. When three diffraction orders were used, the SAW frequency spectrum consisted of two narrow peaks on multiple frequencies of about 300 and 600 MHz. As reported in this paper, more than two spectral peaks can be excited by means of such a setup.

An alternative way to excite laser gratings with multiple frequencies is discussed in [31]. It was shown that the effect of thermal nonlinearity introduced by phase transitions in the SAW excitation region leads to the generation of higher harmonics of the transient grating signal.

3.2.3 Laser Detection of SAWs

Optical methods for SAW detection are based on the influence of the surface acoustic field on the probing light. These effects may be of many kinds, e.g., light diffraction on the surface grid generated by the counterpropagating surface wave train, or deflection of a narrow probe beam by a transient surface bump. The displacement produced by a surface wave shifts the phase of the reflected probe light, which can be measured by means of interferometric methods. In comparison with contact detection devices, optical ones are not so compact and usually more complicated. Therefore, they are not used in microelectronic devices. For scientific purposes, however, such techniques are widespread because of their flexibility and universality. An optical detector does not disturb the acoustic field as contact devices do, so it allows simultaneous measurements at different points. This feature makes laser probing the preferred alternative to contact methods in investigating the spatial evolution of surface waves, such as damping, dispersion, diffraction, or nonlinear distortion.

Laser detection methods can be applied only to surfaces of optical quality — they have to be optically smooth or mirrorlike; i.e., the roughness of the surface within the probe spot must be less than the optical wavelength. The light scattered randomly at the surface roughness increases the noise in the detector and correspondingly reduces detectability.

3.2.3.1 Interferometric Methods. The common feature of the wide class of interferometric techniques is the interference of a light beam reflected from the sample surface with a reference beam, or with itself, but delayed, using an optical path of fixed length. As an example of a reference beam interferometer, we consider the Michelson interferometer, the principle of which is shown schematically in Figure 3.8. The laser beam is split into two beams; one is used as a probe beam and the other as a reference beam. Each of these beams is reflected back so that they are combined again at the beam splitter and after partial deflection are directed onto a photodetector. The light intensity at the photodetector is determined by the superposition of the two waves with different phase shifts and is given by

$$I = I_R + I_P + 2\sqrt{I_R I_P} \cos 2k(\Delta + \xi) \quad (3.20)$$

where I_R and I_P are the intensities of the reference and probe, respectively, k is an optical wavenumber, Δ denotes the constant part of the path difference between probe and reference beams, and ξ is the surface displacement. The response of the light intensity I to relatively small surface displacements ($k\xi \ll 1$) can be expressed as

$$I'_\xi \cdot \xi = -4k\sqrt{I_R I_P} \sin(2k\Delta) \cdot \xi \quad (3.21)$$

Taking into account that $I_R + I_P = I_0$ is constant, it is found that the square root in Eq. 3.21 reaches its maximal value when reference and probe beams have equal intensities after reflection from the surface. The quantity Δ determines

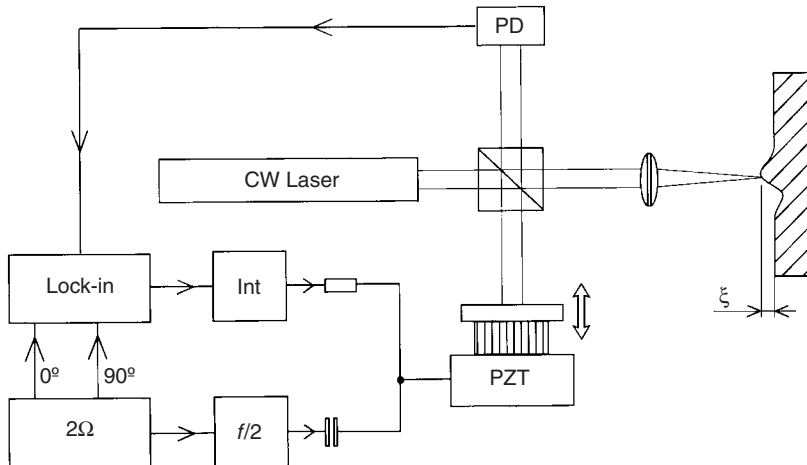


FIG. 3.8. Schematic diagram of a stabilized reference-beam Michelson interferometer.

the operation point of the interferometer and is usually tuned by positioning the reference mirror. As follows from Eq. 3.20, the dependence on Δ has the period of half an optical wavelength, so the operating point must be kept constant with an accuracy significantly less than the wavelength of the laser radiation. At the same time the experimental setup suffers different low-frequency distortions, which affect the optical paths on the scale of micrometers. All kinds of mechanical vibrations, acoustic noise, or temperature deviations can substantially modulate the sensitivity of the interferometer.

In many practical cases the vibrational velocity in a SAW is much higher than these perturbing variations of the optical paths. This allows the operating point to be stabilized by means of an active feedback. The feedback controller determines the deviation of Δ from its optimal value, for which the sine in Eq. 3.21 possesses the value of plus or minus unity. On the basis of this deviation, a signal is produced that shifts the reference mirror back to its optimal position. One practical way to measure deviations from the optimal operational point uses the fact that at this point the sinusoidal oscillation of Δ with frequency Ω causes a maximal photocurrent response at the original frequency Ω and a minimal response at multiple frequencies. In the scheme presented in Figure 3.8, the reference mirror is positioned by a piezotranslation stage (PZT), and an alternating voltage of frequency Ω is applied to it, which modulates the optical reference path. The doubled-frequency component in the photocurrent is selected by a phase-sensitive quadrature lock-in amplifier. Its output is integrated with the time constant τ and then applied to the piezotranslator to shift the reference mirror back to its optimal position.

The method described allows the compensation of slow perturbances with characteristic periods longer than the integration time τ , which is usually chosen to be of the order of 10^{-3} s. The photodiode signal at frequency Ω must be efficiently suppressed by the integrator, $\Omega > \tau^{-1}$, and consequently the low-frequency cutoff of measured surface vibrations is limited to frequencies above Ω .

In quadrature interferometers, the problem of setting the operation point is solved by applying a circularly polarized reference beam [32]. The signal beam is combined with the circularly polarized reference beam, and then a polarizing beam splitter separates mutually orthogonal polarizations, each of which is then measured by a separate photodiode. Signal beams have the same phase at each photodiode, but reference beams have a phase shift of $\pi/2$ with respect to each other. In [32] the signals of both photodetectors were squared and summed, and, as shown in this work, the processed output signal was proportional to the squared surface displacement and did not depend on the operation point. This type of interferometer can be used for measurements of SAW intensities but does not provide the profile of the surface wave. Application of a more complicated signal-processing scheme that takes into

account the phases of both quadrature interference signals allows the signal to be reconstructed proportional to the surface displacement [33].

3.2.3.2 Probe-Beam Deflection Method. This method is a modification of the knife-edge technique that is widely used for measuring the surface disturbances produced by thermoexpansion [34] or surface acoustic waves [35]. The typical arrangement of the probe-beam deflection (PBD) setup is shown in Figure 3.9. The probe beam is focused on a surface, the reflected beam is split into two symmetric parts by a pair of mirrors, and each part is collected by a separate photodetector. Subtraction of the photodetector outputs provides a signal that is sensitive to the position of the reflected beam. For small surface slopes this dependence can be considered to be linear, and for a Gaussian spatial beam profile it is given by

$$\Delta i = i_1 - i_2 = \frac{8}{\sqrt{\pi}} \eta W \cdot \varphi / \theta \quad (3.22)$$

where $i_{1,2}$ are the photocurrents, W is the total power of the reflected probe beam, η is the quantum efficiency of the photodetectors, φ is the surface slope, and θ is the convergence of the probe beam due to focusing. In the approximation of geometrical optics, we obtain $\theta \approx d/l$, where l is the focal length and d is the original beam diameter before the focusing lens. Decreasing the probe beam convergence θ improves the sensitivity, but, on the other hand, it results in an increase of the probe spot size at the surface due to diffraction and thus limits the frequency range.

The surface inclination φ has the meaning of a shear strain $\partial u_3 / \partial x_1$, and in the case of a traveling wave of the form $u = u(x_1 - v_R t)$, φ is equal to the Mach number: $\varphi = \dot{u}_3 / v_R$. Thus the probe-beam deflection method

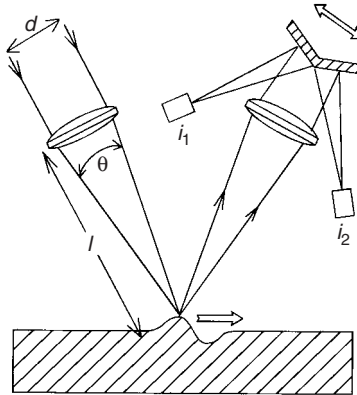


FIG. 3.9. Schematic diagram of a probe-beam deflection (PBD) setup.

provides the value of the surface velocity, in contrast to the reference beam interferometer described in the previous section. This makes such devices insensitive to the low-frequency vibrations and no stabilization is needed. The position of the beam-splitting double mirror with respect to the beam axes is the analog of the operation point in the case of the interferometer. The optimal position is approached by shifting the splitting mirror system across the beam in order to equalize the power in the split beams and so reduce the differential signal to zero, unlike in interferometric devices, where the accuracy required for setting the operation point is related to the optical wavelength. In the present case it is related to the beam diameter at the mirror system, which is of the order of centimeter. Therefore, the accuracy of commercial mechanical translation stages is quite sufficient for this purpose.

Using the differential scheme has a significant advantage in comparison with the knife-edge technique in that it doubles the useful signal and makes the transducer insensitive to fluctuations of the probe beam such as intermode beating or oscillations in the power supply.

The finite size of the probe spot on the surface sets the high-frequency limit of the SAW wavelengths that can be detected. From the general properties of Gaussian beams, the diffraction limit for the probe spot radius is estimated as $a = 2\lambda/(\pi\theta)$, where λ is the optical wavelength and θ is the probe beam convergence after the focusing lens. Let us now estimate the effect of the finite spot size on the system bandwidth. We consider a plane sinusoidal surface wave of the form $u_3 = \sin(2\pi(x - v_R t)/\Lambda)$. The surface inclination in such a wave is given by $\varphi = -2\pi/\Lambda \cdot \cos(2\pi(x - v_R t)/\Lambda)$. In the approximation of geometrical optics, we substitute this expression for φ into Eq. 3.22. Taking into account that W has a Gaussian spatial distribution, we obtain as the transducer response to a SAW of wavelength Λ

$$\Delta i = \frac{8}{\sqrt{\pi}} \eta W(v_3/v_R) \exp(-\pi^2 a^2/\Lambda^2) \quad (3.23)$$

Here v_3 is the normal component of the vibrational velocity and v_R is the phase velocity of the SAW. The ratio v_3/v_R on the right-hand side reflects the fact that the measured value is the shear strain, or shear Mach number, of the surface wave.

The dependence of Eq. 3.23 is shown in Figure 3.10 in normalized form. Since the transducer output is linear with respect to the surface slope and does not introduce any Λ -dependent phase shift, Eq. 3.23 can be used for signal correction to extend the bandwidth in the short-wavelength range.

3.2.3.3 Diffraction Methods. A narrow-band surface wave, which is a long train of one-dimensional periodic corrugation, behaves as a diffraction grid with respect to a relatively broad probe beam. If the irradiated probe-spot diameter is much larger than the SAW period, a pronounced diffraction of

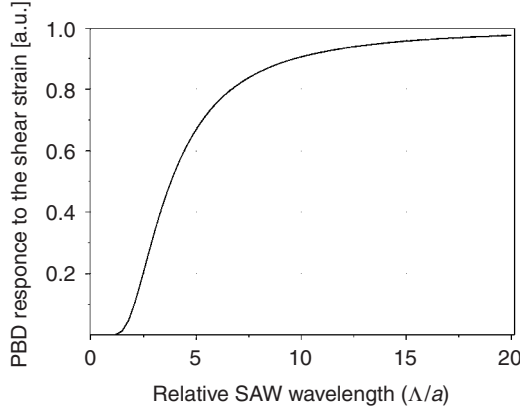


FIG. 3.10. Dependence of PBD response on the SAW wavelength.

the Raman–Nath type is observed. The diffraction signal consists of serial diffraction orders with the angular directions given by

$$\sin \theta_n = \sin \theta_0 + n\lambda/\Lambda, \quad n = 0, \pm 1, \pm 2 \dots \quad (3.24)$$

where θ_n denotes the direction of the n 'th diffraction order and λ and Λ are the optical and SAW wavelengths, respectively.

The relative intensity distribution between the diffraction orders depends on the surface grid shape. For sinusoidal SAWs of the form $u_3 = a \cdot \cos(kx - \omega t)$ the intensity in the n 'th order is given by

$$I_n = I_i R J_n^2(2ka \cos \theta_0) \quad (3.25)$$

where I_i is the incident beam intensity, θ_0 is the angle of incidence in the sagittal plane of the SAW, R is the coefficient of the surface reflectivity, and J_n is the Bessel function of order n . Using the small-argument asymptotic for the Bessel function in the form $J_n(x) = (x/2)^n/n! + O(x^{n+2})$, we obtain the following expression for the SAW parameters:

$$ak = (I_n/I_0)^{1/2} n! / \cos \theta_0 \quad (3.26)$$

In practice, only the first diffraction orders are used ($n = \pm 1$), since higher orders have negligibly small intensities [36].

By means of Eq. 3.26 the amplitude of the vertical vibrational velocity component ak can be evaluated, and, if the wavenumber k of the SAW is known, the surface displacement amplitude can also be calculated. The SAW wavenumber can be determined from Eq. 3.24 if the deflection angles θ_n are measured experimentally.

Since the diffraction method is applied to periodic surface waves, the bandwidth of the receiver can be made very narrow, substantially improving the signal-to-noise ratio. For this purpose the SAW is modulated by a rectangular pulse and then the correspondingly modulated I_1 signal is measured with the help of a lock-in amplifier. As reported in [37], the minimal detectable surface corrugation amplitude is as small as 0.05 \AA at the fundamental SAW frequency of 200 MHz and its multiple harmonics.

3.2.4 Piezoelectric Excitation and Detection

3.2.4.1 Interdigital Transducer. One of the key advances in the field of surface waves was the invention of the interdigital transducer (IDT), which allows the efficient conversion of an electrical signal into an elastic surface wave and then, in the reverse process, the transformation of acoustical energy back to an electrical signal. The transducers consist of a system of periodic metal electrodes (fingers) deposited on a highly polished substrate surface of piezoelectric materials such as quartz, LiNbO_3 , or LiTaO_3 . The periodic elastic deformation is produced by the electric field distribution arising in the substrate when a radio frequency (rf) voltage is supplied to the transducer. With fields localized at the free surface, the coupling can be made quite strong. The transducer possesses a maximum efficiency at the excitation frequency for which the surface wave propagates exactly one transducer period in one rf voltage period (synchronous frequency) $f_0 = v_R/2L$, where L is the length of the spatial electrode periodicity. The highest efficiency is found for equidistant transducer structures whose fingerwidth is equal to the gap between adjacent electrodes. The crystal is oriented such that the charge on adjacent IDTs induces alternating compressive and tensile strains in the piezoelectric material (see Fig. 3.11). The resulting periodic mechanical displacements launch a propagating SAW. If the electrical impedance of the transducer is matched properly to that of the signal source, almost 100% conversion of electrical to acoustic power is possible [3, 38].

Standard lithographic techniques can be used to manufacture interdigitated patterns suitable for SAW generation in the 10-MHz to 1-GHz frequency range (about $1\text{-}\mu\text{m}$ periodicity). Wave trains hundreds of wavelengths long can be generated and detected on a crystal surface a few millimeters long, providing a SAW with well-defined frequency. As the waves propagate along the surface, they can be modulated, manipulated, sampled, etc., between two IDTs used as sender and receiver. Both the velocity and the attenuation of SAWs are sensitive to the acoustic properties of materials placed on top of the propagation surface (acoustic wave sensors) and to the material properties of the substrate to a depth of approximately an inverse acoustic wavenumber. Therefore, it is possible to deposit a piezoelectric film of sufficient thickness on a nonpiezoelectric substrate in such a device. As soon as wireless-telecommunication

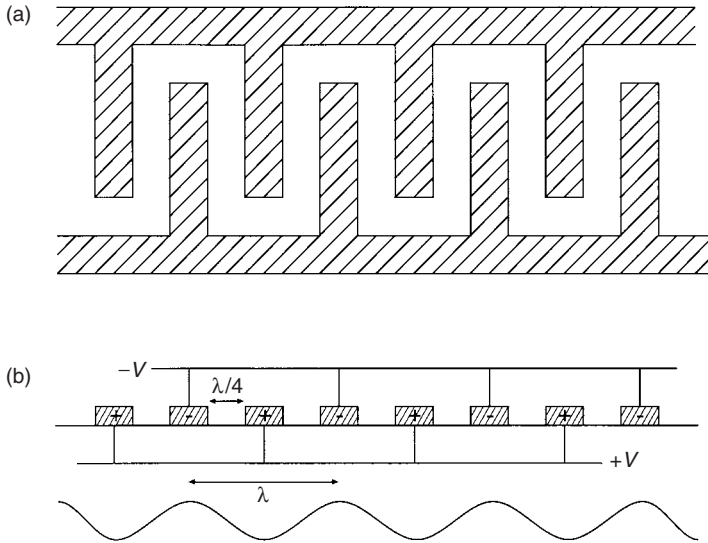


FIG. 3.11. Top (a) and side (b) views of the metallic fingers of an IDT placed on a piezoelectric substrate in alternating configuration and wavelength of the SAW.

applications go beyond 1 GHz, the interest in multilayer systems with a piezoelectric layer of ZnO or LiNbO_3 on a diamond layer and silicon substrate will grow. Since diamond has the highest known acoustic velocity, feature sizes of approximately $1\text{ }\mu\text{m}$ are sufficient to reach 2–3 GHz, whereas the electrode spacings in lithium niobate or quartz would be prohibitively small for current lithographic techniques ($\sim 0.3\text{ }\mu\text{m}$) [39].

3.2.4.2 PVF₂-Foil Transducer. As discussed before, high-quality surfaces are needed for contact-free optical detection of SAWs. The propagation of SAWs on rough surfaces can be monitored with high sensitivity and time resolution using a simple foil transducer, which, however, is not contact free because the piezoelectric foil has to be pressed gently onto the sample surface [40]. A substantially improved device, capable of monitoring frequencies up to 300–400 MHz, has been described in detail in [41].

The design of this broad-band transducer is shown in Figure 3.12. A tungsten rod with a knife edge with a radial curvature of several micrometers supports an electret foil. A short spring connects the tungsten rod to a coaxial connector. This spring also helps to exert a defined force on the knife edge when the transducer is positioned on the surface. Tungsten was selected as backing material because of its high specific acoustic impedance and its ability to obtain and hold a sharp edge. Other metals may be used as well for this purpose, however, with somewhat lower performance. The piezoelectric

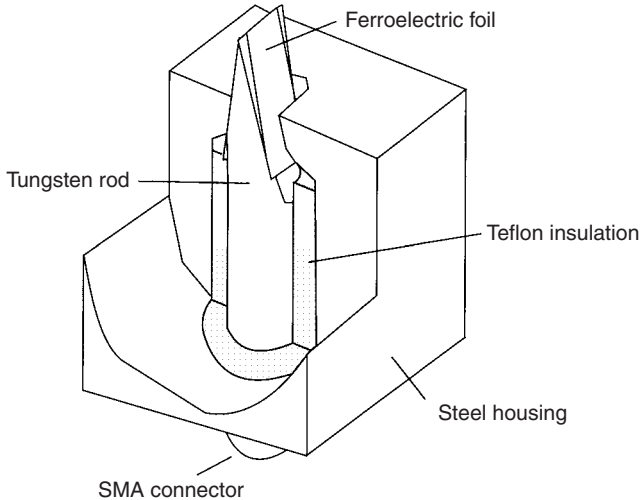


FIG. 3.12. Scheme of the piezoelectric foil transducer for contact measurements of broad-band SAWs.

foil of 6–9- μm thickness consists of a PVF_2 -TrFE (poly(vinylidene fluoride)-trifluoroethylene) copolymer, which, if available, is the material of choice because of its excellent pliability and ferroelectric properties as compared to PVF_2 (poly(vinylidene fluoride)). The side of the electret foil that is in contact with the sample is metalized with an approximately 20-nm-thick aluminum layer. This side of the foil is in electrical and mechanical contact with the grounded steel housing. The back side of the foil is attached to the tungsten rod, which serves also as counter electrode and pickup for the electrical signal induced by a propagating transient SAW pulse.

Such a transducer, with a difficult-to-estimate contact area of, say, approximately 5 μm to 5 mm, is ideally suited to detect plane surface waves. For this purpose the line focus of the laser and the knife edge must be precisely adjusted to a parallel position. The transducer response is quite reproducible; however, the signal varies with the pressure used to press the foil onto the surface. This means that if the detector is removed from the surface, it is difficult to reproduce exactly the previous setting again. Therefore, measurements at several distances require that the transducer be kept stationary on the surface and that the excitation source be moved. An example of the application of this transducer is given in [42], where the Young's modulus and density of thin TiO_2 films has been measured and the transition from the amorphous state at low temperature to anatase was monitored by the change in the Young's modulus as a function of temperature.

The foil transducer is much simpler and cheaper than the noncontact PBD method or Michelson interferometer and allows precision measurements of SAW velocities and pulse shapes on rough surfaces, such as unpolished polycrystalline diamond surfaces (discussed in more detail later on) or unpolished technical surfaces. A setup with a nitrogen laser for SAW pulse excitation and a foil transducer has been developed into a reliable, versatile, and easy-to-handle thin film analyzer that is commercially available [43]. This analyzer has been employed, for example, to determine the Young's modulus of diamond and diamondlike films with a thickness >100 nm [44] and to investigate the damage layer caused by the slicing of GaAs wafers from ingots by studying the dispersion effect [45]. In an averaged elastic modulus of the damaged layer in the as-sawn state was found by SAW measurements to be about 18% less than that of the GaAs single crystal. Damage penetrated to a depth of about $10\text{ }\mu\text{m}$ as verified by stepwise polishing [45].

3.3 SAWs in Anisotropic Solids

3.3.1 Theory of SAWs in Anisotropic Solids

Elastic anisotropy has strong effects on the propagation of acoustic bulk waves. Apart from plane waves propagating in special symmetry directions, they can no longer be classified as purely longitudinal or purely transverse, the degeneracy of the two transverse modes is lifted, and the slowness surface can assume a complicated geometrical structure. Certain features of this structure give rise to the phenomenon of phonon focusing.

In connection with surface acoustic waves, the implications of elastic anisotropy are even more dramatic. For a long time, it was not clear whether Rayleigh waves, which had been discovered by Lord Rayleigh for isotropic materials [46], existed in anisotropic solids for arbitrary crystal cuts and directions of propagation. The solution of this mathematical problem was the subject of the active research field of surface wave existence theory [47–50]. Here, the slowness surface of the acoustic bulk waves of the corresponding homogeneous elastic material plays an important role. From the Barnett-Lothe existence theorem [47], one may conclude that, for a given wavevector \mathbf{q} on a given planar surface with normal $\hat{\mathbf{z}}$ of a homogeneous nonpiezoelectric elastic medium, there is a unique subsonic surface wave whenever there is no plane bulk wave with wavevector $\mathbf{k} = q(\hat{\mathbf{q}} + p\hat{\mathbf{z}})$ which has maximal S_p and at the same time satisfies the traction-free boundary conditions at the surface. Here, $S_p = v^{-1}(\hat{\mathbf{k}})/\sqrt{1 + p^2}$ is the projection on the $\hat{\mathbf{q}}$ -axis of the point on the slowness surface corresponding to the wavevector \mathbf{k} . Situations in which this condition is not satisfied are either covered by the complete version of the existence theorem or have to be (and often have been) investigated separately.

The subsonic surface waves are generalized Rayleigh waves in the sense that they need no longer be polarized in the sagittal plane, and they usually consist of three rather than two partial waves. However, in very special situations, surface waves have been found that are formed by only one partial wave [51, 52]. In piezoelectric media, where the electrostatic potential comes into play as an additional degree of freedom and may be treated as a fourth component of the displacement field [53], generalized Rayleigh waves consist of four partial waves at most. In special situations on certain surfaces of anisotropic elastic media, supersonic surface waves occur [54, 55]. A well-known example is the (001) surface of a cubic crystal. In a certain range of the anisotropy parameter, the following behavior of the generalized Rayleigh waves is found [55]: As the wavevector \mathbf{q} is rotated from the (100) direction toward the (110) direction, the penetration depth of the surface waves increases. Exactly at the (110) direction, it has transformed into a bulk wave, while at the same time a supersonic surface wave has appeared as the endpoint of a branch of leaky waves (or pseudo-surface waves). These are solutions of the equations of motion and traction-free boundary conditions at the surface of the form given in Eqs. 3.1 and 3.2 with a wavevector that has a small imaginary part, describing attenuation along the direction of propagation, while one of the partial waves increases exponentially with depth but has a very small relative amplitude and real part of the exponent α . They are associated with resonances in the reflection of bulk waves from the surface. Although leaky wave solutions formally exist also in isotropic homogeneous half-spaces, it is the anisotropy that can lead to a very high degree of surface localization of leaky waves. It has recently been found that anisotropy can cause leaky waves to have a phase velocity smaller than that of the slowest bulk waves propagating parallel to the surface [56].

As in the case of bulk acoustic waves, anisotropy causes the group velocity of a (generalized) Rayleigh wave normally to point in a different direction than the wavevector. This leads to the effect of beam steering [57], which has to be accounted for in transducer design, as well as diffraction effects in general, which can be strongly influenced by anisotropy [58, 59].

As early as 1961, at a time when it was not yet known that generalized Rayleigh waves exist for most geometries of anisotropic homogeneous half-spaces, the possibility of focusing surface acoustic waves had already been envisaged in [60]. In the meantime, the effect of focusing surface acoustic waves has been analyzed theoretically by a number of authors [61–67], partly even for piezoelectric media [66, 67]. The ray-theoretical description is even simpler than that for bulk acoustic waves, since the slowness surface of Rayleigh waves is a one-dimensional object, i.e., a slowness curve. On the other hand, a full wave-theoretical analysis and the computation of the slowness curve are more complicated because of the boundary conditions to be

satisfied at the traction-free surface and the consequently more complicated structure of the displacement field associated with surface waves as compared to bulk waves.

The effect of phonon focusing is related to the fact that, in anisotropic media, the group velocity and the wavevector associated with a plane wave do not normally point in the same direction. In the case of plane bulk waves, the group velocity is easily calculated from the associated displacement field by using the Hellmann-Feynman theorem. For surface acoustic waves, a compact integral expression can be derived:

$$V_j(\hat{\mathbf{q}}) = -iN^{-1}(\mathbf{q}) \int_0^\infty C_{ljmn} w_l^*(x_3|\mathbf{q}) Q_n(\mathbf{q}) w_m(x_3|\mathbf{q}) dx_3 + c.c. \quad (3.27)$$

where

$$N(\mathbf{q}) = 2\rho q v_R(\hat{\mathbf{q}}) \int_0^\infty w_i^*(x_3|\mathbf{q}) w_i(x_3|\mathbf{q}) dx_3, \quad (3.28)$$

and

$$Q_n(\mathbf{q}) = \delta_{n1} i q_1 + \delta_{n2} i q_2 + \delta_{n3} (\partial/\partial x_3) \quad (3.29)$$

Equations 3.27 and 3.28 are valid for nonpiezoelectric media. In the presence of piezoelectricity, terms involving the piezoelectric coupling constants and dielectric constants have to be added. In both cases, the integrals are trivially evaluated analytically.

Parametrizing the unit vector in the direction of the group velocity as $\hat{\mathbf{V}}(\hat{\mathbf{q}}) = (\cos \phi, \sin \phi)$ and the wavevector $\mathbf{q} = q(\cos \phi, \sin \phi)$, one may define the focusing factor $A = |d\phi/d\theta|^{-1}$, which, in a geometrical acoustics picture, may be associated with the density of rays emerging from a point source. It may be expressed in terms of the Rayleigh wave velocity v_R and its derivatives with respect to θ or by the curvature κ (apart from a constant scale factor) of the slowness curve:

$$\frac{d\phi}{d\theta} = \frac{1 + v_R''/v_R}{1 + (v_R'/v_R)^2} \propto \kappa [v_R^2 + (v_R')^2]^{-1/2} \quad (3.30)$$

where v_R' denotes the first derivative of the Rayleigh wave phase velocity with respect to θ , $v_R' = \partial v_R(\hat{\mathbf{q}}(\theta))/\partial \theta$, and v_R'' is the second derivative. Focusing occurs when the focusing factor A diverges. Equation 3.30 shows that this happens for those wavevector directions $\hat{\mathbf{q}}(\theta_F)$ where the curvature of the slowness curve vanishes, i.e., $\partial^2 v_R/\partial \theta^2 = -v_R$. Focusing directions are the corresponding directions of maximal energy flow, $\hat{\mathbf{V}}(\phi(\theta_F))$.

To determine the displacement field at and near focusing directions, one conveniently starts with the Green's tensor ($\mathcal{G}_{mn}(\mathbf{x}_\parallel - \mathbf{x}_\parallel, x_3, x_3'; t - t')$) of the semi-infinite anisotropic elastic medium with traction-free surface, which

describes the response of the elastic medium to a point source acting at instance t' at location \mathbf{x}' [62]. We confine ourselves here to nonpiezoelectric media. Extension of the theory to piezoelectric media is straightforward [67]. The Green's tensor satisfies the equation of motion

$$\left[\frac{\partial^2}{\partial t^2} \delta_{il} - \frac{1}{\rho} C_{ijlm} \frac{\partial^2}{\partial x_j \partial x_m} \right] \mathcal{G}_{ln}(\mathbf{x}_{\parallel} - \mathbf{x}'_{\parallel}, x_3, x'_3; t - t') = \delta_{in} \delta(t - t') \delta(\mathbf{x} - \mathbf{x}') \quad (3.31)$$

for $x_3, x'_3 > 0$ and the boundary conditions

$$C_{i3lm} \frac{\partial}{\partial x_m} \mathcal{G}_{ln}(\mathbf{x}_{\parallel} - \mathbf{x}'_{\parallel}, x_3, x'_3; t - t')|_{x_3=0, x'_3>0} = 0 \quad (3.32)$$

and Sommerfeld radiation conditions at $x_3 \rightarrow \infty$.

For simplicity, we shall assume that the location \mathbf{x}' of the point source as well as the position \mathbf{x} of the observation point are near the surface such that $x_3, x'_3 \rightarrow 0$ with $x_3 > x'_3$. We indicate the order in which the limits for x_3 and x'_3 going to zero are taken by replacing the arguments x_3 and x'_3 of \mathcal{G} by 0_+ and 0, respectively. One may also show that

$$\frac{1}{\rho} C_{i3lm} \frac{\partial}{\partial x_m} \mathcal{G}_{ln}(\mathbf{x}_{\parallel} - \mathbf{x}'_{\parallel}, x_3, 0; t - t')|_{x_3=0} = \delta_{in} \delta(t - t') \delta(\mathbf{x}_{\parallel} - \mathbf{x}'_{\parallel}) \quad (3.33)$$

From the spectral representation of this Green's tensor, the following decomposition follows:

$$\mathcal{G}_{lm}(\mathbf{x}_{\parallel}, 0_+, 0; t) = \int \frac{d\omega}{2\pi} e^{-i\omega t} \int \frac{d^2 q}{(2\pi)^2} e^{i\mathbf{q} \cdot \mathbf{x}_{\parallel}} G_{lm}(\mathbf{q}, \omega) \quad (3.34)$$

with

$$G_{lm}(\mathbf{q}, \omega) = G_{lm}^{(B)}(\mathbf{q}, \omega) + \frac{W_{lm}(\mathbf{q})}{\omega^2 - \omega_R^2(\mathbf{q})} \quad (3.35)$$

While the first term on the right-hand side of Eq. 3.35 is associated with bulk acoustic waves, the second term has poles at the frequencies $\omega_R(\mathbf{q})$ of Rayleigh waves [68]. In an evaluation of the far field at the surface ($|\mathbf{x}_{\parallel}| \rightarrow \infty$) created by the point source, the contribution $G^{(B)}$ of the bulk waves is normally neglected. Special care has to be taken in the presence of pronounced surface resonances (leaky waves). To evaluate the contribution of the second term to the wavevector integral in Eq. 3.34 for large $|\mathbf{x}_{\parallel}|$ the stationary phase method has been used, which leads to the expression

$$\begin{aligned} \mathcal{G}_{lm}^{(S)}(\mathbf{x}_{\parallel}, 0_+, 0; t) &= \int \frac{d\omega}{2\pi} \sum_{\nu} \frac{\exp[i(\omega/v_R(\theta_{\nu}))|\mathbf{x}_{\parallel}| - i(\text{sgn}(a(\theta_{\nu})) + 2)\pi/4]}{[2\pi|\mathbf{x}_{\parallel}||a(\theta_{\nu})|2\omega\sqrt{v_R^2(\theta_{\nu}) + v_R'^2(\theta_{\nu})}]^{1/2}} \\ &\times W_{lm}([\omega/v_R(\theta_{\nu})]\hat{\mathbf{q}}(\theta_{\nu})) \end{aligned} \quad (3.36)$$

for the surface wave contribution $\mathcal{G}^{(S)}$ to the Green's tensor. Here, v labels the discrete solutions of the equation

$$x_2/x_1 = \tan(\phi(\theta)) \quad (3.37)$$

which means that the group velocity $\mathbf{V}(\hat{\mathbf{q}}(\theta_v))$ points in the direction of \mathbf{x}_{\parallel} , and

$$a = 2v_R[v_R + v_R''] = 2A^{-1}[v_R^2 + v_R'^2] \quad (3.38)$$

In the far field, the wave amplitude decays as $|\mathbf{x}_{\parallel}|^{-1/2}$, like cylindrical waves in the isotropic case, and is proportional to the square root of the focusing factor A . In directions of diverging A , Eq. 3.36 has to be replaced by

$$\begin{aligned} \mathcal{G}_{lm}^{(S)}(\mathbf{x}_{\parallel}, 0_+, 0; t) &= \int \frac{d\omega}{2\pi} \sum_v \frac{\exp[i(\omega/v_R(\theta_v))|\mathbf{x}_{\parallel}| - i\pi/2]}{\Gamma(2/3)[|\mathbf{x}_{\parallel}|\omega|b(\theta_v)|]^{1/3}} \\ &\times W_{lm}([\omega/v_R(\theta_v)]\hat{\mathbf{q}}(\theta_v)) \end{aligned} \quad (3.39)$$

where

$$b = 36v_R[v_R^2 + v_R'^2][2v_Rv_R' + v_R'v_R'' + v_Rv_R'''] \quad (3.40)$$

involving the third derivative v_R''' of the phase velocity with respect to the angle θ . It had already been noticed in [60] that, for directions corresponding to vanishing curvature of the slowness curve, the field amplitude decays less rapidly, namely, $\propto |\mathbf{x}_{\parallel}|^{-1/3}$, with increasing distance from the source. If the coefficient b vanishes simultaneously with a , the field amplitudes decay with an exponent even larger than $-1/3$ [63–65]. Effects beyond the stationary phase approximation have been considered in [69].

3.3.2 Angle Dependence of Linear Wave Propagation

3.3.2.1 The Phonon Focusing Effect. As discussed before in the theoretical section, the phase and group velocities of acoustic waves may differ in direction in elastically anisotropic solids. This means that the direction of energy propagation of the elastic wave is not in general collinear with its wavevector. The anisotropic propagation of elastic energy in anisotropic media is often referred to as phonon focusing. This effect was first observed for the transport of bulk thermal phonons as focusing of ballistic phonons in the 100-GHz range [70]. The observation of this effect for ultrasonic frequencies in the megahertz range was first reported in 1990; focused laser radiation was used as a point source for bulk ultrasonic waves and a small piezoelectric transducer as a point receiver [71]. The acoustic waves launched from a point source contain a broad distribution of wavevectors, which is essential for the observation of the focusing effect. By sampling the wavefront with a point

detector in the case of point excitation, the group velocity is measured and the anisotropy of wave propagation can be obtained directly. The extension of these experiments to SAWs was first reported in [72] using laser excitation and different methods of detection and in [73] employing standard ultrasonic immersion transducers.

The physical reason for the focusing and multiple arrival of SAWs is the elastic anisotropy of the crystal. To discuss this behavior in more detail, we consider the SAW slowness curve, the wavefronts of SAWs propagating from a point source, and the polar plot of the resulting SAW amplitudes. The slowness surface is given by a polar plot of the reciprocal phase velocity, the so-called slowness $s = 1/v_R(\theta)$, which characterizes the anisotropy of the phase velocity. Within a scaling factor the slowness surface coincides with the constant frequency surface $\omega(\mathbf{q}) = \text{constant}$ (see Fig. 3.13). Since for a given wavevector \mathbf{q} the group velocity vector is normal to the constant frequency surface, several wavevectors have group velocities in exactly the same direction in the concave regions with vanishing curvature. This gives rise to a folded wave surface with cusps corresponding to the inflection points of the slowness surface, as described in more detail in [74] for interfering pulses.

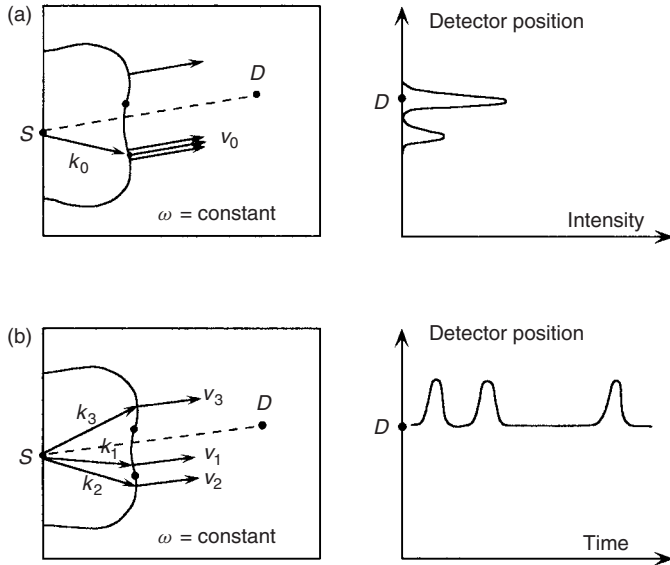


FIG. 3.13. Constant frequency surface with a point source and a point detector, illustrating the phonon-focusing effect and multiple arrivals in pulsed angle-resolved and time-resolved SAW experiments.

This is illustrated schematically in Figure 3.13, which depicts the constant frequency surface in k -space, where S indicates the point source and D the point detector. First a wavevector \mathbf{q}_0 in the direction of zero curvature is considered. Since neighboring \mathbf{q} 's have nearly the same group velocity, this gives rise to high-intensity caustics. There is a second wavevector with the same group velocity direction, however, which arrives at a slightly different time at the detector (two arrivals). If the detector is moved, say, a fraction of a degree, there are three \mathbf{q} 's with the same group velocity direction that reach the detector. Since the moduli of the group velocities of these rays are different, three arrivals are monitored in a time-resolved experiment. With a further slight increase of the observation angle the first and second arrivals merge, enhancing the SAW amplitude in certain directions (phonon focusing).

Up to now the anisotropic behavior of SAWs has been studied mainly in cubic crystals, such as silicon, germanium, and gallium arsenide. The factor of anisotropy $\eta = 2c_{44}/(c_{11} - c_{12})$ increases from Si(111) ($\eta = 1.56$) to Ge(111) ($\eta = 1.66$) to GaAs(111) ($\eta = 1.8$). As can be seen in Figure 3.14,

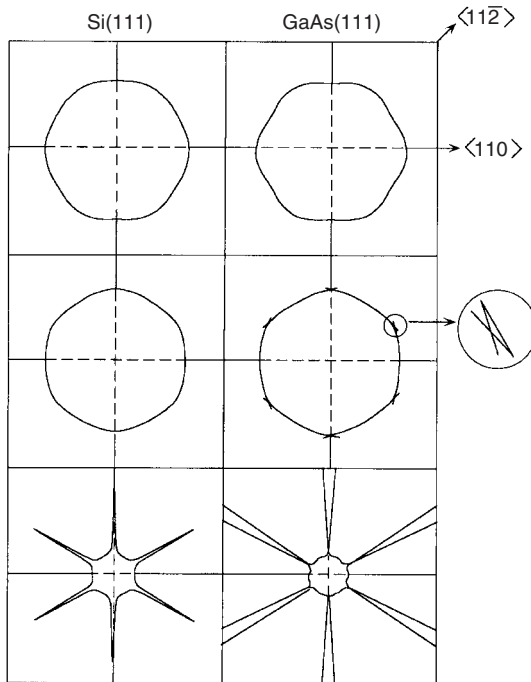


FIG. 3.14. Comparison of the SAW slowness curves, the wave surfaces of SAWs propagating from a point source, and the polar plots of the resulting SAW amplitudes for the Si(111) and GaAs(111) surfaces.

the concave sections of the slowness curve are pronounced for GaAs, leading to the tiny cuspidal structure in the wavefront. In the case of Si(111), which has a weaker anisotropy, theory predicts no singular direction, yielding only one focusing direction, at an angle of $\varphi = 30^\circ$ to the $\langle 110 \rangle$ direction. On the other hand, for GaAs singular directions (caustics) are found theoretically [75], positioned symmetrically about $\varphi = 30^\circ$.

3.3.2.2 First Demonstration of SAW Amplification. The amplification of the acoustic energy flux into certain directions was first visualized by the symmetric dust patterns created by the removal of particles from a dust-covered surface in directions of high SAW amplitude [72, 75]. In these experiments the sample surface, covered with alumina particles of 1–2 μm diameter, was placed vertically in a weak gas flow to avoid reverse settling of the detached particles. The nanosecond laser pulses generated normal vibrational velocities of about 1 m/s and surface accelerations of about 10^8 m/s^2 , sufficient to shake off micrometer-sized particles. The symmetric channeling directions observed in these measurements were confirmed by using a PBD setup to determine the normal surface velocity component as a function of the angle of observation.

Figure 3.15 compares photographs of the Si(111) and GaAs(111) surface, where the areas covered with particles can be seen as light regions. The dark lines are due to the removal of the particles by the passage of the SAW pulses, clearly indicating the directions of phonon focusing. The observed pattern agrees with the symmetry of the elastic properties of the (111) surface, with a threefold axis normal to the surface and its symmetry relative to the center and the $\langle 1\bar{1}0 \rangle$ direction. The direction of maximum acoustic energy concentration is also the direction with maximum phase velocity in silicon but differs by $\pm 2.5^\circ$ for GaAs(111). This simple technique of dust patterning has been applied to a number of materials and crystallographic planes; see, for example, the cuspidal structure in GaAs(111) [75]. However, it does not provide information on the SAW waveforms.

3.3.2.3 Resolution of the Cuspidal Structure. The multiple arrivals of SAW pulses in the cusp region were demonstrated for the GaAs(111) plane in the $\langle 11\bar{2} \rangle$ direction by time-resolved detection of the SAW waveforms [76]. Nanosecond UV laser pulses were focused to a spot of about 50 μm diameter, launching SAW pulses of approximately 20 ns duration. The SAW waveforms were monitored by the PBD technique. The temporal resolution of 4 ns was mainly limited by the finite size of the probe laser spot of about 10 μm diameter. The setup was able to detect a surface slope of 5×10^{-6} rad in the single-shot regime, corresponding to about 0.1 nm displacement of the surface in a SAW pulse.

The normal surface velocities measured for the SAW waveforms at different observation angles with respect to the $\langle 11\bar{2} \rangle$ direction are shown in Figure 3.16.

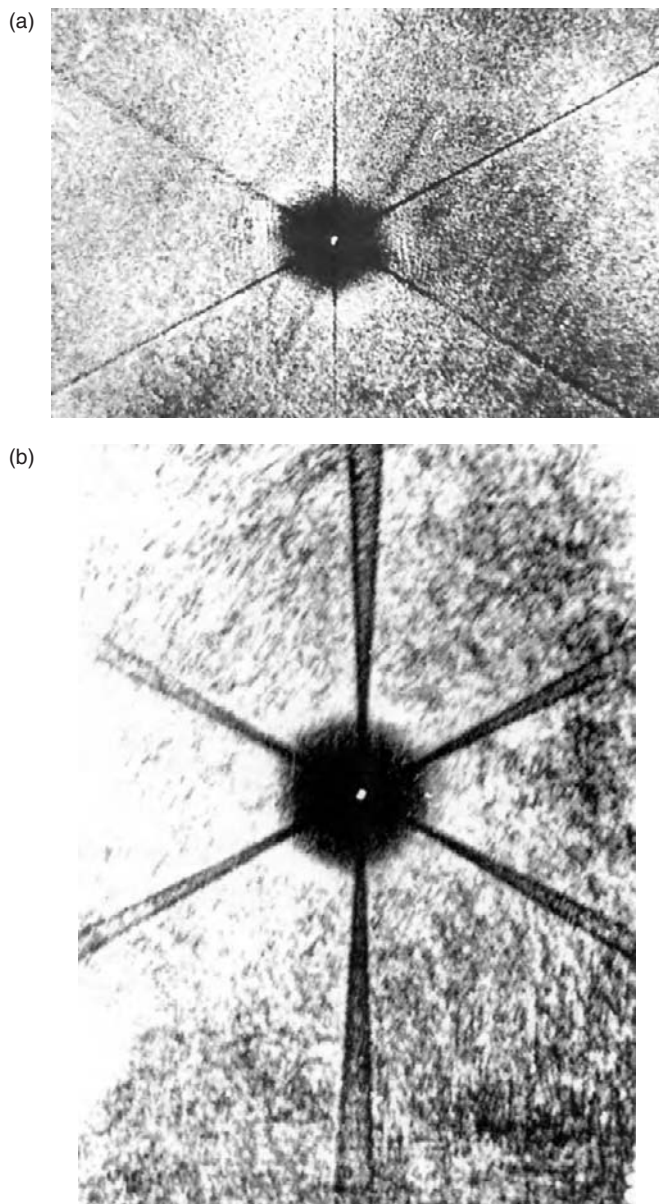


FIG. 3.15. (a) Photograph of a dust-covered Si(111) surface, where the dark lines mark the symmetric propagation directions of the high-amplitude SAWs. (b) The same for GaAs (111).

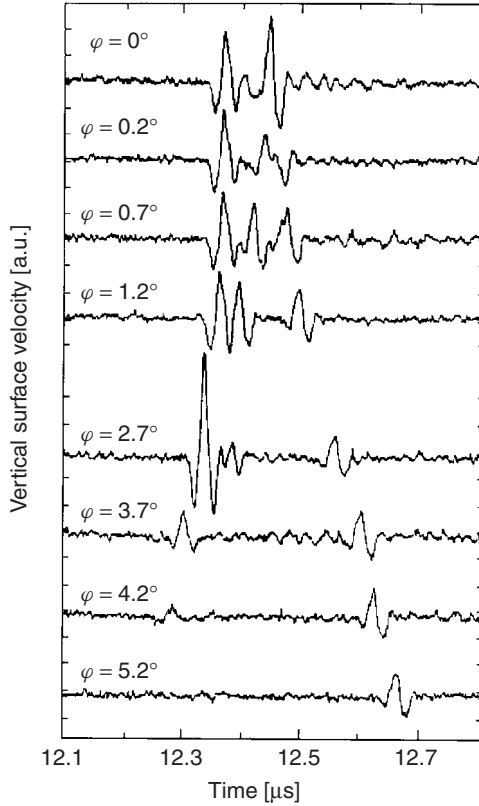


FIG. 3.16. Measurements illustrating the phonon-focusing effect and multiple arrivals of measured SAW waveforms at different angles near the $\langle 11\bar{2} \rangle$ direction on GaAs(111).

Two or three separate pulses corresponding to different branches of the cuspidal structure were observed at angles $|\varphi| \leq 4.5^\circ$. Note that because the ratio of the SAW propagation time to the SAW pulse duration is as large as ~ 1000 , the tiny cuspidal structure could be well resolved in these experiments. At $\varphi = 0^\circ$ the intersection of two branches of the wavefront results in a doubling of the amplitude of the second SAW arrival. This fact can be used for an accurate determination of the $\langle 11\bar{2} \rangle$ direction. When the observation direction deviates more than 0.2° from $\langle 11\bar{2} \rangle$, three arrivals can be clearly discriminated. With a further increase in the observation angle, the second arrival merges with the first one, resulting in a pulse of enhanced amplitude that reaches a maximum around 2.5° in GaAs. Subsequently, its amplitude falls off rapidly, and for $\varphi \geq 5^\circ$ only a single SAW arrival is left.

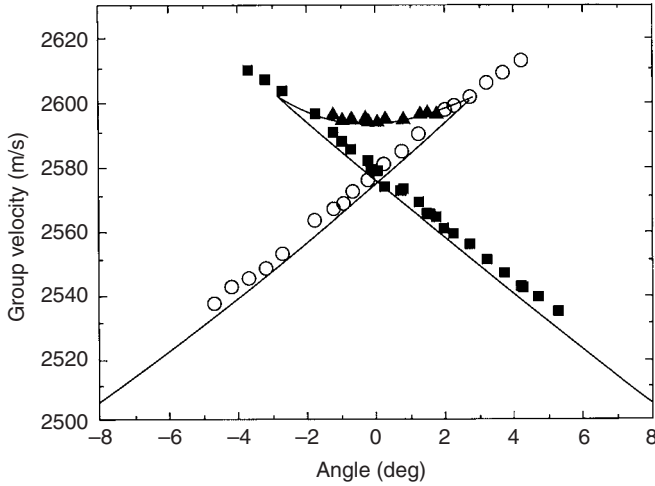


FIG. 3.17. Measured (symbols) and calculated (lines) angular dependence of the SAW group velocity near the $\langle 11\bar{2} \rangle$ direction on GaAs(111) (cuspidal structure). Triangles, open circles, and squares refer to the different arrivals.

The corresponding angular dependence of the group velocity of the SAW pulses, in which the cuspidal structure is resolved with split focusing directions, is presented in Figure 3.17, along with the calculated one [76]. The slight deviation of the calculated curves from the experimental points is well within the uncertainties in the reference data of the elastic constants of GaAs ($c_{11} = 118$ GPa, $c_{12} = 53.5$ GPa, $c_{44} = 59.4$ GPa, $\rho = 5.316$ g/cm³) of about 1%. It should be noted that the measurements of the bulk acoustic wave group velocities in the cuspidal region have been employed for the accurate determination of these elastic constants [77].

3.4 SAWs in Dispersive Media

3.4.1 Theory of Dispersion Effects

The basic equations of elasticity theory (and electroelasticity theory in the case of piezoelectric media) describing long-wavelength acoustic vibrations in solids do not define any length scale. Consequently, acoustic waves propagating in geometries that do not contain a length scale, either, are nondispersive; i.e., their frequency is inversely proportional to their wavelength. This applies to bulk acoustic waves in infinite homogeneous media, guided acoustic waves localized at the planar surface of a semi-infinite medium or the

planar interface of two semi-infinite media, wedge acoustic waves localized at free wedges, or wedge-type boundaries between two or more elastic media. Ideally, acoustic pulses that have been excited in these systems travel without changing their shape or, equivalently, their spectral composition. However, in most cases, there is some length scale present, leading to a nonzero curvature of the dispersion relation and hence to a broadening of acoustic pulses. Among the various dispersion mechanisms, we shall discuss in some detail the effects of surface coating and surface roughness and indicate their theoretical treatment. Others are only briefly mentioned.

3.4.1.1 Layered Media. When the planar surface of a semi-infinite elastic medium is covered by a film of a material different from the substrate, Rayleigh waves become dispersive. The displacement field associated with a surface acoustic wave continues to be of the form in Eq. 3.1. In the substrate, the function $\mathbf{w}(x_3|\mathbf{q})$ is still a linear combination of inhomogeneous plane waves that are exponentially decreasing as $x_3 \rightarrow \infty$ (maximum of three for nonpiezoelectric substrates), and

$$\mathbf{w}(x_3) = \sum_r \mathbf{b}^{(S)}(r) \exp[-\alpha_S(r)x_3] \quad (3.41)$$

for $0 < x_3 < \infty$. Likewise, we have in the film ($-d < x_3 < 0$)

$$\mathbf{w}(x_3) = \sum_r \mathbf{b}^{(F)}(r) \exp[-\alpha_F(r)x_3] \quad (3.42)$$

In Eqs. 3.41 and 3.42 and in the following equations, the sub- and superscripts S and F stand for substrate and film, respectively. In the film, there is no restriction on the exponents $\alpha(r)$. They may have positive or negative real parts or be purely imaginary. Consequently, the sum in Eq. 3.42 runs over a maximum of six partial waves in nonpiezoelectric media.

For a given frequency ω and wavevector \mathbf{q} parallel to the surface, the equations of motion for the displacement field in the film and substrate determine the quantities $\alpha(r)$ and, apart from complex factors, the vectors $\mathbf{b}(r)$. One may therefore write

$$\mathbf{b}(r) = c(r)\mathbf{W}(r) \quad (3.43)$$

with suitably normalized vectors $\mathbf{W}(r)$ determined from the equations of motion and coefficients $c(r)$ that are yet unknown. To determine the latter, the boundary conditions that the displacement field has to satisfy at the surface and at the interface have to be considered. In addition to the condition that the surface be traction-free, i.e.,

$$C_{j3mn}^{(F)} Q_n(\mathbf{q}) w_m(x_3)|_{x_3=-d} = 0 \quad (3.44)$$

for $j = 1, 2, 3$, the stress components σ_{j3} , $j = 1, 2, 3$, and the displacement field itself must be continuous at the interface:

$$C_{j3mn}^{(F)} Q_n(\mathbf{q}) w_m(x_3)|_{x_3=0_-} = C_{j3mn}^{(S)} Q_n(\mathbf{q}) w_m(x_3)|_{x_3=0_+} \quad (3.45)$$

$$w_j(0_-) = w_j(0_+) \quad (3.46)$$

for $j = 1, 2, 3$. Insertion of Eqs. 3.41–3.43 into Eqs. 3.44–3.46 yields a homogeneous linear system of nine equations for the six coefficients $c(r)$ in the film and three coefficients $c(r)$ in the substrate. The corresponding secular equation yields the dispersion relation of the guided waves that can propagate in this layered system. For a given wavevector direction $\hat{\mathbf{q}}$, the quantities $\hat{\alpha}(r) = \alpha(r)/q$ are functions of the ratio ω/q only. From the form of the secular equation following from the boundary conditions, it then becomes obvious that the phase velocity ω/q of the guided waves depends on q and d only via their dimensionless product qd .

For certain highly symmetric geometries or in the case of isotropic media, the shear-horizontal polarization decouples from the sagittal one. Depending on the magnitude of qd , the secular equation may have more than one solution, and the system becomes a multimode waveguide. There are higher-order Rayleigh waves or Sezawa modes and, in contrast to the case of isotropic homogeneous half-spaces, the film localizes shear-horizontal waves at the surface, the well-known Love waves. Their branch of lowest frequency exists for arbitrarily small qd values with phase velocity approaching that of bulk shear waves of the substrate as $qd \rightarrow 0$. These aspects, along with a description of the form of the displacement field for the guided modes, are all described in detail in various reviews and textbooks (see, for example, [78–80]).

Multilayer systems can be treated by a straightforward extension of this approach. Here, the dispersion relation of surface waves is efficiently derived using the transfer matrix method, especially when the sequence of layers is periodic [81] or quasi-periodic [82].

When the wavelength of the Rayleigh waves is much larger than the film thickness, i.e., $qd \ll 1$, the effect of the film on the Rayleigh wave frequency and displacement field can approximately be accounted for by effective boundary conditions at the substrate surface ($x_3 = 0$). The derivation of these effective boundary conditions to first order in qd [83, 84] makes use of the fact that at given \mathbf{x}_{\parallel} the displacement field varies little in the film. Consequently, one may approximate the displacement field $u_j(x_1, x_2, -d; t)$ at the free surface by

$$u_j(x_1, x_2, 0_-; t) - d[\partial u_j(x_1, x_2, x_3; t)/\partial x_3]|_{x_3=0_-} \quad (3.47)$$

and do the same for its derivatives. Eliminating then second x_3 -derivatives of the displacement field in the film with the help of the equation of motion and

making use of the continuity of the displacement field and its derivatives with respect to x_1, x_2 , and t at the interface, one arrives at the desired effective boundary condition:

$$\sigma_{j3}(x_1, x_2, 0_+; t) = d \left[\rho_F \frac{\partial^2}{\partial t^2} u_j(x_1, x_2, 0_+; t) - \sum_{l=1}^3 \sum_{m,n=1}^2 \tilde{C}_{jmln} \frac{\partial^2}{\partial x_m \partial x_n} u_l(x_1, x_2, 0_+; t) \right] \quad (3.48)$$

The right-hand side contains only derivatives with respect to t, x_1 , and x_2 of the displacement field on the substrate side of the interface, and the displacement field in the film does not occur in Eq. 3.48. ρ_F is the mass density of the film material, and the coefficients \tilde{C}_{jmln} are defined as

$$\tilde{C}_{jmln} = C_{jmln}^{(F)} - \sum_{i,k=1}^3 C_{jmi3}^{(F)} \Gamma_{ik} C_{k3ln}^{(F)} \quad (3.49)$$

where (Γ_{ik}) is the matrix inverse of the 3×3 matrix $(C_{i3k3}^{(F)})$.

When expanding the phase velocity of Rayleigh waves in powers of qd ,

$$v_R(\mathbf{q}) = v_R^{(0)}(\hat{\mathbf{q}})[1 + \mu(\hat{\mathbf{q}})qd + O([qd]^2)] \quad (3.50)$$

it is an easy task to determine the coefficient $\mu(\hat{\mathbf{q}})$ with the help of the effective boundary condition (Eq. 3.48) and Green's second integral theorem. The result can be brought into the form

$$\mu(\hat{\mathbf{q}}) = -[v_R(\hat{\mathbf{q}})N(\hat{\mathbf{q}})]^{-1} \sum_{m,n=1}^3 w_m^*(0|\hat{\mathbf{q}}) \left[\rho_F (v_R^{(0)}(\hat{\mathbf{q}}))^2 \delta_{mn} - \sum_{i,j}^2 \tilde{C}_{minj} \hat{q}_i \hat{q}_j \right] w_n(0|\hat{\mathbf{q}}) \quad (3.51)$$

In Eqs. 3.48, 3.49 and 3.51, we have written out the summation symbols explicitly because some of the sums run over 1 and 2 only. The quantity $N(\mathbf{q})$ is defined in Eq. 3.28, where v_R has to be replaced by $v_R^{(0)}$, the Rayleigh wave velocity in the absence of the film. Likewise, the quantities $w_n(0|\hat{\mathbf{q}})$ refer to the displacement field of Rayleigh waves in the absence of a film.

In geometries of high symmetry, Eq. 3.51 takes on a simple form, elucidating the role of the acoustic mismatch between film and substrate in making Rayleigh waves dispersive. If the substrate and film are cubic media with equal orientation and the propagation direction is along a cubic axis on a

(100) surface, one obtains $\mu = 0.5 P M_s$, where the dimensionless quantity P depends on ratios of elastic moduli of the substrate only and the mismatch factor M_s has the explicit form

$$M_s = (\rho_F/\rho_S) - (c_F/c_S) \quad (3.52)$$

with

$$c = [c_{11}^2 - c_{12}^2]/c_{11} \quad (3.53)$$

Depending on the relative values of the mass densities and moduli c of film and substrate, Rayleigh waves may exhibit normal ($\mu < 0$) or anomalous ($\mu > 0$) dispersion.

For small qd , the phase velocity v_{SH} of the lowest Love wave branch in this geometry of cubic media behaves as

$$v_{SH}(q) = v_T [1 - \frac{1}{2} M_{SH}^2 (qd)^2 + O([qd]^4)] \quad (3.54)$$

where v_T is the velocity of shear bulk waves propagating along a cubic axis and

$$M_{SH} = (\rho_F/\rho_S) - (c_{44}^{(F)}/c_{44}^{(S)}) \quad (3.55)$$

The influence of thin layers and capillary effects on the propagation of surface acoustic waves has been reviewed from a theoretical point of view in [4, 84, 85].

In certain situations, the elastic moduli and mass density of a solid vary continuously near the surface, which leads to dispersion of surface acoustic waves. We briefly consider here the case of x_3 -dependent material constants, which may be decomposed as $\rho = \rho_0 + \rho_1(x_3)$ and $C_{ijmn} = C_{ijmn}^{(0)} + C_{ijmn}^{(1)}(x_3)$. The x_3 -dependent parts of the density and elastic moduli are assumed to be small compared to the constant parts and nonzero only near the surface. One may then apply perturbation theory to assess their influence on the frequency of Rayleigh waves and obtain the following dispersion relation to first order in ρ_1 and $C^{(1)}$:

$$v_R(\mathbf{q}) = v_R^{(0)}(\hat{\mathbf{q}}) - [qN(\mathbf{q})]^{-1} \int_0^\infty \left\{ \rho_1(x_3) v_R^{(0)}(\hat{\mathbf{q}}) q^2 w_n^*(x_3|\mathbf{q}) w_n(x_3|\mathbf{q}) \right. \\ \left. - C_{ijmn}^{(1)}(x_3) [\mathcal{Q}_j(-\mathbf{q}) w_i^*(x_3|\mathbf{q})] [\mathcal{Q}_n(\mathbf{q}) w_m(x_3|\mathbf{q})] \right\} dx_3 \quad (3.56)$$

The functions $w_m(x_3|\mathbf{q})$, $m = 1, 2, 3$, and likewise $N(\mathbf{q})$ refer to the Rayleigh wave with wavevector \mathbf{q} propagating in a homogeneous half-space with density ρ_0 and elastic moduli $C^{(0)}$. The overlap integrals may be easily evaluated once the depth profiles of ρ and C are known.

3.4.1.2 Rough Surfaces. Even in homogeneous media, surface acoustic waves are usually dispersive because of surface roughness. Depending on the

preparation of the surface, one may encounter roughness on various length scales. We confine our discussion here to surface corrugations that can be described by a surface profile function $\zeta(x_1, x_2)$. The medium fills the spatial region $x_3 > \zeta(x_1, x_2)$ and, depending on the form of ζ , the surface may now have a nonvanishing local curvature. If the profile function is periodic in its arguments, the wavevector space is divided into Brillouin zones. At the edges of these Brillouin zones, the dispersion relation of surface acoustic waves usually flattens as a result of the interaction between wave components with wavevectors differing by a reciprocal lattice vector, and frequency gaps may open up. This leads to the phenomenon of wave slowing in periodic structures. Another important effect of the periodic corrugation is that surface acoustic waves become leaky from a certain frequency on. We add here that these phenomena also occur with acoustic waves propagating on the surface of acoustic bandgap materials [86] such as a periodic array of elastic cylinders embedded in a material with different elastic moduli and mass density.

When the profile function is periodic in one of its arguments (x_1) and independent of the other (x_2), we are dealing with a periodic grating. Methods for calculating dispersion relations for surface acoustic waves propagating on periodic grating structures have been reviewed in [80, 84, 87, 88]. For wavelengths large compared to the grating period, the velocity of Rayleigh waves has the form of Eq. 3.50, where d now plays the role of the periodicity of the grating, and the coefficient μ depends on its amplitude. In the case of a weak grating, the form of the dispersion relation of Rayleigh waves near the boundary of the Brillouin zone, $q = (\pi/d) - \Delta q$, is of the approximate form [89]

$$\omega(q) = v_R(\pi/d) \pm \sqrt{(\omega_G/2)^2 + (v_R \Delta q)^2} \quad (3.57)$$

with the gap width ω_G being given by

$$\omega_G = v_R S \left(\frac{\pi}{d} \right)^2 \left| \frac{1}{d} \int_{-d/2}^{d/2} \zeta(x_1) e^{i2\pi x_1/d} dx_1 \right| \quad (3.58)$$

The coefficient S depends on ratios of the elastic moduli of the elastic medium.

In the case of randomly rough surfaces, a statistical description is usually adopted to characterize the influence of the surface corrugation on the propagation of surface acoustic waves. In the simplest case, the profile function is assumed to be a stationary Gaussian random process $\langle \zeta(x_1, x_2) \rangle = 0$ and $\langle \zeta(x_1, x_2) \zeta(x'_1, x'_2) \rangle = f(x_1 - x'_1, x_2 - x'_2)$. The angular brackets denote an ensemble average, and $f(x_1, x_2)$ is the correlation function with Fourier transform $g(\mathbf{q}) = \int dx_1 \int dx_2 f(x_1, x_2) \exp[-i(q_1 x_1 + q_2 x_2)]$. It is often taken to be a Gaussian, $f(x_1, x_2) = \delta^2 \exp[-(x_1/d)^2 - (x_2/d')^2]$, with correlation lengths d and d' and mean square deviation δ^2 of the surface profile from

the average planar surface. The influence of random surface roughness on the propagation of surface acoustic waves has been investigated in the past (see [84, 87] for reviews of early work and [90–95] for more recent contributions). It essentially consists of an attenuation due to elastic scattering into bulk and other guided acoustic waves and a wavevector-dependent velocity shift leading to dispersion. The latter has been calculated in [93, 95, 96] for two-dimensional random roughness and in [90, 93] for random gratings ruled on the surface using perturbation theory to second order in the surface profile function. When carrying out such a calculation, it is convenient to start from an effective boundary condition at the average planar surface at $x_3 = 0$ of the form [92]

$$\begin{aligned} \sigma_{j3}(x_1, x_2, 0; t) = & -\zeta(x_1, x_2)\rho \frac{\partial^2}{\partial t^2} u_j(x_1, x_2, 0; t) + \sum_{l,n=1}^2 \sum_{m=1}^3 \frac{\partial}{\partial x_l} \tilde{C}_{jlmn} \\ & \times \left[\zeta(x_1, x_2) \frac{\partial}{\partial x_n} u_m(x_1, x_2, 0; t) \right] \end{aligned} \quad (3.59)$$

correct to first order in ζ . The coefficients \tilde{C}_{jlmn} are related to the elastic moduli of the elastic medium through Eq. 3.49 with the superscript (F) removed. With the help of the Green's tensor Eq. 3.34 for the semi-infinite elastic half-space filling the region $x_3 > 0$, the velocity shift $v_R(\mathbf{q}) - v_R^{(0)}(\hat{\mathbf{q}})$ of the Rayleigh waves due to the random roughness may be expressed as the real part of

$$-N^{-1}(\mathbf{q}) \frac{\rho}{q} \int \frac{d^2 k_{\parallel}}{(2\pi)^2} T_m^*(\mathbf{q}, \mathbf{k}_{\parallel}) G_{mn}(\mathbf{k}_{\parallel}, q v_R^{(0)}(\hat{\mathbf{q}})) T_n(\mathbf{q}, \mathbf{k}_{\parallel}) g(\mathbf{k} - \mathbf{q}) \quad (3.60)$$

where

$$T_m(\mathbf{q}, \mathbf{k}_{\parallel}) = \sum_{n=1}^3 \left\{ \delta_{mn} \left[v_R^{(0)}(\hat{\mathbf{q}}) q \right]^2 - \frac{1}{\rho} \sum_{l,l'=1}^2 \tilde{C}_{mlnl'} k_l q_{l'} \right\} w_n(0|\mathbf{q}) \quad (3.61)$$

In Eq. 3.61, the quantities w_n refer again to the displacement field of Rayleigh waves propagating along a planar surface. Once this displacement field and the Green's tensor for the semi-infinite elastic medium with a planar surface are known, Eq. 3.60 can easily be evaluated. The limit of small correlation lengths $d = d'$ as compared to the wavelength of the Rayleigh waves has been considered in [93] for isotropic and in [95] for anisotropic media and Gaussian correlation functions. The authors find a dispersion relation of the form given in Eq. 3.50 with $\mu(\hat{\mathbf{q}}) = (\delta/d)^2 \tilde{\mu}(\hat{\mathbf{q}})$. The coefficient $\tilde{\mu}(\hat{\mathbf{q}})$ depends on ratios of elastic moduli of the elastic medium as well as on the wavevector direction $\hat{\mathbf{q}}$. An explicit expression for $\tilde{\mu}$ for isotropic media is given in [93],

and numerical results for the dependence of $\tilde{\mu}$ on the propagation direction for various surfaces of anisotropic crystals are given in [95]. μ has been found to be negative (normal dispersion) in the analytic expression and in all numerical examples.

3.4.1.3 Other Dispersion Mechanisms. In piezoelectric media, dispersion may also be introduced by applying a grating of metal electrodes on the surface [97, 98], which modifies the electrical boundary conditions. Here, the spacings of the electrodes and their widths provide the length scales necessary for dispersion. If the electrodes are sufficiently thin, the influence of their mechanical properties is negligible.

When the frequency of surface acoustic waves is so high that their wavelength is no longer much larger than the lattice constant d of the underlying discrete lattice structure, pure elasticity theory is no longer adequate for the description of surface acoustic waves. However, in the spirit of an expansion in powers of qd , one may incorporate lattice dynamical aspects into continuum theory. To lowest order in qd , the effect of discreteness on Rayleigh waves enters via an effective boundary condition at the surface, and a dispersion relation of the form of Eq. 3.50 is found [80, 84].

Surface acoustic waves propagating on curved surfaces, such as the surfaces of cylinders or spheres, are clearly dispersive. A review on the theoretical treatment of Rayleigh waves on curved surfaces is given in [99].

3.4.2 Elastic Film Properties

3.4.2.1 Experiments in Layered Systems. The determination of the elastic constants of films and coatings with micrometer thickness or less in general poses serious experimental problems. Laser excitation of narrow-band wave trains by the laser-induced transient grating (LITG) method or broadband elastic surface pulses by focused laser radiation allows the accurate measurement of elastic film properties. Since the penetration depth of surface waves decreases with increasing frequency, the accuracy of such a measurement depends on the frequency range covered by the technique applied. Surface Brillouin scattering, for example, works at relatively high frequencies, 10–100-GHz region, whereas SAW methods are essentially limited to the 0.05–5-GHz range. On the other hand, Brillouin scattering is based on thermal phonon populations and requires data acquisition times of 20–30 h, while thermoelastic excitation of SAWs enhances the phonon population considerably, and therefore works on the time scale of seconds.

In an investigation with broad-band SAW pulses, the information content and depth resolution depend on the frequency spectrum of the acoustic pulse. The frequency spectrum of laser-excited coherent SAW pulses usually extends over more than a decade. The shorter wavelength spectral components of the elastic pulse, which travel to a larger extent in the film, normally propagate

slower or faster than the longer wavelength spectral components, which penetrate deeper into the substrate. This behavior is due to the difference between the acoustic properties of the substrate and film material. Therefore, the shape of the originally launched bipolar coherent SAW pulse changes with increasing propagation distance into a strongly oscillating pulse form due to interference of the partial waves, as shown schematically in Figure 3.18 [100].

If the high-frequency components of the acoustic pulse travel more slowly than the low-frequency components (softer film material or loading case), the oscillation frequency in the detected signal increases with time. Fourier transformation of the oscillatory signal measured at different distances from the source yields a frequency-dependent phase shift resulting in a decrease of the phase velocity with increasing frequency (normal dispersion). If, on the other hand, the high-frequency components of the pulse travel faster than the low-frequency waves (harder film material or stiffening case), the oscillation frequency of the detected signal decreases with time, as shown in Figure 3.18. This behavior, where the phase velocity increases with frequency, is called anomalous dispersion.

In a transient grating experiment, only a single frequency (narrow range) is available in a single experiment and the dispersion curve has to be constructed point by point by systematically varying either the angle between the two crossed laser pulses or the film thickness [101]. This procedure is time-consuming; however, frequencies of several gigahertz can be reached by LITGs, which are currently not obtainable with short SAW pulses.

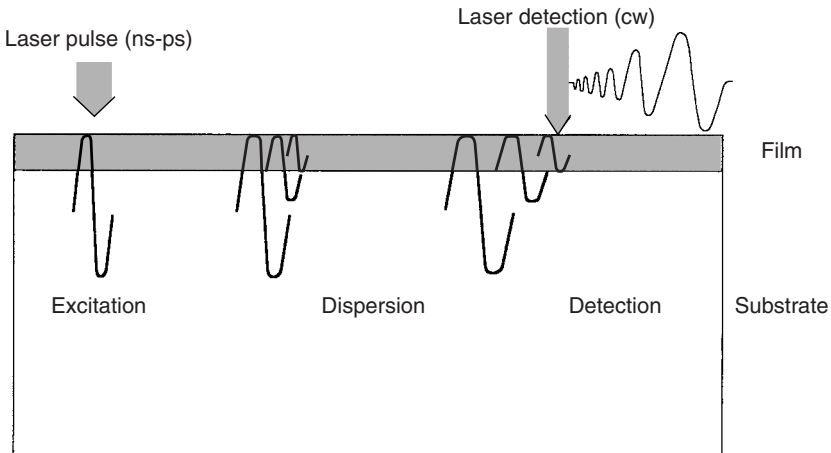


FIG. 3.18. Scheme illustrating the dispersion of a bipolar coherent elastic surface pulse into an oscillating pulse by interference of the spectral components propagating with different velocities.

As mentioned previously, the dispersion effect depends on the relationships between the mechanical and elastic properties of the film and substrate (acoustic contrast). For a given frequency value f and a given combination of the film and substrate properties, the phase velocity of the corresponding spectral components depends on the dimensionless product $\gamma = qd$ of the wavenumber $q = 2\pi f/v(f)$, where $v(f)$ is the phase velocity, and d , the film thickness. From the ratio of film thickness to SAW wavelength, the character of the dispersion effect can be estimated. Propagating surface waves may experience a measurable influence exerted by an ultrathin film as thin as one-hundredth to one-thousandth of their wavelength. In this case, however, only a small linear dispersion effect is observed, which may be used to determine one film property. Let f_{\max} be the maximum frequency in the signal spectrum with a sufficient signal-to-noise ratio and q_{\max} the corresponding wavenumber. Then the capability for the determination of film properties is given by the value of the parameter $\gamma_{\max} = q_{\max} d$. If a value of $\gamma_{\max} < 0.1$ is obtained in the experiment, usually the determination of only one film property is possible (linear dispersion). For larger values of γ_{\max} , two or even three film parameters may be accessible, because the dispersion curve becomes nonlinear [102]. For data analysis the dispersion curve can be described theoretically by the exact solution of the wave equations, taking into account the boundary conditions at the free film surface and substrate interface [78]. The parameters found for the best fit represent the solution of the inverse problem for the determination of the elastic and mechanical film properties.

3.4.2.2 Film Characterization with the Transient Laser Grating Technique. Detailed experimental and theoretical results involving the real-time characterization of surface acoustic modes of thin polymeric films, of about a micrometer thickness, by LITG experiments were reported in [103]. In this work pseudo-Rayleigh and Sezawa acoustic waves propagating in a polyimide coating attached to a silicon substrate were analyzed with the laser grating method.

In these LITG experiments performed in reflection geometry, two picosecond excitation pulses at 355 nm were crossed at the surface. A Q-switched pulse [103], or a gated square pulse from a continuous wave argon ion laser at 514 nm, was used as probe [104]. Figure 3.19 shows the diffracted signal for a 4.4- μm -thick free-standing polymer film with a fringe spacing of 20.55 μm . The oscillations are associated with acoustic standing waves that damp away. The inset shows the signal on microsecond time scales; the slow decay is associated with the thermal component of the response and can be used to determine the in- and out-of-plane thermal diffusivities [104].

We first discuss results obtained for a polymer film tightly bound to silicon. To study the dispersion of the phase velocity in a large $\gamma = qd$ range, the film thickness was varied between 0.92 and 8.46 μm and the wavenumber between

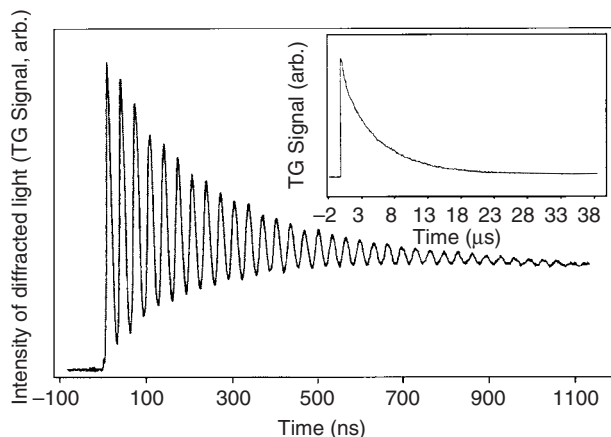


FIG. 3.19. Diffracted signal obtained by LITG measurements on a 4.4- μm free-standing polyimide film (Pyralin 2555) deposited on a silicon substrate. The inset shows the signal on a microsecond time scale; the slow decay is associated with the thermal component of the response.

0.15 and $1.81 \mu\text{m}^{-1}$ in these experiments. As can be seen in Figure 3.20(a), strongly nonlinear dispersion curves were observed, yielding $v_l = 2650 \text{ m/s}$ and $v_t = 1160 \text{ m/s}$ for the longitudinal and transversal velocities, respectively, of the polyimide (DuPont Pyralin 2555) sample. With the known density of 1.45 g/cm^3 , a Young's modulus of $5.4 \pm 0.5 \text{ GPa}$ and a Poisson ratio of 0.38 ± 0.02 could be calculated to characterize the polymer. As predicted from the normal dispersion behavior, the Young's modulus is lower and the Poisson ratio higher than the values of the silicon substrate [103, 105]. Figure 3.20(b) presents results for a free-standing polymer film. The striking differences between the acoustic properties in these two cases are due solely to the mechanical contact of the film to the substrate.

If the elastic constants are known, other system parameters such as the film thickness and/or the density can be determined in a noncontact and nondestructive manner with high precision using the LITG technique described. For example, the thickness of metal films (Cu, Ta, W, Al, and Ti) in the micrometer range deposited on silicon substrates was measured with a repeatability of a few angstroms and data acquisition times of about 1 s [106].

3.4.2.3 Evaluation of Elastic Properties with Broad-band SAW Pulses. As an example of the determination of elastic properties using short SAW pulses, we consider polycrystalline diamond films of about $4 \mu\text{m}$ thickness deposited with the hot filament technique on silicon substrates using methane concentrations of 0.5, 1.0, 1.5, and 2.0% in the hydrogen source gas [107]. The dispersion of the broad-band pulses was employed to determine the film

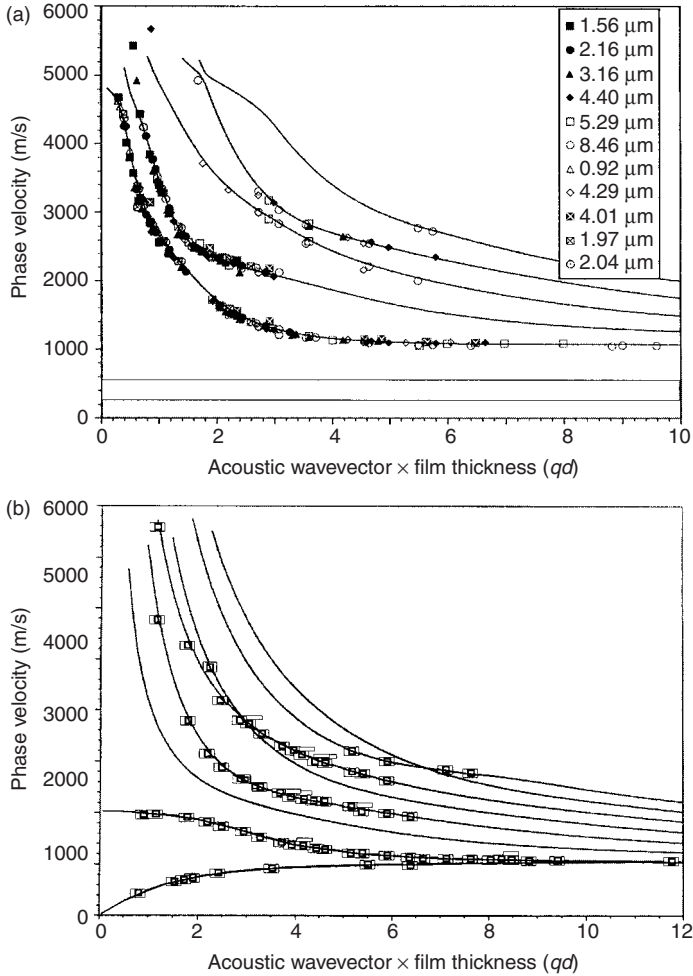


FIG. 3.20. Experimental (symbols) and theoretical pseudo-Rayleigh mode dispersion curves (lines) for Pyralin 2555 films on silicon with the thicknesses indicated (in micrometers). The elastic constants were obtained by the best fit to the data of the two lowest velocity curves of the upper part of the figure. The lower part presents results for a free-standing film.

density, Young's modulus, and Poisson ratio from the transforming profile of the propagating oscillatory SAW pulse.

The absorption of the exciting laser radiation occurs in this system at the grain boundaries of the polycrystalline material and/or at the silicon interface. Since the as-grown polycrystalline diamond films were very rough, no

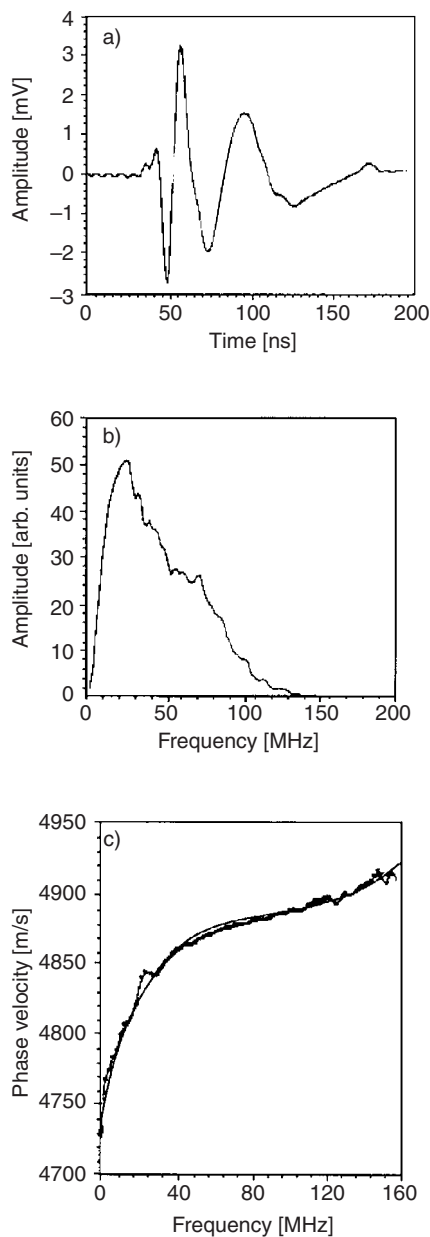


FIG. 3.21. (a) Typical SAW pulse shape with anomalous dispersion. (b) Corresponding amplitude spectrum. (c) Experimental dispersion curve with theoretical fit.

optical detection method could be used. Therefore, suitable detection was possible only with the foil transducer. Figure 3.21 shows a typical SAW pulse shape monitored at a distance of 20 mm from the line source, the corresponding amplitude spectrum of this pulse after Fourier transformation, and the resulting anomalous dispersion curve, obtained by measurements at two or more distances from the source, together with the theoretical fit. The strong nonlinearity of the dispersion of the phase velocity allowed the extraction of three film properties, despite the limitation of the frequency range to about 160 MHz by the system properties. The high information content in the diamond/silicon system is due to the large acoustic contrast between these two materials.

In Table 3.2 the values of the thickness, the roughness obtained by scanning force microscopy (SFM), the Poisson ratio, the density, and the Young's modulus are collected for the four diamond films investigated. As can be seen, the quality of the films improves with decreasing methane concentration in the source gas, approaching the values of single-crystalline diamond. Since the growth rate depends on the methane concentration in the source gas, a much longer deposition time was needed to reach the given film thickness with 0.5% methane. This reduction in the growth rate obviously improves the diamond quality.

Besides these polycrystalline diamond films free-standing polycrystalline diamond plates, grown by electron-assisted hot filament CVD, were investigated using the SAW technique [108]. From the velocities of the longitudinal acoustic bulk waves (LABWs) and SAWs, values of the Poisson ratio of about $\nu = 0.14$ were obtained. The Young's modulus varied between 928 GPa and 1098 GPa. Anomalous dispersion of the SAWs on the nucleation side was observed in some samples. In addition the mean velocity of the SAWs was higher on the nucleation side than on the growth side of the plates. This indicates that the elastic properties changed considerably during the growth process. Measurements of the grain size by scanning electron microscopy (SEM), of the phase purity by Raman spectroscopy, and the texture by X-ray

TABLE 3.2. Results Obtained for Diamond Films by SAW Measurements: Thickness of Diamond Film, Poisson Ratio, Density, and Young's Modulus as a Function of the Methane Concentration

CH_4/H_2 [%]	Film thickness d [μm]	Poisson ratio	Density [kg/m^3]	Young's modulus [GPa]
0.5	4.4 ± 0.1	0.10 ± 0.05	3530 ± 50	1080 ± 20
1.0	4.4 ± 0.1	0.10 ± 0.05	3560 ± 50	1030 ± 20
1.5	3.9 ± 0.1	0.15 ± 0.05	3500 ± 50	1000 ± 30
2.0	3.2 ± 0.2	0.15 ± 0.05	3400 ± 50	925 ± 30

diffraction (XRD) were performed in order to estimate the contribution of different effects to the dispersion and the side dependence of the SAW velocities. In all samples the SAW velocities were higher on the nucleation side than on the growth side, whereas the grain sizes were larger on the growth side. While $\langle 110 \rangle$ -like fibre textures were concurrently measured on the nucleation side of the samples, textures differed for the growth sides. Dispersion was observed for plates which showed a difference in texture between nucleation and growth side. On the other hand, samples without change of texture and without dispersion also exhibited differences in the SAW velocities of 4% between the two sides. While higher SAW velocities can in principle be explained by a lower density and/or a higher Young's modulus, neither Raman spectra (non-diamond carbon phases and inhomogeneous stress distribution) nor the texture (XRD measurements) in the film or the hydrogen content completely explain the results of the SAW measurements.

In addition the elastic constants of several diamond films with grain sizes in the nanometer range were determined. These films possess a relatively smooth surface with a high abrasive resistance. For a film with a grain size in the 10 nm range a Young's modulus of 405 GPa was measured, whereas for a grain size of roughly 50 nm a Young's modulus of 730 GPa and for larger grain sizes values up to 1040 GPa were found [109]. Figure 3.22 provides an overview of the Young's moduli versus density for single crystal diamond,

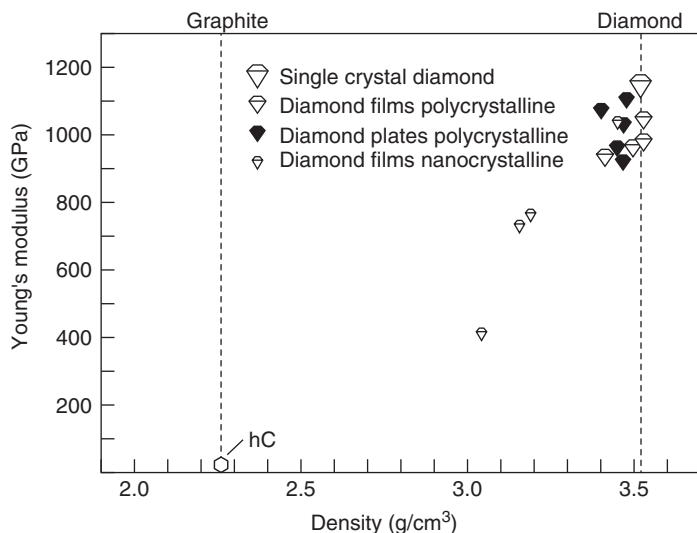


FIG. 3.22. Plot of Young's moduli of single crystal diamond, polycrystalline diamond films and plates, nanocrystalline diamond films, and graphite versus density of the material.

polycrystalline diamond films and plates, as well as nanocrystalline diamond films. In addition, graphite is included for comparison.

Similar to carbon, which exists as the two modifications diamond and graphite, boron nitride exists in two analogous modifications, namely cubic (zinc blende) boron nitride (cBN) and hexagonal boron nitride (hBN) with comparable elastic and mechanical properties. Currently, cBN is a material of growing interest, since it has a hardness of about 70 GPa and elastic constants coming close to those of diamond, as illustrated in Fig. 3.23. With respect to its higher oxidation resistance, greater chemical resistance to ferrous alloys such as steel, and doping properties, cBN is superior to diamond. However, unlike diamond, which can be grown as thick polycrystalline films and plates in optical quality under low-pressure conditions, c-BN has only been deposited as relatively thin nanocrystalline films up to now. Single crystals of cBN up to 3 mm in diameter have been obtained under high-pressure conditions [110], whereas polycrystalline c-BN plates were produced by directly sintering cBN powder at high pressures and temperatures. The elastic properties and density of such polycrystalline disks, measured by the dynamic resonance method, have been reported recently [111] and are included in Fig. 3.23.

Cubic boron nitride (cBN) films of 200–420 nm thickness and high phase purity were deposited on silicon (100) substrates by ion-assisted pulsed

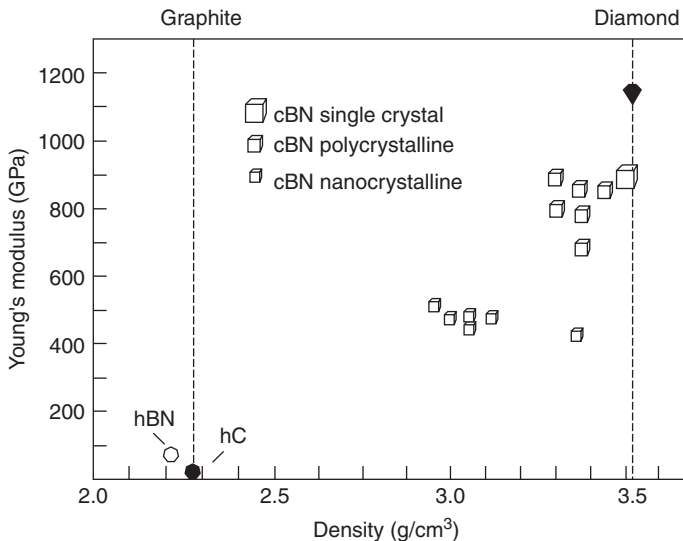


FIG. 3.23. Plot of the Young's modulus of single crystal, polycrystalline, and nanocrystalline cBN, as well as of hBN as a function of density, including for comparison the single crystal diamond and graphite values.

laser deposition from a boron nitride target using a KrF-excimer laser and by plasma-enhanced physical vapor deposition with a hollow-cathode arc evaporation device [112]. In order to improve the cBN film adhesion, hexagonal boron nitride (hBN) films with 25–50 nm thickness were used as buffer layers. The densities and Young's moduli of the c-BN films were obtained by investigating the dispersion of surface acoustic waves. In data analysis a two-layer model was applied in order to take the influence of the hBN layer into consideration. The values for the density vary from $2.95 \pm 0.25 \text{ g/cm}^3$ to $3.35 \pm 0.3 \text{ g/cm}^3$ and those for the Young's modulus from $420 \pm 40 \text{ GPa}$ to $505 \pm 30 \text{ GPa}$ [112]. In Fig. 3.23 the Young's moduli of single crystal, polycrystalline, and nanocrystalline cBN and of hBN are plotted versus density, including single crystal diamond and graphite for comparison with the hardest material.

The development of new materials or the modification of already known composites is a wide and important field of research in materials science and technology. For some purposes materials with versatile properties are needed, while other applications demand only a very specific behavior. Today, with the help of computer simulations, it is possible to estimate the physical and chemical properties of materials. To study the elastic properties of a system with three components amorphous SiC_xN_y films with various compositions were deposited by ion beam sputtering. The bonding characteristics, Young's modulus, and density of the films were investigated using X-ray photoelectron spectroscopy (XPS), Fourier transform infrared (FTIR) spectroscopy, surface acoustic wave spectroscopy (SAWS), X-ray reflection (XRR), and molecular dynamics (MD) simulations [113].

It was observed that the Young's modulus decreases from 260 GPa to 85 GPa while the density decreases from 3.45 g/cm^3 to 2.3 g/cm^3 as the carbon content of the films increases from 0 to 68%, as can be seen in Fig. 3.24. FTIR and XPS spectra indicate an increasing proportion of double and triple bonds with higher carbon content of the films. These experimental results were compared with the Young's moduli and the IR spectra obtained from density-functional-based MD simulations. Also in these model calculations the Young's modulus drops from 237 GPa to 109 GPa as the carbon content increases from 0 to 69% (see Fig. 3.24). It can be seen that the formation of $\text{C}=\text{C}$, $\text{C}=\text{N}$, $\text{C}\equiv\text{C}$, and $\text{C}\equiv\text{N}$ bonds, together with the occurrence of terminating nitrogen atoms for the films with higher carbon content, is responsible for the degradation of the stiff three-dimensional sp^3 -network, and therefore for a lower Young's modulus and density [113]. Thus, the simulation improves our understanding of the dependence of the mechanical properties on the carbon content in the SiC_xN_y composit at the molecular level.

Another interesting problem that can be solved by acoustic dispersion measurements is the determination of the elastic and mechanical properties

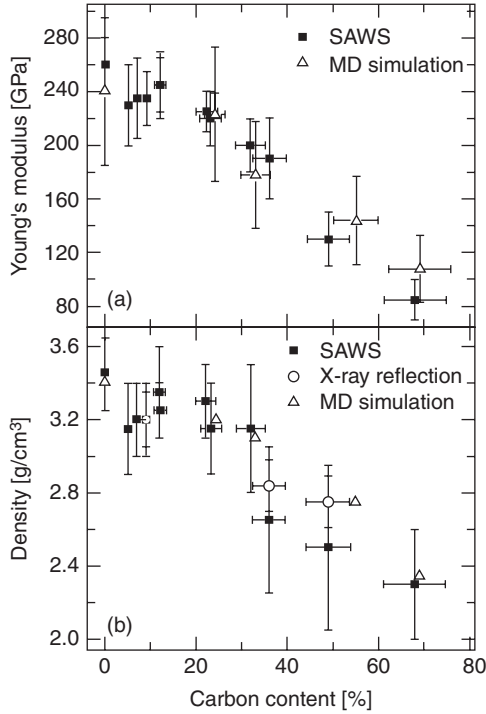


FIG. 3.24. Dependence of the Young's modulus (a) and the density (b) of the $a\text{-SiC}_x\text{N}_y$ films on the carbon content of the composite. The SAWS results are plotted as filled squares, the MD simulations as triangles, and the XRR data as circles.

of a thin surface layer generated by the modification of the surface region of a solid. A technologically important case is the amorphization of silicon by ion implantation. For the measurement of the thickness and homogeneity of an amorphized silicon layer, Rutherford backscattering (RBS) has traditionally been applied in the channeling mode. Broad-band SAW pulses, on the other hand, can be used to measure the elastic constants and the effective thickness of the damaged silicon layer [114].

In these experiments, 180-ps pulses of a Nd:YAG laser at 355 nm were focused to a line to excite plane waves, which were monitored at two distances with an actively stabilized Michelson interferometer, which measures the normal surface displacement with subangstrom resolution [114]. As an example of the extensive results obtained with this method, the dispersion curves measured by varying the implantation energy of the Ar^+ ions between 0.25 and 1.25 MeV at constant dose are displayed in Figure 3.25. A normal dispersion is expected, since ion implantation introduces defects, which reduce the stiffness of the

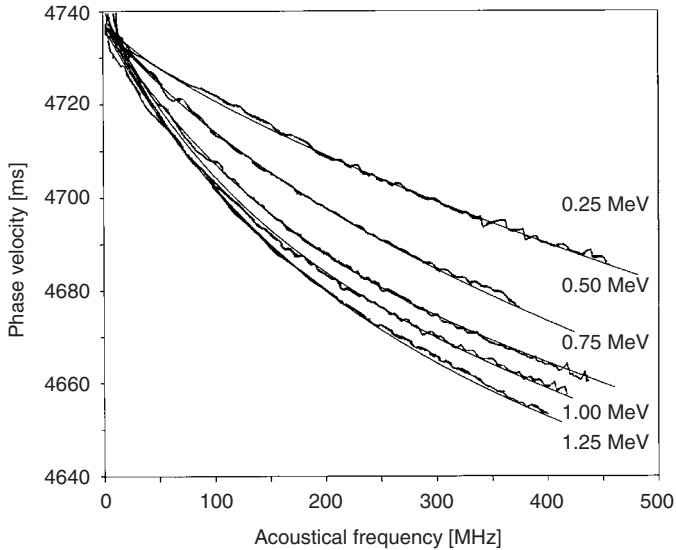


FIG. 3.25. Phase velocity versus frequency for samples implanted with a dose of 5×10^{15} Ar^+ ions/ cm^2 at the implantation energies indicated (normal dispersion).

material and make it softer than the crystal. The highest frequencies realized in these experiments were around 400 MHz with γ_{max} values between 0.3 and 0.9. Thus weak nonlinear dispersion is anticipated and confirmed experimentally. To increase the information content, SAW propagation in the $\langle 112 \rangle$ and $\langle 110 \rangle$ directions on the implanted Si(111) plane was investigated.

Table 3.3 presents the main results for implantation energies of 0.25–1.25 MeV at the fixed dose of 5×10^{15} Ar^+ ions/ cm^2 . This includes the thickness

TABLE 3.3. Experimental Data from RBS and SAWs, for a-Si Layers Formed by Implantation at a Constant Dose of $5 \times 10^{15} \text{Ar}^+$ ions/ cm^2 and Energies between 0.25 MeV and 1.25 MeV

Implant energy (MeV)	RBS	SAW			
	Thickness of amorphous layer (μm)	Thickness of amorphous layer (μm)	Poisson ratio	Density [kg/m^3]	Young's modulus [GPa]
0.25	0.47 ± 0.02	0.50 ± 0.02	0.28 ± 0.02	2300 ± 30	121 ± 3
0.50	0.78 ± 0.02	0.83 ± 0.01	0.28 ± 0.01	2300 ± 30	123 ± 3
0.75	0.04 ± 0.02	1.12 ± 0.02	0.27 ± 0.02	2300 ± 30	125 ± 3
1.00	1.22 ± 0.02	1.35 ± 0.02	0.26 ± 0.02	2310 ± 30	126 ± 2
1.25	1.49 ± 0.02	1.48 ± 0.03	0.26 ± 0.02	2310 ± 30	126 ± 3

of the amorphous layer found by RBS and SAW, the density, the Poisson ratio, and the Young's modulus obtained by SAW measurements [114]. The thicknesses obtained by the two methods are in reasonable agreement. It should be mentioned that no sharp interface can be expected as in the case of a deposited film. The decrease of the density and increase of the Poisson ratio in the amorphous layer are very small. For this reason, the values obtained still agree with the crystal values within the error bars. The Young's modulus is substantially lower than the mean value of the Young's modulus of crystalline silicon of 160 GPa [115] and increases slightly with the implantation energy.

3.5 Nonlinear SAWs

3.5.1 Theoretical Description

Beginning with the early experiments on second harmonic generation of Rayleigh waves [116, 117], there have been numerous experimental and theoretical studies of harmonic generation and frequency mixing of surface acoustic waves. Rayleigh waves are guided along the surface with a penetration depth into the substrate that is of the order of their wavelength. Consequently, high-energy densities and hence large strains can be achieved over propagation distances long in comparison to bulk acoustic waves. This favors nonlinear effects and opens up the possibility of observing nonlinear waveform evolution. With efficient experimental techniques now available for high-intensity excitation of surface acoustic waves and waveform monitoring, nonlinear waveform evolution of surface acoustic waves has become an attractive subject of experimental study for fundamental reasons and also in view of the possibility of extracting information about the nonlinear elastic properties of the substrate material.

A theoretical description of waveform evolution of surface acoustic waves makes use of the fact that the elastic (or electroelastic) nonlinearity is weak; i.e., the length scale on which noticeable changes of the waveform take place is long compared to the wavelengths of "typical" Rayleigh waves excited in the experiments. This allows for the application of asymptotic expansions with multiple time scales or length scales along the propagation direction. In this way, an evolution equation can be derived for the displacement field at the surface, eliminating the depth coordinate x_3 . In doing this, one encounters essentially two difficulties: (i) the absence or at least the weakness of dispersion of Rayleigh-type surface acoustic waves gives rise to a (quasi-)resonant interaction between the harmonics of a fundamental wave, and (ii) the elimination of the coordinate x_3 leads to a complicated nonlocal effective nonlinearity in the evolution equation. It has been shown in pioneering works [118–121] how these difficulties can be mastered, and an evolution equation has been

derived in a rigorous way from nonlinear (electro-)elasticity theory. Since then, numerous theoretical studies on nonlinear surface acoustic waves have been carried out. (For a review of the earlier work, see [122]; more recent contributions are [123–135]). Here, we briefly present the derivation of the evolution equation for nonlinear Rayleigh waves propagating along the x_1 -direction on a planar surface of a homogeneous elastic medium, assuming that the displacement field is independent of x_2 . This assumption is a reasonable approximation in cases of SAWs excited by line sources. We note that evolution equations have also been derived for cylindrical Rayleigh waves, which are relevant for a situation corresponding to a point source [123, 136].

In the derivation, we confine ourselves for simplicity to nonpiezoelectric media. The piezoelectric case has been treated in detail in [137] with the application of different electrical boundary conditions at the surface. Then, a convenient way of deriving simultaneously the equations of motion and the boundary conditions at the traction-free surface starts from the Lagrangian:

$$\mathcal{L} = \int d^3x \{T(\mathbf{x}; t) - \Phi(\mathbf{x}; t)\} \quad (3.62)$$

where

$$T(\mathbf{x}; t) = \frac{1}{2}\rho \left[\frac{\partial}{\partial t} u_j(\mathbf{x}; t) \right] \left[\frac{\partial}{\partial t} u_j(\mathbf{x}; t) \right] \quad (3.63)$$

is the density of kinetic energy, and the potential energy density $\Phi(\mathbf{x})$ may be expanded in powers of displacement gradients,

$$\Phi = \frac{1}{2} C_{ijmn} u_{ij} u_{mn} + \frac{1}{6} S_{ijmnr} u_{ij} u_{mn} u_{rs} + O([u_{ij}]^4) \quad (3.64)$$

Because of the weakness of the elastic nonlinearity, we may truncate the expansion in Eq. 3.64 at the third order of the displacement gradients. The expansion coefficients C_{ijmn} are the second-order elastic moduli, and S_{ijmnr} are linear combinations of second-order and third-order elastic moduli [138],

$$S_{ijmnr} = C_{ijmnr} + \delta_{im} C_{jnrs} + \delta_{ir} C_{jsmn} + \delta_{mr} C_{ijns} \quad (3.65)$$

If the elastic moduli are regarded as functions of x_3 that have a step discontinuity at the surface, the Euler-Lagrange equations following from Eq. 3.62 contain terms proportional to $\delta(x_3)$. The prefactor of this δ -function has to vanish. In this way, one obtains the nonlinear equations of motion

$$\rho \frac{\partial^2}{\partial t^2} u_i(\mathbf{x}; t) = \frac{\partial}{\partial x_j} \sigma_{ij}(\mathbf{x}; t) \quad (3.66)$$

and nonlinear boundary conditions at the surface ($x_3 = 0$)

$$\sigma_{i3}(x_1, x_2, 0; t) = 0 \quad (3.67)$$

with the Piola-Kirchhoff stress tensor

$$\sigma_{ij} = C_{ijmn} \frac{\partial u_m}{\partial x_n} + \frac{1}{2} S_{ijmnr} \frac{\partial u_m}{\partial x_n} \frac{\partial u_r}{\partial x_s} \quad (3.68)$$

In addition, the displacement field is required to decay exponentially to zero for $x_3 \rightarrow \infty$. It has to be emphasized that the argument \mathbf{x} in all of these equations refers to the position of a mass element in the undeformed medium.

The displacement field may be represented as a power series in a dimensionless small parameter $\varepsilon \ll 1$ of the order of a typical strain,

$$\mathbf{u}(\mathbf{x}; t) = \varepsilon \mathbf{u}^{(1)}(x_1, x_3; t; \tau) + \varepsilon^2 \mathbf{u}^{(2)}(x_1, x_3; t; \tau) + O(\varepsilon^3) \quad (3.69)$$

where, in addition, a stretched time coordinate $\tau = \varepsilon t$ has been introduced. Inserting Eq. 3.69 into the equation of motion Eq. 3.66 and boundary condition (Eq. 3.67), one readily finds that $\mathbf{u}^{(1)}$ may be chosen to be of the form

$$\mathbf{u}^{(1)}(x_1, x_3; t; \tau) = \sum_{n=-\infty}^{\infty} e^{inq_0(x_1 - v_R t)} \mathbf{w}(x_3 | nq_0 \hat{\mathbf{x}}) \frac{-i}{nq_0} B_n(\tau) \quad (3.70)$$

which is a superposition of linear Rayleigh waves with strain amplitudes B_n that depend on the stretched time variable τ . The sum on the right-hand side of Eq. 3.70 runs over integer multiples of a fundamental wavenumber $q_0 = 2\pi/\Lambda$. The periodicity Λ may be chosen to be arbitrarily large, and, in the limit $\Lambda \rightarrow \infty$, the Fourier series (Eq. 3.70) may be replaced by a Fourier integral.

At second order of ε , the equation of motion (Eq. 3.66) and boundary condition (Eq. 3.67) with Eq. 3.69 for the displacement field yield a linear inhomogeneous boundary value problem for $\mathbf{u}^{(2)}$:

$$\rho \frac{\partial^2}{\partial t^2} u_i^{(2)} - \frac{\partial}{\partial x_j} C_{ijmn} \frac{\partial u_m^{(2)}}{\partial x_n} = \frac{1}{2} \frac{\partial}{\partial x_j} S_{ijmnr} \frac{\partial u_m^{(1)}}{\partial x_n} \frac{\partial u_r^{(1)}}{\partial x_s} - 2\rho \frac{\partial^2 u_i^{(1)}}{\partial t \partial \tau} \quad (3.71)$$

$$C_{i3mn} \frac{\partial u_m^{(2)}}{\partial x_n} \Big|_{x_3=0} = -\frac{1}{2} S_{i3mnr} \frac{\partial u_m^{(1)}}{\partial x_n} \frac{\partial u_r^{(1)}}{\partial x_s} \Big|_{x_3=0} \quad (3.72)$$

Since we are aiming at describing gradual evolution of wave profiles along the propagation direction, the displacement field must not contain secular terms in t and x_1 . This implies for $\mathbf{u}^{(2)}$ the form

$$\mathbf{u}^{(2)}(x_1, x_3; t; \tau) = \sum_{n=-\infty}^{\infty} e^{inq_0(x_1 - v_R t)} \mathbf{U}(x_3; \tau | nq_0) \quad (3.73)$$

Inserting Eq. 3.70 and Eq. 3.73 into Eq. 3.71, projecting Eq. 3.71 on $\exp(imq_0 x_1) \mathbf{w}(x_3 | mq_0 \hat{\mathbf{x}})$, integrating by parts over x_3 , and making use of

the boundary condition (Eq. 3.72) and the boundary condition satisfied by \mathbf{w} , one obtains the compatibility condition for the solvability of the linear inhomogeneous problem in the form

$$i \frac{\partial}{\partial \tau} B_n = nq_0 \left[\sum_{0 < n' < n} F(n'/n) B_{n'} B_{n-n'} + 2 \sum_{n' > n} (n/n') F^*(n/n') B_{n'} B_{n'-n}^* \right] \quad (3.74)$$

for $n > 0$, which is the desired evolution equation. An equation of the same form has been derived for Stoneley waves and also for Scholte waves [135].

With the form (Eqs. 3.1 and 3.2) of the displacement field of linear Rayleigh waves, the function F can be written as

$$F(k) = \sum_{r, r', r''=1}^3 \frac{G(r, r', r'')}{\hat{\alpha}^*(r) + k\hat{\alpha}(r') + (1-k)\hat{\alpha}(r'')} \quad (3.75)$$

The coefficients $G(r, r', r'')$ are contractions of the tensor (S_{ijklmn}) with the vectors $\mathbf{b}(r)$, $r = 1, 2, 3$, and vectors $\mathbf{K}(r)$, $r = 1, 2, 3$, having components $K_1(r) = i$, $K_2(r) = 0$, $K_3(r) = -\hat{\alpha}(r)$. Explicitly,

$$G(r, r', r'') = -i[2N(\hat{\mathbf{x}})]^{-1} S_{ijklmn} b_i^*(r) K_j^*(r) b_k(r') K_l(r') b_m(r'') K_n(r'') \quad (3.76)$$

The quantity $N(\mathbf{q})$ has been defined in Eq. 3.28. In terms of the vectors $\mathbf{b}(r)$ and decay constants $\hat{\alpha}(r)$, it has the explicit form

$$N(\mathbf{q}) = 2\rho v_R \sum_{r, r'} \frac{b_j^*(r) b_j(r')}{\hat{\alpha}^*(r) + \hat{\alpha}(r')} \quad (3.77)$$

From Eqs. 3.75 and 3.76, it is evident that the function $F(k)$ in the evolution equation depends linearly on the third-order elastic moduli. The linear dependence of the function F on the third-order elastic moduli of the substrate facilitates the extraction of information about these nonlinear elastic moduli from pulse evolution by inverse methods. Once the displacement field of linear Rayleigh waves is known along with the second-order and third-order elastic moduli of the elastic medium, this function is easily calculated. It is complex in the general case. However, in geometries of high symmetry, it can be arranged to be real by a suitable choice of the phase factor in the quantities \mathbf{w} .

To arrive at the form (Eq. 3.74) of the evolution equation that contains summations over positive wavenumbers only, one has to make use of the condition that the displacement field is real. This means that

$$\mathbf{w}(x_3 | -nq_0 \hat{\mathbf{x}}) B_{-n} = \mathbf{w}^*(x_3 | nq_0 \hat{\mathbf{x}}) B_n^* \quad (3.78)$$

In addition, we have chosen $B_{-n} = B_n^*$. Defining the (constant) complex vector $\mathbf{W} = \mathbf{w}(0|\hat{\mathbf{x}})$, we then introduce the (dimensionless) surface strain components

$$E_j(\xi, \tau) = W_j \sum_{n>0} B_n(\tau) e^{nq_0\xi} + c.c. \quad (3.79)$$

where $\xi = x_1 - v_R t$ is the spatial variable in a coordinate frame that travels with the speed of linear Rayleigh waves along the x_1 -direction. The quantities relevant in experiments to detect waveform evolution of surface acoustic waves are usually the particle velocity components normal or parallel to the surface and the surface elevation profile.

Accounting only for the leading-order terms in the expansion parameter ε , these quantities are given by

$$\frac{\partial}{\partial t} u_j(x_1, x_2, 0; t) = -v_R E_j(x_1 - v_R t, \tau) \quad (3.80)$$

$$\begin{aligned} u_3(x_1, x_2, 0; t) &= W_3 \sum_{n>0} B_n(\tau) \frac{1}{inq_0} e^{inq_0(x_1 - v_R t)} + c.c. \\ &= \int_{\xi_0}^{\xi} d\xi' E_3(\xi', \tau) + \text{const} \end{aligned} \quad (3.81)$$

In geometries of high symmetry, when the sagittal polarization decouples from the shear-horizontal one and purely sagittal Rayleigh waves exist, $E_2 = 0$, and the particle velocity components parallel to the surface at $x_3 = 0$, $(-v_R E_1)$, and normal to the surface, $(-v_R E_3)$, are related to each other via

$$E_3(\xi, \tau) = a_1 \frac{1}{\pi} P \int_{-\infty}^{\infty} \frac{E_1(\xi', \tau)}{\xi' - \xi} d\xi' + a_2 E_1(\xi, \tau) \quad (3.82)$$

involving the Hilbert transform. P denotes the Cauchy principle value. The coefficients a_1 and a_2 are the imaginary part and the real part of W_3/W_1 . In the isotropic case as well as in certain anisotropic geometries, the coefficient a_2 vanishes. This includes the situation of vanishing elastic moduli C_{1311} and C_{1333} [139].

When the evolution equation (Eq. 3.74) is transformed into real space [125], it takes on a form that may be regarded as a nonlocal form of the inviscid Burgers equation [140],

$$\frac{\partial}{\partial \tau} E(\xi, \tau) = \frac{\partial}{\partial \xi} \int_{-\Lambda/2}^{\Lambda/2} d\xi' \int_{-\Lambda/2}^{\Lambda/2} d\xi'' L(\xi - \xi', \xi - \xi'') E(\xi', \tau) E(\xi'', \tau) \quad (3.83)$$

We note that the choice of variables $\tau = \varepsilon t$ and $\xi = x_1 - v_R t$, i.e., a “slow” time variable and a “fast” spatial variable in a reference frame moving with the phase velocity of linear Rayleigh waves, is appropriate for initial value

problems. Alternatively, with minor modifications in the derivation, one may introduce a “slow” spatial coordinate $X = \varepsilon x_1$ and a “retarded” time coordinate $\theta = t - x_1/v_R$ to describe the evolution along the propagation direction on the surface of temporal pulse trains with (arbitrary) period $T = \Lambda/v_R$. Representing the displacement field as

$$\mathbf{u}(\mathbf{x}; t) = \varepsilon \mathbf{u}^{(1)}(x_1, x_3; t; X) + \varepsilon^2 \mathbf{u}^{(2)}(x_1, x_3; t; X) + O(\varepsilon^3) \quad (3.84)$$

with

$$\mathbf{u}^{(1)}(x_1, x_3; t; X) = \sum_{n=-\infty}^{\infty} e^{-i2\pi n\theta/T} \mathbf{w}(x_3|q\hat{\mathbf{x}})(-i\Lambda/2\pi n) \tilde{B}_n(X) \quad (3.85)$$

one readily obtains for the amplitudes \tilde{B}_n the evolution equation (Eq. 3.74) with $\partial/\partial\tau$ replaced by $v_R\partial/\partial X$.

Because of the absence of dispersion, one may expect shock formation in finite time when starting from sinusoidal initial conditions, as in physical systems described by the inviscid Burgers equation. Numerical simulations performed with evolution equations (Eq. 3.74), starting with sinusoidal initial conditions, reveal interesting new features in comparison with the Burgers case, especially the formation of cusps in wave profiles [141, 123] (see Fig. 3.26). In particular, shock formation or, more appropriately, wave breaking [141] has been studied and found to differ considerably for different anisotropic materials [134] and even different propagation geometries in the same material [137]. Estimates for the breaking distance have been given [130, 141]. In the simulations it was also found that the waveform evolution is not very sensitive to all details of the function $F(k)$ occurring in Eq. 3.74 [126].

In the simulations, an attenuation term of the form $-i\Gamma n^2 B_n$ has often been added to the right-hand side of Eq. 3.74, mainly for stabilization purposes. Intrinsic attenuation due to phonon viscosity and the thermoelastic effect does indeed give rise to a damping constant of Rayleigh waves that is proportional to the square of their frequency, i.e., $\propto n^2$. Extrinsic damping mechanisms may contribute to the damping constant with terms that depend on frequency in a different way. In the case of surface roughness with small correlation length damping may vary with higher powers of the frequency.

While the theory outlined so far assumes that the displacement field associated with surface acoustic waves does not depend on the coordinate x_2 , there have been extensions that account for a finite beam width [127, 142]. An additional term of the form $(D/n)\partial^2 B_n/\partial Y^2$ appears on the right-hand side of the evolution equation (Eq. 3.74), where $Y = \varepsilon^{1/2}(x_2 - g x_1)$, accounting for diffraction, and $g = V_2(\hat{\mathbf{x}})/V_1(\hat{\mathbf{x}})$ is the ratio of two components of the group velocity. The coefficient D is related to the curvature of the slowness curve of linear Rayleigh waves. Simulations have been carried out on the basis

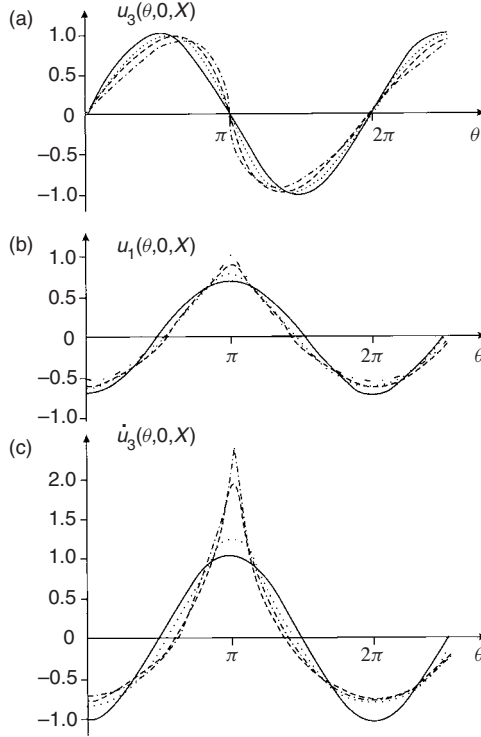


FIG. 3.26. Evolution of an initially sinusoidal waveform on a homogeneous isotropic substrate (for details see [135]). Here $\theta = q_0(x_1 - v_R t)$. (a) Surface elevation profile u_3 . (b) In-plane component of the displacement u_1 . (c) Normal component of the particle velocity \dot{u}_3 .

of the evolution equation (Eq. 3.74) with the diffraction term and the attenuation term discussed previously for isotropic media, and the evolution of beam profiles of a fundamental wave and its higher harmonics have been computed [127].

More recently, effects of dispersion on the propagation of nonlinear surface acoustic waves have been considered, mainly with the prospect of finding surface acoustic solitary waves. The dispersion mechanisms discussed before, as long as they are sufficiently weak, i.e., when Eq. 3.50 applies, lead to the additional term $v_R \mu q_0^2 n^2 d B_n$ on the right-hand side of Eq. 3.74. When transformed into real space, Eq. 3.83 has to be supplemented by the term

$$+v_R \mu d \frac{\partial^2}{\partial \xi^2} \frac{1}{\pi} P \int_{-\infty}^{\infty} \frac{E(\xi', \tau)}{\xi' - \xi} d\xi' \quad (3.86)$$

on its right-hand side and thus takes on a form that may be regarded as a generalization of the Benjamin-Ono equation known in fluid dynamics [143, 144] and having multisoliton solutions [145]. Periodic solutions have been computed for the dispersive evolution equation for Rayleigh waves. They consist of strongly localized pulses. In a certain limit, these periodic solutions converge to solitary waves [133]. As geometry, the (001) direction was chosen on a (001) surface of a silicon substrate. (We note that the dispersion enters the evolution equation only via the constant μ .) The pulse shape was found to resemble a “Mexican hat” for the particle velocity parallel to the surface. Although the evolution equation for dispersive nonlinear Rayleigh waves is not integrable, these periodic pulse train solutions were found to be linearly stable. However, they do not survive collisions between each other and hence are not solitons.

3.5.2 Experimental Results

The first experimental observations of nonlinear effects in SAWs were carried out with initially sinusoidal surface waves generated by means of piezoelectric interdigital transducers [146, 147]. In both investigations the probe-beam diffraction method was used to monitor the SAW amplitudes. It was shown that as the acoustical power density at the surface approached a certain level, which is on the order of $10^3 - 10^4$ W/cm², multiple harmonics of the fundamental frequency appear, resulting in the appearance of diffracted beams at multiple angles.

The amplitude of the n 'th harmonic was evaluated [146] as $u_n = k^{-1} \cos \theta_0 (I_n/I_0)^{1/2}$, where k is an optical wavenumber, θ_0 is the angle of incidence, and I_n the intensity of the n 'th diffraction order. Coincident multiple diffraction orders of the fundamental SAW are normally neglected.

In experiments with a LiNbO₃ crystal [146], the relative power of the fundamental SAW component (at 300 MHz) was measured at a distance of 6 mm from the source transducer as a function of the input acoustic power. A saturation effect was clearly observed starting from the level of 6×10^3 W/cm², which is explained as power transfer into higher harmonics. The propagation characteristics of the first three harmonics were studied by scanning the probe laser along the SAW beam. The observed oscillatory dependence of the amplitude of harmonics on the propagation distance was proved to be a consequence of weak dispersion due to surface roughness.

The same conclusions concerning the oscillatory behavior of harmonics were reached in [147], where the propagation of SAWs was investigated in crystalline quartz. In contrast to the experiments in LiNbO₃, however, the peak of the third harmonic preceded that of the second harmonic. The maximal amplitudes of the fundamental frequency (at 281 MHz) and the second and

third harmonics were measured to be approximately 20, 7, and 2.5 Å, respectively. Correspondingly, the shear strain in the nonlinear SAW was of the order of 10^{-3} .

Nonlinear waveform distortions of a sinusoidal SAW were observed in isotropic glass [148]. A conventional piezoelectric transducer operating at 5 MHz was used for SAW excitation. Detection was achieved with the help of an electrodynamic probe, which consisted of a thin metal strip deposited on the sample surface that was situated in an external magnetic field. In this setup surface oscillations generate a voltage proportional to the vibrational velocity. By changing the orientation of the magnetic field, one can obtain either the in-plane or the out-of-plane component. Recorded experimental profiles show the transformation of the initially sinusoidal wave into a sawtoothlike shape for the in-plane velocity component and into a U-type shape with sharp cusps for the out-of-plane component. These results are fairly consistent with theoretical simulations [149].

The problem of nonlinear SAW propagation in the presence of dispersion was studied experimentally in [97, 150, 151]. In [150] a 50-nm layer of silicon oxide was deposited onto Y-cut LiNbO_3 to obtain the desired normal dispersion. The excitation technique permits acoustic power flux of 10–30 kW/cm^2 at 114 MHz to be obtained. As the sound intensity rose above 10 kW/cm^2 , the initially sinusoidal profile of the in-plane vibrational velocity converged into a wave, for which the period increased with increasing SAW intensity. At an intensity of about 30 kW/cm^2 , the wave profile which resembled a cnoidal wave decayed into two peaks (solitons) with amplitudes in the ratio 1:10. Scanning along the SAW beam shows that the larger soliton propagates faster, and thus the two solitons collide. Similar results are presented in [97], where nonlinear SAW propagation was investigated in a metallic grating waveguide on the surface of LiNbO_3 , which exhibited normal dispersion for SAWs. The evolution of an initially sinusoidal wave was fitted by means of the Korteweg-de Vries (KdV) equation, which predicts the observed effects of wave evolution into a pulse train. The relative velocities of these peaks are in good agreement with that measured experimentally.

The properties of the spatial evolution of the wave harmonics were studied in detail in [151]. Intense SAWs were launched in a LiNbO_3 crystal by means of an interdigital transducer at a frequency of 200 MHz and a maximal power density of about $1.5 \times 10^4 \text{ W/cm}^2$ at the surface. Four spectral harmonics of the SAW were monitored using the diffraction technique. Two series of experiments were carried out, namely, on uncoated samples and on those coated with a 50-nm layer of SiO_2 . For the coated samples, it was shown that the KdV equation described several features, such as the observed oscillatory behavior of the harmonics. It was supposed that for a certain relationship between dispersion and nonlinearity a surface acoustic soliton may exist.

Nonlinear surface acoustic pulses produced by pulsed laser radiation were observed in [152]. In this work the nonlinear propagation of short surface pulses was observed in isotropic fused silica and in a silicon single crystal. The pulsed laser radiation was focused to a line on the sample surface, which was coated with a strongly absorbing liquid layer. The explosive evaporation of the liquid resulted in a strong recoil pressure shock applied to the surface, and thus generated an elastic surface pulse of the ablation type with a Mach number of about 5×10^{-3} and a duration of 10–20 ns. For detection, the probe-beam deflection setup was used, which consisted of two identical channels so that the propagating pulse was recorded at two distances from the source. Nonlinear distortions occurring in both quartz and crystalline silicon broadened the pulse, indicating a frequency-down conversion process (as described by the second term in the right-hand side of Eq. 3.74). This effect cannot be observed in the case of a narrow-band sinusoidal surface wave. Frequency-up conversion appears in the form of sharp cusps in isotropic quartz, similar to those shown in (Fig. 3.26) and shock fronts in silicon (as described by the first term in the right-hand side of Eq. 3.74).

These kinds of nonlinear distortions are well described by the evolution equation (Eq. 3.74). Figure 3.27 presents the theoretical predictions in comparison with the experimentally measured shear strain of the surface acoustic pulse. In theoretical simulations the pulse measured at the first probe spot (dotted line) was represented as a Fourier series of 200 harmonics and substituted into

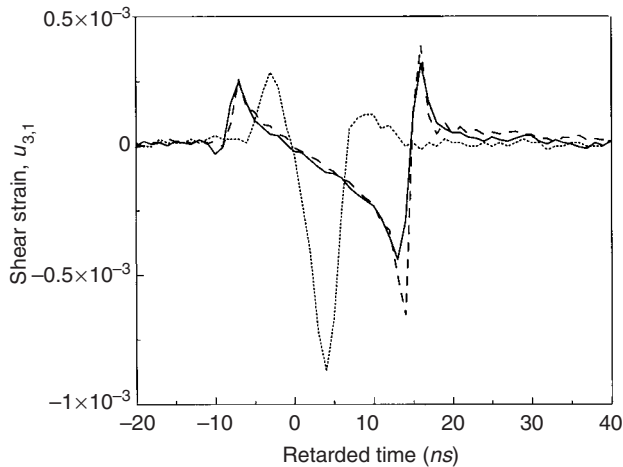


FIG. 3.27. Comparison of theoretical and measured nonlinear distortion of a SAW pulse in silicon (111) cut in the (112) direction. Solid line, measured profile; dashed line, predicted profile; the dotted line shows the original pulse.

Eq. 3.74 as the initial condition. Equation 3.74 is solved numerically using the predictor–corrector method and gives the predicted pulse profile at the position of the second probe spot.

Introduction of dispersion can drastically change the evolution of a nonlinear pulse profile [153]. Experiments in silicon with a thermally grown thin oxide layer show that nonlinearity can compensate for the effect of dispersion. For relatively weak SAW amplitudes, when the dispersion effect dominates, the distorted pulses present typical oscillatory shapes with frequency increasing from the front to the tail, as expected for normal dispersion. In contrast to this, a stronger SAW pulse transforms into a narrower pulse shape propagating faster than the linear Rayleigh wave.

To simulate this regime of strong nonlinearity, an additional term describing the dispersion effect is introduced into Eq. 3.74. The simulation for fused quartz coated with a metal film is shown in Figure 3.28 in comparison with experimental data. In this case the combination of nonlinear elastic properties of the substrate and dispersion results in a decay of the initial profile into a fast bipolar pulse and oscillatory tail. Since the simulation based on Eq. 3.74 provides a satisfying agreement with the experimentally observed pulse shape, it can be applied to predict the further evolution. Such a simulation shows that this bipolar profile is stable with respect to nonlinear and dispersion distortions, and thus it can be called a solitary wave. Note that the in-plane velocity profile has a shape of a “Mexican hat,” obtained theoretically in [133] for propagation in (100) cut of silicon.

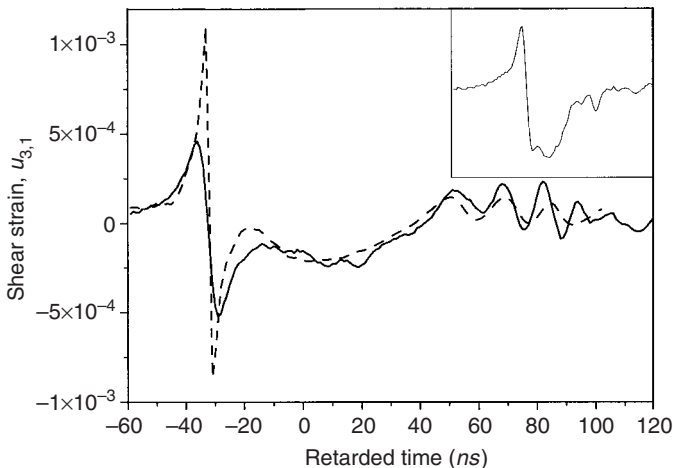


FIG. 3.28. Solitary pulse in isotropic silica covered with a metallic layer. Solid line, measured profile; dashed line, predicted profile. The initial pulse is given in the inset.

References

1. White, R.M. (1970). *Proc. IEEE* **58**: 1238.
2. Farnell, G.W. (1970). In *Physical Acoustics*, p. 109, vol. VI, Mason, W.P., and Thursten, R.N., eds., New York: Academic.
3. Farnell, G.W. (1978). In *Acoustic Surface Waves*, p. 1, vol. 24, Oliner, A.A., ed., Topics Appl. Phys., Berlin: Springer.
4. Krylov, V.V. (1989). *Progress in Surface Science* **32**: 39.
5. Konstantinov, L., Neubrand, A., and Hess, P. (1989). In *Topics in Current Physics*, p. 273, vol. 47, Hess, P., ed., Berlin: Springer.
6. Maradudin, A.A., and Stegeman, G.I. (1991). In *Surface Phonons*, p. 5, Kress, W., and Wette, F.W., eds., Berlin: Springer-Verlag.
7. Viktorov, I.A. (1967). *Rayleigh and Lamb Waves*, New York: Plenum.
8. Auld, B.A. (1990). *Acoustic Fields and Waves in Solids*, vols. I and II, Malabar, Florida: Krieger.
9. Sontag, H., and Tam, A. (1985). *Appl. Phys. Lett.* **46**: 725.
10. Hutchins, D.A., Lundgren, K., and Palmer, S.B. (1989). *J. Acoust. Soc. Am.* **85**: 1441.
11. Desmet, C., Kawalt, U., Mourad, A., Lauriks, W., and Thoen, J. (1996). *J. Acoust. Soc. Am.* **100**: 1509.
12. Gusev, V., and Hess, P. (1994). *Nondestr. Test. Eval.* **11**: 313.
13. Claus, R.O., and Palmer, C.H. (1977). *Appl. Phys. Lett.* **31**: 547.
14. Mattei, Ch., Jia, X., and Quentin, G. (1995). In *Review of Progress in QNDE*, p. 409, vol. 14, Thomson, D.O., and Chimenti, D.E., eds., New York: Plenum.
15. Gusev, V., Desmet, C., Lauriks, W., Glorieux, C., and Thoen, J. (1996). *J. Acoust. Soc. Am.* **100**: 1514.
16. Desmet, C., Gusev, V., Lauriks, W., Glorieux, C., and Thoen, J. (1996). *Appl. Phys. Lett.* **68**: 2939.
17. Desmet, C., Gusev, V., Lauriks, W., Glorieux, C., and Thoen, J. (1997). *Opt. Lett.* **22**: 69.
18. Avanesyan, S.M., Gusev, V.E., Zhdanov, B.V., Kuznetsov, V.I., and Telenkov, S.A. (1986). *Sov. Phys. Acoust.* **32**: 356.
19. Schmidt, M., and Dransfeld, K. (1982). *Appl. Phys.* **A28**: 211.
20. Gusev, V.E., Kolomenskii, A.A., and Hess, P. (1995). *Appl. Phys.* **A61**: 285.
21. Gusev, V.E., and Karabutov, A.A. (1993). *Laser Optoacoustics*, New York: AIP Press.
22. Aussel, J.D., LeBrun, A., and Baboux, J.C. (1988). *Ultrasonics* **16**: 245.
23. Aindow, A.M., Dewhurst, R.J., Hutchins, D.A., and Palmer, S.B. (1981). *JASA* **69**: 449.
24. Scruby, C.B. Drain, L.E., *Laser Ultrasonics* (1990). p. 243, Bristol: Adam Hilger.
25. Kolomenskii, A.A., and Maznev, A.A. (1990). *Sov. Phys. Acoust.* **36**: 463.
26. Kolomenskii, A.A., and Hess, P. (1995). *Proceedings of the 15th International Congress on Acoustics*, Trondheim, Norway, pp. 93–96.
27. Raja, M.Y.A., Reicher, D.W., Brueck, S.R.J., McNeil, J.R., and Oates, D.E. (1990). *Opt. Lett.* **15**: 66.
28. Harata, A., Nishimura, H., and Sawada, T. (1990). *Appl. Phys. Lett.* **57**: 132.
29. Kasinski, J.J., Gomez-Jahn, L.A., Faran, K.J., Gracevski, S.M., and Miller, R.J.D. (1998). *J. Chem. Phys.* **90**: 1253.
30. Rogers, J.A., Fuchs, M., Banet, M.J., Hanselman, J.B., Logan, R., and Nelson, K.A. (1997). *Appl. Phys. Lett.* **71**: 225.

31. Frass, A., Lomonosov, A., Hess, P., and Gusev, V. (2000). *J. Appl. Phys.* **87**: 3505.
32. Vilkomerson, D. (1976). *Appl. Phys. Lett.* **19**(3): 183.
33. Reibold, R., and Molkenstruck, W. (1981). *Acustica* **49**: 205.
34. Olmstead, M.A., and Armer, N.M. (1983). *J. Vac. Sci. Technol.* **B1**(3): 751.
35. Bridoux, E., Rouvaen, J.M., Moriametz, M., Torguet, R., and Hartman, P. (1974). *J. Appl. Phys.* **45**(12): 5156.
36. Burov, J., Tankovsky, N., and Yordanov, B. (1987). *Solid State Communications* **62**(7): 495.
37. Kavalero, V., Katoh, H., Kasaya, N., Inoue, M., and Fujii, T. (1995). *Jpn. J. Appl. Phys.* **34**: 2653.
38. Morgan, D.P. (1985). *Surface-Wave Devices for Signal Process*, New York: Elsevier.
39. Glass, J.T., Fox, B.A., Dreifus, D.L., and Stoner, B.R. (1998). *MRS Bulletin* **23**: 49.
40. Neubrand, A., and Hess, P. (1989). *Materials Science and Engineering A* **122**: 33.
41. Coufal, H., Grygier, R., Hess, P., and Neubrand, A. (1992). *J. Acoust. Soc. Am.* **92**: 2980.
42. Ottermann, C.R., Kuschner, R., Anderson, O., Hess, P., and Bange, K. (1997). *Mat. Res. Soc. Symp. Proc.* **436**: 251.
43. Schneider, D., and Tucker, M.D. (1996). *Thin Solid Films* **290–291**: 305.
44. Schneider, D., Schwarz, Th., Scheibe, J.-J., and Panzner, M. (1997). *Thin Solid Films* **295**: 107.
45. Schneider, D., Hammer, R., and Jurisch, M. (1999). *Semicond. Sci. Technol.* **14**: 93.
46. Rayleigh (Lord). (1885). *Proc. Lond. Math. Soc.* **17**: 4.
47. Lothe, J., and Barnett, D.M. (1976). *J. Appl. Phys.* **47**: 428.
48. Lothe, J., and Barnett, D.M. (1976). *J. Appl. Phys.* **47**: 1799.
49. Barnett, D.M., Lothe, J., and Gundersen, S.A. (1990). *Wave Motion* **12**: 341.
50. Chadwick, P. (1989). *Proc. R. Soc. Lond.* **A422**: 23.
51. Barnett, D.M., Chadwick, P., and Lothe, J. (1991). *Proc. R. Soc. Lond.* **A433**: 699.
52. Norris, A. (1992). *1992 IEEE Ultrasonics Symposium Proceedings*, McAvoy, B.R., ed., p. 671.
53. Taylor, D.B., and Crampin, S. (1978). *Proc. R. Soc. Lond.* **A364**: 161.
54. Figure 4 on page 123 of Reference [2].
55. Gundersen, S.A., Wang, L., and Lothe, J. (1991). *Wave Motion* **14**: 129.
56. Mozhaev, V.G., Bosia, F., and Weihnacht, M. (1998). *1998 IEEE Ultrasonics Symposium Proceedings*, Schneider, S.C., Levy, M., and McAvoy, B.R., eds., p. 143.
57. Slobodnik, Jr., A.J. (1978). In *Acoustic Surface Wave Devices*, p. 195, Oliner, A.A., ed., New York: Springer.
58. Stegeman, G.E., and Nizzoli, F. (1984). In *Surface Excitations*, p. 195, section 3.3.3, Agranovich, V.M., and Loudon, R., eds., Amsterdam: North-Holland. For a recent example, see Knuuttila, J.V., Koskela, J., Tikka, P.T., Salomaa, M.M., Hartmann, C.S., and Plessky, V.P. (1999). *1999 IEEE Ultrasonics Symposium Proceedings*.
59. Seifert, F., Baghai-Wadji, A.R., Wagner, K.C., and Kovacs, G. (1988). In *Recent Developments in Surface Acoustic Waves*, p. 173, Parker, D.F., and Maugin, G.A., Berlin: Springer.

60. Buchwald, V.T. (1961). *Q. J. Mech. Appl. Math.* **14**: 293.
61. Tamura, S.-I., and Honjo, K. (1981). *Jpn. J. Appl. Phys.* **20**, Suppl. **20-3**: 17.
62. Camley, R.E., and Maradudin, A.A. (1983). *Phys. Rev.* **B27**: 1959.
63. Chernozatonskii, L.A., and Novikov, V.V. (1984). *Solid State Communications* **51**: 643.
64. Novikov, V.V., and Chernozatonski, L.A. (1986). *Fiz. Tverd. Tela (Leningrad)* **28**: 419 [*Sov. Phys. Solid State* **28**: 233].
65. Kolomenskii, A.I.A., and Maznev, A.A. (1993). *Phys. Rev.* **B48**, 14502.
66. Shirasaki, H., and Makimoto, T. (1978). *J. Appl. Phys.* **49**: 658.
67. Shirasaki, H., and Makimoto, T. (1978). *J. Appl. Phys.* **49**: 661.
68. Although the decomposition (Eq. 7.35) is not unique, the residues of the Green's tensor at the poles at $\omega_R(q)$ are.
69. Tamura, S., and Yagi, M. (1994). *Phys. Rev.* **B49**: 17378.
70. Taylor, B., Maris, H.J., and Elbaum, C. (1969). *Phys. Rev. Lett.* **23**: 416.
71. Every, A.G., Sachse, W., Kim, K.Y., and Thomson, M.O. (1990). *Phys. Rev. Lett.* **65**: 1446.
72. Kolomenskii, A.I.A., and Maznev, A.A. (1991). *JETP Lett.* **53**: 423.
73. Vines, R.E., Tamura, Shin-ichiro, and Wolfe, J.P. (1995). *Phys. Rev. Lett.* **74**: 2729.
74. Hauser, M.R., Weaver, R.L., and Wolfe, J.P. (1992). *Phys. Rev. Lett.* **68**: 2604.
75. Kolomenskii, A.I.A., and Maznev, A.A. (1993). *Phys. Rev.* **B48**: 14502.
76. Maznev, A.A., Kolomenskii, A.I.A., and Hess, P. (1995). *Phys. Rev. Lett.* **75**: 3332.
77. Kim, K.Y., and Sachse, W. (1994). *J. Appl. Phys.* **75**: 1435.
78. Farnell, G.W., and Adler, E.L. (1972). In *Physical Acoustics*, p. 35, vol. IX, Mason, W.P., and Thurston, R.N., eds., New York: Academic.
79. Auld, B.A. (1973). *Acoustic Fields and Waves in Solids*, p. 94, vol. II, New York: Wiley.
80. Maradudin, A.A. (1985). In *Nonequilibrium Phonon Dynamics*, p. 395, Bron, W.E., ed., New York: Plenum.
81. Djafari-Rouhani, B., Dobrzynski, L., Hardouin Duparc, O., Camley, R.E., and Maradudin, A.A. (1983). *Phys. Rev.* **B28**: 1711.
82. Mayer, A.P. (1989). *J. Phys. Condens. Matter* **1**: 3301.
83. Tiersten, H.F. (1969). *J. Appl. Phys.* **40**: 770.
84. Maradudin, A.A. (1987). In *Physics of Phonons*, p. 82, Paszkiewics, T., ed., New York: Springer.
85. Kosevich, Yu.A. (1997). *Progress in Surface Science* **55**: 1.
86. Tanaka, Y., and Tamura, S. (1998). *Phys. Rev.* **B58**: 7958.
87. Maradudin, A.A. (1988). In *Recent Developments in Surface Acoustic Waves*, p. 100, Parker, D.F., and Maugin, G.A., Berlin: Springer.
88. Baghai-Wadji, A.-R. (1994). *Habilitationsschrift*, Technische Universität Wien.
89. Glass, N.E., Loudon, R., and Maradudin, A.A. (1981). *Phys. Rev.* **B24**: 6843.
90. Huang, X., and Maradudin, A.A. (1987). *Phys. Rev.* **B36**: 7827.
91. Kosachev, V.V., Lokhov, Yu.N., and Chukov, V.N. (1988). *Solid State Communications* **68**: 903; (1990). **73**: 535.
92. Maradudin, A.A., Huang, X., and Mayer, A.P. (1991). *J. Appl. Phys.* **70**: 53.
93. Kosachev, V.V., and Shchegrov, A.V. (1995). *Ann. Phys. (N.Y.)* **240**: 225.
94. Mayer, A.P., and Lehner, M. (1994). *Waves in Random Media* **4**: 321.
95. Shchegrov, A.V. (1995). *J. Appl. Phys.* **78**: 1565.
96. Eguiluz, A.G., and Maradudin, A.A. (1983). *Phys. Rev.* **B28**: 728.
97. Cho, Y., and Miyagawa, N. (1993). *Appl. Phys. Lett.* **63**: 1188.

98. Endoh, G., Hashimoto, K., and Yamaguchi, M. (1995). *Jpn. J. Appl. Phys.* **34**: 2638.
99. Biryukov, S.V., Gulyaev, Yu.V., Krylov, V.V., and Plessky, V.P. (1995). *Surface Acoustic Waves in Inhomogeneous Media*, Chapter 9, Berlin: Springer.
100. Hess, P. (1996). *Appl. Surf. Sci.* **106**: 429.
101. Chen, Y.-C., and Hess, P. (1997). *J. Appl. Phys.* **82**: 4758.
102. Kolomenskii, A.I., Szabadi, M., and Hess, P. (1995). *Appl. Surf. Sci.* **86**: 591.
103. Duggal, A.R., Rogers, J.A., and Nelson, K.A. (1992). *J. Appl. Phys.* **72**: 2823.
104. Rogers, J.A., and Nelson, K.A. (1994). *J. Appl. Phys.* **75**: 1534.
105. Rogers, J.A., and Nelson, K.A. (1995). *Adhesion* **50**: 1.
106. Banet, M.J., Fuchs, M., Rogers, J.A., Reinhold, J.H., Jr., Knecht, J.M., Rothschild, M., Logan, R., Maznev, A.A., and Nelson, K.A. (1998). *Appl. Phys. Lett.* **73**: 169.
107. Kuschnereit, R., Hess, P., Albert, D., and Kulisch, W. (1998). *Thin Solid Films* **312**: 66.
108. Lehmann, G., Schreck, M., Hou, L., Lambers, J., and Hess, P. (2001). *Diam. Relat. Mater.*, **10**: 664.
109. Lehmann, G., Thesis, Universität Heidelberg (2001).
110. Kagamida, M., Kanda, H., Akaishi, M., Nukui, A., Osawa, T., and Yamaoka, S. (1989). *J. Cryst. Growth* **94**: 261.
111. D'Evelyn, M.P., and Taniguchi, T. (1999). *Diamond Relat. Mater.* **8**: 1522.
112. Lehmann, G., Hess, P., Weissmantel, S., Reisse, G., Scheible, P., and Lunk, A. (2001). *Appl. Phys. A* in press.
113. Lehmann, G., Hess, P., Wu, J.-J., Wu, C.T., Wong, T.S., Chen, K.H., Chen, L.C., Lee, H.-Y., Amkreutz, M., and Fraunheim, Th. (2001). Submitted to *Phys. Rev. B*.
114. Szabadi, M., Hess, P., Kellock, A.J., Coufal, H., and Baglin, J.E.E. (1998). *Phys. Rev.* **B58**: 8941.
115. Kuschnereit, R., Fath, H., Kolomenskii, A.A., Szabadi, M., and Hess, P. (1995). *Appl. Phys.* **A61**: 269.
116. Rischbieter, F. (1965). *Acustica* **16**: 75.
117. Løpen, P.O. (1968). *J. Appl. Phys.* **39**: 5400.
118. Reutov, V.P. (1973). *Radiophys. Quant. Electron.* **16**: 1307 [(1973). *Izvestiya Vysshikh Uchebnykh Zavedenii, Radiofizika* **16**: 1690].
119. Kalyanasundaram, N., Ravindran, R., and Prasad, P. (1982). *J. Acoust. Soc. Am.* **72**: 488.
120. Lardner, R.W. (1983). *Int. J. Engng. Sci.* **21**: 1331.
121. Parker, D.F., and Talbot, F.M. (1985). *Elasticity* **15**: 389.
122. Mayer, A.P. (1995). *Phys. Rep.* **256**: 237.
123. Shull, D.J., Hamilton, M.F., Il'insky, Yu.A., and Zabolotskaya, E.A. (1993). *J. Acoust. Soc. Am.* **94**: 418.
124. Porubov, A.V., and Samsonov, A.M. (1995). *Int. J. Non-Linear Mech.* **30**: 861.
125. Hamilton, M.F., Il'insky, Yu.A., and Zabolotskaya, E.A. (1995). *J. Acoust. Soc. Am.* **97**: 882.
126. Hamilton, M.F., Il'insky, Yu.A., and Zabolotskaya, E.A. (1995). *J. Acoust. Soc. Am.* **97**: 891.
127. Shull, D.J., Kim, E.E., Hamilton, M.F., and Zabolotskaya, E.A. (1995). *J. Acoust. Soc. Am.* **97**: 2126.
128. Bonart, D., Mayer, A.P., and Mozhaev, V.G. (1994). In *Proceedings of the Annual Meeting on Advances in Surface and Interface Physics*, Modena, Italy [(1996). *Sci. Technol.* **3/96**: 21].

129. Knight, E.Yu., Hamilton, M.F., Il'inskii, Yu.A., and Zabolotskaya, E.A. (1997). *J. Acoust. Soc. Am.* **102**: 1402.
130. Knight, E.Yu., Hamilton, M.F., Il'inskii, Yu.A., and Zabolotskaya, E.A. (1997). *J. Acoust. Soc. Am.* **102**: 2529.
131. Mayer, A.P., Garova, E.A., and Mozhaev, V.G. (1997). *Proc. Estonian Acad. Sci. Phys. Math.* **40**: 85.
132. Gusev, V.E., Lauriks, W., and Thoen, J. (1997). *Phys. Rev.* **B55**: 9344.
133. Eckl, C., Mayer, A.P., and Kovalev, A.S. (1998). *Phys. Rev. Lett.* **81**: 983.
134. Hamilton, M.F., Il'inskii, Yu.A., and Zabolotskaya, E.A. (1990). *J. Acoust. Soc. Am.* **105**: 639.
135. Meegan, G.D., Hamilton, M.F., Il'inskii, Yu.A., and Zabolotskaya, E.A. (1990). *J. Acoust. Soc. Am.* **106**: 1712.
136. Zabolotskaya, E.A. (1992). *J. Acoust. Soc. Am.* **91**: 2569.
137. Parker, D.F., and David, E.A. (1989). *Int. J. Engng. Sci.* **27**: 565.
138. Leibfried, G., and Ludwig, W. (1960). *Z. Phys.* **160**: 80.
139. Royer, D., and Dieulesaint, E. (1984). *J. Acoust. Soc. Am.* **76**: 1438.
140. Hunter, J.K. (1989). *Contemp. Math.* **100**: 185.
141. Parker, D.F. (1988). *Physics of the Earth and Planetary Interiors* **50**: 16.
142. Kalyanasundaram, N., Parker, D.F., and David, E.A. (1990). *J. Elast.* **24**: 79.
143. Benjamin, T.B. (1967). *J. Fluid Mech.* **29**: 559.
144. Ono, H. (1975). *J. Phys. Soc. Jpn.* **39**: 1082.
145. Joseph, R.I. (1977). *J. Math. Phys.* (N.Y.) **18**: 2251.
146. Nakagawa, Y., Yamanouchi, K., and Shibayama, K. (1974). *J. Appl. Phys.* **45**: 2817.
147. Gibson, J.W., and Meijer, P.H.E. (1974). *J. Appl. Phys.* **45**: 3288.
148. Brysev, A.P., Krasilnikov, V.A., Podgornov, A.A., and Solodov, I.Yu. (1984). *Moscow University Bulletin* **26**: 2104.
149. Parker, D.F. (1988). *Int. J. Eng. Sci.* **26**: 59.
150. Nayanov, V.I. (1986). *JETP Lett.* **44**: 314.
151. Kavalero, V., Katoh, H., Kasaya, N., Inoue, M., and Fujii, T. (1995). *Jpn. J. Appl. Phys.* **34**: 2653.
152. Lomonosov, A., and Hess, P. (1996). In *Nonlinear Acoustics in Perspective*, pp. 106–111, Wei, R.J., ed., Nanjing: Nanjing University Press.
153. Lomonosov, A., and Hess, P. (1999). *Phys. Rev. Lett.* **83**: 3876.

4. QUANTITATIVE ACOUSTIC MICROSCOPY

Pavel V. Zinin

School of Ocean and Earth Science and Technology
University of Hawaii
Honolulu, Hawaii

Science is always wrong. It never solves a problem without creating ten more.
George Bernard Shaw

Abstract

This chapter deals with the elastic characterization of solid media by acoustic microscopy. Three types of microscopy are considered. The first type is conventional acoustic microscopy, which uses monochromatic illumination for measuring elastic properties. The use of conventional acoustic microscopes for evaluating the elastic properties of layered anisotropic solids exploits the fact that this technique is able to measure the velocity of surface acoustic waves (SAWs). In conventional acoustic microscopy, the velocity of the surface acoustic wave is determined from the so-called $V(z)$ curve, the variation of the voltage signal that is measured when the lens of the microscope is translated toward the sample. For isotropic layered materials, the SAW velocity is dependent on the frequency; i.e., there is dispersion. For anisotropic solids, the SAW velocity also exhibits a variation with the direction of propagation, called angular dispersion. The elastic properties of anisotropic solids can be extracted from measured dispersion curves. Acoustic microscopes usually operate within the frequency range of 100 MHz to 2 GHz. At such frequencies the elastic properties of thin layers from several hundred nanometers up to a few tens of microns can be determined. The second type is time-resolved microscopy, which uses pulses for material characterization. This type of microscopy provides an opportunity to measure velocities of bulk waves inside solid layers. A new (third type) type of microscopy, where two lenses are used for quantitative measurements, will be reviewed briefly. The chapter is organized into six sections. A short history of acoustic microscopy is presented in the Introduction (Section 4.1). The basic principles of quantitative acoustic microscopy and the accuracy of measuring SAW velocities by acoustic microscopy are described in Section 4.2. Sections 4.3 and 4.4 concern the acoustic microscopy measurement of dispersion curves of different types of materials and the extraction of the elastic properties from experimental acoustic

data. The application of acoustic microscopy to elastic characterization of nonplane bodies is reviewed in Section 4.5. Finally, acoustic microscopy is compared to other techniques in Section 4.6.

4.1 Introduction

The development of the first high-frequency scanning acoustic microscope was motivated by the idea of using an acoustic field to study the spatial variations of elastic properties of materials with nearly optical resolution [65]. However, it was soon found that the acoustic microscope could be used for measuring the velocity of SAWs. To analyze the image formation in the reflection acoustic microscope, Atalar, Quate, and Wickramasinghe [8] monitored the amplitude of the transducer voltage V as a function of lens-to-sample spacing z , or the $V(z)$ curve. They found that the $V(z)$ curve “has a characteristic response that is dependent upon the elastic properties of the reflecting surface” [8]. Later Weglein and Wilson [109] reported the periodicity of dips appearing in the $V(z)$ curves. They called the central portion of the $V(z)$ curve, which has a periodic character, the acoustic material signature (AMS). It was soon established that the periodicity of the $V(z)$ curve was linked to surface wave propagation [5, 85, 109]. The application of a ray model for wave propagation in the acoustic microscope by Parmon and Bertoni [85] yielded a clear physical picture of signal formation in the reflection acoustic microscope and provided a simple formula for determining the SAW velocity from acoustic microscopy measurements. The next step toward quantitative measurements of anisotropic materials was taken by Kushibiki and coworkers [55], who invented the line-focus-beam (LFB) technique or the line focus acoustic microscope (LFAM). This made it possible to measure the anisotropy of surface acoustic waves on a crystal surface [56]. Considerable progress in quantitative acoustic microscopy of anisotropic multilayered structures has been made since the time of the invention of the acoustic microscope. Today quantitative acoustic microscopy is not limited to the $V(z)$ curve technique. Combining time-of-flight technique with acoustic microscopy [118] allows one to measure, for example, the elastic properties of anisotropic nonflat layers [3] and small superhard samples synthesized from C_{60} under high pressure and high temperature [66]. Different modifications of the acoustic microscope, such as the ultrasonic micrometer [96], the phase or vector contrast scanning ultrasonic microscope [36], the two-point-focus acoustic lenses technique [100], and the ultrasonic force microscope [119], have been developed and are now widely used in the field of elastic characterization of solids. Recent developments in quantitative acoustic microscopy can be found in the series “Advances in Acoustic Microscopy” [18, 19, 119]. This chapter will review the elastic characterization of solids by different types of acoustic microscopy.

Quantitative acoustic microscopy uses a focused acoustic beam to measure velocities of different types of acoustic waves propagating in solid media. Acoustic microscopes used for the characterization of the elastic properties of solids can conveniently be divided into three main groups: conventional microscopy, time-resolved microscopy, and two-lens microscopy.

In conventional acoustic microscopy, a monochromatic sound wave is focused onto a specimen by means of an acoustic lens (Fig. 4.1). At the top of the lens is a piezoelectric transducer, and its other face is ground into a spherical or cylindrical cavity that is coated with a quarter-wavelength matching layer. The same lens is used to record the signal reflected back from the sample. A liquid couplant, usually water, is put between the lens and the sample. The spherical lens, i.e., the lens with a spherical cavity, focuses sound onto a spot of size comparable to the sound wavelength in the fluid (Fig. 4.2[a]). Such a lens is called a point focus lens. Quantitative measurements by conventional microscope with a point focus lens can be

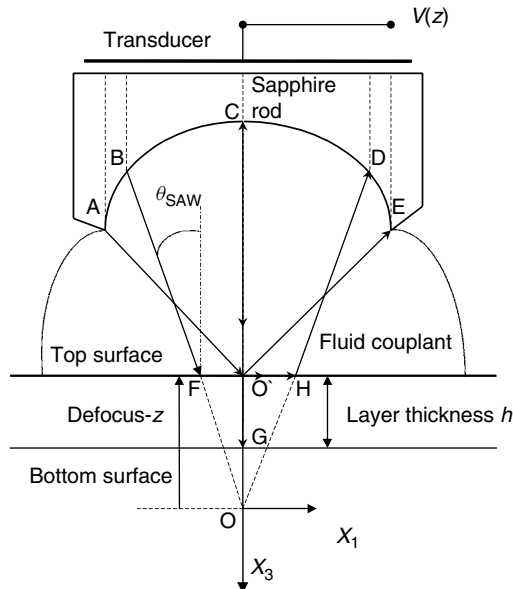


FIG. 4.1. Schematic diagram of the defocused acoustic lens. CO¹ is the trajectory of the specular or geometrical wave (GW). BFHD is the trajectory of the leaky SAW. In the ray model the leaky RW is excited by the ray BF, striking the surface at the angle $\sin \theta_{\text{SAW}} = v_W/v_{\text{SAW}}$. AO'E is the trajectory of the edge wave.

done by measuring the output signal when the lens is translated toward the sample, yielding the $V(z)$ curve. For elastic characterization of anisotropic solids, the LFB lens is preferable. The shape of the lens cavity is the factor that distinguishes the LFB acoustic microscope. The cylindrical lens focuses sound along a line. It is a half-cylinder, as shown in Figure 4.2(b), and surface waves are only excited in the direction perpendicular to the focal line. The rotation of the LFB lens relative to the specimen allows the behavior of the surface waves to be examined in all propagation directions. Most measurements of elastic properties have been done by conventional microscopy, since it has the longest history; therefore, we will discuss it in most detail.

Time-resolved acoustic microscopy adds an additional degree of freedom for quantitative measurement, namely, time [18]. In the time-resolved acoustic microscope, a short sound pulse is sent toward a sample. The returning signal consists of a pulse train, where each pulse is attributed to a particular type of wave, that is excited by the incident pulse. The velocity of the wave can be determined by measuring the time delay of the corresponding pulse. Using a cylindrical lens in the time-resolved microscope provides an opportunity to study the anisotropy of different types of SAWs in crystals.

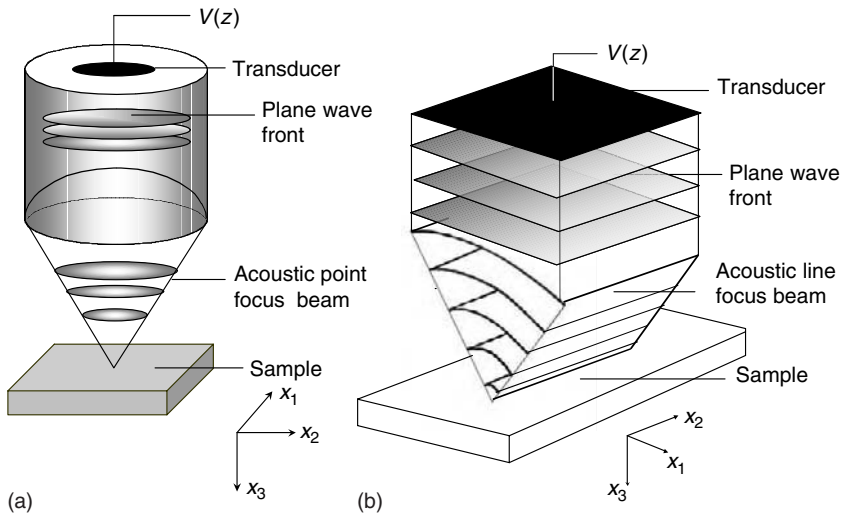
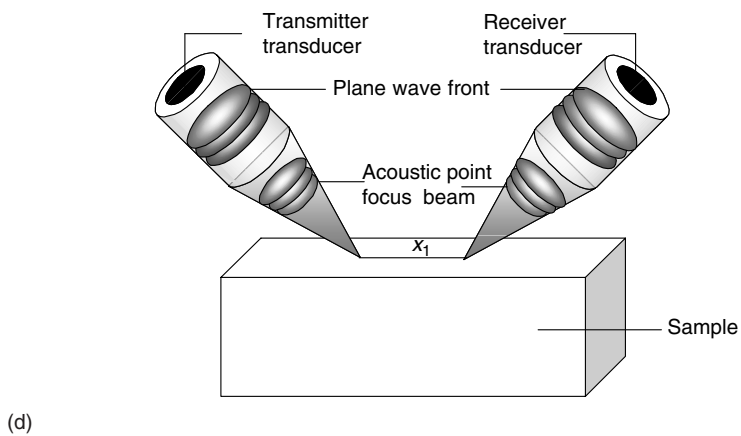
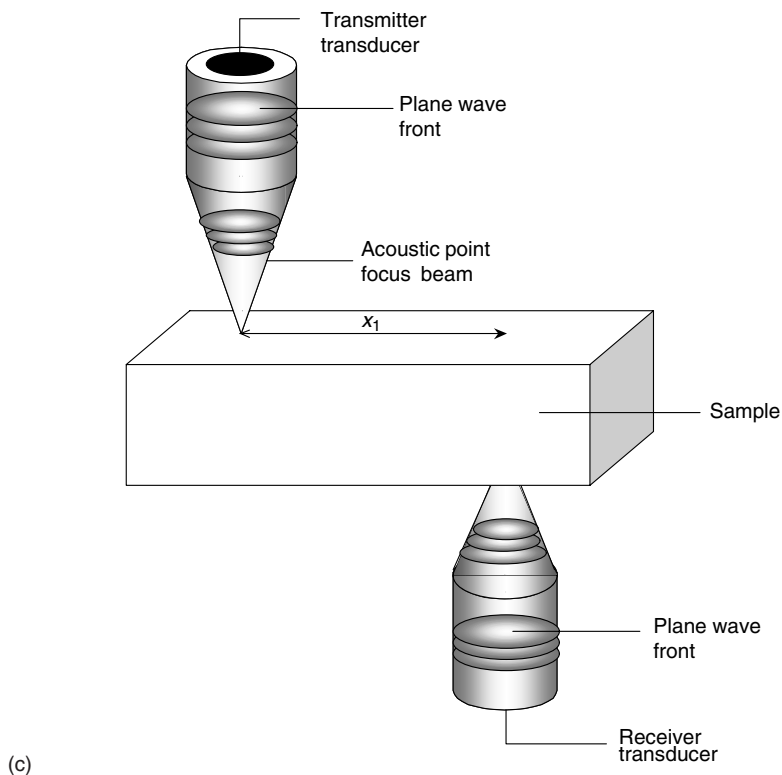


FIG. 4.2. (a) Schematic of the point focus acoustic microscope. (b) Schematic of the line focus acoustic microscope. (c) Schematic of the ultrasonic flux imaging technique. The ultrasound is generated and detected by a pair of focused immersion transducers, one of which is raster-scanned parallel to the sample surface. (d) Sketch of the two-point-focus lenses acoustic imaging system. The sample is immersed in water. The transmitter and receiver transducers are focused to fixed points on the surface of the crystal.

FIG. 4.2. (*continued*)

An additional degree of freedom is added if two lenses are used for measurements. We call such a configuration two-lens acoustic microscopy. In two-lens microscopy one lens transmits the sound pulse and the other lens is used as a receiver. The use of the second lens for quantitative measurements permits a variety of different techniques. A spherical lens as a transmitter and a planar transducer as a receiver are used in ultrasonic micrometry to measure the reflection coefficients of anisotropic solids [96]. In the ultrasonic flux imaging technique [40, 104], two point focus lenses are focused on opposite faces of a crystal (Fig. 4.2[c]). Such a configuration of lenses makes visible a fascinating picture of bulk sound waves propagating in an anisotropic solid, and was found to be a very effective method of determining elastic constants of crystals [116]. The experimental technique, which consists of a pair of point focus [100] or line focus acoustic lenses [115] working in the reflection mode, has brought to light the complex angular and frequency dependence of surface acoustic waves generated on the crystal surface (Fig. 4.2[d]). This type of microscopy is still under development; we will describe briefly the first results in that area.

4.2.1 Wave Theory of the $V(z)$ Curves

To measure the velocity of SAWs by conventional acoustic microscopy, the $V(z)$ technique is usually used. The lens is mechanically translated in the direction normal to the specimen surface. The transducer signal $V(z)$ is detected, processed, and then used to derive the propagation parameters of the SAWs. A typical $V(z)$ curve measured by LFAM [54] is presented in Figure 4.3. To derive an expression for the output signal $V(z)$, two main problems should be addressed. First, the relationship between the input and output signals of the transducer and the acoustic field in the coupling liquid should be established. Second, scattering of the incident focused beam by the specimen, which may be a layered solid, a layer on a substrate, or a substrate alone, needs to be described. The first task involves examining the excitation of the sound waves into the buffer rod by the piezoelectric transducer, propagating the sound inside the buffer rod, and focusing the sound waves into the liquid couplant by the spherical or cylindrical cavity (see Fig. 4.1). An elegant solution of this problem has been developed by Auld [9]. He introduced the reciprocity principle, which provides a general expression relating the output signal and the acoustic field in a solid coupling medium. The solution for the second problem has been provided by Atalar. He applied the Fourier spectrum approach to describe the beam scattering by a layered medium [5].

The following discussion derives an expression for the $V(z)$ curve of the reflection acoustic microscope using Auld's reciprocity principle and the Fourier spectrum approach following Weise *et al.* [112] and Zinin *et al.* [129]. The reader who prefers a simpler phenomenological treatment based on rays should skip to the next subsection. The multilayered flat specimen is located

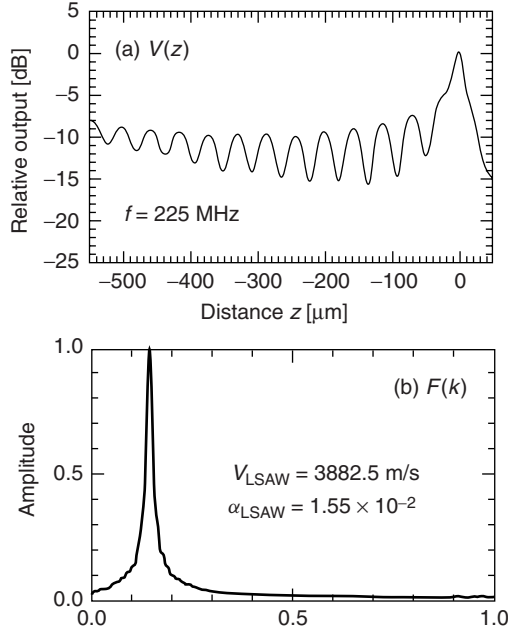


FIG. 4.3. (a) Typical $V(z)$ curve measured for a Z-cut, Y-propagating, undoped LiNbO_3 specimen at 225 MHz. (b) Final spectral distribution ($V(k)$ curve) analyzed by FFT for the $V(z)$ curve shown in (a) (from Kushibiki *et al.* [54]).

at the distance z from the focal plane as depicted in Figure 4.1. I use the three-dimensional coordinate system (x_1, x_2, x_3) with the origin at the focal point O. The axis x_3 is normal to the sample surface and directed away from the lens, and x_1 and x_2 are parallel to the surface. In the case of LFAM, the focal line of the cylindrical lens (Fig. 4.2[b]) is parallel to the axis x_2 and perpendicular to the axis x_1 . Only modes propagating in the sagittal plane ($x_1 x_3$ plane) are considered here: water or any other liquid couplant used in the acoustic microscope does not support transverse modes. A time-harmonic condition is assumed, and the time factor $\exp(-i\omega t)$ is suppressed. For the output signal of the acoustic microscope, one can use the expression derived by the reciprocity principle [6]:

$$V = \int_{-\infty}^{\infty} \int_{-\infty}^{\infty} U_i(-k_1, -k_2) U_s(k_1, k_2) k_3 dk_1 dk_2 \quad (4.1)$$

Here $\boldsymbol{\kappa} = (k_1, k_2, k_3)$ is the wavevector, $k = \omega/v_w$ is the wavenumber, v_w is the velocity of sound in a liquid (water), $\omega = 2\pi f$ is the angular frequency,

f is the frequency, U_i is the Fourier spectrum of the incident acoustic field $u_i(x_1, x_2, x_3)$ for fixed x_3 , and U_s is the Fourier spectrum of the scattered field $u_s(x_1, x_2, x_3)$ at fixed x_3 :

$$U_l(k_1, k_2) = \int_{-\infty}^{\infty} \int_{-\infty}^{\infty} u_l(x_1, x_2, x_3) \exp[-i(k_1 x_1 + k_2 x_2)] dx_1 dx_2, l = i, s. \quad (4.2)$$

In Eq. 4.1 and elsewhere the proportionality constant is omitted. Explicit derivation of the output signal in form (Eq. 4.1) is rather complicated. However, Eq. 4.1 has a straightforward interpretation. The incident spectrum $U_i(k_1, k_2)$ is the emission strength of the emitted plane waves $\exp[i(k_1 x_1 + k_2 x_2)]$, and is also the sensitivity to returning plane waves $\exp[-i(k_1 x_1 + k_2 x_2)]$. Therefore, the contribution of the returning plane wave with an amplitude $U_s(k_1, k_2)$ to the output signal is $U_i(-k_1, -k_2)U_s(k_1, k_2)$. Integration over all the plane waves coming back to the transducer yields the integral (1). The two-dimensional Fourier integral in Eq. 4.1 can be taken at any fixed x_3 position. We take the incident spectrum U_i and the scattered spectrum U_s at the focal plane, where they occur only virtually if the object surface is situated above this point. The coordinate system in the spatial frequency domain (k -space) is chosen so that the k_3 component of waves propagating in the positive x_3 direction of the spatial domain is positive: $k_3 = \sqrt{k^2 - (k_1^2 + k_2^2)}$. Let us suppose we know the spectrum incident on the object and we want to calculate the scattered spectrum. The object is placed at $x_3 = -z$. Since the magnitude of k is fixed, the wavevector is completely specified by the vector $k_{\parallel} = (k_1, k_2)$. To calculate the scattered spectrum, we must integrate over all incident plane waves.

We now express the incident and reflected spectra with respect to the coordinate system with origin at the focus O. For the focused transducer, the spectrum incident at the focal plane U_i in the Debye approximation is equal to [111]

$$U_i(k_1, k_2) = \frac{P(k_1, k_2)}{k_3} \quad (4.3)$$

The pupil function $P(k_1, k_2)$ is here defined as the strength of the field emitted from the point situated in backward prolongation of κ on the transducer [13]. The Fourier spectrum of the acoustic field reflected from an infinite multilayered half-space is the product of the incident field spectrum and the reflection coefficient [16]:

$$U_s(k_1, k_2) = R(k_1, k_2)U_i(k_1, k_2) \quad (4.4)$$

The spatial coordinate system in which both the incident plane wave spectrum and the reflected one are given has its origin at point O in Figure 4.1. To relate the incident spectrum at the focal plane with the spectrum at the object surface

or object plane, we use a property of the spatial Fourier spectrum stating that the spectrum incident at the object plane at the position z is calculated by including a propagation factor $\exp(ik_3z)$ [35]. Since the integration in Eq. (4.1) is taken at the focal plane, we must return with the scattered spectrum to the focal plane by multiplying Eq. 4.4 by $\exp(ik_3z)$. Combining Eqs. 4.1, 4.3, and 4.4 with the back-and-forth propagation factor, $\exp(i2k_3z)$, we finally have the output signal of the reflection microscope:

$$V(z) = \int_{-\infty}^{\infty} \int_{-\infty}^{\infty} P(-k_1, -k_2) P(k_1, k_2) R(k_1, k_2) \exp(2ik_3z) \frac{dk_1 dk_2}{k_3} \quad (4.5)$$

Equation 4.5 represents the $V(z)$ curve of an anisotropic sample in the nonparaxial approximation. The signs in the arguments for the two pupil functions are different, and this is of importance in the investigation of inclined surfaces [111]. Introducing spherical coordinates $k_1 = k \sin \theta \cos \varphi$, $k_2 = k \sin \theta \sin \varphi$, $k_3 = k \cos \theta$, we obtain an expression for the $V(z)$ curve of the acoustic microscope with spherical lens:

$$V(z, \omega) = \int_0^{2\pi} d\varphi \int_0^{\frac{\pi}{2}-i\infty} P(\theta, \varphi) P(\theta, \varphi + \pi) R(\theta, \phi) \exp(2ikz \cos \theta) \sin \theta d\theta \quad (4.6)$$

The reflection coefficient $R(\theta, \varphi)$ depends on the frequency for layered media and therefore $V(z, \omega)$ is a frequency-dependent function for layered solids as well. If the defocus z is fixed and the frequency f is changed, the previous expression is called the $V(f)$ curve [80]. In Eq. 4.6 the angle changes from $\theta = 0$ to $\pi/2 - i\infty$ [16, p. 230]. However, in the Debye approach, the maximum angle of integration is restricted by the semiaperture angle θ_M of the pupil to $\sqrt{k_1^2 + k_2^2} \leq \sin \theta_M$ [67]. This leads to an integration restricted to the real angle domain. For symmetrical pupil function ($P(\theta, \varphi) = P(\theta)$), the expression for the $V(z)$ curve can be rewritten

$$V(z, \omega) = \int_0^{\theta_M} P^2(\theta) R_{kl}(\theta, \omega) \exp(2ikz \cos \theta) \sin \theta d\theta \quad (4.7)$$

$$R_{kl}(\theta, \omega) = \int_0^{2\pi} R(\theta, \varphi, \omega) d\varphi$$

For the cylindrical lens, the pupil function in Eq. 4.5 can be represented as $P(k_1, k_2) = P(k_1)\delta(k_2)$, where $\delta(k_2)$ is the delta function [110]. The cylindrical lens irradiates and receives only acoustic waves propagating normal to the focal line of the cylindrical lens surface ($k_2 = 0$). Substituting the pupil function of the cylindrical lens into the integral (4.5) and integrating over k_2

reduces the expression for the $V(z)$ curve to the one-dimensional integral

$$V(z, \omega) = \int_0^{\theta_M} L^2(\theta) R(\theta, \omega) \exp(2ikz \cos \theta) d\theta \quad (4.8)$$

where $L(\theta)$ is the LFAM pupil function, θ is the polar angle in the x_1x_3 plane, and $R(\theta, \omega)$ is the reflection coefficient in the sagittal plane (x_1x_3) normal to the focal line of the cylindrical lens. We mention that $L(-\theta) = L(\theta)$ was assumed in Eq. 4.8. The computation of the pupil function of the cylindrical lens has been considered by Li *et al.* [70]. Comparing Eqs. 4.7 and 4.8, we note that the difference in the $V(z)$ expressions for spherical and cylindrical lenses is the term $\sin \theta$ in the integrand. This term makes the procedure for extracting the SAW velocity from the $V(z)$ curve different for cylindrical and spherical lenses, as will be shown later. Equation 4.8 shows that the behavior of the $V(z)$ curve is determined by the shape of the reflection coefficient $R(\theta, \omega)$. The reflection coefficient contains all the relevant information related to wave propagation in the sample. A prominent feature is associated with the leaky Rayleigh surface wave and is a 2π change in phase [17]. For a solid half-space, $R(\theta, \omega)$ is independent of frequency. Its amplitude and phase for aluminum are shown in Figure 4.4. For anisotropic solids, a null in the reflection coefficient amplitude has been found at a particular incidence angle [4]. The null in the reflection corresponds to the excitation of the pseudo-SAW. The nature of the pseudo-SAW will be discussed further.

4.2.1.1 Ray Model and Quantitative Analysis of $V(z)$ Curves. The use of conventional acoustic microscopy for evaluating elastic properties of layered anisotropic solids exploits the fact that it is able to measure the velocity

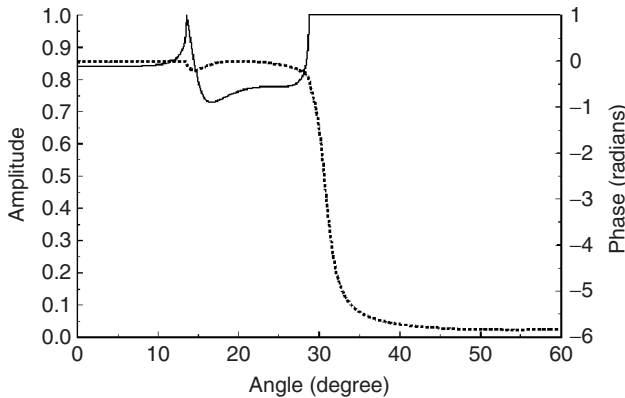


FIG. 4.4. Magnitude (solid line) and phase (dotted line) of the reflection coefficient from water–aluminum interface.

of surface acoustic waves. Layered materials are commonly investigated by SAWs, because surface wave displacements are concentrated within about a wavelength of SAWs from the surface. Therefore, SAWs probe a sample to a depth inversely proportional to the frequency used. For isotropic layered materials, the SAW velocity is dependent on frequency; i.e., there is dispersion. For anisotropic solids, the SAW velocity in addition exhibits variation with the angle of propagation, and this is called the angular dispersion. Determining the elastic constants of a multilayered anisotropic medium by acoustic microscopy involves two main steps: (a) the measurement of the dispersion relation by acoustic microscopy, and (b) the extraction of the material properties of the specimen from the dispersion relation.

As mentioned previously, the standard procedure for determining the elastic constants of anisotropic layered solids by LFAM is to carry out inversion of the measured SAW dispersion relation. Therefore, in order to understand the basic features of the elastic characterization of solids by LFAM, we should consider the propagation of different types of SAWs in anisotropic layered media and the possibility of detecting such waves by LFAM. A wide variety of surface waves that can be generated on layered anisotropic solids have been extensively used in acoustic microscopy. The Rayleigh wave (RW) is the nondispersive acoustic wave (true surface wave) propagating along the stress-free boundary of a semi-infinite isotropic elastic half-space, and it has its energy confined near the surface [32, 41]. Similar waves existing on anisotropic surfaces are called generalized RWs (GRWs) [27]. The solutions of the wave equation for such waves “differ from the true Rayleigh wave on isotropic media only in the form of the variation of the displacement with depth” [32]. In addition, waves that are surfacelike and slowly radiate energy away from the surface, and for which the displacement field does not, therefore, vanish at infinite depth, are called pseudo surface acoustic waves (PSAWs) or leaky SAWs (LSAWs) [32]. PSAWs or LSAWs have a phase velocity higher than that of the lowest of the bulk waves either in a coupling liquid or in the substrate. For simplicity, we refer to those waves radiating energy into the coupling liquid as LSAWs and those irradiating energy into the substrate as PSAWs. Acoustic microscopy is able to detect only LSAWs, i.e., surface waves, having a velocity higher than the velocity of the coupling liquid. Some bulk waves propagating along a liquid–solid interface can also be detected by LFAM. They are the lateral longitudinal waves (LLWs) or the surface-skimming compressive wave (SSCW) and have velocities equal to the bulk velocity of one of the media [12, 16]. The presence of the layer leads to the appearance of an infinite number of waves confined within the layer [33]. For a single layer on solid substrate, these waves are called generalized Lamb waves [10] because of their similarity to the Lamb waves that propagate on isotropic plates with free boundaries. The behavior of the generalized Lamb

waves is determined by the type of layer and substrate and will be discussed further.

Several methods have been developed [20] for extracting the SAW velocity v_{SAW} from the recorded $V(z)$ curve. For practical reasons, only the amplitude of the signal is generally measured, from which velocity and attenuation can be calculated. When the complex-valued signal is available, the reflection coefficient of the investigated solid can be retrieved by applying the inverse Fourier transform to the measured $V(z)$ curve (see Eq. 4.8). This treatment is more complex than the analysis of amplitude data alone [71, 72, 86], and it is not as accurate as the ultrasonic micrometer, a modification of acoustic microscopy used for measuring the complex reflection function of anisotropic solids directly [96]. The standard method of analyzing $V(z)$ curves was developed by Kushibiki and Chubachi [51] in 1985 for the LFAM and is also commonly applied to a point focus lens. The method is based on the ray model proposed by Parmon and Bertoni [85]. They postulated that the periodical character of the $V(z)$ curve is determined by interference of two rays (Fig. 4.1): central ray (CO^1) and the SAW ray (BFHD). Ray CO^1 is incident normally onto the specimen and is reflected back along the same path. Ray BF is incident at a critical angle θ_{SAW} and excites a LSAW wave along the surface. According to the Snell's law, $\sin \theta_{\text{SAW}} = v_W / v_{\text{SAW}}$, where v_{SAW} is the velocity of the SAW. The SAW leaks energy back into the fluid, and the particular ray HD is incident normally onto the lens. Using the ray model, it is not difficult to derive the period of the $V(z)$ oscillations. The phase variations $\phi_S(z)$ and $\phi_{\text{SAW}}(z)$ when the specimen is negatively defocused by an amount z are $\phi_S(z) = -2k_w z$ for the specular ray and $\phi_{\text{SAW}}(z) = -2k_w z / \cos \theta_{\text{SAW}} + 2k_R z \tan \theta_{\text{SAW}} - \pi$ for the SAW ray. The phase of $-\pi$ in the $\phi_{\text{SAW}}(z)$ phase is associated with the phase change of π in the reflection coefficient at the SAW angle. A relative minimum in the $V(z)$ curve appears when the two rays interfere destructively, i.e., when the phase difference between two rays $\Delta\phi(z) = \phi_S(z) - \phi_{\text{SAW}}(z)$ is equal to π : $\Delta\phi(z) = -2k_w z(1 - \cos \theta_{\text{SAW}}) - \pi = \pi$. This condition gives us an expression for the minima in the $V(z)$ curve, Δz :

$$\Delta z = \frac{2\pi}{2k_w(1 - \cos \theta_{\text{SAW}})} \quad (4.9)$$

Equation 4.9 establishes the relation between the $V(z)$ curve periodicity (see Fig. 4.3) and the velocity of the SAW wave propagating in the sample:

$$v_{\text{SAW}} = \frac{v_W}{\sqrt{1 - \left(1 - \frac{v_W}{2f\Delta z}\right)^2}} \quad (4.10)$$

One of the key assumptions in the ray model is a statement that only rays normal to the lens surface make a significant contribution to the output signal. This postulate can be proved by using the method of stationary phase [13] described in detail in Stamnes [93]. According to the method of stationary phase, the integral (22.8) can be calculated with sufficient accuracy only if normal rays to the surface and the edge rays (rays AO'E , Fig. 4.1) are taken into account [93, 113, 129]. In acoustic microscopy the main contribution to the output signal is provided by the normal rays; however, the edge waves can be observed in time-resolved microscopy [122]. They will be considered later in Section 4.2.2.1. The comprehensive ray-optical evaluation of the $V(z)$ curve in the reflection acoustic microscope has been described in a series of papers written by Bertoni and coauthors [12, 13]. It is accepted in acoustic microscopy that the z -axis is directed away from the lens. Thus SAWs are excited and then detected only for negative defocus, with the virtual focus located beneath the sample surface (see Fig. 4.1).

The SAW attenuation is related to Δz , the exponential decay of the $V(z)$ curve, and to α_w , the attenuation associated with the propagation in water (see Fig. 4.3):

$$\alpha = \frac{\delta}{2 \tan \theta_{\text{SAW}}} + \frac{\alpha_w}{\sin \theta_{\text{SAW}}} \quad (4.11)$$

where θ_{SAW} is the angle of SAW excitation or critical angle (see Fig. 4.1). In the presentation of results, the normalized attenuation factor γ is usually used:

$$\gamma = \alpha \frac{v_{\text{SAW}}}{\omega} \quad (4.12)$$

In Kushibiki's method the $V(z)$ curve is considered a linear combination of contributions from the specularly reflected component $V_G(z)$ and the surface wave component $V_{\text{SAW}}(z)$ [7, 51]

$$V(z) = V_G(z) + V_{\text{SAW}}(z) \quad (4.13)$$

For the cylindrical lens it is assumed that the contribution of the specular reflected component $V_G(z)$ is much higher than the contribution from the surface wave component, $V_{\text{SAW}}(z)$: $V_G(z) \gg V_{\text{SAW}}(z)$ [17]. Under such conditions the measured amplitude of the $V(z)$ curve is proportional to $|V_G(z)|[1 + (|V_{\text{SAW}}(z)|/|V_G(z)|) \cos \phi]$, where ϕ is the phase angle between the vectors $V_G(z)$ and $V_{\text{SAW}}(z)$ in the complex plane. The $V_G(z)$ reference curve can be measured using material that exhibits no Rayleigh activity. In practice the $V_G(z)$ is usually the $V(z)$ of Teflon, gold, or lead. The previously mentioned assumption is valid only for $V(z)$ curves obtained with a cylindrical lens. For a spherical lens, the contribution of the specular reflected rays $V_G(z)$ is much less on simple geometrical grounds. As can be seen from Eq. 4.7, the

contribution of the rays received by the lens in the angle $d\theta$ is proportional to $\sin\theta d\theta$ for the spherical lens. Around the central ray CO^1 , $\sin\theta \rightarrow 0$ and the contribution becomes negligible as $\theta \rightarrow 0$. It makes the contribution of the Rayleigh rays comparable to the contribution of the central specular ray [7]. As a consequence, extracting the velocity of SAWs from the spherical lens $V(z)$ curves is more complicated than for the cylindrical lens as described in Briggs [17].

In Kushibiki's method, the absolute value of the reference signal $|V_G(z)|$ is subtracted from the $|V(z)|$ curve: $|V_{\text{SAW}}(z)| = |V(z)| - |V_G(z)|$. At this stage, the curve is an exponential decaying sinusoid. An application of the fast Fourier transform (FFT) to $V_{\text{SAW}}(z)$, $V(k) = \text{FFT}(|V_{\text{SAW}}(z)|)$, (see Fig. 4.3) gives the Δz period of the oscillation of the $V(z)$ curve and the rate of the exponential decay δ . The velocity and the attenuation are then calculated from Eqs. 4.10 and 4.11. Several parameters can influence the results of the analysis, in particular the reference curve, the number of points (or sampling distance), and the length of the signal [61]. One should also note that the kind of coupling liquid used, the operating frequency, and the maximal defocus distance impose a limit on the range of SAW velocity measured by acoustic microscopy. The lower limit of the measurable speed of SAWs is confined by the semiaperture angle of the lens θ_M : $\theta_{\text{SAW}} < \theta_M$, $v_{\text{SAW}} > v_W / \sin\theta_M$. The upper limit of the SAW velocity is determined from the fact that several oscillations must appear on the $V(z)$ curve to use Eq. 4.10 for SAW velocity extraction. The computer simulation performed by Kushibiki *et al.* [58] for an acoustic microscope operating at 216 MHz, with water as an immersed liquid, with the maximal defocus distance 300 μm , and with the semiaperture angle of 60° , showed that only LSAWs with velocity in the range 2.5 to 6.0 km/s can be reliably measured. If a single mode propagates with only a small number of oscillations present in the $V(z)$, the short range of z over which a useful signal can be obtained will give rise to an error in the Fourier transform components. To overcome that, Hirsekorn and Pangraz [42] proposed a method for extracting the velocity of the SAWs from the first oscillation in the $V(z)$ curve. Weglein then simplified the formula given previously by grouping all the parameters into one empirical factor that depended on the geometry of the lens [107]. This method is easy to implement but does not give the attenuation of the wave. In addition, the calculation of the SAW velocity is based on a single distance measurement between two peaks and requires a careful characterization of the lens.

Experiments have shown that for some materials the longitudinal lateral waves can be detected by acoustic microscopy [105]. Bertoni and Chan [12, 21] considered the output signal of the acoustic microscope $V(z)$ as the sum of the contribution of three components: a specular reflected component, a surface wave component, and a lateral wave component, $V_{\text{LLW}}(z)$: $V(z) = V_G(z) +$

$V_{\text{SAW}}(z) + V_{\text{LLW}}(z)$. They found that, for fast materials and for z not near zero, the term $|V_{\text{LLW}}(z)|$ is substantially smaller than $|V_G(z)|$ and $|V_{\text{SAW}}(z)|$ and for a cylindrical lens it decays as $1/|z|^{3/2}$ in amplitude. If $\sin \theta_M < v_W/v_{\text{SAW}}$, the longitudinal lateral wave is the only component that interferes with the geometric component to form an overall oscillating $V(z)$ curve. The speed of the lateral longitudinal wave can be determined from Eq. 4.10. For stiff materials in which both the Rayleigh waves and the lateral longitudinal waves are excited by LFAM, a periodicity associated with longitudinal waves can be found only at a sufficient defocus [92]. The explanation of this is based on the fact that the Rayleigh wave is subject to an exponential decay whereas the lateral waves are subject to algebraic decay [12, 17], and so at large defocus z lateral waves predominate. To enhance the contribution of the lateral wave to the output signal of SAM, two methods have been proposed [24, 37]. It has been shown theoretically and proved experimentally that the efficiency of detection of lateral waves can be improved by using a small-aperture lens. The replacement of the coupling liquid by a heavy liquid, such as mercury, also enhances the efficiency of lateral wave generation. Doghmane *et al.* [24] found that the measured SAW velocity with mercury as a coupling liquid was close to the shear velocity of the substrate.

The high accuracy of SAW velocity measurement is one of the main advantages of LFAM. Accuracy of two kinds has to be distinguished in $V(z)$ measurements: absolute and relative accuracy. The relative accuracy shows how accurately the variation of the SAW velocity can be measured on the same or similar samples: for example, variation of SAW velocity in LiNbO_3 single crystal due to MgO doping [54]. The best relative accuracy, of an order of 0.01%, can be attained by the established measurement procedure [50]. The use of the Fourier transform allows the use of practically all the points on the $V(z)$ curve and hence reduces the accidental error of the experiments. Absolute accuracy exhibits the difference between the SAW velocity of the specimen measured by LFAM and a reference value of SAW velocity measured by other more precise techniques or estimated theoretically. Absolute accuracy of the LFAM is dictated mainly by two factors: (a) the validity of the ray model used for the retrieval of the SAW velocity from the $V(z)$ curve measurements, Eqs. 4.10 and 4.11, and (b) the errors of determining the parameters involved in the model, Eqs. 4.10 and 4.11. It includes the measurement of the water temperature through a thermocouple, leveling of the sample, and monochromaticity of the signal. This has been detailed previously [17, 61], and we do not describe it here. Practically, the temperature and frequency variations and the alignment of samples have small effects on the velocity and the attenuation. The uncertainty induced by these errors in the surface wave velocity measurement was estimated to be around 0.1% [17]. Vertical movement of the microscope stage has been found to be a critical parameter in the

$V(z)$ curve technique that was difficult to substantially improve [61]. Another parameter that has strong influence on the result is the number of oscillations present in the $V(z)$ curve. Since the maximum defocusing distance is limited by the geometry of the lens, at high frequency or for high-speed materials the $V(z)$ curve contains only a few oscillations. For example, high attenuation of sound in water does not allow the radius of the 1-GHz acoustic lens to be larger than 80–100 μm . Then the maximal negative defocus cannot exceed 60 μm , whereas it is 560 μm for a lens operating at 225 MHz. A similar problem also arises if the measured SAW is highly attenuated. Therefore, the error caused by the analysis depends on the materials investigated, and it is not possible to give a general formula to quantify this effect. However, the influence of the attenuation of the SAW and the length of the useful signal can be understood from numerical simulations. Atalar *et al.* [7] and Lefeuvre [61] estimated an error introduced by the $V(z)$ curve analysis. For solids such as aluminum and chromium, values of SAW velocity obtained from the numerical simulation of the $V(z)$ curve and direct calculations performed with SAW dispersion equation differed by only 0.1%. The larger discrepancies were found for stiff materials, such as alumina (0.3%, see [7]) and stiffening layers, such as titanium on steel (1%, see [61]). This happens when the attenuation or the velocity is high and the number of oscillations in the signal is insufficient.

As for the attenuation measurements by LFAM, Kushibiki *et al.* [58] estimated that, for the case of water–solid interface, LFAM operating at 216 MHz is able to measure the attenuation factor (Eq. 4.12) of LSAWs within the range of 5×10^{-3} to 8×10^{-2} . The accuracy of the attenuation determination varies. For the normalized attenuation higher than 0.01, accuracy of a few percent is achieved; when the attenuation is lower, the error can reach 20% [51]. This happens when a PSAW propagates with a velocity close to a velocity of a lateral wave. In this case, the wave decays algebraically rather than exponentially [12] and Eq. 4.11 is no longer valid.

4.2.2 Theory of Time-Resolved Acoustic Microscopy

Yamanaka [118] has applied the time-of-flight acoustic microscopy technique to measure the SAW velocity. It is an alternative to the $V(z)$ curve method. Its accuracy is smaller than that of the $V(z)$ curve technique, but it has the advantage of measuring the speed of SAWs on a small area. Yamanaka proposed using a cylindrical lens to investigate the anisotropic properties of solids. This idea was realized nearly a decade later [43].

A simple expression for the output signal for the time-resolved acoustic microscope can be obtained using a Fourier spectrum approach [103]. Let the defocus z be fixed and a short acoustic pulse $s_o(t)$ be emitted by the lens toward the sample, and $s(t, z)$ be the output signal to the input pulse. We suppose that the lens is aberration-free and that the pupil function is independent of

the frequency. Because of the linearity of the system, the spectrum of the output signal of the SAM $S(z, \omega) = \int_{-\infty}^{\infty} s(t, z) \exp(-i\omega t) dt$ is a product of the spectrum of the input pulse $S_o(\omega) = \int_{-\infty}^{\infty} s_o(t, z) \exp(-i\omega t) dt$ and the frequency response of the system $V(z, \omega)$; i.e.,

$$S(\omega, z) = S_o(\omega) V(z, \omega) \quad (4.14)$$

The shape of a typical pulse $s_o(t)$ and its Fourier spectrum can be seen in Figure 4.5. The second signal in Figure 4.5(b) is an electronic echo [48]. To get the time dependence of the output signal of the microscope $s(t, z)$ in response to the excitation pulse, we apply the inverse Fourier transform to the spectrum $S(\omega, z)$:

$$s(t, z) = \int_{-\infty}^{\infty} S_o(\omega) V(z, \omega) \exp(i\omega t) dt \quad (4.15)$$

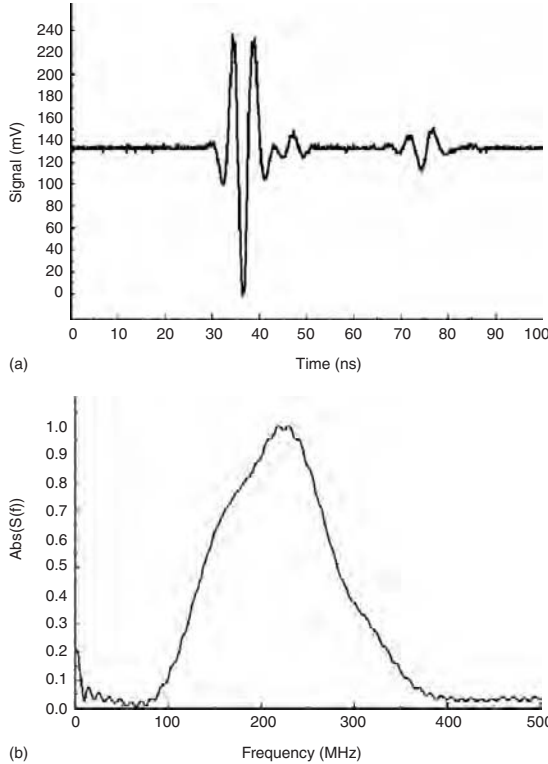


FIG. 4.5. (a) The input pulse $s_o(t)$ (echo from gold surface positioned at a focal plane of the lens: $z = 0$). (b) Absolute value of the Fourier spectrum of input pulse $S_o(2\pi f)$.

where a factor of $1/(2\pi)$ has been omitted. Taking into account properties of the Fourier transform, the output signal $s(t, z)$ can be presented in an alternative form:

$$s(t, z) = \int_{-\infty}^{\infty} s(\xi - t)v(z, \xi)d\xi \quad (4.16)$$

where $v(z, \xi)$ is the inverse Fourier transform of the frequency response function $V(z, \omega)$. Equation 4.16 has been used in numerous papers [69, 90]. The integral in Eq. 4.15 has, however, some advantages for numerical simulations.

To calculate the integral (in Eq. 4.15) numerically, the spectra $S_o(\omega)$ and $V(z, \omega)$ must be determined for both positive and negative frequencies. Since signals $s(t, z)$ and $s_o(t)$ are real functions of time, functions $S_o(\omega)$ and $S(\omega, z)$ must be Hermitian [15, p. 16]. Hence their real parts are even functions of frequency, and their imaginary parts are odd functions of frequency. This property can be succinctly written as $S_o(\omega) = S_o^*(-\omega)$ and $S(\omega, z) = S^*(-\omega, z)$, where the superscript $*$ denotes the complex conjugate. To extend $V(z, \omega)$ to the negative frequency range, we have to first extend the reflection coefficient into the negative frequency range. We recall that the reflection coefficient has been derived for an incident plane wave that has monochromatic time dependence $\exp(-i\omega t)$. Hence the phase of the reflection coefficient is just a phase shift for the plane wave due to reflection. Therefore,

$$R(-\omega, \theta) = |R(\omega, \theta)| \exp[-\arg |R(\omega, \theta)|] \quad (4.17)$$

$R(\theta, \omega)$, and $V(z, \omega)$ are necessarily Hermitian functions as well. In Eq. 4.17 \arg denotes the argument of a complex function. Using properties of Hermitian functions [84] and Eq. 4.8, we can rewrite Eq. 4.15 for LFAM:

$$s(t, z) = \int_0^{\theta_M} L^2(\theta)d\theta \operatorname{Re} \left\{ \int_0^{\infty} S_o(\omega)R(\theta, \omega) \exp \left[i\omega \left(t - \frac{2z}{v_W} \cos \theta \right) \right] d\omega \right\} \quad (4.18)$$

where Re denotes the real part, and a normalizing coefficient is omitted. The internal integral in Eq. 4.18 is the inverse Fourier transform of the function $S_o(\omega)R(\theta, \omega)$ where time is replaced by the expression $t - 2z/v_W \cos \theta$. For the acoustic microscope with the spherical lens, the term $\sin \theta$ should be included in the first integral in Eq. 4.18.

4.2.2.1 Ray Model and Quantitative Analysis of the Time-Resolved Signals. For a layered solid, the signal in time-resolved acoustic microscopy comprises a train of pulses (Fig. 4.6) that can be divided into two types: (a) pulses reflected specularly from the top and bottom surfaces of the layer [44] and (b) pulses generated by the leaky waves propagating along the liquid–solid interface [123]. In Figure 4.6 the pulse *C* is the pulse reflected from the liquid–crystal interface. If the focus of the lens is on the surface of

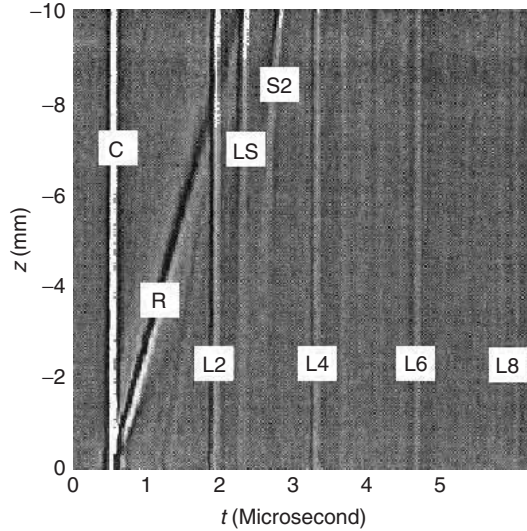


FIG. 4.6. Experimentally scanned wavefront $V(t)$ as a function of defocus distance z , plotted as two-dimensional $v(t, z)$ plot; C , R , L_2 , LS , and S_2 are the arrivals of different waves (from Hsu *et al.* [44]).

a crystal ($z = 0$), only the specularly reflected rays can reach the lens. The probing beam propagates within a specimen mainly as a longitudinal wave pulse. The delay time τ_L between the signal reflected from the front (C -signal) and the back (L_2 -signal) faces determines the value of the longitudinal sound velocity v_L in a specimen: $v_L = 2h\tau_L$. L_4 , L_6 , and L_8 are pulses arising because of multiple reflection of the longitudinal waves from the top and the bottom surface of the crystal. As defocus increases, part of the incident beam impinging obliquely on the specimen surface gives rise to transverse waves through mode conversion at the liquid–solid interface. This transverse wave reflects from the back face as a transverse wave (S_2 pulse) or a longitudinal wave (LS pulse) owing to mode conversion. A prominent feature in Figure 4.6 is the pulse R , the pulse associated with the GRW. The pulses coming from the top surface of the crystal in general have a complex structure [27]. In addition to the GRW, the signal may contain pulses associated with PSAW [44], LLW [123], and the edge waves (EW) [122]. As a rule, the signal generated by the lateral waves is weaker than that generated by the GRWs; however, the LLW signal can play a key role in the elastic characterization of fiber composite materials, where the rays from the surface wave lie beyond the aperture angle of the lens [102, 115]. The arrival time of the LLWs, the leaky Rayleigh waves, and the LSAWs can be estimated by the ray model [122]. The time

delay τ_{RW} between the C and RW signals is related to the Rayleigh wave velocity, v_{RW} , of the specimen and the sound velocity in the liquid, v_W , by $\tau_{RW} = 2z(1 - (1 - \sqrt{1 - (v_W/v_{RW})^2}))/v_W$ [118]. The trajectory of the edge wave is presented in Figure 4.1. The time delay τ_E between C and EW signals is dependent on the semiaperture angle of transducer θ_M and the defocused distance z : $\tau_E = 2z(1 - \cos \theta_M)/v_W$. It has been observed experimentally by Zhang *et al.* [122]. When a pulse reflected from the bottom surface of a layer has a similar shape to the pulse reflected from the top surface, the derivation of the time delay is a simple task [17]. For anisotropic layered solids and plates, the time of flight of different types of bulk waves can be evaluated using the geometrical acoustics approach [3, 102]. However, reflected pulses very often have a complicated shape. In such cases the elastic constants of the layer can be obtained by fitting the experimentally obtained $V(t)$ signal to the theoretical one [69]. The measurements conducted on fused quartz, Si(111), a z -cut sapphire, and steel by a time-resolved acoustic microscope showed that the error was less than 3% for all listed materials [118].

4.2.3 Theory of Two-Lens Acoustic Microscopy

The theoretical description of image formation in the pair lenses acoustic microscope working in the time-resolved mode is rather complicated. However, a simple analytical solution can be obtained for the two-lens system working in the reflection mode. It has been shown by Every and Briggs [28] that the surface Green's function can be used as a quantitative mean for simulating the angular and the time-resolved signal. They assumed that, for cylindrical lenses, the source lens delivers "concentrated line force of short duration normal to the surface of the solid and by reciprocity the receiver transducer measures the normal displacement at its focal line elsewhere on the surface at a later time t " [28]. Then the measured signal can be modeled by the elastodynamic Green's function G_{33} [28]

$$G_{33}(x_1, t > 0) \approx -\frac{i}{\pi|x_1|} \text{Im } \Psi(t/x_1, 0) \quad (4.19)$$

where the function $\Psi(s_1, s_2 = 0)$ where $s_i = k_i/\omega$, is derived as the superposition of three outgoing partial waves for the anisotropic half-space ($N = 3$) or of six for the anisotropic layer ($N = 6$):

$$\Psi(k_1, \omega) = \sum_{n=1}^N \frac{\text{adj } (B)_3^{(n)} U_3^{(n)}}{B} \quad (4.20)$$

B is the boundary condition matrix, $U_3^{(n)}$ are the x_3 components of the polarization vectors for the modes in the solid, and adj is the matrix adjoint. If

the distance x_1 between focal lines of the cylindrical lenses is known, then the Green's function (Eq. 4.19) gives a picture of the arrival time of different types of surface excitations. The Green's function approach reduces the simulation of the time-resolved signal obtained with a pair of line focus acoustic lenses techniques to a purely algebraic problem. The ray picture, describing the propagation of rays in the two-line focus lens system, is very similar to that of LFAM (Fig. 4.1), except that the two-line focus lens microscope does not use specular rays (ray CO¹C, Fig. 4.1), as LFAM does.

For the two-point-focus lenses technique, the output signal can also be expressed in terms of the Green's function approach. If one focus of the lens is considered as a point source of sound located on the surface and a focus of the receiving lens can be considered as a point receiver, the expression of the Green's function for a two-point lens configuration has the form

$$G_{33}(x_1, t > 0) \approx -\frac{i}{2\pi|x_1|} \frac{\partial}{\partial t} \text{Re} \int_{-\infty}^{\infty} ds_2 \Psi(s_1, s_2) \quad (4.21)$$

where x_1 is the distance between two focal points. The difference between the two-line-focus and the two-point-focus technique is that, in the case of the two-line-focus technique, the transmitter lens generates only surface waves in the x_2 direction, and the receiver lens detects only surface wave propagation in this direction. This system, therefore, can be used for measuring the phase velocity of that wave. Acoustic waves generated by a point source constitute a broad distribution of wavevectors, and, when the wavefront is sensed with a point detector, the group velocity is measured [100].

Simulations based on Eq. 4.21 and experimental time-resolved images obtained with the two-point-focus acoustic lens technique for the water-loaded Si(001) surface are presented in Figure 4.7. The simulated image is in very good agreement with the measured image. The intense GRW/PSAW band running across the upper half of the image matches up well with the corresponding observed band. A detailed description of the fine structure of images representing the propagation of the group velocity wavefront can be found in the monograph by Wolfe [114].

4.3 Elastic Properties of Anisotropic Layered Media by Acoustic Microscopy

The SAWs excited by acoustic microscopy are always leaky as water couples the surface of the sample to the transducer. The effect of water loading on the velocity of the SAWs is small ($\sim 0.05\%$) [97] and can be considered negligible compared to an expected experimental error in the measurement

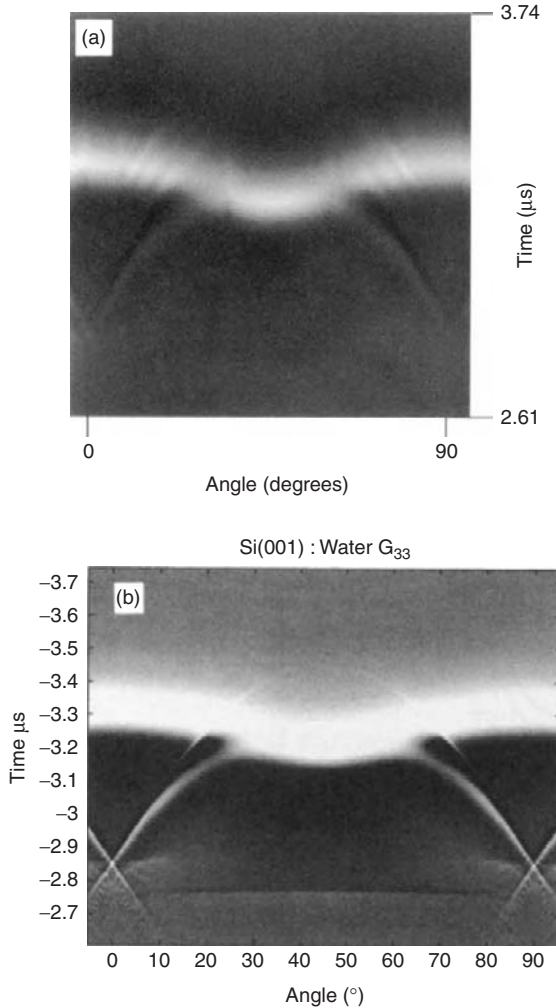


FIG. 4.7. Angle-time images for water loaded Si(001) with $x_1 = 16.13$ mm; (a) Image obtained by a two-point-focus lenses imaging system with short-pulse excitation (from Vines *et al.*, [99]). (b) Green's function simulation by Every *et al.* [29].

system and inversion procedure. The frequency and angular dispersions of SAWs, both with and without fluid loading, are qualitatively the same and the conclusions for the interpretation of the experiments are similar [1, 92]. In contrast to the SAW velocity, the SAW attenuation is significantly increased by the leakage into the liquid. Therefore, we will take into account water loading

for those situations in which the attenuation measurements are necessary. Most of the computations that follow have been performed without fluid loading using the Green's function approach.

The velocity and the attenuation of SAWs that propagate in an anisotropic multilayered media are calculated from the equations of motion and boundary conditions. One method, the modal approach, is described in a number of reviews [32, 33, 75, 82]. However, the velocity and/or attenuation obtained from the analysis of experimental signals, in some particular cases, differs from the intrinsic wave dispersion. In such cases simulations of experimental measurements are necessary [7, 126]. This involves calculating the $V(z)$ curve using Eq. 4.8 from the known elastic parameters of the materials and the known geometry of the lens. The speed and the attenuation are then obtained by the standard procedure for the $V(z)$ curve treatment [51]. This type of simulation, called the LFAM response, is the most rigorous, but it is time-consuming. In this chapter we will use the elastodynamic Green's function approach [124] to understand results obtained by LFAM. This approach has been developed to simulate response of surface Brillouin scattering (SBS) that measures surface acoustic waves excited thermally. Our experience shows that this approach is a very efficient tool in acoustic microscopy as well.

In LFAM, only the phase velocity of the SAWs propagating perpendicular to the focal line of the microscope or along axis x_3 , $\kappa = (k_1, 0)$ can be measured, \mathbf{k}_{\parallel} being the wavevector directed parallel to the surface. The imaginary part of the elastodynamic surface Green's function determines the power spectrum of the surface thermal fluctuation $\langle |U|^2 \rangle_{\omega}$ [23]

$$\langle |U(k_1, \omega)|^2 \rangle \approx \text{Im}[g_{33}(k_1, \omega)] \quad (4.22)$$

where $g_{33}(k_1, \omega)$ is the Fourier coefficient of the dynamic Green's tensor $G_{33}(x_1, t)$ [124] and can be expressed through function Ψ , Eq. 4.20:

$$g_{33}(k_1, \omega) = \frac{i}{\omega} \Psi(k_1, \omega) \quad (4.23)$$

The dispersion equation for SAWs describes the motion of the medium in the absence of the external forces and is conditioned by

$$\det[B] = 0 \quad (4.24)$$

In Green's function calculations the wavevector component k_1 is fixed and real and the power spectrum of the surface thermal fluctuation (Eq. 4.22) or imaginary part of the Green's function is calculated as a function of frequency $\text{Im}[g_{33}(\omega)]$. The true Rayleigh or Sezawa surface waves show up as an S -function singularity at ω_o , and the SAW velocity is given by ω_o/k_1 . A PSAW shows up as a resonance centered on frequency ω_{MAX} , and the velocity of the

PSAW is $v_{\text{SAW}}^P = \omega_{\text{MAX}}^P / k_1$. In contrast to the Green's function approach, in the modal approach a solution of the dispersion equation (Eq. 4.24) is sought for ω fixed. Roots of Eq. 4.24 located on the real axis k_1 correspond to the true Rayleigh and generalized Lamb surface waves, and the velocities obtained by solving the dispersion equation (Eq. 4.24) or by locating the maximum on the Green's function are identical. In contrast, the PSAW is an attenuating SAW, and the corresponding solution (pole) of the dispersion equation is complex [75]. The velocity of the PSAW is understood as the real part of the reciprocal of k_1 ($v_{\text{SAW}} = \text{Re}[\omega/k_1]$) for the pole and its attenuation by the imaginary part. For Green's function simulation, the PSAW is associated with a resonance of finite width. The higher the attenuation or the farther the pole from the real axis, the broader is the PSAW peak in the Green's function, and the higher the discrepancy between the modal and Green's function solutions for PSAW velocity. However, LFAM cannot detect highly damped PSAWs, and the differences between values of the velocities computed by modal and Green's function approaches are within experimental error in most cases [62].

Besides the fact that the Green's function approach provides a means to model the signal [28] in time-resolved LFAM, calculation of the dispersion curves using the Green's function approach has some advantages for conventional acoustic microscopy. In acoustic microscopy the surface waves are excited by the sound waves in the liquid. The driving force that causes the vibration of the liquid–solid interface arising from the pressure in the sound wave is normal to the interface. Therefore the g_{33} component of the Green's function exhibits resonance only for those surface modes that can be excited in acoustic microscopy. This facilitates the interpretation of LFAM.

The Green's function approach is of particular use for hard film characterization by LFAM. Pseudo surface waves propagating in hard films, such as Si_3N_4 or diamond films, transform after the transverse cutoff (frequency or thickness of the layer at which the velocity of the SAW reaches the velocity of the transverse wave in the substrate) into highly damped interfacial waves (IWs) [64]. The modal approach displays the IWs on that part of the dispersion curve where it cannot be detected by LFAM, whereas the SAW dispersion obtained from the Green's function simulation shows a gradual disappearance of this wave from the dispersion curve.

The Green's function approach better predicts the behavior of the SAW dispersion curve measured by LFAM near a transverse cutoff. The modal approach near the cutoff yields a discontinuity, which is proportional to the attenuation coefficient [81]. The dispersion curve measured near the cutoff by LFAM [129] is continuous, as was the dispersion calculated using Eq. 4.8 and the Green's function approach. For a dispersion curve featuring strong cutoff, the Green's function approach is particularly useful in treating the inverse problem, determining the elastic properties from experimental data.

The discontinuity of the SAW dispersion around cutoff makes fitting extremely difficult, and the calculation of the SAW dispersion using an integral presentation of the $V(z)$ curve (Eq. 4.8) with subsequent extraction of the SAW velocity is time-consuming. In this case the Green's function approach is a good compromise between the accuracy and the computing time. Moreover, the Green's function approach illuminates the character of the SAW modes. For example, Figure 4.8 displays the two-dimensional Green's function simulation (Eq. 4.22) for a diamondlike carbon (DLC) layer on the (001) plane of a silicon (Si) substrate. The elastic moduli of the isotropic DCL layer were taken from Chirita *et al.* [22]. The gray-scale image represents the calculated Green's function (Eq. 4.22) as a function of velocity v and angle from [100] direction on the (001) surface of Si. The two bulk wave solutions for symmetry directions, the pure transverse vertical or fast transverse wave (FTW) and the pure transverse horizontal or slow transverse wave (STW), are displayed in Figure 4.8 as solid and dotted lines, respectively. The position of the maximum in the image gives the velocity of the corresponding SAW. The thin, bright line depicts the behavior of the GRW, which propagates without attenuation at the vacuum–solid interface. As the SAW approaches STW cutoff, it veers to approach it. GRW becomes identical with STW in the [110] direction (45°). Beyond the cutoff is a PSAW, which can be considered as the continuation of SAW into the supersonic region. The peak associated with the PSAW is broad, attesting to high attenuation of the PSAW (except in the [110]

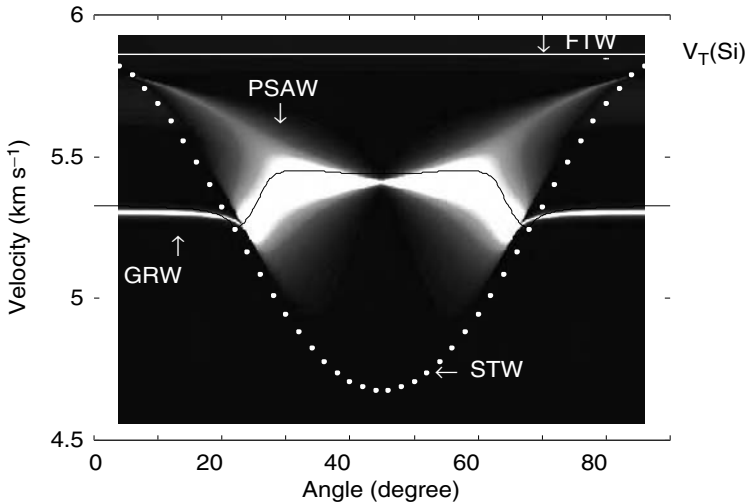


FIG. 4.8. Green's function simulation of the SAW dispersion for DCL layer ($kh = 0.5$) on the (001) plane of Si substrate; v_T (Si) is the transverse velocity in Si.

direction, i.e., 45° on the graph). In this direction the displacement of STW is parallel to the surface, and PSAW turns into a pure surface wave, which is evident from Figure 4.8. The black line traces the maximum of the Green function and hence displays the velocity of the PSAW. In the calculation of the Green function (4.22) at a solid–vacuum interface a small amount of artificial damping [28] is introduced to avoid a true singularity. Simulations of the angular dispersion curves presented here do not include water loading. In practice, all three approaches—the modal simulations (4.24), the response of the microscope (4.8), and the Green’s function approach (4.22) can be used to determine elastic properties from LFAM measurements. The Green’s function approach seems to be the more effective one for many purposes.

In determining the elastic properties of layered anisotropic solids, least-square fitting of the experimental SAW velocities to the theoretical SAW dispersion is usually performed. Here the error sum of squares over all number of experiments n_{exp} [26]

$$\text{ESS} = \sum_{i=1}^{n_{\text{exp}}} (v_{\text{calc}}^i - v_{\text{meas}}^i)^2 \quad (4.25)$$

is minimized with respect to the variation of the elastic constants of the layered solid. In Eq. 4.25 v_{meas}^i are measured values of the SAW velocity and v_{calc}^i are the corresponding theoretical values. Numerical algorithms [1, 49] are available for finding the minimum and variance of the error function (4.25) and thus obtaining the elastic parameters and their errors.

4.4 Acoustic Microscopy of Isotropic Layered Media

4.4.1 Isotropic Half-Space

The elastic properties of isotropic media are described by two elastic constants and density C_{11} , C_{44} , ρ . For isotropic solids the Rayleigh wave is slower than the transverse velocity v_T in the solid, and its velocity v_{RW} is confined inside the following range [98]: $0.87v_T < v_{\text{RW}} < 0.96v_T$. Therefore, measurement of the Rayleigh wave velocity gives a lower estimation of the transverse velocity ($v_T = \sqrt{C_{44}/\rho}$) of the solid, and hence an estimation of C_{44} . When the density is known, the elastic constants C_{11} and C_{44} can be determined if both the lateral longitudinal and the leaky Rayleigh wave velocities can be extracted from $V(z)$ measurements [17]. The longitudinal lateral wave propagates along the liquid–solid interface with a speed of the longitudinal velocity in the solid [16] ($v_L = \sqrt{C_{11}/\rho}$), and therefore its measurement gives the value of C_{11} . The constant C_{44} can then be derived

either from the dispersion equation [98]

$$4k^2qs - (k^2 + s^2)^2 - i \frac{\rho_W q k_T^4}{\rho q_W} = 0 \quad (4.26)$$

or from the approximate equation obtained by Viktorov [98]:

$$v_{RW} = v_T \frac{0.718 - \left(\frac{v_T}{v_L}\right)^2}{0.75 - \left(\frac{v_T}{v_L}\right)^2} \quad (4.27)$$

where ρ is the mass density of the solid, ρ_W is the mass density of liquid, $q = \sqrt{k^2 - k_L^2}$, $s = \sqrt{k^2 - k_T^2}$, $q_W = \sqrt{k_L^2 - k^2}$, and $k_j = \omega/v_j$ ($j = L, T, W$). Without water loading ($\rho_W \rightarrow 0$) Eq. 4.26 reduces to the Rayleigh wave equation, its root is real and corresponds to the true Rayleigh wave. A leaky Rayleigh wave propagating at a liquid–solid interface leaks energy into the fluid, and the corresponding solution of Eq. 4.26 is complex. There is a real root of Eq. 4.26. It corresponds to the Scholte wave, which propagates with a velocity lower than the velocity of sound in the liquid. The Scholte wave in the case of a homogeneous solid does not leak energy into the liquid, and hence it cannot be detected by acoustic microscopy. This is not true for spatially periodic solids, where Scholte-like waves have been detected by an imaging system consisting of a pair of cylindrical lenses [31]. SAW attenuation due to leaking into the liquid can be described by the approximate expression [25]

$$\alpha \lambda_W = \frac{\rho_W v_W^2}{\rho v_{SAW}^2} \quad (4.28)$$

where λ_W is the wavelength of sound in the liquid.

For hard materials the lateral longitudinal wave is very slightly slower than the bulk longitudinal wave [95]. To attain higher accuracy of the elastic constants determination of an isotropic solid from $V(z)$ curve measurements, Li and Achenbach [68] proposed using the following fitting procedure. First, the position and amplitude of the peaks corresponding to the leaky Rayleigh wave and the lateral longitudinal wave on the experimental $V(k)$ curve are determined. The values of the longitudinal and transverse velocities are then extracted by fitting the position and the amplitude of the Rayleigh and the lateral waves obtained experimentally to the theoretical ones. From the results presented by Li and Achenbach [68], it can be concluded that the error does not exceed 0.4% (the highest value obtained for aluminum) for the transverse velocity and 1.3% for the longitudinal velocity.

For very rigid materials such as ceramics, the high-frequency $V(z)$ curve technique does not work well. This is because acoustic microscopy yields $V(z)$ curves with only one maximum besides that from the specular reflection. Hirsekorn and Pangraz [42] proposed evaluating the SAW velocity of a rigid material from the distance between the interference maximum and the maximum of the specular reflection of measured $V(z)$ curves. The disadvantage of this technique is that all the parameters of the acoustic microscope lens need to be known to compute the elastic properties. To overcome this problem, Weglein [107] introduced an empirical formula that relates the distance between the first interference maximum and the specular reflection peak in the $V(z)$ curve. Ghosh *et al.* [34] proposed an alternative method that does not require the knowledge of lens properties for determining SAW velocity. In their method the SAW speed is measured from the first dips of the $V(z)$ and $V(f)$ curves of the lens [34].

If a sample is thick enough that it is possible to separate signals reflected from the top and the bottom of the sample, then time-resolved acoustic microscopy can be used. If the thickness and density of the sample are known, then the shear and longitudinal velocities can be found, as described by Levin *et al.* [66]. In that reference an ultrashort ultrasonic pulse of 30-ns duration was used to measure the elastic constants of a small amount of superhard amorphous carbon synthesized from C_{60} under high pressure (13 GPa) and high temperature (1600–1900 K).

In some cases the thickness of a sample is unknown and only the longitudinal reflected wave can be detected by time-resolved acoustic microscopy. In these cases the velocity of the longitudinal wave in the layer can be obtained by measuring two echo signals: when the lens is focused (a) on the front of the thin sample and (b) on the back of the sample. Geometrical considerations concerning longitudinal wave measurements are discussed by Hanel [39].

4.4.2 Slow Film on Fast Substrate

SAW dispersion for a thin layer on a substrate, as measured by SAM, is very much affected by the type of layer under investigation. For SAWs propagating in the interface between a solid isotropic layer on a solid isotropic substrate, the dispersion equation can be written in an analytical form [14]. Elastic media consisting of a single layer on a substrate are commonly divided within two classes: loading layer or slow-on-fast system, and stiffening layer or fast-on-slow system. A layer is said to stiffen the substrate when its presence, at whatever thickness, increases the velocity of the surface wave above that of the Rayleigh velocity of the substrate and is said to load the substrate if it decreases the Rayleigh velocity [33]. Farnell and Adler [33] found that sufficient conditions for the layer to be loading and stiffening are $\hat{v}_T < \sqrt{2}v_T$ and $\hat{v}_T > \sqrt{2}v_T$, respectively, where v_T is the transverse velocity in the substrate

and \hat{v}_T in that layer. The behaviors of SAWs propagating in loading and stiffening layers are different [61], and therefore we describe the basic features of LFAM measurements for these two systems in some detail. Moreover, it will be shown later that the methods for the inversion of dispersion data used for isotropic layered media can also be applied to the elastic characterization of anisotropic layered solids.

Loading layers have been widely studied with regard to surface wave propagation. As a fairly typical example, the behavior of gold (Au) on fused quartz (Qtz) is discussed here. The two-dimensional Green's function simulation for this system is shown in Figure 4.9. For this and subsequent calculations, unless otherwise specified, all elastic constants have been taken from Briggs [17]. For the loading case, an infinite sequence of surface waves, or generalized Lamb waves, comes into existence with increasing layer thickness [10]. Two types of modes can be distinguished: those with Rayleigh-type behavior, i.e., consisting of coupled shear vertical and longitudinal components, and Love-type modes, which have solely shear-horizontal displacements. The latter do not couple with the fluid and hence are not observed in the acoustic microscope. The lowest velocity mode, depicted in Figure 4.9, is the generalized Rayleigh wave. It starts from the Rayleigh wave velocity of the substrate and with increasing layer thickness approaches asymptotically the Rayleigh wave velocity of the layer. Without liquid loading, GRW is the true SAW because its velocity is below transverse velocity in the substrate for all possible values of the layer thickness (Fig. 4.9). All the additional Lamb modes are leaky waves as the

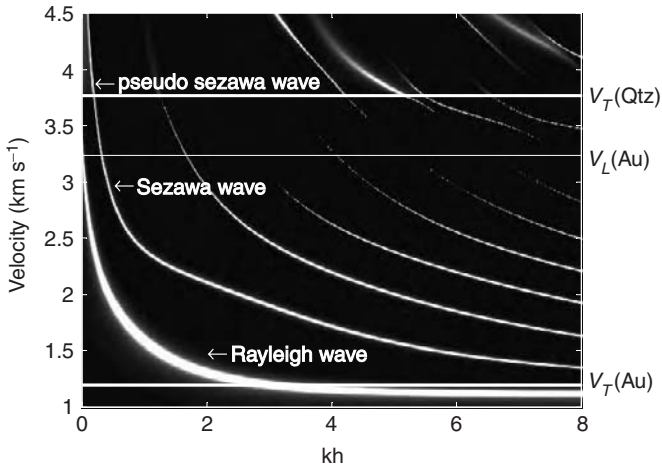


FIG. 4.9. Green's function simulation of the SAW dispersion for gold film on fused quartz.

thickness of the layer approaches zero ($kh \rightarrow 0$). The first additional mode, called a pseudo-Sezawa wave before the critical value of kh (the cutoff), leaks energy in the substrate because its velocity is higher than the shear velocity of the substrate. It is called a Sezawa wave past the cutoff, where it no longer loses energy into the substrate. The Sezawa wave is mainly located in the layer, decaying exponentially in the substrate. As the thickness increases, the behavior of the Sezawa wave depends on the relative material parameters of the layer and substrate [10]. If \hat{v}_T and v_T are appreciably different, this mode approaches a shear wave in the layer when $kh \rightarrow \infty$. However, the Sezawa wave may be transformed into a Stoneley wave as the thickness of the layer increases. The Stoneley wave is a true interfacial wave localized at the interface between layer and substrate. Such a transformation occurs for certain special combinations of material parameters, and when $\hat{v}_T \approx v_T$ [33]. For some materials all higher generalized Lamb waves degenerate into transverse waves in the layer when $kh \rightarrow \infty$.

The Sezawa and pseudo-Sezawa modes are commonly used in acoustic microscopy for extracting the elastic properties of slow-on-fast elastic systems [11, 53]. Kushibiki and colleagues determined three parameters (ρ , C_{44} , h) out of four (ρ , C_{11} , C_{44} , h) of gold films on fused quartz from LFAM measurements in the first Sezawa/pseudo-Sezawa mode. Their measured frequency dependences [53] for velocity and attenuation of SAWs are shown in Figure 4.10. The theoretical attenuation curve (Fig. 4.10) indicates that the two modes can be distinguished. The position of the cutoff was used to determine the thickness of the gold layer, and then the elastic constant C_{44} and density were obtained by computer fitting the dispersion curve. The dispersion curve

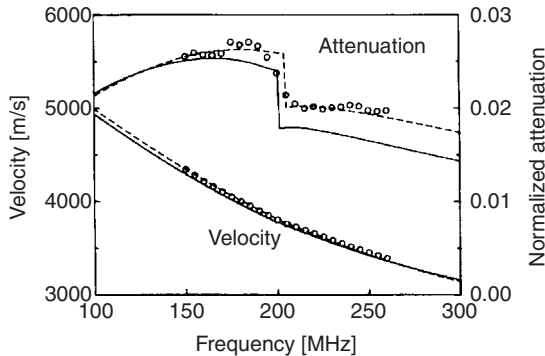


FIG. 4.10. Frequency dependence of measured and calculated propagation characteristics of leaky Sezawa/pseudo-Sezawa wave mode for a gold film on fused quartz substrate. The solid lines are calculated with the bulk constants of gold, and the dotted lines are computer-fitted (from Kushibiki *et al.* [53]).

of the Sezawa mode was found to be insensitive to the variation of the value of the longitudinal velocity in the film. The convergence of the inversion procedure for Sezawa waves has been considered in Behrend *et al.* [11].

Surface waves probe a sample within a depth of about one wavelength, and the higher the frequency the thinner the probed layer. For typical materials, the wavelength can be varied from about 15 μm at 200 MHz to 3 μm at 1 GHz. Acoustic microscopy operating at a frequency of 225 MHz enables characterization of TiN film on MgO substrate between 0.1 and 3 μm [1]. A theoretical estimation made by Yu and Boseck [120, 121] gave layer-thickness accuracy of 5 to 40 nm for an acoustic microscope operating at 1 GHz. However, such an accuracy has not been achieved in experiments because of the high attenuation of sound in liquid at 1 GHz [61].

4.4.3 Fast Film on Slow Substrate

For a fast layer on slow substrate, only one surface wave exists for small thickness of the film ($kh \rightarrow 0$). Generalized Lamb waves appear only at large kh , and they are always highly damped because their velocities are always higher than the transverse velocity in the substrate. Calculations of the dispersion of SAWs in stiffening systems [64] have revealed two types of SAW dispersion for the fast-on-slow system. It was shown that the SAW velocity initially grows with increasing kh . At a critical value kh_{cut} the SAW meets and degenerates with the bulk wave continuum. Beyond this cutoff, while true SAW no longer exists, there is a PSAW, which radiates energy into the substrate and as a result attenuates with distance as it travels along the surface. The attenuation reaches a maximum slightly beyond kh_{cut} and then subsides, either tending toward zero or leveling off at a finite value, depending on the conditions [64]. The first type of behavior comes about when the elastic properties of the layer and the substrate are not very different, and the velocity of the PSAW beyond cutoff increases up to the Rayleigh wave velocity of the layer, while the attenuation of this wave tends asymptotically to zero. This type of behavior is called the nonsplitting type. The second type of behavior, called the splitting type [64], arises when the elastic properties of the two materials are quite dissimilar and the PSAW evolves into a strongly attenuated interfacial mode, while a second mode appears at a higher velocity and transforms into the Rayleigh wave at the free surface of the layer. The acoustic microscope cannot detect the interfacial waves, since they do not couple with the top surface of the layer. This type of wave has been detected at the interface of transparent Si_3N_4 film on GaAs by surface Brillouin scattering (SBS) [128].

Figure 4.11 shows the Green's function representation of the SAW dispersion curve of an oxide layer on aluminum (nonsplitting type). Without water loading (Fig. 4.10), the position of the cutoff can be defined precisely, being the point on the dispersion curve at which the attenuation starts to grow (where

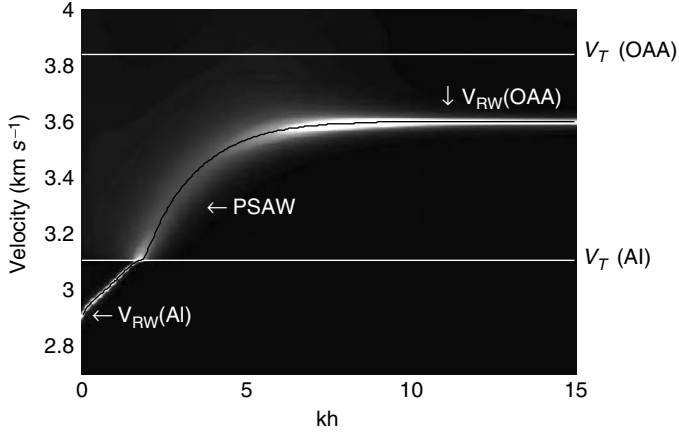


FIG. 4.11. Green's function simulation of the SAW dispersion for oxalic acid anodizing (OAA) film on aluminum (Al). The elastic moduli of the OAA film were taken from Zinin *et al.* [126].

the peak broadens). In contrast to the vacuum-oxide-aluminum system, for water loading (Fig. 4.12[a]) the position of the cutoff point is not defined as clearly as in Figure 4.11. Since the wave leaks energy into the water at all frequencies, there is no longer a sudden change from a nonattenuating wave to an attenuating wave. In contrast to the slow-on-fast system, where only small changes occur [53], for the fast-on-slow system the attenuation exhibits anomalous behavior [126]: it decreases as the velocity approaches the cutoff and sharply increases just above it (Fig. 4.12[b]). This thickness is termed the cutoff thickness for the case of water loading. Nayfeh and Chimenti [83] estimated the thickness at which the cutoff occurs using a thin layer approximation:

$$h_{\text{cut}} = \left(\frac{v_T}{2\pi f} \right) \frac{\left(\frac{\hat{\rho}}{\rho} \right)}{\left[\left(\frac{\hat{v}_T}{v_T} \right)^2 - 1 \right] + \sqrt{1 - \left(\frac{v_T}{v_L} \right)^2}} \quad (4.29)$$

The anomalous behavior of the attenuation near cutoff was used to determine the density of an oxide layer on aluminum [125] and a chromium (Cr) layer on steel [127]. The LFAM measurements performed for a Cr layer on steel between 100 and 260 MHz showed that this method yields an uncertainty in the density determination of 3%. The dispersion curve is sensitive to the value of the shear velocity of the layer (with error of 0.3%) and is

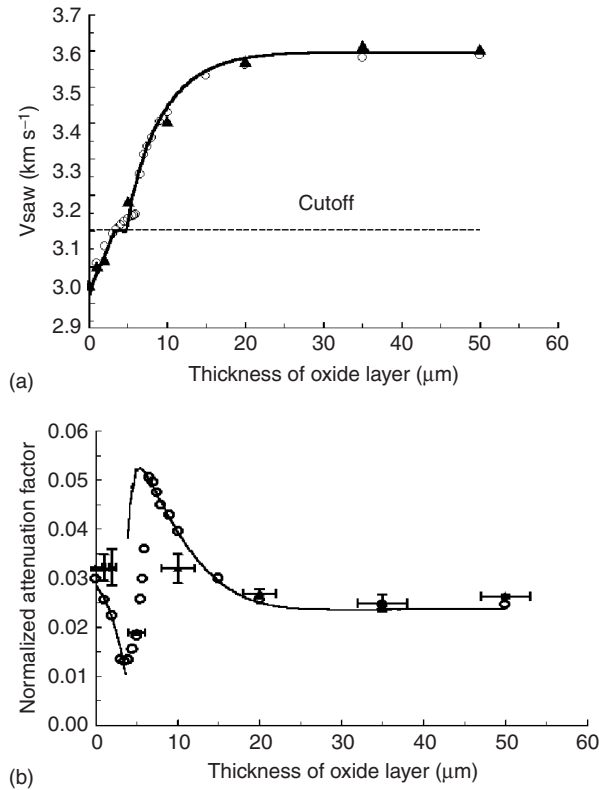


FIG. 4.12. (a) Dispersion of LSAW for a porous oxide film (OAA) on aluminum. Filled triangles are measurements made by a cylindrical lens at 225 MHz. The solid line is the theoretical prediction. Empty circles were obtained by calculating theoretical $V(z)$ curves. (b) Attenuation of LSAW for porous oxide film on aluminum (from Zinin *et al.* [126]).

less sensitive to the velocity of the longitudinal wave (with error of 1.5%). Experimental data showed that acoustic microscopy operating at a frequency of 225 MHz enables the characterization of a stiffening layer between 1 and 50 μm [63, 126].

Measuring the elastic constants of the fast layer can be sufficiently simplified if the lateral wave can be detected by LFAM. Comparing the experimental and theoretical $V(k)$ curves, velocities of the shear and longitudinal waves were determined by Li and Achenbach [68] for titanium film on aluminum. The accuracies of the leaky Rayleigh wave velocity and for LLW determination were found to be 0.5% and 2.3%, respectively.

4.5 Acoustic Microscopy of Anisotropic Solids

Since the standard $V(z)$ technique is not very effective for detecting more than two surface modes, measuring elastic constants by SAM is essentially limited to materials with high elastic symmetry, namely, isotropic, cubic, and hexagonal. Isotropy has been treated earlier. Now we consider the acoustic microscopy of anisotropic layered media of cubic symmetry.

4.5.1 Cubic Symmetry

The invention of the LFAM made it possible to measure the phase velocity of LSAWs as a function of the wave propagation direction in the surface of an anisotropic solid [56], and its application to the characterization of the elastic properties of cubic crystals has been very successful [1]. The behavior of the SAW angular dispersion on a cubic crystal surface is the subject of numerous studies, and its description can be found elsewhere [27, 32]. The acoustic microscope is able to detect only those waves that couple to the transmission liquid, and this fact has to be taken into account in theoretical modeling. A comprehensive analysis of the application of acoustic microscopy for detecting different types of waves propagating on the principal cubic crystal cuts has been reported by Every and Briggs [28]. For cubic crystals, the elastic properties are determined by three elastic constants: C_{11} , C_{12} , and C_{44} and the behavior of the angular dispersion curve, and hence the strategy in LFAM measurements is determined largely by the anisotropy coefficient $\eta = 2C_{44}/(C_{11} - C_{12})$. Consider the (001) surface [17, 30]; if $\eta < 1$, V_{SAW} does not change considerably with the angle and does not degenerate with the bulk STW mode in any direction. It leads to a small variation in the Rayleigh wave velocity with propagation direction. In this case, the (001) plane is not very useful for the LFAM characterization of the anisotropic elastic properties. For $\eta > 1$, as it is for silicon (Si), for example, the angular variation of the SAW, and the PSAW which exists in a certain angular range, provides an opportunity for determining all the elastic constants of a crystal by LFAM. A Green's function simulation of the SAW behavior on the Si (001) surface is presented in Figure 4.13. Comparing the behavior of the GRW and PSAW in Si (Fig. 4.13) and that of DLC film on Si, we see that, though they are qualitatively similar, PSAW on a pure Si surface is considerably less attenuating than with the stiff DCL film. The main features of the SAW dispersion on the Si (001) surface can be observed by a line-focus time-resolved acoustic microscope (Fig. 4.13) [43]. Hsu *et al.* [43] provide a simple algorithm for transforming this wave arrival picture into the wave velocity (V_{SAW} , β) (Fig. 4.14). Using a ray theory model, they show that the velocity of the surface wave V_{SAW} , arriving at time t with respect to t_D , the

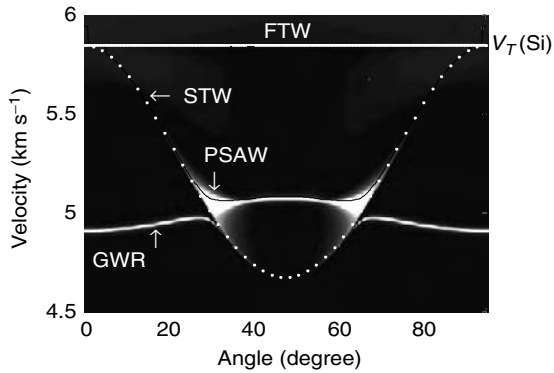


FIG. 4.13. Green's function simulation of the angular SAW dispersion on the (001) plane of Si.

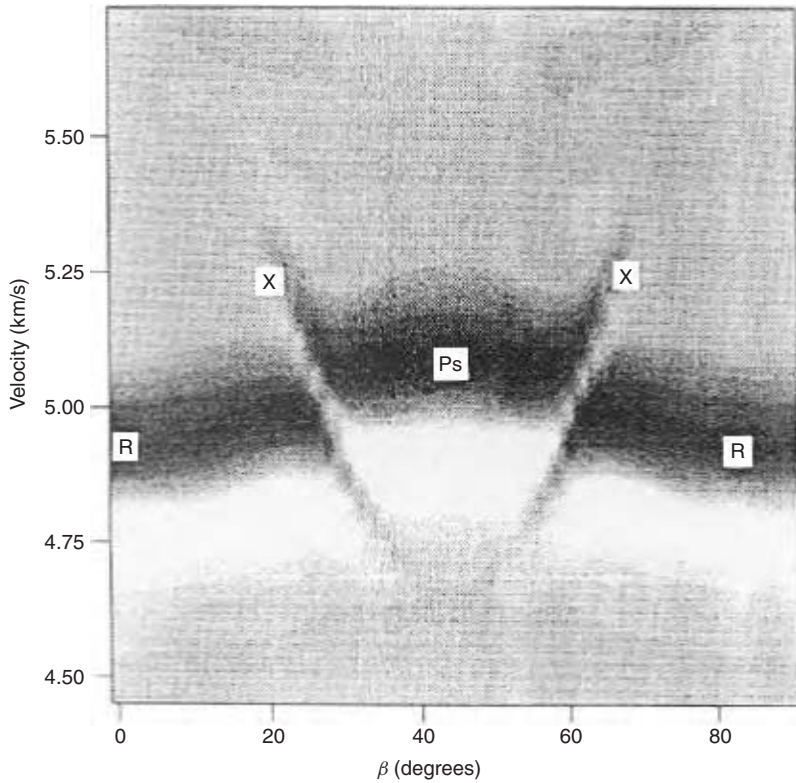


FIG. 4.14. Gray-scale plot of velocity versus orientation on the (001) silicon crystal plane (from Hsu *et al.* [43]).

arrival time of the direct reflected wave, may be written as [43, 117]

$$v_{\text{SAW}} = \frac{v_W}{\sqrt{1 - \left(1 - v_W \frac{t - t_D}{2z}\right)^2}} \quad (4.30)$$

A comparison of the experimental data with theoretical prediction reveals remarkable agreement, particularly near the FT cutoff. Equations 4.19, 4.22, and 4.30 show a deep internal relationship between the dispersion curve computed with the Green's function approach and the time-resolved signal in LFAM.

A detailed description of SAW measurements by LFAM on the (100) surface of Si has been published elsewhere [1, 69]. These studies demonstrated that the ratios of the elastic constants to the mass density (C_{11}/ρ , C_{44}/ρ , C_{12}/ρ) of cubic Si can be determined from the measured SAW angular dispersion, using a preliminary estimated value of the density ρ [60]. The mass density has subsequently been determined using the measurements of the attenuation of LSAWs in the crystal symmetry directions. Constants extracted from LFAM measurements on Si (001) are accurate to within 0.3% for the mass density, 0.8% for C_{11} , 0.3% for C_{12} , and 0.9% for C_{44} [60]. Lee *et al.* [60] conducted a numerical simulation to determine the sensitivity of the SAW velocity to each elastic constant variation. The elastic constants C_{11} and C_{44} are found to have more influence on the SAW velocity than C_{12} . The comparative accuracy of the elastic constants obtained by the conventional LFAM technique and those measured by time-resolved LFAM is described in Li and Achenbach [69].

As is the case for an isotropic solid, the conventional $V(z)$ technique with spherical lens cannot on its own yield all the elastic constants because only one interference maximum appears on the $V(z)$ curve. To use LFAM to characterize high-velocity anisotropic materials, Tourlog *et al.* [94] proposed a modification of the technique developed by Hirsekorn and Pangraz [42]. To extract the elastic constants from LFAM measurements, the distances between the specular reflection peak and the first interference maximum and the minimum of the $V(z)$ curve were measured by LFAM. Then the measured distances were compared to the corresponding distances obtained from the $V(z)$ simulations. Three elastic constants, C_{11} , C_{12} , and C_{44} , of a single-crystal diamond sample were determined by this method [94].

For measuring the elastic properties of a single crystal with symmetry higher than cubic, the two-lens technique seems to be promising. The first step in determining the elastic moduli by the ultrasonic flux imaging technique has been done, however, on a cubic crystal by Wurz *et al.* [116]. The image obtained on cubic gallium arsenide (GaAs) is quite distinct from the images

measured by conventional acoustic microscopy (Fig. 4.13) because it shows the interference between bulk waves propagating inside crystal. To get elastic moduli of the crystal, Wurz *et al.* [116] conducted three-dimensional fitting between experimental and theoretical images. The standard deviation amounted to 0.76%, 1.58%, and 0.54% for C_{11} , C_{12} , and C_{44} , respectively.

Most of the measurements made by LFAM and other microscopic configurations have been done on cubic crystals with the anisotropy coefficient $\eta > 1$. Various metals and semiconductors have been investigated, including nickel [88], MgO [60], gadolinium garnet [50], etc. Other than [001] planes of cubic crystals have not been used for the elastic characterization of single crystals by LFAM, though it has been shown that the velocity of the leaky Rayleigh wave [52] and PSAW on Si(111) can be detected by LFAM with high accuracy [46, 92]. Figure 4.15 displays an anisotropic dependence of the measured SAW velocities on propagation direction for a TiN/(V_{0.3}Nb_{0.7})N (111) superlattice film grown on the (111) plane of a MgO substrate. For cubic crystals having the anisotropy coefficient $\eta < 1$, the (110) and (111) crystal cuts are preferable for elastic characterization by LFAM. The numerical simulations presented in Every and Briggs [28] demonstrated a strong angular dependence

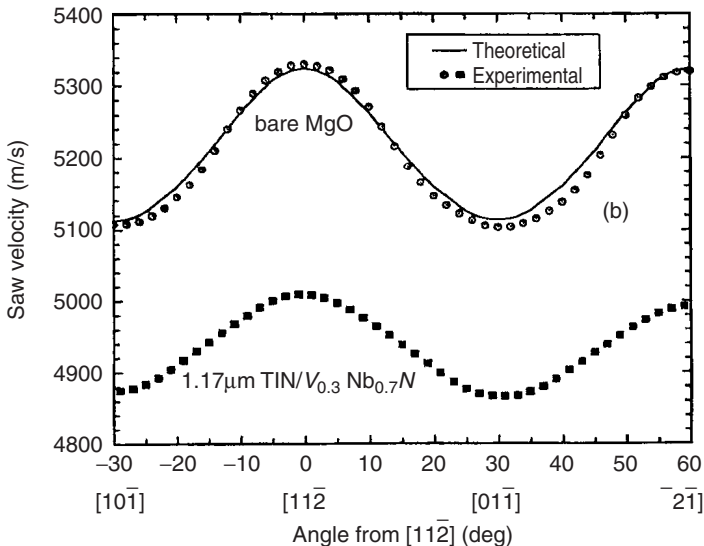


FIG. 4.15. Anisotropic dependence of the SAW velocity measured at 225 MHz for the (111) plane of a TiN/V_{0.3}Nb_{0.7}N superlattice on a MgO substrate and for the MgO substrate alone. The symbols are measured data and the line is theory (from Kim *et al.* [46]).

of leaky Rayleigh waves and PSAWs on the (110) and (111) crystal planes, which can be used for measurements of elastic constants.

4.5.2 Layered Cubic Media

4.5.2.1 Slow Layer on Fast Substrate. The elastic properties of anisotropic layered solids can be investigated either by measuring the frequency or the angular dispersion curves by LFAM. Experimental data for an amorphous carbon film on the (001) plane of Si are presented in Figure 4.16. The transverse velocity of the amorphous carbon film was measured by Kim and Achenbach [45]. The amorphous carbon layer can be considered a loading layer since its transverse velocity \bar{v}_T is lower than the velocity of STW for all directions on (001) Si. The numerical simulations show that, as frequency or thickness of the layer increases, the angular dispersion curve moves downward and the angular range in which the PSAW exists becomes smaller. At a certain film thickness, the velocity of the PSAW in [110] direction reaches the STW cutoff (see Fig. 4.16). For greater thickness the SAW dispersion curve remains below the STW cutoff and the surface waves are true SAWs

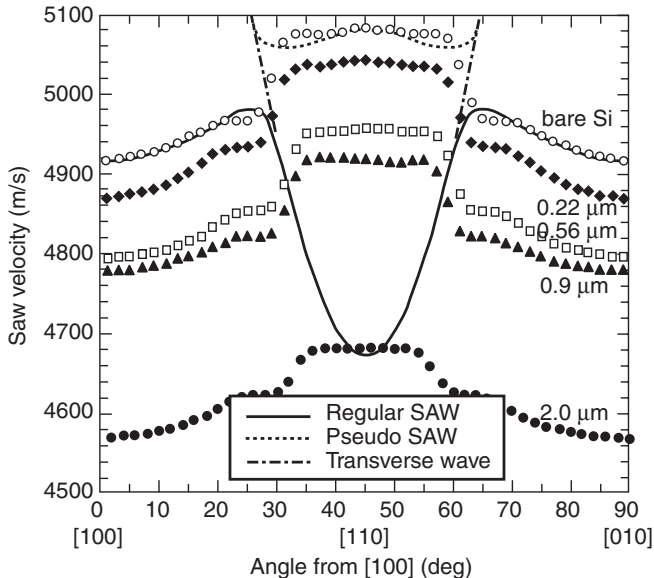


FIG. 4.16. Anisotropic dependence of the SAW velocity measured at 225 MHz for 0.22-, 0.56-, 0.9-, and 2.0- μm amorphous carbon films grown on the (001) plane of Si substrates and for bare Si. Lines show the calculated results for bare Si (from Kim and Achenbach [45]).

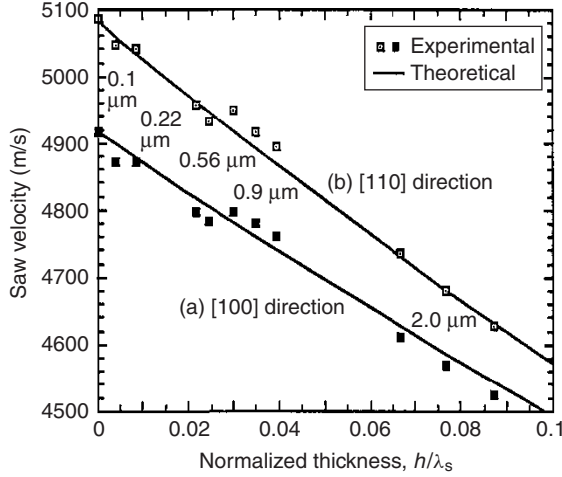


FIG. 4.17. SAW dispersion curves for amorphous carbon films grown on the (001) plane of Si substrates: (a) along the [100] direction and (b) along the [110] direction. The squares are the experimental results. The measurements were carried out for 0.1- and 0.22- μm films at 225 MHz, for 0.56- μm films at 195 and 255 MHz, and for 0.9- and 2.0- μm film at 195, 225, and 255 MHz. Lines show the calculated dispersion curves (from Kim and Achenbach [45]).

in all directions in the absence of water loading (Fig. 4.16). To determine C_{11} and C_{44} of the isotropic amorphous carbon film on the (001) surface of Si, Kim and Achenbach [45] proposed fitting simultaneously the frequency SAW dispersion (SAW as a function of kh) in the [100] and [110] directions of the Si substrate. Figure 4.17 shows the frequency dispersion curves for amorphous carbon films along the [100] and [110] direction of the (001) plane of the Si substrate. The experimental points were taken from the angular dispersion curves measured for different film thicknesses. Lee *et al.* [59, 60] used the angular dispersion curves to determine the elastic moduli (C_{11} , C_{44}) of an isotropic Nb_2O_5 film, C_{11} , C_{12} , C_{44} of cubic titanium nitride (TiN), and cubic vanadium nitride (VN) deposited on the (001) plane of cubic MgO. The elastic constants C_{11} and C_{44} obtained by fitting the angular dispersion curve [59] showed deviations of less than 5% from those reported in Kim *et al.* [47] and Kim and Achenbach [45], where fitting the frequency dispersion curve done in two directions was used. The elastic constant C_{12} showed a large error (more than 10%), which was attributed to the lower sensitivity of the SAW velocity to C_{12} . Kim *et al.* [46] have obtained the elastic properties of transition-metal nitride superlattice films from LFAM measurements. The elastic constants of TiN/NbN and TiN/VN layers on (001) MgO substrate have been determined

by fitting the SAW frequency dispersion curve. Those constants were then used to compute the elastic properties of superlattices.

4.5.2.2 Fast Layer on Slow Substrate. A stiffening layer, in contrast to the loading layer, moves the angular SAW dispersion curve up as the thickness of the layer increases; this has been demonstrated experimentally by Weglein and Kim [108]. Their measurements of the angular SAW dispersion of stiff diamondlike films on (100) Si have been done only for layers that have a SAW velocity lower than the FTW cutoff but greater than the [110] STW cutoff. The shapes of the SAW/PSAW dispersion curves in this case are similar to the SAW dispersion of bare silicon. The numerical simulations (see Fig. 4.8), however, show that the attenuation of the PSAWs increases significantly as the thickness of the layer increases. We note that for the [110] direction (45° in Fig. 4.8) the attenuation of the SAW does not increase because in this direction on grounds of symmetry it is a pure SAW uncoupled from the bulk modes. The directions [100] and [110] on the (001) plane of the cubic substrate are the preferred measuring directions. The behavior of the SAW frequency dispersion curves for a fast isotropic layer on a slow anisotropic substrate is similar to that of the isotropic case, and it has been discussed elsewhere [76, 128].

4.5.3 Solids with Hexagonal and Lower Symmetries

The stiffness matrix of anisotropic solids of hexagonal symmetry contains five independent elastic moduli, and it is a nontrivial matter to determine all five constants from conventional LFAM measurements. LFAM measurements of the angular SAW dispersion on the (10 $\bar{1}$ 0) plane of hexagonal single crystals of fluorapatite and hydroxyapatite have been reported in Sklar *et al.* [91]. It was found that, despite good fit of the experimental data to theoretical predictions, only one of the five elastic constants C_{44} , was accurately determined, which was a “consequence of measuring in only one plane of symmetry” [91]. Two elastic constants and the density of the porous oxide layers with the hexagonal symmetry have been measured by conventional LFAM technique in Zinin *et al.* [125].

Theoretical predictions [28] and experimental studies, [102, 115] show that the combination of LFAM and time-resolved microscopy provides a means for investigating the anisotropy of fiber composites. With the x_1 axis directed along the fiber, the elastic properties of the anisotropic media can be described by five elastic constants (hexagonal symmetry): C_{11} , C_{12} , C_{22} , C_{23} , and C_{55} . Wolfe and Vines [115] have employed an imaging system consisting of a pair of cylindrical or point focus lenses to the study of various anisotropic materials, including fiber composites, superlattices, and phononic lattices [31, 101]. The fiber composite images display complex structures associated with lateral waves.

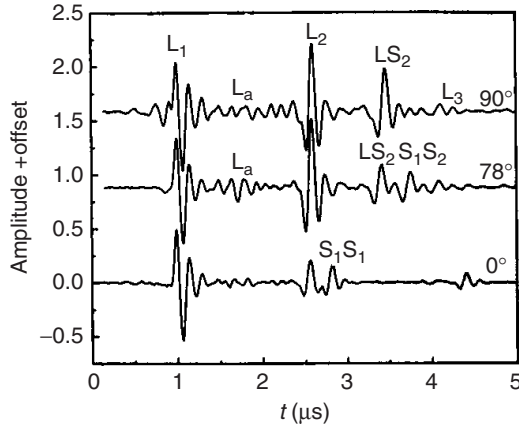


FIG. 4.18. Reflection signals at different rotation angles (from Wang [102]).

Wang [102] investigated an epoxy-graphite fiber composite plate by time-resolved LFAM and demonstrated that four out of five elastic constants can be measured from the time delay of the lateral waves. It has also been found that all five constants could be determined by monitoring the angular dispersion of lateral waves as well as bulk waves reflected from the bottom surface of the plate. Figure 4.18 shows experimental results at different rotation angles with respect to the x_1 axis. L_1 and L_2 stand for the waves reflected specularly from the top and bottom of the plate; LS_2 , S_1S_1 , and S_1S_2 denote other bulk waves reflected from the bottom and undergoing mode conversion, L_a stands for the longitudinal lateral waves, S_1 stands for the FTW, and S_2 stands for the STW wave. Only the longitudinal lateral wave has been detected because only its critical angle was inside the semiaperture angle of the line focus lens. The longitudinal velocity in the direction normal to the fiber is determined by measuring the time delay between the L_1 and L_2 pulses. The remaining four constants have been determined by estimating the time of flight of the LS_2 , S_1S_2 mode sequence at different rotation angles of the plate.

The SAW angular dispersion of anisotropic solids with symmetry lower than hexagonal has been measured by several authors [54, 57, 59]. The first LFAM measurements conducted on the Y -cut of trigonal lithium niobate (LiNbO_3) demonstrated good agreement between the theoretical angular measurements by LFAM [57]. Recently LFAM was used to determine the relationship of the LSAW velocities to the chemical composition ratios of Mg/Li/Nb , densities, and lattice constants of MgO -doped LiNbO_3 [54]. It was shown that the LSAW velocities increase linearly with an increase of the dopant concentration for all the surfaces and all the propagation directions. The authors [54] concluded

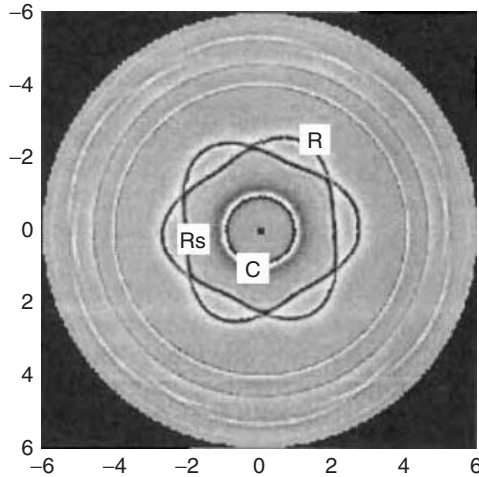


FIG. 4.19. Polar plot of experimentally scanned wavefront $V(t)$ as a function of the transducer alignment meridian angle, for a Z-cut quartz plate at a defocus distance of 11.5 mm. The radial coordinate is time in microsecond; C , R , and R_s , are center-reflected, surface, and pseudo-surface waves (from Hsu *et al.* [44]).

that the application of the LFAM technique provides a means of analyzing and evaluating the spatial variation of chemical compositions and the density of single crystals. Hsu *et al.* [44] and Xiang *et al.* [117] measured the PSAW and the SAW velocities on a Z-cut trigonal crystal quartz by time-resolved LFAM. Figure 4.19 shows their waveform $V(t)$ as a function of angle. The sixfold symmetric figure displays the Rayleigh wave and the PSAW arrival. The line C represents the reflection from the front surface of the plate. The other three rings represent the reflection of bulk waves from the bottom of the plate (see Fig. 4.19). The ability of time-resolved LFAM to detect such a variety of waves provides hope for the future of acoustic microscopy investigations of anisotropic layered solids of a low symmetry.

4.6 Nonplanar Surfaces

Basic research in acoustic microscopy has covered a huge span in the characterization of anisotropic solids. However, in most instances, nondestructive measurements require simple specimen geometry to successfully determine a specific elastic property. Therefore, an important technological barrier is the measurement of the elastic property of systems of complex geometries. An acoustic microscope with a point focus lens is an ideal tool

for characterizing samples with complex shapes. The basic features of nonflat specimen characterization can be understood by considering simple-shaped bodies such as a sphere or a cylinder. Weglein [106] pioneered the field by measuring $V(z)$ curves of spherical steel balls. Later the ray model of the $V(z)$ curve formation on a spherical surface was considered by Hadjoub *et al.* [38], and a wave theory was developed by Maslov *et al.* [78]. The phase difference between central rays and SAW rays for convex surfaces was found to be [38]

$$\Delta\varphi = \frac{4\pi f}{v_{\text{SAW}}} \left\{ \frac{a \sin \theta_{\text{SAW}}}{\cos \left[1 - \frac{(a \sin \theta_{\text{SAW}} - \Delta\varphi_a)^2 - z^2}{2a(a-z)} \right]} - a \cos \theta_{\text{SAW}} + \Delta\varphi_a + z \right\}$$

$$\Delta\varphi_a = (a^2 \cos^2 \theta_{\text{SAW}} + z^2 - 2az)^{1/2} \quad (4.31)$$

where a is the radius of the sphere. The expression for the $V(z)$ curve of the curved surface is more complicated than that of planar surfaces (Eq. 4.10). Moreover, the distance between dips depends on the defocus z . It makes it difficult to apply Kushibiki's technique to the $V(z)$ curve measured on spheres. To overcome this problem, another method has been proposed by Maslov *et al.* [78]. It was found that when the defocus distance is larger than the sphere's radius, two maxima appear on the $V(z)$ curve. They can be attributed to the focusing of longitudinal and shear waves on the back surface of the sphere (Fig. 4.20) and can be expressed as [78, 129]

$$z_{L,T} = \frac{a}{2 \frac{v_{L,T}}{v_w} - 1} \quad (4.32)$$

Measurements of the maxima positions give the velocities of longitudinal and transverse waves inside a spherical particle. The same technique was applied later for characterization of spherical inclusions located inside solid materials [73, 74, 77].

There are only a few papers wherein surfaces more complicated than spherical have been investigated. The use of such sophisticated equipment as a coordinate measuring machine makes the characterization of arbitrarily shaped bodies possible [2]. Amulele and Every [2] studied the elastic properties of an anisotropic nickel-based superalloy layer in the form of a turbine blade. Their measurements constitute two stages. First, a coordinate measuring machine is used for precision measurement of the sample's external profile by means of a touch probe. Measurement of the sample profile can be obtained with an accuracy approaching 1 μm . Then ultrasonic measurements are performed using a motorized manipulator with an ultrasonic transducer. The motorized

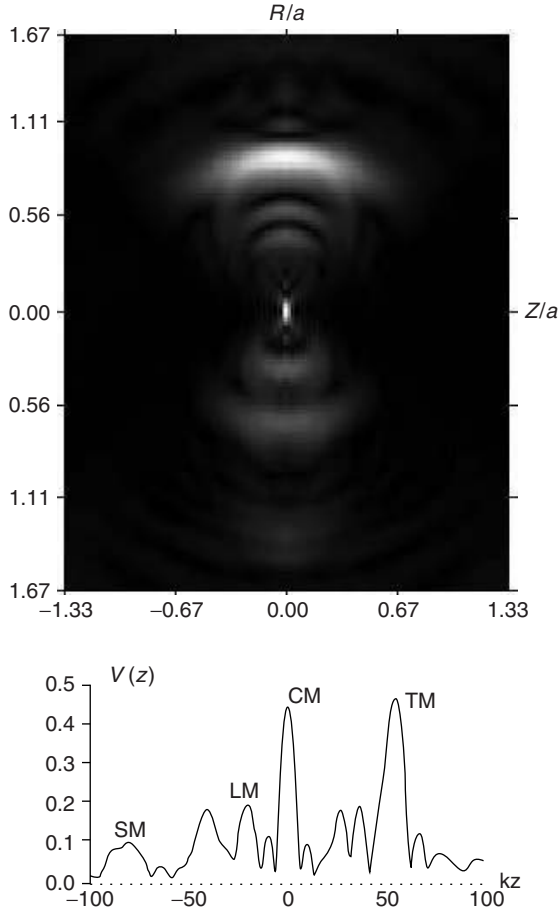


FIG. 4.20. Top: XZ medial section of plexiglass sphere ($ka = 60$, $v_L = 270 \text{ ms}^{-1}$, $v_T = 1100 \text{ ms}^{-1}$, $\rho = 1100 \text{ kg m}^{-3}$) calculated for reflection SAM. Axes scaled in units of the sphere's radius. Bottom: $V(z)$ curve for a plexiglass sphere. TM—Top Maximum; focus of the lens is on the top surface of the sphere. CM—Center Maximum; focus of the lens is in coincidence with sphere center. LM—Longitudinal Maximum. SM—Shear Maximum. Half-aperture angle is equal to 60° (from Zinin *et al.* [129]).

manipulator of a FATHOM IM90 scanning acoustic microscope, working in the time-resolved mode, allows movement of the lens along the surface of an object using the information obtained from the touching probe. First results demonstrated the ability of the system to measure the thickness of the nickel-based superalloy wall of the turbine blade, using a longitudinal acoustic

mode [2], and to study anisotropic properties of the nickel-based signal crystal with the shape of a half-cylinder with a conical top [3].

4.7 Comparison with Other Techniques

The recent surge in the synthesis of new solid materials and films has created a demand for evaluation techniques that can perform nondestructive and noncontacting elastic characterization of these materials. Quantitative acoustic microscopy can be considered one of the most promising methods for meeting such requirements. One of the main features of the acoustic microscope, particularly in its line-focus modification, is the ability to obtain quantitative information with high accuracy. In a recent publication, a relative accuracy of 0.01% in LSAW velocity measurements over the surface of a gadolinium gallium garnet (GGG) crystal has been claimed [50]. For comparison, in surface Brillouin scattering the accuracy of SAW velocity determination is on the order of 0.5% [79]. High accuracy of SAW velocity measurements means that a comparison of different materials is therefore possible from velocity data alone [54]. In the case of Mg-doped LiNbO_3 , for example, there is a linear dependence of the LSAW velocity on the MgO concentration [54]. On a more fundamental level, the measurement of the angular dependence of the Rayleigh wave velocity in the single-grain quasi-crystals of Al-Li-Cu demonstrated the elastic isotropic nature of quasi-crystals [87].

Another advantage of quantitative acoustic microscopy lies in its high resolution in determining SAW velocities and in the short measurement time. These characteristics are ideal for investigating SAW propagation in single crystals. Surface waves provide an attractive method for studying thin coatings because their dispersion characteristics are sensitive to the elastic constants of the coating. The depth probed by acoustic microscopy is of the order of several microns, and therefore layers thicker than 0.5 micron can be investigated. This makes acoustic microscopy complementary to surface Brillouin scattering, which is able to probe layers from several tens of nanometers to 0.5 micron.

The significant aspect of acoustic microscopy for studying SAW propagation is the possibility of detecting the PSAW in addition to the SAW. This can be done because the acoustic microscope excites and receives rays from a surface of a sample confined by a focused beam cone. Inside this cone, the PSAW does not attenuate completely as in the case of the remote detection SAW. Measuring the velocity of the PSAW by acoustic microscopy is found to be crucial for measuring elastic properties of hard and superhard films [63] because the part of the dispersion curve above cutoff can be measured. This gives an advantage over conventional SAW methods, which deal only with true surface waves [89].

Time-resolved point focus acoustic microscopy is a unique tool for characterizing small samples. This feature is of importance in the synthesis of new materials. For example, time-resolved acoustic microscopy made it possible to measure elastic properties of the superhard nanostructures obtained from C_{60} under high pressure and temperature [66]. Only very small samples can be obtained under such extreme conditions.

The main limitation of acoustic microscopy is the low excitation frequency that is currently achievable with the cylindrical acoustic lenses. The depth probed by acoustic microscopy, approximately one SAW wavelength, is of the order of several microns, whereas most structural characteristics in semiconductor surfaces range from a few interatomic spaces to several hundreds of nanometers. Attempts have been made to produce acoustic cylindrical lenses, which operate at higher frequencies, but because of attenuation in the coupling medium, no water-coupled acoustic microscope can work at frequencies higher than 1–2 GHz. Another disadvantage of acoustic microscopy, which causes a problem for the observation of some materials, is the necessity of using water as the coupling fluid. Oxidation reactions can occur between the fluid and the sample, and stains can be left at the surface after acoustic microscopy measurements.

Acknowledgments

The authors would like to thank Dr. Odile Lefeuvre for making corrections; Dr. Wieland Weise for his animated scientific discussions; Prof. Andrew Briggs, Prof. Murli H. Manghnani, Prof. Peter Cawley, and Dr. Max Yaremchuk for their useful comments; and Diane Henderson and Natalia Krokhina for working with the manuscript. I am grateful to Prof. Arthur Every for his patience and great help in writing this chapter. This is SOEST contribution number 5628, H16P contribution number 1100.

References

1. Achenbach, J.D., Kim, J.O., and Lee, Y.C. (1995). Measuring thin-film elastic constants by line-focus acoustic microscope, In *Advances in Acoustic Microscopy*, pp. 153–208, vol. I, Briggs, A., ed., New York: Plenum.
2. Amulele, G., and Every, A.G. (1998). Acoustic microscopy wall thickness measurements on nickel based superalloy gas turbine blades. In *Review of Progress in Quantitative Nondestructive Evaluation*, pp. 2001–2007, vol. 18B, Thompson, D.O., and Chimenti, D.E., eds., New York: Plenum Press.
3. Amulele, G.M., and Every, A.G. (2000). Wave propagation in an anisotropic nickel-based superalloy. *Ultrasonics* **38**(1–8): 252–255.
4. Arikan, O., Telatar, E., and Atalar, A. (1989). Reflection coefficient null of acoustic waves at a liquid-anisotropic-solid interface. *J. Acoust. Soc. Am.* **85**(1): 1–10.

5. Atalar, A. (1978). An angular-spectrum approach to contrast in reflection acoustic microscopy. *J. Appl. Phys.* **49**(10): 5130–5139.
6. Atalar, A. (1980). A backscattering formula for acoustic transducers. *J. Appl. Phys.* **51**(6): 3093–3098.
7. Atalar, A., Koymen, H., Bozkurt, A., and Yaralioglu, G. (1995). Lens geometries for quantitative acoustic microscopy. In *Advances in Acoustic Microscopy*, pp. 117–151, vol. I, Briggs, A., ed., New York: Plenum.
8. Atalar, A., Quate, C.F., and Wickramasinghe, H.K. (1977). Phase imaging in reflection with the acoustic microscope. *Appl. Phys. Lett.* **31**(12): 791–793.
9. Auld, B.A. (1979). General electromechanical reciprocity relations applied to the calculation of elastic wave scattering coefficients. *Wave Motion* **1**: 3–10.
10. Auld, B.A. (1990). *Acoustic Fields and Waves in Solids*. Malabar, FL.: Robert, E. Krieger Publishing Company.
11. Behrend, O., Kulik, A., and Gremaund, G. (1993). Characterization of thin films using numerical inversion of the generalized Lamb wave dispersion relation. *Appl. Phys. Lett.* **62**(22): 2787–2789.
12. Bertoni, H.L. (1984). Ray-optical evaluation of $V(z)$ in the reflection acoustic microscope. *IEEE Trans. Sonic. Ultrason.* **31**(2): 105–116.
13. Bertoni, H.L., and Somekh, M.G. (1985). Ray-optical analysis of spherical focusing transducers for acoustic microscopy. In *IEEE 1985 Ultrasonics Symposium Proceedings*, pp. 715–719, McAvoy, B.R., ed., New York: IEEE Press.
14. Bogy, D.B., and Gracewski, S.M. (1983). On the plane-wave reflection coefficient and nonspecular reflection of bounded beams for layered half-spaces underwater. *J. Acoust. Soc. Am.* **74**(2): 591–599.
15. Bracewell, R.N. (1987). *The Fourier Transform and Its Applications*. New York: McGraw-Hill.
16. Brekhovskikh, L.M. (1980). *Waves in Layered Media*, New York: Academic Press.
17. Briggs, A. (1992). *Acoustic Microscopy*, Oxford: Clarendon Press.
18. Briggs, A., ed. (1995). *Advances in Acoustic Microscopy*, New York: Plenum.
19. Briggs, A., and Arnold, W. (1996). *Advances in Acoustic Microscopy*, New York: Plenum.
20. Briggs, G.A.D., Rowe, J.M., Sinton, A.M., and Spencer, D.S. (1988). Quantitative methods in acoustic microscopy, in *Proceedings of IEEE 1988 Ultrasonics Symposium*, pp. 743–749, vol. 2, McAvoy, B.R., ed., New York: IEEE Press.
21. Chan, K.H., and Bertoni, H.L. (1991). Ray representation of longitudinal lateral waves in acoustic microscopy. *IEEE Trans. Ultrason. Ferroelect. Freq. Cont.* **38**(1): 27–34.
22. Chirita, M., Sooryakumar, R., Xia, H., Monteiro, O.R., and Brown, I.G. (1999). Observation of guided longitudinal acoustic modes in hard supported layers. *Phys. Rev. B* **60**(8): 5153–5156.
23. Cottam, M.G., and Maradudin, A.A. (1984). Surface linear response functions, in *Surface Excitations*, pp. 5–193, Agranovich, V.M., and Loudon, R., eds., London: Elsevier.
24. Doghmane, A., Hadjoub, Z., Alami, K., Saurel, J.M., and Attal, J. (1992). Effects of couplant mass loading on the acoustic signature $V(Z)$. *J. Acoust. Soc. Am.* **92**(3): 1545–1550.
25. Dransfeld, K., and Salzmann, E. (1970). Excitation, detection, and attenuation of high-frequency elastic surface waves, in *Physical Acoustics*, pp. 260–263, vol. III, Mason, W.P., and Thurston, R.N., eds., New York: Academic.

26. Draper, N.R., and Smith, H. (1966). *Applied Regression Analysis*. New York: Wiley.
27. Every, A.G. (1986). Pseudosurface wave structures in phonon imaging. *Phys. Rev. B* **33**(4): 2719–2732.
28. Every, A.G., and Briggs, G.A.D. (1998). Surface response of a fluid-loaded solid to impulsive line and point forces: Application to scanning acoustic microscopy. *Phys. Rev. B* **58**(3): 1601–1612.
29. Every, A.G., Maznev, A.A., and Briggs, G.A.D. (1997). Surface response of a fluid loaded anisotropic solid to an impulsive point force: Application to scanning acoustic microscopy. *Phys. Rev. Lett.* **79**(13): 2478–2481.
30. Every, A.G., Pang, W., Comins, J.D., and Stoddart, P.R. (1998). Brillouin scattering study of guided modes in TiN films on high-speed steel. *Ultrasonics* **36**(1–5): 223–227.
31. Every, A.G., Vines, R.E., and Wolfe, J.P. (1999). Line-focus probe excitation of Scholte acoustic waves at the liquid-loaded surfaces of periodic structures. *Phys. Rev. B* **60**(16): 11755–11760.
32. Farnell, G.W. (1970). Properties of elastic surface waves, in *Physical Acoustics*, pp. 109–166, Mason, W.P., and Thurston, R.N., eds., New York: Academic.
33. Farnell, G.W., and Adler, E.L. (1972). Elastic wave propagation in thin layers, in *Physical Acoustics*, pp. 35–127, Mason, W.P., and Thurston, R.N., eds., New York: Academic.
34. Ghosh, T., Maslov, K.I., and Kundu, T. (1997). A new method for measuring surface acoustic wave speeds by acoustic microscopes and its application in characterizing laterally inhomogeneous materials. *Ultrasonics* **35**(5): 357–366.
35. Goodman, J.W. (1996). *Introduction to Fourier Optics*, New York: McGraw-Hill.
36. Grill, W., Hillmann, K., Wurtz, K.U., and Wesner, J. (1996). Scanning ultrasonic microscopy with phase contrast, in *Advances in Acoustic Microscopy*, pp. 167–218, vol. II, Briggs, A., and Arnold, W., eds., New York: Plenum.
37. Hadjoub, Z., Alami, K., Doghmane, A., Saurel, J.M., and Attal, J. (1991). Acoustic microscopy skimming mode generation using small aperture lenses. *Electron. Lett.* **27**(11): 981–982.
38. Hadjoub, Z., Doghmane, A., Caplain, R., Saurel, J.M., and Attal, J. (1991). Acoustic microscopy investigations of nonplanar surfaces. *Electron. Lett.* **27**(6): 537–539.
39. Hanel, V. (1998). Measurement of sound velocity and thickness of thin samples by time-resolved acoustic microscopy. *J. Appl. Phys.* **84**(2): 668–670.
40. Hauser, M.R., Weaver, R.L., and Wolfe, J.P. (1992). Internal diffraction of ultrasound in crystals: Phonon focusing at long wavelength. *Phys. Rev. Lett.* **(17)**: 2604–2607.
41. Hickernell, F.S. (1999). Surface acoustic wave technology: Macrosuccess through microseims, in *Physical Acoustics*, pp. 136–208, vol. XXIV, Thurston, R.N., Pierce, A.D., and Papadakis, E., eds., New York: Academic.
42. Hirsekorn, S., and Pangraz, S. (1994). Materials characterization with the acoustic microscope. *Appl. Phys. Lett.* **64**(13): 1632–1634.
43. Hsu, N.N., Xiang, D., Fick, S.E., and Blessing, G.V. (1995). Time and polarization resolved ultrasonic measurements using a lensless line-focus transducer, in *Proceedings of IEEE 1995 Ultrasonics Symposium*, pp. 867–871, Levy, M., Schneider, S.C., and McAvoy, B.R., eds., New York: IEEE Press.
44. Hsu, N.N., Xiang, D., and Blessing, G.V. (1998). Time-resolved ultrasonic body wave measurements of material anisotropy using a lensless line-focus transducer,

- in *Proceedings of IEEE 1998 Ultrasonics Symposium*, pp. 1261–1263, Levy, M., Schneider, S.C., and McAvoy, B.R., eds., New York: IEEE Press.
45. Kim, J.O., and Achenbach, J.D. (1993). Line-focus acoustic microscopy measurements of thin-film elastic constants, in *Review of Progress in Quantitative Nondestructive Evaluation*, pp. 1899–1906, vol. 12, Thompson, D., and Chimenti, D., New York: Plenum.
 46. Kim, J.O., Achenbach, J.D., Mirkarimi, P.B., and Barnett, S.A. (1993). Acoustic microscopy measurements of the elastic properties of $\text{Ti}/(\text{V}_{x\text{Nb}1-x})\text{N}$ superlattices. *Phys. Rev. B* **48**(3): 1726–1737.
 47. Kim, J.O., Achenbach, J.D., Mirkarimi, P.B., Shinn, M., and Barnett, S.A. (1992). Elastic constants of single-crystal transition-metal nitride films measured by line-focus acoustic microscopy. *J. Appl. Phys.* **72**(5): 1805–1811.
 48. Knaus, D., Zhai, T., Briggs, G.A.D., and Martin, J.M. (1995). Measuring short cracks by time-resolved acoustic microscopy, in *Advances in Acoustic Microscopy*, pp. 49–77, vol. I, Briggs, A., ed., New York: Plenum.
 49. Kundu, T. (1997). Thin film characterization by acoustic microscopy. *Integr. Ferroelectr.* **15**(1–4): 309–316.
 50. Kushibiki, J., and Arakawa, M. (1998). A method for calibrating the line-focus-beam acoustic microscope. *IEEE Trans. Ultrason. Ferroelect. Freq. Cont.* **45**(2): 421–430.
 51. Kushibiki, J., and Chubachi, N. (1985). Material characterization by line-focus-beam acoustic microscope. *IEEE Trans. Sonic. Ultrason.* **32**(2): 189–212.
 52. Kushibiki, J., Horii, K., and Chubachi, N. (1982). Leaky SAW velocity on water/silicon boundary measured by acoustic line-focus beam. *Electron. Lett.* **18**(1): 732–734.
 53. Kushibiki, J., Ishikawa, T., and Chubachi, N. (1990). Cut-off characteristic of leaky Sezawa and pseudo-Sezawa wave modes for thin-film characterization. *Appl. Phys. Lett.* **57**(19): 1967–1969.
 54. Kushibiki, J., Kobayashi, T., Ishiji, H., and Jen, C.K. (1999). Surface-acoustic-wave properties of MgO -doped LiNbO_3 single crystals measured by line-focus-beam acoustic microscopy. *J. Appl. Phys.* **85**(11): 7863–7868.
 55. Kushibiki, J., Ohkubo, A., and Chubachi, N. (1981). Linearly focused acoustic beams for acoustic microscopy. *Electron. Lett.* **17**(15): 520–522.
 56. Kushibiki, J., Ohkubo, A., and Chubachi, N. (1981). Anisotropy detection in sapphire by acoustic microscope using line-focus beam. *Electron. Lett.* **17**(15): 534–536.
 57. Kushibiki, J., Ohkubo, A., and Chubachi, N. (1982). Propagation characteristics of leaky SAWs on water LiNbO_3 boundary measured by acoustic microscope with line-focus beam. *Electron. Lett.* **18**(1): 6–7.
 58. Kushibiki, J., Ohkubo, A., and Chubachi, N. (1982). Effect of leaky SAW parameters on $V(z)$ curves obtained by acoustic microscopy. *Electron. Lett.* **18**(15): 668–670.
 59. Lee, Y.C., Achenbach, J.D., Nystrom, M.J., Gilbert, S.R., Block, B.A., and Wessels, B.W. (1995). Line-focus acoustic microscopy measurements of $\text{Nb}_2\text{O}_5/\text{MgO}$ and $\text{BaTiO}_3/\text{LaAlO}_3$ thin-film/substrate configurations. *IEEE Trans. Ultrason. Ferroelect. Freq. Cont.* **42**(3): 376–380.
 60. Lee, Y.C., Kim, J.O., and Achenbach, J.D. (1995). Acoustic microscopy measurement of elastic-constants and mass density. *IEEE Trans. Ultrason. Ferroelect. Freq. Cont.* **42**(2): 253–264.

61. Lefeuvre, O. (1998). Characterization of Stiffening Layers by Acoustic Microscopy and Brillouin Spectroscopy. D. Phil. Thesis, Department of Materials, Oxford.
62. Lefeuvre, O., Pang, W., Zinin, P., Comins, J.D., Every, A.G., Briggs, G.A.D., Zeller, B.D., and Thompson, G.E. (1999). Determination of the elastic properties of a barrier film on aluminium by Brillouin spectroscopy. *Thin Solid Films* **350**(1–2): 53–58.
63. Lefeuvre, O., Zinin, P., and Briggs, G.A.D. (1998). Leaky surface waves propagating on a fast on slow system and the implications for material characterization. *Ultrasonics* **36**(1–5): 229–232.
64. Lefeuvre, O., Zinin, P., Briggs, G.A.D., and Every, A. (1998). Surface wave dispersion beyond cut-off for a fast layer on a slow substrate. *Appl. Phys. Lett.* **72**(7): 856–857.
65. Lemons, R.A., and Quate, C.F. (1979). Acoustic microscopy, in *Physical Acoustics*, pp. 1–92, vol. XIV, Mason, W.P., and Thurston, R.N., eds., London: Academic.
66. Levin, V.M., Blank, V.D., Prokhorov, V.M., Soifer, J.M., and Kobelev, N.P. (2000). Elastic properties of solid C_{60} : Measurements and relationship with nanostructure. *J. Phys. Chem. Solids*, **61**(7): 1017–1024.
67. Levin, V.M., Lobkis, O.I., and Maev, R.G. (1990). Investigation of the spatial structure of acoustic field by a spherical focusing transducer. *Soviet Physics Acoustics* **36**(4): 391–395.
68. Li, W., and Achenbach, J.D. (1996). $V(z)$ measurement of multiple leaky-wave velocities for elastic- constant determination. *J. Acoust. Soc. Am.* **100**(3): 1529–1537.
69. Li, W., and Achenbach, J.D. (1997). Determination of elastic constants by time-resolved line-focus acoustic microscopy. *IEEE Trans. Ultrason. Ferroelect. Freq. Cont.* **44**(3): 681–687.
70. Li, Z.L., Achenbach, J.D., and Kim, J.O. (1991). Effect of surface discontinuities on $V(z)$ and $V(z, x)$ for the line-focus acoustic microscope. *Wave Motion* **14**(2): 187–203.
71. Liang, K.K., Bennett, S.D., Khuriyakub, B.T., and Kino, G.S. (1985). Precise phase measurements with the acoustic microscope. *IEEE Trans. Sonic. Ultrason.* **32**(2): 266–273.
72. Liang, K.K., Kino, G.S., and Khuri-Yakub, B.T. (1985). Material characterization by the inversion of $V(z)$. *IEEE Trans. Sonic. Ultrason.* **32**(2): 213–224.
73. Lobkis, O., Kundu, T., and Zinin, P. (1994). Acoustic microscopy for spherical cavities in solids, in *Acoustical Imaging*, vol. 21, Jones, J.P., ed., New York: Plenum.
74. Lobkis, O.I., Maslov, K.I., Kundu, T., and Zinin, P.V. (1996). Spherical inclusion characterization by the acoustical microscope — axisymmetrical case. *J. Acoust. Soc. Am.* **99**(1): 33–45.
75. Lowe, M.J.S. (1995). Matrix techniques for modeling ultrasonic-waves in multi-layered media. *IEEE Trans. Ultrason. Ferroelect. Freq. Cont.* **42**(4): 525–542.
76. Manghnani, M.H., Zhang, X., Tkachev, S., Zinin, P., Feldermann, H., Ronning, C., Hofsass, H., and Every, A.G. (1999). Elastic properties of hard cBN film by surface Brillouin scattering, in *Nondestructive Characterization of Materials IX*, pp. 315–320, Green, R.E., ed., New York: American Institute of Physics.
77. Maslov, K.I., Kundu, T., and Lobkis, O.I. (1996). Acoustic microscopy for spherical inclusion characterization. *J. Acoust. Soc. Am.* **100**(1): 80–85.

78. Maslov, K.I., Zinin, P.V., Lobkis, O.I., and Kundu, T. (1995). $V(z)$ curve formation of solid spherical microparticles in scanning acoustic microscopy. *J. Microsc.* **178**(Pt2): 125–133.
79. Mutti, P., Bottani, C.E., Ghislotti, G., Beghi, M., Briggs, G.A.D., and Sandercock, J.R. (1995). Surface Brillouin scattering—Extending surface wave measurements to 20 GHz, in *Advances in Acoustic Microscopy*, pp. 249–300, vol. I, Briggs, A., ed., New York: Plenum.
80. Nagy, P.B., and Adler, L. (1990). Acoustic material signature from frequency analysis. *J. Appl. Phys.* **67**(8): 3876–3878.
81. Naumenko, N.F., and Didenko, I.S. (1998). Leaky wave propagation in layered structures, in *Proceedings of IEEE 1998 Ultrasonics Symposium*, pp. 149–154, Levy, M., Schneider, S.C., and McAvoy, B.R., eds., New York: IEEE Press.
82. Nayfeh, A.H. (1995). *Wave Propagation in Layered Anisotropic Media: With Applications to Composites*. Amsterdam, New York: Elsevier.
83. Nayfeh, A.H., and Chimenti, D.E. (1984). Reflection of finite acoustic beams from loaded and stiffened half-spaces. *J. Acoust. Soc. Am.* **75**(5): 1360–1368.
84. Papoulis, A. (1962). *The Fourier Integral and Its Applications*. New York: McGraw-Hill.
85. Parmon, W., and Bertoni, H.L. (1979). Ray interpretation of the material signature in the acoustic microscope. *Electron. Lett.* **15**(12): 684–686.
86. Sasaki, Y., Endo, T., Yamagishi, T., and Sakai, M. (1992). Thickness measurement of a thin-film layer on an anisotropic substrate by phase-sensitive acoustic microscope. *IEEE Trans. Ultrason. Ferroelect. Freq. Cont.* **39**(5): 638–642.
87. Sathish, S., Kulik, A., and Gremaud, G. (1991). Elastically isotropic Al-Li-Cu quasicrystal. *Solid State Communications* **77**(6): 403–407.
88. Sathish, S., Mendik, M., Kulik, A., Gremaud, G., and Wachter, P. (1991). Polish-induced surface damage in nickel: Scanning acoustic microscopy and Brillouin scattering study. *Appl. Phys. Lett.* **59**(2): 167–168.
89. Schneider, D., Ollendorf, H., and Schwarz, T. (1995). Nondestructive evaluation of the mechanical behavior of tin-coated steels by laser-induced ultrasonic surface waves. *Appl. Phys. A* **61**(3): 277–284.
90. Sinton, A.M., Briggs, G.A.D., and Tsukahara, Y. (1989). Time-resolved acoustic microscopy of polymer-coatings, in *Acoustical Imaging*, pp. 87–95, vol. XVII, Shimizu, H., Chubachi, N., and Kushibiki, J., eds., New York: Plenum.
91. Sklar, Z., Briggs, G.A.D., Cawley, P., and Kinloch, A.J. (1995). “Quantitative acoustic microscopy of anodized and coated aluminum at frequencies up to 1 GHz. *J. Mater. Sci.* **30**(15): 3752–3760.
92. Sklar, Z., Mutti, P., Stoodley, N.C., and Briggs, G.A.D. (1995). Measuring the elastic properties of stressed materials by quantitative acoustic microscopy, in *Advances in Acoustic Microscopy*, pp. 209–247, vol. I, Briggs, A., ed., New York: Plenum.
93. Stamnes, J.J. (1986). *Waves in Focal Regions*, Bristol: Adam Hilger.
94. Tourlog, A., Li, W., and Achenbach, J.D. (1996). Line-focus acoustic microscopy measurements of elastic constants for materials with high acoustic velocities. *Appl. Phys. Lett.* **69**(24): 3680–3682.
95. Tsukahara, Y., Liu, Y.S., Neron, C., Jen, C.K., and Kushibiki, J. (1994). Longitudinal critical angle singularities and their effect on $V(z)$ of the line-focus-beam acoustic microscope. *IEEE Trans. Ultrason. Ferroelect. Freq. Cont.* **41**(4): 458–466.

96. Tsukahara, Y., Nakaso, N., Ohira, K., and Yanaka, M. (1996). Interaction of acoustic waves with solid surfaces, in *Advances in Acoustic Microscopy*, pp. 103–165, vol. II, Briggs, A., and Arnold, W., eds., New York: Plenum.
97. Victorov, I.G., Grishchenko, E.K., and Kaekina, T.M. (1963). An investigation of the propagation of ultrasonic surface waves at the boundary between a solid and a liquid. *Sov. Phys. Acoust.* **9**: 131–137.
98. Viktorov, I.A. (1967). *Rayleigh and Lamb Waves: Physical Theory and Applications*, New York: Plenum.
99. Vines, R.E., Hauser, M.R., and Wolfe, J.P. (1995). Imaging of surface acoustic waves. *Z. Phys. B* **98**: 255–271.
100. Vines, R.E., Tamura, S., and Wolfe, J.P. (1995). Surface acoustic wave focusing and induced Rayleigh waves. *Phys. Rev. Lett.* **74**(14): 2729–2732.
101. Vines, R.E., Wolfe, J.P., and Every, A.G. (1999). Scanning photonic lattices with ultrasound. *Phys. Rev. B* **60**(17): 11871–11874.
102. Wang, L.G. (1999). Determination of elastic constants of composites by time-resolved acoustic microscopy. *Ultrasonics* **37**(4): 283–289.
103. Weaver, J.M.R., Daft, C.M.W., and Briggs, G.A.D. (1989). A quantitative acoustic microscope with multiple detection modes. *IEEE Trans. Ultrason. Ferroelect. Freq. Cont.* **36**(5): 554–560.
104. Weaver, R.L., Hauser, M.R., and Wolfe, J.P. (1993). Acoustic flux imaging in anisotropic media. *Z. Phys. B* **90**: 27–46.
105. Weglein, R.D. (1979). A model for predicting acoustic material signature. *Appl. Phys. Lett.* **34**(3): 179–181.
106. Weglein, R.D. (1981). Acoustic microscopy of curved surfaces. *Appl. Phys. Lett.* **38**(7): 516–518.
107. Weglein, R.D. (1996). Acoustic material signature extension. *Electron. Lett.* **32**(1): 30–31.
108. Weglein, R.D., and Kim, J.O. (1992). SAW dispersion in diamond films by acoustic microscopy, in *Review of Progress in Quantitative Nondestructive Evaluation*, pp. 1815–1822, vol. 1, Thompson, D.O., and Chimenti, D.E., eds., New York: Plenum.
109. Weglein, R.D., and Wilson, R.G. (1978). Characteristic material signatures by acoustic microscopy. *Electron. Lett.* **14**(12): 352–354.
110. Weise, W. (1999). Private communication.
111. Weise, W., Zinin, P., and Boseck, S. (1994). Modeling of inclined and curved surfaces in the reflection scanning acoustic microscope. *J. Microsc.* **176**(3): 245–253.
112. Weise, W., Zinin, P., and Boseck, S. (1996). Angular spectrum approach for imaging of spherical-particles in reflection and transmission SAM, in *Acoustical Imaging*, pp. 707–712, vol. 22, Tortoli, P., and Masotti, L., eds., New York: Plenum.
113. Weise, W., Zinin, P., Briggs, A., Wilson, T., and Boseck, S. (1998). Examination of the two-dimensional pupil function in coherent scanning microscopes using spherical particles. *J. Acoust. Soc. Am.* **104**(1): 181–191.
114. Wolfe, J.P. (1998). *Imaging Phonons: Acoustic Wave Propagation in Solids*, Cambridge: Cambridge University Press.
115. Wolfe, J.P., and Vines, R.E. (1996). Acoustic wavefront imaging of carbon-fiber/epoxy composites, in *Proceedings of IEEE 1996 Ultrasonics Symposium*, Levy, M., Schneider, S.C., and McAvoy, B.R., eds., New York: IEEE.

116. Wurz, K.U., Wesner, J., Hillmann, K., and Grill, W. (1995). Determination of elastic constants using a scanning acoustic microscope. *Z. Phys. B* **97**(4): 487–492.
117. Xiang, D., Hsu, N.N., and Blessing, G.V. (1999). Imaging of acoustic surface wave slowness. *Appl. Phys. Lett.* **74**(15): 2236–2238.
118. Yamanaka, K. (1983). Surface acoustic wave measurement using an impulse converging beam. *J. Appl. Phys.* **54**: 4323–4329.
119. Yamanaka, K. (1995). New approach in acoustic microscopy for noncontact measurements and ultra high resolution, in *Advances in Acoustic Microscopy*, pp. 301–342, vol. I, Briggs, A., ed., New York: Plenum.
120. Yu, Z., and Boseck, S. (1994). Some considerations in layer-thickness measurement for semiconductor technology by acoustic microscopy. *Optik* **96**(2): 83–92.
121. Yu, Z.L., and Boseck, S. (1995). Scanning acoustic microscopy and its applications to material characterization. *Rev. Mod. Phys.* **67**(4): 863–891.
122. Zhang, J., Baboux, J.C., and Guy, P. (1994). PVDF large aperture spherical transducer in the transient mode, in *Proceedings of IEEE 1994 Ultrasonic Symposium*, pp. 517–520, vol. 3, McAvoy, B.R., Levy, M., and Scheider, S.C., eds., New York: IEEE Press.
123. Zhang, J., Guy, P., Baboux, J.C., and Jayet, Y. (1999). Theoretical and experimental responses for a large-aperture broadband spherical transducer probing a liquid–solid boundary. *J. Appl. Phys.* **86**(5): 2825–2835.
124. Zhang, X., Comins, J.D., Every, A.G., Stoddart, P.R., Pang, W., and Derry, T.E. (1998). Surface Brillouin scattering study of the surface excitations in amorphous silicon layers produced by ion bombardment. *Phys. Rev. B* **58**(20): 13677–13685.
125. Zinin, P., Lefeuvre, O., Briggs, A., Zeller, B.D., Cawley, P., Kinloch, A., Zhou, X., and Thompson, G. (1999). Determination of density and elastic constants of a thin phosphoric acid-anodized oxide film by acoustic microscopy. *J. Acoust. Soc. Am.* **106**(5): 2560–2567.
126. Zinin, P., Lefeuvre, O., Briggs, G.A.D., Zeller, B.D., Cawley, P., Kinloch, A.J., and Thompson, G.E. (1997). Anomalous behavior of leaky surface waves for stiffening layer near cut-off. *J. Appl. Phys.* **82**(3): 1031–1035.
127. Zinin, P., Lefeuvre, O., and Briggs, G.A.D. (1999). Measurement of a stiffening layer density by acoustic microscopy. *J. Mat. Sci. Lett.* **18**(4): 259–261.
128. Zinin, P., Manghnani, M.H., Tkachev, S., Askarpour, V., Lefeuvre, O., and Every, A. (1999). Brillouin spectroscopy of surface in thin film Si_3N_4 on GaAs. *Phys. Rev. B* **60**(3): 2844–2850.
129. Zinin, P., Weise, W., Lobkis, O., and Boseck, S. (1997). The theory of three-dimensional imaging of strong scatterers in scanning acoustic microscopy. *Wave Motion* **25**(3): 213–236.

This Page Intentionally Left Blank

5. RESONANT ULTRASOUND SPECTROSCOPY (RUS)

A. Migliori, T. W. Darling, J. P. Baiardo, and F. Freibert

Los Alamos National Laboratory
Los Alamos, New Mexico

5.1 Introduction

Resonant ultrasound spectroscopy (RUS) uses the mechanical resonances of small cylindrical, rectangular parallelepiped, or spherical samples to extract the elastic modulus tensor. Although many resonance techniques employing roughly similar measurement approaches have been used, RUS is qualitatively different in that the measurements and analysis are highly redundant, and when applied to samples of near unity aspect ratio, sensitive to all the components of the elastic tensor. The technique has been applied to samples with the minimum elastic symmetry (triclinic), though it is most often, and most easily, applied to systems of rhombohedral or higher symmetry. Key to the use of this technique is the ability of modern personal computers to perform calculations nearly as rapidly as the supercomputers of recent years. For example, a modern RUS analysis would require approximately 2 hr per iteration on the first IBM personal computer, 1 sec on the first Cray, and 0.8 sec on an 850 MHz Pentium III. Instrumentation has also been benefited by modern integrated electronics, which enable digital signal processing algorithms to acquire RUS data at rates orders of magnitude higher than in the past, limited only by information theory and thermal noise. In this chapter we describe how RUS works, when to use it, how to make and analyze measurements, and the limitations and accuracy of the technique [1].

5.2 Motivation for the Use of Resonances to Study Elastic Moduli

Why are resonance techniques so valuable for the measurement of elastic moduli? To answer this question, we examine various ultrasonic measuring schemes. Although there are many direct and indirect methods of measuring the elastic modulus tensor [2], we consider here, for the purposes of comparison, only those methods that use a macroscopic stimulus to launch macroscopic mechanical vibrations into the sample to be studied. We shall call such techniques ultrasonic, even though they may be used at audible or subaudible frequencies. Our intent is to exclude coherent optical or neutron-based techniques, because these are typically special purpose, expensive, and imprecise, though of great

power at high frequencies or when the entire acoustic dispersion curve is required. We also exclude static mechanical techniques because they require massive hardware normally found only in metallurgy laboratories. This leaves us with a large group of methods in which some sort of ultrasonic transducer drives a sample and the same or another transducer detects the vibrations.

At one extreme of the ultrasonic measurement techniques are pulse-based methods such as pulse-echo and the like. In a pure pulse-echo system, an acoustic pulse is generated via an electrical impulse to a nonresonant transducer. The pulse is spatially localized and, absent dispersion, travels without change in shape to a receiving transducer. The time of flight (and distance traveled) determine the sound speeds, and hence the elastic moduli. The key measurement is of time, a quantity usually taken to be (with frequency) the most accurately measurable of physical quantities.

The other extreme involves purely resonant schemes such as RUS. A few comparisons can be made immediately between resonance and pulsed techniques. Because resonances are standing waves, there is no propagation involved. Therefore, scattering of the ultrasonic beam is not an issue, and a resonance measurement, via the width of the resonance, measures only the true thermodynamic dissipation, but only for frequencies that correspond to sample resonances. In contrast, pulse methods can see a decrease in the reflected signal from transducer bond material, nonparallelism of the transmit and receive transducers, and scattering of the beam from inhomogeneities of all sorts within the sample, but can measure attenuation at any frequency. Pulse methods can also usually only measure one component of the elastic tensor at a time because only time of flight, a scalar, is measured. Resonances can, in principle, measure all components in a single measurement setup. However, pulsed methods require only a pocket calculator to reduce data, whereas RUS requires a complex algorithm and very large computing capacity (a modern personal computer is just fine). Accuracy is another factor. In round-robin measurements at Los Alamos National Laboratory, National Institute of Standards and Technology (Boulder), University of California, Los Angeles, and University of Wisconsin Milwaukee [3], it has been established that RUS has the highest absolute accuracy of any routine elastic modulus measurement technique; an ordinary RUS measurement can achieve 0.05% absolute accuracy, whereas very carefully set up pulse-echo overlap measurements appear to produce errors nearer 0.1%. Finally, we mention that resonance methods can acquire data on very small samples because the frequencies involved are easily accessible (a 1-mm cube might have its first resonance at 1 MHz), whereas pulsed methods must have extreme bandwidth. To get the time of flight to 0.1% on a 1-mm sample requires 1 GHz receiver bandwidth, causing large increases in system noise. In fact, noise and the ability to obtain all moduli simultaneously on small samples are the key reasons for using RUS.

Before we describe measurement techniques and compare signal/noise of pulse and resonance methods, it is important to understand some intrinsic limitations of both techniques. In a resonance measurement, mechanical resonances are measured using any of a variety of techniques. The shape of an ordinary linear mechanical resonance of a solid object is Lorentzian. That is, if, e.g., the *displacement* $x(\omega, t)$ of the system being measured is plotted against frequency, the (complex) result approximates a Lorentzian function if the resonance is narrow and well separated from others, such that

$$x(\omega, t) = x_0(\omega)e^{-i\omega t}, \text{ with } x_0(\omega) = \frac{iA\omega^2 Q^{-1}}{\omega^2 - \omega_0^2 + i\omega\omega_0 Q^{-1}}. \quad (5.1)$$

A is the peak response and Q is a measure of how narrow the resonance is, or equivalently, how long the resonator would ring after excitation such that

$$Q = \frac{\omega_0 \tau_\ell}{2} = \frac{f}{\Delta f_\ell} \quad (5.2)$$

where τ_ℓ is the characteristic time for exponential decay of displacement (or force, velocity, or any other quantity that is *linearly* related to the forces present). Δf_ℓ is the full width at half-maximum of the real part of the displacement. Note that if power (proportional to the square of a linear response such as displacement) is measured, the decay time is half that in Eq. 5.2, so that

$$Q = \omega_0 \tau_p = \frac{f}{\Delta f_p} \quad (5.3)$$

where Δf_p is the full width at half-maximum of the power driving the resonator. If the *magnitude* (or amplitude) of the displacement is measured as with a meter not sensitive to phase, then the appropriate Δf_ℓ for determination of Q is the full width measured at $1/\sqrt{2}$ of the peak height.

The angular frequency $\omega_r = 2\pi f$ is in fact complex, such that

$$\omega_r = \omega_0 \left(1 - \frac{1}{4Q^2}\right)^{1/2} + i\tau \text{ where } \tau = \frac{2Q}{\omega_0} \quad (5.4)$$

The effect of Eqs. 5.1 and 5.4 is that there is a very real ambiguity in the resonance frequency of a damped oscillator (and, hence, also in the meaning of elastic moduli in dissipative systems). The real part of Eq. 5.4, the frequency where the phase is zero (ω_0), and the frequency of maximum amplitude $\omega_0(1 - \frac{1}{2}Q^2)^{1/2}$ all differ by of order $1/Q^2$. This is a measure of the intrinsic impreciseness of the frequency (or elastic moduli) of a dissipative system where one cannot measure for an arbitrarily long time because the oscillations disappear as heat. However, in a measurement, it is the ability to

measure accurately the width of the resonance that determines how well frequency is determined. This in turn depends on the signal-to-noise ratio, R_n . The *fractional accuracy* of a resonance frequency measurement is limited to approximately $1/(R_n Q)$ up to the point where the error is less than $1/Q^2$, whereupon the intrinsic effects of Eq. 5.4 take over. It is not uncommon to reach this limit. The exactly equivalent property for a pulse system is the decay time for the pulse. One can only measure the travel time of the pulse for a time τ that is the same as the τ for the resonator (longer, and it disappears). Because the pulse itself must have a finite width (of order $1/f$ where f is the driving frequency, even if only a single-cycle pulse is used), the maximum accuracy of a pulse-echo measurement is approximately $1/(R_n \omega \tau)$, the same as for a resonance measurement.

In any measurement, noise intrudes, and because the noise voltage in most well-designed electronic systems is proportional to the square root of the bandwidth, we can estimate the relative R_n of resonant and pulse measurements. Consider a sample with a Q of 10^4 and 10 resonances of average frequency f near 1 MHz required to determine the moduli using RUS. The pulse-echo measurement will require a receiver bandwidth of order 10^9 Hz, with peak power levels of 500 W to obtain an accuracy similar to the RUS measurement at continuous power levels of 5 mW. The RUS measurement must be made on all the modes, so the receiver bandwidth is the number of modes m times the width of each mode, or about mf/Q . The pulse measurement is over in 1 pass of the pulse through the sample; thus at a pulse repetition rate of 10 KHz (limited by the decay time), the duty cycle is a maximum of 0.01 because the transit time is $1/f = 1 \mu s$, in contrast to a duty cycle of unity for RUS. Using these figures, RUS measurements have a voltage R_n conservatively estimated at 200 times greater than pulse methods for the same average power into the sample, shown in Table 5.1.

Surprisingly, there is a continuum of methods in between RUS and pulse techniques, with corresponding changes in R_n . For example, a modification of

TABLE 5.1. A Signal-to-Noise Comparison between Pulsed and RUS Measurements

Parameter	Pulse	Resonance
Transducer drive voltage	160 V into 50 Ω , 1 ns pulse, 10 kHz rep rate = 5 mW average	5 V into 5000 Ω = 5 mW average
Measurement bandwidth	10^9 Hz	10^3 Hz
Electronic noise	10^{-9} V/(Hz) ^{1/2}	10^{-9} V/(Hz) ^{1/2}
Detect duty cycle	0.01	1
Voltage signal/noise ratio R_n	2×10^5	5×10^7

the pulse technique, called pulse-echo-overlap, is to drive the system with a tone burst of moderately well defined frequency. That is, a few tens of cycles of sinusoidal excitation are applied to a resonant transmitting transducer, with a similar receiver. The received pulse is overlapped (mixed) with the next transmitted pulse in such a way that they are out of phase, and the product of the voltage of the two pulses is averaged over the length of the pulse. When they are exactly out of phase, a null is achieved. With such a system, neither the time of flight nor the frequency is measured, but a combination of both. That is, the system looks for information over a *window* of time (the pulse width) within a *band* of frequencies (if the pulse has n cycles in it, the band of frequencies is f/n wide and centered about f) to obtain sound speed. The measurement has an uncertainty of order the pulse period in absolute arrival time (sound speed) but a precision that is determined by the signal-to-noise ratio in a narrow band about the pulse center frequency. That is, the time precision is $1/(R_n f)$, and R_n is improved because the receiver bandwidth is reduced to f/n . Absolute accuracy, however, is limited to approximately the pulse width divided by the transit time.

A resonance method can also be modified toward behaving partly like a pulse method by driving the system with an impulse with frequency components that span all the resonances desired. A Fourier transform of the received signal provides the resonances. Because the receiver bandwidth must now span all the resonances, R_n is degraded over the swept-frequency pure resonant measurement, but acquisition time is reduced, and signal averaging can recover some of the degraded R_n . There are very good reasons to use impulse RUS or pulse-echo-overlap, especially if R_n is already excellent in the former, or, if only precisely determined relative changes (for example, with temperature), are important as in the latter.

5.3 Measurements

Although impulse RUS measurements are used, swept-frequency methods are the technique of choice at low temperatures and in small samples where power dissipation matters, where absolute accuracy is important, and where small changes must be detected. Because the analysis is the same for both techniques, our discussion will mainly center around swept-frequency RUS. A complete swept-frequency RUS measurement system block diagram is shown in Figure 5.1. We next describe desirable features of each of the blocks [4].

5.3.1 Samples

Although any shaped sample resonator can, in principle, be used, there are very substantial savings in computation time if rectangular parallelepiped

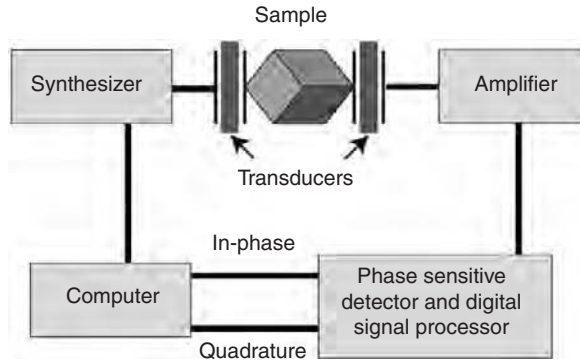


FIG. 5.1. Swept-frequency RUS block diagram.

resonators (RPRs) [5], spherical, or cylindrical ones are used (the time savings is less with cylinders). An RPR sample is generally prepared with the edges parallel to crystallographic symmetry directions for rhombohedral, orthorhombic, tetragonal, hexagonal, or cubic samples. For cylinders, only the axis can be matched to sample symmetry. RUS is rarely used for samples of lower symmetry, and for isotropic samples, alignment is irrelevant. For the higher symmetries, it is also desirable to make the RP sample have different-length edges to prevent resonances from being degenerate, and therefore hard to detect.

The accuracy with which the sample is prepared determines the overall accuracy of the measurement because sample geometry is the most difficult quantity in the measurement to control, and all the analysis codes assume accurate sample geometry. An error in parallelism, perpendicularity, or measured length translates to a similar-sized error in elastic moduli and, worse still, makes the codes unable to compute accurately frequencies that match the measured ones because the mathematical model does not correspond to the sample shape. Many methods are appropriate for preparation of RPR samples, including the use of a conventional surface grinder, precision saws, and manual polishing systems. A typical arrangement for polishing is illustrated in Figure 5.2. This arrangement is very inexpensive, and easily produces samples with geometry accurate to 0.1%.

Measurements on single crystals of rhombohedral or higher symmetry usually require orientation of the sample crystallographic axes with the edges of the RPR, primarily because greater accuracy can be achieved if one needs only to compute elastic moduli, not orientation as well. Although computations of orientation from resonance data have been successful, more resonances are required for an accurate modulus determination if more parameters must be fit.



FIG. 5.2. Plate glass disk with steel shims used to hand-polish RPR samples to produce accurately parallel and perpendicular edges. Wax or other adhesives locate the shims. The sample is the dark area in the center. Lateral finger pressure on the shims ensures perpendicularity if the shims are surface-ground square.

X-ray diffraction, etching to reveal facets, or simply planes appearing during crystal growth have all been used successfully to orient samples.

5.3.2 Transducers

The transducers used for RUS measurements are generally somewhat unusual. The reason relates to the requirement for free-surface boundary conditions for the computation of elastic moduli from frequencies, discussed in following text. Typically, and unlike all other ultrasonic techniques, RUS transducers are most frequently designed to make dry point contact with the sample. For rectangular parallelepiped samples, this means that the corners touch the transducers very lightly (0.01 N is a typical force). Because of the weak, bond-free contact, no transducer corrections are required under most circumstances (long buffer rods are an exception). A typical arrangement is shown in Figure 5.3. The sample shown is about 3 mm on the longest edge, and is mounted to PZT-5A transducers 0.1 mm thick, 1.5 mm in diameter. The transducers are, in turn, fixed with epoxy to a DuPont Kapton film 12 mm in diameter by 25 μm thick and coated with Au to create a ground plane and one electrical contact, shown in Figure 5.4. There is a 1-mm-diameter hole through the Kapton film that enables the sample to make direct contact with the transducer element. The drive or receive electrical contact is made from a 1-mm-wide, 20-mm-long strip of the same Au-coated Kapton used to support the transducer. Although this transducer arrangement is only a typical example, it exhibits several important features. To ensure that the resonances of the transducers are not mistaken for sample resonances, the backload, often single crystal diamond, is chosen to push the first transducer resonance above

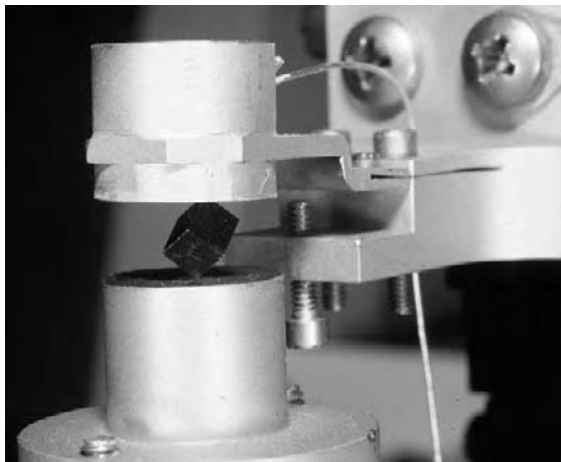


FIG. 5.3. A typical room temperature RUS stage showing transducers and sample [6].

4 MHz. The epoxy bonds and Kapton film provide some damping so that the transducer resonance Q is low, of order 10, thereby making it so broad that it usually appears only as a background behind the sample resonances, which are usually much sharper. The large metallized ground plane disk and the shell to which this assembly is epoxied provide extremely good shielding so that the drive electrical signal that leaks to the receiver electrical contact is much less than the noise floor, even in extremely low noise systems.

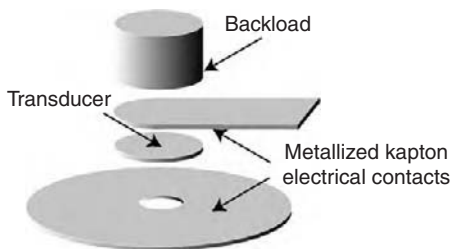


FIG. 5.4. A typical transducer assembly for RUS that has high resonant frequency, high damping, and extremely good electrical shielding. The Kapton components are metallized on the surfaces that contact the transducer. The transducer is 0.1 mm thick LiNbO_3 or PZT-5A, and the backload is single crystal diamond about 1.5 mm diameter by 1 mm long. An alternate scheme, adequate for room temperature, uses a PZT-5A transducer the same size as the diamond, and no backload. The assembly is held together with nonconducting epoxy, which always seems to allow electrical contact between components when compressed during curing.

5.3.3 Electronics

The necessity to preserve a good approximation to free-surface boundary conditions requires weak coupling between transducers and sample. The weak coupling also tends to preserve the Q so that, when attenuation studies are performed, the measured Q corresponds to that of the sample, not the equipment, for samples with a Q less than 10^5 and a mass less than 0.5 g or so. Larger samples are heavier and couple better, and so their Q is degraded because excessive energy leaks into the transducer assemblies.

To capture the weakest signals produced requires considerable care in electronics design. Modern operational amplifiers with very low noise should be used in the preamplifiers. For frequencies above 2 MHz or so, bipolar designs work best, yielding noise values of $2nV/\sqrt{\text{Hz}}$ and $1\text{Pa}/\sqrt{\text{Hz}}$. For lower frequencies, JFET devices can attain values of $6nV/\sqrt{\text{Hz}}$ and $0.005\text{Pa}/\sqrt{\text{Hz}}$ down to about 30 kHz. Below this frequency, typical charge-sensitive preamp designs become more difficult to stabilize, degrading noise, but samples are larger and produce stronger signals, so that in practice there is no real difficulty in making RUS measurements from 20 MHz to nearly DC. In the more typical frequency range around 1 MHz, the capacitance of the cable connecting the receive transducer to the preamplifier, especially in a cryogenic or elevated temperature system, requires that charge-sensitive preamplifiers be used. For example, typical transducer capacitance may be 5pF, and 2 m of coaxial cable may have a capacitance of 100 pF. Thus the voltage developed at the end of the cable is reduced by a factor of 20 if no care is taken to eliminate such capacitive effects. A conventional approach is to use a “guard” actively driven, but at 1 MHz, this is nearly impossible. A more viable approach is to use a charge amplifier, shown in Figure 5.5. Operation, described in the figure caption, is dependent upon the impedance of R being much higher than that of C at the frequencies of interest. R is necessary to prevent the Op-Amp from integrating offset currents until it saturates; thus the charge amplifier only works at frequencies above $1/RC$. Below this frequency, the gain of the preamplifier drops. More importantly, the low-frequency noise voltage is determined by the thermal noise of R . For a typical RUS system, C may be about 10 pF and R 1 M Ω . Thus the low frequency limit begins near 100 kHz. Much below this, the noise output goes from $2\text{nV}/\sqrt{\text{Hz}}$, derived from the Op-Amp, to $(4Rk_bT)^{1/2}$ or about $127\text{nV}/\sqrt{\text{Hz}}$. The total noise from the resistor is confined to frequencies below a few hundred kHz, but is about 80 μV RMS. This is to be compared with the total noise above this frequency range of about 8 μV RMS. The net result is that, unless the remainder of the electronics is not sensitive to noise below a few hundred kHz, serious degradation of the system performance occurs. The way around this at low frequencies for conventional laboratory

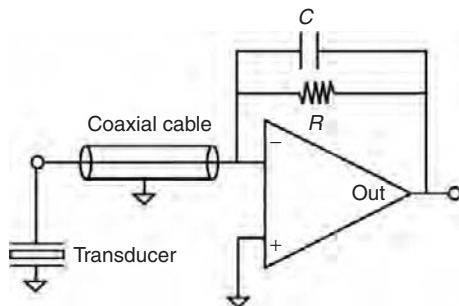


FIG. 5.5. A charge amplifier based on an operational amplifier (Op-Amp). The Op-Amp maintains its inverting terminal (–) at ground so that no voltage is developed between center conductor and shield of the coaxial cable. This ensures that all the charge developed by the transducer appears on the capacitor C as well. If C is set to equal the transducer capacitance, unity gain is achieved, independent of frequency and cable capacitance at frequencies where the impedance of C is much less than that of the DC stabilizing resistor R .

instrumentation is to use a lock-in amplifier, which is sensitive to frequencies within about $1/RC$ of the excitation frequency, and so only sees a narrow slice of the noise, near the signal frequency. Lock-ins have been successfully used for RUS measurements, but there are several drawbacks. One is that a lock-in uses homodyne detection; that is, the signal is mixed (or multiplied with) a reference signal of the same frequency. The result is a DC component with its attendant sensitivity to drift of the electronics with temperature, and with the requirement that one must wait several RC time constants for the signal to stabilize. A better approach is to use a heterodyne system. In a heterodyne system, a reference signal is generated at a fixed difference frequency above or below the frequency used to drive the transducer. When mixed and low-pass-filtered with the signal from the receive transducer preamplifier, the desired resonance information appears at the fixed difference frequency (the intermediate frequency or IF), typically 1 kHz. Digital synthesizers can easily generate the required frequencies rapidly, and, by using a bit of digital signal processing, shown in Figure 5.6, the waiting time for RC filters is reduced. This is not a minor point of convenience. Because the accurate measurement of a resonance may require sweeping through 1000 frequencies around the center frequency, and there may be dozens of frequencies to be measured, an RUS measurement, especially in a cryogenic system where liquid He costs are important, can take a long time. Anything to reduce this time will minimize temperature drifts during a scan and minimize cryogen costs. Remembering that, in almost any measurement performed today, the final result needs to be inside a computer, somewhere along the line an A/D converter is needed.

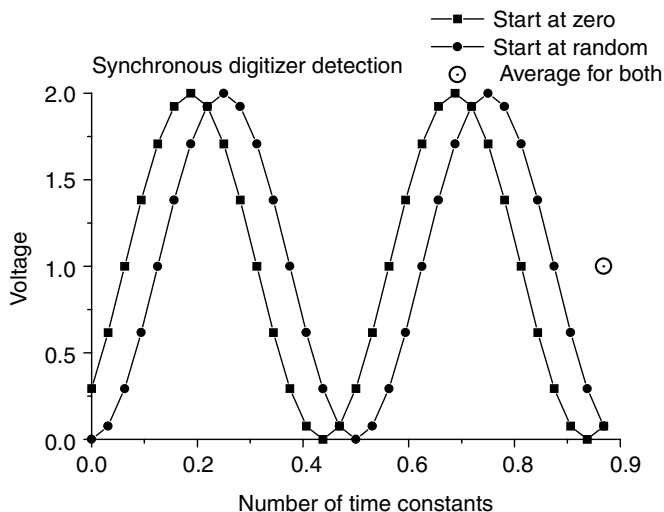


FIG. 5.6. Shown is the synchronous digitization scheme used to acquire stable, low-noise RUS data at as high a rate as possible. No matter where one starts digitizing, as long as the digitizer rate is an integer multiple of the frequency and the digitizer runs for an integer number of cycles, the sum of all the digitized values is the same, with full settling in exactly one cycle, unlike a lock-in.

By driving the A/D at an integer multiple of four times the IF frequency and digitizing for an integral number of IF cycles, shown in Figure 5.6, we can obtain the amplitude of the IF signal. This amplitude, obtained by summing the product of the digitized values multiplied by a similarly digitized reference signal at the IF frequency, is independent of exactly when the digitizer starts, and so the system “settles” instantly, instead of having to wait many RC time constants for stabilization, as in a lock-in. By choosing the number of cycles, we also limit the noise bandwidth. For example, using 10 cycles of a 1 kHz IF takes 10 ms and produces a noise bandwidth of order $1/10 \text{ ms} = 100 \text{ Hz}$. In addition, because the IF reference signal has been digitized, at a rate of four times an integer multiple of its frequency, it is easy to digitally phase-shift this signal and redo the detection process, thereby producing both in-phase and quadrature signals, which are important for data analysis, especially for obtaining Q . All of these operations can be performed before the result ever gets to the data acquisition computer. The net result is that a modern RUS system with only a 10-V drive to the transducer is thermal noise limited, at least an order of magnitude faster than a lock-in based system, and can achieve a dynamic range of 117 dB (the difference in amplitude between the smallest and largest resonance that can be detected is more than 1000).

5.3.4 Apparatus

RUS systems are compact and easy to build, and lend themselves to temperature-controlled environments. There are too many strategies for constructing such systems to describe them here, but suffice it to say that RUS measurements have been performed at 1825–0.25 K [7], and at pressures of up to 150 Bar [8]. However, it is important, to note that the gas surrounding the sample has some effect [5]. At atmospheric pressure, and with strong signals that might be obtained from a 3-mm sample, there is usually little to worry about. At elevated pressures, the gas shifts the resonances in ways which are not fully explored but which affect accuracy; that is, the gas couples to the sample, reducing the perfection of free surface boundary conditions.

At lower temperatures and with submillimeter samples, resonances in the gas can intrude. This is mitigated by reducing the pressure to 100 Pa. Much further reduction will reduce thermal coupling of the sample to the temperature-controlled environment, thereby making accurate determination of sample temperature difficult. Such effects are particularly troublesome if radioactive heating is involved, as it is with U, Pu, and other radioisotopes.

5.3.5 Data

The frequencies of a set of resonances are used to determine elastic moduli, and the widths of those resonances determine ultrasonic attenuation. With in-phase and quadrature data available, one can perform accurate least-squares fits to each resonance to determine these quantities. If this is done, the frequency of a resonance with a Q of 10^4 can be determined to better than a part in 10^6 . Such precision can be of great value in studies at very low temperature or to determine the temperature variation of moduli over very small temperature ranges (the temperature derivative of the elastic moduli of a metal at ambient temperature can usually be determined to an accuracy of 0.3% by measuring over only a 10-K range). However, the absolute determination of moduli is limited by sample geometry, so determining resonance frequencies to about 0.05% is often entirely adequate. This is most easily done by adjusting the phase of a resonance to zero and simply selecting the peak position. The reason for adjusting the phase is that the in-phase component is visually about one-third the width of the amplitude or the quadrature component.

Having acquired data this way, in preparation for the computer-intensive determination of moduli, some important considerations remain. One is that if the sample has, for example, six independent elastic moduli, then it is nearly certain that many more than six resonances are required for a determination of the moduli. The reason, illustrated in Table 5.2, is that many of the lower-lying resonances are determined by the same shear modulus. Thus, for example, the first two resonances may depend only on C_{44} , and hence measurement of

TABLE 5.2. Eighteen Resonances of a Small Sample

n	fex	fr	%err	wt	k	i	df/d	(moduli)	n	fex	fr	%err	wt	k	i	df/d	(moduli)
1	0.488260	0.489423	0.24	1.	4	1	0.00	1.00	1	0.488260	0.486970	-0.26	1.	4	1	0.00	1.00
2	0.578550	0.581709	0.55	1.	4	2	0.00	1.00	2	0.578550	0.577454	-0.19	1.	4	2	0.00	1.00
3	0.662500	0.665424	0.44	1.	6	1	0.10	0.90	3	0.662500	0.662692	0.03	1.	6	1	0.09	0.91
4	0.664360	0.667556	0.48	1.	7	1	0.10	0.90	4	0.664360	0.664805	0.07	1.	7	1	0.09	0.91
5	0.711500	0.715707	0.59	1.	3	1	0.02	0.98	5	0.711500	0.711540	0.01	1.	3	1	0.01	0.99
6	0.714380	0.718480	0.57	1.	2	1	0.01	0.99	6	0.713380	0.714246	-0.02	1.	2	1	0.01	0.99
7	0.758640	0.763605	0.65	1.	8	1	0.01	0.99	7	0.758640	0.758487	-0.02	1.	8	1	0.01	0.99
8	0.766650	0.773214	0.86	1.	1	1	0.04	0.96	8	0.766650	0.767904	0.16	1.	1	1	0.04	0.96
9	0.785160	0.790428	0.67	1.	5	1	0.02	0.98	9	0.785160	0.786240	0.14	1.	5	1	0.02	0.98
10	0.825220	0.831537	0.77	1.	5	2	0.01	0.99	10	0.825220	0.826347	0.14	1.	5	2	0.01	0.99
11	0.836490	0.839861	0.40	1.	6	2	0.32	0.68	11	0.836490	0.836457	0.00	1.	6	2	0.31	0.69
12	0.844280	0.847863	0.42	1.	7	2	0.32	0.68	12	0.844280	0.844243	0.00	1.	7	2	0.31	0.69
13	0.845020	0.848405	0.40	1.	8	2	0.17	0.83	13	0.845020	0.844656	-0.04	1.	8	2	0.17	0.83
14	0.906710	0.870343	-4.01	1.	5	3	0.00	1.00	14	0.000000	0.864396	0.00	0.	5	3	0.00	1.00
15	0.908130	0.910573	0.27	1.	1	2	0.36	0.64	15	0.906710	0.906418	-0.03	1.	1	2	0.34	0.66
16	0.913660	0.912945	-0.08	1.	2	2	0.17	0.83	16	0.908130	0.908173	0.00	1.	2	2	0.16	0.84
17	0.952560	0.918683	-3.56	1.	3	2	0.17	0.83	17	0.913660	0.913771	0.01	1.	3	2	0.16	0.84
18	0.952560	0.952736	0.02	1.	8	3	0.01	0.99	18	0.952560	0.952736	0.02	1.	8	3	0.01	0.99
rms error = 1.3927%									rms error = 0.1028%								

The number of resonances is n , fex are the measured frequencies, and fr are the best fits to a set of computer-determined moduli. %err is the difference in percent between fitted and measured frequencies, wt is the weight given each mode in the fit, k and i are symmetry and harmonic values, and $df/d(\text{moduli})$ are the fractional dependence of each mode on C_{11} and C_{44} for this isotropic sample. RMS error is the rms sum of the errors between fitted and measured resonances. Note that the measurement missed the 14th resonance, so that the fit on the left was poor. Informing the code that a missed resonance exists there immediately produced an adequate fit. Careful examination of the fit on the left reveals how we “guessed” that a resonance was missing. The code used for this is available from Los Alamos National Laboratory.

these two resonances gives information about only one modulus. Typically about three times as many resonances as moduli are required. With present RUS instrumentation, data on modes of up to about 10 MHz are reliable, but limitations of the fitting procedures mean that only the first 40–50 modes are useful for determining quantitative elastic constants.

Another consideration is that occasionally a resonance will be missed. There are two causes. (1) The geometry and exact mounting position of the sample are such that the resonance displacement is zero or along a direction to which the transducer is not sensitive. Note that this will occur much more frequently if the sample makes contact with the transducers at a high symmetry point such as the center of a face instead of the low-symmetry points at the corners. The cure is often as easy as simply remounting or rotating the sample. (2) The shape of the sample produces degeneracies. For example, a perfect cube or cylinder of an isotropic material will have many pairs of resonances that have the same frequencies. Even in anisotropic materials, accidental degeneracies can occur for samples not cut as cubes. If a degeneracy occurs, then a mode will be missed and the data fed to the computation program will have a critical flaw. Recutting the sample may help, but one can often guess at a degeneracy or missing mode by using the analysis program to “predict.” We illustrate this in Table 5.2. It is difficult to give recipes for finding missing modes, but the better the initial guesses for the moduli, the easier this is to do. Unfortunately, some experience is required.

5.3.6 Results

RUS has been used to great effect in physics, materials science, and metallurgy. It has also been used successfully for nondestructive testing [9, 10] by matching the characteristics of the resonances of a manufactured component with those of a known good one, an extensive area beyond the scope of this chapter. What is important here are modulus measurements. In Figure 5.7 we present a typical (neither best nor worst) example of a set of RUS measurements on Be. The data are for a polycrystal and a single crystal sample. Be is hexagonal, with five independent elastic moduli. However, the polycrystal sample will exhibit only two. Directly comparable between the two samples is the bulk modulus, which is expected to be identical. These data confirm this experimentally with very high accuracy. The computations were done with the Los Alamos code, with output discussed at length elsewhere. Of particular note here is a discussion of error bars. At the bottom of Figure 5.7 is a matrix that describes degradation of the fit for a 2% change in chi-square, the conventionally defined goodness-of-fit parameter. The 2% is the result of much experience by us [11] as to how well we can actually determine fit degradation, and is therefore somewhat arbitrary, but it does reflect many direct comparisons of RUS measurements on the same material using differently sized and

Be S200F Textured Polycrystal Be Single Crystal

free moduli are c11, c44

using 10 order polynomials mass= 0.4934 gm
rho= 1.842 gm/cc

free moduli are c33, c23, c12, c44, c66

using 10 order polynomials mass= 0.2264 gm
rho= 1.842 gm/cc

n	fex	fr	%err	wt k i	df/d(moduli)
1	0.633839	0.633252	-0.09	1.00 4 1	0.00 1.00
2	0.635551	0.635684	0.02	1.00 4 2	0.00 1.00
3	0.833434	0.833971	0.06	1.00 6 2	0.21 0.79
4	0.835120	0.835210	0.01	1.00 1 2	0.22 0.78
5	0.835391	0.836387	0.12	1.00 7 2	0.21 0.79
6	0.861719	0.861065	-0.08	1.00 6 3	1.26 -0.26
7	0.862282	0.862273	0.00	1.00 3 2	0.08 0.92
8	0.862721	0.862542	-0.02	1.00 1 3	1.26 -0.26
9	0.000000	0.863094	0.00	0.00 8 2	0.08 0.92
10	0.864708	0.863590	-0.13	1.00 7 3	1.26 -0.26
11	0.864954	0.863766	-0.14	1.00 2 2	0.08 0.92
12	0.981956	0.982200	0.02	1.00 2 3	0.63 0.37
13	0.982327	0.983148	0.08	1.00 8 3	0.63 0.37
14	0.984162	0.984318	0.02	1.00 3 3	0.63 0.37
15	0.000000	0.986349	0.00	0.00 5 1	0.00 1.00
16	0.000000	0.987323	0.00	0.00 5 2	0.00 1.00
17	0.000000	0.988265	0.00	0.00 5 3	0.00 1.00
18	1.021700	1.022765	0.10	1.00 5 4	1.18 -0.18
19	1.023870	1.023852	0.00	1.00 5 5	1.18 -0.18
20	1.057160	1.057543	0.04	1.00 5 6	2.32 -1.32
21	1.185330	1.185270	-0.01	1.00 6 4	0.49 0.51
22	0.000000	1.185470	0.00	0.00 1 4	0.49 0.51
23	0.000000	1.185631	0.00	1.00 7 4	0.49 0.51
24	1.188630	1.187391	-0.10	1.00 4 3	0.30 0.70
25	1.218560	1.219204	0.05	1.00 2 4	0.04 0.96
26	1.220240	1.220656	0.03	1.00 8 4	0.04 0.96

Bulk Modulus= 116.6 GPa

C₁₁ C₆₆
315.5 149.2

d1 d2 d3
0.64471 0.64572 0.64348

loop# 1 **rms error= 0.0704 %**

chisquare increased 2% by the following
% changes in independent parameters
0.02 0.01
0.00 0.03

n	fex	fr	%err	wt k i	df/d(moduli)
1	0.635039	0.635302	0.04	1.00 4 1	0.00 0.00 0.29 0.71
2	0.788106	0.788153	0.01	0.00 6 2	0.00 0.00 0.05 0.15 0.79
3	0.835332	0.834795	-0.06	1.00 1 2	0.00 0.00 0.07 0.00 0.93
4	0.959970	0.957946	-0.21	1.00 3 2	0.00 0.00 0.01 0.00 0.99
5	0.999543	1.001015	0.15	1.00 6 3	0.01 0.00 0.08 0.16 0.76
6	1.036990	1.034969	-0.19	1.00 5 1	0.00 0.00 0.05 0.00 0.95
7	1.047030	1.047225	0.02	1.00 4 2	0.00 0.00 0.00 0.91 0.09
8	1.075950	1.076550	0.06	1.00 7 2	0.00 0.00 0.07 0.00 0.93
9	1.121610	1.122433	0.07	1.00 2 2	0.01 0.00 0.03 0.35 0.61
10	1.149920	1.150491	0.05	1.00 5 2	0.00 0.00 0.07 0.00 0.93
11	1.160580	1.161102	0.04	1.00 8 2	0.01 0.00 0.01 0.69 0.30
12	1.195890	1.196787	0.08	1.00 8 3	0.01 0.00 0.06 0.41 0.53
13	1.254030	1.253338	-0.06	1.00 5 3	0.01 -0.01 0.11 0.00 0.89
14	1.283260	1.280404	-0.22	1.00 2 3	0.01 0.00 0.01 0.89 0.09
15	1.393150	1.395002	0.13	1.00 2 4	0.01 0.00 0.01 0.55 0.43
16	1.480820	1.485443	0.31	1.00 5 4	0.70 -0.01 0.01 0.06 0.24
17	1.487210	1.486888	-0.02	1.00 1 3	0.47 -0.01 0.01 0.11 0.42
18	1.501830	1.500589	-0.08	1.00 7 3	0.02 0.00 0.03 0.00 0.95
19	1.503350	1.503580	0.02	1.00 1 4	0.30 0.01 0.01 0.08 0.60
20	1.525570	1.524154	-0.09	1.00 7 4	0.72 0.00 0.00 0.18 0.10
21	1.527700	1.530233	0.17	1.00 5 5	0.66 -0.01 0.04 0.03 0.28
22	1.534700	1.531091	-0.24	1.00 6 4	0.00 0.00 0.04 0.43 0.53
23	1.549320	1.547966	-0.09	1.00 4 3	0.01 0.00 0.03 0.62 0.33
24	1.562710	1.560613	-0.13	1.00 3 3	0.76 0.00 0.00 0.08 0.15
25	1.612020	1.615287	0.20	1.00 8 4	0.01 0.00 0.02 0.45 0.52
26	1.641860	1.643048	0.07	1.00 3 4	0.01 0.00 0.05 0.00 0.95

Bulk Modulus= 116.5 GPa

C₃₃ C₂₃ C₁₂ C₄₄ C₆₆
356.7 14.00 26.75 162.2 133.4

d1 d2 d3
0.50540 0.60198 0.40390

loop# 3 **rms error= 0.1323 %**

chisquare increased 2% by the following
% changes in independent parameters
0.06 7.55 0.72 -0.02 -0.02
0.01 0.62 -1.81 -0.01 0.11
0.10 -0.54 -0.02 -0.01 -0.02

FIG. 5.7. Results for polycrystal and single crystal Be at 295 K. Note the correspondence between the bulk moduli, which are expected to be the same; d1, d2, and d3 are dimensions in cm.

shaped samples. This matrix has columns that correspond to the free elastic moduli in the order they appear at the top of the fits. The entries in the columns are determined by the principal radii of curvature of the error function used in the fit. These radii are not in the directions of elastic moduli; that is, the n -dimensional bowl formed by the error function (where n is the number of free moduli) has principal curvatures directed along vectors determined by the sample shape and moduli, and these are not along elastic modulus axes. Thus the fit may be degraded much less if several moduli are varied in such a way as to track along a principal curvature direction than if a single modulus is

varied. The entries in the matrix describe how much degradation occurs in the moduli as combinations of moduli are varied along the principal curvature vectors. Only the few shallowest directions (rows) are computed. The effect is as follows. Looking at the hexagonal fit on the right of Figure 5.7, we see that the largest entry in the first column is 0.1%, and this is our estimated error in C_{33} . Similarly, in the second column, the largest entry is 7.55%, and this is our estimated error for C_{23} . Although this error appears large, C_{23} is small, so the effect on the sound speeds and bulk modulus, all of which use C_{23} in combination with C_{33} , is small. Finally, the errors for the shear moduli are always small, such as the 0.02% estimated error for C_{44} . None of these errors are closely related to the 0.132% RMS error for the fit, and it is very wrong to use this RMS error as an error bar for moduli. The principal curvatures of the error function *must* be accounted for.

5.4 Computation of Resonances and Data Analysis

The aim of any spectroscopic technique is to extract information about the sample from the experimentally determined spectrum. In the case of RUS, the information we seek is the linear, second-order elastic tensor. As previously described RUS is used to measure the normal frequencies of vibration of the object under study. These normal frequencies of vibration depend on the physical symmetry of the object (i.e., its shape), the symmetry of its elastic tensor (which is determined by the crystal symmetry of the object—cubic, orthorhombic, isotropic, etc.), its density, and its dimensions. Although RUS has proved quite successful in extracting the elastic moduli of many new materials, including single crystal as well as polycrystalline samples, successful implementation depends on a number of key factors, one of which is the ability to perform very complex computations of resonances.

From a computational perspective, the most important requirement is the availability of a rapid and robust algorithm to compute the normal frequencies of the object given its dimensions, density, and elastic moduli. One can then employ this “forward” computation as part of another algorithm to find a “best fit” (in a least-squares sense) between the observed and calculated spectrum with the elastic moduli as the variable parameters. A variety of such minimization algorithms using different methods to search the parameter space are available. For application to RUS, we chose energy minimization for the forward computation and the Levenberg-Marquardt process [11] for the fitting algorithm, and these have been incorporated into the Los Alamos code, application of which was briefly described in the previous section.

In this section we summarize the essential features of Lagrangian energy minimization techniques for the computation of resonances and highlight the

features necessary for the effective implementation of the “inverse” problem — namely, extraction of the elastic moduli from experimentally measured resonance frequencies.

5.4.1 Formulation of the Problem: Lagrangian Minimization

Because a complete analytical solution for the computation of the free vibrations of solids does not exist, one must rely on available approximate methods. Of these, the most frequently invoked computational approaches have been finite-element methods and energy minimization techniques. Finite-element methods rely on balancing the forces on a differential volume element and calculating its response. This requires complete knowledge of the relevant forces acting on a particular volume element and the forms of solutions that are possible in order to prevent the accidental exclusion of one or more modes. Energy minimization methods, on the other hand, determine the minimum energy, and thus the equilibrium configuration for the object. They are therefore independent of specific solutions and produce energy minima that automatically determine all vibrational modes. Of the energy minimization techniques, that of Lagrangian minimization is the one most used in the analysis of RUS data, having the further advantage of speed because, unlike finite element methods, Lagrangian minimization computational “time” goes roughly as the area of an object, not the volume. Using modern personal computers, for example, the lowest (approximately) 40 modes may be determined in several seconds; equivalent solutions by finite-element methods would require at least several minutes.

The stationary solutions of the mechanical Lagrangian for an elastic solid are precisely the free vibrations of the body — this amounts to finding the solutions to the elastic wave equation with free surface boundary conditions; see Migliori and Sarrao [1] for a complete treatment. The essential procedure begins with an arbitrarily shaped object whose volume, V , is bounded by its free surface, S — a critical point that needs to be remembered when making a measurement. The Lagrangian is given by

$$L = \int_V (KE - PE) dV \quad (5.5)$$

where KE is the kinetic energy density

$$KE = \frac{1}{2} \sum_i \rho \omega^2 u_i^2 \quad (5.6)$$

and PE is the potential energy density

$$PE = \frac{1}{2} \sum_{i,j,k,l} c_{ijkl} \frac{\partial u_i}{\partial x_j} \frac{\partial u_k}{\partial x_l} \quad (5.7)$$

Here, u_i is the i 'th component of the displacement vector; ω , the angular frequency, derives from the assumption of harmonic time dependence (i.e., $u(t) = u_0 e^{i\omega t}$); c_{ijkl} is a component of the elastic tensor; and ρ is the density. Except where noted, subscripts i, j , etc., refer to Cartesian coordinates and run from 1 to 3.

To find the minimum of the Lagrangian (and hence the desired equilibrium configuration of the system), we calculate the differential of L as a function of δu , the arbitrary variation of u in V and on S . Substituting Eqs. 5.6–5.7 in Eq. 5.5, calculating the differentials, keeping only first-order terms, and finally integrating by parts yields

$$\begin{aligned} \delta L = \int_V \left\{ \sum_i \left[\rho \omega^2 u_i - \sum_{j,k,l} c_{ijkl} \frac{\partial^2 u_k}{\partial x_j \partial x_l} \right] \delta u_i \right\} dV \\ - \int_S \left\{ \sum_i \left[\sum_{j,k,l} \bar{n}_j c_{ijkl} \frac{\partial u_k}{\partial x_l} \right] \delta u_i \right\} dS \end{aligned} \quad (5.8)$$

Because δu_i is arbitrary in V and on S , the values of u_i that correspond to stationary points of L , that is $\delta L = 0$, must satisfy the condition that both terms in square brackets in Eq. 5.8 are zero. Setting the first such term equal to zero yields the elastic wave equation. The second square bracketed term is an expression of free surface boundary conditions (and it also describes the surface traction); \bar{n}_j is the unit vector normal to S . For a free body, the latter term sums to zero and need not be considered further.

Thus the set of u_i that satisfies the previously mentioned conditions are precisely those displacements that correspond to ω being one of a discrete set of normal mode frequencies of (free) vibration of the system. This simple result suggests that the normal vibrations of an object may be calculated by applying a variational method to determine both the normal mode frequencies and the description of the physical oscillations. The Rayleigh-Ritz method provides the means to do this.

5.4.2 Application of the Rayleigh-Ritz (R-R) Variational Method

The implementation of such an approach involves expanding the u_i in a complete set of basis functions, substituting that expression into Eq. 5.5, and carrying out the process previously outlined to find the stationary points of the Lagrangian. One arrives at an equation similar to Eq. 5.8 in which the u_i are replaced by expansions in basis functions. This procedure yields an eigenvalue problem easily solved by common techniques.

Let $\{\phi_\lambda\}$ be a complete set of (R) functions suitable for expansion of the displacement vector u_i ; thus

$$u_i = \sum_{\lambda} a_{i\lambda} \phi_\lambda = (\cdots a_\lambda \cdots)_i (\cdots \phi_\lambda \cdots)^T = \mathbf{a}_i \boldsymbol{\phi}^T. \quad (5.9)$$

Equation 5.9 expresses the expansion in matrix notation, where the $()$ terms in parentheses are a product of a row vector with a column vector; and, as usual, $()^T$ denotes the transpose, and $()_i$ denotes the i 'th row of the \mathbf{a} matrix. Substituting this expression for u_i in Eq. 5.5 (via Eqs. 5.6–5.7) eventually gives

$$L = \frac{1}{2}(\omega^2 \mathbf{a}^T \mathbf{E} \mathbf{a} - \mathbf{a}^T \boldsymbol{\Gamma} \mathbf{a}). \quad (5.10)$$

Here, \mathbf{E} and $\boldsymbol{\Gamma}$ are matrices whose order is determined by R , the number of basis functions, and whose elements are given by

$$E_{\lambda i \lambda' i'} = \delta_{ii'} \int_V \phi_\lambda \rho \phi_{\lambda'} dV \quad (5.11)$$

and

$$\Gamma_{\lambda i \lambda' i'} = \sum_{j, j'} c_{ij i' j'} \int_V \frac{\partial \phi_\lambda}{\partial x_j} \frac{\partial \phi_{\lambda'}}{\partial x_{j'}} dV. \quad (5.12)$$

We will return to briefly describe some relevant properties of \mathbf{E} and $\boldsymbol{\Gamma}$ later. Following the earlier prescription to find the stationary points of the Lagrangian, we note that now we should obtain an equation analogous to Eq. 5.8 but with δL in terms of δa , not δu . To obtain δL from Eq. 5.10, we first note that \mathbf{E} and $\boldsymbol{\Gamma}$ are not operators, but are functions of the basis functions ϕ only (and of course the density and elastic tensor, respectively), but not of displacement variables; second, we see that the displacement is now in terms of the expansion coefficients a ; and third, we note that $\mathbf{a}^T \mathbf{M} \mathbf{a} \sim a^2 \langle m \rangle$ and $\partial(a^2 \langle m \rangle)/\partial a = 2a \langle m \rangle$ for any matrix \mathbf{M} , given the previously mentioned constraints. Thus the differential of the Lagrangian (Eq. 5.10) in matrix notation becomes

$$\delta L = \omega^2 \mathbf{E} \mathbf{a} - \boldsymbol{\Gamma} \mathbf{a} = 0 \quad (5.13)$$

In this form, the stationary points of the Lagrangian are found simply by solving the eigenvalue problem that results from Eq. 5.13, namely,

$$\omega^2 \mathbf{E} \mathbf{a} = \boldsymbol{\Gamma} \mathbf{a} \quad (5.14)$$

5.4.3 Choice of Basis Functions

Most samples encountered are homogeneous so that both the density and the elastic moduli are independent of position within the sample. Thus, with

ρ and c constant in Eqs. 5.11 and 5.12, computation of matrix elements for \mathbf{E} and $\mathbf{\Gamma}$ is greatly simplified. The choice of basis functions is quite arbitrary. However, since Eq. 5.14 is a formulation of the problem defined by Eq. 5.8, which is a function of both the displacement functions and their derivatives, it is important that, not only will a series of basis functions converge to any reasonable displacement functions, but also that the series consisting of derivatives of the displacement functions will be convergent. This was first recognized by Demarest [12]. Thus any complete set capable of representing the displacement functions and their derivatives will work. Then, as the number of functions approaches infinity, all the eigenvalues in Eq. 5.14 approach the exact values. Practically, however, one must truncate the basis set to some finite number. The effect of this truncation is that the eigenvalues approach the true value from above as the number of basis functions increases (Cauchy's inequality). The following examples confirm that the choice of functional form for the basis functions is important.

Holland [13] used products of trigonometric functions and the Rayleigh-Rite (R-R) method to compute the resonant properties of a piezoelectric ceramic Rectangular Parallel (RP). These functions were of the form

$$\begin{aligned}\phi_{mnp} &\sim \cos\left(\frac{m\pi x}{l_x}\right) \sin\left(\frac{n\pi y}{l_y}\right) \sin\left(\frac{p\pi z}{l_z}\right); \text{ and } \phi'_{mnp} \\ &\sim \sin\left(\frac{m\pi x}{l_x}\right) \cos\left(\frac{n\pi y}{l_y}\right) \sin\left(\frac{p\pi z}{l_z}\right); \text{ etc.}\end{aligned}\quad (5.15)$$

where l_s ($s = x, y, \text{ or } z$) are the dimensions of the RP. The basis set is then built up by generating various combinations of (m, n, p) triplets; Holland used selected triplets with values of 0 to 15 (not continuous).

Because the first three modes of a cube are triply degenerate and are known exactly, (Lamé modes), Holland computed these for comparison with results obtained using his trial functions. He found that his computation led to a splitting of the lowest Lamé mode (as well as the next higher Lamé mode) into a doublet and a singlet. He used 9, 30, and 99 basis functions and found that, even for 99 functions, the doublet converged to an accuracy limited to $\sim 1\text{--}2\%$ in both cases, but the singlet exhibited much slower convergence—10% for the lower Lamé mode and 4% for the higher one. Demarest [12] used a basis set consisting of products of Legendre polynomials

$$\phi_{ijk} = P_i\left(\frac{2x}{l_x}\right) P_j\left(\frac{2y}{l_y}\right) P_k\left(\frac{2z}{l_z}\right) \quad (5.16)$$

to compute the resonance frequencies of a solid cube. Here, $i, j, \text{ and } k$ are the order of the Legendre polynomial. Demarest found that the maximum order of (i, j, k) triplets depends on the symmetry of the mode represented. For

example, he could use any combination up to $i = j = k = 9$ for antisymmetric torsion and dilation modes, whereas for symmetric flexure modes the total order could not exceed 10 (i.e., $i + j + k \leq 10$). Demarest used a basis set of 60 functions and found that the accuracy with which the four lowest Lamé modes was computed was 0.05% or better. Both Holland and Demarest used similar symmetry considerations in selecting and grouping basis functions, determined the mode shapes of some of the lowest frequency vibrations, and also worked out techniques for extraction of the elastic moduli from their measured resonance spectra. Although the work of Demarest was pivotal in the application of the resonance method to obtain accurate elastic moduli of solids, it was limited to cubic specimens with cubic crystal symmetry.

Ohno [14] then extended the work of Demarest by working out the free vibrations of a crystal of general symmetry and RP geometry. He also used Legendre polynomials as basis functions but worked out the Γ matrix elements, including the symmetry properties imposed by all seven crystal classes. This occurs in Eq. 5.12 because of the symmetry of the c tensor. For example, for a triclinic crystal (lowest symmetry), there are 21 elastic moduli represented in the two-index notation by a 6×6 matrix whose elements $c_{ij} = c_{ji}$ and where c_{ij} are all unique and nonzero. For crystals with higher symmetry, $c_{ij} = 0$ for various i and j , depending on the symmetry: for cubic crystals, for example, only three independent moduli are needed, c_{11} , c_{12} , and c_{44} . The c_{ij} matrix then has $c_{11} = c_{22} = c_{33}$, $c_{44} = c_{55} = c_{66}$, and $c_{12} = c_{13} = c_{23}$, with $c_{ij} = 0$ for all other i and j . A more detailed discussion of the representation of the c matrix for various crystal classes and the conversion of the four-index tensor notation to the two-index matrix notation for c may be found in Migliori and Sarrao [1].

Introduction of the symmetry properties of c in Eq. 5.12 reduces the number of elastic constants to be determined. In addition to crystal symmetry, the physical geometry of the RP sample introduces three mirror planes of symmetry (xy , yz , etc.). The displacement functions must then be invariant to $x \rightarrow -x$, $y \rightarrow -y$, and $z \rightarrow -z$. This reduces the Γ matrix to block diagonal form (eight blocks, corresponding to all combinations of symmetric and antisymmetric with respect to reflection in three mirror planes), thus significantly lowering the computation time in the diagonalization of Eq. 5.14. The previously mentioned considerations require the crystal axes to be parallel with the axes of the RP. If this is not possible, the solution is much more complicated but tractable [1, 15, 16]. For readers interested in a more in-depth treatment of group theoretical applications to mechanical vibrations in RP, Mochizuki [17] also provides a good starting point.

Ohno also reported a scheme for the determination of the elastic moduli from the Resonant Ultrasound spectrum which, although superior to that of Demarest, was not completely amenable to automatic computation. Such a

method was later developed at Los Alamos [4] and will be briefly described in the next section.

As mentioned in a previous section, the resonant ultrasound method has been applied to samples of geometries other than RP with associated advantages and disadvantages. The use of RUS to determine elastic constants for a spherical solid has been called the resonant sphere technique (RST). The basis functions used to treat such spherical samples take advantage of the spherical symmetry and are products of radial functions and spherical harmonics [18, 19, 20, 21].

The choice of an orthonormal basis set simplifies Eq. 5.14 because in this case \mathbf{E} becomes the unit matrix and the resulting eigenvalue problem becomes easier to solve. This is so because, for the more general problem Eq. 5.14, the matrix \mathbf{E} is required to be positive definite.

Visscher [5] was able to show that, using basis functions of simpler form, one can easily compute the vibrations of all sample shapes examined for use in RUS measurements (cube, RP, and sphere) including anisotropic materials, as well as several additional shapes. It is thus the most general method proposed to date. Further, using this general basis, resonances for shapes in transition from one symmetry to another (i.e., sphere to spheroid or ellipsoid) were computed to show the behavior of vibrational modes as a function of symmetry; and, for several shapes, families of spectra were shown as a function of aspect ratio. The basis functions are simple algebraic polynomials in Cartesian coordinates, where ϕ of Eq. 5.9 is of the form

$$\phi_\lambda = x^l y^m z^n \quad (5.17)$$

where $\lambda = (l, m, n)$ serves as a basis function index and has the same meaning as in Eqs. 5.9–5.12. Because of the form of Eq. 5.17, this computational approach has been called the XYZ method, and it has been used in applications of RUS. The XYZ method has also been used by others in conjunction with the Resonant Sphere Technique (RST) [16, 20, 22]. Once again, use of the physical symmetry of the object whose normal vibrations are sought reduces the problem, as was previously mentioned. Visscher also gives an algorithm coded in Fortran to compute the vibrations for the most general case to date, that which occurs for the case where c_{ijkl} has the lowest possible symmetry.

The most unique aspect of the XYZ algorithm is that Eq. 5.17 reduces the matrix elements of both \mathbf{E} and Γ to the following form:

$$f(p, q, r) = \int_V x^p y^q z^r dV \quad (5.18)$$

Here, p , q , and r are positive integers that arise, for example, in the computation of matrix elements of \mathbf{E} in Eq. 5.11 with $\lambda = (l, m, n)$ and $\lambda' = (l', m', n')$

so that $p = l + l'$, $q = m + m'$, and $r = n + n'$. Similar expressions then occur for Γ in Eq. 5.12 because the derivatives of ϕ_λ will be of the same form. Reduction of all necessary integrals to this simple form allows their analytical evaluation for a variety of shapes, V , as mentioned previously. For the case of the RP, Eq. 5.18 becomes

$$f(p, q, r) = \frac{8d_1^{p+1}d_2^{q+1}d_3^{r+1}}{(p+1)(q+1)(r+1)} \quad (5.19)$$

and for the case of the solid sphere, as well as less symmetric objects, one obtains a slightly more complicated expression that is nevertheless only a function of p , q , r , and the dimensions d .

For comparison with discussions of basis set size earlier in this section, the XYZ method selects all basis functions specified by the condition $l + m + n \leq N$, which generates \mathbf{E} and Γ matrices of order $R = 3(N+1)(N+2)(N+3)/6$. The accuracy of the method was checked by direct measurement of a large computer-machined isotropic aluminum sample with no particular symmetry shaped as an ellipsoid with all semimajor axes different [5]. The results indicate that for the lowest 30 modes and a basis set size where $N = 9$, the difference between measured and computed resonances was $<0.3\%$, consistent with the machining accuracy. The XYZ method thus allows the analytical evaluation of all necessary integrals by means of simple algebraic expressions of the form of Eq. 5.19, and is able to calculate both the resonance frequencies and the mode shapes (determined by the eigenvectors in Eq. 5.14) applicable to a variety of shapes and to materials with any crystal symmetry.

Our experience with numerical computations involving Eq. 5.14 is that, as one increases the number of basis functions, \mathbf{E} may no longer be positive definite. This phenomenon is usually mode dependent and may be caused by insufficient numerical precision, even when double precision is used. Similar numerical instabilities were reported by Young and Dickinson [23], for example, who also used the R-R method to compute resonance frequencies of solids of various shapes. The basis set chosen consisted of simple algebraic polynomial series in x , y , and z (as for the XYZ method—of which, apparently, these authors were not aware).

An excellent review of the historical developments leading to RUS as an established technique for elastic moduli determination may be found in Migliori and Sarrao [1].

5.4.4 Determination of the Elastic Moduli from RU Spectra: The Inverse Problem

Several authors have reported work on the problem of extracting elastic moduli from experimental RUS data [4, 12, 14, 18, 24]. However, of these,

only Migliori and coworkers [4] have advanced the solution of the so-called inverse problem significantly enough to enable an automatic algorithm that includes proper error analysis and goodness-of-fit parameters. The algorithm is based on the Levenberg-Marquardt functional minimization scheme [11] and is part of the Los Alamos code for use in RUS applications. This computational package has successfully determined elastic moduli, crystal dimensions, and Euler angles relating crystallographic axes to sample surfaces in the case of a misaligned sample.

Simply stated, the algorithm carries out a nonlinear least-squares fit by minimizing the functional defined by the sum of weighted residuals

$$F = \sum_{i=1}^N w_i (f_i - g_i)^2 \quad (5.20)$$

where \mathbf{g} and \mathbf{f} are the vectors of measured and calculated frequencies, respectively, and w_i is a weighting factor (as usual in such fitting methods, this may be taken as $1/g^2$). N has to be chosen large enough to ensure some amount of overdetermination (i.e., where there are more data than the number of parameters one wishes to fit). The minimization of the previously mentioned functional begins by expansion of F into a Taylor series about x_o , the vector (of length M) containing the initial guesses of the parameters to be determined. The expansion will contain derivatives (first order only are retained) of f with respect to each of the variable parameters. Recall that $f = \omega/2\pi$, with ω obtained from the diagonalization of Eq. 5.14. These derivatives are then used in an iterative scheme to compute the next approximation to the parameters. An in-depth discussion of the fitting procedure as well as a detailed analysis of errors and goodness-of-fit may be found in [1]. Unfortunately, both experience and good initial guesses of elastic moduli are still important for consistent success in using even these well-tested and frequently used codes to analyze RUS data. The rewards, are, however, substantial, as shown by the examples in the next section.

5.5 Examples of Applications of RUS

The data from a RUS experiment are of the form $A(f)$, where f is a set of discrete frequencies in the region of interest. Near a resonance, the sample will take about Q cycles to reach a stable amplitude of oscillation. Each normal mode must therefore be measured for at least $t = Q/f$ sec. For a material with a Q of 10,000 and a resonance near 200 kHz, $t = 50$ mS. Materials with low Q (< 100) can be measured more quickly but rarely produce enough amplitude for accurate measurement. For measurement times less than Q/f , peaks will still appear in $A(f)$, but the line shape may be distorted. The center

frequencies and widths of the peaks are the most useful data—the amplitude is generally such a critical function of the point-contact support that it is not useful. A peak-finder program is useful to extract peak information from a large number of scans, but in noisy data, or where peaks interfere, accurate results are best obtained by fitting to a Lorentzian model. The center frequencies are the input to the RPR codes, discussed elsewhere in this article, which can provide quantitative results for the elastic moduli. The widths represent the internal friction of the specific mode at f . This represents the actual mechanical dissipation (and losses via nonlinear effects), compared to a pulse-echo experiment, where scattering may attenuate a pulse without dissipation. An accurate determination of peak widths clearly requires a sufficient number of data points within each peak.

Even without determining the elastic tensor from the measured resonance frequencies, the experimental setup that RUS uses is so amenable to varying environmental parameters (temperature, magnetic field) that much can be learned from the variation of the frequencies and widths with some parameter. This enables one to obtain useful data from any piece of material—often a randomly shaped fragment—that displays measurable resonances.

The expected behavior of the elastic moduli of a “stable” solid with varying temperature, and thus of the resonance frequencies, is well parameterized within some simple models [26–29]. This general behavior is linear with a negative slope at high temperatures, curving at lower temperatures to approach $T = 0$ with zero gradient. Deviations from this behavior show interesting properties of the material; in particular, since the moduli are derivatives of the free energy with respect to strain, phase transitions of all thermodynamic orders will affect the variation of the resonance frequencies with temperature. The expected deviations may be predicted within various theories (e.g., Landau theory [30]), enabling model parameters, temperature gradients, and the order of a transition to be determined.

Figure 5.8 shows the variation of the frequency of the first four resonances of a single crystal sample of the Colossal Magnetoresistance (CMR) material $\text{La}_{0.83}\text{Sr}_{0.17}\text{MnO}_3$. This composition lies near both a structural and a magnetic phase boundary. The first-order nature of the structural transition is shown by the hysteresis observed, even though the transition does not show a very sharp step. The magnetic transition shows a break in slope without hysteresis and, like the structural transition, is more apparent in some modes.

This material is only slightly distorted from cubic throughout this temperature range, and cubic fits to this sample show the lowest line to be dominantly (cubic) c_{44} , the fourth line to be (cubic) $c^* = (c_{11} - c_{12})/2$, and the middle lines to be mixed modes. By observing just the first and fourth lines, one may see the effects of an applied magnetic field on the shear moduli (Fig. 5.9) without the need to fit the moduli at each field and temperature. The mounting of the

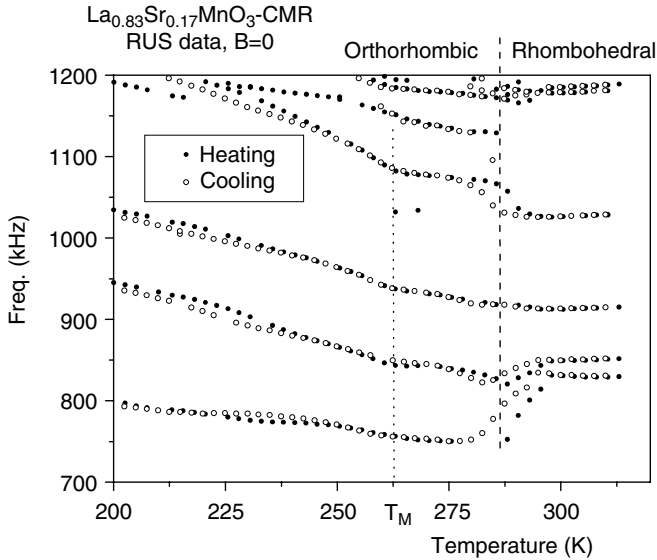


FIG. 5.8. Temperature variation of the center frequencies of the four lowest modes of a single crystal CMR material.

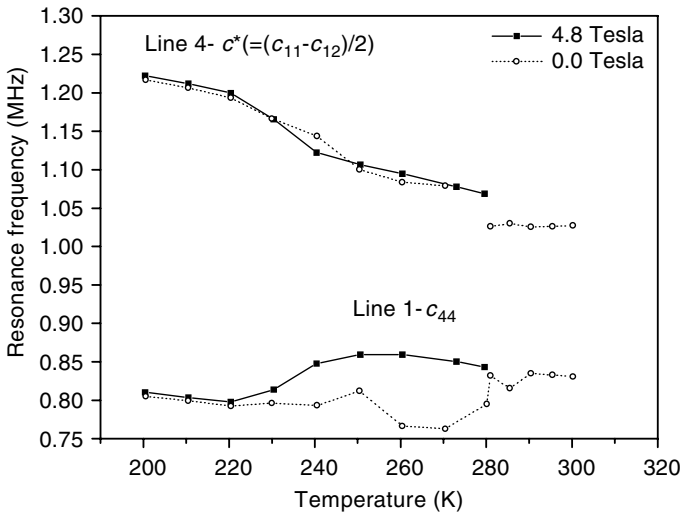


FIG. 5.9. Temperature variation of the (cubic) shear moduli of a single crystal CMR sample at different magnetic fields.

sample within the vertical superconducting magnet constrains the field to be only along a body diagonal. If the atomic structure of the material is known, the actual atomic displacements associated with the strains for the particular mode can be determined and connected to details of the transition [31].

Other anomalous behavior is shown in the B2-structure martensites. The plot for a single crystal of AuZn (Fig. 5.10), shows that many of the modes have a positive temperature coefficient, even at temperatures 150 K above the martensitic transition. The same is true for another B2 system, $\text{Ni}_{0.62}\text{Al}_{0.38}$ (Fig. 5.11), for which only the center frequency and width for the first mode are shown. The hysteresis (not shown) is about 20 K for this transition, but the transition itself is enormously wide, taking nearly 100 K from start to finish. The dissipation, as indicated by the width of the peak, jumps at the first transformation “snap” and then becomes so large at the main bulk transformation that the peak cannot be detected. The low-temperature behavior of the dissipation is presently under more detailed study.

Although qualitative data like these on dissipation are straightforward to extract from RUS data, quantitative results are more difficult and need certain model assumptions to be made. Dissipation can be included as a complex contribution to the elastic modulus and fitted along with the real part, but care must be taken, since relaxation processes may have a large frequency dependence, which may cause variations over the range of a RUS scan [1, 32].

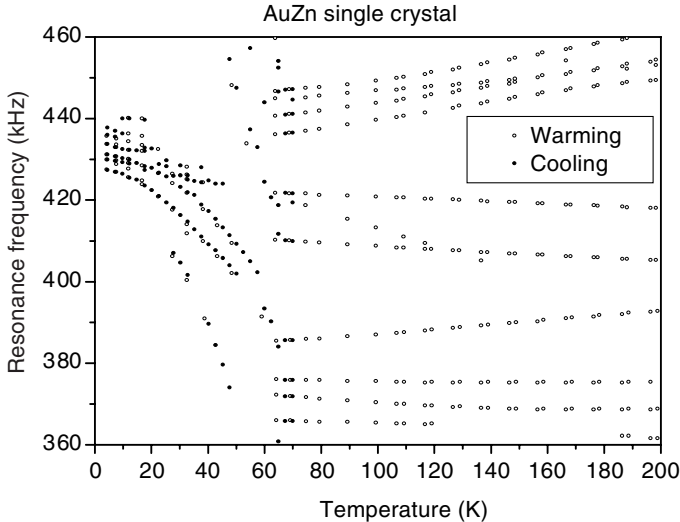


FIG. 5.10. Temperature variation of the mode frequencies for AuZn, $M_s = 64$ K.

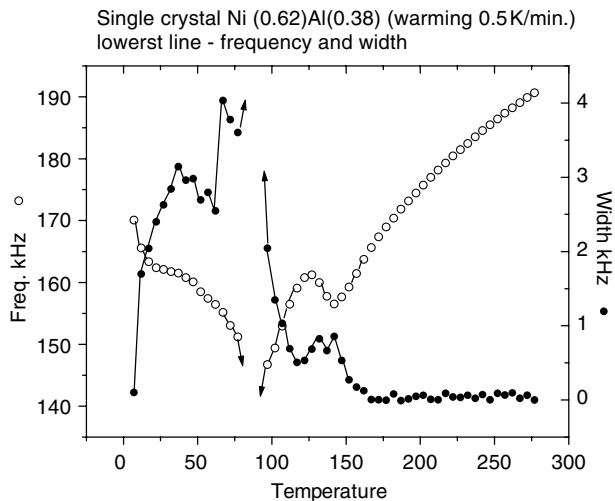


FIG. 5.11. Frequency and width (dissipation) of a C^* shear mode at the martensitic transformation of $\text{Ni}_{0.62}\text{Al}_{0.38}$, $M_s = 78$ K.

The process of fitting the elastic moduli at each temperature can be very time-consuming, but if there are resonances that are dominated by one modulus, the variation of that line will reflect the variation of the c_{ij} . In general, this will require a good fit at one temperature and will only be useful for the diagonal moduli c_{ii} . A test of this was made using a sample of polycrystalline (isotropic) heat-treatable steel (Fig. 5.12), and good agreement between “extrapolated” values and those fitted at each point was found.

Electronic as well as structural effects appear in the free energy and will show up in both the frequency and width data. Figure 5.13 shows the frequency dependence of two resonances of a sample of polycrystal Nb. RUS measurements are intrinsically very precise, but this measurement is only possible because the Q of the sample was $\sim 100,000$. The superconducting transition is clearly visible as a break in the slope of the temperature dependence of these low-frequency resonances. The elastic constants have been found to exhibit the same temperature dependence as the free energy in both states [33].

The narrow-band-gap semiconductor FeSi, because its small activation energy corresponds to nearly room temperature, shows an electronic contribution to the free energy that is apparent at low temperatures. This causes a deviation from the expected elastic behavior, shown in Figure 5.14, by a function of the form used by Varshni. The agreement is good at low temperatures but deviates at higher temperatures. The inset is a plot of the width (dissipation) of a shear resonance. The maximum in the dissipation corresponds to the

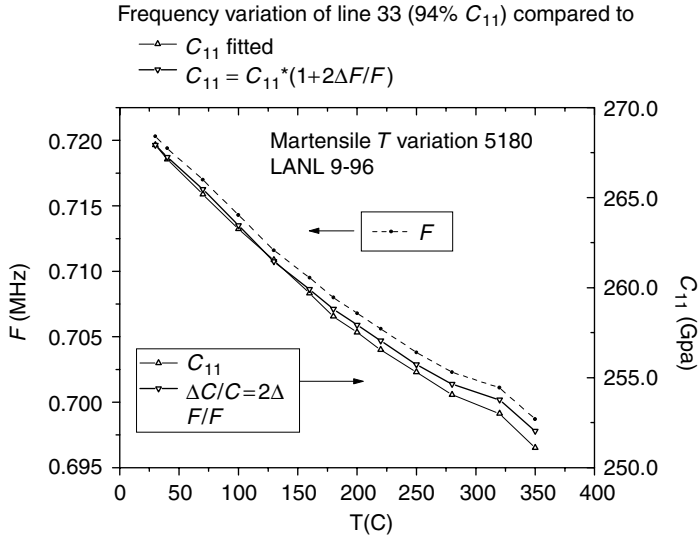


FIG. 5.12. Graph comparing the variation of the frequency, fitted C_{11} modulus, and the value of C_{11} extrapolated from the room temperature fit by assuming $\Delta C/C = 2\Delta f/f$.

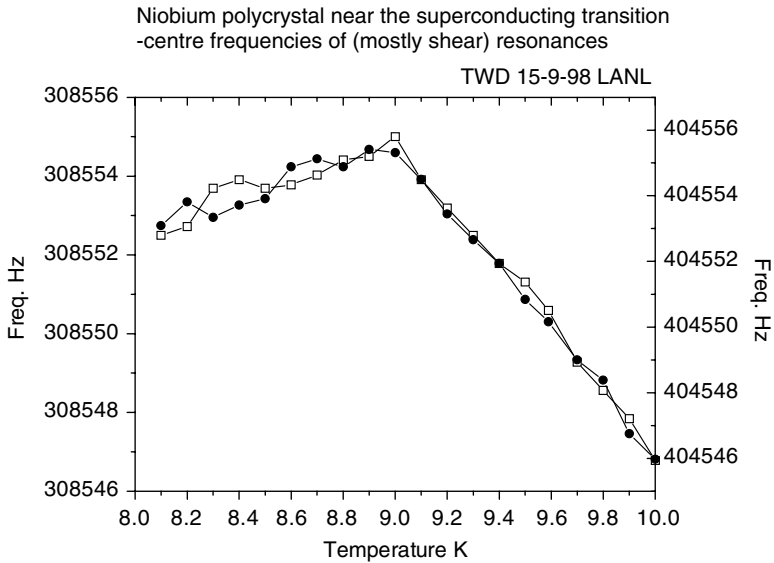


FIG. 5.13. The superconducting transition in polycrystalline Nb.

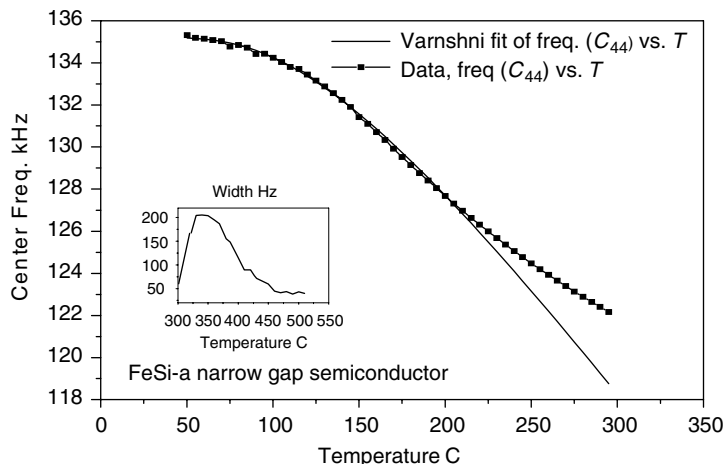


FIG. 5.14. Deviation from expected behavior in the narrow-gap semiconductor FeSi.

activation energy ($\Delta/2$) [34]. These data suggest unusual properties of the electronic density of states near the Fermi level, later confirmed by thermodynamic and photoemission experiments [35, 36].

In summary, RUS has many strengths and a few weaknesses. For a reasonably homogeneous sample of almost any shape, and for sizes down to a fraction of a millimeter, the temperature and magnetic field dependence of the resonance frequencies and widths can be measured, and useful data can be extracted. The mounting configuration used makes it difficult to apply a magnetic field in an arbitrary direction, but transducers using piezoelectric films [37] can be made to overcome this problem.

To extract quantitative results, the sample must conform to a reasonable theoretical model—for moduli, it must be a homogeneous solid of measured size and density, with a well-defined symmetry; for dissipation, one must apply a model of the dissipation mechanism with some idea of the apparent symmetry of the internal friction and its frequency dependence. Without such correspondences, one cannot obtain quantitative results, and for samples with cracks or inclusions, there may even be no useful qualitative results.

RUS does provide a measure of assurance over the results of pulse-echo measurements, where a series of wave velocities will be measured, but whether the results of pulse-echo measurements are consistent with the overall elastic symmetry of the sample may not be certain. However, in both RUS and pulse-echo measurements, it is crucial to prepare samples specifically oriented to enhance measurements that are sensitive to the moduli required.

References

1. Migliori, A. and Sarrao, J.L. (1997). *Resonant Ultrasound Spectroscopy*, New York: Wiley.
2. Schreiber, E., Anderson, O.L., and Soga, N. (1973). *Elastic Constants and Their Measurement*, New York: McGraw-Hill.
3. Renken, M.C., Kim, S., Hollman, K.W., Fortunko, C.M., Schneider, S.C., Levy, M., and McAvoy, B.R. (1997). Accuracy of resonant ultrasound spectroscopy: An experimental study, in *IEEE Ultrasonics Symposium Proceedings*, Canada: Toronto.
4. Migliori, A., Sarrao, J.L., Visscher, W.M., Bell, T., Lei, M., Fisk, Z., and Leisure, R.G. (1993). Resonant ultrasound spectroscopic technique for measurement of the elastic moduli of solids. *Physica* **B183**: 1–24.
5. Visscher, W.M., Migliori, A., Bell, T., and Reinert, R. (1991). On the normal modes of free vibration of inhomogeneous and anisotropic elastic objects. *J. Acoust. Soc. Am.* **90**: 2154–2162.
6. Commercially available systems are made by Dynamic Resonance Systems, Powell, WY and Quasak International, Albuquerque, NM.
7. Goto, T., and Anderson, O.L. (1988). Apparatus for measuring elastic constants of single crystals by a resonance technique up to 1825 K. *Rev. Sci. Instr.* **59**: 1405–1408.
8. Isaak, D.G., Carnes, J.D., Anderson, O.L., and Oda, H. (1998). Elasticity of fused silica spheres under pressure using resonant ultrasound spectroscopy. *J. Acoust. Soc. Am.* **104**: 2200–2206.
9. Migliori, A., and Darling, T.W. (1996). Resonant ultrasound spectroscopy for materials studies and non-destructive testing. *Ultrasonics* **34**: 473–476.
10. Heyliger, P., and Ledbetter, H. (1998). Detection of surface and subsurface flaws in homogeneous and composite solids by resonant ultrasound. *J. Nondestr. Eval.* **17**: 79–87.
11. Press, W.H., Flannery, B.P., Teukolsky, S.A., and Vetterling, W.T. (1986). *Numerical Recipes*, Cambridge University Press, Section 14.5.
12. Demarest, H.H., Jr. (1971). Cube-resonance method to determine the elastic constants of solids. *J. acoust. Soc. am.* **49**(3): 768–775.
13. Holland, R. (1968). Resonant properties of piezoelectric ceramic rectangular parallelepipeds. *J. acoust. Soc. am.* **43**(5): 988–997.
14. Ohno, I. (1976). Free vibration of a rectangular parallelepiped crystal and its application to determination of elastic constants of orthorhombic crystals. *J. Phys. Earth* **24**: 355–379.
15. Sarrao, J.L., Chen, S.R., Visscher, W.M., Lei, M., Kocks, U.F., and Migliori, A. (1994). Determination of the crystallographic orientation of a single crystal using resonant ultrasound spectroscopy. *Rev. Sci. Instr.* **65**: 2139–2140.
16. Oda, H. (1994). Free oscillation of an elastically anisotropic ellipsoid with arbitrary crystal orientation. *J. Phys. Earth* **42**: 97–101.
17. Mochizuki, E. (1988). Sphere-resonance method to determine the elastic constants of crystal. *J. Appl. Phys.* **63**(12): 5668–5673.
18. Oda, H., Isoda, S., Inouye, Y., and Suzuki, I. (1994). Elastic constants and anelastic properties of an anisotropic periclase sphere as determined by the resonant sphere technique. *J. Geophys. Res.* **99**(B8): 15517–15527.
19. Suzuki, I., Oda, H., Isoda, S., Saito, T., and Seya, K. (1992). Free oscillation of an elastically anisotropic sphere and its application to determining the elastic constants of rutile. *J. Phys. Earth* **40**: 601–616.

20. Oda, H., Hirao, J., Suzuki, I., Visscher, W.M., and Anderson, O.L. (1994). Free oscillations of elastically anisotropic spheres and ellipsoids. *Geophysics, J. Int.* **118**: 555–565.
21. Mochizuki, E. (1987). Application of group theory to free oscillations of an anisotropic rectangular parallelepiped. *J. Phys. Earth* **35**: 159–170.
22. Oda, H. (1996). Aspherical correction for free vibration of elastically anisotropic solid by means of the XYZ algorithm. *PAGEOPH* **147**(4): 719–727.
23. Young, P.G., and Dickinson, S. M. (1994). Free vibration of a class of solids with cavities. *Int. J. Mech. Sci.* **36**(12): 1099–1107.
24. Ohno, I., Yamamoto, S., and Anderson, O.L. (1986). Determination of elastic constants of trigonal crystals by the rectangular parallelepiped resonance method. *J. Phys. Chem. Solids* **47**(12): 1103–1108.
25. Oda, H., Suzuki, I., and Ohno, I. (1993). Partial derivatives of eigenfrequencies of a rectangular parallelepiped and a sphere of elastically anisotropic solid. *J. Phys. Earth* **41**: 271–289.
26. Born, M., and Huang, K. (1954). *Dynamical Theory of Crystal Lattices*, Oxford: Oxford University Press.
27. Varshni, Y.P. (1970). Temperature dependence of the elastic constants. *Phys. Rev.* **B2**: 3952–3958.
28. Garber, J.A., and Granato, A.V. (1975). Theory of the temperature dependence of second-order elastic constants in cubic materials. *Phys. Rev.* **B11**: 3990–4007.
29. Sorokin, B.P., Glushkov, D.A., and Aleksandrov, K.S. (1999). Temperature dependence of second-order elastic constants of cubic crystals. *Phys. Solid State* **41**: 208–212.
30. Carpenter, Michael, A., and Salje, Ekhard, K.H. (1998). Elastic anomalies in minerals due to structural phase transitions. *Eur. J. Mineral.* **10**: 693–812.
31. Darling, T.W., Migliori, A., Moshopoulou, E.G., Trugman, S.A., Neumeier, J.J., Sarrao, J.L., Bishop, A.R., and Thompson, J.D. (1998). Measurement of the elastic tensor of a single crystal of $\text{La}_{0.83}\text{Sr}_{0.17}\text{MnO}_3$ and its response to magnetic fields. *Phys. Rev.* **B57**: 5093–5097.
32. Ledbetter, H., Fortunko, C., and Heyliger, P. (1995). Elastic constants and internal friction of polycrystalline copper. *J. Mat. Res.* **10**: 1352–1353.
33. Trivisonno, S., Vatanayon, M., Wilt, J., Washick, J., and Reifenberger, R. (1973). Temperature dependence of the elastic constants of Niobium and Lead in the normal and superconducting states. *J. Low Temp. Phys.* **12**: 153–169.
34. Sarrao, J.L., Mandrus, D., Migliori, A., Fisk, Z., and Bucher, E. (1994). Elastic properties of FeSi. *Physica* **B199–200**: 478–479.
35. Mandrus, D., Sarrao, J.L., Migliori, A., Thompson, J.D., and Fisk, Z. (1995). Thermodynamics of FeSi. *Phys. Rev.* **B51**: 4763–4767.
36. Park, C.-H., Shen, Z.-X., Loeser, A.G., Dessau, D.S., Mandrus, D.G., Migliori, A., Sarrao, J., and Fisk, Z. (1995). Direct observation of a narrow band near the gap edge of FeSi. *Phys. Rev.* **B52**: R16981–16984.
37. Maynard, J.D. (1992). The use of piezoelectric film and ultrasound resonance to determine the complete elastic tensor in one measurement. *J. Acoust. Soc. Am.* **91**: 1754–1762.

6. ELASTIC PROPERTIES AND THERMODYNAMICS

Veerle Keppens

University of Mississippi, NCPA
University, Mississippi

A. Migliori

Los Alamos National Laboratory
Los Alamos, New Mexico

6.1 Introduction

The measurement of the temperature dependence and values of elastic moduli can provide crucial input to fundamental descriptions of the electronic structure and thermodynamics of condensed matter because elastic moduli play a leading role in determining how thermal energy is distributed among internal vibrations, which, for the most part, control the entropy at ambient temperatures and above. Both in systems with and without phase transitions, elastic moduli reflect fundamental thermodynamic properties of the solid and can be used to extract energy scales. These energy scales can be used to determine the relative importance of various components of electronic structure, phonons, and entropy in both theoretical descriptions of the solid and in understanding observed behavior. For example, classical macroscopic measurements of the elastic moduli of FeSi, a novel narrow gap semiconductor, revealed the size of the small semiconducting energy gap [1], later confirmed via photoemission spectroscopy [2]. Although this general approach marks an extensive area for application of ultrasonic methods, we concentrate here on two unusual systems, filled skutterudites with their low-frequency anharmonic local modes but without phase transitions, and Pu, a metal with at least five unusual zero-pressure phases between low temperatures and the melting point. Using these examples we outline general procedures for the use of elastic moduli as important quantitative probes of condensed matter, and present recent data based on such approaches.

6.2 Vibrational Modes, Phonons, and Elastic Moduli

The fundamental electronic structure of a homogeneous solid determines, of course, all of its properties. However, it is not, at present possible to perform an *ab initio* electronic structure calculation at finite temperature with anything approaching an accuracy adequate to explain completely such things as structural

phase transitions e.g., in Pu metal [3] or finite-temperature electronic energy scales in narrow gap semiconductors. It is even more difficult to apply such techniques to systems where local vibrational modes play a role, such as the filled skutterudites. To make the general problem more manageable, it is useful to separate the (Helmholtz) free energy into four components, such that

$$F = F_L + F_H + F_E + F_A \quad (6.1)$$

where F_L is the static lattice energy for electrons and ions in position on the lattice and in the ground state at zero temperature, F_H is the harmonic phonon free energy, F_E is the free energy of thermally excited electronic states, and F_A is a lumped term including such anharmonic effects as phonon–phonon and electron–phonon interactions. The harmonic phonon contribution dominates the temperature dependence of F at higher temperatures, while the electronic piece may dominate in metals at lower temperatures. By constructing a theory for each component suspected to be of importance and comparing to measurements of sound speed and specific heat, constraints can be developed that validate models. To see how this works for harmonic phonons, we construct a simple 1-D phonon dispersion curve, examine the form of the entropy, and indicate schematically how the force constants can be tuned to reconcile sound speeds and specific heat data at various temperatures.

Take a very long string of masses (atoms) a distance a apart and springs (bonds) as shown in Figure 6.1. This simple 1-D model is one for which only nearest neighbors interact. When longer-range interactions occur, things change, as will be sketched here. Looking at one of the masses, we find that the stretching of springs to the left and right of that mass produce an acceleration (Newton's $F = ma$) such that

$$m \frac{d^2 u_i}{dt^2} = -c(u_i - u_{i-1}) + c(u_{i+1} - u_i) \quad (6.2)$$

We can solve Eq. 6.2 to find that there are many different vibrational frequencies with different wavelengths. For each angular frequency $\omega = 2\pi f$, where

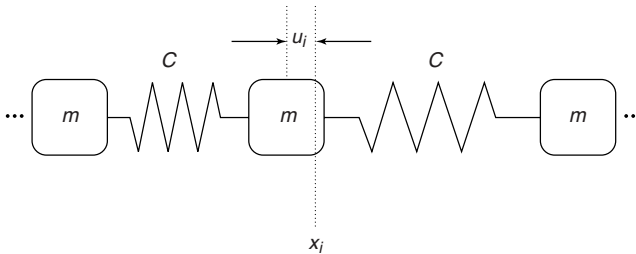


FIG. 6.1. A simple 1-D mass/spring lattice.

λ is the wavelength and s the speed of sound, the displacements $u_i(t)$ are such that

$$\text{if } u_i(t) = u_{i0} e^{i(kx_i - \omega t)} \text{ and } k = \frac{2\pi}{\lambda} \quad \text{then} \quad \omega = \sqrt{\frac{2c}{m}} \sin ka = s \sin ka \quad (6.3)$$

For all the allowed vibrations (corresponding to an integral number of half-wavelengths fitting on the string) the frequencies are given by Eq. 6.3, and these correspond to the (discrete) vibrational modes. In Figure 6.2 we show a plot of this, and also a plot where we have included second-nearest-neighbor springs as well. Because of the number of modes, each plot looks like a continuous line. The slope of the straight solid lines, which are the slopes of the curves at the origin, are what are normally taken to be the sound velocities. The largest value of the wavevector k occurs when the wavelength of the vibration on the string equals twice the distance between masses (any shorter, and we could describe the wave as if it had a longer wavelength and get exactly the same motions). The flattening of the curve at larger k is the effect of the discrete system over the continuous one. For the real solid, the plot is four-dimensional, three for directions of the wavevector, one for frequency. The endpoint of the plot in any direction depends on details of the crystal symmetry (the dispersion curves must come in with zero slope at high symmetry points of the Brillouin zone boundaries). There are, in addition, two shear-like waves and one compressional-like wave in any direction, so that there are three branches to the so-called dispersion curves. The shear wave speeds are usually of order $2/3$ the compressional wave speed. If a plot such as Figure 6.2 can be constructed, then it is straightforward to compute the vibrational entropy of the harmonic solid. As we shall see, however, this is not so easy, and in fact a bootstrapped approach may be required. Such an

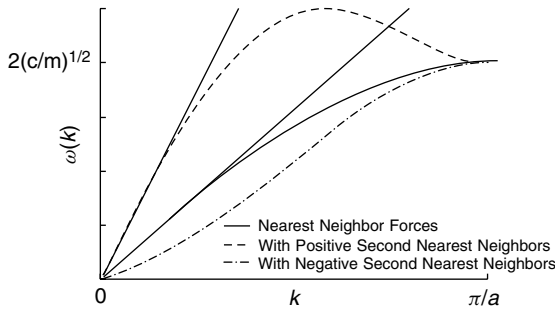


FIG. 6.2. The dispersion curves of a simple 1-D chain with nearest neighbor and both nearest-neighbor and second-nearest-neighbor forces included. Note the very strong similarities with the diffuse neutron scattering computation of Figure 6.4.

approach involves a best guess at the full dispersion curves, with sound speeds anchoring the small- k region, and with specific heat or neutron scattering data assisting with the rest, either directly or by constraining an average.

Considering that the full dispersion curves in fact describe an ensemble of simple harmonic oscillators, we can compute entropy for each element of the ensemble, and then construct mean values that can be compared to measurements. For any individual vibrational mode, we can use the partition function to compute its entropy. Remembering that the energies of each harmonic oscillator or normal mode i are equally spaced such that $E_i = (n + 1/2)\hbar\omega_i$ we find that the average number of quanta \bar{n}_i thermally populating each normal mode (or allowed vibration) can be written as

$$\bar{n}_i = \frac{1}{Z} \sum_{n=0}^{\infty} n e^{-(n+1/2)\frac{\hbar\omega_i}{k_b T}} = \frac{1}{e^{\frac{\hbar\omega_i}{k_b T}} - 1} \quad \text{If } k_b T \gg \hbar\omega_i \text{ then } \bar{n}_i \approx \frac{k_b T}{\hbar\omega_i} \quad (6.4)$$

where we have used the partition function Z to compute the expectation value of the quantum number. Similarly, we can obtain expressions for energy \bar{E}_i , free energy F_i , and entropy S_i , where

$$\bar{E}_i = \hbar\omega_i(\bar{n}_i + 1/2) = k_b \quad (6.5)$$

$$F_i = -k_b T \ln Z \quad \text{where } Z = \frac{1}{e^{\frac{\hbar\omega_i}{2k_b T}} - e^{-\frac{\hbar\omega_i}{2k_b T}}} \quad (6.6)$$

$$T S_i = \bar{E}_i - F \quad \text{If } k_b T \gg \hbar\omega_{\max} \text{ then } T S_i \approx k_b T (1 + \ln \bar{n}_i) \quad (6.7)$$

where ω_{\max} is the highest frequency in the highest phonon branch. To compute the entropy of the entire system, a 3-D average is needed. The Debye temperature, Θ_D is the average temperature corresponding to a certain average phonon frequency, and is the one most familiar. This average is valid when $k_b T \ll \hbar\omega_{\min}$ where ω_{\min} is the highest frequency present in the lowest acoustic phonon branch. It therefore selects out only the lower-frequency modes near the Brillouin zone center, with the result that the specific heat varies as

$$c_v = \frac{2\pi^2 k_b}{5} \left(\frac{k_b T}{\hbar s} \right)^3 \quad (6.8)$$

where $1/s^3$ is the 3-D average of the inverse third power of the sound speeds. In this region, Θ_D contains only information about the linear portion of the phonon dispersion curves. Using this, the low-temperature specific heat is often more accurately found from elasticity measurements than thermal ones.

Differences between the phonon-specific heat calculated from the full elastic tensor and that obtained by measurements is a key indicator of the importance of electronic and other nonphonon effects. At temperatures $k_b T \gg \Theta_{\max}$,

where all the phonon modes are fully populated, we need a different characteristic temperature Θ_0 (average of the $\ln(\omega_i)$) where

$$TS \approx 3Nk_bT [1 + \ln(T/\Theta_0)] \quad (6.9)$$

Equation 6.9 describes the total vibrational entropy of a solid of N atoms at high temperatures, and can be calculated from a measurement of the speed of sound at all wavelengths and in all directions only if optical modes can be neglected, as is often the case.

6.3 Phase Stability of Pu at Higher Temperatures

This simple approach outlined above, especially in the high temperature limit, can quickly establish if a theoretical model is sufficiently robust to be worth pursuing. We illustrate this with data on Pu metal, a mysterious material with at least five zero-pressure stable phases as shown in Figure 6.3 (we omit the so-called δ' bct phase as being thermodynamically unjustified). Electronic structure calculations [4] predict with reasonable certainty the low-temperature phases, but find that the two highest temperature, zero-pressure structures, fcc δ and bcc ϵ are local energy maxima and hence not stable. Can we understand why, quantitatively, from sound speed measurements?

Although the pure fcc phase is not stable at temperatures below 583 K, the addition of 3.3 atomic % Ga will stabilize that phase with very few, if

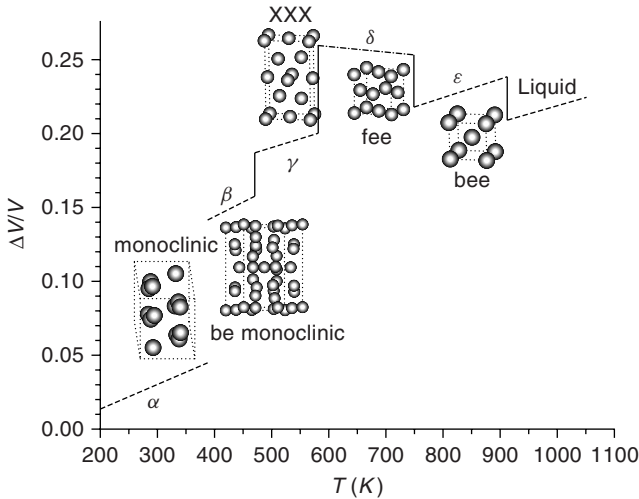


FIG. 6.3. The smoothed measured fractional volume changes and measured structures of Pu at zero pressure.

TABLE 6.1. Elastic Moduli of Pu-3.3 Atomic % Ga δ -phase at Ambient Temperature as Measured by Moment and Ledbetter

C_{11}	36.28 ± 0.36 GPa
C_{44}	33.59 ± 0.11 GPa
$1/2(C_{11} - C_{12}) = c^*$	4.78 ± 0.38 GPa

any, side effects at room temperature, so that not only can single crystals be grown, but measurements can be made as well. The only known single crystal elasticity data for Pu 3.3 atomic % Ga, shown in Table 6.1, was taken by Moment and Ledbetter [4] in 1975 using a composite resonator method on a 0.7-cm long crystal. They found the utterly surprising result that Pu has the highest shear anisotropy, lowest bulk modulus, and the third lowest Θ_D (106 K, above that of Pb and Yb) of any fcc metal. Their measurements stood alone, and an interesting unknown at the time was an accurate prediction for the polycrystal averages. More recently we have made high-accuracy resonant ultrasound spectroscopy (RUS) [5] measurements on available polycrystal samples with varying Ga concentrations that have provided the missing experimental polycrystal values. Interestingly enough, radioactive damage appears to be a stronger effect than Ga concentration, as shown in Table 6.2, where we compare a Kroner [6] average of the single crystal data to our more recent measurements. Note the extremely good agreement between samples of the same age and composition, an encouraging result for accurate thermodynamic analysis.

Missing, however, are accurate data for the shape of the full dispersion curve, and so the high-temperature phonon contribution to the entropy cannot

TABLE 6.2. Summary of Our and Other Measurements of the Elastic Moduli of Pu^a

Sample	C_{11} (GPa)	Bulk (GPa)	Shear (GPa)
Single crystal δ -Pu 3.3 atomic % Ga new	51.4	29.9	16.2
Polycrystal δ-Pu 1.73 atomic % Ga 15y	47.5	26.7	16.3
Polycrystal δ-Pu 2.36 atomic % Ga new	52.3 ± 0.15	30.6	16.3 ± 0.006
Polycrystal δ-Pu 3.3 atomic % Ga new	51.8 ± 0.44	29.6	16.7 ± 0.018
Polycrystal δ-Pu 3.902 atomic % Ga 15y	58.4	34.3	18.1
Polycrystal δ-Pu 5.53 atomic % Ga 44y	50.0	27.0	17.2
Cast α -Pu (Laquer)	104.6	46.6	43.5
Cast α-Pu (new)	109.1	55.8	10.0
Cast α -Pu (DeCadenet)	109.0	54.5	40.9

^aOur results are shown in bold. All measurements were at ambient temperature. Error bars where not noted for our measurements were less than 1% for C_{11} and less than 0.3% for C_{44} . The ages are indicated in years (y) where known.

yet be determined. Normally, inelastic neutron scattering from single crystals can be used to obtain the full phonon dispersion curves with fair, but not great, accuracy. However, single crystals of Pu are unobtainable in sufficient size for such techniques (15 g is a typical size, possible for α -Pu but not likely for any of the other pure phases). In a recent development, Dimitrov, Roder, and Louca have found that a clever and careful analysis of diffuse neutron scattering [7] data could provide those modes, and these authors have produced tentative force constants. Although these data, the only ones available to date, have serious problems associated with container-wall corrections and neutron absorption by Pu^{239} impurities, an estimate can be made using sound speeds as initial slope constraints. From this we obtain $\Theta_0 = 84$ K, yielding a value for $TS = 625$ meV/atom at 753 K, the upper limit of the δ phase boundary. There are, however, specific heat data available for this system from which the actual entropy can be calculated, including electronic and other components. These data, analyzed by Wallace [8] show that at the δ - ϵ phase boundary in the δ phase, $TS = 740$ meV/atom. The difference, 115 meV/atom, though not expected to be very accurate just yet, is probably a good (and the first) upper bound for the entropic contribution of the free electrons.

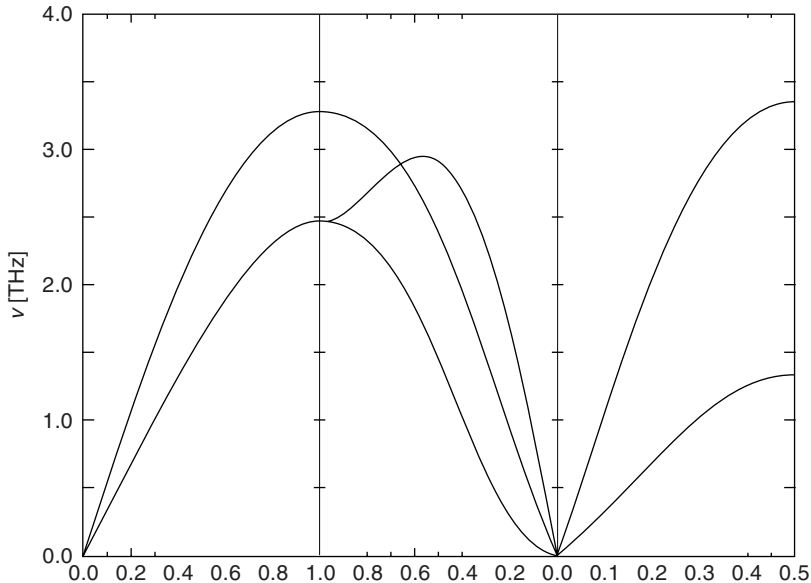


FIG. 6.4. Estimate of the dispersion curves for fcc Pu from careful analysis of diffuse neutron scattering data. Constraints on the initial slope are obtained from elasticity measurements, greatly improving the confidence in such a calculation. Note the obvious presence of second-nearest-neighbor forces.

We should not expect zero-temperature electronic structure calculations (band-structure) to predict anything about such an elastically soft metal as Pu at elevated temperatures because the entropic contributions to the free energy will be unusually high. Compare this to the energy scales over which electronic structure calculations have difficulties. Remembering that such calculations are implicitly performed at zero temperature, results are, strictly speaking, only for the energy, not the free energy. However, in many systems where Θ_D or other phonon averages are near or above room temperature (that is, relatively high), the free energy F is expected to include a much smaller contribution from the entropy. This is not true for Pu especially when one considers the very soft value of c^* and the very low value for the bulk modulus. Therefore, in this metal, entropy is expected to play a much stronger role than in other fcc metals. It is, expected, then, that the failure to include the $TS = 740$ meV/atom in an attempt to understand the phase stability of Pu would leave out the largest contribution to the free energy. From this analysis, it is very likely that it is not the details of the electronic structure that stabilize the high-temperature phases of Pu, but rather it must be vibrational entropy. This is an important point that cannot be overemphasized. In this particular soft f-electron metal, most computations have concentrated on making unlikely or ad hoc changes in the number of itinerant f electrons in order to attempt to understand the properties of Pu. This approach would not have been taken had a careful computation of phonon entropy from available elastic modulus data been made.

6.4 Elastic Moduli and Local Modes

Before looking into examples of solids with “unusual” elastic properties, it might be useful to briefly display “normal” elastic behavior. Such behavior is typified in Figure 6.5; the elastic moduli gradually increase with decreasing temperature, and level off at low temperatures. Attempts have been made to represent this temperature-dependence of elastic constants by empirical equations; the most successful approach has been given by Varshni [9], with the equation

$$c_{ij}^0 = c_{ij} - s/(e^{t/T} - 1) \quad 6.10)$$

with T the temperature, c_{ij}^0 the elastic constant at 0 K and s and t fitting parameters. Using this equation, which has some theoretical justification, Varshni was able to model the elastic constants of over 22 compounds, in a temperature-range from 0 to 300 K.

An elastic system of slightly more complex behavior is one in which local vibrational modes are a strong contributor to the free energy. To understand how this works, first, we can calculate the contribution of a harmonic oscillator

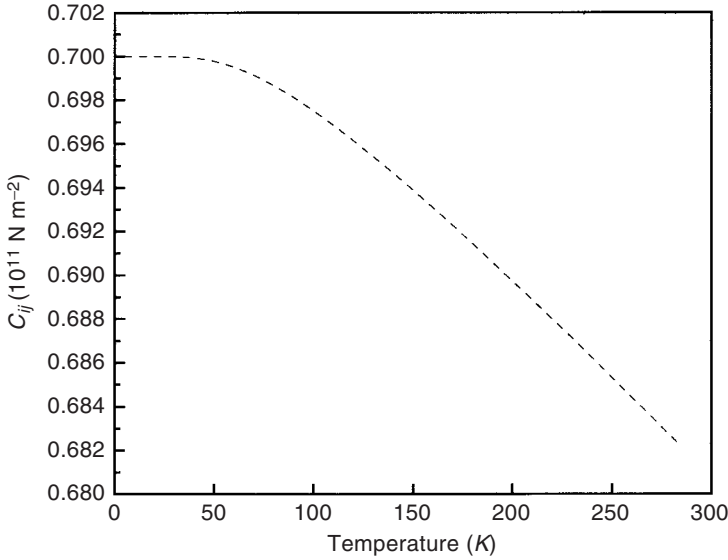


FIG. 6.5. Temperature-dependence of the elastic constants for “normal” solids.

to the elastic tensor. This can be done by taking the second derivative of the Helmholtz free energy F with respect to strain ϵ_{ij} :

$$c_{ij} = \frac{\partial^2 F}{\partial \epsilon_{ij}^2} \quad (6.11)$$

The free energy is linked to the partition function (Eq. 6.6) leading to the following expression for F :

$$F = \frac{1}{2}h\nu + kT \ln(1 - e^{(-h\nu/kT)}) \quad (6.12)$$

If we assume that the energy-difference between the levels, $\Delta = h\nu$, has a linear strain-dependence, $h\nu = A + B\epsilon_{ij}$, we can calculate the elastic moduli using Eq. 6.11:

$$c_{ij} = -N_A k B^2 \frac{\exp((-A - B\epsilon_{ij}/T))}{T(1 - \exp((-A - B\epsilon_{ij})/T))^2} \quad (6.13)$$

This negative contribution would need to be added to the “background” of the material. The elastic moduli of a solid containing one isolated harmonic oscillator could for instance be found by adding Eq. 6.13 to the “Varshni function” (Eq. 6.10).

If the harmonic oscillator were reduced to a simple two-level system, the same approach can be followed, simply replacing the partition function of the harmonic oscillator with that of the two-level system:

$$Z_{2LS} = 1 + e^{-h\nu/kT} \quad (6.14)$$

leading to elastic constants given by

$$c_{ij} = -N_A k B^2 \frac{\exp((-A - B\varepsilon_{ij}/T))}{T(1 + \exp((-A - B\varepsilon_{ij}/T))^2} \quad (6.15)$$

6.5 Local Modes in Filled Skutterudites

We now turn our focus to actual experiments, in which measurements of elastic constants were used to characterize local modes in a solid. Localized vibrational modes are uncommon in solids because of the strong interactions that exist between the constituent atoms. When present, local modes are usually associated with weakly bound guest atoms that reside in the voids of an open-structured host. In this section, we will discuss the presence of low-energy modes in La-filled skutterudites, using this particular class of solids to show how information about the elastic moduli can be used to study local modes in a solid.

The word *skutterudite* is derived from a town in Norway, where minerals with this structure, such as CoAs_3 , were first discovered. Compounds with the filled skutterudite structure were discovered by Jeitschko and Braun in 1977, and have the general formula RM_4X_{12} , where R is a rare-earth element (such as La or Ce), and M is a transition metal (for example Fe or Co) and X is a pnictogen (P, As, Sb) [10]. Their structure can be described as consisting of square planar rings of four pnictogen atoms, the metal (M) atoms form a cubic sublattice and the R atoms are positioned in the two remaining “holes” in the structure. When the R atoms are absent from the structure, the basic skutterudite structure is formed.

The presence of the rare-earth atom in the filled skutterudites has been shown to cause a dramatic decrease in the lattice component of the thermal conductivity, κ_{lattice} while having little effect on the electronic properties of the compound [11–13]. The reduction in κ_{lattice} is believed to be due to the vibrations or “rattling” of the rare-earth atom in the oversized cage.

The first evidence of this rattling came from structure refinements, obtained using either x-ray or neutron scattering on single crystals [10]. An atomic displacement parameter (ADP) can be obtained for each distinct atom in the crystal structure. This parameter measures the mean-square displacement of the atom about its equilibrium position. The ADP values for La in $\text{La}_{0.75}\text{Fe}_3\text{CoSb}_{12}$

are anomalously large, indicating that the La is poorly bonded in the structure and rattles about its equilibrium position.

In order to better characterize the lattice dynamics of filled skutterudites, the elastic moduli of filled and unfilled skutterudites were measured as a function of temperature. High-quality samples of $\text{La}_{0.75}\text{Fe}_3\text{CoSb}_{12}$ and CoSb_3 were cut into $2 \times 2.5 \times 3$ mm rectangular pieces and used for resonant ultrasound spectroscopy (RUS) measurements. RUS is an ultrasonic technique, developed by Migliori *et al.* for determining the complete set of elastic moduli of a solid by measuring the free-body resonances of the sample. This method is unique in that all moduli can be determined simultaneously, avoiding remounts of transducers and multiple temperature sweeps [5]. Measurements have been performed as a function of temperature (5–300 K), for both filled ($\text{La}_{0.75}\text{Fe}_3\text{CoSb}_{12}$) and unfilled (CoSb_3) skutterudites. A polycrystal has two elastic moduli: a shear modulus C_{44} governing transverse waves and a longitudinal modulus C_{11} governing longitudinal waves. The value for both moduli was determined from the RUS measurements. The room temperature values are listed in Table 6.3.

Figure 6.6 shows both the shear and longitudinal modulus for the unfilled skutterudite CoSb_3 , Figure 6.7 shows the moduli for the filled skutterudite $\text{La}_{0.75}\text{Fe}_3\text{CoSb}_{12}$. The solid line through the CoSb_3 data is a model calculation using the Varshni function (Eq. 6.10) discussed in the preceding paragraphs. The elastic response of CoSb_3 can be well described by this Varshni model, indicating that this solid has a “normal” elastic behavior. However, the moduli of the filled skutterudite $\text{La}_{0.75}\text{Fe}_3\text{CoSb}_{12}$ behave anomalously at low temperatures, displaying a much stronger temperature dependence, which is suggestive of unusual low-energy vibrational modes in addition to the normal acoustic modes. The elastic data can be understood by considering the elastic response of a local oscillator. Above, we calculated the elastic response of an Einstein oscillator (Eq. 6.13) and a two-level system (Eq. 6.15), assuming that the level-spacing $\Delta = \hbar\nu$ depends linearly on the strain, that is $\hbar\nu = A + B\epsilon$. To model the experimental data, it is reasonable to start from a background, estimated from the Varshni-fit for unfilled CoSb_3 , taking the same values for the fit parameters s and t , but adjusting c_{ij}^0 to the value of the elastic moduli measured for the filled skutterudite at the lowest temperature. Trying to model

TABLE 6.3. Elastic Constants at Room Temperature for CoSb_3 and $\text{La}_{0.75}\text{Fe}_3\text{CoSb}_{12}$

Compound	$C_{11} (10^{11} \text{N/m}^2)$	$C_{44} (10^{11} \text{N/m}^2)$
CoSb_3	1.598	0.571
$\text{La}_{0.75}\text{Fe}_3\text{CoSb}_{12}$	1.577	0.556

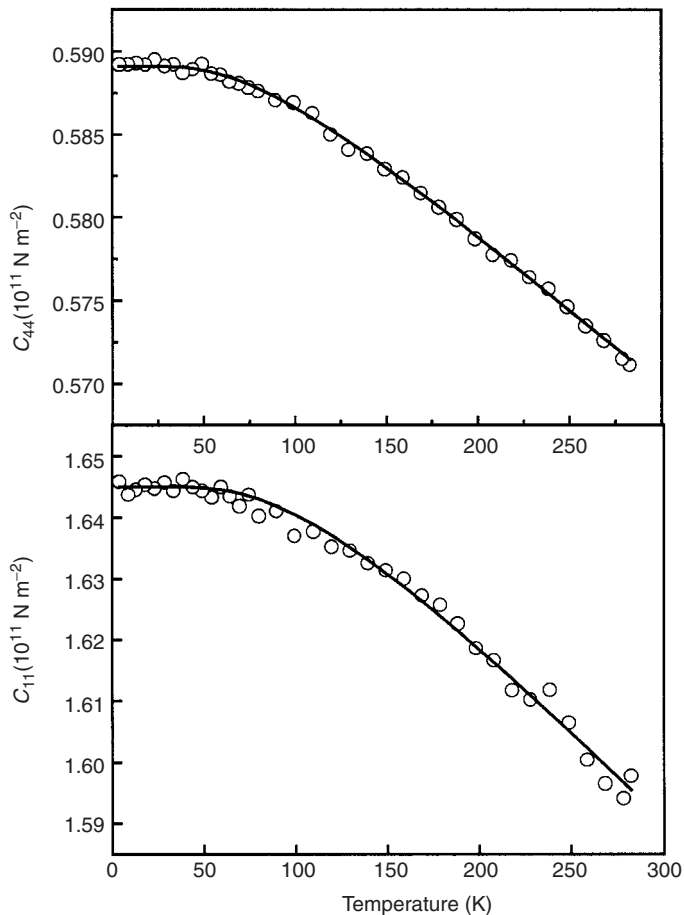


FIG. 6.6. Elastic moduli as a function of temperature for CoSb_3 . The solid line is a fit using the Varshni-function.

the data, we added the contribution of one or more local oscillators, and found that the data can be described reasonably well, by adding the contribution of two two-level systems (2LS): one 2LS with a characteristic energy of 50 K, a second 2LS with $h\nu = 200$ K. [14]. Attempts to model the data using simple Einstein oscillators were not successful.

To further characterize the unusual thermodynamics of filled skutterudites, specific heat measurements were performed on a sample of $\text{LaFe}_3\text{CoSb}_{12}$ from 2 to 300 K [15]. The results are plotted in Figure 6.8, illustrating the difference in the low-temperature behavior of the filled and unfilled materials. Although

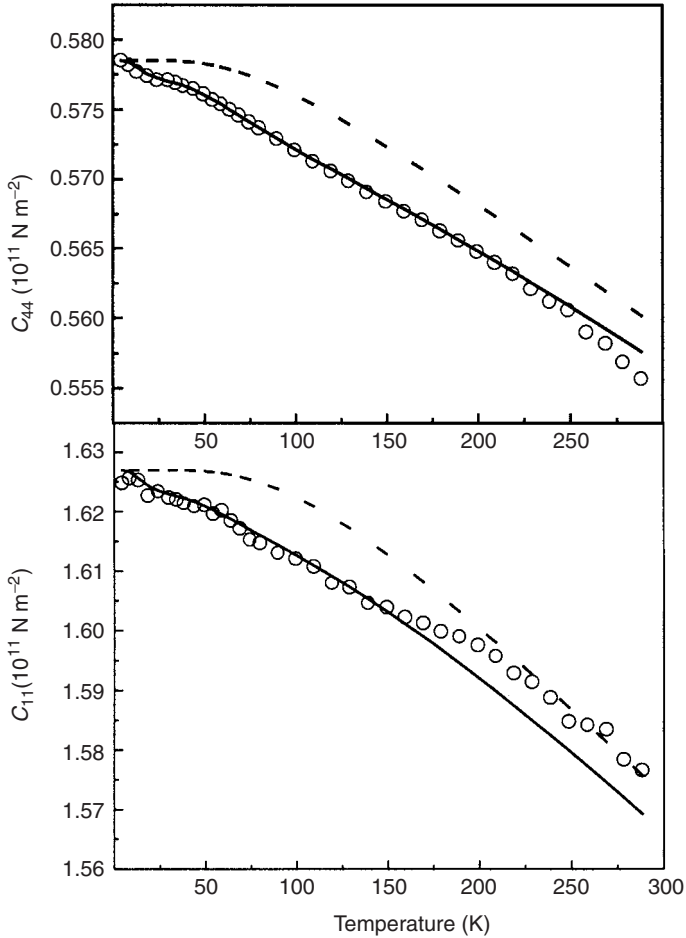


FIG. 6.7. Elastic moduli for $\text{La}_{0.75}\text{Fe}_3\text{CoSb}_{12}$ as a function of temperature. The solid lines represent model calculations using two-level systems. The dashed lines are estimated background moduli.

the specific heat of CoSb_3 deviates somewhat from simple Debye behavior, a model proposed by Feldman and Singh is able to quantitatively account for the data [16]. Using the CoSb_3 data as a background, we find that the addition of two local oscillators is required to model the specific heat of $\text{LaFe}_3\text{CoSb}_{12}$, as illustrated in Figure 6.8. The solid line through the $\text{LaFe}_3\text{CoSb}_{12}$ data in Figure 6.8 represents a model calculation using

$$C_p = C_p(\text{CoSb}_3) + \gamma T + AC_1 + AC_2 \quad (6.16)$$

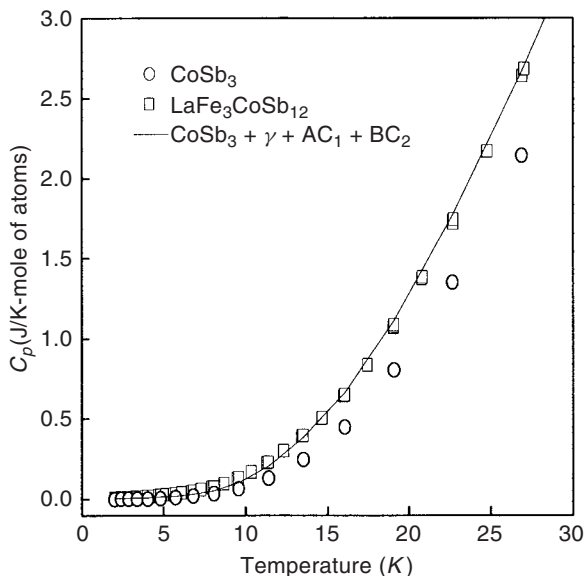


FIG. 6.8. Specific heat versus temperature for CoSb_3 and $\text{LaFe}_3\text{CoSb}_{12}$. The solid line is based on a calculation with the contribution of two local oscillators added to the CoSb_3 data [15].

with $C_p(\text{CoSb}_3)$ the molar specific heat of CoSb_3 , $\gamma = 0.0034 \text{ mol}^{-1}\text{K}^{-2}$, $A = 0.1 \text{ mol}^{-1}\text{K}^{-1}$, $B = 0.12 \text{ mol}^{-1}\text{K}^{-1}$ and T is the temperature. C_1 and C_2 represent contributions from the local oscillators. The data can be modeled using either two Einstein oscillators, with $C = (\theta/T)^2 e^{(\theta/T)} / (e^{(\theta/T)} - 1)^2$, or two 2LS, with $C = (\theta/T)^2 e^{(\theta/T)} / (e^{(\theta/T)} + 1)^2$, with characteristic temperatures $\theta_1 = 70 \text{ K}$ and $\theta_2 = 200 \text{ K}$. Both approaches are indistinguishable in the experimental temperature range (2–300 K). The specific heat data are in excellent agreement with the results obtained from the elastic constant, confirming the presence of two distinct local modes in the filled skutterudites that are absent in the unfilled counterpart.

6.6 Summary

Recent data for solids with and without phase transitions were used to show how elastic moduli reflect fundamental properties of condensed matter. We demonstrated how measurements of the values and the temperature dependence of the elastic constants can contribute to a better understanding of the electronic structure and thermodynamics of solids.

Acknowledgments

It is a pleasure to thank D. Mandrus and B.C. Sales for valuable discussions.

References

1. Mandrus, D., Sarrao, J.L., Migliori, A., Thompson, J.D., and Fisk, Z. (1995). Thermodynamics of FeSi. *Phys. Rev. B* **51**: 4763.
2. Park, C.-H., Shen, Z.-X., Loeser, A.G., Dessau, D.S., Mandrus, D.G., Migliori, A., Sarrao, J.L., and Fisk, Z. (1995). Direct observation of a narrow band near the gap edge of FeSi. *Phys. Rev. B* **52**: 24, R1698.
3. Olle Eriksson, Baker, J.D., Balatsky, A.V., and Wills, J.M. (1999). Novel electronic configuration in d-Pu. *J. Alloys Compd* **287**: 1.
4. Ledbetter, H.M. and Moment, R.L. (1975). Elastic properties of face centered cubic plutonium. *Acta Metall.* **24**: 891.
5. Migliori, A., Sarrao, J.L., Visscher, W.M., Bell, T.M., Lei, M., Fisk, Z., and Leisure, R.G. (1993). Resonant ultrasound spectroscopic techniques for measurement of the elastic moduli of solids. *Physica B* **1**: 183.
6. Hirsekorn, S. (1990). Elastic properties of polycrystals. *Text. and Microstruct.* **12**: 1.
7. Dimitrov, D.A., Roder, H., and Louca, D. (1999). Phonons from neutron powder diffraction. *Phys. Rev. B* **60**: 6204.
8. Duane Wallace, C. (1998). Electronic and phonon properties of six crystalline phases of Pu metal. *Phys. Rev. B* **58**: 15433.
9. Varshni, Y.P. (1970). Temperature dependence of the elastic constants. *Phys. Rev. B* **2**: 3953.
10. Jeitschko, W. and Braun, D. (1977). LaFe₄P₁₂ with filled CoAs₃-type structure and isotypic lanthanoid-transition metal polyphosphides. *Acta Crystallogr. B* **33**: 3401. Braun, D. and Jeitschko, W. (1988). Preparation and structural investigations of antimonides with the LaFe₄P₁₂ structure. *J. Less-Common Met.* **72**: 147.
11. Morelli, D.M. and Meisner, G.P. (1995). Low temperature properties of the filled skutterudite CeFe₄Sb₁₂. *Appl. Phys.* **77**: 3777.
12. Sales, B.C., Mandrus, D., and Williams, R.K. (1996). Filled skutterudite antimonides: a new class of thermoelectric materials. *Science* **272**: 1325.
13. Sales, B.C., *et al.* (1997). Filled skutterudite antimonides: electron crystals and phonon glasses. *Phys. Rev. B* **56**: 15081.
14. Keppens, V., *et al.* (1998). Localized vibrational modes in metallic solids. *Nature* **395**: 878.
15. Unpublished data, courtesy of Mandrus, D. and Sales, B.C.
16. Feldman and Singh (1996). Lattice dynamics of of skutterudites: first principles and model calculations for CoSb₃. *Phys. Rev. B* **53**: 6273. *Erratum* **54**: 712.

This Page Intentionally Left Blank

7. SPEED OF SOUND AS A THERMODYNAMIC PROPERTY OF FLUIDS

Daniel G. Friend

Physical and Chemical Properties Division
Chemical Science and Technology Laboratory
National Institute of Standards and Technology
Boulder, Colorado

Abstract

In this Chapter, we review the principles of sound propagation in fluid systems. From a study of the hydrodynamic equations, sound propagation is shown to be a wave phenomenon. The speed of sound then can be derived at any state point from a knowledge of the thermodynamic surface of the fluid of interest. Several model equations of state are reviewed, and it is shown how the speed of sound can be obtained for a variety of systems. We then focus on several fluids of particular interest, and show the behavior of the sound speed over a wide range of the temperature and pressure variables. Tabulated values of the speed of sound are given for argon, nitrogen, water, and air based on the current standard reference thermodynamic surfaces.

7.1 Introduction

In this Chapter, we discuss the propagation of sound in fluids and provide information about the thermodynamic speed of sound over substantial ranges of the state variables for a variety of fluids. In the context of this chapter, we consider sound to arise from a small periodic and isentropic (constant entropy) perturbation of the local equilibrium in a fluid, which, as we shall see, gives rise to a standard wave equation. The systems under consideration include both pure fluids and mixtures in the liquid, vapor, and supercritical states. Thus the range in temperature is from the melting line to very high temperatures (a dissociation limit), and the range in pressure is from very low values (below which the continuum approximation would not be valid) to the solidification locus (at least in principle).

The major theme of the discussion stems from the relation

$$w = \left\{ \frac{\rho}{M} \left[2 \frac{\partial A}{\partial \rho} \Big|_T + \rho \frac{\partial^2 A}{\partial \rho^2} \Big|_T - \rho \frac{\left(\frac{\partial^2 A}{\partial \rho \partial T} \right)^2}{\frac{\partial^2 A}{\partial T^2} \Big|_\rho} \right] \right\}^{1/2} \quad (7.1)$$

which expresses the speed of sound, w , in terms of derivatives of the molar Helmholtz free energy A and the state point defined by the temperature T and the molar density ρ . In Eq. 7.1, M is the molar mass of the substance in kilograms per mole. Although Eq. 7.1 may not be the simplest expression for the speed of sound, it serves to emphasize that this thermodynamic quantity is easily calculable if the Helmholtz free energy of a fluid system is known. This expression is also appropriate for fluid mixtures, in which case the partial derivatives are to be taken at constant composition.

In the next section, we outline how Eq. 7.1 can be obtained. Although this thermodynamic relationship is straightforward and exact, a few caveats must be given regarding its use. First “thermodynamic” sound model requires isentropic and linear approximations, and thus there are restrictions on the amplitude and frequency of the propagated disturbance. These issues are seldom significant when considering sound in most fluid media under most conditions. The second caveat is more essential: there are only a few fluid systems for which the Helmholtz free energy surface is sufficiently well known to allow sound speeds to be accurately calculated. These surfaces are generally empirical correlations of experimental data, and only when accurate sound speeds are included in the primary data used to determine the thermodynamic surface are the resultant calculated sound speeds obtained with small uncertainty. Experimental determinations of sound speeds, using state-of-the-art techniques as discussed in other chapters, usually produce more accurate values for this quantity. However, more theoretical or predictive models for the Helmholtz free energy surface may be used to obtain useful approximations for the speed of sound for systems that have not been thoroughly characterized through experimental measurements.

Once we have completed a derivation of Eq. 7.1 in the next section, we will explore some of the limits of this approach, and discuss the application to various model systems and to real fluids. Table 7.1 included at the end of this chapter provides reliable speed of sound values for a variety of important fluid systems.

7.2 Wave Equation in a Fluid

From a standard understanding of thermodynamic conventions, it may be difficult to see how sound propagation can be considered a thermodynamic property. Despite a straightforward parsing of the name “thermodynamics,” typical thermodynamic studies deal with unperturbed systems. Other responses to perturbing stresses, such as flow associated with shear stresses, heat flux related to thermal gradients, and diffusive flows caused by composition variations, are not considered thermodynamic in origin, and the separate study of steady-state kinetic theory may be required to obtain viscosity, thermal

conductivity, and diffusion coefficients. The measurement of thermodynamic properties, as with most other physical quantities, may require a perturbing probe (i.e., a temperature change to determine heat capacities), but, in general, thermodynamic processes are equilibrium phenomena. As we will see, it is the linear, reversible, and small amplitude nature of the wave process that serves to connect sound propagation with fluid thermodynamics.

7.2.1 Hydrodynamic Equations

When fluids are considered in the continuum approximation, three conservation laws can be used to determine the response to perturbing influences in an otherwise equilibrated system. These hydrodynamic equations enforce the conservation of mass (or the number of molecules of each species present), the conservation of momentum, and the conservation of energy.

The continuity equation,

$$\frac{\partial \rho}{\partial t} + \nabla \cdot (\rho \mathbf{u}) = 0 \quad (7.2)$$

ensures that the molar density (at a given fixed infinitesimal volume in space) can change only with a flow of molecules into or out of the volume; here, the partial derivative is with respect to time t , and \mathbf{u} represents the macroscopic velocity of fluid flow at the given point. We use the Euler convention in which the frame of reference is fixed in space, so that properties such as ρ are functions of position (\mathbf{r}) and time, and they represent microscopic averages within a volume element centered on \mathbf{r} in this fixed reference frame. The Navier-Stokes equation

$$\left(\frac{\partial}{\partial t} + \mathbf{u} \cdot \nabla \right) \mathbf{u} = \frac{\mathbf{F}}{m} - \frac{1}{M\rho} \nabla (P - \eta_B \nabla \cdot \mathbf{u}) + \frac{\eta}{M\rho} \nabla^2 \mathbf{u} \quad (7.3)$$

is equivalent to Newton's second law and balances changes in momentum with forces acting on the fluid element. The operator $\left(\frac{\partial}{\partial t} + \mathbf{u} \cdot \nabla \right)$ is the material derivative or streaming derivative, and the left side of the equation describes changes in momentum due directly to fluid flow. The forces that act to change the momentum include the external force \mathbf{F} , here divided by the mass m contained in the infinitesimal volume element under consideration, the force on the element due to gradients of pressure P , and forces associated with the viscous nature of any fluid: here, η_B is the bulk viscosity and η is the usual shear viscosity. The pressure tensor has been decomposed, and a linear relationship between the stress and shear has been assumed [1]. Finally, the conservation of energy can be written in the form

$$\left(\frac{\partial}{\partial t} + \mathbf{u} \cdot \nabla \right) T = -\frac{R}{C_v} (\nabla \cdot \mathbf{u}) T + \frac{\lambda}{\rho C_v} \nabla^2 T \quad (7.4)$$

where T is the absolute temperature, R is the molar gas constant, C_v is the molar isochoric heat capacity, and λ is the coefficient of thermal conductivity in a linear, Fourier's law, relationship between thermal gradients and heat flux.

Equations 7.2 to 7.4 are often simplified in the basic development of a wave equation formalism. In particular, we first consider an ideal fluid with no viscous effects or thermal conduction. In the absence of external forces, the Navier-Stokes relationship given by Eq. 7.3 reduces for an ideal fluid to the Euler equation,

$$\left(\frac{\partial}{\partial t} + \mathbf{u} \cdot \nabla \right) \mathbf{u} = -\frac{1}{M\rho} \nabla \quad (7.5)$$

Small disturbances of an equilibrium state can generate sound, and in the derivation of the wave equation, second-order effects in the derivatives can be ignored. Because the equilibrium state corresponds to zero macroscopic velocity, any quadratic terms in \mathbf{u} will also be dropped. These approximations are almost always quite satisfactory in typical acoustic situations, and we will provide some quantitative discussion below.

To lowest order, Eq. 7.5 can then be linearized and written as

$$\nabla P + M\rho_o \frac{\partial \mathbf{u}}{\partial t} = 0 \quad (7.6)$$

where we have now introduced the notation x_o to denote the time-invariant and spatially invariant equilibrium value of a quantity. (In this notation, a physical quantity can be represented by $x = x_o + x_A$, where x_A is then the "acoustic" variable; i.e., P_A is the acoustic pressure, or the deviation of the pressure from its equilibrium value caused by a perturbation.) To the same order, Eq. 7.2 is written as

$$\frac{\partial \rho}{\partial t} + \rho_o \nabla \cdot \mathbf{u} = 0 \quad (7.7)$$

Taking the time derivative of Eq. 7.7 and the divergence of Eq. 7.6 and subtracting the results gives

$$M \frac{\partial^2 \rho}{\partial t^2} - \nabla^2 P = 0 \quad (7.8)$$

Equation 7.8 forms the basis of the wave equation when we recall that the pressure and density can be related through the thermodynamic equation of state or Helmholtz energy surface. For a pure fluid, the pressure can be considered to be a function of the density and a second intensive thermodynamic variable (and for mixtures, the composition must also be given); without specifying the second variable, we write $P = P(\rho, \alpha)$, so that derivatives of the

pressure can be written in terms of derivatives of the density and the parameter α . Again we drop some higher-order terms and write Eq. 7.8 as

$$M \frac{\partial^2 \rho}{\partial t^2} - \left. \frac{\partial P}{\partial \rho} \right|_{\alpha} \nabla^2 \rho - \nabla \cdot \left(\left. \frac{\partial P}{\partial \alpha} \right|_{\rho} \nabla \alpha \right) = 0 \quad (7.9)$$

If we can identify an appropriate variable α which remains constant through the perturbing acoustic signal (i.e., $\nabla \alpha \equiv 0$), then Eq. 7.9 reduces to a standard propagating wave equation with wave speed $[(1/M) \partial P / \partial \rho|_{\alpha}]^{1/2}$. The earliest theoretical acoustic derivations of wave propagation, developed by Newton, essentially assumed that the temperature is constant as the disturbance travels through the system. Although this may seem like a reasonable approximation, it is incorrect and leads to an incorrect value of the speed of sound.

To lowest order, the situation can be further analyzed by examining the energy equation, Eq. 7.4, recalling that we are considering only the ideal fluid with $\lambda = 0$. We can then write

$$\frac{\partial T}{\partial t} + \frac{RT}{C_V} \nabla \cdot \mathbf{u} = 0 \quad (7.10)$$

and use Eq. 7.7 to obtain

$$\frac{\partial}{\partial t} \left[\ln T - \frac{R}{C_V} \ln \rho \right] = 0 \quad (7.11)$$

where we have been consistent in keeping terms of lowest order and have assumed that the isochoric heat capacity is constant to this order. The time invariance of the quantity in the brackets means that $T \rho^{-R/C_V}$ is constant during the perturbation. Using the ideal gas equation of state (discussed below), this leads to the constancy of $P \rho^{-(C_V+R)/C_V}$, which is a common expression for an adiabatic process in an ideal gas. (Recall that the isobaric heat capacity for an ideal gas is given by $C_P = C_V + R$, and the exponent of ρ is then γ , the ratio of heat capacities, which has a value of $5/3$ for an ideal monatomic gas [2].)

Thus, at least in this limit, the perturbing force leads to an adiabatic process which implies that the entropy is constant during passage of an acoustic disturbance. This turns out generally to be a good approximation, and we choose entropy, S , for the variable α in Eq. 7.9. With $\nabla S = 0$, we can write the wave equation

$$M \frac{\partial^2 \rho}{\partial t^2} - \left. \frac{\partial P}{\partial \rho} \right|_S \nabla^2 \rho = 0 \quad (7.12)$$

to represent the hydrodynamic effect of a small disturbance on a fluid in equilibrium. In common with the interpretation of other wave equations in

physical systems, we conclude that the perturbation propagates unchanged with a propagation speed given by

$$w = \sqrt{\left. \frac{1}{M} \frac{\partial P}{\partial \rho} \right|_S} \quad (7.13)$$

Equation 7.13 works remarkably well for a wide variety of fluid acoustic situations despite the approximations made in its derivation. This common expression for speed of sound is often not used directly, because derivatives at constant entropy are not often tabulated. Using a standard definition of the adiabatic compressibility, $\kappa_S = (1/\rho)\partial\rho/\partial P|_S$, we can write

$$w^2 = \frac{1}{M\rho\kappa_S} \quad (7.14)$$

while additional standard thermodynamic relations allow us to write

$$w^2 = \frac{C_P}{MC_V} \left. \frac{\partial P}{\partial \rho} \right|_T \quad (7.15)$$

The relations derived from the Helmholtz free energy then give us the expression in Eq. 7.1. We conclude that a small-amplitude disturbance in an equilibrium ideal fluid will propagate as an isentropic wave with wave speed given by Eq. 7.1; this is a sound wave.

7.2.2 The Speed of Sound

In statistical mechanics, an ideal gas is often considered to be a system of noninteracting point particles; the monatomic noble gases at low densities approximate this ideal condition. In this case, the equation of state can be written as $P = \rho RT$, the molar isochoric heat capacity is generated from the three translational degrees of freedom as $3R/2$, and the isobaric heat capacity is $5R/2$. For this system, Eq. 7.15 immediately gives a value of 322.59 m/s for the speed of sound in argon ($M = 0.039\,948$ kg/mol) at 300 K. A currently accepted reference value at atmospheric pressure is 322.67 m/s, from which we can conclude that this simple theory and model works remarkably well. (Note that this degree of agreement between the properties of a real fluid and the ideal gas model should not generally be expected even at 1 atm, especially for heavier molecules.)

Returning to our basic Eq. 7.1, note that the Helmholtz free energy for such a monatomic ideal gas can be written as

$$A^{ig}(\rho, T) = RT[A^0 + \ln \rho - 3/2 \ln T] \quad (7.16)$$

where A^0 is an integration constant with which we need not be concerned [4]. With this equation for A , the derivatives required for Eq. 7.1 are easily calculable with the result

$$w^2 = \frac{5RT}{3M} \quad (7.17)$$

as previously seen for an ideal monatomic fluid.

More generally, an ideal gas can have additional (intramolecular) degrees of freedom and internal structure. This is reflected in different values or temperature dependences in the ideal gas heat capacities of structured molecules, or, equivalently, in additional temperature dependence in the expression for the ideal gas Helmholtz free energy. With estimates for the translational, rotational, vibrational, and electronic energies based on spectroscopic information, the ideal gas heat capacities, using models as the rigid-rotor harmonic oscillator, can be calculated from statistical mechanics. From this information, values for the speed of sound of low-density systems can be calculated. Alternatively, accurate measurements of the speed of sound at low density can be used to provide estimates of the ideal gas properties of a molecular system. (However, if the frequency associated with the sound is not commensurate with the relaxation time of the modes contributing to the ideal gas calculations, corrections must be considered when connecting measured sound speeds to ideal gas behavior [5].)

Interactions between the particles in a fluid (intermolecular effects) are extremely important when considering the speed of sound, or any other thermodynamic properties, outside the limited region in which the ideal gas approximation is valid. In this case, Eq. 7.16 is not an appropriate representation of the fluid's Helmholtz free energy, and Eq. 7.17 cannot be used to determine the speed of sound. Equations 7.1 and 7.13 through 7.15 are appropriate for compressed gases at elevated pressures, for saturated or compressed liquids, and for supercritical fluids. Explicit examples for the use of these equations in determining the speed of sound in a variety of fluids and over a range of state variables are given Section 7.4.

Two general classes of approximations have been made in our derivation of the wave equation and the equivalent speed of sound expressions of Eqs. 7.1 and 7.13 through 7.15. These require that (1) the amplitude of the wave be small so that the equations can be linearized, and (2) reversibility must be maintained so that isentropic behavior can be assumed. We shall briefly explore these requirements in this Section.

The small-amplitude condition is easily fulfilled in most common examples of sound propagation. The restriction can be made that the maximum relative deviation of the density, the acoustic "condensation," is very small, $|\rho - \rho_o|/\rho_o \ll 1$; alternatively, one can require that $|P - P_o| \ll M\rho_o w^2$. This condition can be satisfied if the pressure perturbations are much smaller than the equilibrium value of the pressure, which is typically the case.

To further quantify the small-amplitude restriction, we note that the sound-intensity level can be defined by a logarithmic ratio of an average energy flux in a propagating wave relative to a reference value for such a flux; $\text{SIL} = 10 \log(I/I_{\text{ref}})$, where SIL is the sound-intensity level expressed in decibels referenced to I_{ref} . (Typically the reference value is 10^{-12} W/m^2 for sound in air, although common practices for this arbitrary reference depend on the application; e.g., for certain underwater acoustics applications, $6.76 \times 10^{-19} \text{ W/m}^2$, equivalent to an acoustic pressure of about $1 \mu\text{Pa}$, may be used.) The energy flux for a plane wave can be approximated as $w^3 M(\rho_A - \rho_o)^2 / (2\rho_o)$, where ρ_A is the maximum value (or amplitude) of the density in the wave. In air at ambient conditions, the small-amplitude approximation breaks down (i.e., $|\rho - \rho_o|/\rho_o = 1$) at a sound-intensity level (re 10^{-12} W/m^2) of about 194 decibels (dB); for comparison, the range of hearing at 1000 Hz is about 0 to 140 dB — so the small-amplitude restriction holds for sounds with an energy of some 250,000 times that which may damage the human ear. For liquid water at ambient conditions, this condition would hold up to about 242 dB (re 10^{-12} W/m^2); with the reference based on $1 \mu\text{Pa}$, this would be about 304 dB. We can conclude that, except in the cases of extraordinarily large “shock” pressures, the linear approximations hold for sound propagation.

The more significant restriction on our derivation of the sound equation is associated with the irreversibility caused by the viscous and heat flux effects that were ignored despite their importance in Eqs. 7.3 and 7.4. Additionally, the inability of a fluid to instantaneously return to an equilibrium state when perturbed can be related to the relaxation times that govern the fluid’s behavior. The energy in a molecular system is distributed among internal (such as vibrational and rotational modes) and translational degrees of freedom; when the time scales for populating these energy levels are not compatible with the frequency of the propagating sound, the derivations given previously will not be accurate. We will not go into details here, but these effects lead to both attenuation of sound and dispersion—the dependence of the speed of sound on the frequency. One can make various approximations to the full hydrodynamic equations to obtain corrections to the speed of sound equations given previously.

The equations can be solved in the complex plane, and to lowest order, the viscous and thermal effects are found to leave the speed of sound unchanged, and contribute only to a frequency-dependent absorption [6]. More generally, one can obtain an expansion of the form

$$w^2(f) = w^2(0)[1 + aX + O(X^2)] \quad (7.18)$$

for the real part of the speed of sound as a function of the frequency, f ; the expansion parameter, X , is related to the relaxation times and the frequency,

and the coefficient a can be evaluated for certain models or treated as an empirical parameter. The solution given by Eq. 7.1 represents the zero frequency limit, and, depending on the particular relaxation mechanisms present, some dispersion effects may be seen at frequencies above 1 GHz. The frequency at which dispersion is important for a given system depends on the rotational and vibrational relaxation times in the molecule; these are generally related to the molecular symmetry. Note that the high-frequency signals correspond to small wavelengths, and it is at small wavelengths that the continuum approximation, essential in the development of hydrodynamic approaches to the fluid state, is inappropriate. Finally, we note that the fluctuation-driven phenomena and the density correlations present in near-critical fluids will have an effect on the isentropic assumption and may contribute to dispersion at even lower frequencies. Details concerning these aspects of the acoustic approximation can be found in the texts listed in “Additional Reading.”

7.3 Equations of State for Fluids

From the previous discussion, we conclude that the speed of sound in a fluid can be determined from its Helmholtz free-energy surface; see Eq. 7.1. In general, an expression for A is formed from the sum of ideal gas and residual contributions: $A(\rho T) = A^{ig}(\rho, T) + A^r(\rho, T)$. The ideal-gas term represents energy associated with noninteracting particles and their internal degrees of freedom — i.e., from the statistical partition function involved with translational, electronic, vibrational, and rotational motions. This quantity can be computed from models of the molecular architecture (i.e., rigid-rotator, harmonic oscillator model for nonlinear polyatomic molecules) and spectroscopic data. Following the format of Eq. 7.16, the ideal gas portion of the Helmholtz energy can be written in general as

$$A^{ig}(\rho, T) = RT[A^0 + \ln \rho + f(T)] \quad (7.19)$$

where f gives all of the temperature dependence. It is often sufficient to consider only the A^{ig} contribution for gas phase systems at very low density; however, the residual contribution becomes important as the pressure is increased. The residual contribution to A describes the effects of interparticle interactions.

An equation of state, typically an expression for the pressure as a function of temperature and density (or volume), can also be decomposed into the ideal gas and residual contributions. The ideal-gas term in the equation of state is known theoretically as $P^{ig} = \rho RT$, and it is the ideal gas heat capacity (or related thermodynamic quantity) that is used to obtain A^{ig} . Accurate expressions for the residual contributions to A or P are generally based on empirical

thermodynamic data. The same decomposition of the Helmholtz free energy into ideal and residual parts holds also for mixtures; in this case, the ideal gas contribution is simply related to a mole fraction average of the pure components' ideal gas values, but cross-interaction effects make the residual values more difficult to determine. In Section 7.4, we see how these two parts of A contribute to the speed of sound in fluids.

In Figures 7.1 and 7.2 we sketch the basic phase topology of simple fluid systems to understand the scope of the Helmholtz energy formulation for fluid systems. All pure fluids have phase diagrams similar to Figure 7.1; however, quantum fluids may look somewhat different at low temperatures, and some fluids may decompose at temperatures within the area depicted. The solid-fluid phase boundary intersects the vapor-liquid equilibrium (VLE) phase boundary at the triple point, a single value of temperature and pressure at which the solid, liquid, and vapor phases coexist. The melting line extends, in principle, to infinite pressures (although there are, of course, other phenomena at extreme conditions), but the VLE phase boundary terminates at a critical point. For temperatures above the critical-point temperature, the fluid is said to be in the supercritical phase; for lower temperatures, the fluid is a vapor at pressures below the VLE phase boundary and a liquid at higher pressures (to the solid-fluid boundary). Along the VLE phase boundary, the fluid is said to be in the saturated liquid or saturated vapor state; inside the two-phase region of

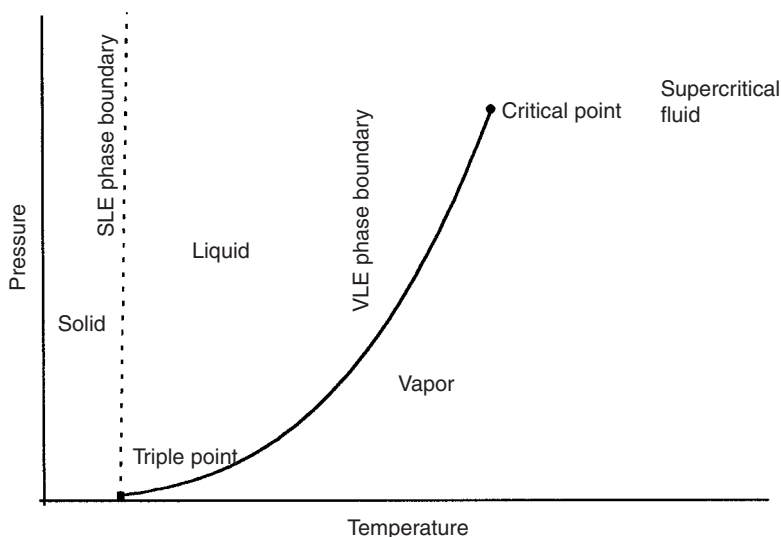


FIG. 7.1. Pressure vs temperature phase diagram of a simple pure fluid. SLE is solid-liquid equilibrium and VLE is vapor-liquid equilibrium.

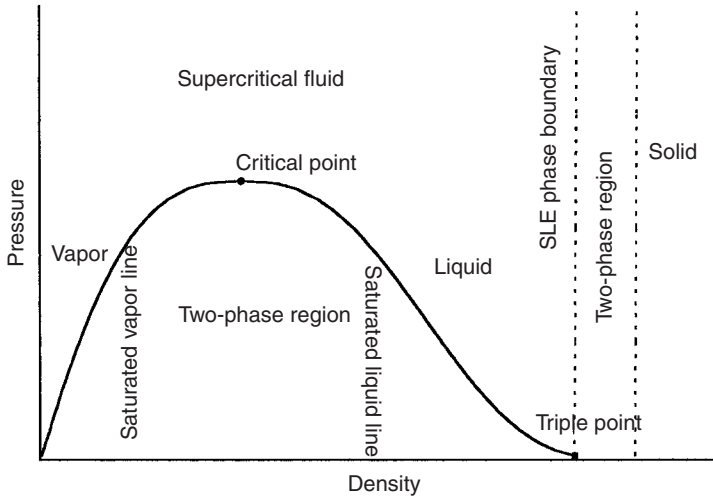


FIG. 7.2. Pressure vs density phase diagram for a simple pure fluid.

Figure 7.2, the equilibrium state consists of two phases, and the speed of sound is not uniquely defined.

The phase topology for mixtures can become significantly more complex. In general, for a system at fixed composition, the VLE phase boundary is no longer a simple line. The liquid will vaporize at a bubble point, and the bubbles may have a composition different from that of the coexisting liquid. The vapor condenses at a dew point, and the coexisting liquid may also have a different composition. The locus of dew points and bubble points for a fixed composition may be joined by a critical point. In addition, there may be liquid-liquid immiscibility in portions of the phase diagram. The speed of sound is well defined for each one-phase point, and the same equations given previously can be used for mixtures.

7.3.1 Simple Equations of State

There are several ways to represent the residual portion of the thermodynamic surfaces of fluids. The virial series is a density expansion for low densities based on statistical-mechanics cluster approaches [4]. The pressure can be written as

$$P = \rho RT[1 + B(T)\rho + C(T)\rho^2 + \dots] = \rho RT[1 + \sum_{i=1} B_i(T)\rho^i] \quad (7.20)$$

In this notation, B is the second virial coefficient, but B_i is the $(i + 1)$ virial coefficient. Although the second and, perhaps, third virial coefficients can

be determined from experimental data, virial coefficients of higher order are difficult to measure, and the series itself does not converge as the critical density is approached. Equation 7.20 is rigorous in the low density limit, and for gases at low and moderate density, up to about one third of the critical density, this type of representation can be quite accurate.

Equation 7.20 yields

$$A^r(\rho, T) = RT \sum_{i=1} \frac{1}{i} B_i(T) \rho^i \quad (7.21)$$

and, using Eq. 7.1, the speed of sound for the virial equation of state is given by

$$w^2 = \frac{1}{M} \left[RT + RT \sum_{i=1} (i+1) B_i \rho^i - \frac{R + 2RT \sum_{i=1} \left(\frac{B_i}{T} + B'_i \right) \rho^i + RT^2 \sum_{i,j=1} \left(\frac{B_i}{T} + B'_i \right) \left(\frac{B_j}{T} + B'_j \right) \rho^{i+j}}{2f' + Tf'' + T \sum_{i=1} \frac{\rho^i}{i} \left(\frac{2B'_i}{T} + B''_i \right)} \right] \quad (7.22)$$

where primes and double primes indicate the first and second temperature derivatives, respectively, of the virial coefficients, B_i and the temperature term in A^{ig} , f from Eq. 7.19. It is straightforward but tedious to expand the denominator in Eq. 7.22 to write a density series of the form

$$w^2 = \frac{RT\gamma^o}{M} \left[1 + \sum_{i=1} K_i(T) \rho^i \right] \quad (7.23)$$

where γ^o is the ratio of the ideal gas heat capacities, $1 - (2Tf + T^2 f'')^{-1}$, in the current notation. The first two terms are given by [7]

$$K_1(T) = 2B_1 + 2(\gamma^o - 1)TB'_1 + \frac{(1 - \gamma^o)^2}{\gamma^o} T^2 B''_1 \quad (7.24)$$

and

$$K_2(T) = \frac{\gamma^o - 1}{\gamma^o} [B_1 + (2\gamma^o - 1)TB'_1 - (1 - \gamma^o)T^2 B''_1]^2 + \frac{2\gamma^o + 1}{\gamma^o} B_2 + \frac{\gamma^{o2} - 1}{\gamma^o} TB'_2 + \frac{(\gamma^o - 1)^2}{2\gamma^o} T^2 B''_2 \quad (7.25)$$

Thus, if the virial coefficients are known, they can be used to calculate the speed of sound in a gas.

In these expressions, we see the intimate connection between the ideal gas value of the speed of sound and the full expression for this property. In Eq. 7.23, the ideal gas contribution is identified with the zero-density value, $w^{ig} = (RT\gamma^o/M)^{1/2}$, but note that a contribution from internal degrees of freedom, γ^o , also affects the higher order terms in the expression for the speed of sound as seen in Eqs. 7.24 and 7.25. It is generally true that the ideal gas speed of sound is consistent with the low-density limit of a thermodynamic expression, and further that the internal modes in a molecular system also affect the sound speed at high densities.

The family of cubic equations of state represents another simple form to describe the thermodynamic surface. In general these equations can be written as [8]

$$P = \frac{\rho RT}{1 - b\rho} - \frac{a\rho^2}{1 + ub\rho + vb^2\rho^2} \quad (7.26)$$

where u and v serve to distinguish between the type of cubic equation (e.g., van der Waals, Peng–Robinson, etc.), b is typically a fluid dependent constant, and a is also fluid dependent, but may be constant or a function of temperature, depending on the model being considered. The residual Helmholtz free energy can then be written as

$$A^r(\rho, T) = -RT \ln(1 - b\rho) - \frac{a^2}{\rho\sqrt{u^2 - 4v}} \ln \frac{2 + b\rho(u + \sqrt{u^2 - 4v})}{2 + b\rho(u - \sqrt{u^2 - 4v})} \quad (7.27)$$

and the speed of sound becomes

$$w^2 = \frac{1}{M} \left[\frac{RT}{(1 - b\rho)^2} - \frac{a\rho(2 + bu\rho)}{[vb^2\rho^2 + bu\rho + 1]^2} - \frac{\left[\frac{R}{1 - b\rho} - \frac{a'\rho}{vb^2\rho^2 + bu\rho + 1} \right]^2}{2Rf' + RTf'' - \frac{a''}{b\sqrt{u^2 - 4v}} \ln \frac{2 + b\rho(u + \sqrt{u^2 - 4v})}{2 + b\rho(u - \sqrt{u^2 - 4v})}} \right] \quad (7.28)$$

The primes again indicate temperature derivatives. The expression simplifies considerably for the original van der Waals equation (where $u = v = 0$ and a is constant), but the general expression of Eq. 7.28 can be used for any of the common cubic equations of state. (Note that in the case of $u = v = 0$, the logarithmic expression can be expanded, and the full equation is still well defined.)

Cubic equations are often used to describe fluids in engineering applications. These equations can provide reasonably good descriptions of a thermodynamic surface, (except near the critical point), and liquid-vapor phase boundary information can be calculated directly from this approach. The sound speeds calculated from expressions such as that given previously may be adequate approximations. For more accurate descriptions of the speed of sound (and other properties), the reference quality equations, as discussed in Section 7.3.2, are required.

In addition to these simple equations that can be used to approximate the properties of real fluid systems, we mention that there are also model systems for which properties can be calculated. For instance, the hard-sphere fluid, consisting of (structureless) spherical particles of diameter σ and relative mass M , interacts with a potential function which is infinite when the particles collide and zero otherwise. This model forms the basis for many computer simulations and theoretical results and is often applied to real systems. The equation of state for this fluid has been shown empirically to be well described by the Carnahan–Starling expression [9]

$$P = \rho RT \frac{1 + \eta + \eta^2 - \eta^3}{(1 - \eta)^3} \quad (7.29)$$

where $\eta = \pi \sigma^3 \rho N_A / 6$ and N_A is the Avogadro number. This leads to a Helmholtz energy expression of the form

$$A = RT \left\{ A^\circ + \ln \rho - \frac{3}{2} \ln T + \frac{4\eta - 3\eta^2}{(1 - \eta)^2} \right\} \quad (7.30)$$

and Eq. 7.1 immediately gives

$$w^2 = \frac{RT}{3M} \left\{ \frac{5 + 10\eta - 3\eta^2 - 24\eta^3 + 37\eta^3 - 22\eta^5 + 5\eta^6}{(1 - \eta)^6} \right\} \quad (7.31)$$

Unfortunately, we are not aware of any computer simulations which have generated the speed of sound of the hard-sphere system, but the model can be used for real fluids with an effective hard-sphere diameter regressed from available data. Of course, alternative ideal gas behavior can also be incorporated into such a hard-sphere model for real fluids.

7.3.2 Other Equation of State Descriptions

The most accurate equations of state are those that seek to represent all available thermodynamic data to within their experimental uncertainty. These are generally expressed by the pressure as a function of temperature and density together with a correlation for the ideal gas properties, or directly

as the Helmholtz free energy as a function of temperature and density. Such equations are available for industrially important fluids and are suitable for purposes such as instrument calibration and custody transfer applications. These equations are developed by regression of large numbers of data over a broad range of state variables and may have 30 to 40 adjustable coefficients to describe the vapor, liquid, and supercritical phases, including the phase boundary information. Of course there are also thermodynamic surfaces of intermediate complexity compared with the simple cubic or virial coefficient representations and the reference quality equations being considered here.

Examples of the accurate reference quality equations of state include the Benedict–Webb–Rubin family of equations, which have the form of

$$P = \rho RT + \sum_{i=1}^{N_1} G_i \rho^{n_i} T^{m_i} + \sum_{i=N_1}^N G_i \rho^{n_i} T^{m_i} \exp(\gamma \rho^2) \quad (7.32)$$

Typical equations of this form [10] have 32 coefficients G_i , with the exponents of density ranging from 2 to 13 and the exponents of temperature ranging from -4 to $\frac{1}{2}$; several important fluids have been described by this functional form with fixed exponents, n_i and m_i , by regressing only the coefficients G_i based on the available experimental data on density, heat capacity, phase boundary, speed of sound, etc. This type of equation can also be converted into an expression for the Helmholtz free energy, and the speed of sound can be calculated from Eq. 7.1 as before.

Recently, several equations of the form

$$\begin{aligned} A(\rho, T) = A^{ig}(\rho, T) + \sum_{i=1}^{N_1} G_i \delta^{n_i} \tau^{m_i} + \sum_{i=N_1}^{N_2} G_i \delta^{n_i} \tau^{m_i} \exp(\delta^{l_i}) \\ + \sum_{i=N_2}^N G_i \delta^{n_i} \tau^{m_i} \exp[g(\delta, \tau)] \end{aligned} \quad (7.33)$$

have been developed for important fluids, where $\delta = \rho/\rho_c$, $\tau = T_c/T$, the subscript “c” indicates a value at the critical point, and g is a function that improves the description of the thermodynamic surface in the critical region. These equations are also determined empirically from the best available experimental data; in this case, the numbers of terms in each sum, the exponents n_i , m_i , l_i , and the function g may be optimized from the data. The resultant “structurally optimized” thermodynamic surface generally provides the best general representation over the full range of fluid states, and the speed of sound determined using Eqs. 7.1 and 7.33 provide an accurate estimate of the property. The sounds speed tabulated in Section 7.6 were generated from models such as those of Eqs. 7.32 and 7.33.

When reference-quality thermodynamic surfaces are not available for a fluid of interest, predictive models for the surface can be used to determine the speed of sound. The residual Helmholtz energy surfaces of similar fluids generally obey a corresponding states principle [4, 8]; thus, with two-scale factors, representing changes in energy and distance scales, one can generate an approximate surface for a fluid based on the thermodynamic surface of a more well-studied fluid. This approach allows reasonable estimates of the speed of sound with a minimal amount of information. The cubic equations of state of Eq. 7.26 can be implemented when values for the critical temperature and pressure are known; the more complex cubic equations require additional information, and other extensions of the corresponding states principle can be implemented that make use of available experimental information. The molecular structure must be considered explicitly to approximate the ideal-gas effects, which are quite significant; group additivity and related methods can be useful for this problem when spectroscopic data are not available. Direct predictions of the heat capacities and compressibilities can also be made; these enter into the speed of sound calculation using Eq. 7.15. Alternatively, corresponding states or related models can be developed for the speed of sound itself, and these can be considered independently of the full Helmholtz energy surface.

Fluid mixtures generally obey the same thermodynamic and hydrodynamic principles as pure fluids, and thus equations of state can be constructed that look similar to those discussed previously, and the speed of sound can be computed using the same equations, with derivatives being taken at fixed composition. Among the special considerations, we note that the continuity equation, Eq. 7.2, must be revised to reflect conservation of each species present, and the irreversibilities associated with demixing upon passage of a sound perturbation must be considered at high frequencies. In addition, as mentioned previously, the phase topology of mixtures generally differs from that of pure fluids, and care must be taken with any calculation of the speed of sound that the appropriate phase has been identified. Thermodynamic surfaces for mixtures can be calculated from a virial equation of state if the pure fluid coefficients are known and the relevant “cross” virial coefficients, representing interactions between the distinct species in the fluid mixture, can be estimated. Cubic equations of state can also be extended to mixtures using well-defined mixing rules and, if available, a set of interaction parameters representing the cross-species effects. Reference quality equations can also be extended to mixtures with appropriate mixing rules; available experimental data over a range of compositions can be used to regress additional correction terms and hence improve the mixture calculations.

As a simple, but explicit, example of a calculation of the speed of sound in a mixture, we consider a system at very low densities, so that the ideal

gas equations are appropriate. The equation of state, $P = \rho RT$, remains valid for ideal gas mixtures, and we denote the isobaric and isochoric ideal gas heat capacities of a mixture as $C_{P,\text{mix}}^{ig}$ and $C_{V,\text{mix}}^{ig}$. Equation 7.15 can be expressed as

$$(w_{\text{mix}}^{ig})^2 = \frac{C_{P,\text{mix}}^{ig}}{C_{V,\text{mix}}^{ig}} \frac{RT}{M_{\text{mix}}} \quad (7.34)$$

Note again that this is the same as for a pure fluid, e.g. Eq. 7.17, although in that case, we considered a monatomic gas with heat capacities $3R/2$ and $5R/2$. The pure components of the mixture (denoted by a subscript i) more generally have ideal gas heat capacities $C_{P,i}^{ig}$ and $C_{V,i}^{ig}$, and they are present with a mole fraction of x_i . It is rigorously correct that the molar mass and ideal gas heat capacities of a mixture can be written as mole-fraction-weighted averages of these quantities for the pure components: $M_{\text{mix}} = \sum x_i M_i$; $C_{P,\text{mix}}^{ig} = \sum x_i C_{P,i}^{ig}$; $C_{V,\text{mix}}^{ig} = \sum x_i C_{V,i}^{ig}$. Then Eq. 7.34 can be written as

$$(w_{\text{mix}}^{ig})^2 = \frac{\sum x_i C_{P,i}^{ig}}{\sum x_i C_{V,i}^{ig}} \frac{RT}{\sum x_i M_i} \quad (7.35)$$

From Eq. 7.35 we see that the speed of sound of a mixture, even in an ideal gas state, cannot generally be calculated as a mole fraction average of the speed of sound of the components.

Near the critical point of a pure fluid or a mixture, none of the equations of state discussed earlier is adequate. At this singularity in the thermodynamic surface, the behavior is governed by fluctuations that have very long length scales rather than by the comparatively short-ranged interactions observed in other regions of the phase diagram [11]. The phenomenon of “critical slowing” affects the hydrodynamics of a near-critical system, so the derivation of the speed of sound as a thermodynamic property must be reexamined [7]. The thermodynamic speed of sound is strictly zero at the critical point, which can be seen by Eq. 7.15 with the additional observation that the strong critical divergence of the isobaric heat capacity is compensated by a similar decrease in the isothermal derivative; thus, the weak divergence of the isochoric heat capacity in the denominator of the expression ensures that the speed of sound approaches zero at the critical point. This value of the speed of sound can be obtained from a classical Helmholtz free energy surface, although a correct description of the approach at the critical point requires a nonanalytical, scaling theory expression for the free energy that is outside the scope of this chapter. The dispersion of sound (i.e., the dependence of the speed of sound on frequency) is very pronounced in the critical region, and it is the low-frequency limit that is governed by these thermodynamic considerations.

In summary, the thermodynamic speed of sound of a fluid system at any temperature, density (or pressure), and composition can be obtained by using Eq. 7.1 if the Helmholtz free energy surface for the fluid is known. The quality of the speed of sound calculated in this manner of course depends on the quality of the thermodynamic surface that is used. The reference quality equations can reliably be used, as they should reflect the uncertainty of the available speed of sound data.

7.4 Speed Of Sound in Fluids

Argon is one of the simplest fluid systems because of its location on the periodic table, and it is also an important commodity chemical. The system has been well studied, and the reference quality Helmholtz energy equation of Tegeler *et al.* [12] provides an excellent basis for examining the behavior of the speed of sound in argon. The equation of [12] is of the form described by Eq. 7.33; in addition, a modified Benedict–Webb–Rubin equation as in Eq. 7.32 is available in [10].

In Figures 7.3 to 7.5, we show the behavior of the speed of sound in various projections over a large range of the state variables. These and other figures are based on the sound speed calculations available in the NIST pure fluids database [3]. In Figure 7.3, the saturation boundary is shown in bold; at a

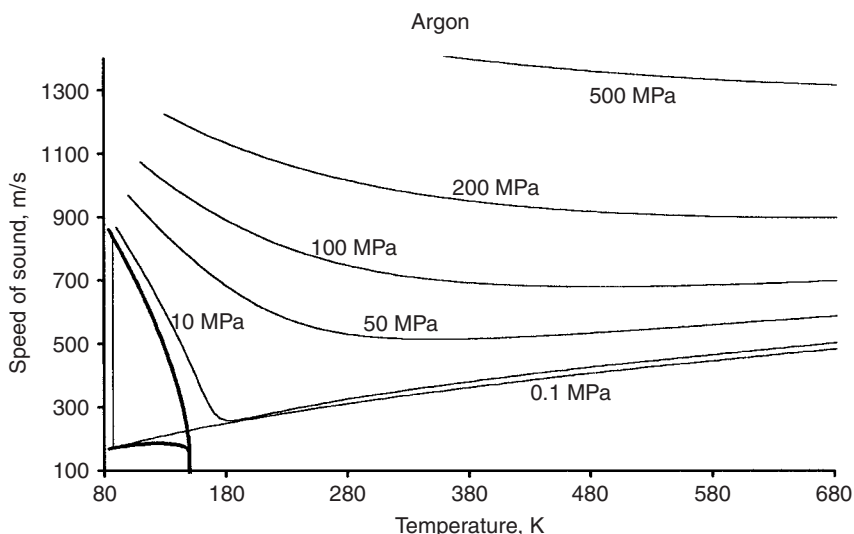


FIG. 7.3. The speed of sound in argon vs temperature along isobars. The heavy lines give values on the saturated liquid and saturated vapor curves.

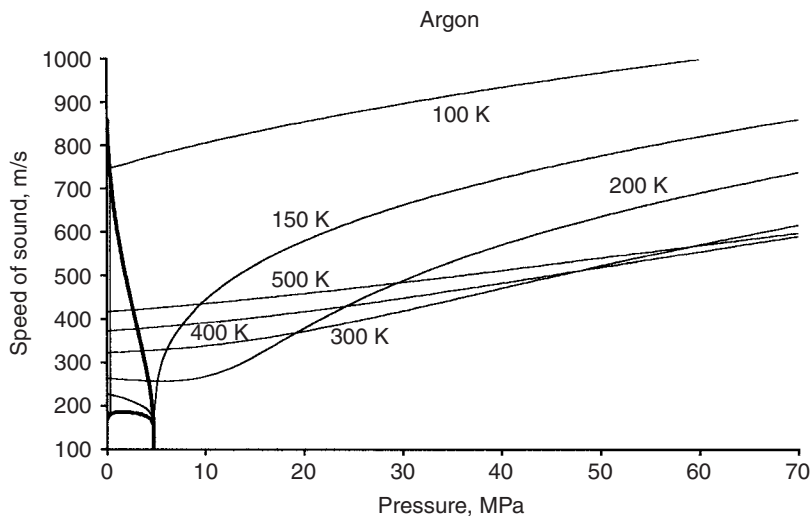


FIG. 7.4. The speed of sound in argon vs pressure along isotherms. The heavy lines give values on the saturated liquid and saturated vapor curves.

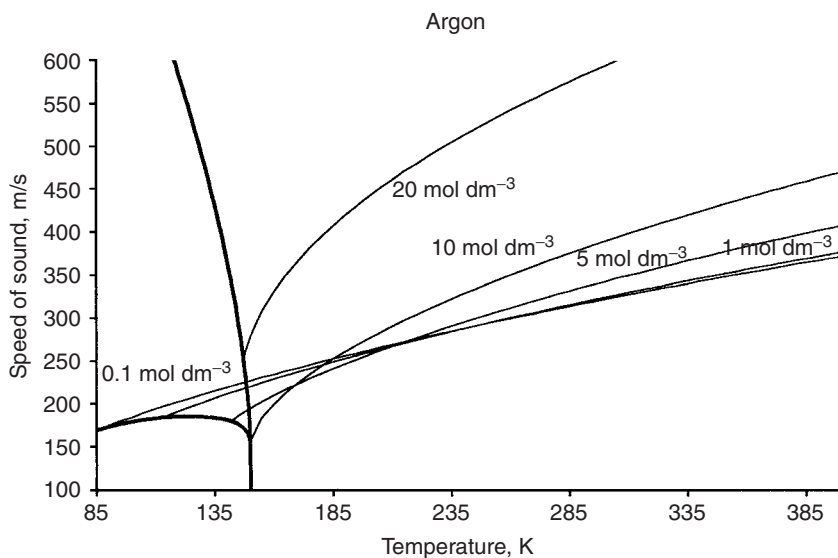


FIG. 7.5. The speed of sound in argon vs temperature along isochores. The heavy lines give values on the saturated liquid and saturated vapor curves.

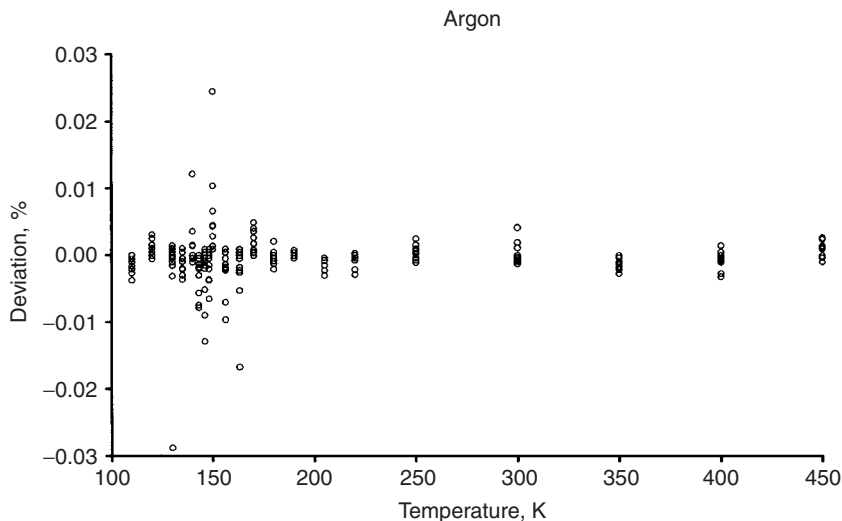


FIG. 7.6. Sample deviations between experimental and calculated values for the speed of sound in argon. Two points (with deviations of -0.26% and 0.54%) are not shown.

fixed temperature, the two lines represent the sound speed in the coexisting vapor and liquid. Note that the sound speeds approach zero at the critical point. Note from Figures 7.3 and 7.4 that the speed of sound isotherms cross in these pressure projections. The isochores (lines of constant density) are also seen to cross in Figure 7.5; for supercritical fluids, the speed of sound tends to increase with density and with temperature along the isochores. In Figure 7.6, we compare the calculated sound speeds with the data of Estrada-Alexanders and Trusler [13]. The 173 data were obtained between 110 K and 450 K for pressures ranging from 6.83 kPa to 19.26 MPa using a spherical acoustic resonator with experimental uncertainties from 0.001 to 0.007%. These data were used in the regression of the thermodynamic surface, and the deviations between the data and this reference quality surface are consistent with the experimental uncertainty assessment.

In general, as discussed previously the reference quality equations of state provide calculations of the speed of sound that are consistent with the experimental data. In Figure 7.7, we compare the 300 K sound speed isotherm for argon as calculated from the equation of state of [12] with the results of various models. A density of 30 mol dm^{-3} for this temperature corresponds to a pressure of about 190 MPa. The dashed line gives the ideal gas value for argon at 300 K, as calculated from Eq. 7.17. This quantity is independent of density, and agrees quite well with the reference equation of state at zero density. In fact, all of the models agree with Eq. 7.17 in this limit. We have included

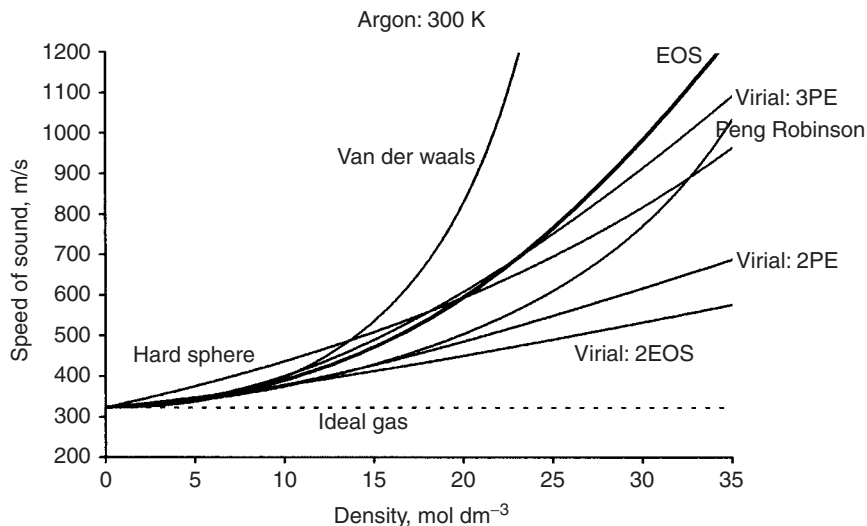


FIG. 7.7. Speed of sound of argon vs density at 300 K. The bold line labeled EOS represents values calculated from the standard reference equation of state. The other lines are values calculated from various models discussed in the text.

three lines to represent the virial expressions of Eqs. 7.20 to 7.25. The line labeled “Virial: 2EOS” used the first two acoustic virial coefficients [Eqs. 7.24 and 7.25], where the pressure virial coefficients and their derivatives were calculated numerically from a computer implementation of the reference thermodynamic surface of Tegeler *et al.* [12]. The line “Virial: 2PE” used the first two acoustic virial coefficients tabulated by Estrada-Alexanders and Trusler [13] that had been determined from an interatomic potential energy function. The differences in these two lines come about because of the difficulty in numerically determining the second temperature derivatives of the pressure virial coefficients and the sensitivity of the acoustic virial coefficients to these quantities. The model (“Virial: 3PE”), using three virial coefficients as tabulated by Estrada-Alexanders and Trusler [13], is seen to provide the best representation of the reference line even to the high pressures which are shown.

The van der Waals and Peng–Robinson equations of state are two forms in the family of cubic equations of state. The parameters of both of these equations are determined from the critical parameters of argon and, in the case of the Peng–Robinson equation, the acentric factor for argon. For the van der Waals equations, both u and v of Eq. 7.28 are zero; for the Peng–Robinson equation of state $u = 2$ and $v = -1$. These equations may have problems reproducing experimental densities at high values of the pressure, and the

speeds of sound are seen to deviate significantly from the reference line. Finally, Figure 7.7 shows the results for the speed of sound of the hard sphere fluid as given in Eq. 7.31. Only a value of the effective hard sphere diameter, σ is needed in order to evaluate the parameter η . We have determined $\sigma = 2.88 \times 10^{-10}$ m by requiring that the hard sphere result be consistent with the sound speed of argon at 20 mol dm^{-3} . The hard sphere expression seems to give somewhat less curvature than the reference line for this isotherm.

Nitrogen provides our second example, and in Figures 7.8 to 7.10 we indicate the behavior of the speed of sound based on the Helmholtz energy formulation of Span *et al.* [14]. The general behaviors of the curves shown are seen to be quite similar to those of argon; for similar state points, nitrogen generally has a larger value of the speed of sound. Figure 7.11 compares the calculated speed of sound with high-quality experimental measurements on argon of Costa Gomes and Trusler [5]. The data were obtained in a spherical resonator operating at frequencies between 5 kHz and 26 kHz, and the experimental uncertainties were estimated [5] as less than 0.01%. A difference between the measured results at these frequencies and the thermodynamic speed of sound, corresponding to zero frequency, was noted by Costa Gomes and Trusler. Figure 7.11 also shows the data as adjusted to zero frequency in [5]. These zero-frequency data were considered in the regression of Span

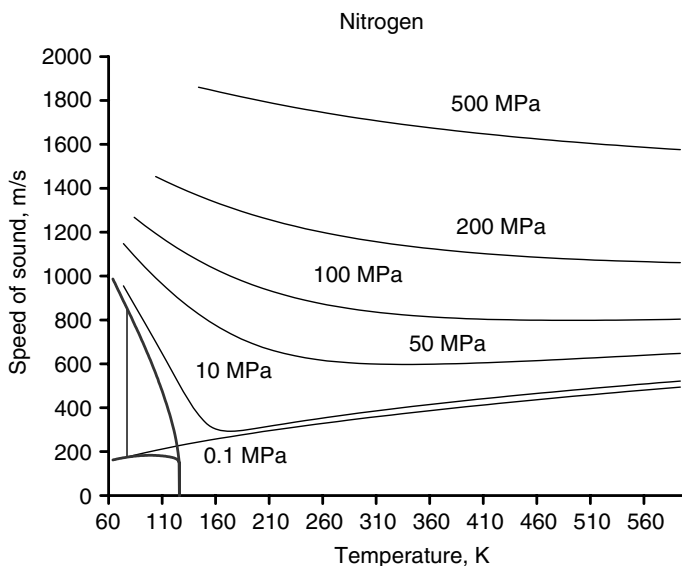


FIG. 7.8. The speed of sound in nitrogen vs temperature along isobars. The heavy lines give values on the saturated liquid and saturated vapor curves.

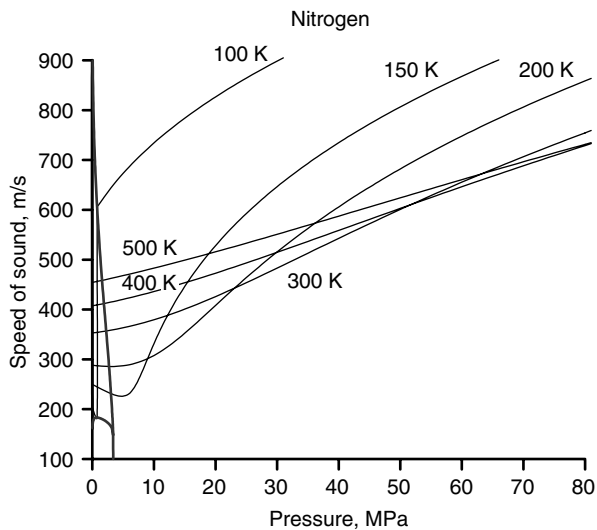


FIG. 7.9. The speed of sound in nitrogen vs pressure along isotherms. The heavy lines give values on the saturated liquid and saturated vapor curves.

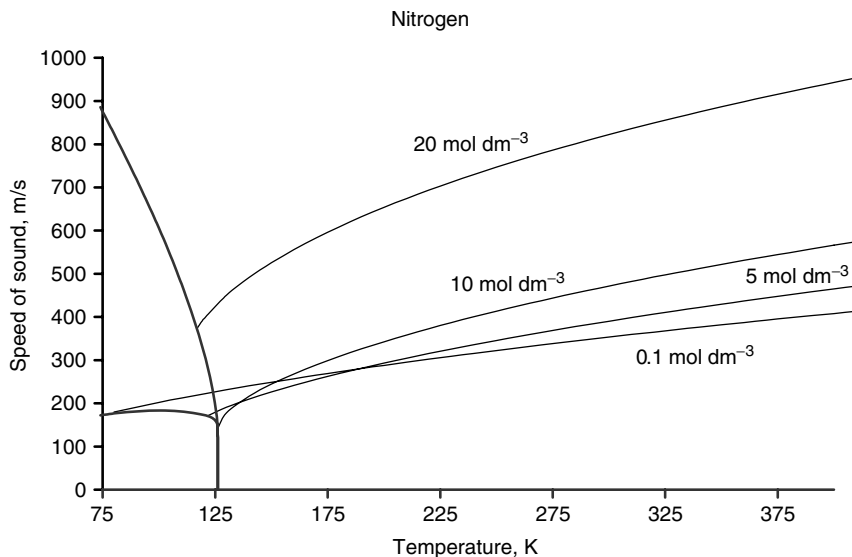


FIG. 7.10. The speed of sound in nitrogen vs temperature along isochores. The heavy lines give values on the saturated liquid and saturated vapor curves.

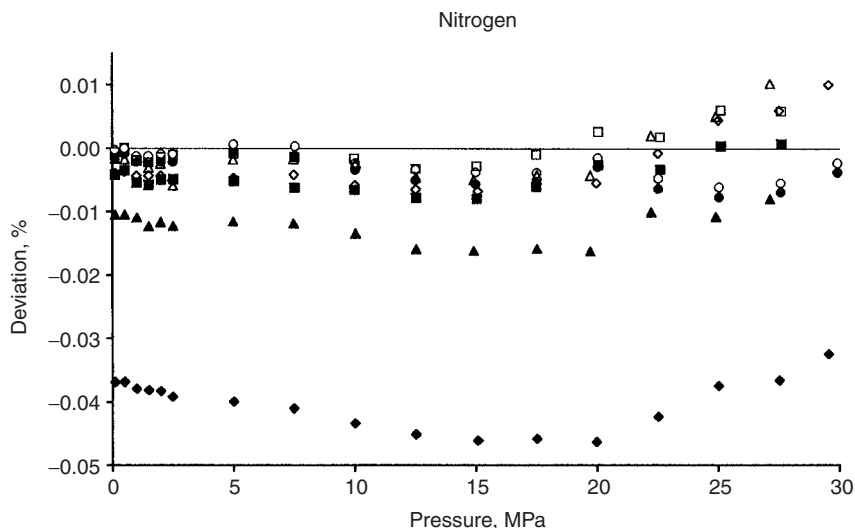


FIG. 7.11. Sample deviations between experimental and calculated values for the speed of sound in nitrogen. The closed symbols represent data obtained at frequencies between 5 kHz and 26 kHz; the open symbols are data corrected to zero frequency. Circles: 250 K; squares: 275 K; triangles: 300 K; diamonds: 350 K.

et al. [14] and, as can be seen, the reference equation of state agrees with the data to within their uncertainty.

The properties of water are well described by the standard formulation adopted by the International Association for the Properties of Water and Steam (IAPWS) [15]. Figures 7.12 to 7.14 show the behavior of the speed of sound of fluid water. Because of the relatively high critical temperature of water (647.096 K) relative to that of argon and nitrogen, the region of phase equilibria is expanded in these figures. The vertical line segments in Figures 7.12 and 7.13 connected the isobars and isotherms, respectively, across the two-phase region. This is the region of liquid-vapor phase separation, and the thermodynamic speed of sound is not defined for the two-phase systems. Figure 7.12 includes a line representing the critical isobar ($P_c = 22.064$ MPa); this isobar intersects the phase boundary at the critical temperature, whereas all subcritical isobars meet the saturation boundary at liquid and vapor points, and supercritical isobars do not intersect the phase boundary. As mentioned earlier the thermodynamic speed of sound should vanish at the critical point, however, the classical equation for water gives a small but non-zero value. For some equations of state, this value may depend on the computer implementation and the particular calculation performed: a value of about 35 m/s can be obtained on the phase boundary at the critical temperature for the IAPWS equation.

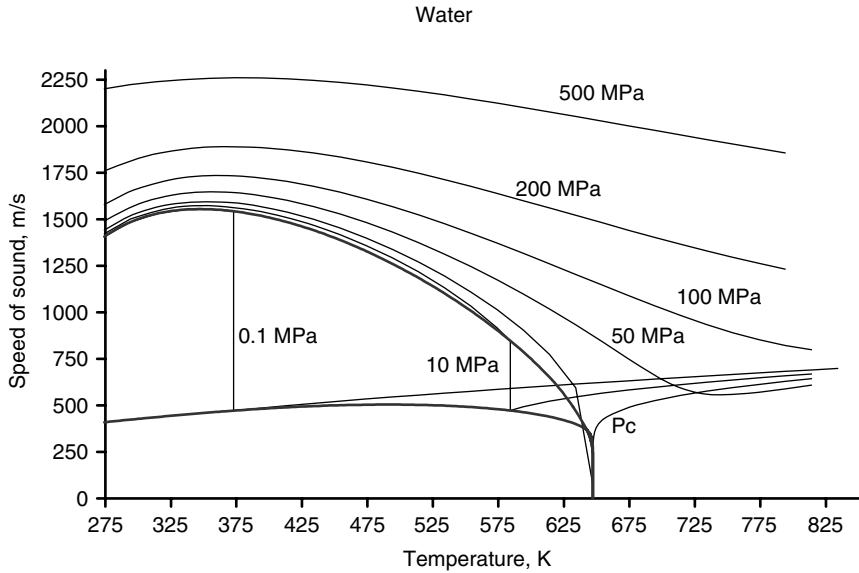


FIG. 7.12. The speed of sound in water vs temperature along isobars. The heavy lines give values on the saturated liquid and saturated vapor curves.

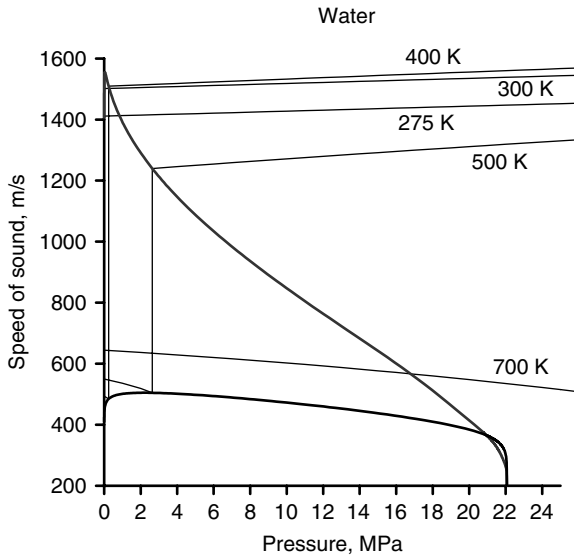


FIG. 7.13. The speed of sound in water vs pressure along isotherms. The heavy lines give values on the saturated liquid and saturated vapor curves.

Several features of the behavior of the speed of sound in water can be observed in Figure 7.13. Note that there is a small region where the speed of sound in the saturated vapor (the lower branch of the phase boundary in most of the figures) is greater than that in the coexisting liquid. This occurs for temperatures between about 643 K and the critical temperature. Near the pure-fluid critical point, the vapor and liquid states become quite similar; although the vapor has a smaller density, the speed of sound in the vapor is larger than that of the liquid in this region. The subcritical isotherms in Figure 7.13 illustrate another feature: note that for fixed pressure (at about 18 MPa, to be specific), the speed of sound at 300 K and 400 K is significantly higher than that at 275 K, and the 500 K isotherm is inverted compared to the trend of the others. This behavior is related to the maxima seen in the isobars in Figure 7.12. Figure 7.14 shows the clear maximum of the speed of sound in the saturated liquid and the broader maximum in that saturated vapor phase.

The behavior of the speed of sound in air is shown in Figures 7.15 to 7.17. These values were calculated from the thermodynamic surface of Lemmon *et al.* [16] which provides a reference quality equation of state for dry air considered at the fixed composition of 0.7812 nitrogen, 0.2096 oxygen, and 0.0092 argon by mole fraction. We see that the general behavior of the mixture isobars (Fig. 7.15), isotherms (Fig. 7.16), and isochores (Fig. 7.17) is quite similar to the trends seen for the pure fluids. Note that the subcritical isobar at 0.1 MPa also shows a segment in the two-phase region. This line is

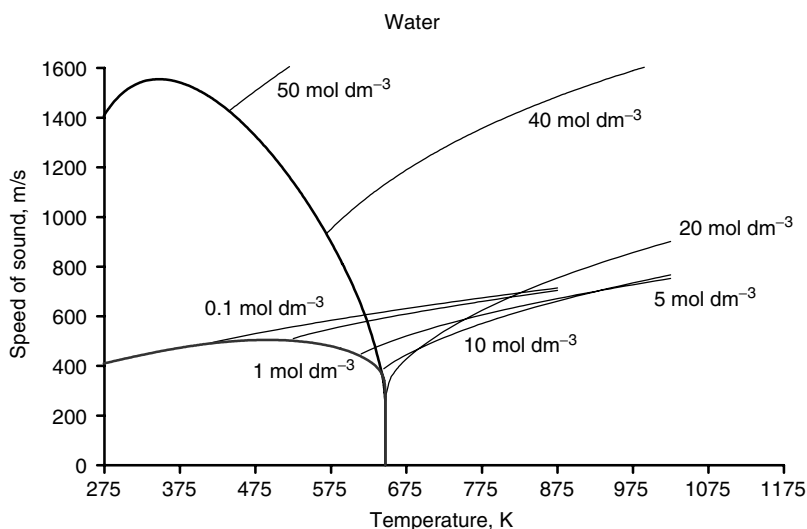


FIG. 7.14. The speed of sound in water vs temperature along isochores. The heavy lines give values on the saturated liquid and saturated vapor curves.

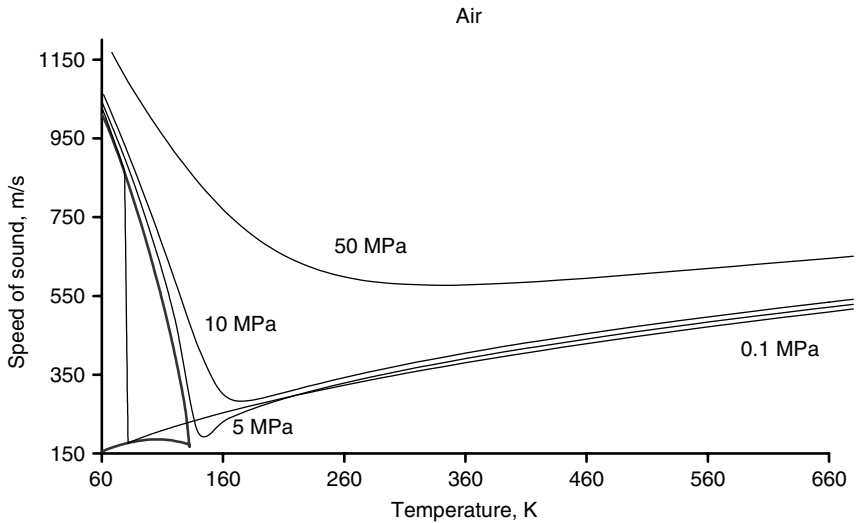


FIG. 7.15. The speed of sound in air vs temperature along isobars. The heavy lines give values on the saturated liquid and saturated vapor curves (bubble-point curve and dew-point curve).

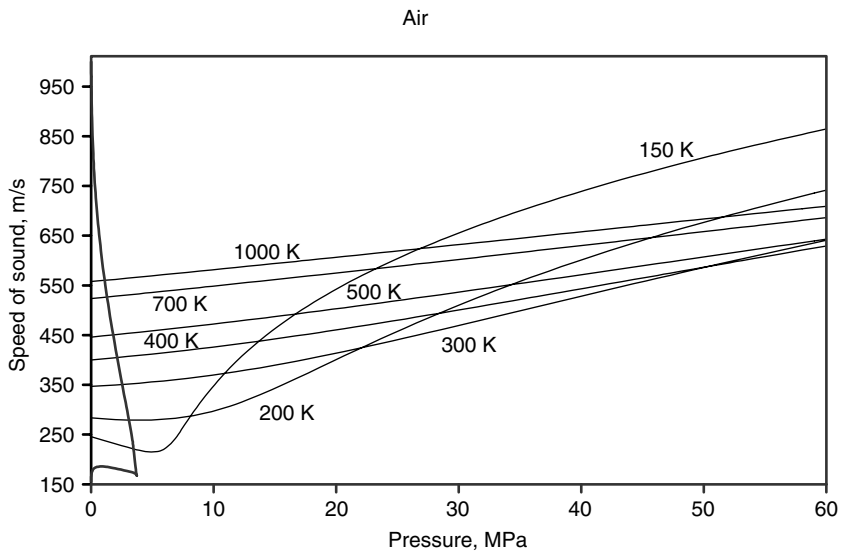


FIG. 7.16. The speed of sound in air vs pressure along isotherms. The heavy lines give values on the saturated liquid and saturated vapor curves (bubble-point curve and dew-point curve).

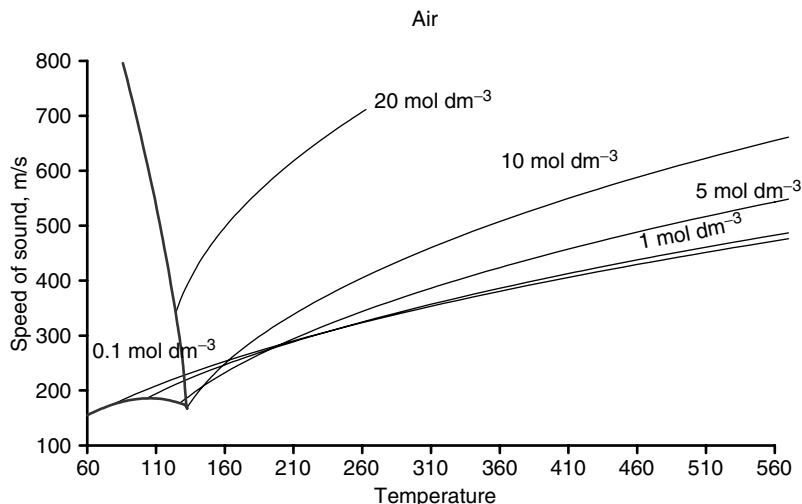


FIG. 7.17. The speed of sound in air vs temperature along isochores. The heavy lines give values on the saturated liquid and saturated vapor curves (bubble-point curve and dew-point curve).

not vertical, however, and does not connect states in equilibrium. The lower saturation boundary is the line of dew points. At 0.1 MPa, the dew-point temperature for the composition specified is at about 81.6 K. The bubble-point temperature is at about 78.8 K. The bubbles in equilibrium with the bulk liquid and the condensate in equilibrium with the bulk vapor have different compositions than the bulk fluid. Again, the thermodynamic speed of sound is not defined in the two-phase region.

Finally, in Figure 7.18 we show some deviations between experimental sound speeds for a natural gas fluid and calculations from a model for the mixture Helmholtz free energy. The data were obtained with a cylindrical cavity for a methane-rich ten-component mixture representing Gulf Coast natural gas [17]. The experimental uncertainty is about 0.05%. The generalized mixture model representing the base line [18] uses the reference quality equation of state for each pure component and a few mixture parameters based primarily on density and phase equilibrium data. The model is seen to agree with the data to nearly within the experimental uncertainty.

7.5 Conclusions

The thermodynamic properties of a fluid system are completely determined by the Helmholtz free energy surface of the system. We have seen that the

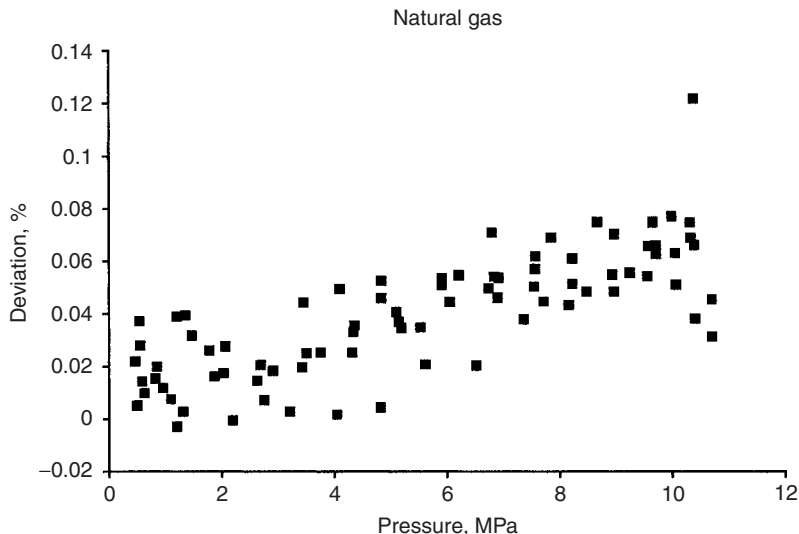


FIG. 7.18. Sample deviations between experimental and calculated values for the speed of sound in a natural gas.

speed of sound in such a system can be considered a thermodynamic property, and that it can be calculated from Eq. 7.1 The available sources for the speed of sound in fluid systems can be considered to be of three types: (1) experimental measurements and compilations of experimental measurements can provide the most accurate values for the speed of sound in well-defined systems; (2) reference quality Helmholtz free energy surfaces have been developed for important fluids and can describe the speed of sound essentially to within the uncertainty of available data; (3) models or predictive schemes can be used for systems for which measurements are not available, including more complex molecular systems and mixtures.

Among the sources for experimental data, the tables [19] of the NIST Thermodynamics Research Center provide an extensive compilation for both hydrocarbon and non-hydrocarbon systems. These tables are available in both printed and electronic form. Researchers at the National Institute of Standards and Technology have developed several reference thermodynamic surfaces based on experimental measurements at NIST and elsewhere, and have compiled reference quality surfaces from several other sources. Such information is available in the form of PC-based computer programs such as the NIST Thermophysical Properties of Pure Fluids Database [3]. NIST also provides predictive computer packages that can be used for pure fluids with limited measurements and for mixtures. The catalog of computer packages from the Standard Reference Data

office of NIST is available on-line at <http://www.nist.gov/srd>. Some information on the thermophysical properties of fluids is available in the NIST chemistry webbook at <http://webbook.nist.gov>. The material in Tables 7.1 through 7.4 was calculated from these PC computer programs.

7.6 Tables of the Speed of Sound in Important Fluids

TABLE 7.1. Argon — Saturation Boundary

T (K)	P (MPa)	Liquid		Vapor	
		ρ (mol/dm ³)	ω (m/s)	ρ (mol/dm ³)	ω (m/s)
84	0.07	35.44	861.10	0.104	168.28
85	0.08	35.28	854.24	0.115	169.08
86	0.09	35.13	847.35	0.127	169.87
87	0.10	34.98	840.43	0.140	170.64
88	0.11	34.82	833.47	0.155	171.39
89	0.12	34.67	826.48	0.170	172.12
90	0.13	34.51	819.45	0.186	172.83
91	0.15	34.35	812.39	0.204	173.52
92	0.16	34.19	805.28	0.222	174.20
93	0.18	34.04	798.14	0.242	174.85
94	0.19	33.87	790.95	0.264	175.49
95	0.21	33.71	783.72	0.286	176.11
96	0.23	33.55	776.45	0.310	176.71
97	0.25	33.39	769.14	0.336	177.29
98	0.28	33.22	761.78	0.363	177.85
99	0.30	33.05	754.37	0.392	178.39
100	0.32	32.89	746.91	0.422	178.91
101	0.35	32.72	739.40	0.454	179.41
102	0.38	32.54	731.83	0.488	179.89
103	0.41	32.37	724.21	0.524	180.36
104	0.44	32.20	716.54	0.562	180.80
105	0.47	32.02	708.81	0.601	181.22
106	0.51	31.84	701.02	0.643	181.62
107	0.54	31.66	693.16	0.687	182.01
108	0.58	31.48	685.24	0.733	182.37
109	0.62	31.30	677.26	0.782	182.71
110	0.67	31.11	669.20	0.833	183.03
111	0.71	30.92	661.08	0.887	183.33
112	0.76	30.73	652.87	0.943	183.61
113	0.81	30.54	644.60	1.002	183.87
114	0.86	30.34	636.24	1.065	184.11
115	0.91	30.14	627.79	1.130	184.33
116	0.97	29.94	619.26	1.198	184.52
117	1.02	29.74	610.64	1.269	184.70
118	1.08	29.53	601.93	1.344	184.85
119	1.15	29.32	593.11	1.423	184.98
120	1.21	29.11	584.19	1.506	185.09
121	1.28	28.89	575.16	1.592	185.17
122	1.35	28.67	566.02	1.683	185.23
123	1.43	28.45	556.75	1.778	185.27
124	1.50	28.22	547.36	1.878	185.29
125	1.58	27.98	537.83	1.982	185.28
126	1.66	27.75	528.16	2.092	185.24
127	1.75	27.50	518.34	2.208	185.18
128	1.84	27.25	508.36	2.330	185.10

TABLE 7.1. (*continued*)

T (K)	P (MPa)	Liquid		Vapor	
		ρ (mol/dm ³)	ω (m/s)	ρ (mol/dm ³)	ω (m/s)
129	1.93	27.00	498.21	2.458	184.98
130	2.03	26.74	487.88	2.592	184.85
131	2.12	26.47	477.36	2.735	184.68
132	2.23	26.20	466.63	2.885	184.49
133	2.33	25.91	455.69	3.043	184.27
134	2.44	25.62	444.51	3.211	184.02
135	2.55	25.32	433.10	3.389	183.74
136	2.67	25.01	421.42	3.579	183.41
137	2.79	24.68	409.47	3.781	183.03
138	2.91	24.35	397.21	3.996	182.60
139	3.04	23.99	384.62	4.228	182.09
140	3.17	23.62	371.63	4.477	181.50
141	3.30	23.23	358.17	4.747	180.81
142	3.44	22.82	344.14	5.041	180.00
143	3.59	22.38	329.41	5.363	179.05
144	3.74	21.90	313.80	5.719	177.93
145	3.89	21.38	297.06	6.119	176.57
146	4.05	20.81	278.88	6.574	174.89
147	4.21	20.16	258.79	7.106	172.74
148	4.38	19.40	236.08	7.750	169.81
149	4.55	18.45	209.33	8.587	165.39
150	4.73	17.03	174.74	9.875	157.01

TABLE 7.2. Argon—Isobar at 0.101 325 MPa

T (K)	ρ (mol/dm ³)	ω (m/s)
90	0.140	173.81
100	0.125	184.14
110	0.113	193.74
120	0.103	202.78
130	0.095	211.38
140	0.088	219.59
150	0.082	227.49
160	0.077	235.09
170	0.072	242.44
180	0.068	249.56
190	0.064	256.48
200	0.061	263.21
210	0.058	269.76
220	0.056	276.15
230	0.053	282.39
240	0.051	288.50
250	0.049	294.48
260	0.047	300.33
270	0.045	306.07
280	0.044	311.70
290	0.042	317.24
300	0.041	322.67
310	0.039	328.02
320	0.038	333.27
330	0.037	338.45
340	0.036	343.55

(continues)

TABLE 7.2. (*continued*)

T (K)	ρ (mol/dm ³)	ω (m/s)
350	0.035	348.57
360	0.034	353.52
370	0.033	358.40
380	0.032	363.21
390	0.031	367.96
400	0.030	372.65
410	0.030	377.28
420	0.029	381.86
430	0.028	386.38
440	0.028	390.85
450	0.027	395.27
460	0.026	399.63
470	0.026	403.95
480	0.025	408.23
490	0.025	412.46
500	0.024	416.65
510	0.024	420.79
520	0.023	424.90
530	0.023	428.96
540	0.023	432.99
550	0.022	436.98
560	0.022	440.93
570	0.021	444.85
580	0.021	448.73
590	0.021	452.58
600	0.020	456.40
610	0.020	460.19
620	0.020	463.94
630	0.019	467.67
640	0.019	471.36
650	0.019	475.03
660	0.018	478.67
670	0.018	482.28
680	0.018	485.87
690	0.018	489.42
700	0.017	492.96

TABLE 7.3. Argon—Isobar at 1 MPa

T (K)	ρ (mol/dm ³)	ω (m/s)
90	34.579	824.17
100	32.955	751.59
110	31.157	672.31
116.5981	29.821	614.12
116.5981	1.240	184.63
120	1.182	189.35
130	1.046	201.51
140	0.945	212.09
150	0.865	221.67
160	0.799	230.54

TABLE 7.3. (*continued*)

T (K)	ρ (mol/dm ³)	ω (m/s)
170	0.744	238.88
180	0.697	246.79
190	0.656	254.34
200	0.619	261.59
210	0.587	268.58
220	0.558	275.34
230	0.532	281.89
240	0.509	288.26
250	0.488	294.47
260	0.468	300.52
270	0.450	306.44
280	0.433	312.22
290	0.418	317.88
300	0.403	323.44
310	0.390	328.88
320	0.377	334.23
330	0.366	339.49
340	0.355	344.66
350	0.344	349.74
360	0.335	354.75
370	0.325	359.68
380	0.317	364.54
390	0.309	369.33
400	0.301	374.06
410	0.293	378.72
420	0.286	383.33
430	0.280	387.87
440	0.273	392.36
450	0.267	396.80
460	0.261	401.19
470	0.256	405.52
480	0.250	409.81
490	0.245	414.06
500	0.240	418.25
510	0.235	422.41
520	0.231	426.52
530	0.226	430.59
540	0.222	434.63
550	0.218	438.62
560	0.214	442.58
570	0.211	446.50
580	0.207	450.39
590	0.203	454.24
600	0.200	458.06
610	0.197	461.85
620	0.194	465.60
630	0.190	469.33
640	0.187	473.02
650	0.185	476.69
660	0.182	480.33
670	0.179	483.94
680	0.176	487.52
690	0.174	491.08
700	0.171	494.61

TABLE 7.4. Argon—Isobar at 5 MPa

T (K)	ρ (mol/dm ³)	ω (m/s)
90	34.879	844.78
100	33.343	777.34
110	31.682	705.93
120	29.828	628.46
130	27.655	541.00
140	24.831	433.54
150	19.159	248.19
160	6.090	206.39
170	4.947	223.58
180	4.307	236.49
190	3.867	247.45
200	3.534	257.20
210	3.269	266.11
220	3.051	274.40
230	2.865	282.20
240	2.706	289.60
250	2.566	296.66
260	2.443	303.44
270	2.332	309.98
280	2.232	316.29
290	2.142	322.42
300	2.060	328.37
310	1.984	334.17
320	1.914	339.82
330	1.849	345.34
340	1.789	350.74
350	1.734	356.03
360	1.681	361.22
370	1.632	366.31
380	1.586	371.31
390	1.543	376.23
400	1.502	381.06
410	1.464	385.82
420	1.427	390.51
430	1.392	395.13
440	1.359	399.69
450	1.328	404.18
460	1.298	408.62
470	1.270	412.99
480	1.242	417.32
490	1.216	421.59
500	1.191	425.81
510	1.167	429.99
520	1.145	434.12
530	1.123	438.20
540	1.101	442.25
550	1.081	446.25
560	1.061	450.21
570	1.043	454.13
580	1.024	458.02
590	1.007	461.87
600	0.990	465.68
610	0.973	469.46
620	0.958	473.21

TABLE 7.4. (*continued*)

T (K)	ρ (mol/dm ³)	ω (m/s)
630	0.942	476.92
640	0.928	480.60
650	0.913	484.26
660	0.899	487.88
670	0.886	491.47
680	0.873	495.04
690	0.860	498.58
700	0.848	502.09

TABLE 7.5. Argon — Isobar at 10 MPa

T (K)	ρ (mol/dm ³)	ω (m/s)
90	35.23	868.40
100	33.78	805.91
110	32.25	741.46
120	30.59	674.25
130	28.76	603.33
140	26.67	527.43
150	24.15	445.10
160	20.87	357.76
170	16.44	284.47
180	12.31	259.27
190	9.89	260.68
200	8.45	267.70
210	7.49	275.72
220	6.78	283.74
230	6.23	291.51
240	5.79	298.98
250	5.42	306.16
260	5.11	313.06
270	4.83	319.72
280	4.60	326.15
290	4.38	332.37
300	4.20	338.42
310	4.02	344.29
320	3.87	350.02
330	3.73	355.60
340	3.60	361.05
350	3.48	366.38
360	3.37	371.60
370	3.26	376.72
380	3.17	381.74
390	3.07	386.67
400	2.99	391.51
410	2.91	396.27
420	2.83	400.96
430	2.76	405.58
440	2.70	410.12
450	2.63	414.60
460	2.57	419.02

(continues)

TABLE 7.5. (*continued*)

T (K)	ρ (mol/dm ³)	ω (m/s)
470	2.51	423.38
480	2.46	427.69
490	2.41	431.94
500	2.36	436.14
510	2.31	440.29
520	2.26	444.39
530	2.22	448.45
540	2.18	452.46
550	2.13	456.43
560	2.10	460.36
570	2.06	464.25
580	2.02	468.10
590	1.99	471.91
600	1.95	475.69
610	1.92	479.44
620	1.89	483.15
630	1.86	486.83
640	1.83	490.47
650	1.80	494.09
660	1.77	497.67
670	1.75	501.23
680	1.72	504.76
690	1.70	508.26
700	1.67	511.73

TABLE 7.6. Argon — Isobar at 50 MPa

T (K)	ρ (mol/dm ³)	ω (m/s)
100	36.26	969.74
110	35.19	927.77
120	34.12	887.55
130	33.05	849.02
140	31.97	812.28
150	30.90	777.44
160	29.83	744.66
170	28.76	714.08
180	27.70	685.82
190	26.65	659.98
200	25.63	636.63
210	24.62	615.80
220	23.65	597.47
230	22.71	581.56
240	21.81	567.93
250	20.96	556.40
260	20.14	546.77
270	19.38	538.85
280	18.66	532.42
290	17.98	527.30
300	17.34	523.31
310	16.75	520.31

TABLE 7.6. (*continued*)

T (K)	ρ (mol/dm ³)	ω (m/s)
320	16.19	518.16
330	15.67	516.73
340	15.18	515.91
350	14.72	515.62
360	14.28	515.78
370	13.88	516.32
380	13.50	517.19
390	13.14	518.35
400	12.80	519.74
410	12.48	521.33
420	12.17	523.11
430	11.88	525.03
440	11.61	527.09
450	11.35	529.26
460	11.10	531.52
470	10.87	533.87
480	10.64	536.29
490	10.43	538.77
500	10.22	541.31
510	10.02	543.89
520	9.83	546.50
530	9.65	549.15
540	9.48	551.83
550	9.31	554.54
560	9.15	557.26
570	9.00	560.00
580	8.85	562.75
590	8.71	565.51
600	8.57	568.28
610	8.43	571.05
620	8.30	573.83
630	8.18	576.62
640	8.06	579.40
650	7.94	582.18
660	7.83	584.97
670	7.72	587.75
680	7.61	590.52
690	7.51	593.30
700	7.41	596.07

TABLE 7.7. Argon—Isobar at 100 MPa

T (K)	ρ (mol/dm ³)	ω (m/s)
110	37.41	1074.29
120	36.57	1043.43
130	35.74	1014.38
140	34.93	987.00
150	34.13	961.21
160	33.35	936.96
170	32.58	914.20

(continues)

TABLE 7.7. (*continued*)

T (K)	ρ (mol/dm ³)	ω (m/s)
180	31.83	892.89
190	31.09	873.00
200	30.37	854.48
210	29.66	837.28
220	28.98	821.35
230	28.31	806.65
240	27.66	793.12
250	27.03	780.71
260	26.42	769.35
270	25.82	759.00
280	25.25	749.60
290	24.69	741.08
300	24.15	733.39
310	23.63	726.46
320	23.13	720.25
330	22.65	714.70
340	22.18	709.76
350	21.73	705.38
360	21.30	701.52
370	20.88	698.13
380	20.47	695.17
390	20.09	692.61
400	19.71	690.42
410	19.35	688.56
420	19.00	687.02
430	18.66	685.75
440	18.34	684.74
450	18.02	683.98
460	17.72	683.43
470	17.43	683.08
480	17.15	682.91
490	16.87	682.92
500	16.61	683.08
510	16.35	683.38
520	16.10	683.81
530	15.86	684.37
540	15.63	685.03
550	15.40	685.80
560	15.19	686.67
570	14.97	687.62
580	14.77	688.65
590	14.57	689.76
600	14.37	690.94
610	14.18	692.17
620	14.00	693.47
630	13.82	694.83
640	13.65	696.23
650	13.48	697.68
660	13.31	699.17
670	13.15	700.71
680	13.00	702.28
690	12.84	703.88
700	12.70	705.52

TABLE 7.8. Nitrogen — Saturation Boundary

T (K)	P (MPa)	Liquid		Vapor	
		ρ (mol/dm ³)	ω (m/s)	ρ (mol/dm ³)	ω (m/s)
64	0.015	30.83	986.57	0.028	162.08
65	0.017	30.69	976.36	0.033	163.20
66	0.021	30.54	966.18	0.038	164.30
67	0.024	30.39	956.04	0.044	165.37
68	0.028	30.24	945.93	0.051	166.41
69	0.033	30.09	935.83	0.059	167.43
70	0.039	29.93	925.74	0.068	168.42
71	0.045	29.78	915.66	0.077	169.39
72	0.051	29.62	905.58	0.088	170.32
73	0.059	29.47	895.49	0.100	171.23
74	0.067	29.31	885.39	0.112	172.10
75	0.076	29.15	875.28	0.126	172.95
76	0.086	28.99	865.15	0.142	173.77
77	0.097	28.83	855.00	0.158	174.55
78	0.109	28.67	844.82	0.176	175.31
79	0.122	28.51	834.61	0.196	176.03
80	0.137	28.34	824.36	0.217	176.72
81	0.153	28.17	814.07	0.240	177.38
82	0.169	28.01	803.74	0.265	178.00
83	0.188	27.84	793.36	0.292	178.60
84	0.208	27.66	782.93	0.320	179.16
85	0.229	27.49	772.44	0.351	179.68
86	0.252	27.32	761.89	0.383	180.17
87	0.276	27.14	751.28	0.418	180.63
88	0.303	26.96	740.60	0.456	181.05
89	0.331	26.78	729.84	0.496	181.43
90	0.360	26.60	719.01	0.538	181.78
91	0.392	26.41	708.09	0.584	182.10
92	0.426	26.22	697.09	0.632	182.38
93	0.462	26.03	685.99	0.683	182.62
94	0.500	25.84	674.80	0.737	182.82
95	0.541	25.64	663.50	0.795	182.99
96	0.583	25.44	652.09	0.856	183.12
97	0.628	25.24	640.57	0.921	183.21
98	0.676	25.03	628.92	0.990	183.26
99	0.726	24.82	617.14	1.063	183.28
100	0.778	24.61	605.23	1.141	183.25
101	0.834	24.39	593.17	1.223	183.18
102	0.892	24.17	580.96	1.310	183.08
103	0.953	23.94	568.58	1.403	182.93
104	1.016	23.71	556.03	1.501	182.74
105	1.083	23.47	543.30	1.605	182.51
106	1.153	23.23	530.37	1.716	182.24
107	1.226	22.98	517.24	1.833	181.93
108	1.303	22.72	503.88	1.958	181.58
109	1.383	22.46	490.29	2.092	181.19
110	1.466	22.18	476.44	2.234	180.76
111	1.553	21.90	462.32	2.386	180.28
112	1.643	21.61	447.92	2.549	179.75
113	1.737	21.31	433.19	2.724	179.15
114	1.835	20.99	418.12	2.912	178.49
115	1.937	20.66	402.67	3.116	177.75

(continues)

TABLE 7.8. (continued)

<i>T</i> (K)	<i>P</i> (MPa)	Liquid		Vapor	
		ρ (mol/dm ³)	ω (m/s)	ρ (mol/dm ³)	ω (m/s)
116	2.043	20.31	386.80	3.337	176.93
117	2.153	19.94	370.43	3.579	176.01
118	2.268	19.55	353.49	3.844	175.00
119	2.387	19.13	335.85	4.137	173.87
120	2.511	18.68	317.33	4.465	172.61
121	2.639	18.19	297.68	4.838	171.17
122	2.773	17.63	276.54	5.270	169.49
123	2.912	17.00	253.32	5.785	167.43
124	3.056	16.23	227.00	6.430	164.67
125	3.207	15.21	195.48	7.324	160.26
126	3.365	13.28	150.97	9.111	148.38

TABLE 7.9. Nitrogen—Isobar at 0.101 325 MPa

<i>T</i> (K)	ρ (mol/dm ³)	ω (m/s)
70	29.94	926.19
77.355	28.77	851.39
77.355	0.1646	174.82
90	0.1392	190.42
110	0.1125	212.07
130	0.0946	231.36
150	0.0817	248.99
170	0.0720	265.37
190	0.0643	280.74
210	0.0581	295.28
230	0.0530	309.11
250	0.0488	322.33
270	0.0452	335.02
290	0.0420	347.22
310	0.0393	359.00
330	0.0369	370.38
350	0.0348	381.40
370	0.0329	392.08
390	0.0312	402.44
410	0.0297	412.51
430	0.0283	422.31
450	0.0271	431.84
470	0.0259	441.12
490	0.0249	450.16
510	0.0239	458.99
530	0.0230	467.60
550	0.0221	476.02
570	0.0214	484.25
590	0.0206	492.31
610	0.0200	500.20
630	0.0193	507.93
650	0.0187	515.51
670	0.0182	522.95

TABLE 7.9. (*continued*)

T (K)	ρ (mol/dm ³)	ω (m/s)
690	0.0177	530.27
710	0.0172	537.45
730	0.0167	544.53
750	0.0162	551.49
770	0.0158	558.34
790	0.0154	565.10
810	0.0150	571.76
830	0.0147	578.33
850	0.0143	584.82
870	0.0140	591.22
890	0.0137	597.55
910	0.0134	603.80
930	0.0131	609.99
950	0.0128	616.10
970	0.0126	622.15
990	0.0123	628.14
1010	0.0121	634.07
1030	0.0118	639.94
1050	0.0116	645.75
1070	0.0114	651.51
1090	0.0112	657.22
1110	0.0110	662.87
1130	0.0108	668.48
1150	0.0106	674.04
1170	0.0104	679.56
1190	0.0102	685.03
1210	0.0101	690.45
1230	0.0099	695.84
1250	0.0097	701.18
1270	0.0096	706.48
1290	0.0094	711.75
1310	0.0093	716.97
1330	0.0092	722.16
1350	0.0090	727.31
1370	0.0089	732.43
1390	0.0088	737.51
1410	0.0086	742.56
1430	0.0085	747.57
1450	0.0084	752.56
1470	0.0083	757.51
1490	0.0082	762.43
1510	0.0081	767.31
1530	0.0080	772.17
1550	0.0079	777.00
1570	0.0078	781.80
1590	0.0077	786.57
1610	0.0076	791.31
1630	0.0075	796.03
1650	0.0074	800.72
1670	0.0073	805.38
1690	0.0072	810.02
1710	0.0071	814.63
1730	0.0070	819.21

(*continues*)

TABLE 7.9. (*continued*)

T (K)	ρ (mol/dm ³)	ω (m/s)
1750	0.0070	823.78
1770	0.0069	828.31
1790	0.0068	832.82
1810	0.0067	837.31
1830	0.0067	841.78
1850	0.0066	846.22
1870	0.0065	850.64
1890	0.0064	855.04
1910	0.0064	859.42
1930	0.0063	863.77
1950	0.0062	868.10
1970	0.0062	872.42
1990	0.0061	876.71

TABLE 7.10. Nitrogen—Isobar at 1 MPa

T (K)	ρ (mol/dm ³)	ω (m/s)
70	30.00	932.51
90	26.69	727.06
103.747	23.77	559.22
103.747	1.48	182.79
110	1.32	194.09
130	1.02	221.53
150	0.8523	243.20
170	0.7359	261.98
190	0.6498	278.91
210	0.5829	294.53
230	0.5291	309.13
250	0.4848	322.92
270	0.4475	336.03
290	0.4158	348.56
310	0.3883	360.58
330	0.3643	372.16
350	0.3432	383.33
370	0.3244	394.13
390	0.3076	404.58
410	0.2925	414.73
430	0.2788	424.57
450	0.2663	434.15
470	0.2549	443.46
490	0.2445	452.53
510	0.2349	461.37
530	0.2260	469.99
550	0.2178	478.42
570	0.2101	486.65
590	0.2030	494.70
610	0.1963	502.58
630	0.1901	510.30
650	0.1843	517.88

TABLE 7.10. (*continued*)

T (K)	ρ (mol/dm ³)	ω (m/s)
670	0.1788	525.31
690	0.1736	532.61
710	0.1687	539.79
730	0.1641	546.84
750	0.1597	553.79
770	0.1556	560.63
790	0.1516	567.37
810	0.1479	574.01
830	0.1443	580.57
850	0.1410	587.04
870	0.1377	593.43
890	0.1346	599.74
910	0.1317	605.98
930	0.1289	612.14
950	0.1262	618.24
970	0.1236	624.27
990	0.1211	630.25
1010	0.1187	636.16
1030	0.1164	642.01
1050	0.1142	647.81
1070	0.1120	653.55
1090	0.1100	659.24
1110	0.1080	664.89
1130	0.1061	670.48
1150	0.1043	676.02
1170	0.1025	681.52
1190	0.1008	686.98
1210	0.0991	692.39
1230	0.0975	697.76
1250	0.0959	703.09
1270	0.0944	708.38
1290	0.0930	713.63
1310	0.0916	718.84
1330	0.0902	724.02
1350	0.0888	729.16
1370	0.0876	734.26
1390	0.0863	739.33
1410	0.0851	744.37
1430	0.0839	749.37
1450	0.0827	754.34
1470	0.0816	759.28
1490	0.0805	764.18
1510	0.0795	769.06
1530	0.0784	773.91
1550	0.0774	778.72
1570	0.0764	783.51
1590	0.0755	788.27
1610	0.0745	793.00
1630	0.0736	797.71
1650	0.0727	802.39
1670	0.0719	807.04
1690	0.0710	811.67
1710	0.0702	816.27

(*continues*)

TABLE 7.10. (*continued*)

T (K)	ρ (mol/dm ³)	ω (m/s)
1730	0.0694	820.84
1750	0.0686	825.39
1770	0.0678	829.92
1790	0.0670	834.42
1810	0.0663	838.90
1830	0.0656	843.36
1850	0.0649	847.79
1870	0.0642	852.20
1890	0.0635	856.59
1910	0.0628	860.96
1930	0.0622	865.31
1950	0.0616	869.63
1970	0.0609	873.94
1990	0.0603	878.22
2010	0.0597	882.48

TABLE 7.11. Nitrogen—Isobar at 5 MPa

T (K)	ρ (mol/dm ³)	ω (m/s)
70	30.283	959.16
90	27.202	772.11
110	23.385	565.77
130	16.433	288.81
150	6.029	226.09
170	4.387	254.67
190	3.605	277.24
210	3.108	296.46
230	2.753	313.52
250	2.483	329.07
270	2.266	343.47
290	2.089	356.96
310	1.940	369.71
330	1.812	381.84
350	1.702	393.42
370	1.605	404.54
390	1.519	415.24
410	1.442	425.55
430	1.373	435.52
450	1.311	445.18
470	1.254	454.54
490	1.202	463.63
510	1.154	472.48
530	1.111	481.09
550	1.070	489.48
570	1.032	497.67
590	0.997	505.67
610	0.965	513.49
630	0.934	521.15
650	0.906	528.65

TABLE 7.11. (*continued*)

T (K)	ρ (mol/dm ³)	ω (m/s)
670	0.879	536.01
690	0.853	543.24
710	0.830	550.33
730	0.807	557.31
750	0.786	564.17
770	0.765	570.93
790	0.746	577.59
810	0.728	584.15
830	0.711	590.62
850	0.694	597.01
870	0.678	603.32
890	0.663	609.55
910	0.649	615.70
930	0.635	621.79
950	0.622	627.81
970	0.609	633.77
990	0.597	639.66
1010	0.585	645.49
1030	0.574	651.27
1050	0.563	657.00
1070	0.553	662.67
1090	0.543	668.29
1110	0.533	673.86
1130	0.524	679.38
1150	0.515	684.86
1170	0.506	690.29
1190	0.498	695.68
1210	0.490	701.02
1230	0.482	706.33
1250	0.474	711.60
1270	0.467	716.82
1290	0.460	722.01
1310	0.453	727.16
1330	0.446	732.28
1350	0.439	737.36
1370	0.433	742.40
1390	0.427	747.42
1410	0.421	752.40
1430	0.415	757.34
1450	0.409	762.26
1470	0.404	767.14
1490	0.399	772.00
1510	0.393	776.82
1530	0.388	781.62
1550	0.383	786.38
1570	0.378	791.12
1590	0.374	795.83
1610	0.369	800.52
1630	0.365	805.17
1650	0.360	809.81
1670	0.356	814.41
1690	0.352	818.99
1710	0.348	823.55

(continues)

TABLE 7.11. (continued)

T (K)	ρ (mol/dm ³)	ω (m/s)
1730	0.344	828.08
1750	0.340	832.59
1770	0.336	837.07
1790	0.332	841.53
1810	0.329	845.97
1830	0.325	850.38
1850	0.322	854.78
1870	0.318	859.15
1890	0.315	863.50
1910	0.312	867.82
1930	0.309	872.13
1950	0.305	876.42
1970	0.302	880.68
1990	0.299	884.93

TABLE 7.12. Nitrogen—Isobar at 10 MPa

T (K)	ρ (mol/dm ³)	ω (m/s)
70	30.60	989.62
90	27.75	819.44
110	24.49	647.61
130	20.41	472.34
150	14.96	331.25
170	10.28	292.70
190	7.87	300.47
210	6.53	315.42
230	5.65	330.91
250	5.02	345.77
270	4.54	359.83
290	4.15	373.13
310	3.84	385.75
330	3.57	397.78
350	3.35	409.27
370	3.15	420.29
390	2.98	430.88
410	2.82	441.09
430	2.69	450.94
450	2.56	460.47
470	2.45	469.71
490	2.35	478.67
510	2.26	487.38
530	2.17	495.85
550	2.09	504.10
570	2.02	512.15
590	1.95	520.01
610	1.89	527.69
630	1.83	535.21
650	1.77	542.57
670	1.72	549.80

TABLE 7.12. (*continued*)

T (K)	ρ (mol/dm ³)	ω (m/s)
690	1.67	556.88
710	1.62	563.84
730	1.58	570.69
750	1.54	577.42
770	1.50	584.05
790	1.46	590.58
810	1.43	597.01
830	1.39	603.36
850	1.36	609.63
870	1.33	615.82
890	1.30	621.93
910	1.27	627.97
930	1.25	633.95
950	1.22	639.86
970	1.20	645.71
990	1.17	651.49
1010	1.15	657.23
1030	1.13	662.90
1050	1.11	668.53
1070	1.09	674.10
1090	1.07	679.62
1110	1.05	685.10
1130	1.03	690.53
1150	1.01	695.92
1170	1.00	701.26
1190	0.981	706.56
1210	0.965	711.82
1230	0.950	717.05
1250	0.935	722.23
1270	0.920	727.37
1290	0.906	732.48
1310	0.893	737.56
1330	0.880	742.59
1350	0.867	747.60
1370	0.855	752.57
1390	0.843	757.51
1410	0.831	762.42
1430	0.820	767.29
1450	0.809	772.14
1470	0.798	776.96
1490	0.787	781.74
1510	0.777	786.50
1530	0.767	791.23
1550	0.758	795.93
1570	0.748	800.61
1590	0.739	805.26
1610	0.730	809.88
1630	0.721	814.48
1650	0.713	819.05
1670	0.704	823.60
1690	0.696	828.12
1710	0.688	832.62
1730	0.680	837.10

(continues)

TABLE 7.12. (continued)

T (K)	ρ (mol/dm ³)	ω (m/s)
1750	0.673	841.55
1770	0.665	845.98
1790	0.658	850.38
1810	0.651	854.77
1830	0.644	859.13
1850	0.637	863.47
1870	0.630	867.79
1890	0.624	872.09
1910	0.617	876.37
1930	0.611	880.63
1950	0.605	884.87
1970	0.599	889.09
1990	0.593	893.29

TABLE 7.13. Nitrogen—Isobar at 50 MPa

T (K)	ρ (mol/dm ³)	ω (m/s)
90	30.52	1061.02
110	28.54	963.85
130	26.61	878.83
150	24.76	806.60
170	22.99	747.47
190	21.35	701.00
210	19.83	665.92
230	18.45	640.44
250	17.22	622.64
270	16.12	610.73
290	15.14	603.25
310	14.28	599.08
330	13.50	597.38
350	12.81	597.50
370	12.19	598.98
390	11.64	601.45
410	11.13	604.67
430	10.67	608.44
450	10.25	612.61
470	9.87	617.08
490	9.51	621.78
510	9.18	626.63
530	8.88	631.59
550	8.60	636.63
570	8.33	641.73
590	8.08	646.85
610	7.85	651.99
630	7.64	657.14
650	7.43	662.28
670	7.24	667.41
690	7.05	672.53
710	6.88	677.63

TABLE 7.13. (*continued*)

T (K)	ρ (mol/dm ³)	ω (m/s)
730	6.72	682.70
750	6.56	687.76
770	6.41	692.79
790	6.27	697.80
810	6.14	702.78
830	6.01	707.74
850	5.88	712.67
870	5.77	717.58
890	5.65	722.46
910	5.54	727.31
930	5.44	732.14
950	5.34	736.95
970	5.24	741.73
990	5.15	746.49
1010	5.06	751.22
1030	4.97	755.93
1050	4.89	760.62
1070	4.81	765.28
1090	4.73	769.92
1110	4.66	774.54
1130	4.59	779.14
1150	4.51	783.71
1170	4.45	788.26
1190	4.38	792.79
1210	4.32	797.30
1230	4.25	801.79
1250	4.19	806.26
1270	4.13	810.70
1290	4.08	815.13
1310	4.02	819.54
1330	3.97	823.92
1350	3.92	828.29
1370	3.87	832.64
1390	3.82	836.96
1410	3.77	841.27
1430	3.72	845.56
1450	3.67	849.83
1470	3.63	854.09
1490	3.59	858.32
1510	3.54	862.54
1530	3.50	866.73
1550	3.46	870.91
1570	3.42	875.08
1590	3.38	879.22
1610	3.34	883.35
1630	3.31	887.46
1650	3.27	891.56
1670	3.24	895.63
1690	3.20	899.70
1710	3.17	903.74
1730	3.13	907.77
1750	3.10	911.78
1770	3.07	915.78

(continues)

TABLE 7.13. (*continued*)

T (K)	ρ (mol/dm ³)	ω (m/s)
1790	3.04	919.76
1810	3.01	923.73
1830	2.98	927.68
1850	2.95	931.61
1870	2.92	935.53
1890	2.89	939.44
1910	2.86	943.33
1930	2.84	947.20
1950	2.81	951.06
1970	2.78	954.91
1990	2.76	958.74

TABLE 7.14. Nitrogen — at 100 MPa

T (K)	ρ (mol/dm ³)	ω (m/s)
90	32.57	1244.55
110	31.03	1173.11
130	29.57	1110.14
150	28.19	1055.27
170	26.90	1008.09
190	25.69	967.97
210	24.57	934.20
230	23.52	906.03
250	22.54	882.74
270	21.63	863.64
290	20.78	848.09
310	19.99	835.56
330	19.26	825.55
350	18.58	817.66
370	17.94	811.52
390	17.35	806.84
410	16.79	803.39
430	16.27	800.95
450	15.79	799.36
470	15.33	798.49
490	14.90	798.21
510	14.49	798.44
530	14.11	799.10
550	13.75	800.12
570	13.41	801.46
590	13.09	803.07
610	12.78	804.91
630	12.49	806.95
650	12.21	809.16
670	11.95	811.53
690	11.69	814.04
710	11.45	816.67
730	11.22	819.40
750	11.00	822.23

TABLE 7.14. (*continued*)

T (K)	ρ (mol/dm ³)	ω (m/s)
770	10.79	825.14
790	10.58	828.12
810	10.39	831.18
830	10.20	834.29
850	10.02	837.46
870	9.85	840.68
890	9.68	843.94
910	9.52	847.25
930	9.36	850.58
950	9.21	853.95
970	9.07	857.35
990	8.93	860.78
1010	8.79	864.23
1030	8.66	867.69
1050	8.53	871.18
1070	8.41	874.68
1090	8.29	878.20
1110	8.17	881.73
1130	8.06	885.27
1150	7.95	888.82
1170	7.84	892.38
1190	7.74	895.95
1210	7.64	899.52
1230	7.54	903.10
1250	7.44	906.68
1270	7.35	910.26
1290	7.26	913.84
1310	7.17	917.43
1330	7.08	921.01
1350	7.00	924.60
1370	6.92	928.18
1390	6.84	931.77
1410	6.76	935.35
1430	6.68	938.93
1450	6.61	942.50
1470	6.54	946.07
1490	6.46	949.64
1510	6.39	953.21
1530	6.33	956.76
1550	6.26	960.32
1570	6.19	963.87
1590	6.13	967.41
1610	6.07	970.95
1630	6.01	974.48
1650	5.95	978.01
1670	5.89	981.53
1690	5.83	985.04
1710	5.77	988.55
1730	5.72	992.05
1750	5.66	995.55
1770	5.61	999.03
1790	5.56	1002.51
1810	5.51	1005.98

(continues)

TABLE 7.14. (continued)

<i>T</i> (K)	ρ (mol/dm ³)	ω (m/s)
1830	5.46	1009.45
1850	5.41	1012.91
1870	5.36	1016.36
1890	5.31	1019.80
1910	5.27	1023.23
1930	5.22	1026.66
1950	5.18	1030.08
1970	5.13	1033.49
1990	5.09	1036.90

TABLE 7.15. Water—Saturation Boundary

<i>T</i> (K)	<i>P</i> (MPa)	Liquid		Vapor	
		ρ (mol/dm ³)	ω (m/s)	ρ (mol/dm ³)	ω (m/s)
275	0.0007	55.50	1411.35	0.0003	410.33
277	0.0008	55.50	1420.78	0.0003	411.77
279	0.0009	55.50	1429.78	0.0004	413.21
281	0.0011	55.50	1438.35	0.0005	414.64
283	0.0012	55.49	1446.51	0.0005	416.06
285	0.0014	55.48	1454.29	0.0006	417.48
287	0.0016	55.47	1461.68	0.0007	418.89
289	0.0018	55.45	1468.71	0.0008	420.29
291	0.0020	55.43	1475.39	0.0008	421.69
293	0.0023	55.41	1481.72	0.0010	423.08
295	0.0026	55.38	1487.72	0.0011	424.46
297	0.0030	55.36	1493.41	0.0012	425.84
299	0.0033	55.33	1498.78	0.0013	427.21
301	0.0038	55.30	1503.86	0.0015	428.57
303	0.0042	55.27	1508.64	0.0017	429.93
305	0.0047	55.23	1513.14	0.0019	431.28
307	0.0053	55.20	1517.37	0.0021	432.62
309	0.0059	55.16	1521.33	0.0023	433.96
311	0.0066	55.12	1525.04	0.0026	435.29
313	0.0073	55.08	1528.49	0.0028	436.61
315	0.0081	55.03	1531.70	0.0031	437.93
317	0.0090	54.99	1534.68	0.0034	439.24
319	0.0100	54.94	1537.42	0.0038	440.54
321	0.0111	54.90	1539.95	0.0042	441.83
323	0.0123	54.85	1542.25	0.0046	443.11
325	0.0135	54.80	1544.35	0.0050	444.39
327	0.0149	54.74	1546.24	0.0055	445.66
329	0.0164	54.69	1547.93	0.0060	446.92
331	0.0180	54.63	1549.43	0.0066	448.17
333	0.0198	54.58	1550.73	0.0072	449.41
335	0.0217	54.52	1551.85	0.0078	450.64
337	0.0238	54.46	1552.80	0.0085	451.87
339	0.0260	54.40	1553.56	0.0093	453.08
341	0.0284	54.34	1554.16	0.010	454.28
343	0.031	54.28	1554.59	0.011	455.48

TABLE 7.15. (continued)

T (K)	P (MPa)	Liquid		Vapor	
		ρ (mol/dm ³)	ω (m/s)	ρ (mol/dm ³)	ω (m/s)
345	0.034	54.21	1554.85	0.012	456.67
347	0.037	54.15	1554.96	0.013	457.84
349	0.040	54.08	1554.91	0.014	459.01
351	0.043	54.01	1554.71	0.015	460.16
353	0.047	53.95	1554.36	0.016	461.30
355	0.051	53.88	1553.86	0.017	462.44
357	0.055	53.81	1553.22	0.019	463.56
359	0.060	53.73	1552.44	0.020	464.67
361	0.065	53.66	1551.52	0.022	465.77
363	0.070	53.59	1550.47	0.023	466.86
365	0.075	53.51	1549.29	0.025	467.93
367	0.081	53.44	1547.98	0.027	469.00
369	0.087	53.36	1546.54	0.029	470.05
371	0.094	53.28	1544.97	0.031	471.09
373	0.101	53.20	1543.29	0.033	472.12
375	0.108	53.12	1541.48	0.035	473.13
377	0.116	53.04	1539.56	0.038	474.14
379	0.125	52.96	1537.52	0.040	475.12
381	0.133	52.88	1535.36	0.043	476.10
383	0.143	52.79	1533.09	0.046	477.06
385	0.153	52.71	1530.71	0.049	478.01
387	0.163	52.62	1528.22	0.052	478.95
389	0.174	52.53	1525.62	0.055	479.87
391	0.186	52.45	1522.92	0.058	480.77
393	0.198	52.36	1520.11	0.062	481.67
395	0.211	52.27	1517.20	0.066	482.54
397	0.224	52.18	1514.18	0.070	483.41
399	0.238	52.08	1511.06	0.074	484.25
401	0.253	51.99	1507.85	0.078	485.09
403	0.269	51.90	1504.53	0.083	485.91
405	0.286	51.80	1501.12	0.087	486.71
407	0.303	51.71	1497.61	0.092	487.50
409	0.321	51.61	1494.00	0.098	488.27
411	0.340	51.51	1490.30	0.103	489.02
413	0.360	51.42	1486.51	0.109	489.76
415	0.381	51.32	1482.62	0.115	490.49
417	0.403	51.22	1478.64	0.121	491.19
419	0.426	51.11	1474.57	0.127	491.88
421	0.449	51.01	1470.41	0.134	492.56
423	0.474	50.91	1466.17	0.141	493.22
425	0.500	50.81	1461.83	0.148	493.86
427	0.527	50.70	1457.40	0.156	494.48
429	0.556	50.59	1452.89	0.164	495.09
431	0.585	50.49	1448.29	0.172	495.68
433	0.616	50.38	1443.60	0.180	496.25
435	0.648	50.27	1438.83	0.189	496.81
437	0.681	50.16	1433.97	0.198	497.35
439	0.716	50.05	1429.03	0.208	497.87
441	0.752	49.94	1424.01	0.218	498.37
443	0.789	49.82	1418.90	0.228	498.86
445	0.828	49.71	1413.71	0.239	499.32
447	0.869	49.60	1408.44	0.250	499.77

(continues)

TABLE 7.15. (continued)

T (K)	P (MPa)	Liquid		Vapor	
		ρ (mol/dm ³)	ω (m/s)	ρ (mol/dm ³)	ω (m/s)
449	0.911	49.48	1403.08	0.261	500.20
451	0.954	49.36	1397.64	0.273	500.62
453	0.999	49.24	1392.12	0.285	501.01
455	1.05	49.13	1386.52	0.298	501.39
457	1.09	49.01	1380.84	0.311	501.74
459	1.15	48.88	1375.08	0.325	502.08
461	1.20	48.76	1369.24	0.339	502.40
463	1.25	48.64	1363.32	0.354	502.70
465	1.31	48.51	1357.32	0.369	502.98
467	1.36	48.39	1351.24	0.385	503.24
469	1.42	48.26	1345.08	0.401	503.49
471	1.49	48.13	1338.84	0.418	503.71
473	1.55	48.01	1332.53	0.435	503.91
475	1.62	47.88	1326.13	0.453	504.09
477	1.68	47.74	1319.66	0.471	504.25
479	1.75	47.61	1313.10	0.491	504.39
481	1.83	47.48	1306.47	0.510	504.51
483	1.90	47.34	1299.76	0.531	504.61
485	1.98	47.21	1292.98	0.552	504.68
487	2.06	47.07	1286.11	0.573	504.74
489	2.14	46.93	1279.16	0.596	504.77
491	2.23	46.79	1272.14	0.619	504.78
493	2.31	46.65	1265.04	0.643	504.77
495	2.40	46.51	1257.85	0.668	504.74
497	2.50	46.36	1250.59	0.693	504.68
499	2.59	46.22	1243.25	0.719	504.60
501	2.69	46.07	1235.83	0.746	504.49
503	2.79	45.92	1228.33	0.774	504.36
505	2.89	45.77	1220.76	0.803	504.21
507	3.00	45.62	1213.10	0.833	504.03
509	3.11	45.47	1205.36	0.863	503.82
511	3.22	45.32	1197.53	0.895	503.59
513	3.34	45.16	1189.63	0.927	503.34
515	3.46	45.00	1181.65	0.961	503.06
517	3.58	44.84	1173.58	0.995	502.75
519	3.70	44.68	1165.43	1.031	502.41
521	3.83	44.52	1157.19	1.068	502.05
523	3.97	44.36	1148.88	1.105	501.65
525	4.10	44.19	1140.47	1.144	501.23
527	4.24	44.02	1131.98	1.185	500.78
529	4.38	43.86	1123.41	1.226	500.30
531	4.53	43.68	1114.74	1.269	499.79
533	4.68	43.51	1105.99	1.313	499.25
535	4.83	43.34	1097.15	1.358	498.68
537	4.99	43.16	1088.21	1.405	498.07
539	5.15	42.98	1079.19	1.453	497.43
541	5.32	42.80	1070.07	1.503	496.76
543	5.49	42.61	1060.86	1.554	496.06
545	5.66	42.43	1051.55	1.607	495.32
547	5.84	42.24	1042.15	1.662	494.54

TABLE 7.15. (continued)

T (K)	P (MPa)	Liquid		Vapor	
		ρ (mol/dm ³)	ω (m/s)	ρ (mol/dm ³)	ω (m/s)
549	6.02	42.05	1032.65	1.718	493.73
551	6.21	41.86	1023.04	1.776	492.88
553	6.40	41.66	1013.34	1.836	491.99
555	6.60	41.46	1003.53	1.898	491.07
557	6.80	41.26	993.61	1.962	490.10
559	7.00	41.06	983.59	2.028	489.10
561	7.21	40.85	973.46	2.096	488.05
563	7.43	40.64	963.21	2.167	486.96
565	7.64	40.43	952.85	2.240	485.83
567	7.87	40.21	942.38	2.315	484.65
569	8.10	40.00	931.78	2.393	483.42
571	8.33	39.77	921.06	2.473	482.15
573	8.57	39.55	910.22	2.556	480.83
575	8.81	39.32	899.25	2.643	479.46
577	9.06	39.08	888.14	2.732	478.04
579	9.32	38.85	876.90	2.824	476.56
581	9.58	38.60	865.53	2.920	475.03
583	9.84	38.36	854.00	3.020	473.44
585	10.12	38.11	842.34	3.123	471.80
587	10.39	37.85	830.52	3.230	470.09
589	10.68	37.59	818.54	3.342	468.32
591	10.97	37.32	806.40	3.458	466.48
593	11.26	37.05	794.09	3.579	464.58
595	11.56	36.77	781.60	3.705	462.60
597	11.87	36.49	768.93	3.836	460.55
599	12.19	36.20	756.07	3.973	458.42
601	12.51	35.90	743.01	4.116	456.21
603	12.83	35.59	729.72	4.265	453.91
605	13.17	35.28	716.21	4.422	451.52
607	13.51	34.95	702.44	4.587	449.04
609	13.86	34.62	688.40	4.760	446.45
611	14.21	34.28	674.06	4.942	443.75
613	14.57	33.92	659.38	5.134	440.93
615	14.94	33.56	644.33	5.337	437.99
617	15.32	33.18	628.86	5.552	434.90
619	15.71	32.78	612.91	5.781	431.67
621	16.10	32.37	596.41	6.025	428.26
623	16.50	31.93	579.28	6.286	424.67
625	16.91	31.48	561.45	6.566	420.87
627	17.33	31.00	542.82	6.869	416.82
629	17.75	30.48	523.31	7.198	412.49
631	18.19	29.93	502.83	7.558	407.83
633	18.63	29.33	481.38	7.956	402.77
635	19.09	28.68	459.03	8.401	397.19
637	19.55	27.97	435.99	8.907	390.93
639	20.02	27.17	412.53	9.496	383.74
641	20.51	26.26	388.55	10.21	375.08
643	21.01	25.15	362.10	11.12	363.84
645	21.52	23.59	325.47	12.46	346.60
647	22.04	19.84	251.20	15.90	285.31

TABLE 7.16. Water — Isobar at 0.101 325 MPa

T (K)	ρ (mol/dm ³)	ω (m/s)
275	55.51	1411.51
295	55.39	1487.89
315	55.04	1531.87
335	54.52	1552.00
355	53.88	1553.96
373.12	53.20	1543.18
373.12	0.0332	472.18
375	0.0330	473.52
395	0.0312	487.03
415	0.0296	499.70
435	0.0282	511.80
455	0.0269	523.44
475	0.0258	534.70
495	0.0247	545.62
515	0.0238	556.23
535	0.0229	566.58
555	0.0220	576.68
575	0.0212	586.55
595	0.0205	596.21
615	0.0199	605.68
635	0.0192	614.95
655	0.0186	624.05
675	0.0181	632.98
695	0.0176	641.75
715	0.0171	650.37
735	0.0166	658.84
755	0.0162	667.18
775	0.0157	675.39
795	0.0153	683.47
815	0.0150	691.43
835	0.0146	699.27
855	0.0143	707.00
875	0.0139	714.63
895	0.0136	722.16
915	0.0133	729.59
935	0.0130	736.92
955	0.0128	744.17
975	0.0125	751.33
995	0.0123	758.41
1015	0.0120	765.41
1035	0.0118	772.33
1055	0.0116	779.17
1075	0.0113	785.95
1095	0.0111	792.66
1115	0.0109	799.30
1135	0.0107	805.88
1155	0.0106	812.40
1175	0.0104	818.86
1195	0.0102	825.26
1215	0.0100	831.61
1235	0.0099	837.90
1255	0.0097	844.14

TABLE 7.17. Water—*isobar at 1 MPa*

T (K)	ρ (mol/dm ³)	ω (m/s)
275	55.53	1412.95
295	55.41	1489.38
315	55.06	1533.44
335	54.54	1553.68
355	53.90	1555.76
375	53.15	1543.41
395	52.29	1519.06
415	51.34	1484.24
435	50.28	1439.85
453.03	49.24	1392.05
453.03	0.286	501.02
455	0.284	502.85
475	0.268	518.73
495	0.255	532.48
515	0.243	545.19
535	0.232	557.16
555	0.223	568.56
575	0.214	579.48
595	0.207	590.01
615	0.199	600.2
635	0.193	610.09
655	0.186	619.72
675	0.181	629.11
695	0.175	638.29
715	0.170	647.26
735	0.165	656.05
755	0.161	664.67
775	0.156	673.12
795	0.152	681.42
815	0.148	689.58
835	0.145	697.61
855	0.141	705.51
875	0.138	713.29
895	0.135	720.95
915	0.132	728.50
935	0.129	735.95
955	0.126	743.30
975	0.124	750.56
995	0.121	757.72
1015	0.119	764.80
1035	0.116	771.80
1055	0.114	778.72
1075	0.112	785.56
1095	0.110	792.33
1115	0.108	799.03
1135	0.106	805.66
1155	0.104	812.22
1175	0.102	818.73
1195	0.101	825.17
1215	0.099	831.56
1235	0.097	837.89
1255	0.096	844.16

TABLE 7.18. Water—Isobar at 5 MPa

T (K)	ρ (mol/dm ³)	ω (m/s)
275	55.64	1419.38
295	55.51	1496.03
315	55.15	1540.44
335	54.64	1561.11
355	54.00	1563.72
375	53.25	1552.01
395	52.40	1528.44
415	51.46	1494.56
435	50.41	1451.34
455	49.27	1399.29
475	48.02	1338.56
495	46.64	1268.87
515	45.09	1189.36
535	43.35	1098.15
537.09	43.15	1087.81
537.09	1.41	498.04
555	1.30	520.81
575	1.22	540.41
595	1.15	557.18
615	1.09	572.16
635	1.04	585.84
655	1.00	598.56
675	0.956	610.51
695	0.921	621.84
715	0.889	632.65
735	0.859	643.03
755	0.832	653.03
775	0.807	662.71
795	0.784	672.09
815	0.762	681.21
835	0.741	690.09
855	0.722	698.76
875	0.704	707.23
895	0.686	715.52
915	0.670	723.65
935	0.655	731.62
955	0.640	739.45
975	0.626	747.14
995	0.612	754.7
1015	0.600	762.15
1035	0.587	769.48
1055	0.576	776.72
1075	0.564	783.85
1095	0.554	790.88
1115	0.543	797.83
1135	0.533	804.69
1155	0.524	811.47
1175	0.515	818.18
1195	0.506	824.81
1215	0.497	831.37
1235	0.489	837.86
1255	0.481	844.29

TABLE 7.19. Water—Isobar at 10 MPa

T (K)	ρ (mol/dm ³)	ω (m/s)
275	55.78	1427.48
295	55.63	1504.34
315	55.27	1549.15
335	54.76	1570.33
355	54.12	1573.56
375	53.38	1562.62
395	52.54	1539.98
415	51.60	1507.23
435	50.58	1465.38
455	49.45	1415.01
475	48.23	1356.38
495	46.88	1289.39
515	45.38	1213.47
535	43.70	1127.35
555	41.78	1028.37
575	39.47	910.76
584.15	38.21	847.33
584.15	3.08	472.51
595	2.85	494.96
615	2.56	524.55
635	2.36	547.42
655	2.21	566.64
675	2.09	583.48
695	1.99	598.63
715	1.90	612.52
735	1.82	625.42
755	1.75	637.54
775	1.69	649.02
795	1.63	659.95
815	1.58	670.42
835	1.53	680.49
855	1.48	690.21
875	1.44	699.62
895	1.40	708.74
915	1.37	717.62
935	1.33	726.27
955	1.30	734.71
975	1.27	742.96
995	1.24	751.03
1015	1.21	758.95
1035	1.19	766.71
1055	1.16	774.33
1075	1.14	781.83
1095	1.12	789.2
1115	1.09	796.46
1135	1.07	803.60
1155	1.05	810.65
1175	1.03	817.60
1195	1.02	824.46
1215	1.00	831.24
1235	0.98	837.93
1255	9.95	844.54

TABLE 7.20. Water—Isobar at 50 MPa

T (K)	ρ (mol/dm ³)	ω (m/s)
275	56.82	1494.62
295	56.59	1570.91
315	56.19	1617.39
335	55.67	1641.44
355	55.05	1648.59
375	54.34	1642.61
395	53.56	1626.02
415	52.70	1600.54
435	51.77	1567.36
455	50.76	1527.34
475	49.69	1481.12
495	48.53	1429.22
515	47.29	1372.03
535	45.96	1309.84
555	44.52	1242.87
575	42.95	1171.23
595	41.23	1094.94
615	39.32	1013.97
635	37.17	928.41
655	34.70	838.86
675	31.78	746.93
695	28.24	659.20
715	24.09	590.51
735	19.85	556.44
755	16.46	556.75
775	14.09	571.69
795	12.44	590.63
815	11.24	609.70
835	10.34	627.78
855	9.62	644.65
875	9.04	660.37
895	8.55	675.07
915	8.13	688.87
935	7.77	701.91
955	7.45	714.26
975	7.17	726.03
995	6.91	737.29
1015	6.68	748.08
1035	6.47	758.46
1055	6.28	768.47
1075	6.10	778.15
1095	5.94	787.53
1115	5.78	796.64
1135	5.64	805.49
1155	5.51	814.11
1175	5.38	822.53
1195	5.26	830.74
1215	5.15	838.77
1235	5.04	846.64
1255	4.94	854.34

TABLE 7.21. Water—Isobar at 100 MPa

T (K)	ρ (mol/dm ³)	ω (m/s)
275	58.00	1583.41
295	57.67	1654.36
315	57.24	1699.71
335	56.71	1724.94
355	56.10	1734.86
375	55.43	1732.90
395	54.69	1721.44
415	53.90	1702.11
435	53.05	1676.13
455	52.14	1644.40
475	51.18	1607.67
495	50.17	1566.57
515	49.11	1521.67
535	47.99	1473.50
555	46.81	1422.55
575	45.58	1369.34
595	44.27	1314.37
615	42.90	1258.17
635	41.45	1201.31
655	39.92	1144.39
675	38.31	1088.12
695	36.62	1033.35
715	34.84	981.04
735	32.99	932.30
755	31.08	888.40
775	29.15	850.76
795	27.24	820.40
815	25.40	797.37
835	23.67	781.16
855	22.08	771.04
875	20.65	766.04
895	19.37	765.04
915	18.24	767.02
935	17.24	771.13
955	16.37	776.73
975	15.59	783.33
995	14.90	790.61
1015	14.28	798.30
1035	13.72	806.26
1055	13.22	814.35
1075	12.76	822.49
1095	12.35	830.64
1115	11.96	838.74
1135	11.61	846.78
1155	11.28	854.73
1175	10.98	862.60
1195	10.70	870.36
1215	10.44	878.01
1235	10.19	885.56
1255	9.95	893.00

TABLE 7.22. Air—Saturation Boundary

<i>T</i> (K)	<i>P</i> (Bubble) (MPa)	Liquid <i>ρ</i> (mol/dm ³)	<i>ω</i> (m/s)	<i>P</i> (Dew) (MPa)	Vapor <i>ρ</i> (mol/dm ³)	<i>ω</i> (m/s)
60	0.006	33.03	1028.29	0.0026	0.005	155.14
61	0.007	32.89	1020.26	0.0033	0.006	156.38
62	0.008	32.74	1012.16	0.0041	0.008	157.61
63	0.010	32.60	1004.00	0.0051	0.010	158.81
64	0.012	32.46	995.77	0.0063	0.012	159.99
65	0.014	32.31	987.48	0.0078	0.014	161.16
66	0.017	32.17	979.13	0.0094	0.017	162.30
67	0.020	32.02	970.72	0.011	0.021	163.42
68	0.024	31.87	962.24	0.014	0.024	164.53
69	0.027	31.72	953.70	0.016	0.029	165.61
70	0.032	31.58	945.10	0.019	0.034	166.66
71	0.037	31.43	936.43	0.023	0.039	167.70
72	0.042	31.28	927.70	0.027	0.046	168.70
73	0.049	31.13	918.90	0.031	0.053	169.69
74	0.056	30.97	910.04	0.037	0.061	170.65
75	0.063	30.82	901.11	0.042	0.069	171.58
76	0.072	30.67	892.11	0.049	0.079	172.49
77	0.081	30.51	883.05	0.056	0.090	173.37
78	0.091	30.36	873.91	0.064	0.101	174.23
79	0.10	30.20	864.71	0.073	0.114	175.05
80	0.11	30.04	855.44	0.082	0.128	175.85
81	0.13	29.88	846.09	0.093	0.143	176.62
82	0.14	29.72	836.67	0.10	0.160	177.36
83	0.16	29.56	827.18	0.12	0.178	178.07
84	0.17	29.40	817.61	0.13	0.198	178.75
85	0.19	29.23	807.96	0.15	0.219	179.40
86	0.21	29.07	798.24	0.16	0.241	180.02
87	0.23	28.90	788.44	0.18	0.266	180.61
88	0.26	28.73	778.56	0.20	0.292	181.17
89	0.28	28.56	768.59	0.22	0.320	181.69
90	0.30	28.38	758.55	0.24	0.351	182.19
91	0.33	28.21	748.42	0.27	0.383	182.65
92	0.36	28.03	738.20	0.29	0.417	183.08
93	0.39	27.85	727.90	0.32	0.454	183.48
94	0.42	27.67	717.51	0.35	0.493	183.84
95	0.46	27.49	707.03	0.38	0.535	184.17
96	0.50	27.30	696.46	0.41	0.580	184.46
97	0.53	27.12	685.80	0.45	0.627	184.72
98	0.57	26.92	675.05	0.49	0.677	184.95
99	0.62	26.73	664.20	0.53	0.730	185.14
100	0.66	26.53	653.26	0.57	0.786	185.30
101	0.71	26.33	642.22	0.61	0.846	185.42
102	0.76	26.13	631.08	0.66	0.909	185.51
103	0.81	25.92	619.84	0.71	0.976	185.55
104	0.87	25.71	608.50	0.76	1.047	185.57
105	0.93	25.50	597.06	0.81	1.122	185.54
106	0.99	25.28	585.51	0.87	1.201	185.48
107	1.05	25.06	573.85	0.93	1.285	185.38
108	1.12	24.83	562.09	0.99	1.374	185.24
109	1.18	24.60	550.21	1.06	1.468	185.07
110	1.26	24.36	538.21	1.13	1.568	184.85
111	1.33	24.12	526.10	1.20	1.674	184.60
112	1.41	23.87	513.86	1.28	1.786	184.30
113	1.49	23.61	501.48	1.35	1.905	183.97
114	1.58	23.35	488.97	1.44	2.032	183.59
115	1.66	23.08	476.31	1.52	2.166	183.17
116	1.75	22.80	463.48	1.61	2.310	182.71

TABLE 7.22. (continued)

T (K)	P (Bubble) (MPa)	Liquid ρ (mol/dm ³)	ω (m/s)	P (Dew) (MPa)	Vapor ρ (mol/dm ³)	ω (m/s)
117	1.85	22.51	450.49	1.70	2.463	182.21
118	1.95	22.22	437.29	1.80	2.626	181.66
119	2.05	21.91	423.89	1.90	2.801	181.08
120	2.16	21.59	410.23	2.01	2.989	180.45
121	2.27	21.25	396.30	2.12	3.191	179.78
122	2.38	20.90	382.04	2.23	3.410	179.06
123	2.50	20.53	367.40	2.35	3.648	178.31
124	2.62	20.14	352.31	2.47	3.908	177.52
125	2.74	19.73	336.67	2.59	4.193	176.68
126	2.87	19.28	320.36	2.73	4.510	175.81
127	3.01	18.79	303.21	2.86	4.865	174.91
128	3.14	18.24	285.00	3.01	5.270	173.96
129	3.28	17.62	265.37	3.15	5.740	172.98
130	3.43	16.86	243.75	3.31	6.307	171.93
131	3.58	15.87	219.07	3.47	7.034	170.79
132	3.72	14.20	189.12	3.65	8.127	169.40

TABLE 7.23. Air—Isobar at 0.101 325 MPa

T (K)	ρ (mol/dm ³)	ω (m/s)
100	0.124	198.21
200	0.061	283.45
300	0.041	347.36
400	0.030	400.50
500	0.024	446.40
600	0.020	487.07
700	0.017	523.89
800	0.015	557.85
900	0.014	589.60
1000	0.012	619.60
1100	0.011	648.15
1200	0.010	675.47
1300	0.0094	701.72
1400	0.0087	727.03
1500	0.0081	751.50
1600	0.0076	775.19
1700	0.0072	798.19
1800	0.0068	820.54
1900	0.0064	842.30
2000	0.0061	863.51
2100	0.0058	884.21
2200	0.0055	904.43
2300	0.0053	924.20
2400	0.0051	943.56
2500	0.0049	962.52
2600	0.0047	981.10
2700	0.0045	999.34
2800	0.0044	1017.25
2900	0.0042	1034.84
3000	0.0041	1052.13
3100	0.0039	1069.14
3200	0.0038	1085.87

(continues)

TABLE 7.23. (continued)

T (K)	ρ (mol/dm ³)	ω (m/s)
3300	0.0037	1102.35
3400	0.0036	1118.58
3500	0.0035	1134.57
3600	0.0034	1150.34
3700	0.0033	1165.89
3800	0.0032	1181.23
3900	0.0031	1196.37
4000	0.0030	1211.31
4100	0.0030	1226.07
4200	0.0029	1240.65
4300	0.0028	1255.05
4400	0.0028	1269.29
4500	0.0027	1283.36
4600	0.0026	1297.27
4700	0.0026	1311.03
4800	0.0025	1324.65
4900	0.0025	1338.12
5000	0.0024	1351.45

TABLE 7.24. Air—Isobar at 1 MPa

T (K)	ρ (mol/dm ³)	ω (m/s)
100	26.59	658.25
106.22	25.23	582.97
108.10	1.38	185.23
200	0.616	281.74
300	0.402	348.45
400	0.300	402.33
500	0.240	448.46
600	0.200	489.16
700	0.171	525.96
800	0.150	559.86
900	0.133	591.54
1000	0.120	621.47
1100	0.109	649.95
1200	0.100	677.21
1300	0.092	703.40
1400	0.086	728.66
1500	0.080	753.07
1600	0.075	776.72
1700	0.071	799.67
1800	0.067	821.98
1900	0.063	843.70
2000	0.060	864.87
2100	0.057	885.53
2200	0.055	905.72
2300	0.052	925.46
2400	0.050	944.79
2500	0.048	963.72
2600	0.046	982.28
2700	0.044	1000.49
2800	0.043	1018.37
2900	0.041	1035.94
3000	0.040	1053.21

TABLE 7.24. (continued)

T (K)	ρ (mol/dm ³)	ω (m/s)
3100	0.039	1070.20
3200	0.038	1086.91
3300	0.036	1103.37
3400	0.035	1119.59
3500	0.034	1135.56
3600	0.033	1151.31
3700	0.032	1166.84
3800	0.032	1182.17
3900	0.031	1197.29
4000	0.030	1212.22
4100	0.029	1226.97
4200	0.029	1241.53
4300	0.028	1255.92
4400	0.027	1270.15
4500	0.027	1284.21
4600	0.026	1298.11
4700	0.026	1311.86
4800	0.025	1325.46
4900	0.025	1338.92
5000	0.024	1352.24

TABLE 7.25. Air—Isobar at 5 MPa

T (K)	ρ (mol/dm ³)	ω (m/s)
100	27.22	710.56
200	3.38	279.42
300	2.02	355.63
400	1.49	411.69
500	1.18	458.30
600	0.983	498.93
700	0.843	535.45
800	0.738	569.01
900	0.657	600.34
1000	0.592	629.93
1100	0.539	658.09
1200	0.494	685.05
1300	0.457	710.97
1400	0.424	735.96
1500	0.396	760.13
1600	0.372	783.56
1700	0.350	806.30
1800	0.331	828.42
1900	0.314	849.96
2000	0.298	870.96
2100	0.284	891.46
2200	0.271	911.50
2300	0.259	931.10
2400	0.249	950.29
2500	0.239	969.10
2600	0.230	987.54
2700	0.221	1005.64
2800	0.213	1023.41
2900	0.206	1040.88

(continues)

TABLE 7.25. (continued)

T (K)	ρ (mol/dm ³)	ω (m/s)
3000	0.199	1058.05
3100	0.193	1074.95
3200	0.187	1091.57
3300	0.181	1107.95
3400	0.176	1124.08
3500	0.171	1139.98
3600	0.166	1155.65
3700	0.162	1171.12
3800	0.158	1186.37
3900	0.154	1201.43
4000	0.150	1216.30
4100	0.146	1230.98
4200	0.143	1245.49
4300	0.139	1259.82
4400	0.136	1273.99
4500	0.133	1288.00
4600	0.130	1301.85
4700	0.127	1315.55
4800	0.125	1329.10
4900	0.122	1342.52
5000	0.120	1355.79

TABLE 7.26. Air—Isobar at 10 MPa

T (K)	ρ (mol/dm ³)	ω (m/s)
100	27.86	763.47
200	7.39	296.30
300	4.04	369.50
400	2.92	425.59
500	2.32	471.81
600	1.93	511.90
700	1.65	547.83
800	1.45	580.83
900	1.29	611.64
1000	1.17	640.74
1100	1.06	668.46
1200	0.975	695.01
1300	0.902	720.56
1400	0.839	745.21
1500	0.784	769.07
1600	0.736	792.20
1700	0.693	814.68
1800	0.655	836.55
1900	0.621	857.85
2000	0.591	878.64
2100	0.563	898.94
2200	0.538	918.78
2300	0.515	938.21
2400	0.494	957.23
2500	0.474	975.87
2600	0.456	994.17
2700	0.440	1012.12
2800	0.424	1029.76
2900	0.410	1047.10

TABLE 7.26. (continued)

T (K)	ρ (mol/dm ³)	ω (m/s)
3000	0.396	1064.15
3100	0.384	1080.92
3200	0.372	1097.44
3300	0.361	1113.71
3400	0.350	1129.74
3500	0.340	1145.54
3600	0.331	1161.12
3700	0.322	1176.49
3800	0.314	1191.66
3900	0.306	1206.63
4000	0.298	1221.42
4100	0.291	1236.03
4200	0.284	1250.46
4300	0.277	1264.72
4400	0.271	1278.82
4500	0.265	1292.76
4600	0.260	1306.55
4700	0.254	1320.19
4800	0.249	1333.68
4900	0.244	1347.04
5000	0.239	1360.25

TABLE 7.27. Air—Isobar at 50 MPa

T (K)	ρ (mol/dm ³)	ω (m/s)
100	30.94	1012.41
200	21.58	670.59
300	15.23	581.66
400	11.68	582.86
500	9.54	604.06
600	8.10	629.50
700	7.06	655.45
800	6.28	680.98
900	5.66	705.86
1000	5.15	730.05
1100	4.74	753.58
1200	4.38	776.48
1300	4.08	798.80
1400	3.82	820.55
1500	3.59	841.78
1600	3.38	862.52
1700	3.20	882.80
1800	3.04	902.63
1900	2.89	922.05
2000	2.76	941.07
2100	2.64	959.73
2200	2.53	978.04
2300	2.43	996.01
2400	2.33	1013.67
2500	2.24	1031.02
2600	2.16	1048.10
2700	2.09	1064.90
2800	2.02	1081.44

(continues)

TABLE 7.27. (continued)

T (K)	ρ (mol/dm ³)	ω (m/s)
2900	1.95	1097.73
3000	1.89	1113.79
3100	1.83	1129.62
3200	1.78	1145.23
3300	1.73	1160.63
3400	1.68	1175.83
3500	1.64	1190.84
3600	1.59	1205.66
3700	1.55	1220.30
3800	1.51	1234.77
3900	1.48	1249.06
4000	1.44	1263.20
4100	1.41	1277.18
4200	1.37	1291.01
4300	1.34	1304.69
4400	1.32	1318.22
4500	1.29	1331.62
4600	1.26	1344.88
4700	1.23	1358.01
4800	1.21	1371.01
4900	1.19	1383.88
5000	1.16	1396.64

TABLE 7.28. Air—Isobar at 100 MPa

T (K)	ρ (mol/dm ³)	ω (m/s)
100	33.16	1192.37
200	26.18	932.01
300	21.14	818.47
400	17.60	779.80
500	15.09	772.41
600	13.23	778.24
700	11.80	790.14
800	10.67	805.13
900	9.75	821.78
1000	8.98	839.35
1100	8.33	857.39
1200	7.77	875.65
1300	7.29	893.95
1400	6.86	912.18
1500	6.48	930.28
1600	6.15	948.19
1700	5.85	965.90
1800	5.57	983.39
1900	5.32	1000.64
2000	5.10	1017.65
2100	4.89	1034.43
2200	4.70	1050.98
2300	4.52	1067.31
2400	4.36	1083.41
2500	4.21	1099.29
2600	4.06	1114.97
2700	3.93	1130.44
2800	3.81	1145.72

TABLE 7.28. (continued)

T (K)	ρ (mol/dm ³)	ω (m/s)
2900	3.69	1160.81
3000	3.58	1175.72
3100	3.48	1190.45
3200	3.38	1205.01
3300	3.29	1219.40
3400	3.20	1233.63
3500	3.12	1247.71
3600	3.04	1261.63
3700	2.97	1275.41
3800	2.90	1289.04
3900	2.83	1302.54
4000	2.76	1315.90
4100	2.70	1329.13
4200	2.64	1342.24
4300	2.59	1355.21
4400	2.53	1368.07
4500	2.48	1380.81
4600	2.43	1393.43
4700	2.38	1405.95
4800	2.34	1418.35
4900	2.29	1430.64
5000	2.25	1442.83

Additional Reading

- Kinsler, L.E., Frey, A.R., Coppens, A.B., and Sanders, J.V. (1982). *Fundamentals of Acoustics* New York: John Wiley & Sons.
- Thompson, P.A. *Compressible-Fluid Dynamics* New York: McGraw Hill. (1972).
- Trusler, J.P.M. (1991). *Physical Acoustics and Metrology of Fluids* Bristol: Adam Hilger.
- Van Dael, W. (1975). In *Experimental Thermodynamics of Non-Reacting Systems* (International Union of Pure and Applied Chemistry, Commission on Thermodynamics and Thermochemistry; Le Neindre, B. and Vodar, B. eds. London: Butterworths. chapter 7, *Thermodynamic Properties and the Velocity of Sound*, pp. 527–575.

References

1. Slattery, J.C. (1981). *Momentum, Energy, and Mass Transfer in Continua*, New York: Krieger Publishing.
2. Thompson, P.A. (1972). *Compressible-Fluid Dynamics* New York: McGraw Hill.
3. NIST Thermophysical Properties of Pure Fluids Database (NIST12, Version 5.0). (2000). Natl. Inst. Stand. Tech., Gaithersburg, MD.
4. McQuarrie, D.A. (1976). *Statistical Mechanics* New York: Harper & Row.

5. Costa Gomes, M.F., and Trusler, J.P.M. (1998). The speed of sound in nitrogen at temperatures between $T = 250$ K and $T = 350$ K and at pressures up to 30 MPa, *J. Chem. Thermodynamics* **30**: 527.
6. Trusler J.P.M. (1991). *Physical Acoustics and Metrology of Fluids* Bristol: Adam Hilger.
7. Van Dael, W. In *Experimental Thermodynamics of Non-Reacting Systems* (International Union of Pure and Applied Chemistry, Commission on Thermodynamics and Thermochemistry Le Neindre, B. and Vodar, B, eds. London: Butterworths, chapter 11: *Thermodynamic properties and the velocity of sound*, pp. 527–575.
8. Reid, R.C., Prausnitz, J.M., and Poling, B.E. (1987). *The Properties of Gases and Liquids* New York: McGraw Hill.
9. Carnahan, N.F., and Starling, K.E. (1969). Equation of state for nonattracting rigid spheres, *J. Chem. Phys.* **51**: 635.
10. Younglove, B.A. (1982). Thermophysical properties of fluids. I. argon, ethylene, parahydrogen, nitrogen, nitrogen trifluoride, and oxygen, *J. Phys. Chem. Ref. Data* **11**, pp. 1–1 to 1–353 (368 pages).
11. Sengers, J.V., and Levelt Sengers, J.M.H. (1978). In *Progress in Liquid Physics* (Croxtan, C.A., ed., Chichester, U.K: Wiley. Chapter 4: *Critical phenomena in classical fluids*, pp. 103–174.
12. Tegeler, Ch., Span, R., and Wagner, W. (1999). A new equation of state for argon covering the fluid region for temperatures from the melting line to 700 K at pressures up to 1000 MPa, *J. Phys. Chem. Ref. Data*, **28**: 779.
13. Estrada-Alexanders, A.F., and Trusler, J.P.M. (1995). The speed of sound in gaseous argon at temperatures between 110 K and 450 K and at pressures up to 19 MPa. *J. Chem. Thermodyn.* **27**: 1075.
14. Span, R., Lemmon, E.W., Jacobsen, R.T., and Wagner, W. (1998). A reference quality equation of state for nitrogen, *Int. J. Thermophys.* **19**: 1121.
15. IAPWS. (1995). Release on the Formulation for the Thermodynamic Properties of Ordinary Water Substance for General and Scientific Use; copies of this and other IAPWS releases can be obtained from the Executive Secretary of IAPWS, Dr. R.B. Dooley, Electric Power Research Institute, 3412 Hillview Ave., Palo Alto, CA 94304 or at <http://www.iapws.org>.
16. Lemmon, E.W., Jacobsen, R.T., Penoncello, S.G., and Friend, D.G. (2000). Thermodynamic properties of air and mixtures of nitrogen, argon, and oxygen from 60 to 2000 K at pressures to 2000 MPa. *J. Phys. Chem. Ref. Data* **29**: 331.
17. Younglove, B.A., Frederick, N.V., and McCarty, R.D. (1993). *Speed of Sound Data and Related Models for Mixtures of Natural Gas Components*, NIST Monograph 178.
18. Lemmon, E.W., and Jacobsen, R.T. (1999). *A Generalized Model for the Thermodynamic Properties of Mixtures*, *Int. J. Thermophys.* **20**: 825.
19. Thermodynamics Research Center; Texas Engineering Experiment Station, College Station, TX (1961–2000): Natl. Inst. Stand. Tech., Boulder, CO (2000–).

8. NONINVASIVE DETERMINATION OF SOUND SPEED AND ATTENUATION IN LIQUIDS

Dipen N. Sinha and Gregory Kaduchak

Electronic Materials and Devices Group
Los Alamos National Laboratory
Los Alamos, New Mexico

Abstract

Swept-Frequency Acoustic Interferometry (SFAI) is a nonintrusive liquid characterization technique developed specifically for detecting and identifying liquids inside sealed munitions. The SFAI technique can rapidly (<20 s) and accurately determine sound speed and sound attenuation of a liquid inside a container over a wide frequency range. From the frequency-dependent sound attenuation measurement, liquid density is determined. The theory of the technique is described. Although SFAI is a frequency domain technique, and we describe how accurate time domain information, equivalent to high-quality pulse-echo measurements, can also be extracted from the data. Sound speed and attenuation measurements using both approaches are presented.

8.1 Introduction

There are many situations in which it is necessary to determine information about the liquid contents inside sealed or otherwise inaccessible containers. In such situations, the only choice is to make measurements from outside the container without any direct physical contact between the sensor and the liquid content. The need for such noninvasive measurement is particularly crucial for highly toxic chemicals, such as the various chemical warfare (CW) agents and many of their precursor chemicals. This is necessary to address the requirements of the Chemical Weapons Convention, the treaty that calls for eventual destruction of all chemical weapons [1], where it is essential to have techniques that can be used to monitor compliance and destruction of existing stockpiles in a verifiable way. If the container has a metal wall, as is the case most often for chemical munitions, then one cannot use any of the commonly used optical, electromagnetic (e.g., microwave and radio frequency), or mass spectrometry techniques for liquid characterization or identification. Information regarding thermal characteristics of the liquid inside may be obtained through calorimetric type measurements but is insufficient to identify a chemical. A good possibility is to use nuclear techniques, with which

it is possible to determine the presence of various elements in the liquid and guess at the chemical composition based on such elemental information. This approach has been quite successful in identifying CW agents in munitions. Unfortunately, such techniques require a radioactive source, a liquid nitrogen cooled detector, and a long particle counting time. A simple solution is to use ultrasound. Ultrasound can easily penetrate the walls of a container and interrogate the liquid content.

Typically, for the noninvasive characterization of any such liquid filler using ultrasound, one needs to determine various physical properties of the liquid, such as sound speed, sound attenuation, and density of the liquid. This information is often sufficient to identify and characterize various subclasses of chemicals. Popular ultrasonic techniques for the measurement of sound speed and sound attenuation in fluids primarily include resonance reverberation, pulse-echo, and ultrasonic interferometry (UI). Of these techniques, UI, developed several decades ago, stands out for its ability to provide frequency-dependent measurements and for its ability to work with small liquid samples [2–5]. Eggers and Kaatz [6] give a comprehensive review on this subject. Unfortunately, this technique requires the transducers to be in direct contact with the test fluid and precision-machined resonator cells, thereby limiting the applicability of this technique primarily to laboratory fluid characterization. Recently, Pope *et al.* [7] applied this technique for noninvasive monitoring of density and concentration of liquids inside pipes. Although the quality of their data was very poor and extremely noisy compared against typical data obtained from traditional ultrasonic measurements, it showed that it is possible to adapt the UI technique for noninvasive liquid characterization.

Sinha *et al.* [8–13] showed for the first time how to properly adapt the UI technique for noninvasive liquid characterization in general containers and called their approach Swept-Frequency Acoustic Interferometry (SFAI). With this adaptation, it is now possible to measure not only sound speed but also sound attenuation over a wide frequency range, density, and viscosity of liquids inside sealed containers. One interesting feature of the SFAI technique is that it takes advantage of the container wall to extract density and viscosity information. A combination of all these physical properties allows a unique identification of various CW agents inside munitions and other containers noninvasively.

The SFAI technique is primarily a frequency domain technique. However, in this chapter we also discuss how to derive high-quality time domain measurement, equivalent to the traditional pulse-echo measurement, from the frequency data and point out the various advantages of this approach. Although the main focus of this chapter is to present data on the sound speed of CW agents and their precursor chemicals, we also present information on how sound attenuation and density are measured noninvasively.

An important objective of this chapter is to present details about how the UI technique is adapted for noninvasive acoustic characterization of liquids. The chapter is organized as follows: In Section 8.2, we discuss the theory behind the SFAI technique and provide details on the frequency domain analysis. In this section, we also show how accurate time domain information can be derived from the frequency domain data. In Section 8.3, we describe the experimental details. The results and discussion are presented in Section 8.4. Finally, Section 8.5 presents our conclusions.

8.2 Theory

An SFAI measurement can be described in terms of planar ultrasonic wave transmission and reflection through a multilayered system consisting of the test fluid sandwiched between symmetric layers of transducer crystal, wear plate, coupling gel, and cell (container) wall. To better understand this multilayered system, it is instructive to first start with the basic single-layer model, as shown in Figure 8.1. It shows a volume of liquid between two identical parallel piezoelectric transducers where one transducer is used as the excitation source and the one on the opposite side as the receiver. If a sine-wave electrical signal

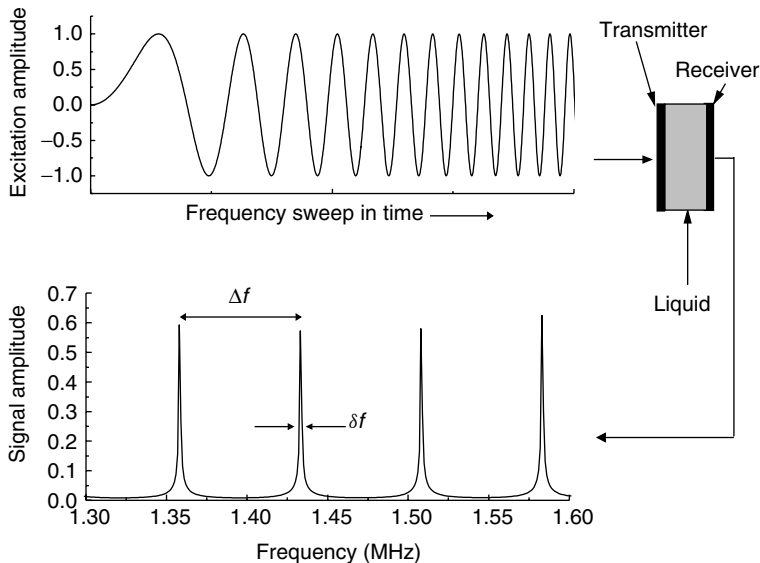


FIG. 8.1. Ultrasonic interferometry with transducers directly in contact with liquid. The top frame shows the excitation signal and the bottom frame shows the interference spectrum due to setting up of standing waves in the liquid at regular intervals.

is applied to the source transducer and its frequency is stepped through in time over a frequency range with appropriate residence time at each frequency step, the signal detected by the receiver transducer is a series of regularly spaced resonance peaks, as shown in the bottom frame of Figure 8.1. The typical regularly spaced interference peaks are observed whenever an integral number of half-wavelengths span the liquid between the two transducers. The sound speed c is then derived from the frequency spacing between any two consecutive resonance peaks Δf as

$$c = 2L\Delta f, \quad (8.1)$$

where L is the liquid path length. Eq. 8.1 provides accurate measurement in practice, in particular if the measurements are made in a frequency range far from the transducer resonance frequency. For measurements closer to the transducer resonance frequency, corrections due to the frequency-dependent transducer transfer function can be included [14, 15]. The width of the peaks (FWHM) is related to the sound attenuation in the liquid and will be discussed later.

The spectrum shown in Figure 8.1 can be easily derived from a simple sound transmission model for a single-layer bounded by infinite media and can be found in many textbooks [16] and articles [17, 18]. The solution is general purpose and can also be used for solids, such as metal plates, at near normal incidence.

In noninvasive measurements, one has to deal with container walls; therefore, the system now becomes a problem of sound transmission through a multilayered medium. For a good description of such sound transmission, refer to the excellent book by Brekhovskikh [19]. Hill and El-Dardiry [20] give simpler expressions for three layers and five layers. When all layers are solid, the situation is somewhat complicated because now both compressional and shear wave propagation through the composite medium needs to be considered. In trying to probe a liquid inside a container, the system becomes much simpler because of the presence of the liquid as the main layer. There is no need to worry about shear wave coupling except at the transducer–wall interface. In practice, it turns out that this effect is quite small and can be neglected unless very accurate liquid attenuation measurement is desired. It does not affect the compressional sound speed measurement in the fluid.

Figure 8.2 shows a typical spectrum obtained from a liquid inside a container with the transducers attached to the outside of the container. The spectrum is now much more complicated than in Figure 8.1. It now shows a composite spectrum where two sets of spectra are coupled together: one from the liquid (as in Fig. 8.1) and the other from each wall, the two walls being identical in thickness and material. The sound transmission through the wall now has a

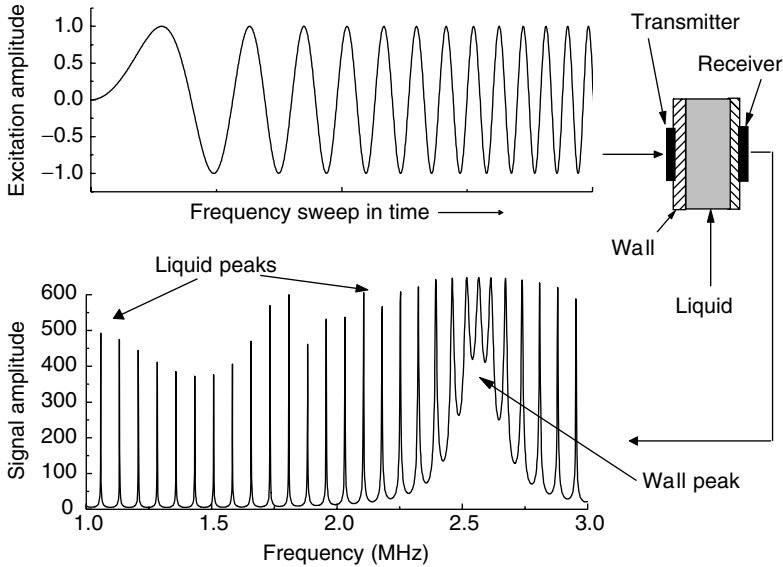


FIG. 8.2. Frequency-sweep measurements in a liquid through a container wall. The irregular variation in transmission amplitude is due to poor resolution in the data.

periodic structure reaching a maximum whenever standing waves set up within the thickness of the wall. This modifies the spectrum obtained from the liquid and forms the composite spectrum. Typically, the path length in the liquid is much larger than the thickness of a wall. Because the sound speed in metals is much higher than in liquids, the frequency spacing of consecutive wall peaks is quite large (see Eq. 8.1). Only a single wall resonance is shown in Figure 8.2. A closer examination of this figure reveals two important features. First, as the wall peak is approached from either side, the liquid peaks get progressively broader, indicating greater loss. This is because of the higher sound transmission through the wall near the wall peaks.

The second feature is the bunching of the liquid peaks near the wall peak: the liquid peak spacing gets progressively shorter as the maximum of the wall peak is approached due to the coupling between the wall and the liquid, and it is very similar to two coupled oscillators. The impedance mismatch between the wall material and the liquid plays a big role in this coupling. The composite spectrum shown in Figure 8.2 is very similar to that observed in traditional interferometry measurements [21] around the transducer crystal resonance, where the transducer is in direct contact with the liquid. The effect of the transducer alone in the traditional interferometry case is similar to the effect of the wall in the present situation, as shown in Figure 8.2. Although

not obvious from the figure, the effect of this wall–liquid coupling extends through the entire frequency range but gets weaker as one moves away from the wall peak. This coupling manifests itself as a small periodic oscillation about its average value in the various observable quantities, such as liquid peak amplitude, liquid width, and liquid peak spacing as a function of frequency. The characteristic of this oscillatory behavior as a function of frequency is the same for each observable quantity. This effect is also observed in traditional interferometry. For example, Gavish *et al.* [22] allude to a fixed oscillatory pattern in the observed sound speed data. A Mathcad program that models the system shown in Figure 8.2 is provided in the Appendix. This program is derived from a straightforward plane wave 1-D propagation model through multiple layers, and it faithfully reproduces the observed behavior in the spectrum described in Figure 8.2.

In practice, the wall–liquid coupling does not affect the sound speed measurement, but it does require care in properly extracting the sound attenuation value in the liquid and will be discussed later. We would like to emphasize here that our goal is to derive sound speed and attenuation values with sufficient accuracy and resolution to be useful for practical applications; this is not meant for high-accuracy acoustic characterization. The SFAI technique shows how to derive proper sound attenuation information by subtracting the effect of the transducer–wall coupling.

It should be pointed out that for use on munitions and other containers, the SFAI technique employs a novel transducer implementation that allows all measurements to be made from only one side of the container using a dual-element transducer system instead of the two transducers on opposite sides, as shown in Figures 8.1 and 8.2.

8.2.1 Frequency Domain Analysis

To derive the physical properties of the liquid from the observed frequency spectrum, the full theory that includes all layers can be used, as presented in the Mathcad program in the Appendix. However, for rapid extraction of such properties, it is more convenient to select an appropriate measurement frequency range to avoid resonance contributions from the walls (e.g., around 4, 6, and 8 MHz in Fig. 8.3). Essentially, in the first order, this reduces the problem to a basic one-layer model, making the analysis significantly straightforward and without introducing significant errors in the measurement of sound speed and sound attenuation. This is similar to avoiding the transducer crystal resonance frequency region in traditional interferometry. The intensity transmission coefficient T for the simplified case of a single fluid layer of path length L , attenuation coefficient α_L ($\alpha_L L \ll 1$), and sound speed c_L between

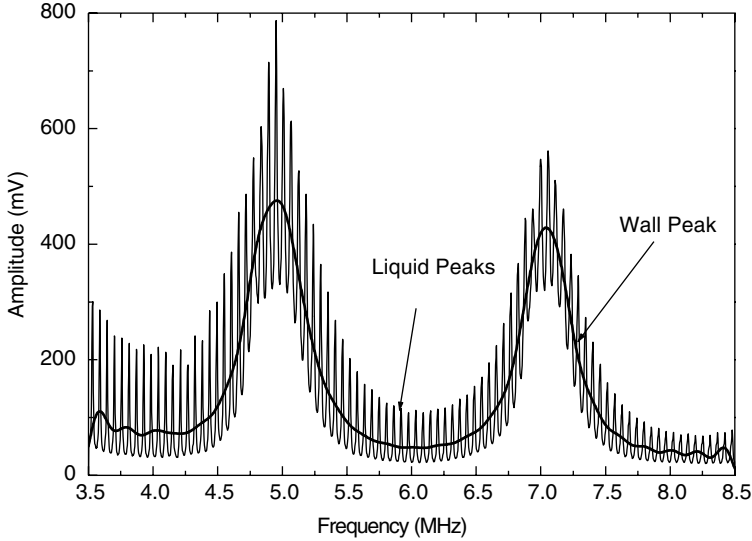


FIG. 8.3. Composite spectra of container wall and liquid. The solid line indicates the sound transmission characteristics of the wall alone. The gradual decrease in the amplitude of the liquid peaks with frequency is due to sound absorption in the liquid. Measurements made in the frequency regions near 4, 6, and 8 MHz (away from the influence of the wall) are similar to measurements without the walls.

two identical wall boundaries can be expressed as

$$T = \frac{1}{\left(1 + \frac{1}{2}\sigma\alpha_L L\right)^2 + \frac{\sigma^2 - 4}{4} \sin^2\left(\frac{\omega}{c_L}L\right)} \quad (8.2)$$

Here, $\sigma = z_w/z_L + z_L/z_w$, ω ($\omega = 2\pi f$) is the angular frequency, z_w and z_L are acoustic impedance (ρc) of wall and liquid, respectively, and ρ is the density. For most liquids inside a metal container, $\sigma \approx z_w/z_L$. T_T in Eq. 8.2 is a periodic function of $\omega L/c_L$ and reaches a maximum (peak) whenever the condition $2\pi f_n L/c_L = n\pi$ is satisfied, where f_n is the n -th peak frequency. From this condition, the sound speed c_L ($c_L = 2L\Delta f$) can be determined if the frequency difference between any two consecutive resonance peaks $\Delta f = f_{n+1} - f_n$ is measured. However, we see from both experiments and model predictions that Δf oscillates ($>1\%$ in most cases in practice) around the mean value over the measurement frequency range due to effects of container wall resonance modulation, a characteristic behavior of the noninvasive measurement as mentioned earlier. Therefore, c_L is obtained using the averaged frequency difference $\langle \Delta f \rangle$ (e.g., between 5.7 and 6.4 MHz in

Fig. 8.3)

$$c_L = 2L\langle\Delta f\rangle \quad (8.3)$$

Next, we discuss how sound attenuation and liquid density are determined from the frequency spectrum. The ratio of transmission coefficient minima, T_{\min} , and maxima, T_{\max} , can be expressed in terms of σ and α_L as [18]

$$\frac{T_{\min}}{T_{\max}} = \frac{2}{\sigma} + L\alpha_L(f^2) \quad (8.4)$$

Equation 8.4 shows that both α_L and σ can be determined from a linear fit of the data of the transmission ratio factor as a function of f^2 . The intercept at zero frequency is related to the acoustic impedance ratio σ . If the impedance of the wall material is known, the liquid density can be determined because the liquid sound speed is determined independently, as discussed above (see Eq. 8.3) and σ is the only unknown.

Another approach to determining the sound attenuation coefficient is to use the half-power bandwidth of observed resonance peaks. From Eq. 8.2, one can derive an inverse solution for the half-power bandwidth, δf , in terms of acoustic properties in the fluid as [13, 18]

$$\delta f = \frac{2c_L}{\pi\sigma L} + \frac{c_L\alpha_L(f^2)}{\pi} \quad (8.5)$$

Similar to Eq. 8.4, the second term is the contribution from liquid sound absorption and is identical to the solution obtained in a previous resonator theory [23, 24] for transducers in direct contact with the test liquid. The first term, the width extrapolated to zero frequency, δf_0 , is independent of frequency and depends on σ , c_L , and L . This term results from the reflection loss at the wall–liquid interface due to the acoustic impedance mismatch and can be used to determine liquid density if the acoustic impedance of the wall is known. Figure 8.4 shows a plot of Eq. 8.5. The intercept is simply the first term in Eq. 8.5 and the slope, the second term. A similar plot is obtained from Eq. 8.4 as well. Either of these approaches can be used to determine sound attenuation and liquid density. From the first term of Eq. 8.5, since c_L is determined independently, the liquid density can be determined if the acoustic impedance of the wall material is known. Typically, one needs to know only the density of the wall material because the sound speed can be determined from the wall peak spacing (see Fig. 8.3).

In practical measurements, however, other loss mechanisms — such as diffraction loss and losses due to the transducer backing and tangential mode generation in the container — although small in magnitude, also contribute to the measured peak width, and their effects need to be included. The diffraction loss effects can be minimized by avoiding the low-frequency region, typically

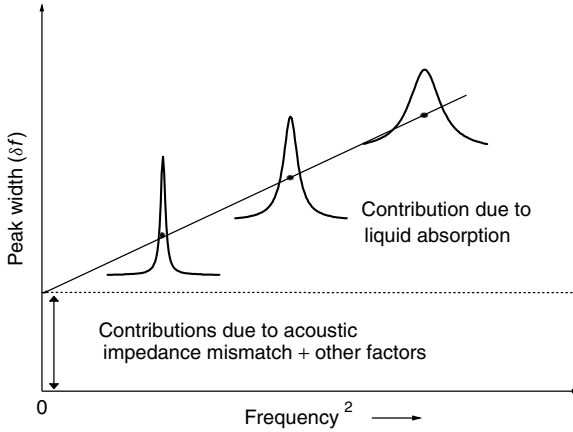


FIG. 8.4. Liquid peak width as a function of square of frequency. The slope of the line provides information on sound attenuation, whereas the intercept extrapolated to zero frequency provides a measure of acoustic impedance mismatch between the container wall and the liquid.

1 MHz and below for most measurements. If the liquid path length inside the container is of comparable dimensions to that of typical commercially available transducers, all the measurements at higher frequencies ensure that a near-field condition is met. Being in this Fresnel region minimizes the beam divergence effects and, therefore, the diffraction loss [24, 25]. However, for accurate determination of sound attenuation and density at any frequency range and particularly for larger containers (path length) where near-field conditions are not ensured, the diffraction loss needs to be subtracted from the measured δf . We have used the standard expression [26] $\delta f_{\text{diff}} = \frac{0.147}{\pi\beta} \left(\frac{2c_r}{D} \right)^3 f^{-2}$, where D is the effective diameter of the transducer and $\beta = z_L/z_W$. Other losses can be accounted for by using a reference liquid of known acoustic properties [6, 23, 26]. Therefore, the attenuation coefficient of the test liquid α_L can be written as

$$\alpha_L = \frac{\pi}{c_L}(\delta f - \delta f_0) - \frac{\pi}{c_L}(\delta f_r - \delta f_{r0}) + \frac{c_r}{c_L}\alpha_r \quad (8.6)$$

Here, δf is the measured half-power bandwidth of the test liquid at any selected frequency, f , and δf_0 is the extrapolated width at $f = 0$. Subscript “ r ” refers to the reference liquid. From Eq. 8.6, the attenuation coefficient factor $\alpha_0 = (\alpha_L/f^2)10^{17}$ np s²/cm can be determined with good accuracy. The density of the test liquid can be determined from

$$\rho_L = \delta f_{0c} \frac{\pi c_w \rho_w L}{2c_L^2} \quad (8.7)$$

Here, δf_{0c} is the extrapolated peak-width value (at $f^2 = 0$) that is corrected for miscellaneous small losses by using a reference liquid. This density determination thus takes advantage of the container wall. On the other hand, the measurement of peak width or the T_{\min}/T_{\max} ratio over a wide range of frequencies allows determination of the sound attenuation in the liquid.

8.2.2 Time Domain Analysis: Traditional Pulse-Echo and Pulse-Echo Transform

Historically, the most popular approach to determining sound velocity has been the pulse-echo time-of-flight technique [27]. In the technique, a narrow electrical pulse is used to excite a transducer attached to a container or in direct contact with a liquid. The pulse generates a pressure pulse that propagates through the liquid, reflects from the opposite wall of the container, and gets detected by either the same transducer or by a second transducer. By measuring the time it took for the pulse to make the round trip travel over the known distance inside the container, it is possible to determine the sound velocity. By transforming the time domain signature to the frequency domain, it is also possible to gather other physical properties of the liquid (e.g., attenuation and density) [28, 29]. This section will describe how to do high-accuracy, high-signal-to-noise measurements in the time domain by taking advantage of the properties of the *analytic* signal and frequency domain data.

The concept of the analytic signal has been around for several decades [30]. It has received much attention by researchers in the radar and sonar community. Its use in NDE applications has been somewhat limited [31, 32]. The analytic signal is described by a real-valued band pass signal that can be represented by complex signals with one-sided spectral densities. In the time domain, the analytic signal is simply written as a real signal, $f(t)$ (which is typically a time-varying quantity measured in an experiment), and its quadrature component, $g(t)$ (phase offset by 90° from the signal $f(t)$) [33].

$$z(t) = f(t) + ig(t) \quad (8.8)$$

This signal has an interesting property in the frequency domain, as shown by the Fourier transform of Eq. 8.8.

$$Z(\omega) = \begin{cases} 2F(\omega) & \omega > 0 \\ 0 & \omega < 0 \end{cases} \quad (8.9)$$

The spectrum of the analytic signal is one-sided and is composed wholly of the positive frequency portion of the real part of the analytic signal. The technique of using only the positive frequency portion of a real signal as shown in Eq. (8.9) is the Hilbert Transform. It is not within the scope of this chapter

to give a detailed account of the analytic signal or the Hilbert transform. For this, the reader is referred to the references.

The analytic signal cannot be appreciated until some examples are given. Consider a measured frequency signature in an experiment such as the one shown in Figure 8.5(a). The spectrum is complex and has been quadrature sampled, as discussed in Section 8.3 of this chapter. The spectrum represents a sinusoidal pulse of center frequency 2 MHz modulated with a Gaussian envelope. The Fourier transform of the spectrum is displayed in Figure 8.5(b). The resultant signal is oscillatory, and a time delay measurement can be made by measuring the location of zero crossings, amplitude extrema, or correlating the pulse with a replica. Now conduct a Hilbert transform on the spectral data in Figure 8.5(a). Erasing the negative frequency components in the spectrum yields the one-sided spectrum in Figure 8.5(c). Performing a Fourier transform on this spectrum yields the analytic signal. The real part of the analytic signal is shown by the oscillatory, solid line in Figure 8.5(d) [and is a replica of the signal seen in Figure 8.5(b)]. But the magnitude of the analytic signal is shown as the bold, solid line in Figure 8.5(d). It is the envelope of the real signal. It can be shown that this envelope is proportional to the rate-of-arrival of the total energy of the pulse at the measuring device. Thus, time-delay

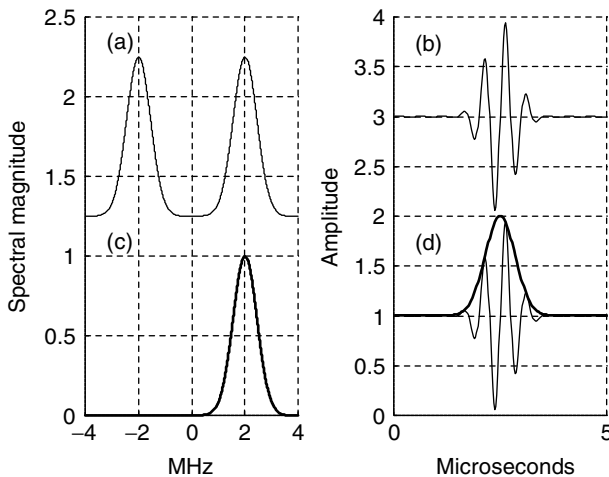


FIG. 8.5. (a) Spectrum of a 2-MHz pulse with a Gaussian envelope. (b) Fourier transform of the spectrum in (a) displaying its time domain representation. (c) Same spectrum as in (a) except the negative frequency components have been set to zero. (d) Fourier transform of the spectrum in (c) representing the results of the Hilbert transform. The bold, solid line is the magnitude of the analytic signal. The real part of the analytic signal is the replica of the signal in (b). The plots in this figure have been offset for clarity.

measurements may be made easily and effectively by locating the maxima of the envelope.

In practice, we derive the analytic signal from swept frequency data. Exactly the same type of parameters may be found from analysis of the analytic signal as from analyzing the data in the frequency domain from an SFAI frequency sweep measurement. Consider the experiment diagrammed in Figure 8.7(b). Instead of applying a frequency sweep, pulse is passed through the wall of a container, propagated through a liquid conduit, and then received after passing through another wall. The frequency spectrum for this experiment is shown in Figure 8.6. After performing the Hilbert transform on this spectral data, the resultant time signature, the band-limited impulse response of the system, is displayed in Figure 8.7(a). It consists of clusters of closely spaced impulses. The first cluster corresponds to the energy, which has traveled once through the liquid conduit. The closely spaced impulses within the cluster represent multiple reflections within the container wall, as shown in Figure 8.7(b). By assuring that the bandwidth B of the measured data obeys the condition

$$\frac{1}{B} \leq \frac{h}{c_w} \quad (8.10)$$

where c_w is the compressional wave speed of the wall material of thickness h , the impulses reverberant within the wall may be temporally isolated. An accurate time-of-flight through the fluid is derived from the time difference between the peaks of the first impulse in each cluster (labeled A and B in the first two clusters). This subtracts out the time the pulse requires to propagate through the container wall, which is not always known for a measurement on

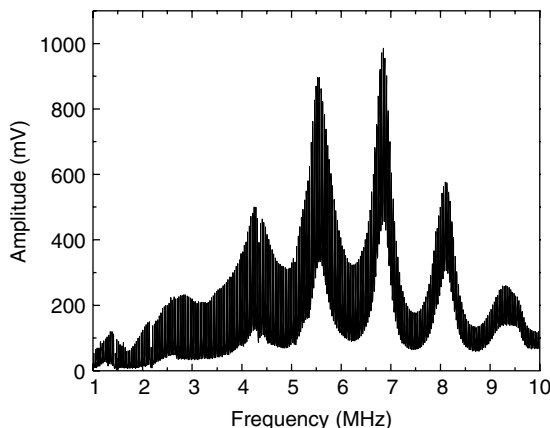


FIG. 8.6. Wide range frequency response of a stainless steel container with ethylene glycol inside.

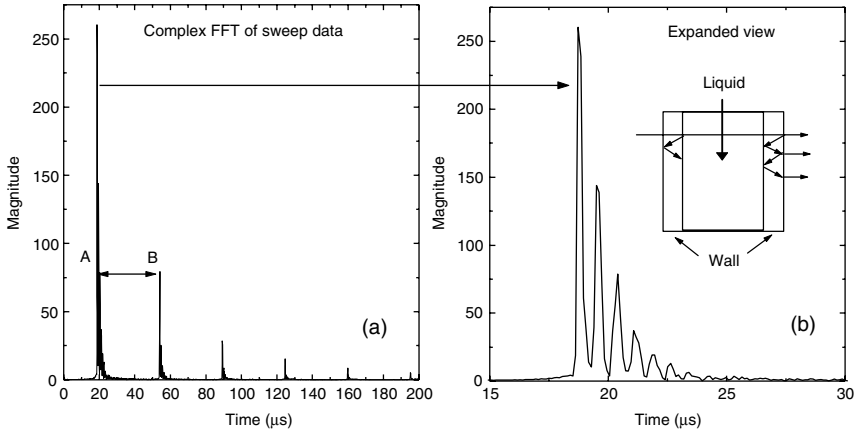


FIG. 8.7. Complex FFT of frequency-sweep data to obtain time domain information. (a) The multiple echoes through the liquid as would be obtained in a typical pulse-echo measurement. (b) An expanded view of the first set of peaks (labeled A) in (a) that clearly shows the multiple reflections in the container wall.

unknown systems. A close-up of the first cluster of echoes labeled A is shown in Figure 8.7(b). Impedance mismatch information about the liquid relative to the container is found in the rate of decay of the peaks in Figure 8.7(b). Using this impedance mismatch information and the decay of the amplitude of the first peak in each cluster shown in Figure 8.7(a) (i.e., A and B), one determines the sound attenuation. This is described in more detail in Section 8.2.1.

One advantage of using this particular type of time domain approach, which is derived from the frequency sweep data, is the ability to achieve much higher signal-to-noise ratios for much lower values of the excitation voltage. In the experiments, measurement at each frequency is made through a narrowband (~ 100 Hz) tracking filter, restricting the received noise to a narrow, sliding frequency window throughout the entire frequency sweep range. In contrast, the noise window for pulse-echo types of measurements would be the equivalent of the entire bandwidth of the transmitted pulse (typically on the order of several megahertz). Thus, for a 10-MHz bandwidth measurement, the SFAI technique can provide a signal-to-noise improvement of approximately five orders of magnitude when comparing the filter widths.

$$\frac{\text{filter width swept-frequency}}{\text{filter width pulse - echo}} = \frac{100 \text{ Hz}}{10,000,000 \text{ Hz}} = 10^5 \quad (8.11)$$

It should be noted that not only is there an increase in the signal-to-noise ratio by recording frequency domain data with a narrow filter, but the system being

measured is allowed to reach a resonant state at each frequency. Thus, the Q of the system will increase the signal levels for a given input drive voltage.

8.2.2.1 Sound Attenuation and Density Determination. The attenuation and density of the fluid in the cell may be calculated by temporally filtering the first impulse (labeled A) in the first cluster and the first impulse (labeled B) in the second cluster from the impulse response shown in Figure 8.7(a) and the expanded view of the impulse in Figure 8.7(b). These pulses refer to disturbances that traverse the thickness of each wall only once and traverse the cavity one or three times, respectively. By calculating the spectrum of the isolated pulses (using a Fourier transform), the ratio of the spectral amplitudes is given by

$$\frac{\text{spectrum}(\text{pulse } B)}{\text{spectrum}(\text{pulse } A)} = \frac{R^2 e^{-\alpha 3 L f^2}}{e^{-\alpha L f^2}} \quad (8.12)$$

where a frequency squared dependence is assumed for the attenuation of the liquid. The unknown quantities are the attenuation coefficient α and the reflection coefficient R of the fluid-wall interface. (All other transmission coefficients which are common to both pulses cancel.) Taking the natural logarithm of this equation yields

$$\ln \left(\frac{\text{spectrum}(\text{pulse } B)}{\text{spectrum}(\text{pulse } A)} \right) = -2\alpha L f^2 + \ln(R^2). \quad (8.13)$$

The right hand side of the equation is a straight line as a function of f^2 with a slope proportional to the attenuation of the liquid and the reflection coefficient (which is proportional to the impedance of the wall and liquid) contained in the y intercept. Note the similarity between Eq. (8.13) and Eq. (8.4).

Based on the analysis presented in this section, a single sweep measurement can be used to derive multiple physical properties of a liquid, including sound speed, sound absorption, frequency dependence of sound absorption, and liquid density. A combination of several of these properties can be used to uniquely identify all the CW compounds and their most significant precursors.

8.3 Experimental

Any conventional electronic system, such as Network Analyzers or Impedance Analyzers, can be used for SFAI measurements. It is also possible to design a simple system based on a computer-controlled function generator (preferably the direct digital synthesis kind) to provide a frequency sweep capability and signal processing electronics that can convert the amplitude of the received sine-wave response from the measurement system. The signal processing circuit can be either an envelope detector or an

RMS-to-DC converter (available as single integrated circuit modules from various electronics vendors). However, to obtain a high signal-to-noise ratio measurement, it is advisable to use a tracking band pass (1 kHz or less bandwidth) filter. Typically, this can be built from a simple heterodyne circuit, such as an AM radio. The amplitude signal can then be digitized and recorded in the computer memory for on-screen display and data analysis.

The SFAI system that we use comprises an electronics unit that consists of a 486DX4-100 MHz embedded PC-104 bus computer and a customized electronics Digital Synthesizer and Analyzer system, model DSA520, made by Nick Electronics, Houston, TX. This instrument is custom designed for SFAI measurements. The DSA520 system contains all electronics for sine-wave sweep signal generation, signal detection, and processing. Another version of this consists of a PC plug-in card (DSA220) that can be used with any desktop PC or any computer with a full-length ISA slot. The sweep frequency range available is 1 kHz to 10 MHz. The sweep rate can be varied from 1 to 800 frequency steps per second. With a resolution of 0.1 Hz over the entire frequency range, the system provides a frequency response directly in real time. Typical excitation voltage levels used for the measurements presented in this chapter varied between 0.1 and 0.5 V peak to peak. The maximum excitation signal available in this system is 10 V.

The transducer system consists off-the-shelf, commercially available broadband piezoelectric transducers. It is preferable that the transducers do not have delay lines attached on the front surface such that the front face can be applied directly on top of the container wall. A thin wear plate on the top surface for protection from mechanical damage is acceptable. Transducers made from 1–3 composite material seem to provide excellent data, but any broadband transducer works fine. The wider the transducer bandwidth, the better the quality of the measurement. This makes the effect of the transducer resonance characteristics less of a problem for attenuation measurement over a wide frequency range. Wide bandwidth means that the transducer frequency response is rather flat compared with a highly peaked response for narrow band transducers. It is particularly important for the time domain analysis.

The signal processing involves a heterodyne mixing technique followed by signal rectification, envelope detection, and 14-bit digitization. The digitized amplitude spectrum is then analyzed in the PC to determine sound speed, sound attenuation, and density of the sample liquid by the methods described in Sections 8.2.1 and 8.2.2. The combined measurement and analysis time is typically <30 s.

For the time domain analysis, we use a homodyne signal processing technique where the real and imaginary components of the received signal are determined. This can be used to obtain both signal amplitude and phase. The

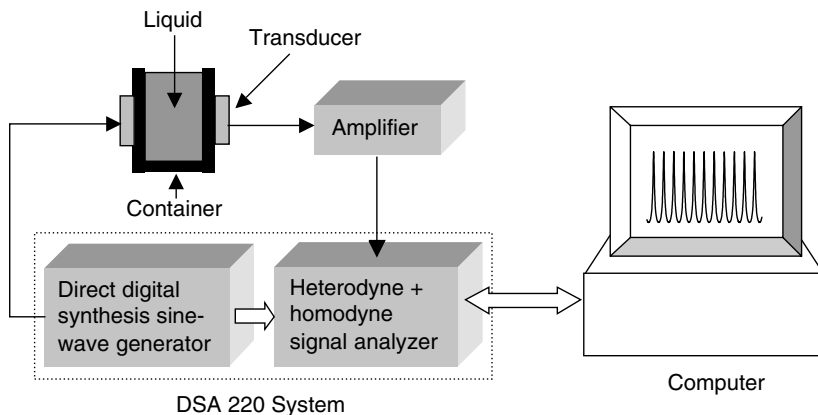


FIG. 8.8. Experimental setup. The DSA220 system is a PC plug-in card that resides inside the desktop computer. It is controlled by the computer through the ISA bus.

bandwidth used for this is ~ 100 Hz. A complex FFT is performed to derive the time domain information, as discussed in the previous section. Both the DSA220 and DSA520 systems have provisions for both heterodyne and homodyne signal processing.

The experimental setup is shown schematically in Figure 8.8. The measurements on CW agents and precursors presented in this chapter were made in cylindrical glass cells used for optical measurements (Catalog Number 32-G-10, Starna Cells, Inc., Atascadero, CA). These cells were made of optical glass, with a path length of 10 mm, wall thickness of 1.25 mm, an exterior diameter of 22 mm, and a volume of 2.8 ml. The transducers used were Panametrics Contact Transducers Videoscan (part number V111-RM), 10-MHz center frequency, and element size of 13 mm. A thin film of ultrasonic gel was used for transducer coupling to the Starna cells. In addition, the transducers had a slight spring loading applied to maintain constant pressure for each measurement. A Peltier cooling–heating system was used to vary the temperature of the Starna cell and its contents and to maintain the temperature to within 1°C . For safety reasons, all experiments were performed under a fume hood in a special laboratory. The transducer and container dimensions are such that all measurements are made in the near-field condition, which minimizes the effect due to diffraction, and the analysis is straightforward. The sound field inside the Starna cell between the two opposite transducers can be considered as plane waves confined inside a cylindrical place [24, 25] of the near-field Fresnel region. Because of the use of identical receiver and transmitter, the transmitted signal as detected by the receiver transducer is effectively integrated over the beam diameter.

8.4 Results and Discussion

We show results of SFAI measurements in optically polished rectangular glass cells of liquid path length 1.0 cm and wall thickness 0.125 cm for various chemicals, including CW compounds. Sound speed can be accurately determined from Eq. 8.3. Figure 8.9 shows the sound speed measurements for glycerine, ethylene glycol, water, toluene, benzene, and isopropanol in a glass cell over a frequency range of 1–12 MHz. For these liquids, the maximum standard deviation relative to the mean values of sound speeds is 0.59%. The scatter (actually an oscillation) in the sound speed data is not due to measurement error but primarily to the wall resonance modulation effect, as discussed in Section 8.2.1, see Eq. 8.3. This oscillation is also seen in predictions from our theoretical model and is discussed in Section 8.2.

Figure 8.10(a) compares the sound attenuation measurement for ethylene glycol in two very different containers, a small glass cell (as in Fig. 8.8) and a cylindrical stainless steel shell with an inner diameter of 5.27 cm and a wall thickness of 0.225 cm. The resonance peak width is plotted as a function of the square of the frequency. The data are consistent with Eq. 8.5. Because the acoustic impedances are very different for glass and steel, the intercepts are different. For the cylindrical container, the effect of curvature on the peak width is now included in the intercept and can be separated. It is evident in the experimental data that qualitatively the same behavior in the frequency-dependent peak width is observed for both planar and cylindrical containers. The slopes of the two lines are the same, indicating the same sound attenuation values.

Figure 8.10(b) shows determination of sound attenuation and density using the Time Domain Analysis technique as described in Section 8.2.1. The

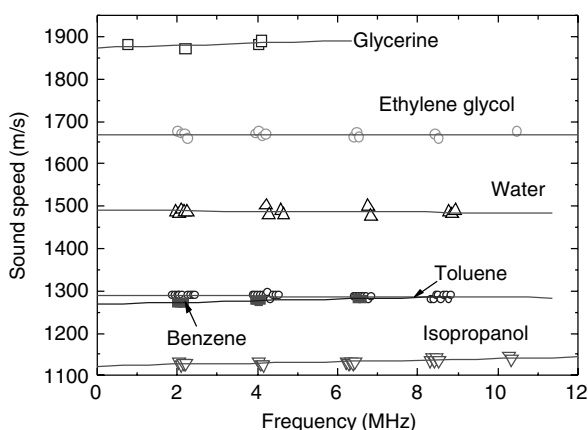


FIG. 8.9. Sound speed determination for six chemicals using Eq. 8.3.

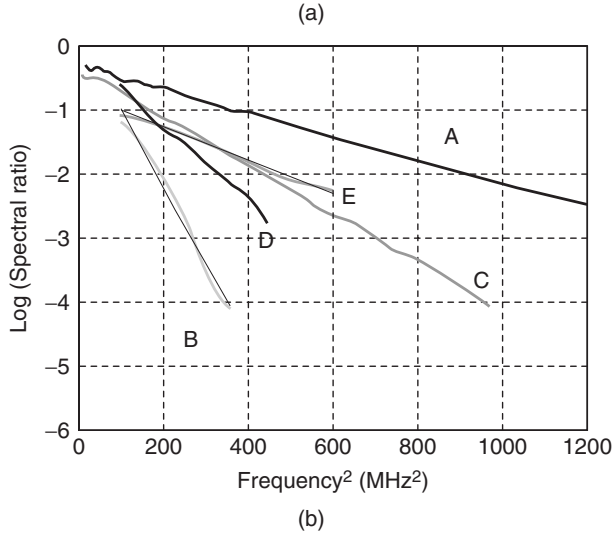
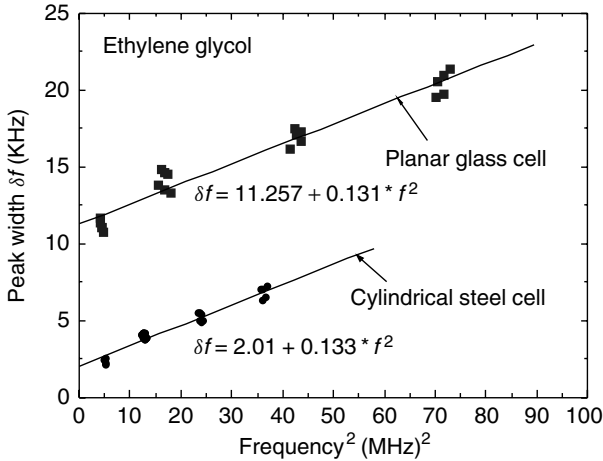


FIG. 8.10. SFAI measurements using both frequency-domain and time-domain approaches. (a) Shows measurements on planar glass cell and cylindrical steel shell filled with ethylene glycol. (b) Shows measurements with the same liquid (isopropanol) but in five different containers.

data, logarithm of spectral ratio as a function of the square of frequency (see Eq. 8.13), shown are for experiments conducted with cells of different material construction (identified by the letters A–E), wall thickness h , and cavity length L . These cell characteristics are defined in Table 8.1. All the cells contained isopropanol as the test fluid. The straight lines superimposing

TABLE 8.1. Cell Characteristics

Cell material	Wall thickness (mm)	Cell length (mm)
A Quartz	1.2	10
B Quartz	1.2	50
C Aluminum	2.5	10
D SS304	2.0	25
E Glass	1.2	20

the experimental data are the plots of Eq. 8.13 using the experimental values of attenuation and density mentioned below. The measurements compare extremely well with literature values:

Attenuation (α):	9.0 Np/(m MHz ²)	Literature
	9.3 ± 0.05 Np/(m MHz ²)	Experiment
Density:	800 kg/m ³	Literature
	850 ± 0.6 kg/m ³	Experiment

This demonstrates that reliable sound attenuation measurements can be made using the SFAI technique regardless of the container geometry and container wall material properties.

Figure 8.11 presents the results of the noninvasive SFAI characterizations of the most common CW compounds. The data presented are for measurements made in Starna glass cells using CW agents that are more than 90% pure and at an ambient temperature of 23 °C. The density for each liquid was determined using Eq. 8.4. This forms the basis for the SFAI technique in noninvasive CW agent identification. Note that in a 3-D representation of the measured data, each liquid is clearly separated from the others, and this separation is many times larger than the accuracy of the measurement. For measurements using the Starna cells, the accuracy of sound speed measurement is approximately 0.5% and that of sound attenuation is more than 3%. Density determination is somewhat less accurate and is typically 5%. All measurements were made over a temperature range between 4 and 35 °C using a specially built Peltier heater–cooler based temperature-controlled system.

The sound speed values of the CW agents and 40 precursor chemicals are presented in Tables 8.2 and 8.3.

8.5 Conclusions

In this chapter, we showed how acoustic characterization of liquids can be made noninvasively. In particular, sound speed, sound attenuation, and density can be determined over a wide frequency range. The equipment used limits the

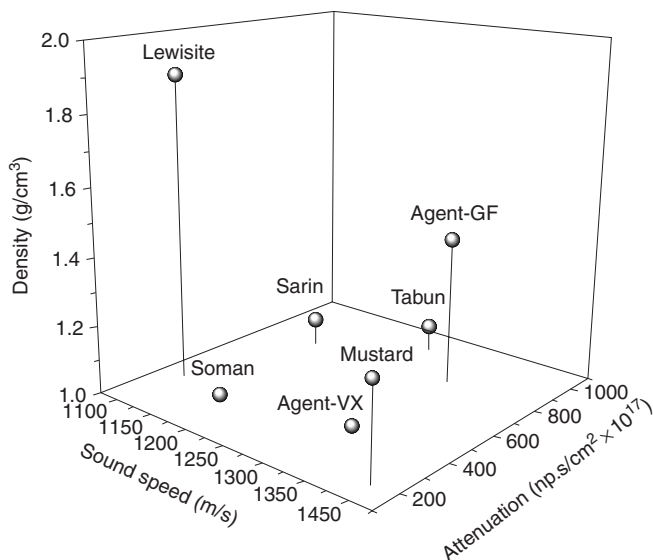


FIG. 8.11. Sound speed, sound attenuation, and density determination for seven chemical warfare agents using the swept-frequency acoustic interferometry technique using glass Starna cells of path length 1 cm and at 26.5 °C.

frequency range. The approach is based on an adaptation of the UI technique. In this particular adaptation, one can take advantage of the container wall itself to determine liquid density. Moreover, it is shown that if the frequency region of analysis is chosen away from the wall resonance (thickness mode), then the analysis reduces to traditional interferometry where the transducers are in direct contact with the liquid. The methodology presented is applicable for containers that are both planar and cylindrical. Although this is a frequency

TABLE 8.2. Sound Speed Values of CW Agents at Several Temperatures

Chemical agents	Sound speed (m/s)				Density at 25 °C (g/cm ³)
	13 °C	17.5 °C	26.5 °C	35 °C	
Tabun (GA)	1290.3	1272.8	1253.21	1220.5	1.073
Sarin (GB)	1196.77	1181.9	1154.1	1129.4	1.088
Soman (GD)	1211.79	1194.3	1172.49	1149.5	1.022
GF	1354.17	1345.7	1322.29		1.434
Sulfur mustard (HD)	1458.18	1421.8	1398.18	1367.8	1.268
Lewisite (L)	1141.82	1124.8	1107.15	1080.3	1.890
VX	1356.60	1340.10	1317.38	1283.62	1.008

TABLE 8.3. Sound Speed of Precursor Chemicals at Three Different Temperatures

Chemical name	Sound speed (m/s)			Density (g/cm ³)
	20 °C	25 °C	30 °C	Density (g/cm ³)
1,4-Butanediol		1601.71	1576.63	1.017
1,5 Pentanediol	1593.96	1582.15	1573.82	0.978
Sulfur monochloride 98%	1202.47	1187.60	1163.69	1.690
<i>N,N</i> -Diethylethanolamine 99%	1346.42	1431.56	1317.50	0.892
4-Picoline	1439.52		1279.20	0.955
Diethyl phosphite 98%	1257.14	1261.98	1247.96	0.920
Phosphorus trichloride	986.78	957.46	933.10	1.574
Phosphorus oxychloride 99%	995.51	986.70	977.14	1.645
<i>N</i> -Ethyl diethanolamine 98%	1504.13	1522.41	1490.79	1.013
Triethyl phosphite 98%	1117.02	1126.04	1093.79	0.963
Pinacolone 98%	1186.76	1180.64	1164.39	0.723
Ethylsonicotinate 98%	1413.71	1407.60	1394.29	0.993
1,4-Dichloro butane 97%	1289.43	1346.62	1269.92	1.141
3,3-Dimethyl-2-butanol 98%	1210.55	1215.84	1188.07	0.812
Triethanol amine 98%	1601.82	1622.15	1593.41	1.124
1,3-Dichloropropane	1243.37	1244.95	1193.68	1.187
<i>N</i> -Methyl diethanolamine	1567.91	1576.54	1559.50	1.038
Dimethyl methyl phosphonate 97%	1378.52	1376.97	1355.02	1.151
Triisopropyl phosphite 95%	1080.70	1091.23	1059.50	0.968
Diethyl methyl phosphonate 97%	1267.73	1268.96	1244.09	1.041
2-(Diisopropylamino)-ethanol 99%	1328.84	1325.29	1309.19	0.826
1,5-Dichloropentane 99%	1293.18	1312.17	1294.63	1.101
2-Chloroethyl ether 99%	1328.11	1328.31	1308.47	1.220
Diethyl chlorothiophosphate 97%	1158.77	1182.44	1134.78	1.183
Ethyl bromoacetate 98%		1119.91	1102.26	1.503
Trimethyl phosphite	1128.10	1154.63	1106.96	1.052
2-Mercapo ethanol 98%	1485.48	1483.74	1469.46	1.114
Diethyl dithiophosphate	1278.52	1276.89	1262.66	1.247
2,2-Thiodiethanol 99%	1680.16	1683.37	1668.15	1.075
2-Chloroethanol	1356.92	1358.18	1340.48	1.202
Thionyl chloride	1040.71	1038.59	1022.87	1.803
Sulfur dichloride	1104.76	1112.68	1087.47	1.620
Dimethyl phosphite 98%	1336.94	1333.71	1318.52	1.200
Dimethyl sulfate 99%	1240.13	1239.43	1221.93	1.332
Dichloro methane 99.6%	1079.49	1096.40		1.326
Carbon disulfide 99.9%	1150.11	1145.45		1.255
Diisopropylamine	1101.63	1093.98	1073.23	0.715
Diethanolamine 99%	1722.46	1699.62	1707.18	1.097
Arsenic(III) chloride 99.99%	1021.23	1016.68	1007.52	2.150
2-Methyl-2-butane 99%	1080.72	1066.29		0.662
Pinacolyl alcohol		1230.34		0.812
<i>O,O'</i> -Diisopropyl methylphosphonate		1184.88		1.036
Diisopropyl [hydrogen] phosphite		1186.30		0.997

domain technique, the complex frequency spectrum can be Hilbert transformed to derive high signal-to-noise ratio time domain measurements. The technical approach presented here is meant primarily to derive sound speed, sound attenuation, and density values with sufficient accuracy for practical use. This is not designed for the highest quality measurements to define fluid characterization standards. Using the methodology presented in this chapter, we determined the sound speed and attenuation for all the common CW agents. This is the first such systematic measurement of these types of chemicals. We also present sound speed data on 40 precursor chemicals to these CW agents.

Appendix

This program analyzes in one-dimension acoustic plane wave interactions normally incident on a system consisting of five distinct regions with the following boundaries: glass–quartz, water–glass, glass–water, and quartz–glass. The program is customized for the glass Starna cells used for the measurements presented in the chapter. It can be easily adapted for other systems by simply replacing the wall thickness, density, attenuation, and sound speed values for glass with other material. The transmitted amplitude is calculated as a pressure, defined as the inverse of the absolute value of the average of components z_3 and z_4 .

$d_1 = 0.01$	the thickness of the liquid region (m)
$c_0 = 5750$	the speed of sound in crystal (approximated) (m/s)
$d_2 = 0.00125$	the thickness of the Pyrex glass (m)
$c_1 = 1480$	the speed of sound in water (m/s)
$\rho_0 = 0.1$	the density of crystal (measured) (g/cm^3)
$c_3 = 5640$	speed of sound in Pyrex glass (m/s)
$\rho_1 = 1.0$	the density of water (g/cm^3)
$i = \sqrt{-1}$	complex number defined
$\rho_3 = 2.6$	the density of Pyrex glass (g/cm^3)
$j = 0.999$	the range variable (Mathcad starts at 0)
points = 1000	number of data points
startf = 1.0	the initial frequency in MHz
stopf = 5.0	the final frequency in MHz
stepf = $\frac{\text{stopf} - \text{startf}}{\text{points}}$	the incremental frequency step size as determined by the number of points
$f_j = \text{startf} + \text{stepf} \cdot j$	the frequency range in MHz
$\omega_j = 2 \cdot \pi \cdot f_j \cdot 10^6$	the conversion of linear frequency to angular frequency

$$\alpha_1 = 25.3 \cdot 10^{-15}$$

the absorption coefficient for water

$$\alpha_3 = 2.5 \cdot 10^{-17}$$

the absorption coefficient for Pyrex glass

Glass–Quartz Interface

$$k0_j = \frac{\omega_j}{C_0}$$

propagation constant in quartz

$$k3_j = \frac{\omega_j}{C_3}$$

propagation constant in glass

$$e1_j = \exp[-\alpha_3 \cdot (f_j)^2 \cdot 10^{12} \cdot d_2]$$

the exponential dependence of the attenuation coefficient for Pyrex glass

$$z_{al} = \frac{\rho_0}{\rho_3}$$

ratio of quartz to Pyrex glass densities: equivalent to the sum of the psi field amplitude coefficients ($B + C$)

$$zr1_j = \frac{k0_j}{k3_j + i \cdot \alpha_3 \cdot (f_j)^2 \cdot 10^{12}}$$

the difference of the amplitude psi field coefficients ($B - C$)

$$zb_j = \frac{(z_{al} + zr1_j)}{2}$$

solution of the psi field amplitude coefficients B and C

$$zc_j = \frac{(z_{al} - zr1_j)}{2}$$

$$\text{ang}1_j = k3_j \cdot d_2$$

the phase shift in Pyrex glass through distance d_2 , and modified by the sweep in frequency

$$\text{euler}1_j = \cos(\text{ang}1_j) + i \cdot \sin(\text{ang}1_j)$$

the sum and difference of the complex Euler angles in Pyrex glass

$$\text{euler}2_j = \cos(\text{ang}1_j) - i \cdot \sin(\text{ang}1_j)$$

$$zb2_j = \frac{zb_j \cdot \text{euler}2_j}{e1_j}$$

evaluation of the psi field at an infinitesimal amount within boundary 2

$$zc2_j = zc_j \cdot \text{euler}1_j \cdot e1_j$$

Water–Glass Interface

$$k1_j = \frac{\omega_j}{c_1}$$

propagation constant in water

$$z_{am} = \frac{\rho_3}{\rho_1}$$

equivalent to the sum of the amplitude coefficients ($E + F$) divided by the sum of the amplitude coefficients ($B + C$)

$$zr2_j := \frac{k3_j + i \cdot \alpha_3 \cdot (f_j)^2 \cdot 10^{12}}{k1_j + i \cdot \alpha_1 \cdot (f_j)^2 \cdot 10^{12}}$$

equivalent to the difference of the amplitude coefficients ($E - F$) divided by the difference of the coefficients ($B - C$)

$$zd_j := z_{am} \cdot (zb2_j + zc2_j)$$

$$ze_j := zr2_j \cdot (zb2_j - zc2_j)$$

imposing boundary conditions at boundary 2

$$zr3_j := \frac{zd_j + ze_j}{2}$$

$$zr4_j := \frac{zd_j - ze_j}{2}$$

solution of the psi field amplitude coefficients E and F

$$ang2_j := k1_j \cdot d_1$$

the phase shift in water through distance d_1 , and modified by the sweep in frequency

$$euler3_j := \cos(ang2_j) - i \cdot \sin(ang2_j)$$

$$euler4_j := \cos(ang2_j) + i \cdot \sin(ang2_j)$$

the sum and difference of the complex Euler angles in water
exponential dependence of the attenuation coefficient for water

$$e2_j := \exp[-\alpha_1 \cdot (f_j)^2 \cdot 10^{12} \cdot d_1]$$

$$zb3_j := \frac{zr3_j \cdot euler3_j}{e2_j}$$

evaluation of the psi field at an infinitesimal amount within boundary 3

$$zc3_j := zr4_j \cdot euler4_j \cdot e2_j$$

Glass–Water Interface

$$z_{an} := \frac{\rho_1}{\rho_3}$$

equivalent to the division of the amplitude coefficients ($G + H$) by the amplitude coefficients ($E + F$)

$$zr5_j := \frac{k1_j + i \cdot \alpha_1 \cdot (f_j)^2 \cdot 10^{12}}{k3_j + i \cdot \alpha_3 \cdot (f_j)^2 \cdot 10^{12}}$$

equivalent to the difference of the amplitude coefficients ($G - H$) divided by the difference of the coefficients ($E - F$)

$$zf_j := z_{an} \cdot (zb3_j + zc3_j)$$

$$zg_j := zr5_j \cdot (zb3_j - zc3_j)$$

imposing boundary conditions at boundary 3

$$zr6_j := \frac{zf_j + zg_j}{2}$$

$$zr7_j := \frac{zf_j - zg_j}{2}$$

solution of the psi field amplitude coefficients G and H

$$zb4_j := \frac{zr6_j \cdot euler2_j}{e1_j}$$

evaluation of the psi field at an infinitesimal amount within boundary 4

$$zc4_j := zr7_j \cdot euler1_j \cdot e1_j$$

Now Calculate the Input PSI Field

$$z3_j := \frac{\rho_3}{\rho_0} \cdot (zb4_j + zc4_j)$$

equivalent to the sum of the psi field amplitude coefficients ($P + A$)

$$zs_j := \frac{k3_j + i \cdot \alpha_3 \cdot (f_j)^2 \cdot 10^{12}}{k0_j}$$

equivalent to the difference of the psi field amplitude coefficients ($P - A$)

$$z4_j := zs_j \cdot (zb4_j - zc4_j)$$

imposing boundary condition at boundary 4

$$trans_j := \frac{z3_j + z4_j}{2}$$

solution of psi field coefficient P

$$pressure_j \frac{1}{|trans_j|}$$

the transmitted pressure amplitudes as a function of swept frequency

$$reflected_j := \frac{(z3_j - z4_j)}{2}$$

solution of psi field coefficient A

$$backpressure_j \frac{1}{|reflected_j|}$$

the reflected amplitudes as a function of swept frequency

Acknowledgments

This work was supported by the Defense Threat Reduction Agency. We are grateful to Kendall Springer and David Lizon for support with the measurements on CW agents and precursor chemicals. We are indebted to Wei Han for developing the methodology and extensive analysis of the data. We thank Mike Keleher for many valuable discussions on CW agents, Fred Mueller for deriving the 1-D multilayer wave propagation model, and Roger Hasse for writing the Mathcad program.

References

1. Barnaby, F. (1994). The Destruction of chemical warfare agents. *Interdisc. Sci. Rev.* **19**: 190.

2. Hubbard, J.C. (1931). The acoustic resonator interferometer: I. the acoustic system and its equivalent electric network. *Phys. Rev.* **38**: 1011.
3. Fox, F. (1937). Ultrasonic interferometry for liquid media. *Phys. Rev.* **52**: 973.
4. Pethrick, R.A. (1972). The swept frequency acoustic resonant interferometer: Measurement of acoustic dispersion parameters in the low megahertz frequency range. *J. Phys. E* **5**: 571.
5. Eggers, F., and Funck, Th. (1976). Ultrasonic relaxation spectroscopy in liquids. *Naturwissenschaften* **63**: 280.
6. Eggers, F. and Kaatz, U. (1996). Broad-band ultrasonic measurement techniques for liquids. *Meas. Sci. Technol.* **7**: 1–19.
7. Pope, N.G., Veirs, D.K., Claytor, T.N., and Hestand, M.B. (1992). Fluid density and concentration measurement using noninvasive in situ ultrasonic resonance interferometry, in *Proceedings IEEE 1992 Ultrasonic Symposium*, vol. 2, McAvoy, B.R., ed., p. 855.
8. Sinha, D.N., Anthony, B.W., and Lizon, D.C. (1995). Swept Frequency Acoustic Interferometry Technique for Chemical Weapons Verification and Monitoring, Third International Conference On Site Analysis, Houston, January 22–25, Los Alamos Unclassified Report: 95–610.
9. Sinha, D.N., Springer, K., Lizon, D., and Hasse, R. (1996). Applications of Swept-Frequency Acoustic Interferometry Technique in Chemical Diagnostics, Fourth International Conference On Site Analysis, Orlando, January 22–25, Los Alamos Unclassified Report: 96–449.
10. Sinha, D.N., Springer, K.N., Han, W., Lizon, D.C., and Houlton, R.B. (1997). Swept-Frequency Acoustic Interferometry for Noninvasive Chemical Diagnostics, Fifth International On Site Analysis Conference, Seattle, February 3–5, Los Alamos Unclassified Report: 96–4561.
11. Sinha, D.N., Springer, K., Han, W., Lizon, D., and Kogan, S. (1977). Applications of Swept Frequency Acoustic Interferometer for Nonintrusive Detection and Identification of Chemical Warfare Compounds, presented at the 1977 Fall American Chemical Society Meeting, Las Vegas, Nevada, September 7–11. Los Alamos Unclassified Report: 97–3113.
12. Sinha, D.N. (1997). Applications of Ultrasonic Interferometry, Proceedings of the Symposium Sponsored by the Office of Naval Research, Resonance Meeting, Asilomar Conference, Pacific Grove, CA, May 11–15. Available from National Center for Physical Acoustics, University of Mississippi. ncpa@olemiss.edu.
13. Han, W., Sinha, D.N., Springer, K., and Lizon, D. (1998). Noninvasive measurement of acoustic properties of fluids using and ultrasonic interferometry technique, in *Nondestructive Characterization of Material VIII*, Green, R.E., ed., p. 393, New York: Plenum Press.
14. Leon, H.I. (1955). Fixed path, variable frequency acoustic interferometer. *J. Acoust. Soc. Am.* **27**: 1107.
15. Behrends, R., Eggers, F., Kaatz, U., and Telgmann, T. (1996). Ultrasonic spectrometry of liquids below 1 MHz: Biconcave resonator cell with adjustable radius of curvature. *Ultrasonics* **34**: 59.
16. Kinsler, L.E., Frey, A.R., Coppens, A.B., and Sanders, J.V. (1982). *Fundamentals of Acoustics*, Third Edition, New York: John Wiley & Son.
17. Katahara, K.W., Rai, C.S., Manghnani, M.B., and Balogh, J. (1981). An interferometric technique for measuring velocity and attenuation in molten rocks. *J. Geophys. Res.* **86**: 779.

18. Guidarelli, G., Marini, A., and Palmieri, L. (1993). Ultrasonic method for determining attenuation coefficients in plate-shaped materials, *J. Acoust. Soc. Am.* **94**: 1476.
19. Brekhovskikh, L.M. (1980). *Waves in Layered Media*, New York: Academic Press.
20. Hill, R. and El-Dardiry, S.M.A. (1980). A theory for optimization in the use of acoustic emission transducers. *J. Acoust. Soc. Am.* **67**: 673.
21. Eggers, F. (1994). Analysis of phase slope or group delay time in ultrasonic resonators and its applications for liquid absorption and velocity measurements. *Acustica* **80**: 397.
22. Gavish, B., Gratton, E., Hardy, C.J., and St. Dennis, A. (1983). Differential sound velocity apparatus for the investigation of protein solutions. *Rev. Sci. Instrum.* **54**: 1756.
23. Eggers, F. and Funck, Th. (1973). Ultrasonic measurements with milliliter liquid samples in the 0.5–100 MHz range. *Rev. Sci. Instrum.* **44**: 969–977.
24. Povey, M.J.W. (1977). *Ultrasonic Techniques for Fluids Characterization*, Orlando, FL: Academic Press. Water.
25. Champion, J.V., Langton, C.M., Meeten, G.H., and Sherman, N.E. (1990). Near-field ultrasonic measurement apparatus for fluids. *Meas. Sci. Technol.* **1**: 786.
26. Labhardt, A. and Schwarz, G. (1976). A high resolution and low volume ultrasonic resonator method for fast chemical relaxation measurements. *Ber. Bunsenges. Phys. Chem.* **80**: 83–92.
27. McClements, D.J. and Fairley, P. (1991). Ultrasonic pulse echo reflectometer. *Ultrasonics* **29**: 58–62.
28. Papadakis, E.P., Fowler, K.A., and Lynnworth, L.C. (1973). Ultrasonic attenuation by spectrum analysis of pulses in buffer rods: Method and diffraction correction. *J. Acoust. Soc. Am.* **53**: 1336–1343.
29. Adamowski, J.C., Buochi, F., Simon, C., Silva, E.C.N., and Sigelmann, R.A. (1995). Ultrasonic measurement of density of liquids, *J. Acoust. Soc. Am.* **97**: 354–361.
30. Gabor, D. (1946). Theory of communication, *J. Inst. Electric. Engrs.* **93**: 429–457.
31. Gammel, P.M. (1981). Improved ultrasonic detection using the analytic signal magnitude. *Ultrasonics* **19**: 73–76.
32. Duncan, M.G. (1990). Real-time analytic signal processor for ultrasonic nondestructive testing. *IEEE Trans. Inst. Meas.* **39**: 1024–1029.
33. Stremler, F.G. (1982). *Introduction to Communication Systems*, pp. 244–252, Reading, MA: Addison-Wesley.

This Page Intentionally Left Blank

9. INTRODUCTION TO THE ELASTIC CONSTANTS OF GASES

Henry E. Bass

National Center for Physical Acoustics
The University of Mississippi
University, Mississippi

9.1 Introduction

Although gases are compressible and exert a restoring force when compressed, it is not common to address the elastic properties of gases. More often the speed of sound or attenuation in a gas are discussed. This slightly different terminology arises from the fundamental physics. Gases are a collection of individual particles that are not bound together but are usually forced to be in the same volume as other particles through the existence of walls or other constraints. A description of the elastic properties of a gas, then, is an attempt to assign a group property to a collection of individual gases. Such a description must rely on a statistical treatment [1]. The most common starting point for such a treatment is the Boltzmann Equation. There are, however, regimes where a rigorous consideration of the Boltzmann Equation is not required, conditions under which the gas behaves as a continuum. Such regimes span most of the experimental space. The major exception where a particle description becomes important is at very low pressures where the sample volume does not contain a sufficient number of particles to provide a statistical average.

Many measurements of elastic properties of gas are made using acoustics. In that case, the appropriate volume over which averages are made is that defined by the scale of the acoustic wavelength. When the acoustic wavelength becomes comparable to the mean free paths between collisions, the continuum description of gases is no longer appropriate. A measure of this condition is the frequency to pressure ratio. Frequency is inversely proportional to wavelength, and mean free path is inversely proportional to gas pressure, so when that ratio is very large, the wavelength approaches the mean free path. The exact value of f/P where a particle description is required depends on the mass of the particles but, in general, is in the neighborhood of 10^{11} Hz/atm. At higher f/P ratios, solutions to Boltzmann's Equation that maintain some of the particle nature of the gas are available [2]. The characteristics of gases at this extreme condition are appropriate for astronomical applications, interstellar gas clouds, for example.

In those f/P regimes most often encountered, gases can be treated as a continuum. This continuum is isotropic so the stress tensor is simple compared to many solids. A standard form for the stress tensor is [3]

$$\sigma_{ij} = (-P + \eta' \nabla \bullet u) \delta_{ij} + 2\eta \varepsilon_{ij} \quad (9.1)$$

where P is the hydrostatic pressure, η is the coefficient of viscosity, η' is the so-called second coefficient of viscosity, u is the displacement vector, δ_{ij} is zero if $i \neq j$ and 1 if $i = j$, and ε is the strain. Note that the shear terms exist only when there is a change in strain. This is different from a solid where a static shear stress can exist. Although this stress tensor looks simple, the individual terms can become quite complex. The following sections deal with the individual terms; the final section revisits the very high f/P regime.

Much of what follows comes from an excellent book by Robert Beyer and Stephen Letcher [4]. Professor Beyer has been kind enough to allow this author to make extensive use of his work.

9.2 Ideal Gas

An ideal gas has no internal losses, so η' and η are both zero. Since the gas is isotropic, we can further simplify the mathematics by assuming motion in only the x direction. Recognizing that we will be interested in determining the elastic constants from the speed of sound, we will write and solve Newton's second law. From the stress gradient,

$$F_i = \partial \sigma_{ij} / \partial x_j \quad (9.2)$$

This force causes an acceleration

$$\rho_o \partial^2 u_i / \partial t^2 = \partial \sigma_{ij} / \partial x_j \quad (9.3)$$

where ρ_o is the mass density. For the simple case of no shear,

$$\rho_o \partial^2 u_i / \partial t^2 = -\partial p / \partial x \quad (9.4)$$

In the same notation, the equation of continuity (or conservation of mass) can be written as [4]

$$-\partial(\rho u) / \partial x = \partial \rho / \partial t \quad (9.5)$$

The first law of thermodynamics can be written in the form

$$\Delta Q = dU - \Delta W \quad (9.6)$$

where ΔQ is the heat added (per mole) to the system in an infinitesimal process, dU is the corresponding increase in the internal energy of the system,

and ΔW is the work done on the system during the same process. Assume that no heat enters or leaves the system during the process so that $\Delta Q = 0$. Replace ΔW with

$$\Delta W = -PdV = M(P/\rho_o^2)d\rho \quad (9.7)$$

where M is the gram molecular weight of the gas, $dU = C_v dT$, where C_v is the heat capacity per mole at constant volume.

In the general case, the equation of state is an expression of the form

$$P = P(\rho, T) \quad (9.8)$$

For an ideal gas, $P = \rho_o RT/M$, where R is the gas constant (per mole). In many cases, however, the more general form of Eq. 9.8 is required. The most notable cases are gases at high pressure where the gas behaves less ideally and those cases where even small deviations from ideal gas behavior are important. Both of these exceptions are treated in this chapter.

With the simplifications shown previously, the velocity of propagation of acoustic plane waves becomes

$$c_0^2 = \omega^2/k^2 = (\partial P/\partial \rho)_T + (M P_0/\rho_o^2 C_v)(\partial P/\partial T)_\rho \quad (9.9)$$

where a distinction is now made between P , the local hydrostatic pressure, and P_o , the ambient pressure in the absence of the acoustic disturbance. The same distinction is made for the densities ρ and ρ_o . By making a number of thermodynamic transformations, it is possible to show that to terms in first order, Eq. 9.9 is indeed equivalent to the general expression for the square of the sound velocity in a nondissipative medium, namely, $c_0^2 = (\partial p/\partial \rho)_s$. In the particular case of an ideal gas,

$$(\partial P/\partial \rho)_T = P_o/\rho_o \text{ and } (\partial P/\partial T)_\rho = P_o/T = \rho_o R/M \quad (9.10)$$

so that

$$c_0^2 = (P_o/\rho_o)(1 + R/C_v) = \gamma(P_o/\rho_o) = \gamma RT/M \quad (9.11)$$

In terms of the isothermal bulk modulus, B_T , the sound velocity is

$$c_o^2 = \gamma B_T/\rho_o \quad (9.12)$$

The isothermal bulk modulus is the quantity that would be measured in a static experiment and serves as a basis for comparing static and dynamic results.

At this point it is useful to examine some of the approximations that have been made to arrive at Eqs. 9.11 and 9.12. The first assumption made was that the acoustic wavelength is much greater than the mean free path. Relaxation of that assumption will be made in the section on rarified gases.

The second assumption was that the gas is nonviscous, actually, that there are no time-dependent components of the elastic constants. Several physical processes violate this assumption. Polyatomic gases do have a measurable bulk viscosity. In addition, energy is lost due to thermal conduction and diffusion. For polyatomic molecules, relaxation processes associated with relaxation of rotational and vibrational degrees of freedom can introduce a significant source of absorption. This additional absorption may be introduced through the bulk viscosity η' , but that approach is not taken here. Since absorption and velocity dispersion are related through a Kramers-Kronig relation [5], the velocity is also affected by these processes. The frequency-dependent specific heat gives rise to a frequency dependence in the thermal conduction. And, since thermal conduction and viscosity are related, including transport into the equations of motion could become complicated. To simplify the mathematics, each of the contributions to the time-dependent elastic properties of gases is treated separately in the following sections. The variation of the transport properties with frequency is a second-order effect that can be assumed to be small if the absorption due to those terms is small compared with the speed of sound.

In the derivation of Eqs. 9.11 and 9.12, it was assumed that the gas obeys the ideal gas law. This is true for monatomic gases at low pressures, but real gases exhibit deviations from ideal behavior that affect the measured speed of sound. Nonideal gas contributions to the speed of sound will be treated in the next section. The additional approximation that has been made is that the gas behaves linearly. Extreme pressures will be treated in separate chapters. But the result of dynamically changing the stress by large amounts leads to interested nonlinear elastic behavior not unlike that observed for solids. Some comments will be offered in a later section.

9.3 Real Gas Corrections

Real gas corrections to the speed of sound can be deduced by introducing a modified equation of state. The virial equation of state in the form

$$PV = RT(1 + B(T)/V + C(T)/V^2 + \dots) \quad (9.13)$$

can be used as a correction to ideal gas law in most cases. The disadvantage of Eq. 9.13 is that connections to the underlying physics are obscure. The coefficients can be computed from a knowledge of the interaction potential between molecules [6]. Much of the physics can be recovered by writing the equation of state in the form

$$(P + a/V^2)(V - b) = RT \quad (9.14)$$

In Eq. 9.14, b represents the volume occupied by individual molecules, volume that is not available to other molecules. The term “ a ” accounts for attractive forces between molecules.

Bhatia [7] expresses the correction to the equation of state in the form of Eq. 9.13 with $C(T) = 0$ and then writes for the specific heat at constant volume,

$$C_V = C_{Vi} - (R/V)(2B'T + B''T^2) \quad (9.15)$$

where $B' = dB/dT$, $B'' = dB'/dT$, and C_{Vi} is the constant volume specific heat in the ideal gas limit. Neglecting powers of B' and B'' higher than first order, Bhatia finds that for this nonideal gas, the sound velocity can be written as

$$c = c_i(1 - gP) \quad (9.16)$$

where

$$-g = B/RT + (\gamma_i - 1)B'/R + (\gamma_i - 1)^2TB''/(2R\gamma_i) \quad (9.17)$$

and $\gamma_i = (1 + R/C_{Vi})$.

Near standard temperature and pressure, this leads to a small correction in the speed of sound. Bhatia [7] gives values of g for CH_4 and CCl_4 as 0.000424 and 0.04422, respectively. The measured values of c at atmospheric pressure are [8] about 420 m/s (25 °C) and 145 m/s (97 °C). This suggests a nonideal gas correction of 1 part in a million and 300 parts per million, respectively. The best measurements could be expected to yield an accuracy of 10 parts in a million, so for CH_4 an ideal gas correction would be required only at very high pressures. For CCl_4 such a correction should be made even at atmospheric pressures. For gases where a large correction is required, measurements of the speed of sound can be used to experimentally determine B .

9.4 Contribution of Transport Processes on Speed of Sound

Up to this point, the contributions of viscous drag, thermal conduction, and, in the case of gas mixtures, diffusion have been ignored. It is most simple to visualize the contributions of these effects to absorption. Since that absorption and velocity dispersion are related through a Kramers-Kronig relation, we could solve for absorption then transform to get velocity. Relating velocity dispersion to elastic moduli is then straightforward. In practice it is easier to solve for a complex propagation constant and get the velocity directly.

Using the general form of the stress tensor, Eq. 9.1, the equation of motion, Eq. 9.4, becomes the Stokes-Navier equation. For the one-dimensional case,

$$\partial/\partial t(\rho\partial u/\partial t) = -\partial P/\partial x + (\eta' + 4\eta/3)\partial^2/\partial x^2(\partial u/\partial t) \quad (9.18)$$

where η is the coefficient of shear viscosity. The quantity η' is known as the bulk viscosity and corresponds to the viscous drag that would be experienced in a pure volume dilatation, in which no shearing motions can occur.

The nature and value of η' forms one of the most interesting problems in the historical development of ultrasonic wave propagation. It was assumed by Stokes that η' was identically zero, and, to a large extent, this assumption marks the difference between classical and modern theories of ultrasonic absorption and dispersion. The bulk viscosity can be used to account for dispersion and absorption due to relaxation of internal molecular modes. This chapter calculates the effects directly. We set $\eta' = 0$.

A question often raised at this point is why the shear viscosity should enter into the description of the motion of a plane wave of large extent, since no shearing motions are immediately obvious. The answer to this question lies in the fact that one cannot restrict all the motion to one direction without doing it as a combination of deformations in all the coordinate directions. The analysis has been given by Kittel [9] for the elastic case.

Consider a unit cube of material [Fig. 9.1(a)] that is to be stretched in the x direction to a strain ε_{11} , with no net change in either the y or z directions. This will be done in three steps:

1. Uniform strain by an amount $\varepsilon_{11}/3$ [Fig. 9.1(b)].
2. Extension in the x direction to a total strain $2\varepsilon_{11}/3$, with simultaneous compression to zero in the y direction, preserving a constant volume in the process [Fig. 9.1(c)].
3. Extension in the x direction to a total ε_{11} and simultaneous compression in the z direction to zero, again preserving a constant volume [Fig. 9.1(d)].

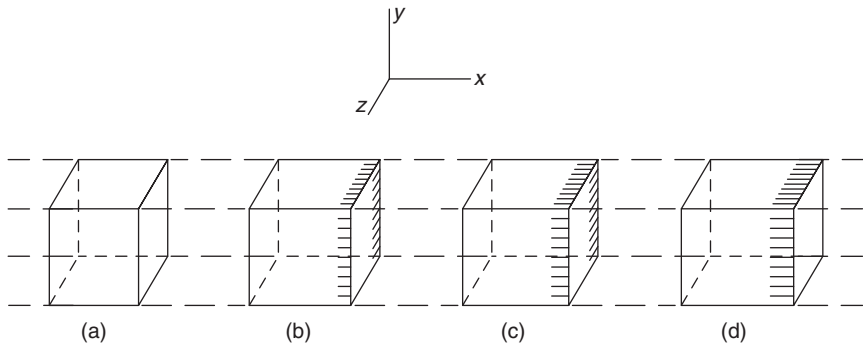


FIG. 9.1. Steps showing that a longitudinal dilation involves both compression and shear moduli. See [4] for description.

In the first step, the stresses are uniform and given by

$$\sigma_{11} = B \frac{\Delta V}{V} = \frac{B}{3}(\varepsilon_{11} + \varepsilon_{22} + \varepsilon_{33}) = B\varepsilon_{11} \quad (9.19)$$

where B is the bulk modulus, since $\varepsilon_{11} + \varepsilon_{22} + \varepsilon_{33}$ in the present case. In the second step, we have a process that can be described as a shear of angle $2\varepsilon_{11}/3$, so that the stress in the x direction will be $\mu \cdot 2\varepsilon_{11}/3$, where μ is the shear modulus. The situation in the third step is identical to that in the second except that y is replaced by z . Hence, the total stress in the x direction will be equal to $(B + \frac{4}{3}\mu)$. To proceed to a discussion of the effect of the shear viscosity on the propagation of sound, we replace Eq. 9.4 by Eq. 9.18 with $\eta' = 0$, and make the linear approximation, thus obtaining

$$\partial v / \partial t = -\rho_0^{-1} \partial P / \partial x + \frac{4}{3}(\eta / \rho_0) \partial^2 v / \partial x^2 \quad (9.20)$$

or, for harmonic waves of frequency ω ,

$$(\omega - \frac{4}{3}i(\eta / \rho_0)k^2)v - (k / \rho_0)P = 0 \quad (9.21)$$

where v is $\partial u / \partial t$. This leads to the result

$$k^2 / \omega^2 = [c_0^2 + i\frac{4}{3}(\eta / \rho_0)\omega]^{-1} \quad (9.22)$$

The presence of the imaginary term on the right side of Eq. 9.22 makes k complex. Setting $k = k_r - i\alpha$, α is the amplitude absorption coefficient while k_r is the real wave number, equal to ω divided by the phase velocity c .

The substitution of $k_r - i\alpha$ in Eq. 9.22 leads to the equations

$$k_r^2 - \alpha^2 = \frac{\omega^2 c_0^2}{c_0^4 + (16/9)(\eta^2 / \rho_0^2)\omega^2} \quad (9.23)$$

$$2k_r\alpha = \frac{(4/3)(\eta / \rho_0)\omega^3}{c_0^4 + (16/9)(\eta^2 / \rho_0^2)\omega^2} \quad (9.24)$$

In virtually all cases, $k_r^2 \gg \alpha^2$ (and hence $(16/9)(\eta^2 \omega^2 / \rho_0^2) \ll c_0^4$) so that, to an excellent approximation

$$\begin{aligned} k_r &= \omega / c_0 \\ k_r\alpha &= \frac{2}{3}(\eta \omega^3 / \rho_0 c_0^4) \text{ or } \alpha = \frac{2}{3}(\eta \omega^2 / \rho_0 c_0^3) \end{aligned} \quad (9.25)$$

In oxygen, at 20° and at atmospheric pressure, α is $1.68 \times 10^{-13} \nu^2$ in cgs units so $\alpha / k_r = 0.88 \times 10^{-8} \nu$ and the approximation $k_r^2 \gg \alpha^2$ is valid to frequencies on the order of 10^8 Hz at 1 atm of pressure.

Viscosity results from the transport of momentum from one element of the gas to another. This collisional transport of momentum is always accompanied by a transport of energy. Phenomenologically, this energy transport can be described by heat flow. To include heat conduction into the wave propagation calculations, a term can be added to the energy conservation equation (Eq. 9.6), which represents the heat removed per second per mole ($\partial Q'/\partial t$). From the Fourier's law for heat conduction,

$$\partial Q/\partial t = (M\kappa/\rho_0)\partial^2\theta/\partial x^2 \quad (9.26)$$

where κ is thermal conductivity and θ is the temperature. Repeating the derivation in the usual way [4],

$$\frac{k^2}{\omega^2} = \frac{1}{c_0^2} \frac{1 - i\zeta}{1 - i(\zeta/c_0^2)(\partial p/\partial \rho)_T} \quad (9.27)$$

where

$$\zeta = \kappa k^2 / \rho_0 \omega c_v \quad (9.28)$$

As written, Eq. 9.27 is not an explicit solution for k^2 , since k is also contained in ζ . The quantity ζ is small, however, and it is customary to replace k in ζ by ω/c_0 so that $\zeta = k\omega/\rho_0 c_0^2 c_v$. Setting $k = k_r - i\alpha$, for the case of thermal conduction (after some algebra),

$$\begin{aligned} k_r^2 &= \omega^2/c_0^2 \\ 2k_r\alpha &= \frac{\omega^2}{c_0^2} \left[1 - \left(\frac{\partial p}{\partial \rho} \right)_T \frac{1}{c_0^2} \right] \\ \alpha &= \frac{\omega^2 \kappa}{2c_v \rho_0 c_0^3} \left[1 - \frac{1}{c_0^2} \left(\frac{\partial p}{\partial \rho} \right)_T \right] \end{aligned} \quad (9.29)$$

For an ideal gas (in the sense that $B = 0$), $(1/c_0^2)(\partial P/\partial \rho)_T = 1/\gamma$, and

$$\alpha = \frac{\omega^2 \kappa}{2c_p \rho_0 c_0^3} (\gamma - 1) \quad (9.30)$$

where $c_p = \gamma c_v$ is the heat capacity per unit mass (at constant pressure).

9.5 Changes in Elastic Properties Due to Relaxation Processes

Studies of acoustic absorption and dispersion have proven to be an effective tool in developing a physical description of molecular interactions in gases.

Experimentally, absorption or velocity dispersion is measured as a function of frequency/pressure. The measured quantities are computed using the theory outlined below that requires some insight into the particular physical processes that give rise to the absorption or dispersion (e.g., vibrational relaxation). Computed values are compared to experiment, and the assumed physical process or interaction parameters are varied until agreement is achieved. The theoretical model that gives rise to predicted absorption and dispersion, which agree with experiment, is assumed to correctly represent the interactions taking place at the microscopic level.

Some of the microscopic processes studied acoustically can also be studied using optical techniques. In those cases, the physical model and numerical values for the parameters describing the interactions are found to be consistent provided a proper theoretical link between microscopic model and measured quantities is used.

For the purpose of developing an understanding of relaxation processes, first consider a gas made up of diatomic molecules. The individual molecules are free to move translationally in three directions, rotate about two perpendicular axes (actually three but the third has zero moment of inertia so has no energy), and vibrate along the bond joining the atoms. Some energy is associated with each of these allowed motions.

Translational motion can typically be considered nonquantized. Any energy is allowed. As the molecules translate, they collide, exchanging energy with their collision partners. At atmospheric pressure, assuming a hard sphere molecular model, a single molecule suffers about 10^{11} collisions/second. A single collision is typically sufficient to transfer translational energy from one molecule to another. However, a certain period of time is required to randomize energy associated with excess velocity in a particular direction. This time is often referred to as the translational relaxation time. Kohler following Maxwell [11] associates viscosity with this relaxation time, writing $\tau_{tr} = \eta/P = 1.25\tau_c$, where P is gas pressure and τ_c is the time between collisions. As pressure is lowered, the rate of collisions decreases proportionately. At 1 torr (1/760 atm), the translational relaxation time is about 10^{-8} sec; at 1 millitorr, 10^{-6} sec. These time regimes can be effectively studied using ultrasonics.

Unlike translational motion, rotation and vibration are noticeably quantized. During a collision, a change in rotational or vibrational state can only occur if the change in energy of another state is sufficient to allow at least a one-quantum jump. For rotational energy transfer, the spacing between energy levels is given by $2(J+1)B$, where J is the rotational quantum number, $B = \hbar^2/2I$ and I is the effective moment of inertia. If one assumes J is the most probable value (from a Boltzmann distribution), the value of $2(J+1)B$ for a typical molecule (say N_2) in units of kT is about 1 K. This means that

in a gas above 1 K, essentially all collisions will have sufficient translational energy to cause multiple changes in J . As a result, rotation rapidly equilibrates with translation.

An exception is hydrogen, which has much larger rotational energy level spacing due to the small moment of inertia. On average, as many as 350 collisions [12] may be necessary to transfer a quantum of rotational energy in H_2 . At a pressure of 1 atm, this gives a relaxation time of about 2×10^{-8} sec. It should be noted that a given collision does or does not transfer a quantum of energy. The 350-collision average means that only 1 collision in 350 has the proper geometry and energy to cause a transfer of one quantum of rotational energy. The number of collisions necessary, on average, to transfer one quantum of energy is referred to as the collision number Z . When rotational energy is involved, the subscript "rot" is typically added (Z_{rot}). The inverse of this dimensionless quantity is the probability of transferring a quantum in a collision (P_{rot}). Since rotational energy level spacings are unequal, a $1 \rightarrow 2$ transition should be more probable than a $2 \rightarrow 3$ transition. These events are distinguished by using the symbols P_{rot}^{1-2} or P_{rot}^{2-3} .

Generally speaking, the probability for transferring a quantum of energy in a collision decreases rapidly with the size of the quantum transferred. Since vibrational levels are much more widely spaced than rotational energy levels, vibrational relaxation times are much longer than rotational. Vibrational levels in a single vibrational mode are approximately equally spaced. This means that energy can be exchanged between levels (i.e., the vibrational quantum number goes up in one molecule and down in the other) with very little energy exchanged between vibration and translation. The result is that such $v-v$ exchanges take place very rapidly. In this case, the vibrational relaxation time is controlled by the time it takes energy to transfer between translation and the lowest lying vibrational level. Since this energy level varies greatly for different molecules, so do the probabilities of vibrational energy transfer during a collision. During $N_2 - N_2$ collisions, Z_{10} is near 1.5×10^{11} , so the relaxation time is near 1.5 sec [13] (Z_{10} is the number of collisions needed to transfer energy from the lowest vibrational level to translation). Large molecules have vibrational energy levels that are very close together. A molecule such as C_2H_6 requires only 100 collisions to transfer a quantum of vibrational energy from the first vibrational level into translation [12]. This very wide range of relaxation times presents interesting experimental challenges.

To this point, there has been no attempt to rigorously define relaxation times in terms of energy transfer probabilities. In fact, such a relation is possible in a simple form for only the few cases where gases exhibit a single relaxation time. Nevertheless, the simple case provides valuable insight into the behavior of more complex systems and deserves a detailed description.

Consider the case where the population of a vibrational state is excited to an energy E_v , which is greater than the energy $E_v(T_{tr})$, which it would have in Boltzmann equilibrium with translation. In this case, the excess vibrational energy will equilibrate with translation according to a standard relaxation equation,

$$-\frac{dE_v}{dt} = \frac{1}{\tau}[E_v - E_v(T_{tr})] \quad (9.31)$$

The return to equilibrium occurs due to energy transfer during individual collisions.

The rate of energy transfer k_{10} is defined as the rate at which molecules go from the first excited state to the ground state due to collisions at a pressure of 1 atm. This rate is just the collision frequency, M , times the probability of energy transfer, $P^{1 \rightarrow 0}$, times the mole fraction of molecules in the first excited state, x_1 . During some collisions, the reverse process will occur, that is, some molecules in the ground state will become excited at a rate k_{01} . In equilibrium, equal numbers of molecules go in both directions, so

$$k_{10}x_1 - k_{01}x_0 = 0 \quad (9.32)$$

As explained previously, energy is quickly transferred from the first excited level of the vibrational mode to higher levels of the mode by v - v exchanges. Assuming quantum mechanical laws hold for probabilities of energy exchanges between vibrational levels of a harmonic oscillator, Landau and Teller [15] showed

$$-\frac{dE_v}{dt} = k_{10}(1 - e^{-h\nu/kT})[E_v - E_v(T_{tr})] \quad (9.33)$$

where ν is the vibrational frequency of the relaxing mode. By comparison with Eq. 9.31

$$\tau = \frac{1}{k_{10}(1 - e^{-h\nu/kT})} \quad (9.34)$$

The relationship between the relaxation time and ultrasonic absorption and dispersion may be understood by noting that the relaxation process makes the specific heat of the gas time (or frequency) dependent. This time dependence can be obtained from the energy relaxation equation. Consider, as previously, that the specific heat of a simple gas can be divided into translational, rotational, and vibrational contributions. For now, assume that the translational and rotational energies both equilibrate rapidly enough to follow any acoustically induced temperature variations. In this case, the effective specific heat can be written as

$$(C_v)_{\text{eff}} = C_v^{\infty} + C' \frac{dT'}{dT_{tr}} \quad (9.35)$$

where C_v^∞ is the sum of rotational and translational specific heats, C' is the relaxing specific heat, and T' is the instantaneous temperature of the relaxing mode (in this case, vibration). From the energy relaxation equation (Eq. 9.33), for small periodic variations in T_{lr} and T_v about their equilibrium values,

$$(C_v)_{\text{eff}} = C_v^\infty + \frac{C'}{1 + i\omega\tau} \quad (9.36)$$

where ω is the angular frequency of the acoustic wave.

The acoustic propagation constant can be written in the form

$$\frac{k^2}{\omega^2} = \left(\frac{1}{c} - \frac{i\alpha}{\omega} \right)^2 = \frac{\rho_0 \kappa_T}{\gamma_{\text{eff}}} \quad (9.37)$$

where c is the acoustic velocity, α is the attenuation, ρ_0 is the equilibrium density, κ_T is the compressibility, and

$$\gamma_{\text{eff}} = [(C_v)_{\text{eff}} + R]/(C_v)_{\text{eff}} \quad (9.38)$$

with R the gas constant. For this simple single relaxation, assuming $\alpha/\omega \gg 1/c$ [16],

$$\alpha\lambda = \pi \left(\frac{c}{c_0} \right)^2 \varepsilon \frac{\omega\tau_s}{1 + (\omega\tau_s)^2} \quad (9.39)$$

and

$$\left(\frac{c_0}{c} \right)^2 = 1 - \frac{\varepsilon\omega^2\tau_s^2}{1 + (\omega^2\tau_s^2)} \quad (9.40)$$

where

$$\varepsilon = \left(\frac{c_\infty^2 - c_0^2}{c_\infty^2} \right) \quad (9.41)$$

and where λ is the wavelength, c_0 is the speed of sound for $\omega\tau_s \ll 1$, and c_∞ is the speed of sound at frequencies much greater than the relaxation frequency. The adiabatic relaxation time τ_s , is related to the isothermal relaxation time τ used earlier by

$$\tau_s = (C_v + R)/(C_v^\infty + R)\tau \quad (9.42)$$

The relaxation frequency, f_r , defined as the frequency at which the maximum absorption per wavelength occurs, is related to τ_s by

$$f_r = 1/2\pi\tau_r = c_\infty/c_0(1/2\pi\tau_s) \quad (9.43)$$

In the case of polyatomic gases or mixtures of relaxing diatomic gases, the different relaxing modes can be coupled together by $v-v$ exchanges.

Such complex or multiple relaxation processes exhibit the general behavior given by Eqs. 9.39 and 9.40, but the magnitude of the absorption and dispersion and the relaxation frequencies can take on new meaning. In the case of multiple relaxing internal energy modes, Eqs. 9.39 and 9.40 take on the form [18]

$$\left(\frac{c}{c^\infty}\right)^2 = 1 + \sum_j \frac{\delta_j k_s / k_s^\infty}{1 + (\omega \tau_{s,j})^2} \quad (9.44)$$

$$\alpha \lambda \left(\frac{c}{c^\infty}\right)^2 = -\pi \sum_j \frac{\delta_j k_s / k_s^\infty}{1 + (\omega \tau_{s,j})^2} \omega \tau_{s,j} \quad (9.45)$$

where $\delta_j k_s / k_s^\infty$ is a relaxing adiabatic compressibility (negative) and j indicates that there might be more than one relaxation process. In these complex

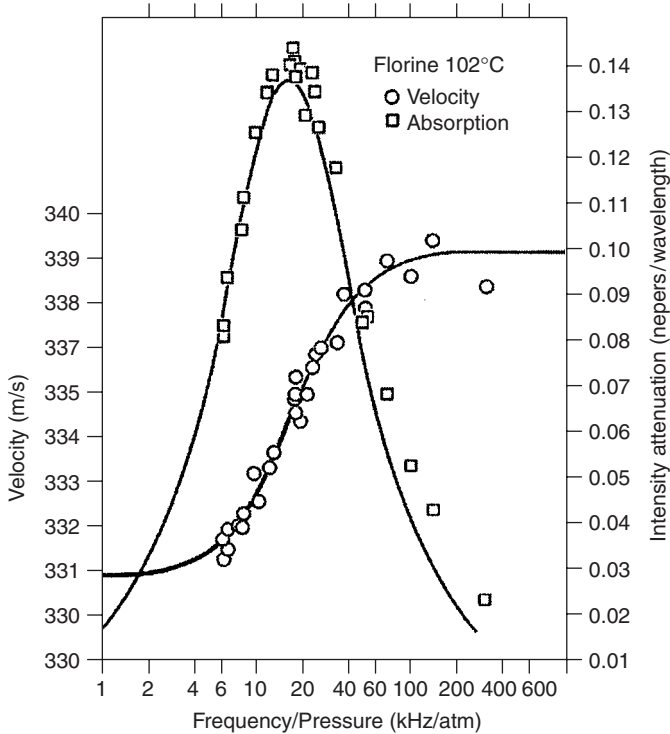


FIG. 9.2. Typical curves for absorption per wavelength and velocity dispersion to a single relaxation process. The example here is F_2 at 102°C. The figure compares curves representing the previous theory with measured values [17].

cases, $\tau_{s,j}$ can no longer be related to a single energy transfer reaction and $\delta_j k_s / k_s^\infty$ can no longer be related to relaxing energy of a specific mode. Instead, the various modes and reaction pathways are coupled. The sums in Eqs. 9.44 and 9.45 are over eigenvalues of the energy transfer matrix, which simultaneously accounts for all reactions. Eqs. 9.44 and 9.45 is used to calculate the sound absorption in moist air as a function of frequency and temperature in a later section. The American National Standard for sound absorption in the atmosphere is now based on these equations.

Not only can Eqs. 9.44 and 9.45 be used to calculate sound absorption and velocity, but the reverse process is also possible, i.e., the transition rates can be extracted from measured values of absorption and velocity. However, the number of possible relaxation paths multiplies rapidly with an increase in the number of relaxing modes, and the identification of specific rates becomes a tedious process and usually involves some assumptions. It has been done for only a few special cases.

A further complication arises from chemical reactions. For a reversible chemical reaction with heat of reaction ΔH , ΔH enters into the relaxation equations in a manner similar to ΔE for vibrational relaxation. A major difference is that chemical reactions allow the possibility that the number density of molecules can change. Such changes bring about additional relaxation absorption and dispersion.

9.6 Measurements at Moderate Pressures

Before modern techniques were available for measuring transients, most ultrasonic absorption and velocity measurements were made with ultrasonic interferometers [19–22]. This instrument continues to be used with refined precision and modern methods of control and measurement [23]. Both velocity and absorption can be measured with the interferometer. A column of gas or liquid of varying length forms the load on a quartz crystal vibrating at its resonant frequency. The loading effect of the gas or liquid column increases whenever the length of the gas column is a whole multiple of a half wavelength of the sound. This loading effect is reflected in the driving circuit of the crystal. The separation between the peak values as the two path lengths changes determines the sound wavelength, and the variation of the magnitude of the peaks with length of the column allows the determination of the absorption coefficient.

Another continuous-wave method for measuring velocity and absorption in gases uses a source and receiver whose separation can be varied mounted in a tube so as to avoid standing waves [24, 25]: see Fig. 9.3. This method has been used to make measurements at audible frequencies and reduced pressures and, therefore, is capable of measurements over the f/p range where many

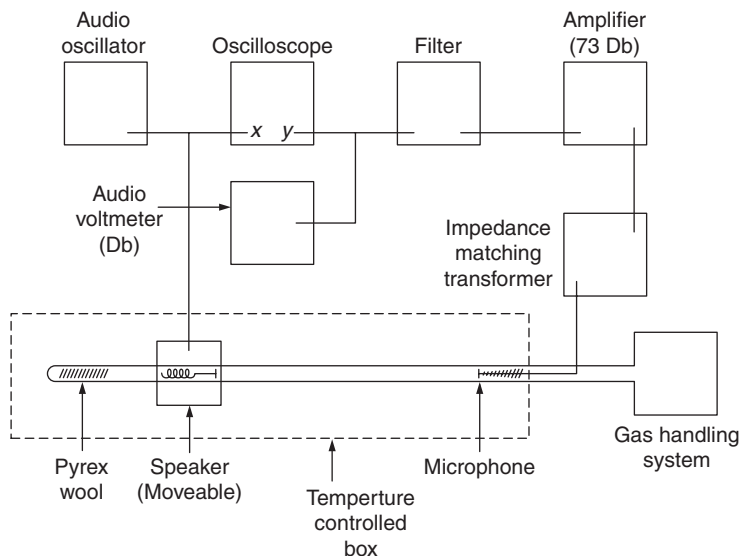


FIG. 9.3. Schematic diagram of the apparatus for measuring the attenuation of sound [24, 25].

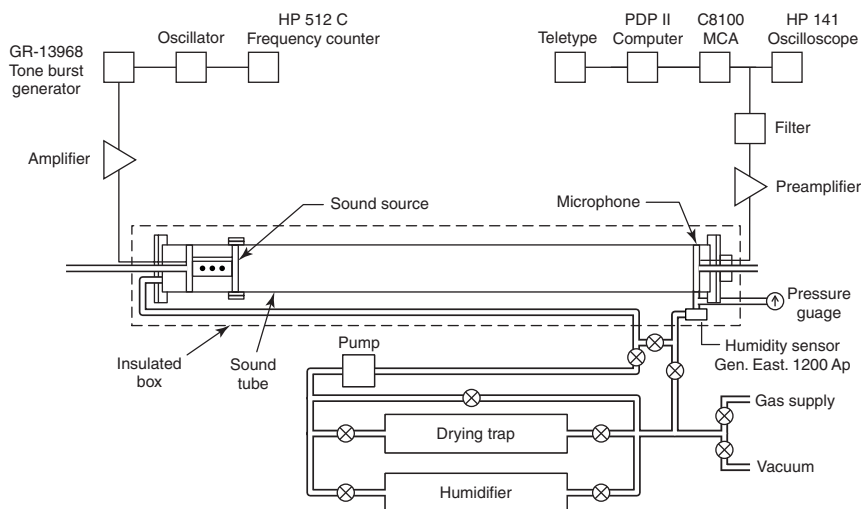


FIG. 9.4. Diagram of experimental system for measuring sound absorption, using pulse-echo.

of the interesting relaxation processes occur in gases and gas mixtures. The absorption is determined from the decrease in sound amplitude at the receiver as the source-receiver separation is increased. The wavelength of the sound is equal to the distance between points of equal phase in the received sound. This change in phase is easily observed by comparing the receiver and source signals.

With the development of the capability for generating and measuring tone bursts, it has been possible to use the pulse-echo technique [26, 27]. In this case, the sound velocity is determined from time of flight and the absorption from the variation of the tone burst amplitude with source and receiver separation.

At lower frequency-to-pressure ratios, resonant tubes are used [13]. The velocity is determined from the resonant frequency and the absorption from the width of the resonant peak.

When relaxation effects are studied, absorption measurements are designed to provide absorption as a function of frequency divided by pressure over a range of values, where the period of the sound wave is approximately equal to the relaxation time. When studying relaxation in molecular N_2 , this requires measurements of very small absorption (less than 1 dB/m) at f/p values as low as a fraction of a hertz per atmosphere. On the other hand, measurements of absorption in UF_6 involve very large attenuation (~ 100 dB/m) at f/p values as high as 10 MHz/atm [28].

To separate the effects due to vibrational relaxation, the measured absorption must be corrected for (1) viscous and thermal losses in the body of the gas, (2) viscous and thermal losses to the measuring chamber walls, (3) radiation or leakage losses from the chamber, (4) spreading losses, and (5) losses due to rotational relaxation.

These different effects are generally small enough to be additive. The quantity usually reported is the absorption coefficient, α , in terms of which the amplitude of the plane wave is written as

$$A = A_0 e^{-\alpha(x_2 - x_1)} \quad (9.46)$$

Plotting $\log A$ vs x gives α as the slope in nepers/m. The measured α is due to a combination of the losses listed previously. Careful design of the experimental apparatus is necessary if accurate corrections are to be made for wall and/or spreading losses.

A common geometry for sound absorption measurements is a cylindrical tube. This method generally avoids losses c and d (due to spreading and leakage) above and involves well-known corrections for a and b . In this case, the total absorption is given by

$$\alpha_{\text{tot}} = \alpha_{cl} + \alpha_{\text{rot}} + \alpha_{tu} + \alpha_v \quad (9.47)$$

where α_{cl} (classical absorption) is the absorption due to viscosity and thermal conductivity, α_{rot} is absorption due to relaxation processes not of interest to the study (rotational relaxation, for example). α_{tu} is the tube absorption, and α_v is the absorption due to the relaxation process of interest. The term α_{cl} can be computed from known or measured values of viscosity and thermal conductivity [29]; it is proportional to f^2 . The term α_{rot} generally is estimated based on other studies. At frequencies well below the rotational relaxation frequency it also is proportional to f^2 . The tube absorption, α_{tu} , depends upon the viscosity, thermal conductivity, and tube radius (r).

Only plane waves will be present in the tube if the sound frequency is below the cutoff frequency for the first nonplane mode, i.e., $f < 0.586 c/d$, where c is the sound speed and d is the tube diameter. Plane waves can be maintained for higher frequencies if the transducer generating the waves fills the tube and is carefully maintained perpendicular to the tube axis and if its surface vibrates as a piston [31]. Interferometers used for high-frequency measurements in liquids and gases will generally satisfy these conditions. As the wavelength becomes small compared with the tube diameter, wall losses become negligible.

In the previous discussion, relaxation absorption and dispersion of sound resulted when a finite time was required for the passage of the energy of translation into the vibrational energy of the gas molecules. Relaxation mechanisms can also be studied in special cases using the reverse processes. Laser light of a particular frequency is used to excite a vibrational mode. This excess vibrational energy then relaxes into translational energy generating an increase in translational temperature and pressure. If the laser light is chopped, a sound wave is generated. This phenomena is referred to as the “optoacoustic effect” and the device as a “spectrophone” [32]. The relaxation time can be determined from the phase relations between modulated laser light and the resulting sound pressure.

The primary attraction of optoacoustic measurements is the ability to excite a specific internal mode and observe how energy from the mode makes its way to translation. Experimentally, only a limited number of internal modes can be excited with available lasers, which limits the list of systems that can be studied.

9.7 Typical Results

For the purposes of this chapter, specific studies will be selected that illustrate the physics involved. Three cases will be treated. The first is the halogen family of diatomic molecules, specifically, F_2 , Cl_2 , Br_2 , and I_2 . This example illustrates the functional forms presented earlier for absorption due to relaxation processes, gives typical values for probability of energy transfer,

$P^{1 \rightarrow 0}$, and provides some indication of how $P^{1 \rightarrow 0}$ varies with temperature, molecular weight, and vibrational frequency. The second example is a more complex molecule, SO_2 , in mixtures with Ar and O_2 . This example illustrates the complexity of the relaxation process when different vibrational modes exchange energy.

Shields used an acoustic traveling wave tube similar to that developed by Angora [24] to measure acoustic absorption in F_2 , Cl_2 , Br_2 , and I_2 as a function of frequency, pressure, and temperature [17, 33]. Results for Cl_2 at five different temperatures are plotted in Figure 9.5. The absorption and velocity in F_2 at 102°C are shown in Figure 9.2. The curves drawn through the experimental points were calculated using the theory discussed previously.

Several features of these curves are interesting. First, when more than one point is plotted for the same value of f/p , it means that absorption was measured at two different pressures but at different frequencies so that the ratio was the same. The agreement between such measured values confirms that the classical and tube corrections were being made correctly and that the relaxation absorption varied as f/p . Second, note that the relaxation time decreases as temperature increases (the relaxation frequency increases). This means that although the density is lower for a given pressure, the probability of energy transfer increases more rapidly than the collision frequency decreases. Finally, note that the maximum absorption increases as the temperature increases. This is a result of increasing vibrational specific heat. The Plank-Einstein relation

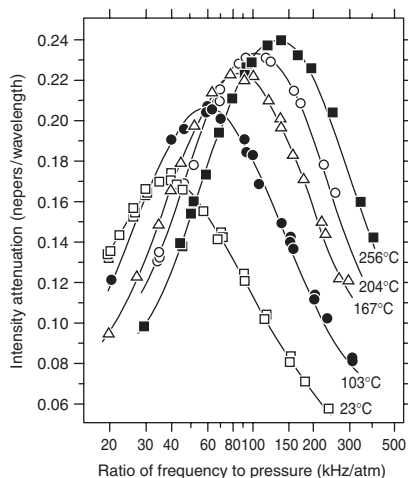


FIG. 9.5. Relaxation absorption coefficient per wavelength vs log (frequency/pressure) for chlorine. The solid curves are theoretical absorption with values of relaxation amplitude and frequency adjusted to give the best fit of the experimental points.

predicts that

$$C' = R(\theta/T)^2 [e^{\theta/T} / (e^{\theta/T} - 1)^2] \quad (9.48)$$

where C' is the vibrational specific heat, θ is the vibrational temperature, and T is the gas temperature.

Results of Shields' study are summarized in Figure 9.6, which shows the probability for deexciting the first excited vibrational level in a collision.

The log of this probability is plotted vs $T^{-1/3}$. This type of plot was suggested by an early theory by Landau and Teller [15]. They predicted an approximately linear relationship between $\log P^{1 \rightarrow 0}$ vs $T^{-1/3}$. From similar measurements on a great many other gases, one can expect the following trends for v-t transitions:

- (1) The log of the transition probability decreases roughly linearly with $T^{-1/3}$ for a particular molecular collision pair. The reasons for this dependence are complex but can be thought of in terms of the speed molecules are traveling when they collide. The more rapidly they are moving, the more energy they carry into the collision. As the temperature increases (move to the left in Figure 9.6), the average speed of each molecule increases; hence, there is a greater probability of energy transfer.
- (2) The transition probability is very sensitive to the amount of energy that must be transferred between vibration and translation in the transition, increasing rapidly as this energy decreases. This can be thought of the same as the temperature dependence. When two molecules collide with

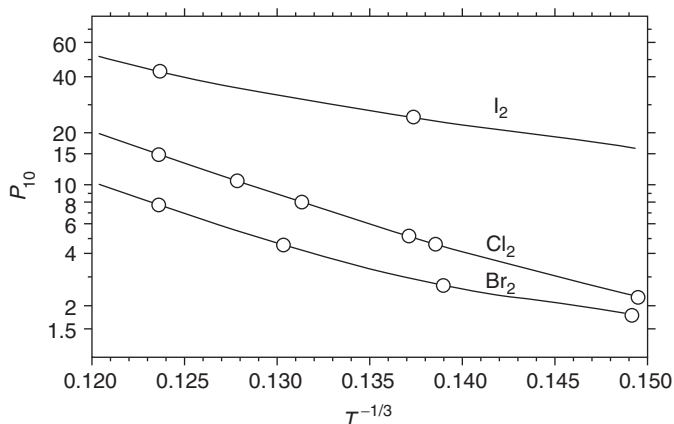


FIG. 9.6. Log of collision efficiency vs absolute temperature to the minus one-third power. The values of the ordinate should be multiplied by 10^{-5} for Cl_2 and by 10^{-4} for Br_2 and I_2 .

translational energy less than a quantum of vibration, the probability of a transition is classically zero.

- (3) The transition probability is very sensitive to the time involved in the molecular collisions increasing rapidly as this time decreases. This means that the transition probability increases with increasing temperature [see trend (1)] and with decreasing molecular mass. This effect is due to the requirement that momentum as well as energy be conserved in the collision.
- (4) For polyatomic molecules, bending vibrations are more easily excited than stretching vibrations (as one might expect from the geometry of the collision process). There are larger collision cross sections for excitation of a bending mode.
- (5) Water vapor and a few other molecules with low moments of inertia, and, therefore, high rotational velocities, are very efficient in shortening relaxation times when added to gases, even in small amounts. For such mixtures, the relaxation time is much less sensitive to temperature change and can even increase with temperature. This effect is attributed to the coupling between vibration and rotation in such collisions [34–38].
- (6) The probability of the transition is sensitive to the nature of the intermolecular potential. Figure 9.7 shows some simple potentials. These can give reasonable results for atom–diatom collisions and for molecules that have electron clouds that are reasonably spherical. For these cases, the probability of a transition depends on the depth of the potential and the steepness of the repulsive part of the potential.

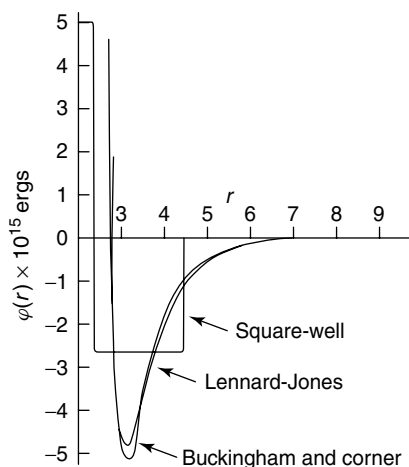


FIG. 9.7. Potential energy of interaction.

As an example of the use of sound absorption measurements to determine the relaxation scheme in a polyatomic gas mixture consider the case of SO_2/O_2 mixtures [39]. SO_2 has three vibrational modes. These can be classified as a bending mode, with a fundamental vibrational frequency of 518 cm^{-1} ; a symmetrical stretching mode, and an asymmetrical stretching mode, with frequencies of 1151 and 1361 cm^{-1} , respectively. O_2 has a vibrational frequency of 1580 cm^{-1} . SO_2 was one of the first gases in which the sound absorption vs frequency curve evidenced more than one relaxation time. Figure 9.8 shows measurements in three different SO_2/O_2 mixtures at 500°K . Twelve different transition rates were adjusted to make the theoretical curves simultaneously fit these data and the data for pure SO_2 , SO_2/Ar mixtures [40, 41], and pure O_2 [42].

As an illustration of the kind of information that can be obtained from such studies, the following conclusions from the SO_2/O_2 and SO_2/Ar measurements are listed:

- (1) The relaxation in SO_2 is primarily a series process. Translational energy flows into the bending mode and from there is shared with the symmetrical stretch through a two quantum for one exchange and from symmetric stretch to the asymmetrical stretch with a one for one exchange.

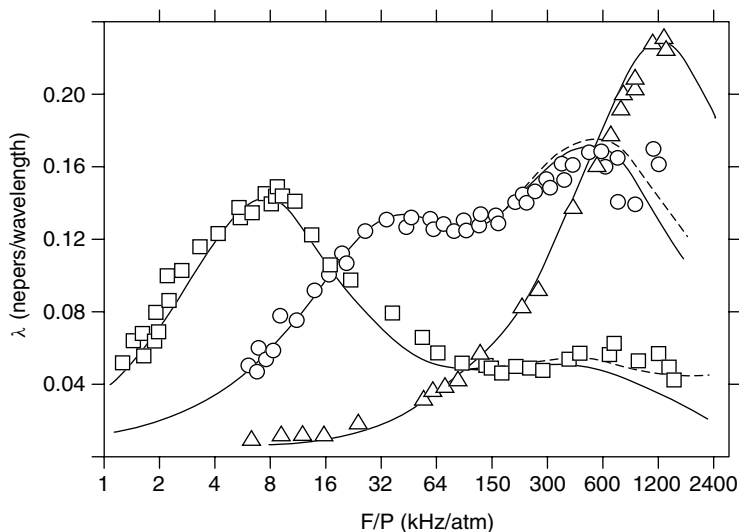


FIG. 9.8. Relaxation absorption in 75% $\text{SO}_2/25\%$ O_2 (Δ), 20% $\text{SO}_2/80\%$ O_2 (\circ), and 5% $\text{SO}_2/95\%$ O_2 (\square) at 500°K . The solid curve is the theoretical curve for the series relaxation process.

- (2) Argon is only about one tenth and O_2 about one fourth as effective as another SO_2 molecule in deexciting the bending vibration in SO_2 .
- (3) The first excited level of the O_2 vibration exchanges energy in vibration-to-vibration exchange primarily with the first excited level of the asymmetric stretch mode of SO_2 .
- (4) The transition rate for the SO_2 vibration to vibration transfer increases with temperature faster than the vibration-to-translation rates. This is a peculiar property of SO_2 and has been attributed to its dipole moment.

An excellent example of combining knowledge of microscopic property measurements to determine elastic properties of a gas can be seen in the treatment of the absorption and velocity of sound in air. Combining absorption due to viscosity and heat conduction,

$$\alpha = [\omega^2 / (2\gamma P c)] [4\mu/3 + (\gamma - 1)\kappa / (\gamma c_v)] \quad (9.49)$$

in $Np\ m^{-1}$. The Eucken expression [43]

$$\kappa = (15R\mu/4)[4c_v/(15R) + 3/5] \quad (9.50)$$

in $J\ (kg\ mol)^{-1}\ K^{-1}\ kg\ m^{-1}\ sec^{-1}$, can be used to relate κ and μ for real air. For dry air over the temperature range 225–370 °K, the ratio c_v/R has the value $5/2 \pm 0.4\%$. For moist air, over the same temperature range, the c_v/R ratio becomes increasingly larger than the ideal gas value as the concentration of water vapor increases, but only by a small amount. For example, at a temperature of 370 °K and 100% relative humidity, $c_v/R = 2.565$ or just 2.6% more than the ideal gas value [44]. Therefore, if we assume $c_v/R = 5/2$, the computed value for κ cannot be more than 1% different from the value calculated using the correct value of c_v/R . This assumption yields $\kappa = 19R\mu/4$. For an ideal gas, $c_p = c_v + R$. Thus, with $c_v/R = 5/2$, the ratio $c_p/R = 7/2$. Substituting $\kappa = 19R\mu/4$ into Eq. 9.49 and using $(\gamma - 1)R/(\gamma c_v) = 4/35$ with $\gamma = c_p/c_v = 1.4$ gives

$$\alpha = [2\pi^2 f^2 / (\gamma P c)] (1.88\mu) \quad (9.51)$$

in $Np\ m^{-1}$ where f is now used to denote frequency in Hz.

For mixtures of gases, there is, in general, an additional term due to internal diffusion. It has been shown, however, that for air, this term is small and will be ignored here.

The classical absorption given by Eq. 9.51 changes with temperature due to changes in the speed of sound c , and the coefficient of viscosity μ . For an ideal gas (and air at STP is close to ideal), c varies as $T^{1/2}$. The coefficient of viscosity for dry air can be written in the form of Sutherland's

equation [43]

$$\mu = \frac{\beta T^{1/2}}{1 + (S/T)} \quad (9.52)$$

in $\text{kg m}^{-1} \text{sec}^{-1}$, where B and S are empirical parameters. For air, the parameters $B = 1.458 \times 10^{-6} \text{ kg m}^{-1} \text{sec}^{-1} \text{K}^{-1/2}$ and $S = 110.4 \text{ K}$ are standard values [45] that provide a satisfactory fit to experimental data and permit reasonably accurate calculations of μ for the range of temperatures between 273.15 and 313.15 K (0° and 40°C).

Using the standard values of γ , R , and M for air from the Society of Automotive Engineers [46] and defining a reference temperature T_0 to be 293.15 K gives

$$c = 343.23(T/T_0)^{1/2} \quad (9.53)$$

in m sec^{-1} , and

$$\mu = 7.318 \times 10^{-3} \frac{(T/T_0)^{3/2}}{T + 110.4} \quad (9.54)$$

in $\text{kg m}^{-1} \text{sec}^{-1}$, so Eq. 9.51 becomes

$$\alpha_{cl} = 5.578 \times 10^{-9} \frac{T/T_0}{T + 110.4} f^2 / (P/P_0) \quad (9.55)$$

in Np m^{-1} , where P_0 is the reference pressure of $1.01325 \times 10^5 \text{ N m}^{-2}$ or 1 atm, the pressure P is in N m^{-2} , and the temperature T is in Kelvin.

It was shown earlier that for a single relaxing degree of freedom

$$\alpha = -\frac{\delta K_s / K_s^\infty}{2c} \frac{\omega^2 \tau'_{vs}}{1 + (\omega \tau'_{vs})^2} \quad (9.56)$$

in Np m^{-1} , where K_s^∞ is the instantaneous adiabatic compressibility (in units of N m^{-2}) and equal to $P c_p^\infty / c_v^\infty$; δK_s is the relaxing compressibility; and τ'_{vs} is the relaxation time at the partial pressure of the reactants in the mixture, at constant volume and under adiabatic conditions. For a single relaxing degree of freedom, $(\delta K_s / K_s^\infty) = -R c' / [c_p^\infty (c_v^\infty + c')]$, where c' is the specific heat of the relaxing mode in $J (\text{kg mol})^{-1} \text{K}^{-1}$; c_p^∞ is the specific heat at constant pressure at frequencies $\gg 1/(2\pi \tau'_{vs})$; and c_v^∞ is the specific heat at constant volume under the same conditions. For frequencies $< 1/(2\pi \tau'_{vs})$, the specific heat at constant volume c_v equals $c_v^\infty + c'$.

Oxygen, nitrogen, and carbon dioxide all have rotational degrees of freedom and hence a rotational specific heat c' for rotational relaxation equal to the universal gas constant R . Water vapor has three rotational degrees of freedom and a rotational specific heat of $3R/2$; however, since the mole fraction of

water vapor in air is at most 8% in the temperature range 273–313 °K [44], the rotational specific heat of air can be closely approximated by R .

Each rotational energy level relaxes with a different relaxation time, and the resultant absorption as a function of frequency can be quite complex. However, the principal constituents of air (oxygen, nitrogen, and water vapor) have rotational energy levels that are closer together than the average thermal energy. As a result, the rotational relaxation process for air behaves as though the rotational energy levels were continuous and can be described by a single relaxation time for isometric and adiabatic conditions $\tau'_{vs,rot}$. At all frequencies less than 10 MHz, $\tau'_{vs,rot}$ is $\ll \omega^{-1}$. For this case, and the value of $\delta K_s/K_s^\infty$ discussed previously, with $c_v = c_v^\infty + c' = c_v^\infty + R$ and $R/c_v = \gamma - 1$, Eq. 9.56 becomes

$$\alpha_{rot} = \{[\pi R(\gamma - 1)]/(cc_p^\infty)\}(f^2/f_{r,rot}) \quad (9.57)$$

in Np m^{-1} , where

$$f_{r,rot} = 1/(2\pi \tau'_{vs,rot}) \quad (9.58)$$

in Hertz is the rotational relaxation frequency.

Now consider again Eq. 9.56. Write

$$\alpha = f^2 \left(\frac{c}{c_o^2} \right) \left(\frac{c_\infty^2 - c_o^2}{c_\infty^2} \right) \frac{2\pi^2 \tau_{ps}}{1 + \omega^2 \tau_{ps}^2} \quad (9.59)$$

where c_o is the low frequency limit of sound speed. Experimentally, one finds that τ for rotational relaxation is very small so that below 10 MHz, $\omega^2 \tau_{ps}^2 \approx 0$. Then

$$\alpha = \text{const} \cdot f^2 \cdot \tau_{ps} \quad (9.60)$$

If we write $\tau_{ps} = \text{const} \cdot Z_{rot}/P$, where Z_{rot} is the rotational collision number, we find that

$$\alpha_{rot} = [2\pi^2 f^2/(\gamma P c)] \mu [\gamma(\gamma - 1)R/(1.25c_p^o)] Z_{rot} \quad (9.61)$$

in Np m^{-1} . Again, assuming that $\gamma = 1.4$ and $c_p^o/R = 7/2$, the term in brackets becomes 0.128, a value that is independent of temperature since the specific heat of rotation does not change with temperature. Comparing Eqs. 9.51 and 9.61, we can now write

$$\alpha_{rot}/\alpha_{cl} = 0.128 Z_{rot}/1.88 = 0.0681 Z_{rot} \quad (9.62)$$

For dry air, the rotational collision number Z_{rot} has been measured near room temperature by Greenspan [47] and at higher temperatures by Bass and

Keeton [48]. A summary of these experimental results can be written in the form

$$Z_{\text{rot}} = 61.1 \exp(-16.8T^{1/3}) \quad (9.63)$$

over the temperature range 293–690 °K.

Acknowledging the presence of water vapor but ignoring the relaxation of the small water-vapor rotational specific heat, the rotational collision number can be written as

$$Z_{\text{rot}} = \{[X(\text{N}_2 + \text{O}_2)/Z_{\text{rot}}(\text{N}_2 + \text{O}_2) + X(\text{H}_2\text{O})/Z_{\text{rot}}(\text{N}_2 + \text{O}_2 + \text{H}_2\text{O})]\}^{-1} \quad (9.64)$$

where $X(\text{N}_2 + \text{O}_2)$ is the mole fraction of nitrogen plus the mole fraction of oxygen; $Z_{\text{rot}}(\text{N}_2 + \text{O}_2)$ is the rotational collision number for dry air; $X(\text{H}_2\text{O})$ is mole fraction of water; and $Z_{\text{rot}}(\text{N}_2 + \text{O}_2 + \text{H}_2\text{O})$ is the number of H_2O collisions required for N_2 and O_2 to establish rotational equilibrium. This latter quantity can take on values from ∞ to 1 (probability 0–1). The resultant Z_{rot} will be most dependent on $X(\text{H}_2\text{O})$ if $Z_{\text{rot}}(\text{N}_2 + \text{O}_2 + \text{H}_2\text{O}) = 1$. Since $Z_{\text{rot}}(\text{N}_2 + \text{O}_2) \cong 5$, when $X(\text{H}_2\text{O}) < 0.02$, the rotational collision number for the mixture can change by no more than 2%, so $Z_{\text{rot}} \cong (\text{N}_2 + \text{O}_2)$; hence, we are justified in ignoring the effect of water vapor on the rotational collision number.

Combining Eqs. 9.62 and 9.63 with Eq. 9.55 gives the combined absorption due to classical absorption factors and rotational relaxation α_{cr} as

$$\alpha_{cr} = 5.578 \times 10^{-9} \frac{T/T_0}{T + 110.4} \frac{[1 + 4.16 \exp(-16.8T^{-1/3})]f^2}{P/P_0} \quad (9.65)$$

Evaluating Eq. 9.65 for various temperatures indicates that a simplified empirical equation of the form

$$\alpha_{cr} = 1.83 \times 10^{-11} \frac{(T/T_0)^{1/2} f^2}{P/P_0} \quad (9.66)$$

in Np m^{-1} , is within 2% of Eq. 9.65 for temperatures between 213 and 373 °K.

The relaxation strengths of the two vibrational relaxation processes important in air are near to those one would expect for a simple single relaxation of N_2 and O_2 . With $\lambda = c/f$ and $\omega = 2\pi f$, Eq. 9.56 can be written as

$$\alpha_{\text{vib},j} = \frac{\pi s}{c} f \frac{f^2/f_{r,j}}{1 + (f/f_{r,j})^2} \quad (9.67)$$

in Np m^{-1} , where $j = 0$ or N ; $s_j = c'_j/R[c_p^\infty(c_p^\infty + c'_j)]$; and $f_{r,j} = 1/(2\pi\tau_{\text{vs},j})$. The relaxation strength s_j can be related to the particular

atmospheric constituent and the temperature by using the Planck-Einstein relation [47],

$$c'_j/R = \frac{X_j(\theta_j/T)^2 e^{-\theta_j/T}}{(1 - e^{-\theta_j/T})^2} \quad (9.68)$$

where X_j is the mole fraction of the component considered; i.e., 0.20948 for oxygen and 0.78084 for nitrogen [45]; θ_j is the characteristic vibrational temperature (2239.1°K for oxygen and 3352.0°K for nitrogen). For the temperature range 0–40°C, c'_j is small with respect to c_j^∞ , and thus $c_j^\infty \cong c_p$ and $c_v^\infty + c'_j = c_v$. Therefore, $s_j \cong (c'_j/R)(R^2/c_p c_v)$. Using the same reasoning that led to the approximations described in developing Eq. 9.51, the quantity $(R^2/c_p c_v)$ can be set equal to $(\gamma - 1)R/c_p$, which, with $\gamma c_v = c_p$, was shown to be equal to 4/35. Thus, with Eq. 9.68, Eq. 9.67 can be written as

$$\alpha_{\text{vib},j} = \frac{4\pi X_j}{35c} \frac{(\theta_j/T)^2 e^{-\theta_j/T}}{(1 - e^{-\theta_j/T})^2} \frac{f^2/f_{r,j}}{1 + (f/f_{r,j})^2} \quad (9.69)$$

in Np m^{-1} . Using Eq. 9.56, the absorption due to vibrational relaxation can be computed if the $f_{r,j}$ frequencies for oxygen and nitrogen are known.

The frequencies of maximum absorption for oxygen and nitrogen vibrational relaxation have been computed by using the general theory described earlier [50]. To a good approximation,

$$f_{r,O} = (P/P_0)\{24 + 4.41 \times 10^4 h[(0.05 + h)/(0.391 + h)]\} \quad (9.70)$$

in hertz, where h is the mole fraction of water vapor in percent. The various constants in Eq. 9.69 can be determined from the general theory or from experimental measurements in air.

The frequency of maximum absorption for nitrogen is theoretically less difficult to determine than that for oxygen, since it is dominated by direct vibration-translation (V-T) deexcitation of the excited nitrogen molecules by water vapor (or a one-step V-V transfer to H_2O). Carbon dioxide provides an alternate relaxation path at very low water-vapor concentrations. The form of the relaxation frequency is

$$f_{r,N} = (P/P_0)(T/T_0)^{-1/2}[9 + 350h \exp\{-6.142[(T/T_0)^{-1/3} - 1]\}] \quad (9.71)$$

in hertz.

An alternative model for nitrogen relaxation gives

$$f_{r,N} = (P/P_0)(9 + 200h) \text{ (Hz)} \quad (9.72)$$

The contribution to atmospheric absorption due to vibration relaxation processes can now be determined from Eqs. 9.69–9.72 if the percent mole

fraction of water vapor is known. By Avogadro's law, the percent mole fraction is equal to the ratio of the partial pressure of water vapor P_w to the atmospheric pressure P of the sample volume of moist air, in percent. Thus,

$$h = 100P_w/P \quad (9.73)$$

in percent. Introducing the saturation vapor pressure of pure water over liquid water P_{sat} , Eq. 9.73 can be written as

$$h = (100P_w/P_{\text{sat}})(P_{\text{sat}}/P) \quad (9.74)$$

or

$$h = h_r(P_{\text{sat}}/P) \quad (9.75)$$

in percent, where h_r is by definition the relative humidity for a given sample of moist air under pressure P and at a temperature T , in percent, a quantity that is usually available from experiments. For convenience, Eq. 9.75 is written in terms of the standard atmospheric pressure P_0 as

$$h = \frac{h_r(P_{\text{sat}}/P_0)}{P_0} \quad (9.76)$$

in percent. The quality P_{sat} can be determined from standard references or computed from the relation

$$\begin{aligned} \log_{10}(P_{\text{sat}}/P_0) = & 10.79586[1 - (T_{01}/T)] \\ & - 5.02808 \log_{10}(T/T_{01}) \\ & + 1.50474 \times 10^{-4}(1 - 10^{-8.29692}[(T/T_{01}) - 1]) \\ & + 0.42873 \times 10^{-3}(10^{4.76955}[1 - T_{01}/T] - 1) \\ & - 2.2195983 \end{aligned} \quad (9.77)$$

where T is the air temperature, T_{01} is the air triple-point temperature (273.16 °K). Once h is known, the relaxation frequencies can be completed. Combining all the absorption terms,

$$\begin{aligned} \alpha = f^2 \left\{ 1.83 \times 10^{-11}(P_0/P)(T/T_0)^{1/2} + (T_0/T)^{5/2} \right. \\ \times \left(1.278 \times 10^{-2} \frac{e^{-2239.1/T}}{f_{r,o} + (f^2/f_{r,o})} \right) \\ \left. + \left(1.069 \times 10^{-1} \frac{e^{-3352/T}}{f_{r,N} + (f^2/f_{r,N})} \right) \right\} \end{aligned} \quad (9.78)$$

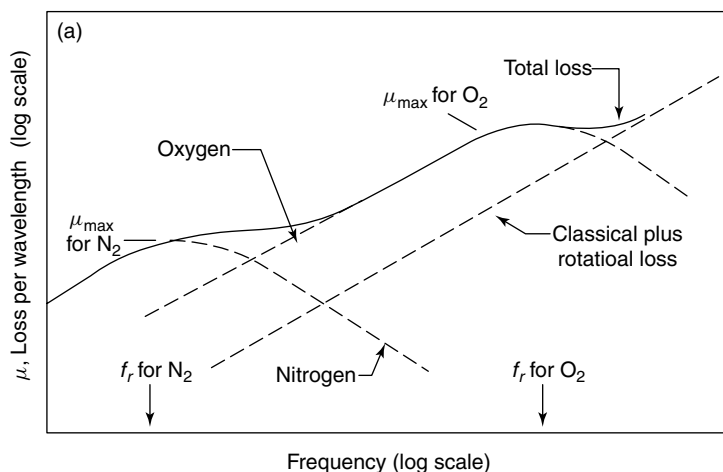


FIG. 9.9(a). Components and general behavior of total air absorption in air in terms of loss per wavelength: $\mu \sim \frac{2(f/f_r)}{1 + (f/f_r)^2}$.

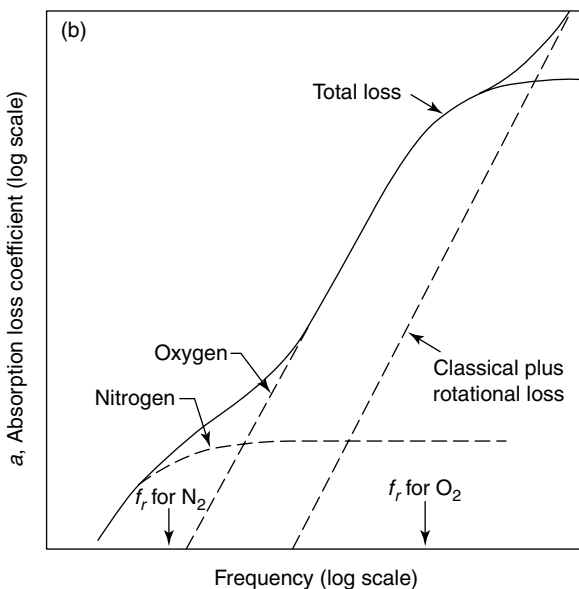


FIG. 9.9(b). Components and general behavior of total air absorption in air in terms of absorption loss coefficient: $\alpha \sim \frac{(f/f_r)^2}{1 + (f/f_r)^2}$.

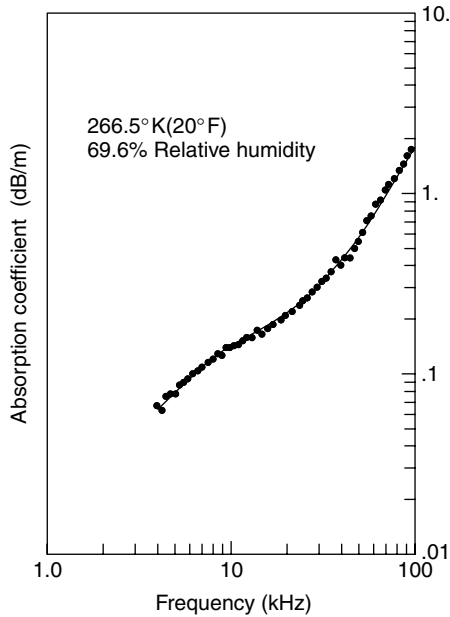


FIG. 9.9(c). Total free-field sound absorption in air at 266.5°K and 69.9% relative humidity; points represent experimental data; solid line calculated using the computational technique described here.

where f is the acoustic frequency in Hz, P is the atmospheric pressure, P_0 is the reference atmospheric pressure (1 atm), T is the atmospheric temperature in K, T_0 is the reference atmospheric temperature (293.15°K), $f_{r,O}$ is the relaxation frequency of molecular oxygen (Eq. 9.70), and $f_{r,N}$ is the relaxation frequency of molecular nitrogen (Eq. 9.71 or 9.72).

Figures 9.9(a) and 9.9(b) show the relative contributions of the different relaxation mechanisms. Figure 9.9(c) shows comparison between theory and experiment.

9.8 Diffusion

There is yet another source of sound absorption that must be considered in gas mixtures. When there is local pressure or temperature gradient, less massive molecules with their higher thermal speeds move toward a condition of equilibrium more rapidly than heavier molecules. The diffusion due to the pressure gradient is accompanied by preferential diffusion of the lighter

molecules due to the thermal gradient. The result is an additional absorption due to this diffusion given by [51]

$$\alpha = \frac{2\pi^2 f^2 \gamma X_1 X_2 P D_{12}}{P c^3} \left[\frac{M_2 - M_1}{M} + \frac{(\gamma - 1)k_T}{\gamma D_{12} X_1 X_2} \right]^2 \quad (9.79)$$

in Np m^{-1} , where X_1 , X_2 and M_1 , M_2 are the mole fractions and molecular weights of gases 1 and 2, respectively; M is the molecular weight of the mixture of gases 1 and 2; D_{12} is the concentration diffusion coefficient and the product of pressure P and D_{12} is in units of $N \text{ sec}^{-1}$; and k_T is the thermal diffusion coefficient in $\text{m}^2 \text{ sec}^{-1}$.

The calculation of absorption due to the combination of pressure and thermal diffusion terms requires that $P D_{12}$ and the ratio k_T/D_{12} be known. These quantities can be calculated from kinetic theory [43], but experimental values are sparse. For air, the term $P D_{12}$ is largest when considering $\text{O}_2/\text{H}_2\text{O}$ collisions; however, in this case, not only is the product $X_1 X_2$ small, but the ratio $k_T/(X_1 X_2)$ is also small. For O_2/N_2 collisions, X_1 and X_2 are both relatively large in air, but the differences in molecular weights ($M_2 - M_1$) and k_T are both small. Ignoring relaxation, Bauer [1] has shown that for air, 99.5% of the total classical absorption can be attributed to the viscosity and thermal conduction. Hence, additional absorption due to diffusion need not be considered for air. For mixtures where $M_2 - M_1$ is large, however, this situation could change dramatically.

9.9 Gases at Low Pressure

Early in this chapter, it was assumed that the f/P ratio in the gas is sufficiently large that the gas can be considered a continuum and the Navier-Stokes Equation is applicable. This description is adequate when the mean distance between collision is very small compared with a wavelength. When this condition is no longer met, treating the gas as a continuous media is no longer accurate. One must resort to a microscopic description of molecular energy and momentum transfer even for the transfer of translational energy. In this case, the governing equation is the Boltzmann Equation.

Very low frequency sound waves naturally occur in the very low density regions of space. The general trend towards favoring low frequency (long wavelength propagation) still applies giving rise to wavelengths that might be measured in light years. The interaction between particular that support wave propagation can be gravitational, or in the case of plasmas, very strong electromagnetic interactions. As a result, the wave equation is complex and the wave speeds not well understood. G. Bertin and C. C. Lin [52] have recently written an excellent book that summarizes current knowledge. For

the discussion that follows, we will assume that interactions are described as hard sphere collisions. Hopefully, future versions of the handbook will include more comprehensive descriptions of this intriguing and evolving field.

Sound propagation in dilute gases has been investigated by Greenspan [2] (Helium at 1 MHz; He, Ne, Ar, Kr, X at 11 MHz), Meyer and Sessler [53] (Ar at 100 and 200 kHz), and Hassler [54] (Ar at 100 and 200 kHz). These data are plotted in Figure 9.10 on the universal abscissa $\eta f/p = \omega \tau_c/2\pi$. One sees that the rare gases obey the Kirchhoff-Stokes theory for $\omega \tau_c < 0.2$.

In Figure 9.10, only those measurements that correspond to the conditions “inside” the gas are included. In dilute gases the experimental conditions are very unfavorable: the small density and the large absorption reduces the signal so much that measurements are taken more and more in the very neighborhood of the sound transmitter, i.e., at the “margin” of the gas. Here, where the molecules coming from the sound transmitter have not suffered a collision with other molecules, special phenomena show up.

The most detailed description of a system containing a single monatomic ideal gas in terms of a distribution function $f(c, r, t)$ is presented in [1]. Some of the main features of that article are included here for reference. Note that in this section, f represents the number of molecules in the differential space dr at r , which possess at t a velocity within dc of c . f can be understood as the density of particles in space/momentum hyperspace.

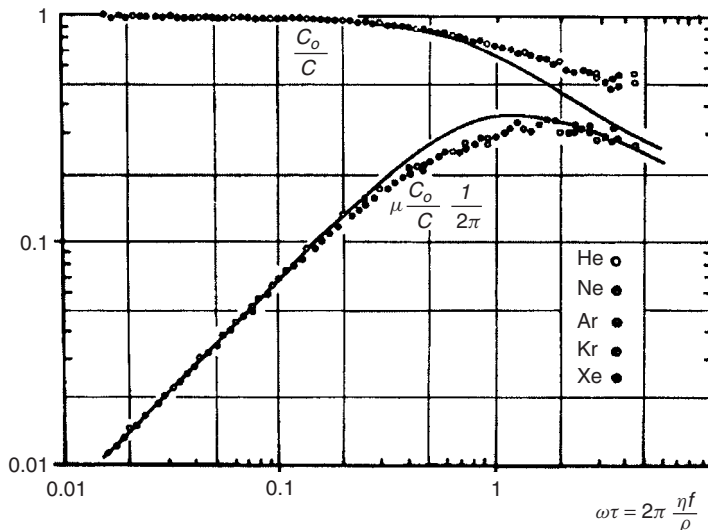


FIG. 9.10. Sound propagation in monatomic gases (Greenspan); Kirchhoff-Stokes theory. Courtesy of Academic Press, New York.

The thermodynamic variables and the irreversible fluxes are given by the moments of the distribution function. The zero moment yields the number density

$$n = \int f dc \quad (9.80)$$

The first moment yields the mean (macroscopic) velocity

$$v = \int c(f/n)dc \quad (9.81)$$

The kinetic energy relative to a frame moving with v defines the kinetic temperature,

$$\frac{3}{2}kT = \frac{m}{2} \int (c - v)^2 (f/n)dc \quad (9.82)$$

Internal friction means transport of a component of the linear momentum $m(\underline{c}_\mu - \underline{v}_\mu)$ with the speed $(c_\nu - v_\nu)(\mu, \nu = x, y, z)$. In tensor notation that establishes the pressure tensor

$$\underline{\underline{P}} = m \int (\underline{c} - \underline{v})(\underline{c} - \underline{v}) f dc \quad (9.83)$$

The trace of Eq. 9.83 is the threefold static pressure $3p = 3nkT$. The heat conduction stems from the transport of kinetic energy (relative to \underline{v}) $m(\underline{c} - \underline{v})^2/2$ in the direction $(\underline{c} - \underline{v})$. Therefore, the transport of kinetic energy is represented by q

$$q = \frac{m}{2} \int (\underline{c} - \underline{v})(\underline{c} - \underline{v})^2 f dc \quad (9.84)$$

where \underline{q} is the trace of the third tensorial moment. Higher moments do not possess a particular thermodynamic meaning and therefore have no names. If we succeed in finding an equation for $f(c, r, t)$, the friction tensor and the heat current can be calculated by insertion of the solution into Eqs. 9.83 and 9.84. Together with the conservation equation, which also represents equations between the moments, the dispersion equation for sound propagation is obtained. For that purpose, the moments may be linearized: since f contains members proportional to the sound amplitude, we can substitute $(c - v)$ by c in Eqs. 9.82 and 9.83. In the case of Eq. 9.84, the same procedure would include convective energy transport,

$$q = \frac{m}{2} \int \underline{c}^2 c f dc - \frac{5}{2}nkT \underline{v} = \frac{m}{2} \int \left(c^2 - \frac{5}{2\beta} \right) \underline{c} f d\underline{c} \quad (9.85)$$

where $5/2nkT$ denotes the enthalpy per unit volume.

A complete description of momentum and energy transport requires a knowledge of the distribution f . The equation for f is the Boltzmann equation. We report in the following some of its properties; more details can be gathered from the literature (e.g., [55, 56]).

The local variation of the distribution function with time is affected (neglecting external fields and walls) (1) by the flight of the molecules — when the time dt has elapsed, dr now contains molecules formerly- cdt apart; (2) by collisions between two molecules that throw these out of or into the velocity range dc at c ; and (3) by the action of external fields, which we assume to be absent.

If one neglects the duration of a collision against the mean free time (or the range of the intermolecular potential against the mean free path), the changes (1) and (2) are independent of each other,

$$\frac{\partial f}{\partial t} = -\underline{c} \cdot \text{grad } f + \left. \frac{\partial f}{\partial t} \right|_{\text{collision}} \quad (9.86)$$

In elastic collisions of identical particles (velocities \underline{c} and \underline{c}_1), the motion of the center of mass and the amount of the velocity difference is maintained, thus the velocity difference $\underline{c} - \underline{c}_1 = \underline{g}$ is only rotated by angle X into a new direction (unit vector \underline{e}'). The velocities of both particles \underline{c}' and \underline{c}'_1 after the collision are, therefore,

$$\underline{c}' = \frac{1}{2}(\underline{c} + \underline{c}_1) \pm \frac{1}{2}|\underline{c} - \underline{c}_1|\underline{e}' \quad (9.87)$$

The probability of such rotation can be expressed in a differential cross section $\sigma(g, X)$, which depends on the intermolecular potential. Now we can formulate the loss of molecules out of $d\mathbf{c}$,

$$d\underline{c} \left. \frac{\partial f}{\partial t} \right|_{\text{loss}} = d\underline{c} \int g \sigma f(\underline{c}) f(\underline{c}_1) d\underline{e}' d\underline{c}_1 \quad (9.88)$$

g stems from the proportionality between collision rate and velocity difference, $f(\underline{c})f(\underline{c}_1)d\underline{c}d\underline{c}_1$ is the density of the colliding and the target molecules; the integration over the angle ($d\underline{e}'$) takes into account all products of the collision, the integration over $d\underline{c}_1$ considers all velocities of the target molecules. To calculate the gain we have to look for collisions that force the colliding molecules into $d\underline{c}$ at \underline{c} . If, in addition, the target molecule changes its velocity into $d\underline{c}_1$ at \underline{c}_1 , then, for molecules without spin, we look for the “inverse” collisions, which we obtain from Eq. 9.88 by time reversal. Since the equations of motion of the molecules are reversible, those “inverse” collisions possess the same probability σ . By multiplication with the distribution function of colliding and target molecule at those \underline{c}' and \underline{c}'_1 values compatible with

Eq. 9.88, and integration over all possibilities ($d\mathbf{e}'$) and final velocities of the target molecules ($d\mathbf{c}_1$), we obtain the production rate of molecules at c ,

$$d\mathbf{c} \left. \frac{\partial f}{\partial t} \right|_{\text{gain}} = d\mathbf{c} \int g\sigma(\mathbf{c}') \int (\mathbf{c}'_1) d\mathbf{e}' d\mathbf{c}_1 \quad (9.89)$$

The loss-gain balance is the Boltzmann Equation in the absence of external fields

$$\frac{\partial f}{\partial t} + \mathbf{c} \cdot \text{grad } f = \int g\sigma(f'f'_1 - f'f'_1) d\mathbf{e}' d\mathbf{c}_1 \quad (9.90)$$

As usual, the argument of f is abbreviated, i.e., $f_1 = f(\mathbf{c}_1)$, $f' = f(\mathbf{c}')$. $f'f'_1$ therefore corresponds to Eq. 9.87. The nonlinear integro-differential equation for f is highly complex, and for our purpose linearization is allowed.

Equation 9.90 possesses one simple (and the only exactly known) solution, the Maxwell distribution:

$$f_M(\mathbf{c}) = n \left(\frac{\beta}{\pi} \right)^{3/2} \exp(-\beta(\mathbf{c} - \mathbf{v})^2), \quad \beta = m/2kT \quad (9.91)$$

with number density n , mean velocity \mathbf{v} , and temperature T constant in time and space. For the Maxwell distribution $(f'f'_1 - f'f'_1)$ vanishes identically. However, there are systems with n , \mathbf{v} , $T = F(r, t)$ for which Eq. 9.90 is a good zero-order approximation. That is the case if the left-hand side of Eq. 9.89 is so small that a minute deviation of the distribution function from the Maxwellian, if inserted into the then nonvanishing collision integral, is sufficient to satisfy Eq. 9.89. Since the collision integral implies the division of the distribution function by a mean free time (in the sense of a dimensional analysis), we can think of two cases.

- (1) The variations of n , T , and \mathbf{v} in time and space are small within a mean free time or a mean free path, respectively, while the total variation may be considerable. Then we suppose the solution to be a small deviation from a local Maxwellian Eq. 9.91 with n , \mathbf{v} , $\beta = n$, \mathbf{v} , $\beta(r, t)$ and have

$$f = f_M(\mathbf{r}, t)[1 + \phi(\mathbf{c}, \mathbf{r}, t)] \quad (9.92)$$

- (2) The amplitudes of the variables n , \mathbf{v} , T are small. Then even with “steep” gradients and “fast” variations the deviation from an absolute Maxwellian (constant in time and space) will be small,

$$f = f_0[1 + \Phi(\mathbf{c}, \mathbf{r}, t)] \quad (9.93)$$

That is the case in the propagation of small-amplitude sound. We therefore introduce Eq. 9.93 into Eq. 9.89 and obtain the linearized Boltzmann Equation

by neglecting terms quadratic in Φ , because $f'_0 f'_{01} = f_0 f_{01}$, the linearized Boltzmann Equation

$$f_0 \left\{ \frac{\partial \Phi}{\partial t} + \underline{c} \cdot \text{grad } \Phi \right\} = \int g \sigma \int_0 \int_{01} [\Phi(\underline{c}_1) + \Phi(\underline{c}') - \Phi(\underline{c}_1) - \Phi(\underline{c})] d\underline{c}' d\underline{c}_1 \quad (9.94)$$

The collision integral on the right-hand side of Eq. 9.94 represents the rate of change of deviation from the Maxwellian distribution $f_0 \Phi(\underline{c})$ at the velocity \underline{c} . It depends on the shape of that deviation and consists of four parts: encounters with Maxwellian-distributed target molecules diminish an excess of the colliding molecules $f_0 \Phi(\underline{c})$ at \underline{c} (last term of Eq. 9.94; an excess in other velocity ranges consistent with Eq. 9.87; $\Phi(\underline{c}')$; increases in the excess at c (second term). The collisions of the Maxwellian-distributed part of the colliding molecules against target molecules distributed according to $f_0(1 + \Phi)$ produce a gain (first term) and a loss (third term) at \underline{c} . In general, the rate of change of the relative deviation from the Maxwellian, $\Phi(\underline{c})$, will be different at different velocities. Such relative deviations, which change at every velocity with a rate proportional to $\Phi(\underline{c})$, conform to the eigenfunctions of the collision operator. They decay under retention of their shape.

Consider a region near the sound transmitter in which most of the molecules come directly from the oscillating surface without a binary collision in between. The Boltzmann Equation is

$$\frac{\partial f}{\partial t} + c_x \frac{\partial f}{\partial x} = 0 \quad (9.95)$$

A solution is any distribution function that contains the combination $c_x - x/t$. Specific solutions are found by applying the boundary conditions at the transmitter. The simplest case is the emission of a Maxwellian from a transmitter surface located at the origin, facing to the right, oscillating according to

$$w = \hat{w} \sin \omega t' \quad (9.96)$$

Then the molecules with direction to the right (coming from the transmitter) have a distribution in the laboratory frame [58]

$$f_+(x=0) = n_0 \left(\frac{\beta}{\pi} \right)^{3/2} \exp[-\beta(c_x - \hat{w} \sin \omega t')^2 - \beta c_y^2 - \beta c_z^2] \quad (9.97)$$

Molecules flying to the left have no harmonic history, they shall be Maxwellian

$$f_-(x=0) = n_0 \left(\frac{\beta}{\pi} \right)^{3/2} e^{-\beta c^2} \quad (9.98)$$

Half-range expansions of the form of Eqs. 9.97 and 9.98, but with more complicated f_+ , and other assumptions regarding momentum accommodation at the oscillating surface have been introduced by Maidnik *et al.* [57] For small amplitudes, \hat{w} , Eq. 9.97 may be linearized

$$f_+(x=0) = n_0 \left(\frac{\beta}{\pi} \right)^{3/2} \exp[-\beta c_x^2 - 2\beta \hat{w} c_x \sin \omega t' - \beta c_y^2 - \beta c_z^2] \quad (9.99)$$

or

$$f(x=0) = f_0[1 + U(c_x)2\beta \hat{w} c_x \sin \omega t'] \quad (9.100)$$

$U(x)$ is the unit step. The propagator $\delta(t' - t + x/c_x)$ moves the distribution function (100) from the point $x = 0$ to x ,

$$f = f_0[1 + U(c_x)2\beta \hat{w} c_x e^{j\omega(t-x/c_x)}] \quad (9.101)$$

The received pressure is the flux of linear momentum per unit time and area, if we assume full accommodation (molecules that collide with the surface take on the momentum of that surface). It contains a part oscillating with ω , the amplitude of which is

$$\begin{aligned} \Delta P_{xx} &= 2\beta \hat{w} e^{j\omega t} \int f_0 c_x^3 e^{-j\omega x/c_x} dc \\ &= 2\beta \hat{w} e^{j\omega t} n_0 \left(\frac{\beta}{\pi} \right)^{3/2} \int_0^\infty e^{-\beta c_x^2} c_x^3 e^{-j\omega x/c_x} dc_x \end{aligned} \quad (9.102)$$

Higher harmonics, expected by Kahn and Mintzer [58], are not present. The integral (Eq. 9.102) cannot be solved in closed form. First we discuss the situation close to the transmitter.

- (1) *Short distance to the transmitter.* For small values of x , the factor $\exp(-j\omega x/c_x)$ can be expanded for almost all molecules except the very slow ones. The integration can then be performed. If we force the result into an exponential representation again, we obtain (with the mean velocity $c_m = (4/\pi\beta)^{1/2}$),

$$\begin{aligned} \frac{\Delta P_{xx}}{p} &\approx \frac{\sqrt{2}}{c_m} \hat{w} e^{j\omega t} \\ &\times \exp \left[-j \frac{\omega x}{c_m} + \left(\frac{1}{2} - \frac{2}{\pi} \right) \frac{\omega^2 x^2}{c_m^2} + j \left(\frac{1}{3} - \frac{2}{3\pi} \right) \frac{\omega^3 x^3}{c_m^3} + \dots \right] \end{aligned} \quad (9.103)$$

The phase is no longer a linear function of the distance. From the phase term

$$\begin{aligned} & \exp \left(-j \int_0^x k(x') dx' \right) \\ &= \exp \left[-j \frac{\omega x}{c_m} + \left(\frac{1}{2} - \frac{2}{\pi} \right) \frac{\omega^3 x^2}{c_m^2} + j \left(\frac{1}{3} - \frac{2}{3\pi} \right) \frac{\omega^2 x^3}{c_m^3} + \dots \right] \end{aligned} \quad (9.104)$$

we gain differentiation as

$$k(x) = \frac{\omega}{c_m} \left[1 - j \left(\frac{4}{\pi} - 1 \right) \frac{\omega x}{c_m} - \left(1 - \frac{2}{\pi} \right) \frac{\omega^2 x^2}{c_m^2} + \dots \right] \quad (9.105)$$

This result is readily interpreted. The phase velocity near the transducer is the phase of the molecules. The phase velocity increases with increasing distance, and we notice an absorption proportional to the distance. That behavior results from the fact that in the region $\omega x/c_x \ll 1$, almost all molecules contribute to the propagation, while for greater values of x the phase factor $\exp(-j\omega x/c_x)$ begins to oscillate for the slow molecules. Fewer molecules support propagation further from the transducer, and these are faster in the mean.

(2) *General solution.* Because

$$\Delta P_{xx} = \Delta \hat{P}_{xx} e^{j\omega t} \exp \left(-j \int_0^x k(x') dx' \right) \quad (9.106)$$

we obtain $k(x)$ from Eq. 9.104 as

$$k(x) = j \frac{\partial}{\partial x} \ln P_{xx} = \int_0^\infty c_x^2 e^{-\beta c_x^2} e^{-j\omega x/c_x} dc_x / \int_0^\infty c_x^3 e^{-\beta c_x^2} e^{-j\omega x/c_x} dc_x \quad (9.107)$$

A relation similar to Eq. 9.107 but with modified accommodation and without the factor c_x^2 resulting from the weighting of the momentum transport, has been given by Meyer and Sessler [53] and solved by expansion techniques.

There are two standard methods of solution of the linearized Boltzmann Equation and its application to the problem of sound propagation in rarefied gases. These methods differ considerably in approach but they yield the same class of solutions, the so-called normal solutions, and the same expressions for the pressure tensor $P_{\mu\nu}$ and the heat current q_ν . Bauer [1] discusses them in the Chapman-Enskog version and applies them to the Boltzmann Equation

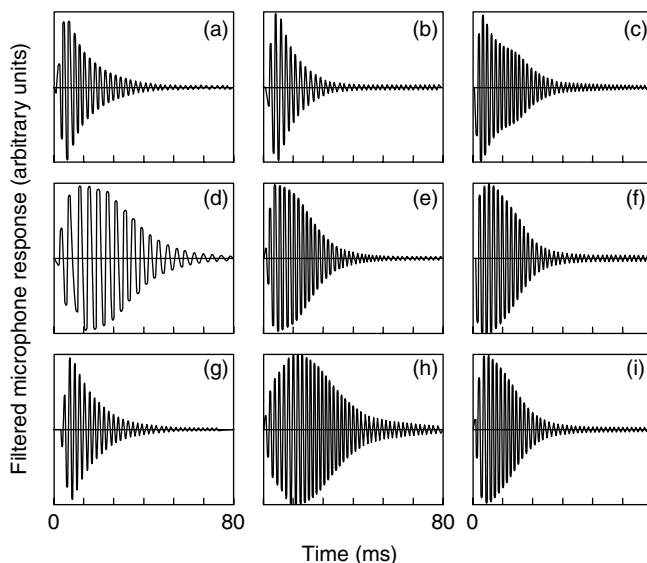


FIG. 9.11. Filtered microphone response. In moving from the central graph (e), only one of the four variables changes. For (c), (e), and (f), the sound frequency increases; (d) is the fundamental of the 60-cm tube; (e) is the fundamental for the 30-cm tube. Corresponding frequencies are approximately 340, 680, and 1360 Hz. For (b), (e), and (h) the pressure increases from 20 to 40 to 80 torr. For (a), (e), and (i) the H₂ concentration increases from 0 to 10% to 20%. For (g), (e), and (c) the energy per mole deposited by the discharge in the gas increases from 3700 to 7000 to 9000 J/mol. If all of this energy were to go into vibrations, the corresponding initial vibrational temperatures would be 1600, 2100, and 2400 °K.

linearized about an absolute Maxwellian, Eq. 9.95. Then the calculation gains in simplicity, and the method becomes clear (the original method was based on the nonlinear Boltzmann Equation itself or a linearization about a local Maxwellian). In principle, the method is an iteration: a lower-order approximation $\phi^{(i-1)}$ is inserted into the differential part; in doing that the integro-differential equation is converted into an ordinary integral equation for a higher-order solution $\phi^{(I)}$. The dispersion relations obtained by that method and also the pertinent literature have been listed by Greenspan [2].

9.10 Systems Not in Equilibrium

To this point the treatment has included only those systems that are in equilibrium on a scale large compared with a mean free path. Modern research is much more involved with propagation in systems far removed

from equilibrium. Thermoacoustics occurs when sound propagates through a region where there is a temperature gradient. Thermoacoustics occurs when sound propagates through a region in which the gas is in close thermal contact with a solid surface with an imposed temperature gradient. Under the correct phasing conditions, heat from the solid matrix is converted to mechanical work and a net gain in acoustic energy or intensity occurs. The stack amplifies the incident acoustic wave. A system in equilibrium could not do this without violating the third law of thermodynamics but when a temperature gradient is present, energy flow occurs, and acoustic gain can result. There are other cases where negative absorption has been observed. Shields [59] has observed gain for a wave propagating through a gas vibrationally excited by an electric discharge. He can predict and observe negative gain.

9.11 Summary

A discussion of the elastic properties of gases quickly involves processes that store energy in the gas. These processes affect the dynamic elastic properties but have no noticeable effect on the static properties. Such behavior is also observed in solids but not to the extent of liquids. Not mentioned in any of the above discussion are nonlinear effects. Gases do exhibit nonlinearity as do solids. In most cases the nonlinear behavior is straightforward and involves no new properties of the gas. For a good discussion of the nonlinear behavior of gases, see [60].

References

1. Bauer, H.J. (1972). Influences of transport mechanisms on sound propagation in gases. *Adv. Mol. Relaxation Proc.* **2**: 319.
2. Greenspan, M. (1965). In *Physical Acoustics IIA*, pp. 1–45, New York: Academic Press.
3. Bhatia, A.B. (1967). *Ultrasonic Absorption: An Introduction to the Theory of Sound Absorption and Dispersion in Gases, Liquids, and Solids*, pp. 50–51, Oxford: Clarendon Press.
4. Beyer, R.T. and Letcher, S.V. (1969). *Physical Ultrasonics*, pp. 91–96, New York: Academic Press.
5. O'Donnell, M., Jaynes, E.T., and Miller, J.G. (1981). Kramers-Kronig relationship between ultrasonic attenuation and phase velocity. *J. Acoust. Soc. Am.* **69**.
6. Hirschfelder, J.O., Curtiss, C.F., and Bird, R.B. (1954). *Molecular Theory of Gases and Liquids*, pp. 147–148, New York: John Wiley & Sons.
7. Bhatia, A.B. (1967). Ultrasonic absorption: an introduction to the theory of sound absorption and dispersion in gases, liquids, and solids, pp. 14–15, Oxford: Clarendon Press.
8. Landolt-Bornstein. (1967). *Numerical Data and Functional Relationships in Science and Technology: Molecular Acoustics*, vol 5, pp. 8–9, New York: Springer-Verlag.

9. Kittel, C. (1948). *Rept. Progr. Phys.* **11**: 205.
10. Beyer, R.T. and Letcher, S.V. (1969). *Physical Ultrasonics*, pp. 359–360, New York: Academic Press.
11. Herzfeld, K.F. and Litovitz, T.A. (1959). *Absorption and Dispersion of Ultrasonic Waves*. New York: Academic Press.
12. Winter, T.G. and Hill, G.L. (1967). High-temperature ultrasonic measurements of rotational relaxation in hydrogen, deuterium, nitrogen, and oxygen. *J. Acoust. Soc. Am.* **42**: 848.
13. Zuckerwar, A.J. and Griffin, W.A. (1980). Resonant tube for measurement of sound absorption in gases at low frequency/pressure ratios. *J. Acoust. Soc. Am.* **68**: 218.
14. Hill, G.L. and Winter, T.G. (1968). The effect of temperature on the rotational and vibrational relaxation times of some hydrocarbons. *J. Chem. Phys.* **49**: 440.
15. Landau, L. and Teller, E. (1936). Zur theorie der schall dispersion. *Phy. Z. Soviet-Union* **10**: 34.
16. Beyer, R.T. and Letcher, S.V. (1969). *Physical Ultrasonics*, chapter 5, New York: Academic Press.
17. Shields, F.D. (1962). Thermal relaxation in fluorine. *J. Acoust. Soc. Am.* **34**: 271.
18. Bass, H.E., Sutherland, L.C., Piercy, J., and Evans, L. (1984). Absorption of sound by the Atmosphere. *Phys. Acoust.* **VXII**, 161.
19. Hubbard, J.C. (1931). The acoustic resonator interferometer: the acoustic system and its equivalent electric network. *Phys. Rev.* **38**: 1011.
20. Counter, J.V. (1958). Ultrasonic dispersion in oxygen. *J. Acoust. Soc. Am.* **30**: 297.
21. Steward, E.S. and Stewart, J.L. (1952). Rotational dispersion in the velocity, attenuation, and reflection of ultrasonic waves in hydrogen and deuterium. *J. Acoust. Soc. Am.* **24**: 194.
22. Lagemann, R.T. (1952). The use of glass parts in ultrasonic interferometers. *J. Acoust. Soc. Am.* **24**: 86.
23. Jacobs, B., Carain, R., Olson, J.R., and Aunne, R.C. (1990). Vibrational relaxation in $s_i f_\gamma$ using a computer controlled ultrasonic interferometer. *J. Acoust. Soc. Am.* **88**: 2812–2815.
24. Angora, F.A. (1953). Attenuation of sound in a tube. *J. Acoust. Soc. Am.* **25**: 336.
25. Shields, F.D. (1959). Measurement of thermal relaxation in CO₂ extended to 300°C. *J. Acoust. Soc. Am.* **31**: 248.
26. Bass, H.E., Winter, T.G., and Evans, L.B. (1971). Vibrational and rotational relaxation in sulfur dioxide. *J. Chem., Phys.* **54**: 644.
27. Shields, F.D., Bass, H.E., and Bolen, L.N. (1977). Review of acoustical patents. *J. Acoust. Soc. Am.* **62**: 236–253.
28. Cravens, D., Shields, F.D., Bass, H.E., and Breshears, W.D. (1979). Vibrational relaxation of UF₆: ultrasonic measurements in mixtures with argon and N₂. *J. Chem. Phys.* **71**: 2797–2802.
29. Shields, F.D. and Lagemann, R.T. (1957). Tube corrections in the study of sound absorption. *J. Acoust. Soc. Am.* **29**: 470.
30. Shields, F.D. and Faughn, J. (1969). Sound velocity and absorption in low-pressure gases confined to tubes of circular cross section. *J. Acoust. Soc. Am.* **46**: 158. Shields, F.D. (1975). An acoustical method for determining the thermal and momentum accommodation coefficients of gases on solids. *J. Chem. Phys.* **62**: 1248.
31. Shields, F.D. and Faughn, J. (1969). Sound velocity and absorption in low-pressure gases confined to tubes of circular cross section. *J. Acoust. Soc. Am.* **46**: 158.

- Shields, F.D. (1975). An acoustical method for determining the thermal and momentum accommodation coefficients of gases on solids. *J. Chem. Phys.* **62**: 1248.
32. Bass, H.E. and Yan, H.X. (1983). Pulsed spectrophone measurements of vibrational energy transfer in CO₂. *J. Acoust. Soc. Am.* **74**: 1817.
33. Shields, F.D. (1960). Sound absorption in the halogen gases. *J. Acoust. Soc. Am.* **32**: 180.
34. Lewis, J.W.L. and Lee, K.P. (1965). Vibrational relaxation in carbon dioxide/water vapor mixtures. *J. Acoust. Soc. Am.* **38**: 813.
35. Shields, F.D. and Burks, J.A. (1968). Vibrational relaxation in CO₂/D₂O mixtures. *J. Acoust. Soc. Am.* **43**: 510.
36. Shields, F.D. (1969). Sound absorption and velocity in H₂S and CO₂/H₂S mixtures. *J. Acoust. Soc. Am.* **45**: 481.
37. Shields, F.D. and Carney, G.P. (1970). Sound absorption in D₂S and CO₂/D₂S mixtures. *J. Acoust. Soc. Am.* **47**: 1269.
38. Bass, H.E. and Shields, F.D. (1974). Vibrational relaxation and sound absorption in O₂/H₂O mixtures. *J. Acoust. Soc. Am.* **56**: 856.
39. Anderson, B., Shields, F.D., and Bass, H.E. (1974). Vibrational relaxation and sound absorption in O₂/H₂O mixtures. *J. Acoust. Soc. Am.* **56**: 856.
40. Shields, F.D. (1967). Vibrational relaxation in SO₂ and SO₂/Ar mixtures. *J. Chem. Phys.* **46**: 1063.
41. Shields, F.D. and Anderson, B. (1971). More on vibrational relaxation in SO₂/Ar mixtures. *J. Chem. Phys.* **55**: 2636.
42. Shields, F.D. and Lee, K.P. (1963). Sound absorption and velocity measurements in oxygen. *J. Acoust. Soc. Am.* **35**(2): 251.
43. Hirschfelder, J.O., Curtiss, C.F., and Bird, R.B. (1958). Molecular theory of gases and liquids. New York: Wiley.
44. National Bureau of Standards, Talks of Thermodynamic and Transport Properties of Air, Argon, Carbon Dioxide, Carbon Monoxide, Hydrogen, Nitrogen, Oxygen and Steam, (Pergamon, New York, 1960).
45. U.S. Standard Atmosphere, 1962, U.S. Gov. Print. Off. Washington, DC.
46. Society of Automotive Engineers, Committee A-21, Standard Values of Atmospheric Absorption as a Function of Temperature and Humidity for Use in Evaluating Aircraft Flyover Noise, SAE Aerosp. Recomm. Pract. ARP 86 (6), (August, 1964).
47. Greenspan, M.J. (1959). Rotational relaxation in nitrogen, oxygen and air. *J. Acoust. Soc. Am.* **31**: 155.
48. Bass, H.E. and Keeton, R.G. (1975). ultrasonic absorption in air at elevated temperatures. *J. Acoust. Soc. Am.* **58**: 110.
49. Holman, J.P. (1969). Thermodynamics. New York: McGraw-Hill, **169**.
50. Evans, L.B., Bass, H.E., and Sutherland, L.C. (1972). Atmospheric absorption of sound: theoretical predictions. *J. Acoust. Soc. Am.* **51**: 1565.
51. Cottrell, T.L. and McCoubrey, J.C. (1961). Molecular energy transfer in gases. Butterworth: London.
52. Bertin, G. and Lin, C.C. In *Spiral Structure in Galaxies, A Density Wave Theory* (MIT Press, 1996, Cambridge, Massachusetts).
53. Meyer, E. and Sessler, G. (1957). *Z. Phys.* **149**: 15.
54. Hassler, H. (1968). *Acoustica* **20**: 271.
55. Walsman, L., Handbuch der Physik XII, pp. 345 (Springer, Heidelberg, 1958).
56. Grad, H., Handbuch der Physik XII, pp. 205–295 (Springer, Heidelberg, 1958).

57. Maidnik, G. and Heckl, M. (1965). *Phys. Fluids* **8**: 266.
58. Kahn, D. and Mintzer, D. (1965). *Phys. Fluids* **8**: 1090.
59. Douglas Shields, F. (1987). Propagation of sound in vibrationally excited n_2 /mixtures. *J. Acoust. Soc. Am.* **81**: 87–92.
60. Hamilton, M.F. and Blackstock, D.T. (1998). *Nonlinear acoustic*. New York: Academic Press.

10. ACOUSTIC MEASUREMENTS IN GASES

M. R. Moldover, K. A. Gillis, J. J. Hurly, J. B. Mehl,
and J. Wilhelm¹

Process Measurements Division
National Institute of Standards and Technology
Gaithersburg, Maryland

Abstract

Cylindrical acoustic resonators developed at the National Institute of Standards and Technology (NIST) are routinely used to measure the speed of sound in gases with uncertainties of 0.01% or less. The pressure dependence of the data is fitted with model intermolecular potentials to obtain virial coefficients as well as gas densities ρ and heat capacities C_p with uncertainties of 0.1%. The model intermolecular potentials are also used to estimate the viscosity η and thermal conductivity λ of gases with uncertainties of less than 10%. These techniques have been applied to numerous gases, and the results are tabulated. The gases include candidate replacement refrigerants, helium-xenon mixtures used in thermoacoustic machinery, and very reactive gases used in semiconductor processing. The viscosity can be measured directly with uncertainties of less than 1% using the Greenspan acoustic viscometer, a novel acoustic resonator developed at NIST. A second novel resonator is used to measure the Prandtl number ($Pr \equiv \eta C_p / \lambda$) with uncertainties on the order of 2%. The thermal conductivity is determined by combining the Prandtl number with the acoustically determined density, viscosity, and heat capacity. Spherical acoustic resonators are used to measure the speed of sound with the highest possible accuracy. An argon-filled spherical resonator was used to redetermine the universal gas constant R with a fractional standard uncertainty of 1.7×10^{-6} . The same resonator was used to measure imperfections of the internationally accepted temperature scale (ITS-90) in the range 217 to 303 K. This work is being extended to 800 K. In effect, very accurate speed-of-sound measurements will be used to calibrate thermometers.

10.1 Introduction and Scope

We describe a research program at the National Institute of Standards and Technology (NIST) that uses gas-filled acoustic resonators to obtain

¹Guest Scientist from Fachbereich Chemie, Universität Rostock, D-18051 Rostock, Germany.

thermodynamic and transport property data for solving both engineering and standards problems. The NIST program has determined the thermodynamic properties of more than 20 gases used in engineering; tables of these properties are in the database associated with this chapter. Acoustic measurements to determine the transport properties of these gases are proceeding. In the area of standards, this program has used an argon-filled spherical acoustic resonator to determine the internationally recognized [1] value of the universal gas constant R [2]. Subsequently, the same resonator was used to measure the imperfections of the internationally accepted temperature scale (ITS-90) in the range 216 to 303 K [3]. The study of ITS-90 is now being extended to temperatures as high as 800 K. In addition to data, this research program has led to a thorough understanding of spherical acoustic resonators [4]; cylindrical acoustic resonators [5]; Greenspan acoustic viscometers [6, 7]; and practical, reliable methods of interpolating and extrapolating speed-of-sound data [8, 9]. (We adapted several ideas for interpolation and extrapolation from Trusler and his collaborators [10–12].)

This NIST program began in 1978 when one of the present authors (M.R.M.) was asked to find an alternative method of determining the universal gas constant R . The request was stimulated by the presence of mutually inconsistent values of R in the literature [13]. In 1976, a group at Britain's National Physical Laboratory (NPL) reported a "new" value for R that had a standard uncertainty of 20 ppm (1 ppm = 1 part in 10^6) [14] and was 159 ppm larger than the value of R that had been accepted in 1972 with an uncertainty of 31 ppm [15]. The new NPL value of R was based on speed-of-sound data obtained with a cylindrical acoustic resonator and extrapolated to zero pressure using an empirical, quadratic function. Guided by the theory of the virial equation of state, Rowlinson and Tildesley [16] used a linear extrapolation of the NPL data to obtain a value of R in agreement with the 1972 value. Three years later, the NPL group reported a revised value of R and stated that its 1976 value of R was erroneous because an unsuspected nonlinearity in an acoustic transducer had led them to use a quadratic function for extrapolating [13]. Thus, NPL unintentionally demonstrated the value of the theoretical considerations that we present in Section 10.2. By the time of NPL's revision, this NIST program had begun. Ultimately, NIST confirmed the revised value of R with a much smaller standard uncertainty, 1.7 ppm.

The present review begins by describing the connections between the thermodynamic properties of dilute gases and the speed of sound. These connections lead us to recommend the use of model intermolecular potentials for analyzing speed-of-sound data (and for extrapolation to zero pressure). The data tables are based on such model potentials. Then, we describe four gas-filled resonators: (1) a cylinder used to measure the speed of sound in industrially significant gases, (2) a dumbbell-shaped Helmholtz resonator

used to measure the viscosity, (3) a cylinder with sheet-metal inserts to determine the Prandtl number, and (4) the large spherical shell that was used to redetermine R and to measure the imperfections in ITS-90.

10.2 Acoustic Measurements and Thermodynamic Properties of Dilute Gases

Rigorous statistical mechanical arguments lead to the convenient virial expansion of the pressure p of gases as a function of density ρ and the thermodynamic temperature T

$$p = \rho RT(1 + B\rho + C\rho^2 + D\rho^3 + \cdots) \quad (10.1)$$

Here, the density virial coefficients $B(T)$, $C(T)$, $D(T)$, etc., are functions of the temperature only. All of the thermodynamic properties of dilute gases can be computed by straightforward differentiations and integrations from the density virial coefficients and the zero-pressure limit of the constant-pressure heat capacity $C_p^0(T)$. Often, $B(T)$, $C(T)$, $D(T)$, etc., are parametrized with arbitrary functions (e.g., polynomials in $1/T$) and the parameters are determined from some limited set of thermodynamic data. If this procedure is followed using speed-of-sound data, unacceptable results may be obtained, especially when the functions are extrapolated beyond the range of the data. Much better results can be obtained by using virial coefficients generated from model intermolecular potentials to represent the speed of sound $u(p, T)$.

In the limit of zero frequency, the speed of sound is a thermodynamic quantity:

$$u^2 = \left(\frac{\partial p}{\partial \rho} \right)_S = \frac{1}{\rho \beta_S} = \frac{\gamma}{\rho \beta_T} \quad (10.2)$$

Here, S is the entropy, β_S is the adiabatic compressibility, β_T is the isothermal compressibility, and $\gamma \equiv C_p/C_V$ is the ratio of the molar heat capacity at constant pressure to the molar heat capacity at constant volume. In this work, we consider audio frequencies and gases at pressures of 50 kPa or higher. Under these circumstances, the zero-frequency limit is an excellent approximation, except for those few gases composed of symmetric molecules in which the conversion of kinetic energy into vibrational energy requires unusually many collisions (e.g., very dry carbon dioxide).

Usually, one measures the speed of sound $u(p, T)$ as a function of the temperature and the pressure (instead of the density). The results may be expressed as the power series

$$u^2 = \frac{\gamma^0 RT}{M} \left(1 + \frac{\beta_a p}{RT} + \frac{\gamma_a p^2}{RT} + \frac{\delta_a p^3}{RT} + \frac{\varepsilon_a p^4}{RT} + \cdots \right) \quad (10.3)$$

Here, $\gamma^0(T) = C_p^0(T)/C_v^0(T)$ is the zero-pressure limit of the heat capacity ratio and M is the molecular mass. The temperature-dependent “acoustic virial coefficients” $\beta_a(T)$, $\gamma_a(T)$, $\delta_a(T)$, and $\varepsilon_a(T)$ can be calculated explicitly from the density virial coefficients $B(T)$, $C(T)$, etc., using rigorous thermodynamic relationships [8]. The relationships for $\beta_a(T)$ and $\gamma_a(T)$ are

$$\beta_a = 2B + 2(\gamma^0 - 1)B' + \frac{(\gamma^0 - 1)^2}{\gamma^0}B'' \quad (10.4)$$

and

$$\begin{aligned} \gamma_a = \frac{(\gamma^0 - 1)}{RT\gamma^0} [B + (2\gamma^0 - 1)B' + (\gamma^0 + 1)B'']^2 \\ + \frac{1}{RT\gamma^0} \left[(2\gamma^0 + 1)C + [(\gamma^0)^2 - 1]C' + \frac{(\gamma^0 - 1)^2}{2}C'' \right] \end{aligned} \quad (10.5)$$

In Eqs. 10.4 and 10.5, the primed functions B' and B'' denote $T(dB/dT)$ and $T^2(d^2B/dT^2)$, respectively. As illustrated by Eqs. 10.4 and 10.5, $\beta_a(T)$ and $\gamma_a(T)$ are related to the density virial coefficients by second-order differential equations. Similar, more complicated equations for $\delta_a(T)$ and $\varepsilon_a(T)$ appear in [8]. These equations can be integrated numerically provided that the acoustic virial coefficients and $C_p^0(T)$ [or equivalently $\gamma^0(T)$] are known from speed-of-sound measurements and provided that the initial values for the integration are determined by additional thermodynamic data. For many gases, the initial values are not available. When the initial values are at low temperatures and the integrations proceed toward higher temperatures, the integrations are stable in the sense that the effects of errors in the initial values decrease as the temperature increases. When the initial values are at high temperatures and the integration proceeds to lower temperatures, the uncertainties grow [11].

We recommend another way of analyzing $u^2(p, T)$. We begin with an algebraic expression for the ideal-gas heat capacity $C_p^0(T)$ that contains several parameters and following Trusler [10] a model intermolecular pair potential $\varphi(r)$ that also contains several parameters. (Here, r is the radial coordinate that measures the distance between pairs of molecules.) To obtain the temperature-dependent density virial coefficients and their derivatives, the model potential is weighted by the Boltzmann factor, integrated with respect to r , and differentiated with respect to T . Then, using Eqs. 10.4 and 10.5, etc., we compute $u^2(p, T)$ for those states where the data were taken. These computations are repeated to find the best-fit values of the parameters in $C_p^0(T)$ and $\varphi(r)$. This procedure does not require additional thermodynamic data and it solves the differential equations relating $B(T)$ and $C(T)$ to $\beta_a(T)$ and $\gamma_a(T)$ exactly. The procedure is not perfect because the true functional form of $\varphi(r)$ is not known.

For analyzing $u^2(p, T)$ data, we have used two model potentials for $B(T)$: (1) hard-core square-well potentials and (2) the hard-core Lennard-Jones potential. When we used a square-well potential for $B(T)$, we used a separate square-well function for $C(T)$. When we used a Lennard-Jones potential for $B(T)$, we included an Axilrod-Teller triple dipole term in $C(T)$. We note that Trusler [10] has used yet another potential introduced by Maitland and Smith.

The hard-core square-well potentials can be integrated to obtain very convenient, closed-form expressions for $B(T)$ and $C(T)$; we reproduce these expressions here:

$$B(T) = b_0[1 - (\lambda^3 - 1)\Delta] \quad (10.6)$$

$$\begin{aligned} C(T) &= \frac{1}{8}b_0^2(5 - c_1\Delta - c_2\Delta^2 - c_3\Delta^3) \\ c_1 &= \lambda^6 - 18\lambda^4 + 32\lambda^3 - 15 \\ c_2 &= 2\lambda^6 - 36\lambda^4 + 32\lambda^3 + 18\lambda^2 - 16 \\ c_3 &= 6\lambda^6 - 18\lambda^4 + 18\lambda^2 - 6 \end{aligned} \quad (10.7)$$

where $\Delta \equiv \exp(\varepsilon/k_B T) - 1$, k_B is Boltzmann's constant, $b_0 \equiv (2/3)\pi N_A \sigma^3$ is the molar volume excluded by the hard cores, and N_A is Avogadro's constant. The adjustable parameters are ε , λ , and σ , where ε is the well depth, σ is the radius of the hard core, and λ is the ratio of the width of the well to σ . We allowed each virial coefficient to have its own values for ε , λ , and σ ; thus, we do not attribute physical significance to the values that resulted from fitting the data. When the data extended to high enough pressures, we also used square-well functions for $D(T)$ and an empirical form for $E(T)$ [8].

The form of the hard-core Lennard-Jones 6-12 potential is:

$$\varphi(r_{ij}) = 4\varepsilon \left\{ \left(\frac{\sigma - 2a}{r_{ij} - 2a} \right)^{12} - \left(\frac{\sigma - 2a}{r_{ij} - 2a} \right)^6 \right\} \quad (10.8)$$

where r_{ij} is the intermolecular separation between molecules i and j , ε is the well depth, σ is the value of r_{ij} where $\varphi(r)$ crosses zero, and a is the radius of the hard core. This potential has three adjustable parameters: ε , σ , and a . The same values for these parameters are used to compute both $B(T)$ and $C(T)$.

As an example of what can be done with the hard-core Lennard-Jones potential, we consider the data for WF_6 . We calculated $B(T)$ and $C(T)$ and their temperature derivatives classically using references [17, 18]. The calculation of $C(T)$ required the inclusion of three-body contributions. This added a fourth adjustable parameter, v_{123} . Following Trusler [10], we used the Axilrod-Teller triple-dipole term [19],

$$\varphi(r_{123}) = \frac{v_{123}(1 + \cos \theta_1 \cos \theta_2 \cos \theta_3)}{(r_{12}^3 r_{13}^3 r_{23}^3)} \quad (10.9)$$

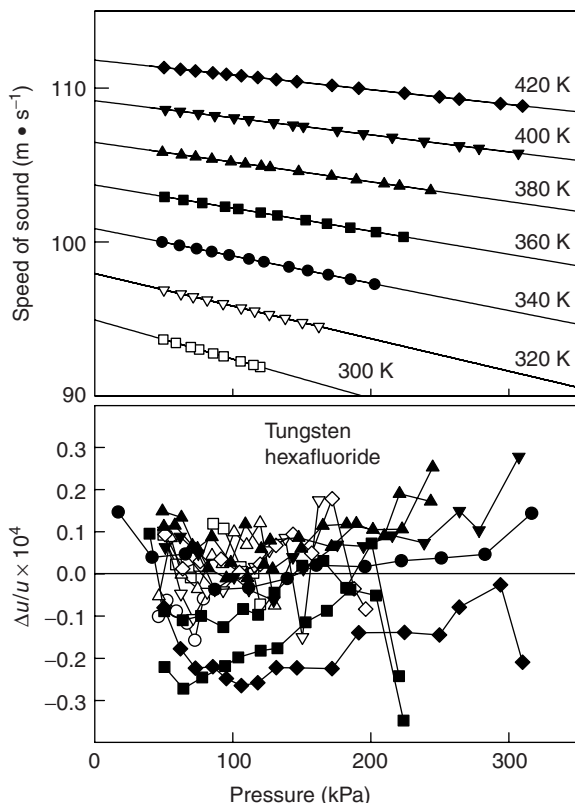


FIG. 10.1. Top, Speed-of-sound data for WF_6 . Bottom, Deviations of all of the data in the top panel from a fit to a model hard-core Lennard-Jones potential.

where ν_{123} is the dispersion coefficient and θ_i is defined as the angle subtended at molecule i by molecules j and k . This is the first term in the three-body corrections to the dispersion energy for monatomic species.

Figure 10.1 displays speed-of-sound data for WF_6 and their deviations from a seven-parameter fitting function. Three of the parameters were used to represent the ideal-gas heat capacity:

$$C_p^0/R = 5.207 + 0.04251(T/K) - 3.931 \times 10^{-5}(T/K)^2$$

$$290 \text{ K} \leq T \leq 420$$
10.10)

The remaining four parameters were ε , σ , a , and ν_{123} . These four parameters define the density virial equation up to $C(T)$; however, the derivatives of $B(T)$ and $C(T)$ do make noticeable contributions to the acoustic virials $\delta_a(T)$, and

$\varepsilon_a(T)$, and these terms were included when fitting the speed-of-sound data for WF_6 . Figure 10.1 shows that the data are represented almost to within their noise. We also analyzed these data with the Maitland-Smith potential and obtained slightly larger deviations.

Because of experimental problems, the data for WF_6 did not extend to pressures above 300 kPa. For several other gases, the $u^2(p,T)$ data extend to higher densities. For such gases, we used hard-core square-well expressions for $D(T)$ and empirical expressions for $E(T)$. In these cases, we first completed a preliminary analysis using only the low-pressure data to find the best values of the parameters in $C_p^0(T)$. Then, we held the parameters in $C_p^0(T)$ fixed and found the best values of the remaining parameters.

To a small extent, the results for $B(T)$, $C(T)$, etc., depend on the functional forms of the model potentials. For several gases, (e.g., light alkanes), the published $u^2(p,T)$ data are accurate and span a very wide temperature range. In such cases, we found that the more realistic potentials (e.g., hard-core Lennard Jones, Maitland-Smith, etc.) yield better results than the hard-core square-well potentials, especially when extrapolated to very high temperatures. Nevertheless, even the hard-core square-well potentials yield equations of state $p(\rho,T)$ with uncertainties of less than 0.1% over a wide range of conditions [8].

The tables of data attached to this chapter were obtained from model intermolecular potentials. For each gas, we have tabulated values of $C_p^0(T)$, $B(T)$, and $C(T)$, and for those gases where our data extend to high enough densities, we have tabulated $D(T)$. We have also tabulated the acoustic virial coefficients $\beta_a(T)$, $\gamma_a(T)$, and $\delta_a(T)$.

Figure 10.2 is another demonstration of the utility of fitting model potentials to $u^2(p,T)$ data. The solid curves represent the viscosity of three gases (HBr, SF_6 , and BCl_3) at low pressures. These curves were calculated from model hard-core Lennard-Jones potentials that were obtained from $u^2(p,T)$ data [20]. For SF_6 , the viscosities from the model potential are, on average, 4% smaller than published viscosity measurements (filled symbols). Also, every published measurement falls within 10% of the calculated curve. Equally good agreement has been obtained for CF_4 , C_2F_6 [9] and C_3H_8 [10]. From these experiences, we conclude that one can use $u^2(p,T)$ data to predict the viscosity of difficult-to-handle gases such as HBr and BCl_3 over a wide range of temperatures with uncertainties on the order of 10% or less.

In concluding this section, we emphasize that model potentials provide physically motivated functions for extrapolating $u^2(p,T)$ data to zero pressure. Such extrapolations to zero pressure are exactly what is required to determine $C_p^0(T)$, R , and the thermodynamic temperature from acoustic data. Indeed, as mentioned in the Section 10.1, Rowlinson and Tildesley [16] detected the extrapolation error in the earlier NPL determination of R [14] by using a

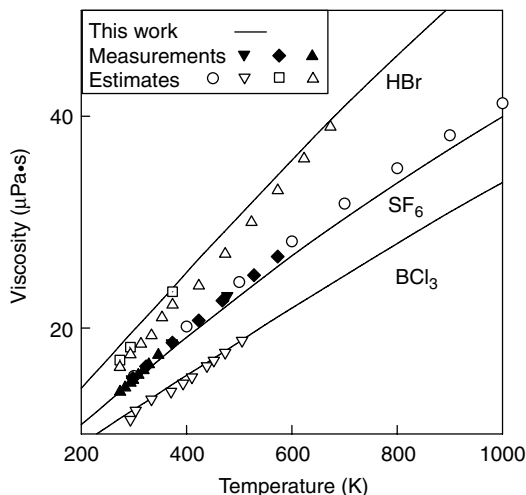


FIG. 10.2. Viscosity of three gases at zero pressure. The curves are estimates from speed-of-sound data. The filled symbols are direct measurements. For SF₆, the direct measurements differ by less than 10% from the curve. The open symbols are other estimates. For references and details, see [20].

semiempirical model potential to extrapolate the $u^2(p, T)$ data from NPL to zero pressure.

10.3 Measuring the Speed of Sound

10.3.1 Under What Conditions Are Resonance Methods Most Useful?

Gas-filled acoustic resonators are well suited for measuring $u^2(p, T)$ with fractional uncertainties of less than 10^{-4} throughout the approximate density range $50 \text{ mol} \cdot \text{m}^{-3} < \rho < 10^4 \text{ mol} \cdot \text{m}^{-3}$. Under these conditions, $u^2(p, T)$ can be determined from measurements of resonance frequencies and the application of very small corrections that depend on other properties of the gas and the properties of the resonator. When the density of the gas is reduced below the lower end of this range (which corresponds to a density near that of ambient air), the corrections from viscous and thermal dissipation at the boundary between the gas and the walls of the resonator grow as $1/\rho^{1/2}$ and the signal-to-noise ratio decreases in proportion to ρ^2 . (For certain gases at low pressures, the attenuation of sound throughout the volume of the gas is important and the signal-to-noise ratio decreases as ρ^3 .) These effects set the lower density limit. When the density of the gas is raised above $10^4 \text{ mol} \cdot \text{m}^{-3}$ (corresponding approximately to the critical density for most gases), the uncertainties increase

because the coupling between oscillations of the gas within the resonator to oscillations of the shell enclosing the gas increases. A measure of the coupling is the frequency perturbation:

$$\Delta f_{\text{shell}}/f = \mathcal{F}(\text{geometry, frequency}) \times (\rho u^2)/(\rho_{\text{shell}} u_{\text{shell}}^2) \quad (10.11)$$

where ρ_{shell} and u_{shell} are the density and the longitudinal speed of sound in the shell. In Eq. 10.11, the function \mathcal{F} depends on the shape of the resonator (spherical, cylindrical, etc.) and on the resonance mode under consideration. The magnitude of \mathcal{F} becomes large when the frequency of the gas's oscillations is close to one of the resonance frequencies of the empty shell, which themselves depend on u_{shell} . For radially symmetric oscillations of a gas within a spherical shell of radius a and thickness t , the function of frequency and geometry in Eq. 10.11 is approximately

$$\mathcal{F}(\text{geometry, frequency}) = \frac{a/(2t)}{1 - (f/f_{\text{breathing}})^2} \quad (10.12)$$

where $f_{\text{breathing}} \approx 0.22 \times u_{\text{shell}}/a$ is the frequency of the breathing oscillation of the empty shell. For resonators of other shapes, this function will have a larger zero-frequency limit. At high densities, where $\Delta f_{\text{shell}}/f$ is always large, the speed of sound can be measured more accurately by using high-frequency time-of-flight techniques than by using resonance techniques. Even at low densities, reliable measurements cannot be obtained from any mode of a gas oscillation that has a frequency that happens to be close to a resonance frequency of the empty shell.

10.3.2 Resonators for Speed-of-Sound Measurements

The resonators designed to obtain accurate values of $u^2(p, T)$ should have (1) walls that are thick and stiff, (2) transducers that are small and stiff, (3) a small surface-to-volume ratio, (4) smooth interior surfaces, and (5) a carefully designed port for admitting and removing gas. The first two qualities are desirable because they reduce hard-to-calculate corrections to the resonance frequencies from the compliance of the walls ($\Delta f_{\text{shell}}/f$) and the transducers. The third and fourth qualities ensure that the corrections from viscous and thermal dissipation can be calculated and are small. Ideally, a valve is built into the wall of the resonator to seal any port used to admit gas. When this is done, the port introduces negligible perturbations to the resonance frequencies. A very simple and frequently used alternative is to use a long, narrow capillary tube to admit gas. However, a capillary slows the pumping of gas out of the resonator so much that flushing must be used whenever samples are changed. A more sophisticated alternative to a valve is to choose the length of the port and its exterior termination to simultaneously achieve a high acoustic impedance

at the resonance frequencies and a low impedance to the quasi-steady flows used to fill and empty the resonator [21].

In “routine” measurements of $u^2(p, T)$ in industrially significant gases at NIST, we have used cylindrical resonators with a circular cross section. (Typical dimensions are 14 cm long and 3 cm in radius.) When results of the highest possible accuracy are needed, we have used spherical resonators with internal volumes of 1/4, 1, or 3 liters. For spherical resonators, one can model Δf_{shell} most accurately and one can attain the lowest possible viscous and thermal attenuation at the gas-shell boundary by using the radially symmetric modes. Then, one has the smallest possible frequency perturbations from the boundary and the highest possible signal-to-noise ratio.

In principle, the measurement of the resonance frequency of a single acoustic mode is sufficient to determine the speed of sound. In practice, the redundancy that comes with measuring the frequencies f and the halfwidths g of several resonance modes provides checks of the calculated corrections. These checks are practical only if the modes under study are nondegenerate, i.e., the resonance frequencies are well separated from each other. For a spherical resonator, only the radially symmetric modes are nondegenerate; thus, they are the only ones used for practical purposes. For a cylindrical resonator, we have typically used the four lowest-frequency longitudinal modes together with the lowest-frequency radial and azimuthal modes.

For studies of gases where intramolecular relaxation is slow and for studies of the strong attenuation of sound that occurs extremely close to all liquid-vapor critical points, compact resonators with low-resonance frequencies are desirable. For such studies, Garland and Williams [22] used a torroidal resonator. Recently, we measured $u^2(p, T)$ with uncertainties on the order of 0.02% using a double Helmholtz resonator designed as an acoustic Greenspan viscometer (Section 10.4). At the frequency of the Helmholtz resonance, the wavelength of sound was 1.1 m, even though the resonator was only 6 cm long. We plan to use this resonator for measurements near the critical point of xenon.

10.3.3 Calibration Using a Gas of Known Properties

The resonance method of measuring $u^2(p, T)$ requires a resonator, frequency standard, pressure gauge, and thermometer that are stable. In practice, exacting temperature and dimensional measurements are avoided by “calibrating” the resonator with a gas, such as argon, for which the speed of sound is accurately known. The calibration is conducted by measuring the resonance frequencies of several acoustic modes when the resonator is filled with argon at the temperatures and pressures of interest. These frequencies are corrected for the thermal and viscous boundary layers and are then used to determine the relevant dimensions of the resonator. The resonator is then filled with the test

gas, and the resonance frequencies of exactly the same modes are measured. After making the boundary layer corrections, these frequencies are used to determine the speed of sound in the test gas, $u_{\text{test}}(p, T)$. To a high degree, the dimensions of the resonator drop out of the determination. In effect, one determines $u_{\text{test}}(p, T)/u_{\text{argon}}(p, T)$ from the frequency ratios $f_{\text{test}}/f_{\text{argon}}$ for several modes.

A numerical example illustrating the benefits of calibration is instructive. Consider an acoustic determination of $C_p^0(T)$ for propane in the temperature range 220–460 K. In this range, γ^0 decreases from 1.18 to 1.09 and $(u_{\text{propane}})^2$ increases by 105%; however, $(u_{\text{argon}}/u_{\text{propane}})^2 = (f_{\text{argon}}/f_{\text{propane}})^2$ increases by only 16%. To determine $C_p^0(T)$ directly from u_{propane}^2 (without calibration), the data are analyzed using the first equality in Eq. 10.13.

$$\begin{aligned} \frac{C_p^0(T)}{R} &= \lim_{p \rightarrow 0} \left(\frac{(M \cdot u^2)_{\text{propane}}}{(M \cdot u^2)_{\text{propane}} - RT} \right) = \frac{\gamma^0}{\gamma^0 - 1} \\ &= \lim_{p \rightarrow 0} \left(1 - \frac{3}{5} \frac{M_{\text{argon}}}{M_{\text{propane}}} \left(\frac{f_{\text{argon}}}{f_{\text{propane}}} \right)^2 \right)^{-1} \end{aligned} \quad (10.13)$$

To attain a fractional uncertainty of 0.1% of $C_p^0(T)$, the combined fractional uncertainties of $M \cdot u^2$ and T must be less than 9×10^{-5} . Thus, the uncertainty of T must be less than 0.04 K at 460 K. In contrast, if one calibrates with argon using the zero-pressure result $(M \cdot u^2(0, T))_{\text{argon}} = (5/3)RT$ and the last equality in Eq. 10.13, then $C_p^0(T)$ can be determined to within 0.1% if the uncertainty of T is as large as 0.56 K. Of course the temperature of the calibration must be reproduced within 0.04 K when making the test measurements; however, this is a much easier task than knowing the temperature to 0.04 K. Indeed, temperature differences on the order of 0.5 K across parts of the resonator can be tolerated, provided that the calibration is conducted in the same thermal environment as the test measurements.

10.3.4 Effects of Impurities

In our experience, the presence of unknown impurities is often the most important contribution to the uncertainties of $u^2(p, T)$ and $C_p^0(T)$ deduced from measurements of acoustic resonance frequencies. The importance of impurities is implied by the ratio of masses in the last equality in Eq. 10.13. To make an explicit estimate of the importance of impurities, we use a thermodynamic result that can be derived from the virial equation of state for a mixture [23]. If the virial expansion is truncated after the term $B\rho$, one finds

$$u_{\text{mix}}^2 = (C_{p, \text{mix}}/C_{V, \text{mix}})RT/M_{\text{mix}} \quad (10.14)$$

where the subscript “mix” denotes a mole-fraction average for each property of the mixture. Consider the limit of an ideal gas (where $C_p^0 - C_v^0 = R$), with properties denoted by the subscript “1.” An undetected impurity of component “2” with a small mole fraction x will change u_1 to u_{mix} . We consider the value of $C_{p,\text{mix}}^0$ computed from $(u_{\text{mix}})^2$ via the first equality in Eq. 10.13. The fractional change in $C_{p,\text{mix}}^0$ in the limit of x approaching zero is

$$\frac{1}{C_{p1}^0} \frac{\partial C_{p1}^0}{\partial x} = (C_{p2}^0/C_{p1}^0 - 1) - \frac{(1 - M_2/M_1)}{(\gamma_1^0 - 1)} + \dots \quad (10.15)$$

Usually, the first term on the right hand side of Eq. 10.15 is less than the second term. For propane, where $(\gamma_1^0 - 1) \approx 0.1$, the mole fraction of ethane must be less than 3×10^{-4} if its effect on C_p^0 is to be less than 0.1%. Impurities with very large values of M_2/M_1 are particularly troublesome.

10.3.5 Transducers

At gas densities greater than approximately $50 \text{ mol}\cdot\text{m}^{-3}$, it is possible to make accurate measurements of $u^2(p, T)$ using acoustic pressures as small as 10^{-6} times the pressure of the test gas. Large, efficient acoustic transducers are not needed to generate and detect such small acoustic pressures when a gas in a modest volume is resonating with a Q on the order of 10^3 to 10^4 . Recognizing this, we have placed small transducers within the resonator or we have used external transducers that are coupled very weakly to the resonator. These arrangements ensure that the transducers make only very small perturbations to the resonance frequencies.

We have always used two independent transducers, one functioning as a sound generator and a second functioning as a sound detector. When measuring $u^2(p, T)$ in inert gases, we used commercially manufactured transducers that were embedded within the walls of resonators in such a way as to be flush with an interior surface. To work with reactive test gases, we built thin, stainless steel or monel diaphragms into one or two walls of the resonator to separate the test gas within the resonator from an inert gas at the same pressure outside the resonator (see Fig. 10.3). In some cases, we placed transducers immediately behind the diaphragms. In other cases, acoustic wave guides filled with inert gas conducted the sound between two remote transducers and the diaphragms. This wave guide arrangement is particularly versatile because the transducers can be at ambient temperature while the resonator is at either a very high or a very low temperature [24]. Near the diaphragms, a short length of each wave guide is filled with a screen formed of fine stainless steel wires. The screen attenuates sound, thereby preventing the occurrence of high- Q , longitudinal resonances within the wave guides. Such unintentional resonances would have

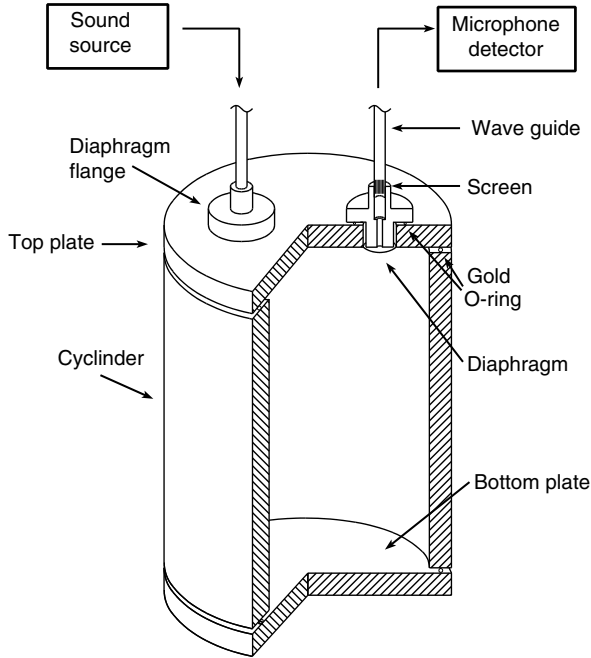


FIG. 10.3. Cylindrical acoustic resonator designed for speed-of-sound measurement.

interfered with measurements of the resonances of the test gas within the resonator.

10.3.6 Measurements of Resonance Frequencies and Halfwidths

At each state point (p, T) , the frequency of the sound generator is stepped through each resonance while recording in-phase (x) and quadrature signals (y) from the detector. Typically, measurements are made at 11 frequencies separated by steps of $g_m/5$ spanning the range $f_m \pm g_m$, where g_m is the halfwidth of the resonance and the subscript “m” denotes the indices that identify the mode under study. Then, the theoretically expected, complex function of the frequency is fitted to the values $x + iy$ to obtain both f_m and g_m and also their uncertainties. The fitting function is

$$x + iy = \frac{if\mathbf{A}_m}{(f^2 - \mathbf{F}_m^2)} + \mathbf{B} + \mathbf{C}(f - f_1) \quad (10.16)$$

Here, \mathbf{A}_m , \mathbf{B} , and \mathbf{C} are complex constants, $\mathbf{F}_m = f_m + ig_m$ is the complex resonance frequency, and f_1 is an arbitrary constant. In Eq. 10.16, the

parameters **B** and **C** account for possible crosstalk and for the effects of the “tails” of modes other than the one under study. The quality factor of a typical resonance was in the range $10^3 < Q \equiv f_m/2g_m < 10^4$ and the standard deviation of f_m was less than $10^{-5}f_m$. Under ideal conditions, the statistical uncertainty of f_m is on the order of $10^{-7}f_m$.

10.3.7 Determination of the Speed of Sound

The speed of sound u in the test gas is determined from the measured resonance frequencies f_m by $u = 2\pi f_m/k_m$. Expressions for the wave number k_m for resonances in a cylindrical cavity with a radius a and length l appear in [5]. Expressions for a spherical cavity appear in [4]. If the resonator is calibrated (Section 10.3.3) using a gas with a known speed of sound, accurate values of the dimensions of the resonator and the wave number are not needed.

The measured resonance frequencies are corrected for the thermal and viscous losses at the boundaries as well as for the small effects of the duct used to move the sample into and out of the resonance cavity [9, 10].

10.3.8 Corrections for Boundary Losses and Fill Duct

Dissipative heat exchange between the test gas and the walls of the resonator occurs within a gas layer adjacent to the walls. The thickness of this thermal boundary layer is characterized by the thermal penetration length δ_t . Similarly, momentum exchange is characterized by the viscous penetration length δ_v . These lengths are defined in terms of the acoustic frequency and the gas's properties by

$$\delta_t^2 \equiv \frac{\lambda}{\rho C_p \pi f}; \quad \delta_v^2 \equiv \frac{\eta}{\rho \pi f} \quad (10.17)$$

The thermal and viscous boundary layers perturb the resonance frequencies and halfwidths by $\Delta \mathbf{F}_t = -\Delta f_t + i g_t$ and $\Delta \mathbf{F}_v = \Delta f_v + i g_v$, respectively. For a typical resonator, such as the one shown in Figure 10.3, these perturbations have magnitudes on the order of the volume of the gas in the boundary layers divided by the volume of the gas inside the resonator, i.e., $\Delta f_t/f_m \sim g_t/f_m \sim (\gamma - 1) \times \delta_t \times A_{\text{resonator}}/V_{\text{resonator}} \sim (\gamma - 1)10^{-4}$ and $\Delta f_v/f_m \sim g_v/f_m \sim \delta_v \times A_{\text{resonator}}/V_{\text{resonator}} \sim 10^{-4}$. For the monatomic gases at low pressures, the factor $(\gamma - 1)$ is 2/3; it is much smaller for polyatomic gases (e.g., 0.09 for propane at 460 K). Therefore, the temperature changes associated with the sound wave and the corresponding frequency perturbations $\Delta \mathbf{F}_t$ are much smaller in polyatomic gases than in monatomic gases.

Expressions for $\Delta \mathbf{F}_t$ and $\Delta \mathbf{F}_v$ for cylindrical resonators appear in [5]; the corresponding expressions for spherical resonators appear in [4]. For other geometries, the corrections may be calculated using boundary perturbation

theory. As in [4], boundary perturbation theory may also be used to account for any fill duct that may be present.

10.4 Resonance Measurements of Transport Properties

Cylindrical resonators, such as the one sketched in Figure 10.3, are not well suited to determine the viscosity η and the thermal conductivity λ . In the following paragraph, we discuss the reasons for this to motivate the design of the Greenspan acoustic viscometer and the Prandtl number resonator. The Prandtl number is defined by $Pr \equiv \eta C_p / \lambda$ and is widely used to correlate the heat transfer from a solid to a moving fluid. We plan to measure the Prandtl number in many gases and to deduce the thermal conductivity from it, together with the acoustically determined values of C_p and η .

As mentioned in Section 10.3.8, typical perturbations from viscous and thermal losses are on the order of (volume of the boundary layer)/(volume of the resonator). For the cylindrical resonators designed to measure $u^2(p, T)$, this ratio is 10^{-3} or even smaller. The halfwidths g_m of the resonances are measured with relative uncertainties on the order of 10^{-2} or less. In principle, one could use these measured values of g_m for several modes to determine the lengths δ_t and δ_v and from these lengths one could determine η and λ . However, several factors would lead to uncertainties in η and λ of several percent or more. One factor is the difficult-to-calculate contributions to g_m . Such contributions come from motion of the shell at high pressures, sound attenuation throughout the volume of the gas at low pressures, and dissipation within the transducer assemblies. A second factor is the difficulty in determining the effective internal area of a resonator within 1%. Surface roughness on the scale of δ_t and δ_v may cause the effective area to increase with pressure (as δ_t and δ_v decrease with pressure). A pressure-dependent contribution to the effective area may result from crevices that were formed where the parts of a resonator were joined during its assembly. Finally, accurate measurements of small values of g_m require a high signal-to-noise ratio and very fine temperature control during the measurement. These considerations led us to consider using a Greenspan acoustic viscometer to measure η and another specially designed resonator to measure the Prandtl number.

10.4.1 Greenspan Acoustic Viscometer

The Greenspan acoustic viscometer is a dumbbell-shaped double Helmholtz resonator that has a low-frequency, low- Q resonance in which the gas oscillates through a duct connecting two chambers (see Fig. 10.4). The low frequency leads to relatively large values of δ_v that reduce the requirements for a fine

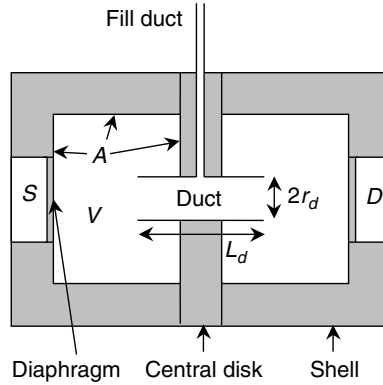


FIG. 10.4. Schematic cross section of a Greenspan acoustic viscometer [7]. This viscometer had an outer diameter of 6.2 cm and a length of 7.2 cm. The source and detector transducers (denoted “S” and “D,” respectively) were PZT stacks. The volume of the chamber on the left is indicated by “V” and its inner surface area is indicated by “A.”

surface finish. The low Q reduces the relative importance of the difficult-to-estimate contributions to g_m and also reduces the need to maintain very high temperature stability. In the lowest-order approximation, the Helmholtz resonance frequency f_m is

$$f_m^2 \approx \frac{u^2 r_d^2}{2\pi L_d V} \quad (10.18)$$

where V is the volume of each of the chambers and L_d and r_d are the length and radius of the duct that connects the chambers. In many important cases, the halfwidth of the Helmholtz resonance can be expressed as the sum of four terms:

$$\begin{aligned} \frac{2g_m}{f_m} = \frac{1}{Q} \approx & \frac{\delta_v}{r_d} + 2\varepsilon_{\text{orif}} \frac{\delta_v}{L_d} + (\gamma - 1) \frac{\delta_t A}{2V} \\ & + (\gamma - 1) \frac{C_{\text{relax}}}{C_p} \frac{2\pi f_m \tau_{\text{relax}}}{1 + (2\pi f_m \tau_{\text{relax}})^2} \end{aligned} \quad (10.19)$$

The first term on the right hand side (r.h.s.) of Eq. (10.19) is the desired term that is used to determine the viscosity from the radius of the duct r_d and ρ (that appears in δ_v). The second term on the r.h.s. of Eq. (10.19) accounts for flows that converge into and diverge out of each end of the duct. This term contains the “orifice resistance parameter” $\varepsilon_{\text{orif}}$ that Mehl calculated numerically [25]. For the resonator described in [7] and sketched in Figure (10.4), $\varepsilon_{\text{orif}} \approx 0.97$.

The third term² on the r.h.s. of Eq. (10.19) accounts for the heat exchange between the gas and the walls of the resonator; it is proportional to the ratio of the volume of the thermal boundary layer in one chamber $\delta_t A$ to the volume V of that chamber. The last term on the r.h.s. of Eq. 10.19 applies to certain gases (e.g., CH_4 , CO_2) that have symmetries such that many intermolecular collisions are required for their internal degrees of freedom to adjust to the temperature change associated with the acoustic oscillation. In such gases, the acoustic dissipation throughout the volume of the gas is characterized by the product $C_{\text{relax}} \cdot \tau_{\text{relax}}(\rho)$ where C_{relax} is the heat capacity associated with the slowly relaxing degrees of freedom and $\tau_{\text{relax}}(\rho)$ is the relaxation time, which is proportional to ρ^{-1} .

For the viscometer described by Wilhelm *et al.* [7], the transducers were piezoelectric “stacks” that were separated from the test gas by 0.1-mm-thick stainless steel diaphragms. In tests with five gases (He, Ar, Xe, N_2 , CH_4), the $Q \equiv f_m/2g_m$ was in the range $20 < Q < 200$ for pressures in the range $0.2 \text{ MPa} < p < 3.2 \text{ MPa}$. Less than 10% of Q^{-1} came from heat transfer between the gas and the walls of the chambers; thus, λ had to be known to 10% to determine η to 2%. The relaxation term for methane contributed less than 0.3% to Q^{-1} .

Figure 10.5 compares the viscosities determined with the Greenspan acoustic viscometer with data from the literature obtained by other methods. To obtain the results in the upper panel of Figure 10.5, the Greenspan viscometer was used as an absolute instrument, i.e., the viscosity was calculated from measurements of its dimensions and its frequency response. The root mean square (r.m.s.) deviation of the Greenspan viscometer data from the base line is 0.47%.

The bottom panel of Figure 10.5 shows the smaller deviations (0.12% r.m.s.) that remained after the data from the literature were used to calibrate the Greenspan viscometer. This illustrates how the instrument would perform if it were used as a relative instrument. For the calibration, we assumed that the literature values of η were correct and we replaced the values of $\varepsilon_{\text{orif}}$ and A with effective values. On reducing the calculated value of $\varepsilon_{\text{orif}}$ by 3%, all of the deviations on Figure 10.5 were shifted upward by 0.5%. This small change in $\varepsilon_{\text{orif}}$ would result if the right angles (that were assumed in the calculations)

²By mistake, the equivalent of this third term was reduced by a factor of $2/\pi$ in three publications. The mistake appears in Eq. (9) of Ref. [6], Eq. (4) of Ref. [7], and Eq. (19) of M. R. Moldover, K. A. Gillis, J. J. Hurly, J. B. Mehl, and J. Wilhelm, “Chapt 12 Acoustic Measurements in Gases: Applications to Thermodynamic Properties, Transport Properties, and the Temperature Scale” in *HANDBOOK OF ELASTIC PROPERTIES OF SOLIDS, FLUIDS, AND GASES*, edited by Levy, Bass and Stern, Volume IV (Academic Press, New York, 2000). In these earlier publications, the correct term was to analyze data.

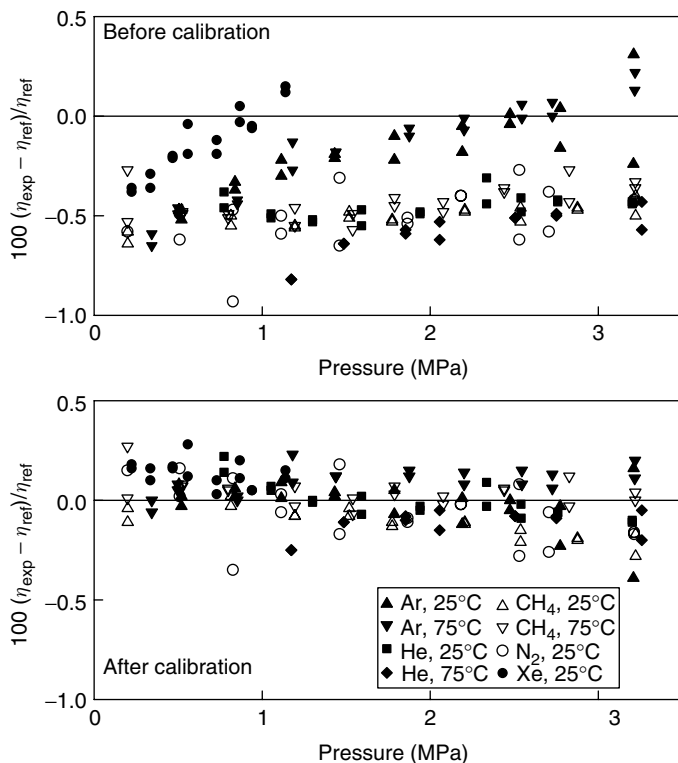


FIG. 10.5. Comparison of viscosities determined with a Greenspan acoustic viscometer with literature values. Top, Results obtained using the viscometer as an absolute instrument. Bottom, Results obtained after calibration.

at the ends of the duct were rounded with a radius of only $2.5\ \mu\text{m}$ [25]. Such rounding is consistent with the way in which the duct was manufactured.

The data for the noble gases in the top panel of Figure 10.5 have a positive slope before calibration. This slope was eliminated by replacing A with effective values that were 1–5% larger than the value calculated from dimensional measurements and by assuming that A varied inversely as δ_t . The cause for this δ_t -dependent increase in A was not determined; it may be related to rough surfaces where the diaphragms and the duct were soldered into place. Alternatively, there may have been a narrow crevice where metal O-rings were used to seal the chambers to the central disk (Fig. 10.4).

The frequency of the Helmholtz mode of the Greenspan viscometer can be used to determine the speed of sound $u(p, T)$. This is a by-product of the viscosity measurement and was not expected to be particularly accurate. It

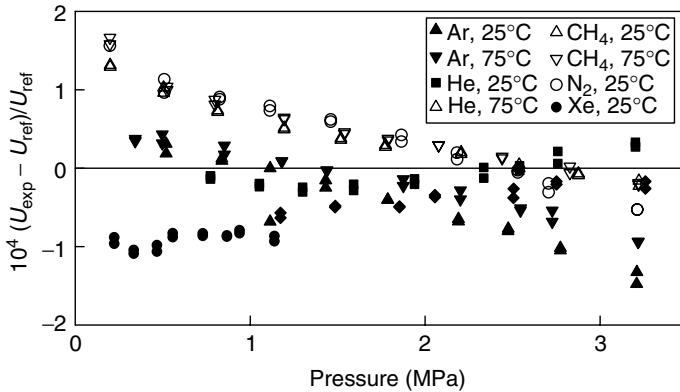


FIG. 10.6. Comparison of speed-of-sound results from a Greenspan viscometer with results from the literature. See [7] for details.

was a pleasant surprise to find that the values of $u(p, T)$ for He, Ar, Xe, N₂, and CH₄ were consistently between 0.16 and 0.20% larger than values from the literature. If the volumes of the chambers were replaced with effective volumes that were 0.36% smaller, all of the speed of sound data would fall within $\pm 0.02\%$ of published values (see Fig. 10.6). The difference between the effective volume and the geometric volume is on the order of the volume displaced by the solder used to hold the diaphragms and the duct in place.

Apparently, a calibrated Greenspan viscometer can be used for simultaneously measuring the viscosity and the speed of sound in a gas. However, if one were to use only the Helmholtz mode of such a resonator, the redundancy that is usually available in resonance speed-of-sound measurements would be missing and the possibility of undetected systematic errors would be greatly increased. Alternatively, one could design a Greenspan viscometer with three chambers connected by two ducts. Such a resonator would have two low-frequency modes that could provide some redundancy.

10.4.2 Resonators for Measuring the Prandtl Number

Figure 10.7 is a sketch of a prototype resonator that was designed to measure the Prandtl number. This resonator was a cylinder with an internal length, $L = 13.2$ cm, and an internal radius of $R = 4.8$ cm. A honeycomb-shaped array of hexagonal ducts was installed into the center of the resonator. Ignoring the honeycomb and the viscous and thermal boundary layers, the longitudinal modes of the cylindrical resonator have frequencies f_n

$$f_n = un/(2L); \quad n = 1, 2, 3, \dots \quad (10.20)$$

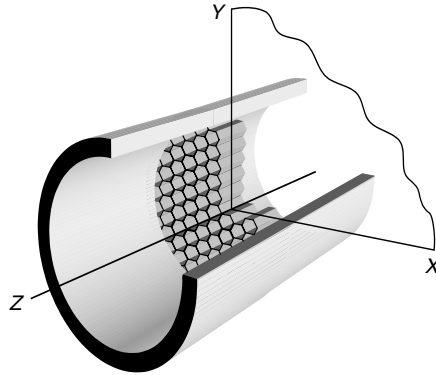


FIG. 10.7. Schematic section of the resonator used to measure the Prandtl number. The hexagonal ducts are oriented parallel to the axis of the cylindrical resonator and located midway between the ends of the cylinder. The odd longitudinal modes have a velocity antinode in the plane bisecting the resonator and the ducts. The even longitudinal modes have a temperature antinode in the same plane.

The surface area of the honeycomb was approximately five times larger than the surface area of the cylinder even though the length of the honeycomb was much less than that of the cylinder. Thus, most of the damping of the longitudinal modes occurred within the honeycomb.

The odd longitudinal modes ($n = 1, 3, 5, \dots$) had velocity antinodes in the plane of symmetry bisecting the honeycomb and the axis of the cylinder. In each hexagonal duct, viscosity damped the gas motion within the boundary layer (of thickness δ_v) surrounding the duct's surfaces. The quality factor of these odd modes was approximately $Q_{\text{odd}} \approx (\text{volume of resonator})/[\delta_v \times (\text{area of honeycomb})]$. In the same plane bisecting the honeycomb, the even longitudinal modes ($n = 2, 4, 6, \dots$) had a velocity node and a corresponding antinode in the pressure and the temperature. Heat exchange between the honeycomb and the gas within the thermal boundary layer (of thickness δ_t) strongly damped the even longitudinal modes. The quality factor of the even modes was approximately $Q_{\text{even}} \approx (\text{volume of resonator})/[(\gamma - 1)\delta_t \times (\text{area of honeycomb})]$. In this crude approximation, the ratio $Q_{\text{even}}/Q_{\text{odd}}$ is independent of the volume of the resonator and of the area of the honeycomb, and the Prandtl number can be calculated from measurements of the frequencies and halfwidths of an even and odd mode:

$$\begin{aligned}
 Pr &= \frac{\eta C_p}{\lambda} = \frac{f_{\text{odd}}}{f_{\text{even}}} \left(\frac{\delta_v}{\delta_t} \right)^2 = \frac{f_{\text{odd}}}{f_{\text{even}}} \left(\frac{(\gamma - 1)Q_{\text{even}}}{Q_{\text{odd}}} \right)^2 \\
 &= \frac{f_{\text{even}}}{f_{\text{odd}}} \left(\frac{(\gamma - 1)g_{\text{even}}}{g_{\text{odd}}} \right)^2
 \end{aligned} \tag{10.21}$$

The prototype Prandtl number resonator was assembled by installing a stainless steel honeycomb into the center of a cylindrical resonator. The honeycomb was similar to the “stack” built into thermoacoustic refrigerators and heat engines. Each hexagonal duct was 2.6 cm long and had a diameter (from flat side to flat side) of 1 mm. The stainless steel sheets comprising the honeycomb were 0.05-mm thick, and the average hydraulic radius r_h of the hexagonal ducts was 0.430 mm. [$r_h \equiv 2 \times (\text{cross-sectional area of duct})/(\text{perimeter of duct})$] Piezoelectric (PZT) “stack” transducers were placed behind diaphragms in each end of the resonator, much like the arrangement for the Greenspan viscometer sketched in Figure 10.4.

The frequency response of the resonator was measured as a function of pressure on an isotherm for argon, xenon, and sulfur hexafluoride. The acoustic amplitudes used for these measurements were always small enough that non-linear contributions to the Q were negligible.

The measured frequency response was compared with predictions that account for several effects not included in Eq. 10.21, namely, the viscous and thermal losses at the cylindrical boundaries of the resonator, the “end effects” at both ends of each hexagonal duct, the reduction of the resonator’s cross section by the honeycomb, and the duct used to admit and remove gas from the resonator [26].

Figure 10.8 displays preliminary results obtained with the Prandtl number resonator. For several modes and for the three gases, the measured halfwidths are compared with halfwidths calculated using data from the literature. For xenon the data span the pressure range $0.2 \text{ MPa} < p < 1.2 \text{ MPa}$, corresponding to the range $50 < Q < 300$; for argon, the ranges are $0.1 \text{ MPa} < p < 1 \text{ MPa}$ and $25 < Q < 160$; for SF_6 , the ranges are $0.15 \text{ MPa} < p < 0.4 \text{ MPa}$ and $250 < Q < 1000$.

The results in Figure 10.8 for the odd modes are plotted as a function of δ_v/r_h and the results for the even modes are plotted as a function of δ_t/r_h . Nearly all the results in the bottom panel of Figure 10.8 fall within $\pm 2\%$ of a smooth curve, indicating that the effective area of the honeycomb is a smooth function of the length scale (δ_v or δ_t) used to determine the area. Probably, some of this dependence results from the sensitivity of the end corrections to the presence of sharp corners or burrs. Another contribution to scale dependence of the effective area may result from the partially obstructed and oddly shaped ducts that were located at the boundary between the honeycomb and the cylindrical shell of the resonator.

One can fit the data in the bottom panel of Figure 10.8 by an empirical equation that represents the effective area as a function of δ_v or δ_t . If this fit is used as a calibration, the Prandtl number of another gas can be determined with a standard uncertainty on the order of 2%. This is a very encouraging result from a prototype instrument. We conjecture that the importance of the

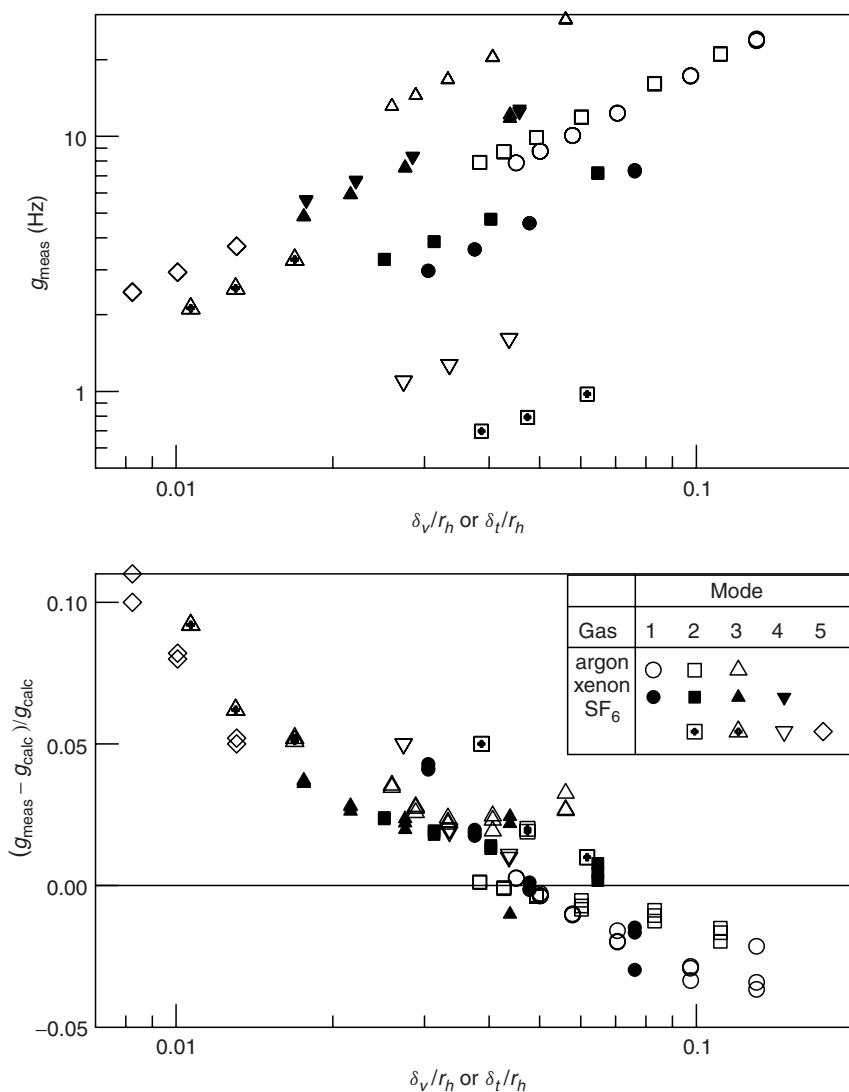


FIG. 10.8. Top, Halfwidths g of the longitudinal resonances of the Prandtl number resonator. Because SF₆ has a small value of $(\gamma - 1)$, the even, thermally damped modes for this gas have conspicuously smaller values of g . Bottom, Fractional differences between measured and calculated halfwidths. If a smooth curve were drawn through the differences, most of that data would fall within $\pm 2\%$ of it.

calibration function would be reduced if the ends of the honeycomb were rounded, perhaps by electropolishing.

10.5 Acoustic Thermometry

10.5.1 Principles of Acoustic Thermometry

Primary acoustic thermometry relies on the connection between the speed of sound in a gas and the thermodynamic temperature of that gas. Hydrodynamics and the kinetic theory of dilute gases relate the thermodynamic temperature T , the average kinetic energy E in one degree of freedom, and the speed of sound u . In the simplest approximation,

$$3E = \frac{1}{2}mv_{\text{rms}}^2 = \frac{3}{2}k_B T, \quad u^2 = \frac{\gamma}{3}v_{\text{rms}}^2 \quad (10.22)$$

Here, v_{rms} is the root mean square speed of a gas molecule, m is its mass, and k_B is the Boltzmann constant. For monatomic gases, $\gamma \rightarrow 5/3$ as $p \rightarrow 0$. The International System of Units assigns the exact value 273.16 K to the temperature of the triple point of water T_w . From this assignment and from Eq. 10.22, the Kelvin thermodynamic temperature T of a gas can be determined from the zero-pressure limit of the ratio of speed of sound measurements at T and T_w using the equation

$$\frac{T}{273.16 \text{ K}} = \lim_{p \rightarrow 0} \left(\frac{u^2(p, T)}{u^2(p, T_w)} \right) \quad (10.23)$$

In the NIST program, the speed-of-sound ratios were determined using the spherical, stainless steel shell that had been used to acoustically redetermine the universal gas constant R . This shell had a 2-cm-thick wall bounding a spherical cavity with a radius of 9 cm. A schematic drawing of the shell appears in Figure 10.9. We measured the frequencies $f_\mu(T)$ of the microwave resonances of the cavity while it was evacuated to deduce the thermal expansion of the cavity. (Here, the subscripts α and μ distinguish acoustic frequencies from microwave frequencies.) We also measured, as a function of the temperature and the pressure, the resonance frequencies $f_\alpha(p, T)$ of the radially symmetric acoustic modes of the cavity while it was filled with argon. To deduce $u^2(p, T)$, the acoustic frequencies were combined with the volume of the resonator at T_w from [2] and the thermal expansion deduced from $f_\mu(T)$. To obtain zero-pressure ratios of $u^2(p, T)/u^2(p, T_w)$, the values of $u^2(p, T)$ on each isotherm were fitted by the virial expansion Eq. 10.3 with an additional term proportional to p^{-1} that accounted for a mean free-path effect at low pressures.

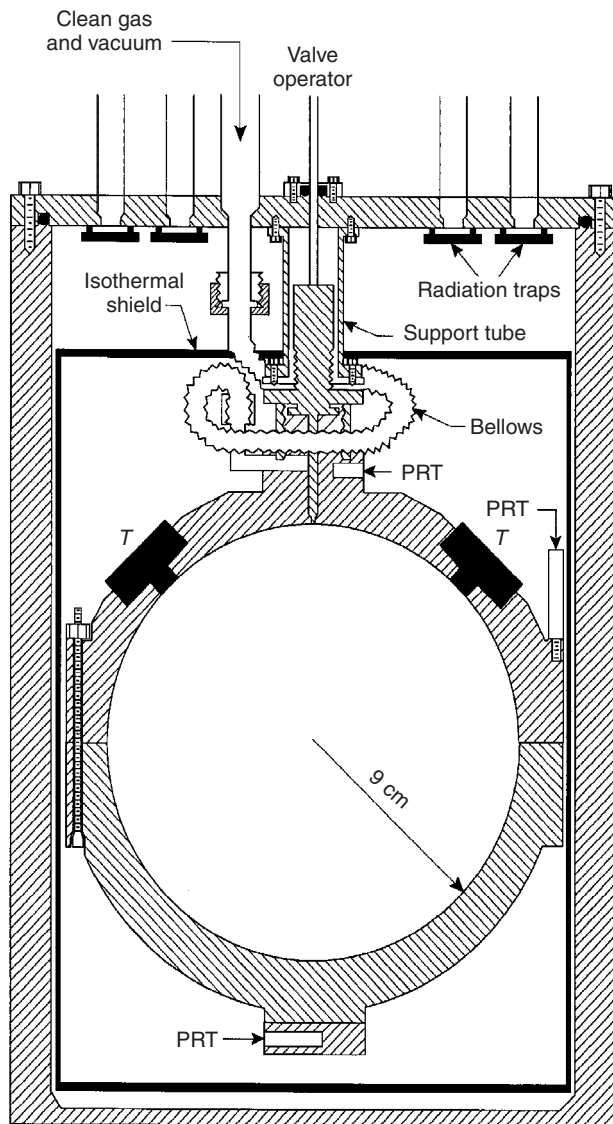


FIG. 10.9. Schematic cross section of the resonator used to measure the universal gas constant R and the difference between the international temperature scale ITS-90 and the Kelvin thermodynamic temperature. The resonator is shown within a pressure vessel. The pressure vessel was immersed in a stirred, thermostated bath that is not shown. The transducers are denoted "T" and the platinum resistance thermometers are denoted "PRT."

The Kelvin thermodynamic temperature was determined approximately from the measured quantities by

$$\frac{T}{273.16 \text{ K}} = \left(\frac{\langle f_\mu(T_w) + \Delta f_\mu(T_w) \rangle}{\langle f_\mu(T) + \Delta f_\mu(T) \rangle} \right)^2 \times \lim_{p \rightarrow 0} \left(\frac{f_\alpha(p, T) + \Delta f_\alpha(p, T)}{f_\alpha(p, T_w) + \Delta f_\alpha(p, T_w)} \right)^2 \quad (10.24)$$

Because there are no radially symmetric microwave modes, it was necessary to use appropriately weighted averages of the microwave frequencies; this is indicated by the brackets “ $\langle \dots \rangle$ ” in Eq. 10.24 [9]. (Partially resolved triplets of microwave modes were used.) In Eq. 10.24, the terms $\Delta f_\alpha(p, T)$ and $\Delta f_\mu(T)$ represent small corrections that must be applied to the acoustic and microwave frequencies, respectively. For the acoustic frequencies, these corrections depend on the thermal conductivity of the argon and the mechanical response of the shell to the acoustic pressure, as discussed in Section 10.3.1 in connection with other acoustic resonators. For the microwave frequencies, the electrical resistivity of the stainless steel shell was needed to account for the penetration of the microwave fields into a thin layer of metal at the inner boundary of the resonator. The microwave penetration length δ_μ is analogous to the thermal and viscous lengths δ_t and δ_v insofar as it leads to a Q for the microwave modes on the order of (radius of resonator)/ δ_μ and a fractional frequency shift on the order of Q^{-1} .

The derivation of Eq. 10.24 requires that the same acoustic and microwave modes be used for the frequency measurements at the temperatures T and T_w and that the gas has the same value of γ at both temperatures. Maintaining the purity of the argon was a major concern and is discussed in [3]. As implied by the absence of the resonator's dimensions and eigenvalues in Eq. 10.24, and as emphasized by Mehl and Moldover [27], the spherical cavity plays a limited role in measuring u/c , the ratio of the speed of sound in a monatomic gas to the speed of microwaves (light). One may view the cavity as a temporary artifact that must remain dimensionally stable just long enough to measure $f_\alpha(p)$ and $\langle f_\mu \rangle$ at the temperature T and that must not change its shape too much when the frequency measurements are repeated at T_w .

10.5.2 Why Spherical Resonators?

For thermometry, we require speed-of-sound measurements of the highest possible precision. To meet this requirement, the radially symmetric acoustic modes within a spherical cavity have several advantages compared with the acoustic modes of other cavities, including those of more easily manufactured cylindrical cavities.

For radially symmetric acoustic oscillations in a spherical cavity, the gas's motion is perpendicular to the shell everywhere; thus, it is not subject to

viscous damping where the gas contacts the shell. The small surface-to-volume ratio of the spherical shell leads to the smallest possible thermal dissipation in the thermal boundary layer. The absence of viscous losses and the small thermal losses lead to higher Q s and correspondingly higher signal-to-noise ratios. The latter permits measurements at lower pressures, thereby reducing the uncertainties in extrapolating $u^2(p, T)$ to zero pressure.

The high Q s of the radially symmetric modes permit the use of small transducers embedded in the shell. The transducers were selected because they had a very small effective volume that produced only weak perturbations to the measured frequencies.

For the radially symmetric modes, the frequency perturbation from the thermal boundary layer is as small as possible for a resonator of a given volume. Thus, the dependence of the measured frequencies (and the temperatures deduced from them) on the thermal conductivity is as small as possible. For the NIST resonator, a 0.3% uncertainty in the thermal conductivity of argon propagates into a 0.2 mK uncertainty in the temperatures determined in the range 216 to 303° K. This uncertainty is a fraction of the overall standard uncertainty of the results: 0.6 mK.

As mentioned in Section 10.3.1, the coupling of the motion of the gas to the motion of the shell leads to pressure-dependent frequency perturbations. In comparison with other geometries, these perturbations are smallest for spherical shells. Also, they have been modeled quantitatively.

10.5.3 Measurements of the Thermodynamic Temperature

In the NIST acoustic thermometry (and in the acoustic redetermination of R discussed in Section 10.6), five nondegenerate acoustic modes spanning the frequency range 2.5–9.5 kHz were used. Also, three microwave triplets spanning the frequency range 1.5–5.0 GHz were used. The redundant acoustic and microwave measurements helped determine some components of the uncertainty in measuring $(T - T_{90})$, the difference between the Kelvin thermodynamic temperature T and the temperature measured on ITS-90. The redundancy also tested the theories for the corrections $\Delta f_\alpha(T)$ and $\Delta f_\mu(T)$. We now consider, in turn, the measurements of the four variables that appear in Eq. 10.24: f_μ , f_α , T , and p .

The microwave resonances had quality factors of more than 5000. The values of $\langle f_\mu(T) \rangle$ could be determined with uncertainties of a few parts in 10^7 using off-the-shelf instruments and a relatively simple analysis program. The uncertainties of $\langle f_\mu(T) + \Delta f_\mu(T) \rangle$ made a negligible contribution to the uncertainty of $(T - T_{90})$.

For argon, the acoustic measurements were made on near to six isotherms: 217.0950, 234.3156, 253.1500, 273.1600, 293.1300, and 302.9166 K. These measurements spanned the density range 10–200 mol·m⁻³. At these densities,

the correction terms $\Delta f_\alpha(p, T)$ were small, and in some cases they tended to cancel out the ratios in Eq. 10.24. At low pressures, the contribution to $\Delta f_\alpha(p, T)$ from the thermal boundary layer in the argon where it contacts the shell grows as $p^{-1/2}$ and the signal-to-noise ratio for measuring $f_\alpha(T)$ declines as p^2 . At high pressures, the term in $\Delta f_\alpha(p, T)$ from the mechanical response of the shell to the acoustic pressure grows as p and the terms resulting from the nonideality of the argon grow as p , p^2 , *etc.* Thus, the argon data were taken over the limited range of intermediate densities where they were most useful for determining $(T - T_{90})$.

Three capsule-style standard platinum resistance thermometers were calibrated at the triple points of argon, mercury, water, and gallium and then installed in the resonator. The uncertainty of the thermometry resulted from the uncertainty of each calibration measurement and from drifts in the system (thermometers + resistance bridge + standard resistor) during the weeks between calibrations. ITS-90 is inherently nonunique because different platinum resistance thermometers meeting ITS-90 specifications will indicate different temperatures when they are compared at temperatures not used in their calibration [28]. In this work, the nonuniqueness of ITS-90 contributed an uncertainty of approximately 0.2 mK to the temperature measurements on the isotherms at 217, 253, and 293 K. An additional uncertainty resulted from the small temperature difference (≤ 0.5 mK) between the thermometers embedded in the top and in the bottom of the spherical shell. We estimate that our imperfect knowledge of the volume average of the temperature within the argon was less than 0.1 mK relative to the thermometer calibrations.

We used a calibrated, fused-quartz, bourdon tube gage to measure the pressure of the argon. On the isotherm at 303 K, the worst case, u^2 changes only 0.3% over the range of pressure spanned by the data. The uncertainty of the pressure measurement made a negligible contribution to the uncertainty of $(T - T_{90})$.

The analysis of the acoustic data is a complicated subject that is described in detail in [3]. Here, we emphasize the quality of the results, as illustrated in Figure 10.10. Note that all the fractional deviations of u^2 are within $\pm 4 \times 10^{-6}$. These results are approximately a factor of 10 more precise than those obtained with the cylindrical resonator (Fig. 10.1, bottom panel) and approximately a factor of 100 more precise than those obtained with the dumbbell-shaped Greenspan viscometer (Fig. 10.6).

With a few well-understood exceptions, $u^2(p, T)$ results obtained from resonance frequency measurements spanning a factor of 20 in pressure, a factor of 4 in frequency, and the temperature range $216 \text{ K} \leq T \leq 303 \text{ K}$, could all be represented with a relative standard deviation of only 1.1×10^{-6} . This representation had 11 parameters of which six were the determined thermodynamic temperatures. The other 5 parameters were used to represent the departures

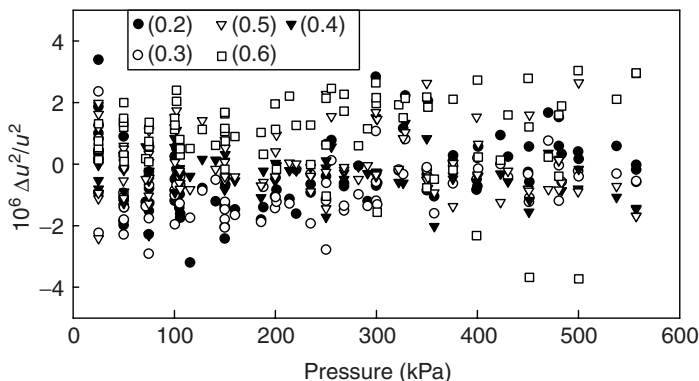


FIG. 10.10. Deviations of measurements of the speed of sound in argon from an augmented virial equation of state ($\Delta u^2 \equiv u_{\text{measured}}^2 - u_{\text{fitted}}^2$). The various symbols show the results for different radially symmetric acoustic modes, which are denoted (0,2), (0,3), etc.

of the acoustic virial coefficients $\beta_a(T)$ and $\gamma_a(T)$ in Eq. 10.3 from a model argon-argon potential.

The values of $(T - T_{90})$ ranged from (-3.6 ± 0.6) mK at 217 K to (4.6 ± 0.6) mK at 303 K. The resonator that was used at NIST to produce the data in Figure 10.10 has been remanufactured and is now being used to determine values of $(T - T_{90})$ up to 800 K. This study may lead to replacing ITS-90 with a new temperature scale based, in part, on speed-of-sound data. If that happens, the calibration of practical thermometers will be based on acoustic measurements and the nonuniqueness inherent in ITS-90 may be reduced.

10.6 Acoustic Determination of the Universal Gas Constant R

The most accurate measurement of the speed of sound ever made in a gas had a relative standard uncertainty of only 0.6×10^{-6} . This measurement (made at NIST) led to the value of the universal gas constant $R = (8.314\,472 \pm 0.000\,015) \text{ J} \cdot \text{mol}^{-1} \cdot \text{K}^{-1}$, which has a relative standard uncertainty of 1.7×10^{-6} and was internationally accepted in 1998 [1]. The physics underlying this acoustic redetermination of R is the same physics underlying the acoustic determination of the thermodynamic temperature; however, the redetermination of R had two additional complexities. First, only ratios of u^2 are needed to determine the temperature; however, an absolute measurement

of u^2 is required to determine R . Any absolute measurement of u^2 requires difficult dimensional measurements. Second, any monatomic gas may be used to determine the temperature; however, a gas of known molecular mass M must be used to determine R . The mass m of a single atom (of a known isotope) is extremely well known on a scale of atomic mass units; however, the uncertainty of the average value of m for any pure gas is much larger because of the uncertainties of the relative isotopic abundances and the uncertainty of the Avogadro constant N_A . (The Avogadro constant relates the Boltzmann constant to the gas constant $R = N_A k_B$ and it relates the molecular mass to the molar mass $M = N_A m$.)

Equations 10.22 imply that a measurement of the speed of sound in a dilute, monatomic gas at the temperature T_w (which, by definition, is exactly 273.16 K) will determine R through the relations

$$R = N_A k_B = \frac{m N_A}{T_w} \lim_{p \rightarrow 0} (u^2 / \gamma) = \frac{3M}{5T_w} \lim_{p \rightarrow 0} (f_m V^{1/3} / z_m)^2 \quad (10.25)$$

To obtain the last equality of Eq. 10.25, we replaced γ with its zero-pressure limit 5/3 for the monatomic gases, and we replaced u with $(f_m V^{1/3} / z_m)$, where z_m is the exactly known eigenvalue associated with the radially symmetric mode of a gas in a perfect spherical shell of volume V , and f_m is the unperturbed resonance frequency of that mode.

The eigenvalues z_m have a very weak sensitivity to smooth departures from a perfect spherical geometry, provided that the departures do not change the volume. For acoustic measurements, this symmetry is discussed in [4] and [29]; for microwave measurements, a detailed discussion appears in [27]. This symmetry allowed NIST to use careful weighing in place of very difficult and less accurate measurements of the internal dimensions of the assembled spherical shell.

The NIST redetermination of R used a spherical shell assembled from two hemispherical parts that had been manufactured in NIST's machine shop. The shell had departures from sphericity on the order of a few parts in 10^4 . The volume of the shell was determined by weighing the mercury required to fill it and by using the known density of that lot of mercury. The weighing was done with a relative standard uncertainty of 0.3×10^{-6} at ambient temperature; however, the uncertainty of $V^{2/3}$ at T_w was larger (0.7×10^{-6}) because of the uncertainty of the integrated thermal expansion of the mercury between ambient temperature and T_w .

Commercially purchased argon gas was used for the measurements; however, the relative abundances of the isotopes Ar^{36} , Ar^{38} , and Ar^{40} were not

known accurately enough to calculate the mean molar mass M . Instead, a small sample of isotopically enriched Ar^{40} was purchased and chemically purified and then used as a standard for M . The spherical acoustic resonator was used to compare the speed of sound in this standard to the speed of sound in the commercial argon used for the main measurements. The relative standard uncertainty of the comparisons was 0.2×10^{-6} of u and it contributed a relative standard uncertainty of 0.4×10^{-6} to the value of R .

As in the case of acoustic thermometry, a significant contribution to the uncertainty of R (0.7×10^{-6}) resulted from the multiparameter fits used to extrapolate the speed-of-sound data to zero pressure. A smaller uncertainty resulted from the uncertainty of the thermal conductivity of argon. The thermal conductivity was needed to correct the resonance frequencies for the thermal boundary layer.

Today, the constants R and k_B are best known from acoustic measurements. They appear in relationships connecting energy to temperature. For example, the power per unit area radiated by a black body is $\pi^2(k_B T)^4 / (60\hbar^3 c^2)$, where c is the speed of light and $2\pi\hbar$ is Planck's constant. Thus, one can use the acoustically established value of k_B and a measurement of the power radiated to determine the temperature of the radiator.

10.7 Concluding Remarks

We have described gas-filled acoustic resonators with four different shapes (1) cylindrical, (2) dumbbell, (3) spherical, and (4) cylindrical with an internal honeycomb of parallel ducts. These resonators compose a tool kit for accurately measuring the thermophysical properties of pure gases and gas mixtures. To use these tools effectively, we used model intermolecular potentials to obtain thermodynamic properties from the resonance frequency data. In the future, we will also use model intermolecular potentials to obtain transport properties from the halfwidth's of the resonances. The model intermolecular potentials obtained by simultaneously fitting virial coefficients and transport properties will permit reliable calculations of the thermophysical properties of gases beyond the temperature range of the acoustic data.

We have used our resonance frequency measurements to determine the ideal-gas heat capacity and the parameters in model intermolecular potentials for more than 20 gases. From these model potentials, we have computed and tabulated the density virial coefficients and the acoustic virial coefficients. The tables include the ideal-gas heat capacity; thus, they can be used to calculate any thermodynamic property of the gases. We plan to add the viscosity and the thermal conductivity to this database, and we plan to extend the database to include most of the gases for which industry requires accurate values of thermophysical properties.

10.8 Preface to Tables

The following tables contain the thermodynamic properties of 24 gases. For each gas, we provide ideal-gas heat capacities, density virial coefficients, and acoustic virial coefficients. The units for each property are shown in the heading of each column. The tabulated values should be multiplied by the power of 10 given in parentheses immediately following the value. Thus, $-6.674(-4)$ is to be understood as -6.674×10^{-4} .

All of the virial coefficients were computed from model intermolecular potential functions containing parameters that were fitted to speed-of-sound data. The temperature span of each table corresponds to the temperature span of the underlying acoustic data. Each table includes the maximum pressure of the acoustic data and a reference to a publication containing the acoustic data. The tables are ordered by the area of the industrial application.

For modeling vapor-compression refrigerators, we present data for 3 ethers, 11 partially halogenated hydrocarbons, and methane. For these gases, the chemical formulas and the refrigeration industry's abbreviation (in parentheses) are $\text{CF}_3\text{-O-CF}_2\text{H}$ (E125), $\text{CHF}_2\text{-O-CHF}_2$ (E134), $\text{CF}_3\text{CH}_2\text{-O-CHF}_2$ (E245), CCl_2HCF_3 (R123), CHFCl-CF_3 (R124), C_2HF_5 (R125), $\text{CF}_3\text{-CH}_2\text{F}$ (R134a), $\text{CFCl}_2\text{-CH}_3$ (R141b), $\text{CF}_2\text{-CH}_3$ (R143a), $\text{CHF}_2\text{-CH}_3$ (R152a), $\text{CF}_3\text{-CHF-CHF}_2$ (R236ea), $\text{CF}_3\text{-CH}_2\text{-CF}_3$ (R236fa), $\text{CHF}_2\text{-CF}_2\text{-CH}_2\text{F}$ (R245ca), $\text{CHF}_2\text{-CF}_2\text{-CF}_2\text{-CH}_2\text{F}$ (R338mccq), and CH_4 (R50).

For calibrating mass flow controllers used in the semiconductor processing industry and for process modeling, we present data for three surrogate gases — CF_4 , C_2F_6 , and SF_6 — and data for three process gases — WF_6 , HBr , and BCl_3 .

The data for three noble gases — Xe , He , and Ar — may be useful for modeling thermoacoustic machinery and carrier gases used in semiconductor processing.

The uncertainty of the tabulated values of C_p^0 is on the order of 0.1%. It is difficult to provide a statement of the uncertainty of densities calculated from the acoustically derived virial coefficients that is both concise and accurate. Instructive examples are provided in [8]. In one example, the acoustic data for pentafluoroethane (R125) in the ranges $0.71 < T/T_c < 1.18$ and $0.05 < p/\text{MPa} < 1$ was analyzed. ($T_c = 339 \text{ K}$ is the critical temperature.) The resulting densities were all within 0.07% of independently measured values of the density at pressures up to the lesser of 1 MPa or 80% of the vapour pressure. Larger density differences occurred very close to the vapour pressure curve. See [8] for examples in different temperature and pressure ranges.

The tabulated values of the acoustic virial coefficients can be used to calculate the speed of sound from which they were derived with uncertainties on the order of 0.01%.

Name: pentafluorodimethyl ether (CAS # 3822-68-2)
 Formula: $\text{CF}_3-\text{O}-\text{CF}_2\text{H}$
 M.W.: 0.13602 kg/mol
 Max. Pressure: 1000 kPa
 Reference: Hurlly, J.J., Schmidt, J.W., Gillis, K.A. (1997). Virial equation of state and ideal-gas heat capacities of pentafluoro-dimethyl ether. *Int. J. Thermophys.* **18**: 137–159.

T (K)	$C_p^0(T)/R$	$B(T)$ ($\text{m}^3 \cdot \text{mol}^{-1}$)	$C(T)$ ($\text{m}^6 \cdot \text{mol}^{-2}$)	$D(T)$ ($\text{m}^9 \cdot \text{mol}^{-3}$)	$\beta_a(T)$ ($\text{m}^3 \cdot \text{mol}^{-1}$)	$\gamma_a(T)$ ($\text{m}^3 \cdot \text{mol}^{-1} \cdot \text{Pa}^{-1}$)	$\delta_a(T)$ ($\text{m}^3 \cdot \text{mol}^{-1} \cdot \text{Pa}^{-2}$)
260	11.645	-6.674(-4)	2.090(-9)	-1.34(-10)	-1.066(-3)	-2.59(-10)	-2.3(-16)
265	11.780	-6.358(-4)	1.621(-8)	-1.11(-10)	-1.019(-3)	-2.21(-10)	-1.8(-16)
270	11.915	-6.063(-4)	2.639(-8)	-9.25(-11)	-9.748(-4)	-1.90(-10)	-1.4(-16)
275	12.050	-5.788(-4)	3.357(-8)	-7.68(-11)	-9.331(-4)	-1.64(-10)	-1.1(-16)
280	12.183	-5.531(-4)	3.848(-8)	-6.37(-11)	-8.940(-4)	-1.42(-10)	-9.1(-17)
285	12.316	-5.290(-4)	4.168(-8)	-5.27(-11)	-8.571(-4)	-1.23(-10)	-7.3(-17)
290	12.448	-5.063(-4)	4.358(-8)	-4.35(-11)	-8.223(-4)	-1.07(-10)	-5.9(-17)
295	12.579	-4.850(-4)	4.451(-8)	-3.59(-11)	-7.894(-4)	-9.40(-11)	-4.7(-17)
300	12.709	-4.650(-4)	4.472(-8)	-2.94(-11)	-7.583(-4)	-8.23(-11)	-3.8(-17)
305	12.838	-4.461(-4)	4.440(-8)	-2.40(-11)	-7.289(-4)	-7.23(-11)	-3.0(-17)
310	12.967	-4.283(-4)	4.370(-8)	-1.94(-11)	-7.010(-4)	-6.36(-11)	-2.4(-17)
315	13.094	-4.114(-4)	4.273(-8)	-1.56(-11)	-6.745(-4)	-5.60(-11)	-1.9(-17)
320	13.221	-3.954(-4)	4.158(-8)	-1.24(-11)	-6.493(-4)	-4.94(-11)	-1.5(-17)
325	13.346	-3.803(-4)	4.031(-8)	-9.67(-12)	-6.253(-4)	-4.35(-11)	-1.2(-17)
330	13.471	-3.659(-4)	3.898(-8)	-7.38(-12)	-6.025(-4)	-3.84(-11)	-9.5(-18)
335	13.594	-3.523(-4)	3.762(-8)	-5.47(-12)	-5.807(-4)	-3.38(-11)	-7.3(-18)
340	13.716	-3.393(-4)	3.626(-8)	-3.86(-12)	-5.600(-4)	-2.97(-11)	-5.6(-18)
345	13.838	-3.270(-4)	3.492(-8)	-2.51(-12)	-5.401(-4)	-2.61(-11)	-4.1(-18)
350	13.958	-3.152(-4)	3.363(-8)	-1.38(-12)	-5.212(-4)	-2.29(-11)	-3.0(-18)
355	14.077	-3.040(-4)	3.238(-8)	-4.43(-13)	-5.030(-4)	-2.00(-11)	-2.0(-18)
360	14.194	-2.933(-4)	3.118(-8)	3.37(-13)	-4.856(-4)	-1.73(-11)	-1.2(-18)
365	14.311	-2.831(-4)	3.005(-8)	9.82(-13)	-4.690(-4)	-1.50(-11)	-5.8(-19)
370	14.426	-2.733(-4)	2.899(-8)	1.51(-12)	-4.530(-4)	-1.28(-11)	-6.6(-20)
375	14.541	-2.639(-4)	2.799(-8)	1.94(-12)	-4.376(-4)	-1.09(-11)	3.5(-19)
380	14.653	-2.550(-4)	2.705(-8)	2.29(-12)	-4.229(-4)	-9.11(-12)	6.9(-19)
385	14.765	-2.464(-4)	2.618(-8)	2.57(-12)	-4.087(-4)	-7.49(-12)	9.5(-19)
390	14.875	-2.381(-4)	2.537(-8)	2.79(-12)	-3.951(-4)	-6.01(-12)	1.2(-18)
395	14.984	-2.302(-4)	2.463(-8)	2.96(-12)	-3.819(-4)	-4.65(-12)	1.3(-18)
400	15.091	-2.226(-4)	2.394(-8)	3.09(-12)	-3.693(-4)	-3.41(-12)	1.5(-18)

Name: tetrafluorodimethyl ether (CAS # 1691-17-4)
 Formula: $\text{CHF}_2-\text{O}-\text{CHF}_2$
 M.W.: 0.118031 kg/mol
 Max. Pressure: 90 kPa
 Reference: Gillis, K.A. (1994). Thermodynamic properties of two halogenated ethers from speed-of-sound measurements: Difluoromethoxy-difluoromethane and 2-difluoromethoxy-1,1,1-trifluoroethane. *Int. J. Thermophys.* **15**: 821–847.

T (K)	$C_p^0(T)/R$	$B(T)$ ($\text{m}^3 \cdot \text{mol}^{-1}$)	$C(T)$ ($\text{m}^6 \cdot \text{mol}^{-2}$)	$D(T)$ ($\text{m}^9 \cdot \text{mol}^{-3}$)	$\beta_a(T)$ ($\text{m}^3 \cdot \text{mol}^{-1}$)	$\gamma_a(T)$ ($\text{m}^3 \cdot \text{mol}^{-1} \cdot \text{Pa}^{-1}$)	$\delta_a(T)$ ($\text{m}^3 \cdot \text{mol}^{-1} \cdot \text{Pa}^{-2}$)
255	10.482	-1.229(-3)	—	—	-1.826(-3)	-1.05(-9)	-1.3(-15)
260	10.672	-1.156(-3)	—	—	-1.731(-3)	-8.57(-10)	-9.6(-16)
265	10.852	-1.089(-3)	—	—	-1.644(-3)	-7.08(-10)	-7.4(-16)
270	11.022	-1.028(-3)	—	—	-1.563(-3)	-5.89(-10)	-5.7(-16)
275	11.184	-9.726(-4)	—	—	-1.488(-3)	-4.93(-10)	-4.4(-16)
280	11.338	-9.213(-4)	—	—	-1.418(-3)	-4.15(-10)	-3.4(-16)
285	11.483	-8.741(-4)	—	—	-1.353(-3)	-3.52(-10)	-2.7(-16)
290	11.622	-8.305(-4)	—	—	-1.293(-3)	-3.00(-10)	-2.2(-16)
295	11.753	-7.902(-4)	—	—	-1.236(-3)	-3.66(-10)	-2.4(-16)

T (K)	$C_p^0(T)/R$	$B(T)$ ($\text{m}^3 \cdot \text{mol}^{-1}$)	$C(T)$ ($\text{m}^6 \cdot \text{mol}^{-2}$)	$D(T)$ ($\text{m}^9 \cdot \text{mol}^{-3}$)	$\beta_a(T)$ ($\text{m}^3 \cdot \text{mol}^{-1}$)	$\gamma_a(T)$ ($\text{m}^3 \cdot \text{mol}^{-1} \cdot \text{Pa}^{-1}$)	$\delta_a(T)$ ($\text{m}^3 \cdot \text{mol}^{-1} \cdot \text{Pa}^{-2}$)
300	11.879	-7.528(-4)	—	—	-1.183(-3)	-3.29(-10)	-2.0(-16)
305	11.998	-7.182(-4)	—	—	-1.134(-3)	-2.96(-10)	-1.7(-16)
310	12.113	-6.859(-4)	—	—	-1.087(-3)	-2.67(-10)	-1.5(-16)
315	12.222	-6.559(-4)	—	—	-1.044(-3)	-2.42(-10)	-1.2(-16)
320	12.328	-6.278(-4)	—	—	-1.003(-3)	-2.19(-10)	-1.1(-16)
325	12.429	-6.016(-4)	—	—	-9.641(-4)	-1.99(-10)	-9.1(-17)
330	12.527	-5.770(-4)	—	—	-9.277(-4)	-1.81(-10)	-7.8(-17)
335	12.622	-5.540(-4)	—	—	-8.934(-4)	-1.65(-10)	-6.7(-17)
340	12.716	-5.323(-4)	—	—	-8.610(-4)	-1.51(-10)	-5.8(-17)
345	12.807	-5.120(-4)	—	—	-8.304(-4)	-1.38(-10)	-5.0(-17)
350	12.897	-4.928(-4)	—	—	-8.015(-4)	-1.27(-10)	-4.4(-17)
355	12.986	-4.747(-4)	—	—	-7.741(-4)	-1.16(-10)	-3.8(-17)
360	13.075	-4.577(-4)	—	—	-7.481(-4)	-1.07(-10)	-3.3(-17)
365	13.164	-4.415(-4)	—	—	-7.235(-4)	-9.86(-11)	-2.9(-17)
370	13.254	-4.263(-4)	—	—	-7.001(-4)	-9.10(-11)	-2.6(-17)
374	13.327	-4.146(-4)	—	—	-6.822(-4)	-8.54(-11)	-2.3(-17)

Name: 2-(difluoromethoxy)-1,1,1-trifluoroethane (CAS # 1885-48-9)

Formula: $\text{CF}_3\text{CH}_2\text{O}-\text{CHF}_2$

M.W. 0.150048 kg/mol

Max. Pressure: 50 kPa

Reference: Gillis, K.A. (1994). Thermodynamic properties of two halogenated ethers from speed-of-sound measurements: Difluoromethoxy-difluoromethane and 2-difluoromethoxy-1,1,1-trifluoroethane. *Int. J. Thermophys.* **15**: 821–847.

T (K)	$C_p^0(T)/R$	$B(T)$ ($\text{m}^3 \cdot \text{mol}^{-1}$)	$C(T)$ ($\text{m}^6 \cdot \text{mol}^{-2}$)	$D(T)$ ($\text{m}^9 \cdot \text{mol}^{-3}$)	$\beta_a(T)$ ($\text{m}^3 \cdot \text{mol}^{-1}$)	$\gamma_a(T)$ ($\text{m}^3 \cdot \text{mol}^{-1} \cdot \text{Pa}^{-1}$)	$\delta_a(T)$ ($\text{m}^3 \cdot \text{mol}^{-1} \cdot \text{Pa}^{-2}$)
278	15.395	-1.499(-3)	—	—	-2.430(-3)	-1.42(-9)	-1.9(-15)
280	15.474	-1.464(-3)	—	—	-2.379(-3)	-1.35(-9)	-1.8(-15)
285	15.670	-1.383(-3)	—	—	-2.259(-3)	-1.20(-9)	-1.4(-15)
290	15.864	-1.309(-3)	—	—	-2.149(-3)	-1.06(-9)	-1.2(-15)
295	16.054	-1.241(-3)	—	—	-2.046(-3)	-9.46(-10)	-9.9(-16)
300	16.242	-1.178(-3)	—	—	-1.952(-3)	-8.45(-10)	-8.2(-16)
305	16.427	-1.120(-3)	—	—	-1.864(-3)	-7.57(-10)	-6.9(-16)
310	16.610	-1.066(-3)	—	—	-1.782(-3)	-6.80(-10)	-5.8(-16)
315	16.789	-1.017(-3)	—	—	-1.706(-3)	-6.13(-10)	-4.9(-16)
320	16.966	-9.706(-4)	—	—	-1.635(-3)	-5.53(-10)	-4.1(-16)
325	17.141	-9.278(-4)	—	—	-1.568(-3)	-5.01(-10)	-3.5(-16)
330	17.312	-8.880(-4)	—	—	-1.506(-3)	-4.55(-10)	-3.0(-16)
335	17.481	-8.509(-4)	—	—	-1.448(-3)	-4.14(-10)	-2.6(-16)
340	17.647	-8.162(-4)	—	—	-1.393(-3)	-3.77(-10)	-2.2(-16)
345	17.810	-7.837(-4)	—	—	-1.342(-3)	-3.44(-10)	-1.9(-16)
350	17.971	-7.533(-4)	—	—	-1.294(-3)	-3.15(-10)	-1.7(-16)
355	18.129	-7.247(-4)	—	—	-1.248(-3)	-2.89(-10)	-1.4(-16)
360	18.284	-6.979(-4)	—	—	-1.205(-3)	-2.66(-10)	-1.3(-16)
365	18.436	-6.726(-4)	—	—	-1.164(-3)	-2.44(-10)	-1.1(-16)
370	18.586	-6.489(-4)	—	—	-1.126(-3)	-2.25(-10)	-9.6(-17)
375	18.733	-6.264(-4)	—	—	-1.090(-3)	-2.08(-10)	-8.4(-17)
380	18.877	-6.052(-4)	—	—	-1.055(-3)	-1.92(-10)	-7.4(-17)
384	18.991	-5.891(-4)	—	—	-1.029(-3)	-1.81(-10)	-6.7(-17)

Name: 2,2-dichloro-1,1,1-trifluoroethane (CAS # 306-83-2)
 Formula: $\text{CCl}_2\text{-HCF}_3$
 M.W. 0.15293 kg/mol
 Max. Pressure: 80 kPa
 Reference: Goodwin, A.R.H., and Moldover, M.R. (1991). Thermophysical properties of gaseous refrigerants from speed-of-sound measurements, III: Results for 1,1-dichloro-2,2,2-trifluoroethane ($\text{CHCl}_2\text{-CF}_3$) and 1,2-dichloro-1,2,2-trifluoroethane (CHClF-CClF_2). *J. Chem. Phys.* **95**: 5236–5242.

T (K)	$C_p^0(T)/R$	$B(T)$ ($\text{m}^3 \cdot \text{mol}^{-1}$)	$C(T)$ ($\text{m}^6 \cdot \text{mol}^{-2}$)	$D(T)$ ($\text{m}^9 \cdot \text{mol}^{-3}$)	$\beta_a(T)$ ($\text{m}^3 \cdot \text{mol}^{-1}$)	$\gamma_a(T)$ ($\text{m}^3 \cdot \text{mol}^{-1} \cdot \text{Pa}^{-1}$)	$\delta_a(T)$ ($\text{m}^3 \cdot \text{mol}^{-1} \cdot \text{Pa}^{-2}$)
260	11.410	-1.518(-3)	-1.099(-6)	—	-2.373(-3)	-2.23(-9)	-3.3(-15)
265	11.541	-1.440(-3)	-8.814(-7)	—	-2.261(-3)	-1.90(-9)	-2.6(-15)
270	11.670	-1.367(-3)	-7.057(-7)	—	-2.156(-3)	-1.62(-9)	-2.1(-15)
275	11.796	-1.300(-3)	-5.634(-7)	—	-2.059(-3)	-1.40(-9)	-1.7(-15)
280	11.920	-1.238(-3)	-4.479(-7)	—	-1.969(-3)	-1.20(-9)	-1.3(-15)
285	12.042	-1.180(-3)	-3.539(-7)	—	-1.884(-3)	-1.04(-9)	-1.1(-15)
290	12.161	-1.126(-3)	-2.772(-7)	—	-1.805(-3)	-9.05(-10)	-8.7(-16)
295	12.278	-1.076(-3)	-2.145(-7)	—	-1.730(-3)	-7.89(-10)	-7.0(-16)
300	12.393	-1.030(-3)	-1.632(-7)	—	-1.661(-3)	-6.90(-10)	-5.8(-16)
305	12.506	-9.859(-4)	-1.213(-7)	—	-1.595(-3)	-6.05(-10)	-4.7(-16)
310	12.617	-9.450(-4)	-8.690(-8)	—	-1.533(-3)	-5.32(-10)	-3.9(-16)
315	12.725	-9.066(-4)	-5.876(-8)	—	-1.475(-3)	-4.69(-10)	-3.2(-16)
320	12.831	-8.705(-4)	-3.574(-8)	—	-1.420(-3)	-4.14(-10)	-2.7(-16)
325	12.935	-8.366(-4)	-1.694(-8)	—	-1.368(-3)	-3.67(-10)	-2.2(-16)
330	13.037	-8.046(-4)	-1.614(-9)	—	-1.318(-3)	-3.25(-10)	-1.8(-16)
335	13.316	-7.744(-4)	-1.084(-8)	—	-1.272(-3)	-2.89(-10)	-1.5(-16)

Name: 1-chloro-1,2,2,2-tetrafluoroethane (CAS # 2837-89-0)
 Formula: CHFCl-CF_3
 M.W. 0.136477 kg/mol
 Max. Pressure: 900 kPa
 Reference: Gillis, K.A. (1997). Thermodynamic properties of seven gaseous halo-genated hydrocarbons from acoustic measurements: CHClFCF_3 , CHF_2CF_3 , CF_3CH_3 , CHF_2CH_3 , $\text{CF}_3\text{CHFCHF}_2$, $\text{CF}_3\text{CH}_2\text{CF}_3$ and $\text{CHF}_2\text{CF}_2\text{CH}_2\text{F}$. *Int. J. Thermophys.* **18**: 73–135.

T (K)	$C_p^0(T)/R$	$B(T)$ ($\text{m}^3 \cdot \text{mol}^{-1}$)	$C(T)$ ($\text{m}^6 \cdot \text{mol}^{-2}$)	$D(T)$ ($\text{m}^9 \cdot \text{mol}^{-3}$)	$\beta_a(T)$ ($\text{m}^3 \cdot \text{mol}^{-1}$)	$\gamma_a(T)$ ($\text{m}^3 \cdot \text{mol}^{-1} \cdot \text{Pa}^{-1}$)	$\delta_a(T)$ ($\text{m}^3 \cdot \text{mol}^{-1} \cdot \text{Pa}^{-2}$)
250	10.664	-9.906(-4)	-8.375(-9)	—	-1.537(-3)	-6.61(-10)	-6.4(-16)
255	10.791	-9.395(-4)	-9.785(-10)	—	-1.465(-3)	-5.79(-10)	-5.2(-16)
260	10.916	-8.924(-4)	5.278(-9)	—	-1.398(-3)	-5.08(-10)	-4.2(-16)
265	11.040	-8.487(-4)	1.057(-8)	—	-1.335(-3)	-4.47(-10)	-3.4(-16)
270	11.163	-8.083(-4)	1.504(-8)	—	-1.276(-3)	-3.94(-10)	-2.8(-16)
275	11.285	-7.708(-4)	1.880(-8)	—	-1.222(-3)	-3.48(-10)	-2.3(-16)
280	11.406	-7.358(-4)	2.198(-8)	—	-1.171(-3)	-3.08(-10)	-1.9(-16)
285	11.526	-7.032(-4)	2.464(-8)	—	-1.123(-3)	-2.73(-10)	-1.6(-16)
290	11.645	-6.727(-4)	2.686(-8)	—	-1.077(-3)	-2.42(-10)	-1.3(-16)
295	11.762	-6.442(-4)	2.871(-8)	—	-1.035(-3)	-2.15(-10)	-1.1(-16)
300	11.879	-6.175(-4)	3.023(-8)	—	-9.949(-4)	-1.91(-10)	-9.0(-17)
305	11.995	-5.924(-4)	3.148(-8)	—	-9.571(-4)	-1.70(-10)	-7.5(-17)
310	12.109	-5.688(-4)	3.250(-8)	—	-9.214(-4)	-1.51(-10)	-6.2(-17)
315	12.223	-5.466(-4)	3.331(-8)	—	-8.876(-4)	-1.35(-10)	-5.2(-17)
320	12.335	-5.256(-4)	3.394(-8)	—	-8.556(-4)	-1.20(-10)	-4.3(-17)
325	12.446	-5.058(-4)	3.442(-8)	—	-8.252(-4)	-1.07(-10)	-3.6(-17)
330	12.557	-4.871(-4)	3.477(-8)	—	-7.963(-4)	-9.52(-11)	-3.0(-17)
335	12.666	-4.694(-4)	3.501(-8)	—	-7.689(-4)	-8.48(-11)	-2.5(-17)
340	12.774	-4.526(-4)	3.515(-8)	—	-7.428(-4)	-7.54(-11)	-2.1(-17)
345	12.881	-4.367(-4)	3.522(-8)	—	-7.180(-4)	-6.71(-11)	-1.7(-17)

T (K)	$C_p^0(T)/R$	$B(T)$ ($\text{m}^3 \cdot \text{mol}^{-1}$)	$C(T)$ ($\text{m}^6 \cdot \text{mol}^{-2}$)	$D(T)$ ($\text{m}^9 \cdot \text{mol}^{-3}$)	$\beta_a(T)$ ($\text{m}^3 \cdot \text{mol}^{-1}$)	$\gamma_a(T)$ ($\text{m}^3 \cdot \text{mol}^{-1} \cdot \text{Pa}^{-1}$)	$\delta_a(T)$ ($\text{m}^3 \cdot \text{mol}^{-1} \cdot \text{Pa}^{-2}$)
350	12.987	-4.216(-4)	3.521(-8)	—	-6.943(-4)	-5.96(-11)	-1.4(-17)
355	13.092	-4.072(-4)	3.514(-8)	—	-6.717(-4)	-5.29(-11)	-1.2(-17)
360	13.196	-3.935(-4)	3.501(-8)	—	-6.500(-4)	-4.69(-11)	-9.9(-18)
365	13.299	-3.804(-4)	3.485(-8)	—	-6.294(-4)	-4.14(-11)	-8.1(-18)
370	13.400	-3.680(-4)	3.465(-8)	—	-6.096(-4)	-3.65(-11)	-6.6(-18)
375	13.501	-3.561(-4)	3.441(-8)	—	-5.907(-4)	-3.21(-11)	-5.3(-18)
380	13.601	-3.448(-4)	3.415(-8)	—	-5.725(-4)	-3.20(-11)	-5.0(-18)
385	13.699	-3.339(-4)	3.387(-8)	—	-5.551(-4)	-2.81(-11)	-4.0(-18)
390	13.797	-3.236(-4)	3.357(-8)	—	-5.384(-4)	-2.46(-11)	-3.2(-18)
395	13.893	-3.136(-4)	3.326(-8)	—	-5.223(-4)	-2.14(-11)	-2.5(-18)
400	13.989	-3.041(-4)	3.294(-8)	—	-5.069(-4)	-1.86(-11)	-1.9(-18)

Name: pentafluoroethane (CAS # 354-33-6)
Formula: C_2HF_5
M.W. 0.12002 kg/mol
Max. Pressure: 1000 kPa
Reference: Gillis, K.A., and Moldover, M.R. (1996). Practical determination of gas densities from the speed of sound using square-well potentials. *Int. J. Thermophys.* **17**: 1305–1324.

T (K)	$C_p^0(T)/R$	$B(T)$ ($\text{m}^3 \cdot \text{mol}^{-1}$)	$C(T)$ ($\text{m}^6 \cdot \text{mol}^{-2}$)	$D(T)$ ($\text{m}^9 \cdot \text{mol}^{-3}$)	$\beta_a(T)$ ($\text{m}^3 \cdot \text{mol}^{-1}$)	$\gamma_a(T)$ ($\text{m}^3 \cdot \text{mol}^{-1} \cdot \text{Pa}^{-1}$)	$\delta_a(T)$ ($\text{m}^3 \cdot \text{mol}^{-1} \cdot \text{Pa}^{-2}$)
240	9.967	-6.330(-4)	-8.029(-8)	-1.35(-10)	-9.776(-4)	-2.88(-10)	-2.7(-16)
245	10.090	-6.011(-4)	-4.822(-8)	-1.12(-10)	-9.319(-4)	-2.40(-10)	-2.1(-16)
250	10.212	-5.715(-4)	-2.450(-8)	-9.31(-11)	-8.891(-4)	-2.01(-10)	-1.6(-16)
255	10.333	-5.440(-4)	-7.043(-9)	-7.74(-11)	-8.492(-4)	-1.69(-10)	-1.3(-16)
260	10.453	-5.184(-4)	5.710(-9)	-6.44(-11)	-8.117(-4)	-1.44(-10)	-1.0(-16)
265	10.573	-4.945(-4)	1.492(-8)	-5.37(-11)	-7.766(-4)	-1.22(-10)	-7.9(-17)
270	10.691	-4.722(-4)	2.145(-8)	-4.47(-11)	-7.435(-4)	-1.05(-10)	-6.3(-17)
275	10.810	-4.513(-4)	2.597(-8)	-3.73(-11)	-7.124(-4)	-9.00(-11)	-5.0(-17)
280	10.927	-4.317(-4)	2.896(-8)	-3.11(-11)	-6.830(-4)	-7.77(-11)	-4.0(-17)
285	11.044	-4.132(-4)	3.082(-8)	-2.59(-11)	-6.553(-4)	-6.73(-11)	-3.2(-17)
290	11.160	-3.959(-4)	3.183(-8)	-2.15(-11)	-6.291(-4)	-5.84(-11)	-2.5(-17)
295	11.275	-3.795(-4)	3.221(-8)	-1.79(-11)	-6.042(-4)	-5.09(-11)	-2.0(-17)
300	11.390	-3.641(-4)	3.212(-8)	-1.48(-11)	-5.807(-4)	-4.44(-11)	-1.6(-17)
305	11.504	-3.495(-4)	3.171(-8)	-1.22(-11)	-5.583(-4)	-3.88(-11)	-1.3(-17)
310	11.617	-3.357(-4)	3.105(-8)	-1.00(-11)	-5.370(-4)	-3.39(-11)	-1.0(-17)
315	11.730	-3.226(-4)	3.024(-8)	-8.19(-12)	-5.168(-4)	-2.97(-11)	-8.2(-18)
320	11.841	-3.102(-4)	2.932(-8)	-6.63(-12)	-4.975(-4)	-2.59(-11)	-6.5(-18)
325	11.952	-2.984(-4)	2.834(-8)	-5.32(-12)	-4.792(-4)	-2.27(-11)	-5.1(-18)
330	12.063	-2.872(-4)	2.733(-8)	-4.20(-12)	-4.616(-4)	-1.98(-11)	-3.9(-18)
335	12.173	-2.765(-4)	2.632(-8)	-3.27(-12)	-4.449(-4)	-1.72(-11)	-3.0(-18)
340	12.281	-2.664(-4)	2.532(-8)	-2.48(-12)	-4.288(-4)	-1.49(-11)	-2.2(-18)
345	12.390	-2.567(-4)	2.435(-8)	-1.81(-12)	-4.135(-4)	-1.29(-11)	-1.6(-18)
350	12.497	-2.474(-4)	2.341(-8)	-1.25(-12)	-3.988(-4)	-1.10(-11)	-1.1(-18)
355	12.604	-2.386(-4)	2.252(-8)	-7.74(-13)	-3.847(-4)	-9.36(-12)	-6.5(-19)
360	12.710	-2.301(-4)	2.168(-8)	-3.78(-13)	-3.712(-4)	-7.87(-12)	-3.1(-19)
365	12.816	-2.220(-4)	2.088(-8)	-4.77(-14)	-3.582(-4)	-6.51(-12)	-2.9(-20)
370	12.920	-2.143(-4)	2.013(-8)	2.28(-13)	-3.458(-4)	-5.28(-12)	2.0(-19)
375	13.024	-2.069(-4)	1.944(-8)	4.56(-13)	-3.338(-4)	-4.16(-12)	3.8(-19)
380	13.128	-1.997(-4)	1.879(-8)	6.44(-13)	-3.223(-4)	-3.14(-12)	5.2(-19)
385	13.230	-1.929(-4)	1.820(-8)	7.97(-13)	-3.112(-4)	-2.20(-12)	6.4(-19)
390	13.332	-1.863(-4)	1.765(-8)	9.22(-13)	-3.005(-4)	-1.34(-12)	7.3(-19)
395	13.433	-1.800(-4)	1.714(-8)	1.02(-12)	-2.901(-4)	-5.53(-13)	8.0(-19)
400	13.534	-1.739(-4)	1.668(-8)	1.10(-12)	-2.802(-4)	1.74(-13)	8.5(-19)

Name: 1,1,1,2-tetrafluoroethane (CAS # 811-97-2)
 Formula: $\text{CF}_3-\text{CH}_2\text{F}$
 M.W. 0.10203 kg/mol
 Max. Pressure: 600 kPa
 Reference: Gillis, K.A., and Moldover, M.R. (1996). Practical determination of gas densities from the speed of sound using square-well potentials. *Int. J. Thermophys.* **17**: 1305–1324.

T (K)	$C_p^0(T)/R$	$B(T)$ ($\text{m}^3 \cdot \text{mol}^{-1}$)	$C(T)$ ($\text{m}^6 \cdot \text{mol}^{-2}$)	$D(T)$ ($\text{m}^9 \cdot \text{mol}^{-3}$)	$\beta_a(T)$ ($\text{m}^3 \cdot \text{mol}^{-1}$)	$\gamma_a(T)$ ($\text{m}^3 \cdot \text{mol}^{-1} \cdot \text{Pa}^{-1}$)	$\delta_a(T)$ ($\text{m}^3 \cdot \text{mol}^{-1} \cdot \text{Pa}^{-2}$)
233	8.728	-1.013(-3)	4.006(-8)	—	-1.429(-3)	-6.39(-10)	-7.0(-16)
235	8.776	-9.863(-4)	3.908(-8)	—	-1.396(-3)	-6.01(-10)	-6.3(-16)
240	8.894	-9.238(-4)	3.681(-8)	—	-1.318(-3)	-5.17(-10)	-5.0(-16)
245	9.012	-8.673(-4)	3.482(-8)	—	-1.246(-3)	-4.46(-10)	-3.9(-16)
250	9.129	-8.158(-4)	3.310(-8)	—	-1.181(-3)	-3.87(-10)	-3.1(-16)
255	9.245	-7.690(-4)	3.163(-8)	—	-1.121(-3)	-3.36(-10)	-2.5(-16)
260	9.360	-7.261(-4)	3.040(-8)	—	-1.065(-3)	-2.93(-10)	-2.0(-16)
265	9.475	-6.868(-4)	2.937(-8)	—	-1.014(-3)	-2.56(-10)	-1.6(-16)
270	9.588	-6.507(-4)	2.853(-8)	—	-9.664(-4)	-2.24(-10)	-1.3(-16)
275	9.701	-6.174(-4)	2.786(-8)	—	-9.223(-4)	-1.96(-10)	-1.1(-16)
280	9.813	-5.867(-4)	2.734(-8)	—	-8.812(-4)	-1.72(-10)	-8.5(-17)
285	9.924	-5.583(-4)	2.695(-8)	—	-8.428(-4)	-1.51(-10)	-6.9(-17)
290	10.034	-5.319(-4)	2.669(-8)	—	-8.070(-4)	-1.33(-10)	-5.6(-17)
295	10.143	-5.074(-4)	2.653(-8)	—	-7.735(-4)	-1.16(-10)	-4.6(-17)
300	10.252	-4.846(-4)	2.646(-8)	—	-7.421(-4)	-1.02(-10)	-3.7(-17)
305	10.360	-4.634(-4)	2.648(-8)	—	-7.126(-4)	-8.95(-11)	-3.0(-17)
310	10.467	-4.435(-4)	2.657(-8)	—	-6.849(-4)	-7.83(-11)	-2.4(-17)
315	10.573	-4.249(-4)	2.672(-8)	—	-6.588(-4)	-6.83(-11)	-2.0(-17)
320	10.678	-4.075(-4)	2.693(-8)	—	-6.342(-4)	-5.93(-11)	-1.6(-17)
325	10.782	-3.912(-4)	2.719(-8)	—	-6.109(-4)	-5.13(-11)	-1.2(-17)
330	10.885	-3.758(-4)	2.749(-8)	—	-5.889(-4)	-4.41(-11)	-9.7(-18)
335	10.988	-3.613(-4)	2.782(-8)	—	-5.681(-4)	-3.77(-11)	-7.5(-18)
340	11.090	-3.477(-4)	2.819(-8)	—	-5.484(-4)	-3.19(-11)	-5.6(-18)

Name: 1,1-dichloro-1-fluoroethane (CAS # 1717-00-6)
 Formula: $\text{CFCl}_2-\text{CH}_3$
 M.W. 0.11695 kg/mol
 Max. Pressure: 70 kPa
 Reference: Goodwin, A.R.H., and Moldover, M.R. (1991). Thermophysical properties of gaseous refrigerants from speed-of-sound measurements, II: Results for 1,1-dichloro-1-fluoroethane (CCl_2FCH_3). *J. Chem. Phys.* **95**: 5230–5235.

T (K)	$C_p^0(T)/R$	$B(T)$ ($\text{m}^3 \cdot \text{mol}^{-1}$)	$C(T)$ ($\text{m}^6 \cdot \text{mol}^{-2}$)	$D(T)$ ($\text{m}^9 \cdot \text{mol}^{-3}$)	$\beta_a(T)$ ($\text{m}^3 \cdot \text{mol}^{-1}$)	$\gamma_a(T)$ ($\text{m}^3 \cdot \text{mol}^{-1} \cdot \text{Pa}^{-1}$)	$\delta_a(T)$ ($\text{m}^3 \cdot \text{mol}^{-1} \cdot \text{Pa}^{-2}$)
260	9.792	-1.388(-3)	—	—	-2.118(-3)	-1.26(-9)	-1.7(-15)
265	9.897	-1.321(-3)	—	—	-2.023(-3)	-1.12(-9)	-1.4(-15)
270	10.003	-1.259(-3)	—	—	-1.934(-3)	-1.01(-9)	-1.2(-15)
275	10.108	-1.201(-3)	—	—	-1.851(-3)	-9.01(-10)	-9.7(-16)
280	10.213	-1.147(-3)	—	—	-1.773(-3)	-8.09(-10)	-8.1(-16)
285	10.319	-1.096(-3)	—	—	-1.700(-3)	-7.29(-10)	-6.9(-16)

T (K)	$C_p^0(T)/R$	$B(T)$ ($\text{m}^3 \cdot \text{mol}^{-1}$)	$C(T)$ ($\text{m}^6 \cdot \text{mol}^{-2}$)	$D(T)$ ($\text{m}^9 \cdot \text{mol}^{-3}$)	$\beta_a(T)$ ($\text{m}^3 \cdot \text{mol}^{-1}$)	$\gamma_a(T)$ ($\text{m}^3 \cdot \text{mol}^{-1} \cdot \text{Pa}^{-1}$)	$\delta_a(T)$ ($\text{m}^3 \cdot \text{mol}^{-1} \cdot \text{Pa}^{-2}$)
290	10.424	-1.049(-3)	—	—	-1.631(-3)	-6.57(-10)	-5.8(-16)
295	10.530	-1.004(-3)	—	—	-1.566(-3)	-5.94(-10)	-5.0(-16)
300	10.635	-9.623(-4)	—	—	-1.504(-3)	-5.37(-10)	-4.2(-16)
305	10.740	-9.228(-4)	—	—	-1.446(-3)	-4.87(-10)	-3.6(-16)
310	10.846	-8.856(-4)	—	—	-1.391(-3)	-4.42(-10)	-3.1(-16)
315	10.951	-8.505(-4)	—	—	-1.338(-3)	-4.02(-10)	-2.7(-16)

Name: 1,1,1-trifluoroethane (CAS # 420-46-2)
Formula: CF_3-CH_3
M.W. 0.0840412 kg/mol
Max. Pressure: 1000 kPa
Reference: Gillis, K.A. (1997). Thermodynamic properties of seven gaseous halo-genated hydrocarbons from acoustic measurements: CHClFCF_3 , CHF_2CF_3 , CF_3CH_3 , CHF_2CH_3 , $\text{CF}_3\text{CHFCHF}_2$, $\text{CF}_3\text{CH}_2\text{CF}_3$ and $\text{CHF}_2\text{CF}_2\text{CH}_2\text{F}$. *Int. J. Thermophys.* **18**: 73–135.

T (K)	$C_p^0(T)/R$	$B(T)$ ($\text{m}^3 \cdot \text{mol}^{-1}$)	$C(T)$ ($\text{m}^6 \cdot \text{mol}^{-2}$)	$D(T)$ ($\text{m}^9 \cdot \text{mol}^{-3}$)	$\beta_a(T)$ ($\text{m}^3 \cdot \text{mol}^{-1}$)	$\gamma_a(T)$ ($\text{m}^3 \cdot \text{mol}^{-1} \cdot \text{Pa}^{-1}$)	$\delta_a(T)$ ($\text{m}^3 \cdot \text{mol}^{-1} \cdot \text{Pa}^{-2}$)
250	8.324	-6.466(-4)	8.478(-9)	-4.48(-11)	-9.408(-4)	-2.09(-10)	-1.5(-16)
255	8.444	-6.140(-4)	2.271(-8)	-3.73(-11)	-8.985(-4)	-1.76(-10)	-1.2(-16)
260	8.561	-5.838(-4)	3.301(-8)	-3.11(-11)	-8.590(-4)	-1.49(-10)	-9.2(-17)
265	8.676	-5.557(-4)	4.031(-8)	-2.61(-11)	-8.220(-4)	-1.26(-10)	-7.2(-17)
270	8.790	-5.297(-4)	4.533(-8)	-2.20(-11)	-7.873(-4)	-1.07(-10)	-5.7(-17)
275	8.901	-5.054(-4)	4.860(-8)	-1.86(-11)	-7.547(-4)	-9.15(-11)	-4.5(-17)
280	9.011	-4.828(-4)	5.055(-8)	-1.58(-11)	-7.241(-4)	-7.82(-11)	-3.5(-17)
285	9.119	-4.616(-4)	5.152(-8)	-1.35(-11)	-6.952(-4)	-6.69(-11)	-2.8(-17)
290	9.226	-4.418(-4)	5.173(-8)	-1.15(-11)	-6.679(-4)	-5.73(-11)	-2.2(-17)
295	9.331	-4.233(-4)	5.140(-8)	-9.88(-12)	-6.422(-4)	-4.91(-11)	-1.7(-17)
300	9.434	-4.058(-4)	5.066(-8)	-8.50(-12)	-6.178(-4)	-4.21(-11)	-1.4(-17)
305	9.537	-3.894(-4)	4.964(-8)	-7.34(-12)	-5.947(-4)	-3.60(-11)	-1.1(-17)
310	9.638	-3.740(-4)	4.841(-8)	-6.35(-12)	-5.728(-4)	-3.08(-11)	-8.5(-18)
315	9.738	-3.594(-4)	4.706(-8)	-5.51(-12)	-5.521(-4)	-2.63(-11)	-6.7(-18)
320	9.837	-3.456(-4)	4.563(-8)	-4.80(-12)	-5.323(-4)	-2.23(-11)	-5.2(-18)
325	9.935	-3.326(-4)	4.417(-8)	-4.18(-12)	-5.135(-4)	-1.88(-11)	-3.9(-18)
330	10.032	-3.202(-4)	4.270(-8)	-3.65(-12)	-4.956(-4)	-1.58(-11)	-2.9(-18)
335	10.128	-3.085(-4)	4.124(-8)	-3.20(-12)	-4.786(-4)	-1.31(-11)	-2.2(-18)
340	10.223	-2.974(-4)	3.982(-8)	-2.81(-12)	-4.623(-4)	-1.07(-11)	-1.5(-18)
345	10.318	-2.869(-4)	3.844(-8)	-2.47(-12)	-4.468(-4)	-8.64(-12)	-9.7(-19)
350	10.412	-2.768(-4)	3.712(-8)	-2.18(-12)	-4.320(-4)	-6.76(-12)	-5.4(-19)
355	10.505	-2.673(-4)	3.586(-8)	-1.92(-12)	-4.178(-4)	-5.09(-12)	-2.0(-19)
360	10.599	-2.582(-4)	3.466(-8)	-1.70(-12)	-4.042(-4)	-3.58(-12)	-8.8(-20)
365	10.691	-2.495(-4)	3.352(-8)	-1.50(-12)	-3.912(-4)	-2.23(-12)	-3.2(-19)
370	10.784	-2.412(-4)	3.246(-8)	-1.33(-12)	-3.787(-4)	-1.01(-12)	-5.0(-19)
375	10.876	-2.332(-4)	3.145(-8)	-1.18(-12)	-3.667(-4)	9.85(-14)	-6.5(-19)
380	10.968	-2.256(-4)	3.052(-8)	1.31(-15)	-3.552(-4)	-9.11(-13)	9.6(-19)
385	11.061	-2.184(-4)	2.964(-8)	1.31(-15)	-3.442(-4)	1.28(-13)	1.0(-18)
390	11.153	-2.114(-4)	2.883(-8)	1.31(-15)	-3.336(-4)	1.08(-12)	1.1(-18)
395	11.245	-2.048(-4)	2.808(-8)	1.31(-15)	-3.233(-4)	1.94(-12)	1.1(-18)
400	11.338	-1.983(-4)	2.738(-8)	1.31(-15)	-3.135(-4)	2.74(-12)	1.1(-18)

Name: 1,1-difluoroethane (CAS # 75-37-6)
 Formula: CHF_2-CH_3
 M.W. 0.0660508 kg/mol
 Max. Pressure: 1000 kPa
 Reference: Gillis, K.A. (1997). Thermodynamic properties of seven gaseous halo-genated hydrocarbons from acoustic measurements: CHClFCF_3 , CHF_2CF_3 , CF_3CH_3 , CHF_2CH_3 , $\text{CF}_3\text{CHFCHF}_2$, $\text{CF}_3\text{CH}_2\text{CF}_3$ and $\text{CHF}_2\text{CF}_2\text{CH}_2\text{F}$. *Int. J. Thermophys.* **18**: 73–135.

T (K)	$C_p^0(T)/R$	$B(T)$ ($\text{m}^3 \cdot \text{mol}^{-1}$)	$C(T)$ ($\text{m}^6 \cdot \text{mol}^{-2}$)	$D(T)$ ($\text{m}^9 \cdot \text{mol}^{-3}$)	$\beta_a(T)$ ($\text{m}^3 \cdot \text{mol}^{-1}$)	$\gamma_a(T)$ ($\text{m}^3 \cdot \text{mol}^{-1} \cdot \text{Pa}^{-1}$)	$\delta_a(T)$ ($\text{m}^3 \cdot \text{mol}^{-1} \cdot \text{Pa}^{-2}$)
243	7.119	-9.318(-4)	-1.850(-7)	-2.99(-10)	-1.243(-3)	-5.46(-10)	-7.3(-16)
245	7.154	-9.092(-4)	-1.573(-7)	-2.76(-10)	-1.216(-3)	-5.05(-10)	-6.5(-16)
250	7.242	-8.561(-4)	-1.004(-7)	-2.27(-10)	-1.154(-3)	-4.19(-10)	-4.9(-16)
255	7.330	-8.076(-4)	-5.754(-8)	-1.88(-10)	-1.096(-3)	-3.49(-10)	-3.8(-16)
260	7.420	-7.631(-4)	-2.544(-8)	-1.56(-10)	-1.043(-3)	-2.92(-10)	-2.9(-16)
265	7.510	-7.223(-4)	-1.513(-9)	-1.31(-10)	-9.938(-4)	-2.46(-10)	-2.3(-16)
270	7.601	-6.848(-4)	1.618(-8)	-1.10(-10)	-9.483(-4)	-2.08(-10)	-1.8(-16)
275	7.692	-6.501(-4)	2.911(-8)	-9.24(-11)	-9.059(-4)	-1.77(-10)	-1.4(-16)
280	7.784	-6.181(-4)	3.480(-8)	-7.82(-11)	-8.665(-4)	-1.51(-10)	-1.1(-16)
285	7.876	-5.884(-4)	4.489(-8)	-6.65(-11)	-8.296(-4)	-1.29(-10)	-9.0(-17)
290	7.968	-5.608(-4)	4.926(-8)	-5.67(-11)	-7.952(-4)	-1.11(-10)	-7.2(-17)
295	8.061	-5.352(-4)	5.200(-8)	-4.85(-11)	-7.629(-4)	-9.57(-11)	-5.8(-17)
300	8.154	-5.113(-4)	5.352(-8)	-4.17(-11)	-7.327(-4)	-8.27(-11)	-4.7(-17)
305	8.247	-4.889(-4)	5.411(-8)	-3.59(-11)	-7.042(-4)	-7.17(-11)	-3.8(-17)
310	8.341	-4.680(-4)	5.401(-8)	-3.10(-11)	-6.773(-4)	-6.22(-11)	-3.1(-17)
315	8.434	-4.485(-4)	5.340(-8)	-2.69(-11)	-6.520(-4)	-5.41(-11)	-2.5(-17)
320	8.528	-4.301(-4)	5.243(-8)	-2.33(-11)	-6.281(-4)	-4.71(-11)	-2.1(-17)
325	8.621	-4.128(-4)	5.120(-8)	-2.03(-11)	-6.055(-4)	-4.10(-11)	-1.7(-17)
330	8.715	-3.996(-4)	4.980(-8)	-1.77(-11)	-5.841(-4)	-3.57(-11)	-1.4(-17)
335	8.808	-3.813(-4)	4.829(-8)	-1.55(-11)	-5.638(-4)	-3.11(-11)	-1.1(-17)
340	8.901	-3.668(-4)	4.672(-8)	-1.36(-11)	-5.445(-4)	-2.70(-11)	-9.3(-18)
345	8.993	-3.532(-4)	4.513(-8)	-1.20(-11)	-5.262(-4)	-2.34(-11)	-7.6(-18)
350	9.086	-3.403(-4)	4.355(-8)	-1.05(-11)	-5.087(-4)	-2.03(-11)	-6.2(-18)
355	9.178	-3.281(-4)	4.200(-8)	-9.31(-12)	-4.921(-4)	-1.74(-11)	-5.0(-18)
360	9.269	-3.165(-4)	4.050(-8)	-8.23(-12)	-4.762(-4)	-1.49(-11)	-4.0(-18)
365	9.360	-3.055(-4)	3.905(-8)	-7.28(-12)	-4.611(-4)	-1.27(-11)	-3.2(-18)
370	9.450	-2.950(-4)	3.767(-8)	-6.46(-12)	-4.466(-4)	-1.07(-11)	-2.5(-18)
375	9.540	-2.851(-4)	3.635(-8)	-5.74(-12)	-4.327(-4)	-8.83(-12)	-2.0(-18)
380	9.629	-2.756(-4)	3.511(-8)	-5.33(-15)	-4.195(-4)	-9.96(-12)	-2.6(-19)
385	9.717	-2.666(-4)	3.394(-8)	3.53(-15)	-4.068(-4)	-8.27(-12)	-2.9(-20)
390	9.804	-2.580(-4)	3.285(-8)	3.53(-15)	-3.946(-4)	-6.73(-12)	1.6(-19)
395	9.891	-2.498(-4)	3.183(-8)	3.53(-15)	-3.829(-4)	-5.32(-12)	3.2(-19)
400	9.976	-2.419(-4)	3.088(-8)	3.53(-15)	-3.717(-4)	-4.04(-12)	4.5(-19)

Name: 1,1,1,2,3,3-hexafluoropropane (CAS # 431-63-0)
 Formula: $\text{CF}_3-\text{CHF}-\text{CHF}_2$
 M.W. 0.152039 kg/mol
 Max. Pressure: 600 kPa
 Reference: Gillis, K.A. (1997). Thermodynamic properties of seven gaseous halo-genated hydrocarbons from acoustic measurements: CHClFCF_3 , CHF_2CF_3 , CF_3CH_3 , CHF_2CH_3 , $\text{CH}_3\text{CHFCH}_2$, $\text{CF}_3\text{CH}_2\text{CF}_3$ and $\text{CHF}_2\text{CF}_2\text{CH}_2\text{F}$. *Int. J. Thermophys.* **18**: 73–135.

T (K)	$C_p^0(T)/R$	$B(T)$ ($\text{m}^3 \cdot \text{mol}^{-1}$)	$C(T)$ ($\text{m}^6 \cdot \text{mol}^{-2}$)	$D(T)$ ($\text{m}^9 \cdot \text{mol}^{-3}$)	$\beta_a(T)$ ($\text{m}^3 \cdot \text{mol}^{-1}$)	$\gamma_a(T)$ ($\text{m}^3 \cdot \text{mol}^{-1} \cdot \text{Pa}^{-1}$)	$\delta_a(T)$ ($\text{m}^3 \cdot \text{mol}^{-1} \cdot \text{Pa}^{-2}$)
267.15	14.593	-1.032(-3)	-1.576(-6)	-5.60(-9)	-1.741(-3)	-1.53(-9)	-4.2(-15)
270	14.678	-1.006(-3)	-1.286(-6)	-4.75(-9)	-1.699(-3)	-1.31(-9)	-3.5(-15)
275	14.826	-9.622(-4)	-8.900(-7)	-3.58(-9)	-1.628(-3)	-1.01(-9)	-2.5(-15)
280	14.973	-9.214(-4)	-6.032(-7)	-2.73(-9)	-1.561(-3)	-7.89(-10)	-1.9(-15)

T (K)	$C_p^0(T)/R$	$B(T)$ ($\text{m}^3 \cdot \text{mol}^{-1}$)	$C(T)$ ($\text{m}^6 \cdot \text{mol}^{-2}$)	$D(T)$ ($\text{m}^9 \cdot \text{mol}^{-3}$)	$\beta_a(T)$ ($\text{m}^3 \cdot \text{mol}^{-1}$)	$\gamma_a(T)$ ($\text{m}^3 \cdot \text{mol}^{-1} \cdot \text{Pa}^{-1}$)	$\delta_a(T)$ ($\text{m}^3 \cdot \text{mol}^{-1} \cdot \text{Pa}^{-2}$)
285	15.119	-8.830(-4)	-3.957(-7)	-2.10(-9)	-1.498(-3)	-6.23(-10)	-1.4(-15)
290	15.264	-8.467(-4)	-2.458(-7)	-1.63(-9)	-1.438(-3)	-4.97(-10)	-1.0(-15)
295	15.408	-8.125(-4)	-1.380(-7)	-1.27(-9)	-1.382(-3)	-4.02(-10)	-7.8(-16)
300	15.552	-7.801(-4)	-6.109(-8)	-1.00(-9)	-1.328(-3)	-3.30(-10)	-6.0(-16)
305	15.694	-7.495(-4)	-6.785(-9)	-7.95(-10)	-1.277(-3)	-2.73(-10)	-4.6(-16)
310	15.835	-7.204(-4)	-3.095(-8)	-6.35(-10)	-1.229(-3)	-2.30(-10)	-3.6(-16)
315	15.976	-6.929(-4)	-5.654(-8)	-5.11(-10)	-1.182(-3)	-1.95(-10)	-2.8(-16)
320	16.116	-6.667(-4)	-7.327(-8)	-4.13(-10)	-1.139(-3)	-1.68(-10)	-2.2(-16)
325	16.254	-6.418(-4)	-8.356(-8)	-3.36(-10)	-1.097(-3)	-1.45(-10)	-1.8(-16)
330	16.392	-6.180(-4)	-8.920(-8)	-2.75(-10)	-1.057(-3)	-1.27(-10)	-1.4(-16)
335	16.529	-5.954(-4)	-9.153(-8)	-2.26(-10)	-1.018(-3)	-1.12(-10)	-1.2(-16)
340	16.665	-5.738(-4)	-9.152(-8)	-1.87(-10)	-9.819(-4)	-9.97(-11)	-9.6(-17)
345	16.800	-5.532(-4)	-8.992(-8)	-1.55(-10)	-9.469(-4)	-8.89(-11)	-7.9(-17)
350	16.934	-5.335(-4)	-8.726(-8)	-1.30(-10)	-9.134(-4)	-7.97(-11)	-6.5(-17)
335	17.067	-5.147(-4)	-8.394(-8)	-1.09(-10)	-8.812(-4)	-7.16(-11)	-5.4(-17)
360	17.199	-4.967(-4)	-8.024(-8)	-9.15(-11)	-8.504(-4)	-6.44(-11)	-4.5(-17)
365	17.330	-4.794(-4)	-7.638(-8)	-7.74(-11)	-8.208(-4)	-5.80(-11)	-3.7(-17)
370	17.460	-4.628(-4)	-7.251(-8)	-6.57(-11)	-7.923(-4)	-5.22(-11)	-3.1(-17)
375	17.590	-4.469(-4)	-6.874(-8)	-5.59(-11)	-7.649(-4)	-4.70(-11)	-2.6(-17)
377	17.641	-4.407(-4)	-6.727(-8)	-1.47(-11)	-7.543(-4)	-5.25(-11)	-9.6(-18)

Name: 1,1,1,3,3,3-hexafluoropropane (CAS # 690-39-1)

Formula: $\text{CF}_3\text{-CH}_2\text{-CF}_3$

M.W. 0.152039 kg/mol

Max. Pressure: 1000 kPa

Reference: Gillis, K.A. (1997). Thermodynamic properties of seven gaseous halo-genated hydrocarbons from acoustic measurements: CHClFCF_3 , CHF_2CF_3 , CF_3CH_3 , CHF_2CH_3 , $\text{CF}_3\text{CHFCHF}_2$, $\text{CF}_3\text{CH}_2\text{CF}_3$ and $\text{CHF}_2\text{CF}_2\text{CHF}_2$. *Int. J. Thermophys.* **18**: 73–135.

T (K)	$C_p^0(T)/R$	$B(T)$ ($\text{m}^3 \cdot \text{mol}^{-1}$)	$C(T)$ ($\text{m}^6 \cdot \text{mol}^{-2}$)	$D(T)$ ($\text{m}^9 \cdot \text{mol}^{-3}$)	$\beta_a(T)$ ($\text{m}^3 \cdot \text{mol}^{-1}$)	$\gamma_a(T)$ ($\text{m}^3 \cdot \text{mol}^{-1} \cdot \text{Pa}^{-1}$)	$\delta_a(T)$ ($\text{m}^3 \cdot \text{mol}^{-1} \cdot \text{Pa}^{-2}$)
275	14.292	-9.136(-4)	-7.494(-7)	-3.63(-10)	-1.536(-3)	-9.69(-10)	-1.0(-15)
280	14.442	-8.748(-4)	-5.534(-7)	-2.97(-10)	-1.473(-3)	-7.88(-10)	-7.7(-16)
285	14.592	-8.384(-4)	-4.033(-7)	-2.45(-10)	-1.414(-3)	-6.45(-10)	-5.9(-16)
290	14.743	-8.040(-4)	-2.884(-7)	-2.02(-10)	-1.358(-3)	-5.31(-10)	-4.6(-16)
295	14.893	-7.716(-4)	-2.004(-7)	-1.68(-10)	-1.305(-3)	-4.41(-10)	-3.5(-16)
300	15.044	-7.409(-4)	-1.330(-7)	-1.41(-10)	-1.255(-3)	-3.68(-10)	-2.8(-16)
305	15.194	-7.119(-4)	-8.153(-8)	-1.18(-10)	-1.207(-3)	-3.09(-10)	-2.2(-16)
310	15.344	-6.844(-4)	-4.237(-8)	-9.95(-11)	-1.162(-3)	-2.61(-10)	-1.7(-16)
315	15.495	-6.582(-4)	-1.274(-8)	-8.42(-11)	-1.118(-3)	-2.22(-10)	-1.4(-16)
320	15.645	-6.334(-4)	9.514(-9)	-7.16(-11)	-1.077(-3)	-1.89(-10)	-1.1(-16)
325	15.796	-6.098(-4)	2.604(-8)	-6.11(-11)	-1.038(-3)	-1.62(-10)	-8.9(-17)
330	15.946	-5.874(-4)	3.812(-8)	-5.23(-11)	-1.000(-3)	-1.40(-10)	-7.2(-17)
335	16.096	-5.659(-4)	4.676(-8)	-4.50(-11)	-9.645(-4)	-1.21(-10)	-5.9(-17)
340	16.247	-5.455(-4)	5.274(-8)	-3.88(-11)	-9.302(-4)	-1.06(-10)	-4.8(-17)
345	16.397	-5.260(-4)	5.667(-8)	-3.35(-11)	-8.974(-4)	-9.21(-11)	-4.0(-17)
350	16.548	-5.074(-4)	5.902(-8)	-2.91(-11)	-8.660(-4)	-8.06(-11)	-3.3(-17)
355	16.698	-4.895(-4)	6.017(-8)	-2.53(-11)	-8.358(-4)	-7.08(-11)	-2.7(-17)
360	16.848	-4.725(-4)	6.041(-8)	-2.21(-11)	-8.069(-4)	-6.22(-11)	-2.2(-17)
365	16.999	-4.561(-4)	5.997(-8)	-1.93(-11)	-7.791(-4)	-5.48(-11)	-1.9(-17)
370	17.149	-4.404(-4)	5.903(-8)	-1.70(-11)	-7.525(-4)	-4.83(-11)	-1.6(-17)
375	17.300	-4.253(-4)	5.773(-8)	-1.49(-11)	-7.268(-4)	-4.26(-11)	-1.3(-17)
380	17.450	-4.109(-4)	5.618(-8)	2.68(-16)	-7.021(-4)	-4.41(-11)	-7.5(-18)
385	17.600	-3.970(-4)	5.448(-8)	2.66(-16)	-6.783(-4)	-3.93(-11)	-6.1(-18)
390	17.751	-3.836(-4)	5.268(-8)	2.68(-16)	-6.554(-4)	-3.50(-11)	-5.0(-18)
395	17.901	-3.707(-4)	5.083(-8)	2.68(-16)	-6.333(-4)	-3.11(-11)	-4.0(-18)
400	18.052	-3.584(-4)	4.898(-8)	2.68(-16)	-6.120(-4)	-2.76(-11)	-3.2(-18)

Name: 1,1,2,2,3-pentafluoropropane (CAS # 679-86-7)
 Formula: $\text{CHF}_2-\text{CF}_2-\text{CH}_2\text{F}$
 M.W. 0.134049 kg/mol
 Max. Pressure: 1000 kPa
 Reference: Gillis, K.A. (1997). Thermodynamic properties of seven gaseous halo-generated hydrocarbons from acoustic measurements: CHClFCF_3 , CHF_2CF_3 , CF_3CH_3 , CHF_2CH_3 , $\text{CF}_3\text{CHFCHF}_2$, $\text{CF}_3\text{CH}_2\text{CF}_3$ and $\text{CHF}_2\text{CF}_2\text{CH}_2\text{F}$. *Int. J. Thermophys.* **18**: 73–135.

T (K)	$C_p(T)/R$	$B(T)$ ($\text{m}^3 \cdot \text{mol}^{-1}$)	$C(T)$ ($\text{m}^6 \cdot \text{mol}^{-2}$)	$D(T)$ ($\text{m}^9 \cdot \text{mol}^{-3}$)	$\beta_a(T)$ ($\text{m}^3 \cdot \text{mol}^{-1}$)	$\gamma_a(T)$ ($\text{m}^3 \cdot \text{mol}^{-1} \cdot \text{Pa}^{-1}$)	$\delta_a(T)$ ($\text{m}^3 \cdot \text{mol}^{-1} \cdot \text{Pa}^{-2}$)
310	14.696	-8.264(-4)	-2.319(-7)	-5.00(-10)	-1.394(-3)	-4.68(-10)	-5.2(-16)
315	14.885	-7.950(-4)	-1.520(-7)	-4.34(-10)	-1.344(-3)	-3.93(-10)	-4.2(-16)
320	15.071	-7.653(-4)	-9.126(-8)	-3.78(-10)	-1.296(-3)	-3.32(-10)	-3.4(-16)
325	15.252	-7.370(-4)	-4.531(-8)	-3.30(-10)	-1.250(-3)	-2.82(-10)	-2.8(-16)
330	15.430	-7.102(-4)	-1.078(-8)	-2.88(-10)	-1.206(-3)	-2.42(-10)	-2.3(-16)
335	15.604	-6.846(-4)	1.494(-8)	-2.52(-10)	-1.165(-3)	-2.08(-10)	-1.9(-16)
340	15.774	-6.603(-4)	3.385(-8)	-2.21(-10)	-1.125(-3)	-1.80(-10)	-1.6(-16)
345	15.940	-6.371(-4)	4.749(-8)	-1.95(-10)	-1.086(-3)	-1.57(-10)	-1.3(-16)
350	16.102	-6.150(-4)	5.708(-8)	-1.71(-10)	-1.050(-3)	-1.38(-10)	-1.1(-16)
355	16.260	-5.939(-4)	6.355(-8)	-1.51(-10)	-1.015(-3)	-1.21(-10)	-9.4(-17)
360	16.414	-5.737(-4)	6.763(-8)	-1.33(-10)	-9.808(-4)	-1.07(-10)	-8.0(-17)
365	16.564	-5.544(-4)	6.989(-8)	-1.18(-10)	-9.484(-4)	-9.53(-11)	-6.8(-17)
370	16.711	-5.359(-4)	7.078(-8)	-1.05(-10)	-9.173(-4)	-8.50(-11)	-5.8(-17)
375	16.853	-5.182(-4)	7.065(-8)	-9.27(-11)	-8.874(-4)	-7.59(-11)	-4.9(-17)
380	16.991	-5.012(-4)	6.976(-8)	1.64(-13)	-8.586(-4)	-7.65(-11)	-1.8(-17)
385	17.126	-4.848(-4)	6.833(-8)	1.64(-13)	-8.309(-4)	-6.91(-11)	-1.5(-17)
390	17.256	-4.692(-4)	6.652(-8)	1.64(-13)	-8.042(-4)	-6.24(-11)	-1.3(-17)
395	17.383	-4.541(-4)	6.446(-8)	1.64(-13)	-7.785(-4)	-5.65(-11)	-1.1(-17)
400	17.506	-4.396(-4)	6.225(-8)	1.64(-13)	-7.537(-4)	-5.12(-11)	-9.2(-18)

Name: 1,1,1,2,2,3,3,4-octafluorobutane (CAS # 662-35-1)
 Formula: $\text{CF}_3-\text{CF}_2-\text{CF}_2-\text{CH}_2\text{F}$
 M.W. 0.202047 kg/mol
 Max. Pressure: 400 kPa
 Reference: Defibaugh, D.R., Carrillo, N.E., Hurly, J.J., Moldover, M.R., Schmidt, J.W., Weber, L.A. (1997). Thermodynamic properties of HFC-338mccq , $\text{CF}_3\text{CF}_2\text{CF}_2\text{CH}_2\text{F}$, 1,1,1,2,2,3,3,4-octafluorobutane. *J. Chem. Eng. Data* **42**: 488–496.

T (K)	$C_p(T)/R$	$B(T)$ ($\text{m}^3 \cdot \text{mol}^{-1}$)	$C(T)$ ($\text{m}^6 \cdot \text{mol}^{-2}$)	$D(T)$ ($\text{m}^9 \cdot \text{mol}^{-3}$)	$\beta_a(T)$ ($\text{m}^3 \cdot \text{mol}^{-1}$)	$\gamma_a(T)$ ($\text{m}^3 \cdot \text{mol}^{-1} \cdot \text{Pa}^{-1}$)	$\delta_a(T)$ ($\text{m}^3 \cdot \text{mol}^{-1} \cdot \text{Pa}^{-2}$)
300	19.748	-1.162(-3)	-6.284(-7)	—	-2.037(-3)	-1.30(-9)	-1.3(-15)
305	19.899	-1.114(-3)	-4.808(-7)	—	-1.955(-3)	-1.11(-9)	-1.0(-15)
310	20.053	-1.069(-3)	-3.632(-7)	—	-1.878(-3)	-9.44(-10)	-8.0(-16)
315	20.208	-1.026(-3)	-2.695(-7)	—	-1.805(-3)	-8.09(-10)	-6.4(-16)
320	20.366	-9.861(-4)	-1.948(-7)	—	-1.736(-3)	-6.96(-10)	-5.1(-16)
325	20.528	-9.480(-4)	-1.353(-7)	—	-1.671(-3)	-6.01(-10)	-4.2(-16)
330	20.692	-9.120(-4)	-8.793(-8)	—	-1.609(-3)	-5.21(-10)	-3.4(-16)
335	20.860	-8.778(-4)	-5.031(-8)	—	-1.550(-3)	-4.54(-10)	-2.8(-16)
340	21.033	-8.453(-4)	-2.053(-8)	—	-1.494(-3)	-3.96(-10)	-2.3(-16)
345	21.209	-8.145(-4)	2.934(-9)	—	-1.441(-3)	-3.48(-10)	-1.9(-16)
350	21.390	-7.852(-4)	2.130(-8)	—	-1.390(-3)	-3.06(-10)	-1.5(-16)
355	21.576	-7.573(-4)	3.556(-8)	—	-1.342(-3)	-2.69(-10)	-1.3(-16)
360	21.768	-7.308(-4)	4.651(-8)	—	-1.296(-3)	-2.38(-10)	-1.1(-16)
365	21.965	-7.054(-4)	5.478(-8)	—	-1.252(-3)	-2.11(-10)	-8.8(-17)
370	22.168	-6.812(-4)	6.090(-8)	—	-1.210(-3)	-1.88(-10)	-7.4(-17)
375	22.378	-6.581(-4)	6.529(-8)	—	-1.169(-3)	-1.67(-10)	-6.2(-17)
380	22.594	-6.359(-4)	6.828(-8)	—	-1.131(-3)	-1.49(-10)	-5.2(-17)
385	22.818	-6.148(-4)	7.016(-8)	—	-1.094(-3)	-1.33(-10)	-4.4(-17)

$\frac{LT}{(K)}$	$\frac{C_p^0(T)}{R}$	$\frac{B(T)}{(m^3 \cdot mol^{-1})}$	$\frac{C(T)}{(m^6 \cdot mol^{-2})}$	$\frac{D(T)}{(m^9 \cdot mol^{-3})}$	$\frac{\beta_a(T)}{(m^3 \cdot mol^{-1})}$	$\frac{\gamma_a(T)}{(m^3 \cdot mol^{-1} \cdot Pa^{-1})}$	$\frac{\delta_a(T)}{(m^3 \cdot mol^{-1} \cdot Pa^{-2})}$
390	23.049	-5.945(-4)	7.116(-8)	—	-1.059(-3)	-1.19(-10)	-3.7(-17)
395	23.287	-5.750(-4)	7.146(-8)	—	-1.025(-3)	-1.07(-10)	-3.1(-17)
400	23.534	-5.564(-4)	7.120(-8)	—	-9.920(-4)	-9.58(-11)	-2.6(-17)

Name: methane (CAS # 74-82-8)

Formula: CH₄

M.W. 0.016043 kg/mol

Max. Pressure: 3000 kPa

Reference: Gillis, K.A., and Moldover M.R. (1996). Practical determination of gas densities from the speed of sound using square-well potentials. *Int. J. Thermophys.* **17**: 1305–1324.

T (K)	$\frac{C_p^0(T)}{R}$	$\frac{B(T)}{(m^3 \cdot mol^{-1})}$	$\frac{C(T)}{(m^6 \cdot mol^{-2})}$	$\frac{D(T)}{(m^9 \cdot mol^{-3})}$	$\frac{\beta_a(T)}{(m^3 \cdot mol^{-1})}$	$\frac{\gamma_a(T)}{(m^3 \cdot mol^{-1} \cdot Pa^{-1})}$	$\frac{\delta_a(T)}{(m^3 \cdot mol^{-1} \cdot Pa^{-2})}$
125	4.003	-2.565(-4)	1.923(-9)	2.64(-13)	-3.100(-4)	-6.74(-11)	-3.2(-17)
130	4.004	-2.379(-4)	2.357(-9)	3.44(-13)	-2.869(-4)	-5.43(-11)	-2.2(-17)
135	4.004	-2.214(-4)	2.667(-9)	3.77(-13)	-2.662(-4)	-4.39(-11)	-1.6(-17)
140	4.005	-2.065(-4)	2.885(-9)	3.82(-13)	-2.476(-4)	-3.56(-11)	-1.1(-17)
145	4.005	-1.932(-4)	3.034(-9)	3.70(-13)	-2.307(-4)	-2.90(-11)	-8.2(-18)
150	4.006	-1.811(-4)	3.132(-9)	3.50(-13)	-2.155(-4)	-2.37(-11)	-5.9(-18)
155	4.006	-1.702(-4)	3.190(-9)	3.25(-13)	-2.015(-4)	-1.94(-11)	-4.3(-18)
160	4.007	-1.602(-4)	3.219(-9)	2.98(-13)	-1.887(-4)	-1.58(-11)	-3.1(-18)
165	4.009	-1.511(-4)	3.227(-9)	2.72(-13)	-1.770(-4)	-1.29(-11)	-2.2(-18)
170	4.010	-1.426(-4)	3.217(-9)	2.47(-13)	-1.662(-4)	-1.05(-11)	-1.6(-18)
175	4.012	-1.349(-4)	3.196(-9)	2.24(-13)	-1.562(-4)	-8.50(-12)	-1.1(-18)
180	4.015	-1.277(-4)	3.165(-9)	2.03(-13)	-1.470(-4)	-6.84(-12)	-7.8(-19)
185	4.018	-1.211(-4)	3.128(-9)	1.84(-13)	-1.384(-4)	-5.44(-12)	-5.2(-19)
190	4.021	-1.149(-4)	3.087(-9)	1.67(-13)	-1.304(-4)	-4.28(-12)	-3.2(-19)
195	4.026	-1.092(-4)	3.042(-9)	1.52(-13)	-1.229(-4)	-3.30(-12)	-1.8(-19)
200	4.031	-1.038(-4)	2.996(-9)	1.38(-13)	-1.160(-4)	-2.47(-12)	-7.4(-20)
205	4.036	-9.882(-5)	2.948(-9)	1.27(-13)	-1.094(-4)	-1.77(-12)	-3.7(-21)
210	4.042	-9.412(-5)	2.900(-9)	1.17(-13)	-1.033(-4)	-1.18(-12)	6.1(-20)
215	4.049	-8.970(-5)	2.852(-9)	1.08(-13)	-9.754(-5)	-6.80(-13)	1.0(-19)
220	4.057	-8.554(-5)	2.805(-9)	1.00(-13)	-9.212(-5)	-2.56(-13)	1.3(-19)
225	4.066	-8.162(-5)	2.759(-9)	9.33(-14)	-8.701(-5)	1.04(-13)	1.5(-19)
230	4.075	-7.792(-5)	2.713(-9)	8.76(-14)	-8.219(-5)	4.09(-13)	1.6(-19)
235	4.085	-7.442(-5)	2.669(-9)	8.28(-14)	-7.763(-5)	6.68(-13)	1.7(-19)
240	4.097	-7.110(-5)	2.626(-9)	7.86(-14)	-7.332(-5)	8.87(-13)	1.7(-19)
245	4.109	-6.796(-5)	2.585(-9)	7.52(-14)	-6.923(-5)	1.07(-12)	1.8(-19)
250	4.122	-6.498(-5)	2.544(-9)	7.23(-14)	-6.535(-5)	1.23(-12)	1.7(-19)
255	4.136	-6.214(-5)	2.506(-9)	6.99(-14)	-6.167(-5)	1.36(-12)	1.7(-19)
260	4.151	-5.944(-5)	2.468(-9)	6.79(-14)	-5.817(-5)	1.47(-12)	1.7(-19)
265	4.166	-5.687(-5)	2.432(-9)	6.63(-14)	-5.484(-5)	1.56(-12)	1.6(-19)
270	4.183	-5.441(-5)	2.398(-9)	6.51(-14)	-5.166(-5)	1.64(-12)	1.6(-19)
275	4.201	-5.207(-5)	2.365(-9)	6.41(-14)	-4.864(-5)	1.70(-12)	1.5(-19)
280	4.219	-4.983(-5)	2.333(-9)	6.35(-14)	-4.575(-5)	1.75(-12)	1.5(-19)
285	4.239	-4.769(-5)	2.302(-9)	6.30(-14)	-4.299(-5)	1.79(-12)	1.4(-19)
290	4.259	-4.563(-5)	2.273(-9)	6.27(-14)	-4.034(-5)	1.82(-12)	1.4(-19)
295	4.280	-4.366(-5)	2.245(-9)	6.27(-14)	-3.782(-5)	1.84(-12)	1.3(-19)
300	4.303	-4.178(-5)	2.218(-9)	6.27(-14)	-3.539(-5)	1.86(-12)	1.2(-19)
305	4.326	-3.996(-5)	2.192(-9)	6.29(-14)	-3.307(-5)	1.87(-12)	1.2(-19)
310	4.349	-3.822(-5)	2.167(-9)	6.32(-14)	-3.084(-5)	1.88(-12)	1.1(-19)
315	4.374	-3.655(-5)	2.143(-9)	6.36(-14)	-2.870(-5)	1.88(-12)	1.1(-19)
320	4.399	-3.493(-5)	2.121(-9)	6.41(-14)	-2.664(-5)	1.88(-12)	1.0(-19)
325	4.426	-3.338(-5)	2.099(-9)	6.46(-14)	-2.465(-5)	1.87(-12)	9.9(-20)
330	4.453	-3.189(-5)	2.078(-9)	6.52(-14)	-2.274(-5)	1.87(-12)	9.4(-20)
335	4.480	-3.048(-5)	2.058(-9)	6.59(-14)	-2.090(-5)	1.86(-12)	9.0(-20)
340	4.508	-2.905(-5)	2.038(-9)	6.66(-14)	-1.913(-5)	1.84(-12)	8.6(-20)
345	4.537	-2.771(-5)	2.020(-9)	6.73(-14)	-1.741(-5)	1.83(-12)	8.2(-20)

(continues)

(continued)

T (K)	$C_p^0(T)/R$	$B(T)$ ($\text{m}^3 \cdot \text{mol}^{-1}$)	$C(T)$ ($\text{m}^6 \cdot \text{mol}^{-2}$)	$D(T)$ ($\text{m}^9 \cdot \text{mol}^{-3}$)	$\beta_a(T)$ ($\text{m}^3 \cdot \text{mol}^{-1}$)	$\gamma_a(T)$ ($\text{m}^3 \cdot \text{mol}^{-1} \cdot \text{Pa}^{-1}$)	$\delta_a(T)$ ($\text{m}^3 \cdot \text{mol}^{-1} \cdot \text{Pa}^{-2}$)
350	4.566	-2.641(-5)	2.002(-9)	6.18(-14)	-1.575(-5)	1.81(-12)	7.9(-20)
355	4.596	-2.515(-5)	1.985(-9)	6.88(-14)	-1.415(-5)	1.80(-12)	7.5(-20)
360	4.627	-2.394(-5)	1.969(-9)	6.96(-14)	-1.260(-5)	1.78(-12)	7.2(-20)
365	4.657	-2.276(-5)	1.953(-9)	7.04(-14)	-1.109(-5)	1.76(-12)	6.9(-20)
370	4.688	-2.163(-5)	1.938(-9)	7.13(-14)	-9.634(-6)	1.74(-12)	6.6(-20)
375	4.719	-2.053(-5)	1.924(-9)	7.21(-14)	-8.219(-6)	1.72(-12)	6.3(-20)

Name: tetrafluoromethane (CAS # 75-73-0)

Formula: CF_4

M.W. 0.08805 kg/mol

Max. Pressure: 1500 kPa

Reference: Hurly, J.J. (1999). Thermophysical properties of gaseous CF_4 and H_2F_6 from speed-of-sound measurements. *Int. J. Thermophys.* **20**: 455–484.

T (K)	$C_p^0(T)/R$	$B(T)$ ($\text{m}^3 \cdot \text{mol}^{-1}$)	$C(T)$ ($\text{m}^6 \cdot \text{mol}^{-2}$)	$D(T)$ ($\text{m}^9 \cdot \text{mol}^{-3}$)	$\beta_a(T)$ ($\text{m}^3 \cdot \text{mol}^{-1}$)	$\gamma_a(T)$ ($\text{m}^3 \cdot \text{mol}^{-1} \cdot \text{Pa}^{-1}$)	$\delta_a(T)$ ($\text{m}^3 \cdot \text{mol}^{-1} \cdot \text{Pa}^{-2}$)
175	5.257	-3.005(-4)	5.144(-9)	—	-3.897(-4)	-6.15(-11)	-2.5(-17)
180	5.344	-2.830(-4)	6.076(-9)	—	-3.688(-4)	-6.11(-11)	-1.9(-17)
185	5.432	-2.670(-4)	6.766(-9)	—	-3.494(-4)	-4.25(-11)	-1.4(-17)
190	5.520	-2.523(-4)	7.269(-9)	—	-3.313(-4)	-3.54(-11)	-1.1(-17)
195	5.608	-2.387(-4)	7.624(-9)	—	-3.145(-4)	-2.94(-11)	-7.9(-18)
200	5.697	-2.260(-4)	7.865(-9)	—	-2.988(-4)	-2.43(-11)	-5.9(-18)
205	5.785	-2.143(-4)	8.016(-9)	—	-2.841(-4)	-2.01(-11)	-4.4(-18)
210	5.874	-2.034(-4)	8.096(-9)	—	-2.703(-4)	-1.65(-11)	-3.2(-18)
215	5.962	-1.932(-4)	8.122(-9)	—	-2.574(-4)	-1.35(-11)	-2.4(-18)
220	6.050	-1.837(-4)	8.105(-9)	—	-2.451(-4)	-1.09(-11)	-1.7(-18)
225	6.138	-1.748(-4)	8.055(-9)	—	-2.335(-4)	-8.65(-12)	-1.2(-18)
230	6.225	-1.664(-4)	7.980(-9)	—	-2.226(-4)	-6.76(-12)	-7.7(-19)
235	6.312	-1.586(-4)	7.886(-9)	—	-2.122(-4)	-5.14(-12)	-4.6(-19)
240	6.398	-1.512(-4)	7.778(-9)	—	-2.024(-4)	-3.75(-12)	-2.3(-19)
245	6.483	-1.442(-4)	7.659(-9)	—	-1.930(-4)	-2.57(-12)	-6.1(-20)
250	6.568	-1.376(-4)	7.533(-9)	—	-1.841(-4)	-1.55(-12)	6.8(-20)
255	6.652	-1.313(-4)	7.403(-9)	—	-1.756(-4)	-6.72(-13)	1.6(-19)
260	6.735	-1.254(-4)	7.270(-9)	—	-1.675(-4)	7.83(-14)	2.3(-19)
265	6.817	-1.198(-4)	7.136(-9)	—	-1.598(-4)	7.22(-13)	2.8(-19)
270	6.899	-1.145(-4)	7.002(-9)	—	-1.524(-4)	1.27(-12)	3.1(-19)
275	6.980	-1.094(-4)	6.869(-9)	—	-1.453(-4)	1.75(-12)	3.3(-19)
280	7.060	-1.046(-4)	6.738(-9)	—	-1.386(-4)	2.15(-12)	3.4(-19)
285	7.139	-9.995(-5)	6.609(-9)	—	-1.321(-4)	2.49(-12)	3.4(-19)
290	7.217	-9.556(-5)	6.484(-9)	—	-1.258(-4)	2.79(-12)	3.4(-19)
295	7.294	-9.136(-5)	6.361(-9)	—	-1.198(-4)	3.03(-12)	3.4(-19)
300	7.370	-8.735(-5)	6.242(-9)	—	-1.140(-4)	3.24(-12)	3.3(-19)
305	7.446	-8.352(-5)	6.126(-9)	—	-1.085(-4)	3.42(-12)	3.2(-19)
310	7.520	-7.984(-5)	6.014(-9)	—	-1.032(-4)	3.56(-12)	3.0(-19)
315	7.594	-7.631(-5)	5.905(-9)	—	-9.801(-5)	3.68(-12)	2.9(-19)
320	7.667	-7.293(-5)	5.800(-9)	—	-9.305(-5)	3.77(-12)	2.7(-19)
325	7.738	-6.969(-5)	5.699(-9)	—	-8.826(-5)	3.85(-12)	2.6(-19)
330	7.809	-6.657(-5)	5.602(-9)	—	-8.364(-5)	3.91(-12)	2.4(-19)
335	7.879	-6.357(-5)	5.508(-9)	—	-7.917(-5)	3.95(-12)	2.3(-19)
340	7.948	-6.068(-5)	5.418(-9)	—	-7.486(-5)	3.98(-12)	2.2(-19)
345	8.016	-5.790(-5)	5.331(-9)	—	-7.068(-5)	4.00(-12)	2.0(-19)
350	8.083	-5.522(-5)	5.248(-9)	—	-6.665(-5)	4.01(-12)	1.9(-19)
355	8.150	-5.264(-5)	5.168(-9)	—	-6.274(-5)	4.01(-12)	1.8(-19)
360	8.215	-5.014(-5)	5.090(-9)	—	-5.895(-5)	4.00(-12)	1.6(-19)
365	8.279	-4.774(-5)	5.016(-9)	—	-5.528(-5)	3.99(-12)	1.5(-19)
370	8.343	-4.541(-5)	4.945(-9)	—	-5.172(-5)	3.96(-12)	1.4(-19)
375	8.406	-4.317(-5)	4.877(-9)	—	-4.827(-5)	3.94(-12)	1.3(-19)
380	8.467	-4.099(-5)	4.812(-9)	—	-4.492(-5)	3.91(-12)	1.2(-19)

T (K)	$C_p^0(T)/R$	$B(T)$ ($\text{m}^3 \cdot \text{mol}^{-1}$)	$C(T)$ ($\text{m}^6 \cdot \text{mol}^{-2}$)	$D(T)$ ($\text{m}^9 \cdot \text{mol}^{-3}$)	$\beta_a(T)$ ($\text{m}^3 \cdot \text{mol}^{-1}$)	$\gamma_a(T)$ ($\text{m}^3 \cdot \text{mol}^{-1} \cdot \text{Pa}^{-1}$)	$\delta_a(T)$ ($\text{m}^3 \cdot \text{mol}^{-1} \cdot \text{Pa}^{-2}$)
385	8.528	-3.889(-5)	4.749(-9)	—	-4.167(-5)	3.88(-12)	1.1(-19)
390	8.588	-3.686(-5)	4.688(-9)	—	-3.851(-5)	3.84(-12)	1.0(-19)
395	8.647	-3.488(-5)	4.630(-9)	—	-3.545(-5)	3.80(-12)	9.6(-20)
400	8.706	-3.297(-5)	4.575(-9)	—	-3.246(-5)	3.76(-12)	8.8(-20)
405	8.763	-3.112(-5)	4.521(-9)	—	-2.956(-5)	3.72(-12)	8.1(-20)
410	8.820	-2.933(-5)	4.470(-9)	—	-2.674(-5)	3.67(-12)	7.4(-20)
415	8.875	-2.758(-5)	4.421(-9)	—	-2.400(-5)	3.63(-12)	6.8(-20)
420	8.930	-2.589(-5)	4.374(-9)	—	-2.132(-5)	3.58(-12)	6.2(-20)
425	8.984	-2.425(-5)	4.329(-9)	—	-1.872(-5)	3.54(-12)	5.6(-20)
430	9.038	-2.265(-5)	4.285(-9)	—	-1.619(-5)	3.49(-12)	5.1(-20)
435	9.090	-2.110(-5)	4.244(-9)	—	-1.372(-5)	3.44(-12)	4.6(-20)
440	9.142	-1.959(-5)	4.204(-9)	—	-1.131(-5)	3.39(-12)	4.1(-20)
445	9.193	-1.812(-5)	4.165(-9)	—	-8.960(-6)	3.34(-12)	3.7(-20)
450	9.243	-1.670(-5)	4.128(-9)	—	-6.670(-6)	3.29(-12)	3.3(-20)
455	9.293	-1.531(-5)	4.093(-9)	—	-4.435(-6)	3.24(-12)	2.9(-20)
460	9.341	-1.395(-5)	4.059(-9)	—	-2.255(-6)	3.20(-12)	2.6(-20)
465	9.389	-1.263(-5)	4.027(-9)	—	-1.259(-7)	3.15(-12)	2.2(-20)
470	9.437	-1.135(-5)	3.995(-9)	—	-1.953(-6)	3.10(-12)	1.9(-20)
475	9.483	-1.010(-5)	3.965(-9)	—	-3.983(-6)	3.05(-12)	1.6(-20)

Name: hexafluoroethane (CAS # 76-16-4)

Formula: C_2F_6

M.W.: 0.138012 kg/mol

Max. Pressure: 1500 kPa

Reference: Hurly, J.J. (1999). Thermophysical properties of gaseous CF_4 and H_2F_6 from speed-of-sound measurements. *Int. J. Thermophys.* **20**: 455–484.

T (K)	$C_p^0(T)/R$	$B(T)$ ($\text{m}^3 \cdot \text{mol}^{-1}$)	$C(T)$ ($\text{m}^6 \cdot \text{mol}^{-2}$)	$D(T)$ ($\text{m}^9 \cdot \text{mol}^{-3}$)	$\beta_a(T)$ ($\text{m}^3 \cdot \text{mol}^{-1}$)	$\gamma_a(T)$ ($\text{m}^3 \cdot \text{mol}^{-1} \cdot \text{Pa}^{-1}$)	$\delta_a(T)$ ($\text{m}^3 \cdot \text{mol}^{-1} \cdot \text{Pa}^{-2}$)
210	10.244	-5.772(-4)	-3.057(-8)	-2.47(-12)	-9.171(-4)	-2.84(-10)	-1.9(-16)
215	10.401	-5.472(-4)	-1.734(-8)	-2.30(-12)	-8.725(-4)	-2.40(-10)	-1.5(-16)
220	10.557	-5.194(-4)	-7.094(-9)	-2.14(-12)	-8.309(-4)	-2.03(-10)	-1.1(-16)
225	10.712	-4.936(-4)	8.205(-10)	-1.99(-12)	-7.921(-4)	-1.73(-10)	-9.0(-17)
230	10.865	-4.696(-4)	6.914(-9)	-1.84(-12)	-7.557(-4)	-1.47(-10)	-7.0(-17)
235	11.017	-4.473(-4)	1.158(-8)	-1.70(-12)	-7.216(-4)	-1.26(-10)	-5.5(-17)
240	11.168	-4.264(-4)	1.512(-8)	-1.57(-12)	-6.896(-4)	-1.08(-10)	-4.4(-17)
245	11.316	-4.069(-4)	1.777(-8)	-1.44(-12)	-6.594(-4)	-9.23(-11)	-3.4(-17)
250	11.464	-3.886(-4)	1.973(-8)	-1.31(-12)	-6.310(-4)	-7.91(-11)	-2.7(-17)
255	11.609	-3.714(-4)	2.113(-8)	-1.19(-12)	-6.042(-4)	-6.78(-11)	-2.2(-17)
260	11.753	-3.552(-4)	2.209(-8)	-1.08(-12)	-5.789(-4)	-5.81(-11)	-1.7(-17)
265	11.896	-3.400(-4)	2.272(-2)	-9.70(-13)	-5.548(-4)	-4.98(-11)	-1.3(-17)
270	12.037	-3.257(-4)	2.307(-8)	-8.64(-13)	-5.321(-4)	-4.26(-11)	-1.0(-17)
275	12.176	-3.121(-4)	2.321(-8)	-7.62(-13)	-5.105(-4)	-3.63(-11)	-8.2(-18)
280	12.313	-2.992(-4)	2.319(-8)	-6.63(-13)	-4.899(-4)	-3.09(-11)	-6.3(-18)
285	12.449	-2.871(-4)	2.303(-8)	-5.68(-13)	-4.704(-4)	-2.62(-11)	-4.8(-18)
290	12.583	-2.755(-4)	2.278(-8)	-4.76(-13)	-4.518(-4)	-2.21(-11)	-3.6(-18)
295	12.715	-2.646(-4)	2.246(-8)	-3.88(-13)	-4.340(-4)	-1.86(-11)	-2.7(-18)
300	12.846	-2.541(-4)	2.208(-8)	-3.02(-13)	-4.171(-4)	-1.54(-11)	-1.9(-18)
305	12.975	-2.442(-4)	2.166(-8)	-2.19(-13)	-4.009(-4)	-1.27(-11)	-1.3(-18)
310	13.102	-2.348(-4)	2.121(-8)	-1.39(-13)	-3.854(-4)	-1.03(-11)	-7.5(-19)
315	13.227	-2.257(-4)	2.075(-8)	-6.12(-14)	-3.706(-4)	-8.19(-12)	-3.4(-19)
320	13.351	-2.171(-4)	2.028(-8)	1.40(-14)	-3.564(-4)	-6.34(-12)	-1.7(-20)
325	13.473	-2.089(-4)	1.980(-8)	8.70(-14)	-3.428(-4)	-4.70(-12)	2.4(-19)
330	13.594	-2.010(-4)	1.933(-8)	1.58(-13)	-3.298(-4)	-3.26(-12)	4.5(-19)
335	13.712	-1.935(-4)	1.886(-8)	2.26(-13)	-3.172(-4)	-1.99(-12)	6.1(-19)
340	13.829	-1.862(-4)	1.840(-8)	2.93(-13)	-3.052(-4)	-8.69(-13)	7.4(-19)
345	13.945	-1.793(-4)	1.795(-8)	3.58(-13)	-2.936(-4)	1.21(-13)	8.4(-19)
350	14.059	-1.727(-4)	1.751(-8)	4.20(-13)	-2.824(-4)	9.95(-13)	9.1(-19)
355	14.171	-1.663(-4)	1.709(-8)	4.81(-13)	-2.717(-4)	1.77(-12)	9.7(-19)

(continues)

(continued)

T (K)	$C_p(T)/R$	$B(T)$ ($\text{m}^3 \cdot \text{mol}^{-1}$)	$C(T)$ ($\text{m}^6 \cdot \text{mol}^{-2}$)	$D(T)$ ($\text{m}^9 \cdot \text{mol}^{-3}$)	$\beta_a(T)$ ($\text{m}^3 \cdot \text{mol}^{-1}$)	$\gamma_a(T)$ ($\text{m}^3 \cdot \text{mol}^{-1} \cdot \text{Pa}^{-1}$)	$\delta_a(T)$ ($\text{m}^3 \cdot \text{mol}^{-1} \cdot \text{Pa}^{-2}$)
360	14.281	-1.601(-4)	1.668(-8)	5.41(-13)	-2.613(-4)	2.45(-12)	1.0(-18)
365	14.390	-1.542(-4)	1.629(-8)	5.99(-13)	-2.513(-4)	3.05(-12)	1.0(-18)
370	14.497	-1.485(-4)	1.591(-8)	6.55(-13)	-2.417(-4)	3.58(-12)	1.1(-18)
375	14.603	-1.430(-4)	1.555(-8)	7.09(-13)	-2.324(-4)	4.05(-12)	1.1(-18)
380	14.706	-1.378(-4)	1.520(-8)	7.63(-13)	-2.234(-4)	4.46(-12)	1.1(-18)
385	14.809	-1.327(-4)	1.487(-8)	8.14(-13)	-2.147(-4)	4.83(-12)	1.1(-18)
390	14.910	-1.278(-4)	1.455(-8)	8.65(-13)	-2.063(-4)	5.15(-12)	1.1(-18)
395	15.009	-1.230(-4)	1.425(-8)	9.14(-13)	-1.982(-4)	5.43(-12)	1.0(-18)
400	15.106	-1.184(-4)	1.396(-8)	9.62(-13)	-1.903(-4)	5.67(-12)	1.0(-18)
405	15.202	-1.140(-4)	1.369(-8)	1.01(-12)	-1.827(-4)	5.88(-12)	1.0(-18)
410	15.297	-1.097(-4)	1.343(-8)	1.05(-12)	-1.753(-4)	6.07(-12)	9.9(-19)
415	15.390	-1.056(-4)	1.318(-8)	1.10(-12)	-1.682(-4)	6.23(-12)	9.7(-19)
420	15.481	-1.016(-4)	1.294(-8)	1.14(-12)	-1.613(-4)	6.36(-12)	9.5(-19)
425	15.571	-9.767(-5)	1.272(-8)	1.19(-12)	-1.545(-4)	6.48(-12)	9.3(-19)
430	15.660	-9.390(-5)	1.251(-8)	1.23(-12)	-1.480(-4)	6.58(-12)	9.1(-19)
435	15.747	-9.025(-5)	1.231(-8)	1.27(-12)	-1.416(-4)	6.66(-12)	8.9(-19)
440	15.832	-8.670(-5)	1.212(-8)	1.31(-12)	-1.355(-4)	6.73(-12)	8.7(-19)
445	15.916	-8.327(-5)	1.194(-8)	1.35(-12)	-1.295(-4)	6.78(-12)	8.5(-19)
450	15.999	-7.993(-5)	1.177(-8)	1.38(-12)	-1.236(-4)	6.83(-12)	8.3(-19)
455	16.080	-7.669(-5)	1.161(-8)	1.42(-12)	-1.180(-4)	6.86(-12)	8.1(-19)
460	16.160	-7.354(-5)	1.146(-8)	1.46(-12)	-1.125(-4)	6.88(-12)	7.9(-19)
465	16.238	-7.048(-5)	1.132(-8)	1.49(-12)	-1.071(-4)	6.90(-12)	7.7(-19)
470	16.315	-6.750(-5)	1.119(-8)	1.53(-12)	-1.019(-4)	6.91(-12)	7.5(-19)
475	16.391	-6.461(-5)	1.106(-8)	1.56(-12)	-9.678(-5)	6.91(-12)	7.3(-19)

Name: sulfur hexafluoride (CAS # 2551-62-4)

Formula: SF_6

M.W.: 0.146054 kg/mol

Max. Pressure: 1500 kPa

Reference: Hurly, J.J., Defibaugh, D.R., and Moldover, M.R. (2000). Thermodynamic properties of sulfur Hexafluoride. *Int. J. Thermophys.* **21**: 739–765.

T (K)	$C_p(T)/R$	$B(T)$ ($\text{m}^3 \cdot \text{mol}^{-1}$)	$C(T)$ ($\text{m}^6 \cdot \text{mol}^{-2}$)	$D(T)$ ($\text{m}^9 \cdot \text{mol}^{-3}$)	$\beta_a(T)$ ($\text{m}^3 \cdot \text{mol}^{-1}$)	$\gamma_a(T)$ ($\text{m}^3 \cdot \text{mol}^{-1} \cdot \text{Pa}^{-1}$)	$\delta_a(T)$ ($\text{m}^3 \cdot \text{mol}^{-1} \cdot \text{Pa}^{-2}$)
230	9.367	-4.868(-4)	-2.852(-8)	-7.24(-12)	-7.636(-4)	-1.88(-10)	-1.1(-16)
235	9.552	-4.645(-4)	-1.950(-8)	-7.65(-12)	-7.320(-4)	-1.63(-10)	-8.6(-17)
240	9.734	-4.437(-4)	-1.219(-8)	-7.96(-12)	-7.022(-4)	-1.41(-10)	-7.0(-17)
245	9.913	-4.242(-4)	-6.272(-9)	-8.18(-12)	-6.740(-4)	-1.22(-10)	-5.8(-17)
250	10.088	-4.059(-4)	-1.478(-9)	-8.32(-12)	-6.473(-4)	-1.06(-10)	-4.8(-17)
255	10.261	-3.888(-4)	2.399(-9)	-8.40(-12)	-6.221(-4)	-9.25(-11)	-4.0(-17)
260	10.430	-3.726(-4)	5.528(-9)	-8.44(-12)	-5.981(-4)	-8.06(-11)	-3.4(-17)
265	10.596	-3.574(-4)	8.042(-9)	-8.42(-12)	-5.753(-4)	-7.02(-11)	-2.8(-17)
270	10.759	-3.430(-4)	1.005(-8)	-8.38(-12)	-5.536(-4)	-6.12(-11)	-2.4(-17)
275	10.919	-3.295(-4)	1.165(-8)	-8.30(-12)	-5.330(-4)	-5.34(-11)	-2.0(-17)
280	11.077	-3.166(-4)	1.291(-8)	-8.20(-12)	-5.133(-4)	-4.65(-11)	-1.7(-17)
285	11.231	-3.045(-4)	1.388(-8)	-8.07(-12)	-4.945(-4)	-4.05(-11)	-1.5(-17)
290	11.382	-2.929(-4)	1.463(-8)	-7.93(-12)	-4.766(-4)	-3.53(-11)	-1.3(-17)
295	11.531	-2.820(-4)	1.518(-8)	-7.78(-12)	-4.595(-4)	-3.07(-11)	-1.1(-17)
300	11.676	-2.715(-4)	1.558(-8)	-7.62(-12)	-4.431(-4)	-2.66(-11)	-9.7(-18)
305	11.819	-2.616(-4)	1.585(-8)	-7.44(-12)	-4.275(-4)	-2.30(-11)	-8.5(-18)
310	11.959	-2.521(-4)	1.601(-8)	-7.27(-12)	-4.124(-4)	-1.98(-11)	-7.4(-18)
315	12.096	-2.431(-4)	1.608(-8)	-7.09(-12)	-3.981(-4)	-1.70(-11)	-6.5(-18)
320	12.230	-2.345(-4)	1.608(-8)	-6.90(-12)	-3.842(-4)	-1.46(-11)	-5.8(-18)
325	12.362	-2.262(-4)	1.603(-8)	-6.72(-12)	-3.710(-4)	-1.24(-11)	-5.1(-18)
330	12.491	-2.184(-4)	1.592(-8)	-6.53(-12)	-3.582(-4)	-1.04(-11)	-4.5(-18)
335	12.617	-2.108(-4)	1.578(-8)	-6.35(-12)	-3.460(-4)	-8.67(-12)	-4.1(-18)
340	12.741	-2.036(-4)	1.561(-8)	-6.16(-12)	-3.342(-4)	-7.13(-12)	-3.6(-18)
345	12.862	-1.966(-4)	1.541(-8)	-5.98(-12)	-3.228(-4)	-5.76(-12)	-3.3(-18)
350	12.980	-1.900(-4)	1.520(-8)	-5.80(-12)	-3.119(-4)	-4.54(-12)	-2.9(-18)

T (K)	$C_p(T)/R$	$B(T)$ ($\text{m}^3 \cdot \text{mol}^{-1}$)	$C(T)$ ($\text{m}^6 \cdot \text{mol}^{-2}$)	$D(T)$ ($\text{m}^9 \cdot \text{mol}^{-3}$)	$\beta_a(T)$ ($\text{m}^3 \cdot \text{mol}^{-1}$)	$\gamma_a(T)$ ($\text{m}^3 \cdot \text{mol}^{-1} \cdot \text{Pa}^{-1}$)	$\delta_a(T)$ ($\text{m}^3 \cdot \text{mol}^{-1} \cdot \text{Pa}^{-2}$)
355	13.096	-1.836(-4)	1.497(-8)	-5.63(-12)	-3.013(-4)	-3.45(-12)	-2.6(-18)
360	13.210	-1.774(-4)	1.474(-8)	-5.46(-12)	-2.911(-4)	-2.48(-12)	-2.4(-18)
365	13.320	-1.715(-4)	1.449(-8)	-5.29(-12)	-2.813(-4)	-1.62(-12)	-2.2(-18)
370	13.429	-1.658(-4)	1.424(-8)	-5.13(-12)	-2.718(-4)	-8.46(-13)	-2.0(-18)
375	13.535	-1.603(-4)	1.399(-8)	-4.97(-12)	-2.627(-4)	-1.58(-13)	-1.8(-18)
380	13.638	-1.550(-4)	1.374(-8)	-4.81(-12)	-2.538(-4)	4.55(-13)	-1.6(-18)
385	13.740	-1.499(-4)	1.349(-8)	-4.66(-12)	-2.452(-4)	1.00(-12)	-1.5(-18)
390	13.839	-1.450(-4)	1.325(-8)	-4.52(-12)	-2.369(-4)	1.49(-12)	-1.4(-18)
395	13.935	-1.402(-4)	1.300(-8)	-4.38(-12)	-2.289(-4)	1.92(-12)	-1.3(-18)
400	14.029	-1.356(-4)	1.276(-8)	-4.24(-12)	-2.211(-4)	2.31(-12)	-1.2(-18)
405	14.121	-1.312(-4)	1.253(-8)	-4.11(-12)	-2.136(-4)	2.65(-12)	-1.1(-18)
410	14.211	-1.269(-4)	1.229(-8)	-3.98(-12)	-2.063(-4)	2.96(-12)	-1.0(-18)
415	14.299	-1.227(-4)	1.207(-8)	-3.86(-12)	-1.992(-4)	3.23(-12)	-9.3(-19)
420	14.384	-1.187(-4)	1.185(-8)	-3.74(-12)	-1.923(-4)	3.47(-12)	-8.7(-19)
425	14.467	-1.148(-4)	1.164(-8)	-3.63(-12)	-1.856(-4)	3.68(-12)	-8.1(-19)
430	14.548	-1.110(-4)	1.143(-8)	-3.52(-12)	-1.791(-4)	3.86(-12)	-7.6(-19)
435	14.627	-1.073(-4)	1.123(-8)	-3.42(-12)	-1.728(-4)	4.03(-12)	-7.1(-19)
440	14.704	-1.038(-4)	1.104(-8)	-3.32(-12)	-1.667(-4)	4.17(-12)	-6.7(-19)
445	14.779	-1.003(-4)	1.085(-8)	-3.22(-12)	-1.607(-4)	4.29(-12)	-6.3(-19)
450	14.852	-9.700(-5)	1.067(-8)	-3.13(-12)	-1.549(-4)	4.40(-12)	-5.9(-19)
455	14.923	-9.374(-5)	1.049(-8)	-3.04(-12)	-1.493(-4)	4.49(-12)	-5.6(-19)
460	14.992	-9.059(-5)	1.032(-8)	-2.96(-12)	-1.438(-4)	4.57(-12)	-5.3(-19)

Name: tungsten hexafluoride (CAS 7783-82-6)
Formula: WF_6
M.W.: 0.29784 kg/mol
Max. Pressure: 300 kPa
Reference: Hurly, J.J. (2000). Thermophysical properties of gaseous tungsten hexafluoride from speed-of-sound measurements. *Int. J. Thermophys.* **21**: 185–206.

T (K)	$C_p^0(T)/R$	$B(T)$ ($\text{m}^3 \cdot \text{mol}^{-1}$)	$C(T)$ ($\text{m}^6 \cdot \text{mol}^{-2}$)	$D(T)$ ($\text{m}^9 \cdot \text{mol}^{-3}$)	$\beta_a(T)$ ($\text{m} \cdot \text{mol}^{-1}$)	$\gamma_a(T)$ ($\text{m}^3 \cdot \text{mol}^{-1} \cdot \text{Pa}^{-1}$)	$\delta_a(T)$ ($\text{m}^3 \cdot \text{mol}^{-1} \cdot \text{Pa}^{-2}$)
290	14.229	-7.955(-4)	-1.113(-7)	—	-1.341(-3)	-4.71(-10)	-3.2(-16)
295	14.326	-7.637(-4)	-8.388(-8)	—	-1.289(-3)	-4.13(-10)	-2.6(-16)
300	14.422	-7.338(-4)	-6.120(-8)	—	-1.241(-3)	-3.63(-10)	-2.1(-16)
305	14.516	-7.057(-4)	-4.245(-8)	—	-1.196(-3)	-3.20(-10)	-1.8(-16)
310	14.607	-6.791(-4)	-2.695(-8)	—	-1.152(-3)	-2.82(-10)	-1.5(-16)
315	14.697	-6.541(-4)	-1.415(-8)	—	-1.112(-3)	-2.50(-10)	-1.2(-16)
320	14.785	-6.305(-4)	-3.597(-9)	—	-1.073(-3)	-2.21(-10)	-1.0(-16)
325	14.871	-6.081(-4)	5.087(-9)	—	-1.036(-3)	-1.97(-10)	-8.4(-17)
330	14.954	-5.869(-4)	1.221(-8)	—	-1.001(-3)	-1.75(-10)	-7.1(-17)
335	15.036	-5.668(-4)	1.803(-8)	—	-9.681(-4)	-1.56(-10)	-5.9(-17)
340	15.116	-5.477(-4)	2.277(-8)	—	-9.365(-4)	-1.39(-10)	-5.0(-17)
345	15.194	-5.295(-4)	2.658(-8)	—	-9.064(-4)	-1.24(-10)	-4.2(-17)
350	15.270	-5.123(-4)	2.964(-8)	—	-8.777(-4)	-1.11(-10)	-3.5(-17)
355	15.344	-4.958(-4)	3.205(-8)	—	-8.503(-4)	-9.98(-11)	-3.0(-17)
360	15.416	-4.801(-4)	3.393(-8)	—	-8.240(-4)	-8.96(-11)	-2.5(-17)
365	15.486	-4.652(-4)	3.536(-8)	—	-7.989(-4)	-8.04(-11)	-2.1(-17)
370	15.554	-4.509(-4)	3.641(-8)	—	-7.749(-4)	-7.23(-11)	-1.8(-17)
375	15.620	-4.372(-4)	3.715(-8)	—	-7.519(-4)	-6.50(-11)	-1.5(-17)
380	15.684	-4.242(-4)	3.762(-8)	—	-7.298(-4)	-5.84(-11)	-1.3(-17)
385	15.747	-4.116(-4)	3.788(-8)	—	-7.087(-4)	-5.26(-11)	-1.1(-17)
390	15.807	-3.996(-4)	3.795(-8)	—	-6.883(-4)	-4.73(-11)	-9.2(-18)
395	15.865	-3.881(-4)	3.788(-8)	—	-6.688(-4)	-4.26(-11)	-7.8(-18)
400	15.921	-3.771(-4)	3.768(-8)	—	-6.500(-4)	-3.83(-11)	-6.6(-18)
405	15.976	-3.665(-4)	3.739(-8)	—	-6.319(-4)	-3.45(-11)	-5.5(-18)
410	16.028	-3.563(-4)	3.701(-8)	—	-6.145(-4)	-3.10(-11)	-4.6(-18)
415	16.078	-3.465(-4)	3.656(-8)	—	-5.977(-4)	-2.78(-11)	-3.9(-18)
420	16.127	-3.371(-4)	3.607(-8)	—	-5.815(-4)	-2.50(-11)	-3.2(-18)

Name: hydrogen bromide (CAS # 10035-10-6)
 Formula: HBr
 M.W.: 0.080912 kg/mol
 Max. Pressure: 1500 kPa
 Reference: Hurly, J.J. (2000). Thermophysical properties of gaseous HBr and BCl₃ from speed-of-sound measurements. *Int. J. Thermophys.*

T (K)	$C_p^0(T)/R$	$B(T)$ (m ³ · mol ⁻¹)	$C(T)$ (m ⁶ · mol ⁻²)	$D(T)$ (m ⁹ · mol ⁻³)	$\beta_a(T)$ (m ³ · mol ⁻¹)	$\gamma_a(T)$ (m ³ · mol ⁻¹ · Pa ⁻¹)	$\delta_a(T)$ (m ³ · mol ⁻¹ · Pa ⁻²)
230	3.503	-3.277(-4)	-1.608(-8)	—	-3.668(-4)	-8.14(-11)	-2.5(-17)
235	3.503	-3.118(-4)	-1.079(-8)	—	-3.482(-4)	-6.88(-11)	-2.0(-17)
240	3.503	-2.971(-4)	-6.686(-9)	—	-3.310(-4)	-5.85(-11)	-1.6(-17)
245	3.503	-2.835(-4)	-3.494(-9)	—	-3.150(-4)	-5.00(-11)	-1.3(-17)
250	3.503	-2.708(-4)	-1.020(-9)	—	-3.001(-4)	-4.29(-11)	-1.0(-17)
255	3.503	-2.590(-4)	8.906(-10)	—	-2.863(-4)	-3.70(-11)	-8.5(-18)
260	3.503	-2.480(-4)	2.358(-9)	—	-2.734(-4)	-3.21(-11)	-6.9(-18)
265	3.503	-2.377(-4)	3.476(-9)	—	-2.613(-4)	-2.79(-11)	-5.6(-18)
270	3.503	-2.281(-4)	4.318(-9)	—	-2.500(-4)	-2.43(-11)	-4.6(-18)
275	3.503	-2.190(-4)	4.941(-9)	—	-2.394(-4)	-2.13(-11)	-3.8(-18)
280	3.503	-2.105(-4)	5.392(-9)	—	-2.294(-4)	-1.87(-11)	-3.1(-18)
285	3.503	-2.025(-4)	5.707(-9)	—	-2.200(-4)	-1.64(-11)	-2.6(-18)
290	3.503	-1.949(-4)	5.914(-9)	—	-2.111(-4)	-1.45(-11)	-2.1(-18)
295	3.503	-1.878(-4)	6.036(-9)	—	-2.027(-4)	-1.28(-11)	-1.8(-18)
300	3.503	-1.810(-4)	6.092(-9)	—	-1.948(-4)	-1.13(-11)	-1.5(-18)
305	3.504	-1.746(-4)	6.096(-9)	—	-1.873(-4)	-9.96(-12)	-1.2(-18)
310	3.504	-1.686(-4)	6.060(-9)	—	-1.801(-4)	-8.82(-12)	-1.0(-18)
315	3.504	-1.628(-4)	5.994(-9)	—	-1.733(-4)	-7.81(-12)	-8.6(-19)
320	3.504	-1.573(-4)	5.905(-9)	—	-1.669(-4)	-6.92(-12)	-7.2(-19)
325	3.504	-1.521(-4)	5.798(-9)	—	-1.608(-4)	-6.12(-12)	-6.0(-19)
330	3.505	-1.472(-4)	5.680(-9)	—	-1.549(-4)	-5.42(-12)	-5.0(-19)
335	3.505	-1.425(-4)	5.553(-9)	—	-1.493(-4)	-4.79(-12)	-4.2(-19)
340	3.505	-1.380(-4)	5.420(-9)	—	-1.440(-4)	-4.22(-12)	-3.4(-19)
345	3.506	-1.337(-4)	5.285(-9)	—	-1.389(-4)	-3.72(-12)	-2.8(-19)
350	3.506	-1.296(-4)	5.149(-9)	—	-1.340(-4)	-3.26(-12)	-2.3(-19)
355	3.506	-1.257(-4)	5.014(-9)	—	-1.294(-4)	-2.85(-12)	-1.9(-19)
360	3.507	-1.219(-4)	4.880(-9)	—	-1.249(-4)	-2.48(-12)	-1.5(-19)
365	3.507	-1.183(-4)	4.749(-9)	—	-1.206(-4)	-2.15(-12)	-1.2(-19)
370	3.508	-1.148(-4)	4.622(-9)	—	-1.165(-4)	-1.85(-12)	-9.6(-20)
375	3.509	-1.115(-4)	4.498(-9)	—	-1.125(-4)	-1.57(-12)	-7.4(-20)
380	3.509	-1.083(-4)	4.379(-9)	—	-1.087(-4)	-1.32(-12)	-5.5(-20)
385	3.510	-1.053(-4)	4.264(-9)	—	-1.050(-4)	-1.09(-12)	-3.8(-20)
390	3.511	-1.023(-4)	4.154(-9)	—	-1.015(-4)	-8.84(-13)	-2.4(-20)
395	3.511	-9.949(-5)	4.049(-9)	—	-9.812(-5)	-6.94(-13)	-1.3(-20)
400	3.512	-9.676(-5)	3.948(-9)	—	-9.485(-5)	-5.20(-13)	-2.5(-21)
405	3.513	-9.413(-5)	3.852(-9)	—	-9.169(-5)	-3.61(-13)	5.9(-21)
410	3.514	-9.159(-5)	3.761(-9)	—	-8.864(-5)	-2.15(-13)	1.3(-20)
415	3.515	-8.914(-5)	3.675(-9)	—	-8.570(-5)	-8.13(-14)	1.9(-20)
420	3.516	-8.678(-5)	3.593(-9)	—	-8.286(-5)	4.18(-14)	2.4(-20)
425	3.517	-8.450(-5)	3.515(-9)	—	-8.011(-5)	1.55(-13)	2.9(-20)
430	3.518	-8.229(-5)	3.442(-9)	—	-7.745(-5)	2.59(-13)	3.2(-20)
435	3.519	-8.016(-5)	3.373(-9)	—	-7.488(-5)	3.55(-13)	3.5(-20)
440	3.520	-7.810(-5)	3.308(-9)	—	-7.239(-5)	4.44(-13)	3.7(-20)

Name: boron trichloride (CAS # 10294-34-5)
 Formula: BCl_3
 M.W.: 0.11717 kg/mol
 Max. Pressure: 1500 kPa
 Reference: Hurly, J.J. (2000). Thermophysical properties of gaseous HBr and BCl_3 from speed-of-sound measurements, *Int. J. Thermophys.*

T (K)	$C_p^0(T)/R$	$B(T)$ ($\text{m}^3 \cdot \text{mol}^{-1}$)	$C(T)$ ($\text{m}^6 \cdot \text{mol}^{-2}$)	$D(T)$ ($\text{m}^9 \cdot \text{mol}^{-3}$)	$\beta_a(T)$ ($\text{m}^3 \cdot \text{mol}^{-1}$)	$\gamma_a(T)$ ($\text{m}^3 \cdot \text{mol}^{-1} \cdot \text{Pa}^{-1}$)	$\delta_a(T)$ ($\text{m}^3 \cdot \text{mol}^{-1} \cdot \text{Pa}^{-2}$)
290	7.447	-7.649(-4)	-2.992(-7)	—	-1.216(-3)	-5.17(-10)	-3.6(-16)
295	7.490	-7.376(-4)	-2.492(-7)	—	-1.176(-3)	-4.55(-10)	-2.9(-16)
300	7.533	-7.118(-4)	-2.068(-7)	—	-1.138(-3)	-4.02(-10)	-2.4(-16)
305	7.574	-6.873(-4)	-1.707(-7)	—	-1.103(-3)	-3.55(-10)	-2.0(-16)
310	7.616	-6.641(-4)	-1.400(-7)	—	-1.068(-3)	-3.15(-10)	-1.7(-16)
315	7.656	-6.420(-4)	-1.137(-7)	—	-1.036(-3)	-2.79(-10)	-1.4(-16)
320	7.696	-6.211(-4)	-9.126(-8)	—	-1.004(-3)	-2.48(-10)	-1.2(-16)
325	7.735	-6.011(-4)	-7.207(-8)	—	-9.747(-4)	-2.21(-10)	-1.0(-16)
330	7.774	-5.821(-4)	-5.563(-8)	—	-9.462(-4)	-1.97(-10)	-8.4(-17)
335	7.812	-5.640(-4)	-4.156(-8)	—	-9.189(-4)	-1.76(-10)	-7.1(-17)
340	7.849	-5.467(-4)	-2.950(-8)	—	-8.927(-4)	-1.57(-10)	-5.9(-17)
345	7.886	-5.302(-4)	-1.917(-8)	—	-8.676(-4)	-1.40(-10)	-5.0(-17)
350	7.922	-5.144(-4)	-1.032(-8)	—	-8.435(-4)	-1.25(-10)	-4.2(-17)
355	7.957	-4.993(-4)	-2.741(-9)	—	-8.203(-4)	-1.12(-10)	-3.6(-17)
360	7.992	-4.848(-4)	3.736(-9)	—	-7.981(-4)	-1.00(-10)	-3.0(-17)
365	8.026	-4.709(-4)	9.266(-9)	—	-7.766(-4)	-8.99(-11)	-2.5(-17)
370	8.059	-4.576(-4)	1.398(-8)	—	-7.560(-4)	-8.06(-11)	-2.1(-17)
375	8.092	-4.448(-4)	1.798(-8)	—	-7.362(-4)	-7.22(-11)	-1.8(-17)
380	8.124	-4.325(-4)	2.138(-8)	—	-7.170(-4)	-6.46(-11)	-1.5(-17)
385	8.156	-4.207(-4)	2.424(-8)	—	-6.985(-4)	-5.79(-11)	-1.3(-17)
390	8.187	-4.093(-4)	2.665(-8)	—	-6.807(-4)	-5.18(-11)	-1.1(-17)
395	8.217	-3.983(-4)	2.866(-8)	—	-6.635(-4)	-4.63(-11)	-9.0(-18)
400	8.247	-3.878(-4)	3.032(-8)	—	-6.469(-4)	-4.13(-11)	-7.5(-18)
405	8.276	-3.776(-4)	3.169(-8)	—	-6.308(-4)	-3.69(-11)	-6.2(-18)
410	8.304	-3.678(-4)	3.279(-8)	—	-6.152(-4)	-3.28(-11)	-5.1(-18)
415	8.332	-3.583(-4)	3.367(-8)	—	-6.001(-4)	-2.92(-11)	-4.2(-18)
420	8.359	-3.492(-4)	3.436(-8)	—	-5.856(-4)	-2.59(-11)	-3.4(-18)

Name: xenon (CAS # 7440-63-3)
 Formula: Xe
 M.W.: 0.1313 kg/mol
 Max. Pressure: 1500 kPa
 Reference: Hurly, J.J., Schmidt, J.W., Boyes, S.J., and Moldover, M.R. (1997). Virial equation of state of helium, xenon, and helium-xenon mixtures from speed-of-sound and burnett P rho T measurements. *Int. J. Thermophys.* **18**: 579–634.

T (K)	$C_p^0(T)/R$	$B(T)$ ($\text{m}^3 \cdot \text{mol}^{-1}$)	$C(T)$ ($\text{m}^6 \cdot \text{mol}^{-2}$)	$D(T)$ ($\text{m}^9 \cdot \text{mol}^{-3}$)	$\beta_a(T)$ ($\text{m}^3 \cdot \text{mol}^{-1}$)	$\gamma_a(T)$ ($\text{m}^3 \cdot \text{mol}^{-1} \cdot \text{Pa}^{-1}$)	$\delta_a(T)$ ($\text{m}^3 \cdot \text{mol}^{-1} \cdot \text{Pa}^{-2}$)
210	2.5	-2.501(-4)	6.598(-11)	—	-2.381(-4)	-4.11(-11)	-9.6(-18)
215	2.5	-2.395(-4)	1.425(-9)	—	-2.257(-4)	-3.52(-11)	-7.8(-18)
220	2.5	-2.295(-4)	2.503(-9)	—	-2.142(-4)	-3.01(-11)	-6.3(-18)
225	2.5	-2.202(-4)	3.355(-9)	—	-2.034(-4)	-2.59(-11)	-5.2(-18)
230	2.5	-2.115(-4)	4.026(-9)	—	-1.933(-4)	-2.33(-11)	-4.2(-18)
235	2.5	-2.033(-4)	4.548(-9)	—	-1.838(-4)	-1.92(-11)	-3.4(-18)
240	2.5	-1.955(-4)	4.951(-9)	—	-1.749(-4)	-1.65(-11)	-2.8(-18)
245	2.5	-1.882(-4)	5.257(-9)	—	-1.664(-4)	-1.43(-11)	-2.3(-18)
250	2.5	-1.813(-4)	5.483(-9)	—	-1.585(-4)	-1.23(-11)	-1.9(-18)
255	2.5	-1.747(-4)	5.646(-9)	—	-1.510(-4)	-1.06(-11)	-1.5(-18)
260	2.5	-1.685(-4)	5.755(-9)	—	-1.439(-4)	-9.11(-12)	-1.2(-18)

(continues)

(continued)

T (K)	$C_p^0(T)/R$	$B(T)$ ($\text{m}^3 \cdot \text{mol}^{-1}$)	$C(T)$ ($\text{m}^6 \cdot \text{mol}^{-2}$)	$D(T)$ ($\text{m}^9 \cdot \text{mol}^{-3}$)	$\beta_a(T)$ ($\text{m}^3 \cdot \text{mol}^{-1}$)	$\gamma_a(T)$ ($\text{m}^3 \cdot \text{mol}^{-1} \cdot \text{Pa}^{-1}$)	$\delta_a(T)$ ($\text{m}^3 \cdot \text{mol}^{-1} \cdot \text{Pa}^{-2}$)
265	2.5	-1.626(-4)	5.823(-9)	—	-1.371(-4)	-7.82(-12)	-1.0(-18)
270	2.5	-1.570(-4)	5.856(-9)	—	-1.307(-4)	-6.69(-12)	-8.1(-19)
275	2.5	-1.517(-4)	5.861(-9)	—	-1.246(-4)	-5.70(-12)	-6.6(-19)
280	2.5	-1.466(-4)	5.844(-9)	—	-1.188(-4)	-4.83(-12)	-5.2(-19)
285	2.5	-1.417(-4)	5.809(-9)	—	-1.133(-4)	-4.07(-12)	-4.2(-19)
290	2.5	-1.371(-4)	5.760(-9)	—	-1.080(-4)	-3.40(-12)	-3.3(-19)
295	2.5	-1.327(-4)	5.699(-9)	—	-1.030(-4)	-2.80(-12)	-2.5(-19)
300	2.5	-1.284(-4)	5.630(-9)	—	-9.819(-5)	-2.28(-12)	-1.9(-19)
305	2.5	-1.244(-4)	5.554(-9)	—	-9.359(-5)	-1.81(-12)	-1.4(-19)
310	2.5	-1.205(-4)	5.473(-9)	—	-8.917(-5)	-1.40(-12)	-9.8(-20)
315	2.5	-1.168(-4)	5.388(-9)	—	-8.494(-5)	-1.03(-12)	-6.3(-20)
320	2.5	-1.132(-4)	5.301(-9)	—	-8.088(-5)	-7.06(-13)	-3.5(-20)
325	2.5	-1.098(-4)	5.213(-9)	—	-7.699(-5)	-4.16(-13)	-1.1(-20)
330	2.5	-1.064(-4)	5.123(-9)	—	-7.324(-5)	-1.58(-13)	7.6(-21)
335	2.5	-1.033(-4)	5.034(-9)	—	-6.963(-5)	7.14(-14)	2.3(-20)
340	2.5	-1.002(-4)	4.946(-9)	—	-6.617(-5)	2.76(-13)	3.6(-20)
345	2.5	-9.726(-5)	4.858(-9)	—	-6.282(-5)	4.59(-13)	4.6(-20)
350	2.5	-9.442(-5)	4.771(-9)	—	-5.960(-5)	6.21(-13)	5.4(-20)
355	2.5	-9.168(-5)	4.686(-9)	—	-5.649(-5)	7.66(-13)	6.0(-20)
360	2.5	-8.903(-5)	4.603(-9)	—	-5.350(-5)	8.96(-13)	6.4(-20)
365	2.5	-8.648(-5)	4.522(-9)	—	-5.060(-5)	1.01(-12)	6.8(-20)
370	2.5	-8.401(-5)	4.442(-9)	—	-4.780(-5)	1.11(-12)	7.0(-20)
375	2.5	-8.162(-5)	4.365(-9)	—	-4.509(-5)	1.20(-12)	7.2(-20)
380	2.5	-7.931(-5)	4.290(-9)	—	-4.247(-5)	1.28(-12)	7.3(-20)
385	2.5	-7.707(-5)	4.217(-9)	—	-3.994(-5)	1.36(-12)	7.3(-20)
390	2.5	-7.491(-5)	4.146(-9)	—	-3.749(-5)	1.42(-12)	7.3(-20)
395	2.5	-7.281(-5)	4.078(-9)	—	-3.511(-5)	1.48(-12)	7.3(-20)
400	2.5	-7.078(-5)	4.012(-9)	—	-3.280(-5)	1.53(-12)	7.2(-20)

Name: helium (CAS # 7440-59-7)

Formula: He

M.W.: 0.0040026 kg/mol

Max. Pressure: 1500 kPa

Reference: Hurly, J.J., Schmidt, J.W., Boyes, S.J., and Moldover, M.R. (1997).
 Virial equation of state of helium, xenon, and helium-xenon mixtures
 from speed-of-sound and Burnett P rho T measurements. *Int. J. Thermophys.* **18**: 579–634.

T (K)	$C_p^0(T)/R$	$B(T)$ ($\text{m}^3 \cdot \text{mol}^{-1}$)	$C(T)$ ($\text{m}^6 \cdot \text{mol}^{-2}$)	$D(T)$ ($\text{m}^9 \cdot \text{mol}^{-3}$)	$\beta_a(T)$ ($\text{m}^3 \cdot \text{mol}^{-1}$)	$\gamma_a(T)$ ($\text{m}^3 \cdot \text{mol}^{-1} \cdot \text{Pa}^{-1}$)	$\gamma_a(T)$ ($\text{m}^3 \cdot \text{mol}^{-1} \cdot \text{Pa}^{-2}$)
210	2.5	1.216(-5)	1.197(-10)	—	2.324(-5)	3.95(-14)	-9.7(-22)
215	2.5	1.214(-5)	1.188(-10)	—	2.316(-5)	3.75(-14)	-9.1(-22)
220	2.5	1.213(-5)	1.179(-10)	—	2.308(-5)	3.57(-14)	-8.6(-22)
225	2.5	1.212(-5)	1.171(-10)	—	2.229(-5)	3.39(-14)	-8.1(-22)
230	2.5	1.210(-5)	1.162(-10)	—	2.291(-5)	3.22(-14)	-7.6(-22)
235	2.5	1.208(-5)	1.153(-10)	—	2.282(-5)	3.07(-14)	-7.2(-22)
240	2.5	1.207(-5)	1.144(-10)	—	2.274(-5)	2.92(-14)	-6.7(-22)
245	2.5	1.205(-5)	1.136(-10)	—	2.265(-5)	2.78(-14)	-6.4(-22)
250	2.5	1.203(-5)	1.127(-10)	—	2.257(-5)	2.65(-14)	-6.0(-22)
255	2.5	1.202(-5)	1.119(-10)	—	2.249(-5)	2.53(-14)	-5.7(-22)
260	2.5	1.200(-5)	1.111(-10)	—	2.240(-5)	2.42(-14)	-5.4(-22)
265	2.5	1.198(-5)	1.103(-10)	—	2.232(-5)	2.31(-14)	-5.1(-22)
270	2.5	1.196(-5)	1.095(-10)	—	2.224(-5)	2.21(-14)	-4.9(-22)
275	2.5	1.194(-5)	1.087(-10)	—	2.216(-5)	2.12(-14)	-4.6(-22)
280	2.5	1.192(-5)	1.080(-10)	—	2.209(-5)	2.03(-14)	-4.4(-22)
285	2.5	1.190(-5)	1.072(-10)	—	2.201(-5)	1.95(-14)	-4.2(-22)
290	2.5	1.188(-5)	1.065(-10)	—	2.194(-5)	1.87(-14)	-4.0(-22)
295	2.5	1.186(-5)	1.058(-10)	—	2.186(-5)	1.80(-14)	-3.8(-22)

T (K)	$C_p^0(T)/R$	$B(T)$ ($\text{m}^3 \cdot \text{mol}^{-1}$)	$C(T)$ ($\text{m}^6 \cdot \text{mol}^{-2}$)	$D(T)$ ($\text{m}^9 \cdot \text{mol}^{-3}$)	$\beta_a(T)$ ($\text{m}^3 \cdot \text{mol}^{-1}$)	$\gamma_a(T)$ ($\text{m}^3 \cdot \text{mol}^{-1} \cdot \text{Pa}^{-1}$)	$\gamma_a(T)$ ($\text{m}^3 \cdot \text{mol}^{-1} \cdot \text{Pa}^{-2}$)
300	2.5	1.184(−5)	1.050(−10)	—	2.180(−5)	1.73(−14)	−3.6(−22)
305	2.5	1.182(−5)	1.043(−10)	—	2.173(−5)	1.66(−14)	−3.4(−22)
310	2.5	1.180(−5)	1.037(−10)	—	2.166(−5)	1.60(−14)	−3.3(−22)
315	2.5	1.178(−5)	1.030(−10)	—	2.160(−5)	1.54(−14)	−3.1(−22)
320	2.5	1.176(−5)	1.023(−10)	—	2.154(−5)	1.49(−14)	−3.0(−22)
325	2.5	1.174(−5)	1.017(−10)	—	2.149(−5)	1.44(−14)	−2.9(−22)
330	2.5	1.172(−5)	1.011(−10)	—	2.143(−5)	1.39(−14)	−2.7(−22)
335	2.5	1.169(−5)	1.004(−10)	—	2.138(−5)	1.35(−14)	−2.6(−22)
340	2.5	1.167(−5)	9.982(−11)	—	2.134(−5)	1.31(−14)	−2.5(−22)
345	2.5	1.165(−5)	9.922(−11)	—	2.130(−5)	1.27(−14)	−2.4(−22)
350	2.5	1.163(−5)	9.863(−11)	—	2.126(−5)	1.23(−14)	−2.3(−22)
355	2.5	1.161(−5)	9.806(−11)	—	2.123(−5)	1.19(−14)	−2.2(−22)
360	2.5	1.159(−5)	9.749(−11)	—	2.120(−5)	1.16(−14)	−2.1(−22)
365	2.5	1.157(−5)	9.694(−11)	—	2.117(−5)	1.13(−14)	−2.0(−22)
370	2.5	1.155(−5)	9.639(−11)	—	2.115(−5)	1.10(−14)	−1.9(−22)
375	2.5	1.152(−5)	9.586(−11)	—	2.114(−5)	1.07(−14)	−1.9(−22)
380	2.5	1.150(−5)	9.533(−11)	—	2.113(−5)	1.05(−14)	−1.8(−22)
385	2.5	1.148(−5)	9.482(−11)	—	2.112(−5)	1.02(−14)	−1.7(−22)
390	2.5	1.146(−5)	9.431(−11)	—	2.112(−5)	1.00(−14)	−1.6(−22)
395	2.5	1.144(−5)	9.382(−11)	—	2.113(−5)	9.81(−14)	−1.6(−22)
400	2.5	1.142(−5)	9.333(−11)	—	2.114(−5)	9.62(−14)	−1.5(−22)

Name: argon (CAS # 7440-37-1)

Formula: Ar

M.W.: 0.039948 kg/mol

Max. Pressure: 1500 kPa

Reference: Aziz, R.A. (1993). A highly accurate interatomic potential for argon.

J. Chem. Phys. **99**: 4518–4525.

T (K)	$C_p^0(T)/R$	$B(T)$ ($\text{m}^3 \cdot \text{mol}^{-1}$)	$C(T)$ ($\text{m}^6 \cdot \text{mol}^{-2}$)	$D(T)$ ($\text{m}^9 \cdot \text{mol}^{-3}$)	$\beta_a(T)$ ($\text{m}^3 \cdot \text{mol}^{-1}$)	$\gamma_a(T)$ ($\text{m}^3 \cdot \text{mol}^{-1} \cdot \text{Pa}^{-1}$)	$\delta_a(T)$ ($\text{m}^3 \cdot \text{mol}^{-1} \cdot \text{Pa}^{-2}$)
100	2.5	−1.824(−4)	−8.830(−10)	—	−1.804(−4)	−4.58(−11)	−1.6(−17)
110	2.5	−1.531(−4)	1.080(−9)	—	−1.449(−4)	−2.50(−11)	−7.2(−18)
120	2.5	−1.305(−4)	1.853(−9)	—	−1.182(−4)	−1.41(−11)	−3.3(−18)
130	2.5	−1.126(−4)	2.114(−9)	—	−9.735(−5)	−8.01(−12)	−1.5(−18)
140	2.5	−9.809(−5)	2.150(−9)	—	−8.061(−5)	−4.42(−12)	−6.5(−19)
150	2.5	−8.606(−5)	2.087(−9)	—	−6.688(−5)	−2.24(−12)	−2.5(−19)
160	2.5	−7.596(−5)	1.985(−9)	—	−5.542(−5)	−8.81(−13)	−6.7(−20)
170	2.5	−6.736(−5)	1.871(−9)	—	−4.573(−5)	−2.25(−14)	2.0(−20)
180	2.5	−5.995(−5)	1.760(−9)	—	−3.742(−5)	5.23(−13)	5.6(−20)
190	2.5	−5.350(−5)	1.656(−9)	—	−3.022(−5)	8.67(−13)	6.9(−20)
200	2.5	−4.785(−5)	1.561(−9)	—	−2.393(−5)	1.08(−12)	6.9(−20)
210	2.5	−4.785(−5)	1.477(−9)	—	−1.839(−5)	1.21(−12)	6.4(−20)
220	2.5	−3.840(−5)	1.402(−9)	—	−1.348(−5)	1.27(−12)	5.7(−20)
230	2.5	−3.442(−5)	1.335(−9)	—	−9.091(−6)	1.30(−12)	5.0(−20)
240	2.5	−3.084(−5)	1.276(−9)	—	−5.155(−6)	1.30(−12)	4.3(−20)
250	2.5	−2.759(−5)	1.225(−9)	—	−1.605(−6)	1.29(−12)	3.6(−20)
260	2.5	−2.465(−5)	1.179(−9)	—	−1.610(−6)	1.23(−12)	3.0(−20)
270	2.5	−2.196(−5)	1.138(−9)	—	−4.535(−6)	1.23(−12)	2.5(−20)
280	2.5	−1.950(−5)	1.102(−9)	—	7.205(−6)	1.19(−12)	2.1(−20)
290	2.5	−1.724(−5)	1.070(−9)	—	9.650(−6)	1.14(−12)	1.7(−20)
300	2.5	−1.516(−5)	1.041(−9)	—	1.190(−5)	1.10(−12)	1.4(−20)
310	2.5	−1.323(−5)	1.015(−9)	—	1.397(−5)	1.06(−12)	1.1(−20)
320	2.5	−1.145(−5)	9.921(−10)	—	1.588(−5)	1.02(−12)	8.9(−21)
330	2.5	−9.792(−6)	9.714(−10)	—	1.765(−5)	9.74(−13)	7.0(−21)
340	2.5	−8.249(−6)	9.527(−10)	—	1.929(−5)	9.34(−13)	5.4(−21)
350	2.5	−6.809(−6)	9.357(−10)	—	2.082(−5)	8.94(−13)	4.1(−21)
360	2.5	−5.462(−6)	9.204(−10)	—	2.225(−5)	8.57(−13)	3.0(−21)
370	2.5	−4.021(−6)	9.064(−10)	—	2.358(−5)	8.21(−13)	2.1(−21)
380	2.5	−3.017(−6)	8.936(−10)	—	2.482(−5)	7.87(−13)	1.3(−21)

(continues)

T (K)	$C_p^0(T)/R$	$B(T)$ ($\text{m}^3 \cdot \text{mol}^{-1}$)	$C(T)$ ($\text{m}^6 \cdot \text{mol}^{-2}$)	$D(T)$ ($\text{m}^9 \cdot \text{mol}^{-3}$)	$\beta_a(T)$ ($\text{m}^3 \cdot \text{mol}^{-1}$)	$\gamma_a(T)$ ($\text{m}^3 \cdot \text{mol}^{-1} \cdot \text{Pa}^{-1}$)	$\delta_a(T)$ ($\text{m}^3 \cdot \text{mol}^{-1} \cdot \text{Pa}^{-2}$)
390	2.5	-1.904(-6)	8.820(-10)	—	2.599(-5)	7.54(-13)	6.3(-22)
400	2.5	-8.558(-7)	8.713(-10)	—	2.708(-5)	7.23(-13)	8.1(-23)
410	2.5	1.326(-7)	8.164(-10)	—	2.811(-5)	6.93(-13)	-3.7(-22)
420	2.5	1.066(-6)	8.524(-10)	—	2.908(-5)	6.65(-13)	-7.5(-22)
430	2.5	1.948(-6)	8.440(-10)	—	2.999(-5)	6.39(-13)	-1.1(-21)
440	2.5	2.784(-6)	8.362(-10)	—	3.085(-5)	6.13(-13)	-1.3(-21)
450	2.5	3.576(-6)	8.290(-10)	—	3.166(-5)	5.89(-13)	-1.5(-21)
460	2.5	4.328(-6)	8.222(-10)	—	3.242(-5)	5.66(-13)	-1.7(-21)
470	2.5	5.042(-6)	8.159(-10)	—	3.315(-5)	5.44(-13)	-1.8(-21)
480	2.5	5.722(-6)	8.100(-10)	—	3.383(-5)	5.24(-13)	-1.9(-21)
490	2.5	6.368(-6)	8.045(-10)	—	3.449(-5)	4.17(-13)	-3.0(-21)
500	2.5	6.984(-6)	7.993(-10)	—	3.510(-5)	4.00(-13)	-3.0(-21)

Acknowledgments

This work was supported in part by the Office of Naval Research. We thank the Deutscher Akademischer Austauschdienst (Germany), which provided a stipend to one of the authors (J.W.), thereby facilitating his participation in this work.

References

1. Mohr, P.J., and Taylor, B.N. (1999). CODATA Recommended Values of the Fundamental Physical Constants: 1998. *J. Phys. Chem. Ref. Data* **28**: 1713–1852.
2. Moldover, M.R., Trusler, J.P.M., Edwards, T.J., Mehl, J.B., and Davis, R.S. (1988). Measurement of the universal gas constant R using a spherical acoustic resonator. *J. Res. Nat. Bureau Stand. (US)* **93**: 85–144.
3. Moldover, M.R., Boyes, S.J., Meyer, C.W., and Goodwin, A.R.H. (1999). Thermodynamic temperatures of the triple points of mercury and gallium and in the interval 217 K to 303 K. *J. Res. Natl. Inst. Stand. Tech.* **104**: 11–46.
4. Moldover, M.R., Mehl, J.B., and Greenspan, M. (1986). Gas-filled spherical resonators: Theory and experiment. *J. Acoust. Soc. Am.* **79**: 253–272.
5. Gillis, K.A. (1994). Thermodynamic properties of two gaseous halogenated ethers from speed-of-sound measurement: Difluoromethoxy-difluoromethane and 2-difluoromethoxy-1,1,1-trifluoroethane. *Int. J. Thermophysics* **15**: 821–847.
6. Gillis, K.A., Mehl, J.B., and Moldover, M.R. (1996). Greenspan acoustic viscometer for gases. *Rev. Sci. Instrum.* **67**: 1850–1857.
7. Wilhelm, J., Gillis, K.A., Mehl, J.B., and Moldover, M.R. (2000). An improved Greenspan acoustic viscometer. *Int. J. Thermophysics* **21**: 983–997.
8. Gillis, K.A., and Moldover, M.R. (1996). Practical determination of gas densities from the speed of sound using square-well potentials. *Int. J. Thermophys.* **17**: 1305–1324.
9. Hurly, J.J. (1999). Thermophysical properties of gaseous CF_4 and C_2F_6 from speed-of-sound measurements. *Int. J. Thermophys.* **20**: 455.
10. Trusler, J.P.M. (1997). Equation of state for gaseous propane determined from the speed of sound. *Int. J. Thermophys.* **18**: 635–654.
11. Estrada-Alexanders, A.F., Trusler, J.P.M., and Zarari, M.P. (1995). Determination of thermodynamic properties from the speed of sound. *Int. J. Thermophys.* **16**: 663–673.

12. Trusler, J.P.M., Wakeham, W.A., and Zarari, M. (1997). Model intermolecular potentials and virial coefficients determined from the speed of sound. *Mol. Phys.* **90**: 695–703.
13. Colclough, A.R., Quinn, T.J., and Chandler, T.R.D. (1979). An acoustic redetermination of the gas constant. *Proc. R. Soc. Lond. A* **368**: 125–139.
14. Quinn, T.J., Colclough, A.R., and Chandler, T.R.D. (1976). A new determination of the gas constant by an acoustical method. *Phil. Trans. R. Soc. Lond. A* **283**: 367–420.
15. Batuecas, T. (1972). Volume normal moléculaire, V_o , des gaz à l'état idéal, in *Atomic Masses and Fundamental Constants*, vol. 4, Sanders, J.H., and Wapstra, A.H., eds., pp. 534–542, New York: Plenum.
16. Rowlinson, J.S., and Tildesley, D.J. (1977). The determination of the gas constant from the speed of sound. *Proc. R. Soc. Lond. A* **358**: 281–286.
17. Mason, E.A., and Spurling, T.H. (1969). *The Virial Equation of State*. Oxford: Pergamon Press.
18. Dulla, R.J., Rowlinson, J.S., and Smith, W.R. (1971). Effective pair potentials in fluids in the presence of three-body forces. II. *Mol. Phys.* **21**: 299–315.
19. Axilrod, B.M., and Teller, E.J. (1943). Interaction of the van der Waals type between three atoms. *J. Chem. Phys.* **11**: 299–300.
20. Hurly, J.J. (in press). Thermophysical properties of gaseous HBr and BCl₃ from speed-of-sound measurement. *Int. J. Thermophys.*
21. Goodwin, A.R.H. (1988). *Thermophysical Properties from the Speed of Sound*, pp. 113–117, PhD Thesis, University College London.
22. Garland, C.W., and Williams, R.D. (1974). Low-frequency sound velocity near the critical point of xenon. *Phys. Rev. A* **10**: 1328–1332.
23. Van Dael, W., (1975). Thermodynamic properties and the velocity of sound, in *Experimental Thermodynamics*, vol. II, Le Neindre, B., and Vodar, B., eds., pp. 527–577, London: Butterworths.
24. Gillis, K.A., Moldover, M.R., and Goodwin, A.R.H. (1991). Accurate acoustic measurements in gases under difficult conditions. *Rev. Sci. Instrum.* **62**: 2213–2217.
25. Mehl, J.B. (1999). Greenspan acoustic viscometer: Numerical calculations of fields and duct-end effects. *J. Acoust. Soc. Am.* **106**: 73–82.
26. Gillis, K.A., Mehl, J.B., and Moldover, M.R. (in preparation). Acoustic resonator for Prandtl number measurements.
27. Mehl, J.B., and Moldover, M.R. (1986). Measurement of the ratio of the speed of sound to the speed of light. *Phys. Rev. A* **34**: 3341–3344.
28. Strouse, G.F. (1992). NIST assessment of ITS-90 non-uniqueness for 25.5 Ω SPRTs at gallium, indium, and cadmium fixed points, in *Temperature: Its Measurement and Control in Science and Industry*, vol 6, Schooley, J.F., ed., pp. 175–178, New York: American Institute of Physics.
29. Mehl, J.B. (1986). Acoustic resonance frequencies of deformed spherical resonators: I. *J. Acoust. Soc. Am.* **71**: 1109–1113; Mehl, J.B. (1982). Acoustic resonance frequencies of deformed spherical resonators: II. *J. Acoust. Soc. Am.* **79**: 278–285.

This Page Intentionally Left Blank

INDEX

A

Ablation pulse, 79
Absorption
 for plane shear waves, 2
Acoustic virial coefficients, 380
Air
 saturation boundary, 263
 sound speed, 262–264
Al
 thermal generation of SAWs in, 78
Analytic signal, 316–318, 333
Angle dependence of propagation, 94
Anisotropic solids
 phonon image, 45
 Rayleigh waves in, 90
Antisymmetric mode, 52
Argon
 measurement derivations, 401
 saturation boundary, 254
 sound speed, 254, 256, 258
Atomic displacement parameter (ADP), 230
Attenuation coefficient
 phase velocity and, 33
Attenuation, 28
AuZn, 215

B

Barnett-Lothe theorem, 90
Benedict-Webb-Rubin equation, 254
Benzene, sound speed measurement, 323
Boltzmann Equation, 335, 364, 367–369,
 371–372
 rarified gas, 337, 371
Boron trichloride, thermodynamic properties,
 423
Brillouin scattering, 107
Broad-band SAWs
 pulsed laser excitation of, 71
Bulk modulus, 1, 22–25, 29

C

Capillary fracture waveform data, 51
Carnahan-Starling expression, 250
Chemical warfare agents, 326, 331
Chemical warfare agents, sound speed
 determination in, 323, 326
 frequency domain analysis, 309, 312
 introduction to, 333
 liquid density, 307, 314, 320, 326
 loss mechanisms, 314
 precursor chemicals, 308, 328

 results, 323, 325
 shear wave coupling, 310
 swept frequency data, 318
 time domain analysis, 323
 wall resonance modulation, 313, 323
 wave interactions, 328
Chemical Weapons Convention, 307
Christoffel-Pochhammer wave equation, 21,
 25
(CMR) (Colossal Magnetoresistance)
 material, 213
Compressional/dilatational strains, 3
Cr
 SAW velocity in, 150
Crystal structures, 1, 4, 6, 10
Cubic crystals
 phase velocity of LSAWs in, 168
Cubic matrix, 1
 elastic wave in, 1
Cylindrical acoustic resonators, 378
 calibration, 386
 conditions most useful, 384
 fill duct corrections, 391
 sound speed measurements, 384
 transport properties measurements, 391
 universal gas constant determination, 404

D

Debye temperature, 224
Determination of the elastic constants, 107
Diffusion
 gas mixture, 363, 339
Difluoromethoxy-1,1,1-trifluoroethane,
 2-thermodynamic properties, 408–409
Dispersion curves, 223–224, 227
Dispersion effects
 on nonlinear propagation, 125
 piezoelectric media, 107
 theory of, 100
DLC (diamondlike carbon)
 on Si, elastic constants for, 159
Dynamic Green's functions, 38

E

Elastic compliance, 5–6
Elastic constant matrices, reduced, 1, 10–12
Elastic constants, 1, 2, 4, 10–13, 16, 18–20,
 35
 gases, 335, 373

Elastic constants (*continued*)

- symmetry plane measurements for, 53

Elastic film

- film characterization, 109

Elastic isotropy, 21–22

Elastic waves

- in hexagonal crystals, 18
- in cubic crystals, 16
- in isotropic media, 21

Elasticity theory, 100, 107

Electroelasticity theory, 100

- Epoxy–graphite fiber composite, elastic properties of, 175

Equation of state

- critical point, 260
- cubic, 249, 251, 257
- fluid, 250, 256
- ideal, 337
- reference quality, 250–251, 256, 262, 265
- simple, 247
- thermodynamic, 240–241
- virial, 247, 252, 338, 378

F

- FeSi, 216, 218, 220

Fiber composites

- elastic properties of, 174

- Filled skutterudites, 231, 234

- Flexural mode, 53

Fluids

- argon, 262
- continuity equation, 239
- critical point and, 262
- Euler equation, 240
- equations of state, 245
- hard sphere, 258
- hard-sphere, 250
- hydrodynamic equations, 237, 244
- particle interactions, 243, 245
- phase topology, 246–247
- simple, 249, 252
- sound as thermodynamic property, 237, 253
- sound speed, 249–250, 254, 264
- thermodynamic, 241
- vapor-liquid equilibrium phase boundary, 246
- wave equation, 237–238, 243

Fourier transform

- chemical warfare agents, 316

G

GaAs

- diffraction image of, 46

- elastic constants, 47

- phase velocity of LSAWs in, 170

Gases

- 1,1,1,2,2,3,3,4-octafluorobutane, 416
- 1,1,1,2,3,3-hexafluoropropane, 414
- 1,1,1,2-tetrafluoroethane, 412
- 1,1,1,3,3,3-hexafluoropropane, 415
- 1,1,1-trifluoroethane, 413
- 1,1,2,2,3-pentafluoropropane, 416
- 1,1-difluoroethane, 414
- 1-chloro-1,2,2,2-tetrafluoroethane, 410
- 2,2-dichloro-1,1,1-trifluoroethane, 410
- acoustic measurements, 378
- acoustic propagation constant, 346
- acoustic thermometry, 399
- acoustic virial coefficients, 380
- acoustics measurements, 335
- boron trichloride, 423
- calibration, 386
- collisions, 344, 354
- convective energy transport, 366
- corrections for boundary losses and fill duct, 390
- determining, 378, 391
- diatomic, 346
- diffusion, 363
- distribution function, 365–367
- eigenvalues, 405
- elastic constants, 335, 373
- equation of continuity, 336
- equation of motion, 339
- equation of state, virial, 338, 387
- Greenspan acoustic viscometer, 391
- halfwidths measurements, 396
- halogen, 351
- hard-core Lennard-Jones potential, 381
- helium, 424
- hexafluoroethane, 419
- hydrogen bromide, 422
- ideal, 336
- impurities, effects of, 387
- inverse collisions, 367
- low pressure measurements, 364
- low-pressure gas, 374
- Maxwell distribution, 368
- measurement results, 364
- methane, 417
- model potential form, 383
- moderate pressure measurements, 348
- pentafluorodimethyl ether, 408
- pentafluoroethane, 407
- polyatomic, 346
- Prandtl number, 391

- real gas corrections, 338
- relaxation processes, 342, 351, 360
- resonance frequencies measurements, 384
- resonance methods, 384
- resonators for, 385
- rotation, 343
- rotational energy levels, 358
- sound speed, 338–339, 395
- spherical resonators, 401
- Stokes-Navier equation, 339
- sulfur hexafluoride, 420
- systems not in equilibrium, 372
- tables of thermodynamic properties, 407
- tetrafluorodimethyl ether, 408
- tetrafluoromethane, 418
- thermodynamic properties of dilute, 379
- thermodynamic temperature measurements, 402
- transducers, 388
- translational motion, 343
- transport processes contributions, 339
- tungsten hexafluoride, 421
- ultrasonic absorption/dispersion, 345
- universal gas constant, 377–378
- v-t transitions, 353
- vibration, 343, 346
- virial coefficients tables, 407
- viscosity, 377
- viscosity of, 384
- xenon, 423
- Gaussian envelope, 317
- GGG (Gd/Ga garnet), velocity of LSAWs in, 179
- Glycerine, sound speed, 323
- Green's functions
 - dynamic, 39
 - half-space, 40, 49
 - in infinite continuum, 39, 51
 - to determine dispersion, 160
- Greenspan acoustic viscometer, 377–378, 391–392, 394, 426–427
- Group velocity, 2, 31–32
- H**
 - Hard-core Lennard-Jones potential, 382
 - Hard-core square-well potential, 383
 - Hard-core square-well potentials, 381
 - Helium
 - thermodynamic properties, 424
 - Helmholtz free energy, 229, 238, 242–243, 246, 249, 251, 253–254, 264–265
 - fluid systems, 254
 - ideal gas, 245
 - monatomic ideal gas, 242
 - natural gas fluid deviations, 264
 - Hexagonal crystals
 - elastic constants of, 168
 - Hexagonal matrix, 1
 - elastic waves in, 1
 - Hilbert transform, 316–318
 - Hooke's law, generalized
 - elastic constants, 2, 4
 - Hydrogen
 - rotational energy level, 344
 - Hydrogen bromide thermodynamic properties, 422
- I**
 - Impedance analyzers, 320
 - Interdigital transducer (IDT), 87
 - Interdigital transducers (IDTs), 71
 - Interferometry
 - quadrature, 83
 - Interferometry
 - gas velocity measurement techniques, 348
 - Swept-Frequency Acoustic, 326, 332
 - to detect SAWs, 81
 - International Association for the Properties of Water and Steam (IAPWS), 260
 - Internationally accepted temperature scale (ITS-90), 377–378
 - Isopropanol, sound speed measurement, 323
 - Isotropic layered materials
 - SAW velocity in, 135, 145
 - Isotropic matrix, 14
 - Isotropic solids
 - elastic constants of, 160
- L**
 - Lamé constants, 10, 14, 22–24
 - Laser
 - to detect SAWs, 81
 - Lasers
 - mode locked, to generate narrow-band SAWs, 80
 - Lateral longitudinal waves (LLWs), 145
 - Leaky surface acoustic waves, 145
 - LFAM response, 157
 - Line-focus beam microscopy (LFB, LFAM)
 - advantages of, 136
 - Longitudinal waves, 23, 25, 27, 30, 32
 - Love waves, 70, 102
- M**
 - Mathcad program, 312, 331
 - Maxwell distribution, 368
 - Micrometry, ultrasonic, 140
 - Monoclinic matrix, 1

Monte Carlo methods, of generating phonon intensity patterns, 44
 Motion, equations of, 14–15, 27

N

Narrow-band SAWs
 generation of, 80
 National Institute of Standards and Technology (NIST)
 sound speed in gases measurements, 377
 universal gas constant value, 404
 Thermophysical Properties of Pure Fluids Database, 265
 Navier-Stokes, 240
 Navier-Stokes Equation, 364, 239
 Nb, 216–217
 Network analyzers, 320
 Newton's second law, 14
 Nitrogen gas, cylindrical acoustic resonance measurements
 relaxation, 360
 Nondispersive wave, 100
 Nonlinear SAWs
 experimental observations, 126
 isotropic glass, 127
 Nonplanar surfaces, determining elastic properties, 176

O

OAA (oxalic acid anodizing) film on Al,
 SAW properties in, 166
 Octafluorobutane, 1,1,1,2,2,3,3,4-,
 thermodynamic properties, 416
 Optoacoustic effect, 351
 Orthorhombic matrix, 1
 Oxygen, vibrational relaxation, 360

P

Pentafluoro-dimethyl, thermodynamic properties, 408
 Phase velocity, attenuation and, 2, 33
 Phonon focusing effect, 94–95
 Phonon imaging
 of crystal anisotropy, 43
 Phononic lattices, elastic properties of, 174
 Phonons, 235
 Planck-Einstein relation, 360
 Plane, 2
 Plane longitudinal waves, 29
 Plane shear waves, 27
 Plane wave interaction
 glass–quartz, 328
 glass–water, 328
 glass–quartz interface, 329
 input PSI field, 331
 water–glass, 328

Plate modes, 53
 Point focus acoustic microscopy, 180
 Point-source/point-receiver (PS/PR) methods
 advantages of, 37
 described, 38
 techniques for, 37–38
 Poisson's ratio, 1, 22–23
 Polycrystalline, 204, 216–217, 220
 Prandtl number, 391
 Probe-beam deflection
 to detect SAWs, 84
 Pseudo surface acoustic waves (pSAWs), 145
 Pu phase stability at higher temperatures, 225
 Pulse-echo technique
 transform, 316
 Pulse-echo technique
 gas measurements, 350
 time-of-flight, 316
 Pupil function, 142

Q

Quantitative acoustic microscopy
 frequency range of, 135
 history of, 135
 limitations of, 179
 of anisotropic solids, 136
 principal of, 135
 principles of, 137
 Quasi-crystals, isotropic nature of, 179

R

Raman–Nath diffraction, 86
 Rattling, 230
 Rayleigh waves, 65–66, 68, 70, 73, 78,
 90–91, 93, 101–107, 119–124, 126
 characteristic, 68
 leaky, 70, 172
 Rayleigh-Ritz method, 206, 208
 Reciprocity principle, 140–141
 Reduced tensor notation, 5
 Reflection acoustic microscopy, 181
 Reflection coefficient, 142–144, 146, 152,
 180–181
 Relaxation effects
 gases elastic properties, 350
 Resonant ultrasound spectroscopy (RUS),
 226, 231
 applications of, 210, 212
 electronics for, 189
 evaluation of, 211
 for samples, 194–195, 197, 202, 218
 measurements in, 210
 motivation for use of, 189
 transducers, 195
 transducers for, 195

S

Scanning transmission acoustic microscopy, 45–46

Scholte wave, 161

Scholte waves, 70, 122

Shear strains, 4

Si

epicentral wave for, 51

plate modes of, 53

Skutterudites, 221–222, 230–231

Sound

as a thermodynamic property of fluids, 237–238, 240, 242, 244, 246, 248, 250, 252, 254, 256, 258, 260, 262, 264, 266, 268, 270, 272, 274, 276, 278, 280, 282, 284, 286, 288, 290, 292, 294, 296, 298, 300, 302, 304, 306

Sound attenuation

chemical warfare agents, 308, 320

Sound propagation

low pressure gas, 365

multilayered medium, 310

Sound speed

fluid, 266

chemical warfare agents, 308

sound speed measurement, 310, 325

Space

low frequency sound waves, 364

Spectrophone, 351

Spectroscopy

resonant ultrasound, 189, 219

Spherical surface, determining elastic

properties of, 177

Stoneley waves, 122

Stress tensors, 5

Sulfur dioxide

relaxation, 355, 374

vibrational modes, 355

Sulfur Hexafluoride, thermodynamic

properties, 420

Superconducting transition in, 217

Superconductors, high T_c , 18

Superlattice, elastic properties of, 173

Surface acoustic waves (SAWs)

displacement field associated with, 65

velocity measurement of, 135

amplification of, 97

broad-band, 68, 89, 110

depth of penetration of, 66

depth penetration of, 66

described, 65

diffraction method, 87

diffraction methods of detecting, 85

frequencies of, 71

generated by, 70

generation of, 77

in thermoelastic regime, 72

mode-locked laser pulses generated, 80

piezoelectric excitation and detection of, 87

propagation of, 88

slowness curve, 95

surface velocity, 97

types of, 68

velocities of, 68

in anisotropic solids, 90

in dispersive media, 100

nonlinear, 119

Swept-Frequency Acoustic Interferometry (SFAI), 307–308

electronic system, 320

theory behind, 309

transducer, 308

T

Taylor's expansion, 3

Tetragonal matrix, 1

The time domain, 316

Thermodynamics

filled skutterudites, 232

Thermodynamics Research Center, 265

Ti on steel, SAW velocity in, 150

Time Domain Analysis, 316

signal-to-noise ratio, 319

Time-resolved microscopy, 135, 137

evaluation of, 147

theory of, 174

TiN

on MgO, SAW properties in, 165

Toluene, sound speed measurement, 323

Transducer

interdigital (IDT), 87

Swept-Frequency Acoustic Interferometry (SFAI), 309

Transducers

gas measurements, 388

Transient grating, 81, 107

experimental use of, 108

Transverse waves, 2, 18, 23, 25–27

Triclinic matrix, 1, 11

Trigonal matrix, 1

Tungsten hexafluoride, thermodynamic properties, 421

Two-point focus acoustic lenses technique theory of, 136

U

Ultrasonic micrometer, 136, 146

Ultrasound

point-source/point-receiver, 37, 52

V

Vapor-liquid equilibrium phase boundary,
246–247

Varshni model, 231

Vector contrast scanning ultrasonic
microscope, 136

Velocity measurements, 19

Vibrational modes, 222–223, 228, 230–231,
235

Vibrational modes, phonons, and, 221

Virial

equation of state, 248

Viscosity

gas, 383

Voigt

notation, 5

W

Water

saturation boundary, 260

attenuation of sound in, 150

Water, sound speed in, 262

measurements, 328

tables, 265

Wave arrivals, observation of, 48, 50–53,
54

Wave equations, Christoffel–Pochhammer,
24

Wave surface of, 48, 50

waveform studies of, 48

X

Xenon, thermodynamic properties, 423

Y

Young's modulus, 1, 22–23, 32